Design and analysis of a scanning beam interference lithography system for patterning gratings with nanometer-level distortions

by

Paul Thomas Konkola

Bachelor of Science in Mechanical Engineering
University of California at Berkeley, May 1995

Master of Science in Mechanical Engineering
Massachusetts Institute of Technology, February 1998

Submitted to the Department of Mechanical Engineering
in partial fulfillment of the requirements for the degree of

Doctor of Philosophy

at the

MASSACHUSETTS INSTITUTE OF TECHNOLOGY

June 2003

Author .....
Department of Mechanical Engineering
May 2, 2003

Certified by .....
Mark L. Schattenburg
Principal Research Scientist, Center for Space Research
Thesis Supervisor

Accepted by .....
Professor David L. Trumper
Department of Mechanical Engineering
Thesis Committee Chairman

Accepted by .....
Ain A. Sonin
Chairman, Department Committee on Graduate Students

Design and analysis of a scanning beam interference lithography system for patterning gratings with nanometer-level distortions

by

Paul Thomas Konkola

Submitted to the Department of Mechanical Engineering
on May 2, 2003, in partial fulfillment of the
requirements for the degree of
Doctor of Philosophy

Abstract

This thesis describes the design and analysis of a system for patterning large-area gratings with nanometer level phase distortions. The novel patterning method, termed scanning beam interference lithography (SBIL), uses the interference fringes between two coherent laser beams to define highly coherent gratings in photo resist. The substrate is step and scanned under the interference pattern to expose large gratings.

Our experimental system, the "Nanoruler", employs interference lithography optics, an X-Y air bearing stage, column referencing displacement interferometry, refractometry, a grating length-scale reference, a beam alignment system, and acousto-optic fringe locking. Supporting systems also include an environmental enclosure, a beam steering system, and vibration isolation with feedforward. The system can pattern 300 mm diameter substrates. The errors are categorized and analyzed.

The image-to-substrate motion during writing is comprised of "servo error", which is calculated from interferometric measurements, and unobservable error. The Nanoruler contains a built-in metrology capability where it can measure directly the image-to-substrate motions, which includes the unobservable error. In this special metrology mode, measurements can be performed at all substrate locations and on the fly — a capability possessed by no other patterning machine. This feature is used to assess the image-to-substrate motions. On-the-fly writing and metrology is further noted to be important because periodic errors in the interferometry can be eliminated.

I control the fringe placement with a novel system of stage control and acousto-optic fringe locking. The experimentally verified system performance allows control of the servo error to the limits of quantization and latency. The impacts of stage controller performance and vibration isolation feedforward performance on unobservable errors are modeled and verified. Extremely high resonant frequency metrology frames were designed that provided unusual insensitivity to disturbances. The vibration errors are estimated to be sub angstrom (0 to 100 Hz).

Based on my results and modeling, it is concluded that SBIL is capable of satis-

fying sub nanometer placement requirements. In my work I have demonstrated long term (1 hour) fringe placement stability of 1.4 nm, 3σ (0 to 1.4 Hz). Also, the short term placement stability is less than 4 nm, 3σ (0 to 5 kHz). When considering the integrated intensity of the scanned image traveling at 100 mm/s, the dose placement stability is 2.1 nm, 3σ. The wafer mapping repeatability was shown to be 2.9 nm, 3σ while measuring a 100 mm substrate. The repeatability is consistent with error models. The index of air uniformity and the thermal stability of assemblies currently limit the repeatability. An improved system of thermal control, enclosed beam paths, and lower coefficient of thermal expansion components is critical for achieving sub nanometer placement error.

Thesis Supervisor: Mark L. Schattenburg
Title: Principal Research Scientist, Center for Space Research

Acknowledgments

I thank my research advisor, Dr. Mark L. Schattenburg. Mark originated the SBIL concept, contributed many ideas, and was an eager source of advice. He always had great enthusiasm for gratings and metrology.

I thank the thesis committee members Professor David L. Trumper and Professor Alexander H. Slocum. I also thank Professor Henry I. Smith. Their suggestions, questions, and support greatly enhanced this thesis.

Carl Chen was the only other person to work full time on SBIL for most of the project's duration. We spent countless hours discussing the many aspects of the system. The credit for the interference lithography optics goes to him. I am grateful to have worked with him and to have him as a friend.

I thank the students and staff in the Space Nanotechnology Laboratory and the Nanostructures Laboratory. Bob Fleming greatly aided with the many facilities requirements of the system. Ralf Heilmann was responsible for the fringe locking optics. Ed Murphy's expert processing is most appreciated. The MIT Central Machine Shop staff was very helpful and performed great work. Many students and staff contributed to or supported the research in many ways. I thank Chi Chang, Pat Everett, Craig Forest, Andy Lapsa, Chulmin Joo, Mike McGuirck, Juan Montoya, G.S. Pati, Yanxia Sun, Shi Yue, David Carter, Jimmy Carter, Jim Daley, Juan Ferrera, Dario Gil, Todd Hastings, Mark Mondol, Euclid Moon, Tim Savas, and Mike Walsh.

I thank my friends and family. I especially thank my parents, John and Mirjam Konkola. I could not have completed this research without their support and encouragement.

DARPA and NASA sponsored this research.

Contents

List of Figures

List of Tables

Symbols

Note: Vectors and matrices appear in bold face type.

b	dashpot constant (Ns/m)
C	compressibility (1/Pa)
c_s	speed of sound (340 m/s in air)
d	$1/e^2$ intensity diameter for a Gaussian beam (m)
D	dose (J/m^2)
e	periodic error (m)
E	Young's modulus (Pa)
e_A	normalized dose amplitude error (NA)
f	frequency (1/s)
f_G	normalized Gaussian frequency (NA)
f_n	normalized frequency (NA)
g	gravitational acceleration (9.81 m/s^2)
G_r	ratio of Rowland ghosts of first order to their parent line (NA)
h	total substrate thickness (m)
j	$\sqrt{-1}$ (NA)
k	time index (NA)
l	linewidth (m)
L_c	length of cavity for the fundamental acoustic resonance (m)
n	interference scale factor (equals four for a double pass interferometer)
m	order of diffraction (NA)
m	mass (kg)
M	moving average transfer function (NA)
M_d	discrete time moving average transfer function (NA)
N_o	Avogadro's number (6.0221×10^{23})
p	phase meter counts per period
P	pressure (Pa)
$\mathcal{P}$	Power (W)
PM	phase meter signal (counts)
R	Refractometer cavity length (m)
R	Universal gas constant (8.314 J/mol/K)
s	Laplace transform variable (rad/sec)
t	time (s)
u	in-plane distortion (m)
w_o	$1/e^2$ intensity radius for a Gaussian beam (m)
x	data (NA)
w	out-of-plane distortion (m)
x_{die}	displacement interferometer error (m)
x_{fle}	fringe locking error (m)
x_{nl}	phase nonlinearity (m)

y_d	discrete time moving average data (NA)
y	data (NA)
z	Z transform variable (NA)
α	fringe angle with respect to the y-axis (rad)
γ	specific heat ratio (1.4 for air) (NA)
ϕ	phase (rad)
ϕ_m	metrology block interferometer phase (rad)
λ_{DMI}	vacuum wavelength of displacement measurement interferometer (m)
λ_{il}	vacuum wavelength of the interference lithography laser (m)
Λ	nominal period of the interference fringes in the substrate plane (m)
Λ_g	period of a diffraction grating(m)
Λ_o	nominal period of the interference fringes measured perpendicular to them (m)
ν	Poisson ratio (NA)
ω	frequency (rad/s)
θ_{Zsm}	differential yaw motion between the stage and the metrology block (rad)
τ	integration time (s)

Chapter 1

Introduction

We proposed interferometrically produced fiducials for metrology of sub-100 nm device generations [86]. In this method, distortions produced by processing, mastering, or replication are measured by comparing the distorted pattern to an accurate reference grating or grid. The gratings are interferometrically produced. The grids combine two orthogonal grating exposures.

The goal of my work was to advance interference lithography and fiducials as metrological tools. The manufacture of gratings with nanometer level linearity is the main challenge for this advancement. Since state-of-the art patterning tools lack the accuracy required to pattern the desired gratings, we developed scanning beam interference lithography (SBIL) to produce nanometer accuracy gratings and grids over large areas (≈300 mm diameter). While the system uses beam sizes on the order of 1 mm radius, large grating areas are exposed in photoresist by scanning the substrate. In this thesis, I discuss the design and analysis of this novel paradigm for patterning gratings.

In addition to semiconductor metrology, gratings and grids are important components in optics. The diffractive property of gratings is exploited in many applications including position measurement, beam splitters, alignment [100], and spectroscopy. Gratings are the building blocks for filters in optoelectronics [69]. Also, periodic patterns are required for devices such as magnetic storage, distributed feedback lasers, and field emitter displays [97]. Gratings are viewed as a fundamental component and

more accurate diffraction gratings than those available today will enable important advances in many applications.

The SBIL system can not only write gratings but it can read grating phase. The reading characterizes the system phase placement errors and the accuracy of the written gratings. The capability to read gratings makes SBIL a placement metrology tool in addition to patterning tool.

The long term goal for SBIL is to pattern gratings over 300 mm diameter areas with about a nanometer of accuracy. For my design purposes, only repeatability and not accuracy for linear gratings was considered. Accuracy is left for future work. Accuracy approaching the repeatability can be achieved after applying self calibration methods [23, 83, 104]. Moreover, repeatability is a necessary precondition for accuracy since the accuracy can never be better than the repeatability for a given set of measurements.

1.1 Patterning accuracy goals

The requirements for SBIL are driven by requirements for semiconductor metrology. Table 1.1 shows placement requirements as specified by the International Technology Roadmap for Semiconductors [52, 53]. The mask image placement requirement for year 2003 is 21 nm of error. The desired metrology precision is 1/10 the image placement. For year 2003, the metrology precision is 2.1 nm over the 132 mm square patterning area of a 152 mm square reticle. Additionally, the table includes the wafer overlay requirements. In year 2003, the wafer overlay requirement is 35 nanometers and the metrology precision, which is 1/10 the overlay, is 3.5 nm. The future requirements are tabulated up to year 2016. The SBIL gratings are intended to solve the long term metrology requirements for the semiconductor industry and thus nanometer level accuracies are useful. Subnanometer placement accuracy for research applications are also desirable.

Year of First Product Shipment	2002	2003	2004	2005	2006	2007	2010	2013	2016
Technology Generation (nm)	115	100	90	80	70	65	45	32	22
Mask size (assumes EUVL follows optical) (mm, square)	152	152	152	152	152	152	152	152	152
Mask image placement (assumes 4x magnification) (nm)	24	21	19	17	15	14	11	8	6
Mask image placement metrology precision (nm)	2.4	2.1	1.9	1.7	1.7	1.6	1.1	0.8	0.6
Wafer size (mm, ϕ)	300	300	300	300	300	300	300	450	450
Minimum (field area)$^{1/2}$ (mm)	28	24	24	24	24	24	24	24	24
Wafer overlay (nm)	40	35	32	28	25	23	18	13	9
Wafer overlay metrology precision (nm)	4.0	3.5	3.2	2.8	2.5	2.3	1.8	1.3	0.9

Table 1.1: Mask and wafer lithography and metrology requirements from the International Technology Roadmap for Semiconductors

1.2 Metrology by interferometrically produced fiducials

Grids can by applied to lithography metrology as shown in Figure 1-1. Here, the moire image formed between a reticle grid and a substrate grid is the phase map of the stepper distortion – if the grids are perfect. Image placement stability can also be assessed. Additionally, the magnification of the stepper is set when zeroing out the linear phase in the Moire pattern. This in-situ metrology is quicker, more accurate, and provides information over a wider range of spatial frequencies than the traditional placement accuracy methods.

The spatial phase locked electron beam lithography (SPLEBL) [94, 26] concept in Figure 1-2 is another application for grids. In this technique, a readable grid is fabricated on a substrate that is also patternable by an e-beam lithography system. The grid serves as a metrology reference for the electron beam, which in turn can

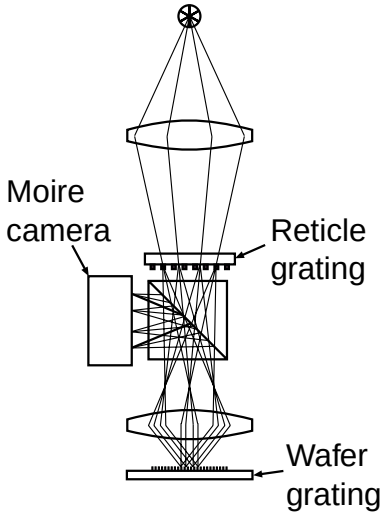

Figure 1-1: Application of grids to lithography metrology. If the reticle and substrate grids are perfect, the observed moire pattern is the phase map of the stepper distortion.

fabricate arbitrary patterns. Since the electron beam performs metrology at the exposure interface, the metrology information is extremely accurate. Therefore, the accuracy of the patterning can be limited by the accuracy of the grid on the substrate. The detector signal will typically be secondary electrons but they might be photons if the grid is scintillating.

Gratings can also be used for calibration of more generic electron beam lithography systems. The grating is read and used to correct inaccuracy of the ebeam system. Reference [3] uses a holographically produced grating for correction of a single scan field. However, there is no reason why this same technique couldn't be applied over the entire stage travel if a large grating could be produced with sufficient accuracy. The accurate gratings and grids would greatly simplify the calibration of ebeam and scanned laser writing tools.

SBIL is useful as a process metrology tool. Distortions due to etching, plating, and deposition can be assessed by measuring the processed grating with SBIL. Diffractive techniques have also been exploited for process monitoring and control [95].

Displacement measurement is another important application for fiducials. Figure 1-3 shows an individual linear encoder and an example of a grating based stage topology. The grating would be patterned onto a low CTE substrate such as Zerodur.

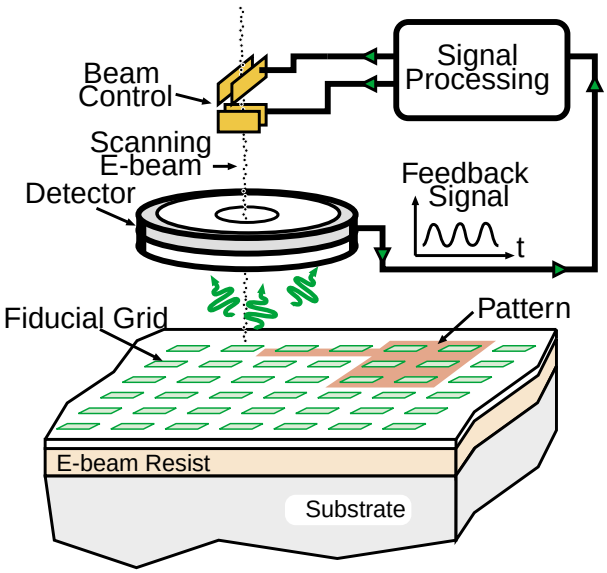

Figure 1-2: Application of grids to Spatial Phase Locked Electron Beam Lithography.

The read head can be designed to provide measurement of motion perpendicular to the grating and the height. There are many read head design possibilities, some of which are commercially implemented [40, 90]. The read head for a semiconductor stage would need to be designed to have very low heat dissipation for the required thermal stability. The stage schematic shows a scanner where the reticle and wafer stage reference linear encoders. Each stage has six degree of freedom measurement with three linear encoder plates. If the optical column is not sufficiently stable, additional stage-encoder-to-column-encoder metrology is also required. The beam paths for this additional metrology can be enclosed in vacuum. Heterodyne [103] and homodyne phase detections schemes are possible with grating based metrology. Other stage encoder designs might use grids. Reference [7] shows a stage topology where the grating is upside down on the stage. There, the laser enters from beneath the stage.

Grating-based distance measurement has several advantages over displacement measurement interferometry [7, 106]. The deadpath in an encoder-based system may be only a millimeter or two compared to at least 150 mm for a stage with enough travel to expose a 300 mm diameter substrate. The smaller deadpath provides insensitivity to air index variations and changes of the vacuum wavelength of the laser.

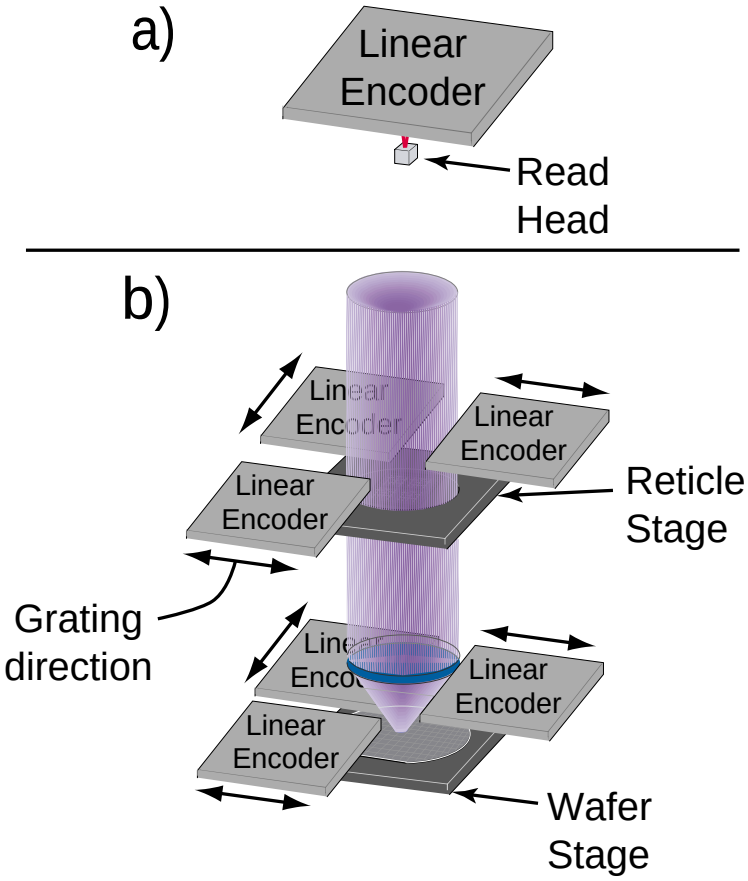

Figure 1-3: Application of gratings to a) a linear encoder and b) six-degree-of-freedom stage metrology.

Another advantage includes the unusually stable length scale provided by a grating written on a low thermal expansion substrate such as Zerodur. The encoders also allow lighter weight moving parts because the stage will no longer have interferometer mirrors. The lighter weight parts will have a higher resonant frequency and require less control effort. A higher resonant frequency implies less metrology frame deflections in the pressence of disturbances. Less control effort implies higher accelerations and lower heat dissipation. Looking at Figure 1-3, the large encoder plates might be argued to be disadvantageous since vibration induced motion between the large encoder plates will cause errors. After reading this thesis, one will understand that the vibration levels using a commercial vibration isolation system can be low enough that a 500 Hz resonant coupling of the encoders will be sufficient for angstrom level

vibration errors. One will also understand that the errors due to air index nonuniformity can be much larger. Currently the index nonuniformity error is in fact much larger than the vibration errors in the Nanoruler. Additionally, the decoupling of the optical column frame and the stage frame, which is typically done anyway for scanner applications, and even better vibration isolation would relax the requirement on the encoder coupling. The encoder-based stage topology is advantageous considering that the stage vibration sensitivity is the most important. Moreover, the stage has much larger vibration levels than the metrology and optical frames due to scanning related accelerations and disturbances; the absence of interferometer mirrors on the moving part enables a lighter, higher resonant frequency stage.

All the state-of-the-art high accuracy stages use linear interferometers. Because gratings with sufficient accuracy are not available, gratings cannot even be considered for these applications today.

1.3 Prior art

There are many methods for fabricating gratings. The predominant patterning technologies include electron beam lithography, scanned laser writing, interference lithography (also called holography), and mechanical ruling. No one has produced gratings with sufficient accuracy for semiconductor metrology. In this section I discuss the state-of-the-art in high performance grating fabrication, general patterning, and placement metrology.

Reference [107] contains an excellent collection of classic papers on ruled and holographic gratings. It also contains milestone papers on theory and application of gratings. A general book on gratings is written by Hutley [51]. Reference [80] provides a high level overview of gratings. Evans [22] reviews the history of diffraction gratings and provides a nice bibliography that covers ruling engines.

Mechanical ruling of gratings dates back to Fraunhofer in 1821 [70]. Advances in technology such as laser interferometers, control systems, and mechanical accuracy [74] were critical to the ruling engine development [35]. Although its history is inter-

esting, the ruling approach is slow and fundamentally limited by diamond wear. A large grating may require many kilometers of diamond travel. For instance, reference [12] comments that the greater than 280 km of diamond travel required to pattern a 40 cm $\times$ 40 cm grating with 1800 lines/mm far exceeds the acceptable limit of diamond wear. Ruling can take weeks or months and the diamond wear leads to varying groove profile, including line-space ratios. On the positive side, ruled gratings can have higher diffraction efficiency than holographic gratings produced with conventional processes because the groove profile can be defined by the shape of the diamond [68].

Spectroscopy seems to have been the driving force behind the ruling engine development. The spectroscopic resolution is limited by diffraction in addition to the quality of the grating. Harrison [35] cites Lord Rayleigh's papers, where he "showed that resolving power is not greatly reduced if rays that are to interfere constructively are not more than $\lambda/4$ out of phase." The variable λ is the wavelength of the light. From this, Lord Rayleigh deduced the gratings can have errors of $\Lambda/(4m)$ where Λ is grating period and m is the order of diffraction.

Random errors in the grating will result in scattering of the light and widening of the spectrum line. However, periodic errors cause erroneous daughter spikes in the spectrum. If the periodic errors occur over a large scale (change in period over many grooves), the so-called Rowland ghosts appear in the spectrum. Here pairs of lines appear – one line on each side of every strong line. From Harrison, the ratio of Rowland ghosts of first order to their parent line is

$$G_r = \left(\frac{\pi m e}{\Lambda}\right)^2 \tag{1.1}$$

The periodic error e defines the amplitude of the periodic error. Then the period control is

$$\frac{e}{\Lambda} = \sqrt{G_r}/\left(\pi m\right). \tag{1.2}$$

Equation 1.2 can be used to calculate the periodic error given the ratio of Rowland ghosts. Additionally, so-called Lyman ghosts are due to short scale (within two or

three grooves) periodic errors. The Lyman ghosts are widely separated from the parent line [51]. The Fourier transform principles of optics [33] provide a way to visualize the effect of periodic errors.

The manufacturers of ruled gratings tend not to specify grating nonlinearity in their catalogs. However, Loewen [70] shows the Littrow interferogram of a 6.3 μm period grating in the -18 diffraction order. The photograph indicates this 250mm wide grating has a nonlinear error on the order of $\lambda/4$ which corresponds to about 35 nm of grating nonlinearity. The ghosts were not detectable at the 10^{-5} level, which from Equation 1.2 implies large scale period control to better than 60 ppm. The reference reports producing gratings with resolution that are 80% of maximum.

Ruled gratings are typically very expensive and are usually used as grating masters. The replication [108] of these masters typically adds further distortion.

The highest resolution spectrometers are no longer grating-based. The Fabry-Perot interferometer can have much better spectral resolution than the grating spectrometer [38]. Even Harrison [36] conceded the demise of large gratings for spectroscopy – the resolution of a grating spectrometer is proportional to the width of the grating. Moreover, the spectroscopy applications no longer fuel the demand for more accurate and larger linear gratings. Gratings that are suitable for spectroscopy can have distortions that are more than an order of magnitude worse than those suitable for semiconductor placement metrology and still function near the diffraction limit.

Electron beam lithography is another method for the production of gratings and it is also suitable for general patterning. NTT developed an e-beam mask writer appropriate for proximity x-ray lithography [77]. Called EB-X3, it is a shaped-beam system that provides an image-placement reproducibility of <15 nm (3σ) over a 20 mm square area and is expected to soon achieve <10 nm ($3\ \sigma$) [93]. Among commercially available masks, image placement accuracies of 20 nm have been achieved by the Next Generation Lithography Mask Center of Competence, which is a collaboration between Photronics and IBM. Among commercially available tools, the MEBES 5500 from Etec Systems Incorporated has a 30 nm placement accuracy specification [21].

The most accurate commercially available encoder that I identified is available from Heidenhain. The CT 60 length gage has 50 nm of nonlinearity over a 60 mm measurement range [41]. I suspect the phase grating was written with a good mask writing tool and the specification accounts for distortions due to replication.

The highest performance placement metrology tools to date are based on a mark detection via a microscope and substrate positioning via an interferometrically controlled stage. The placement metrology tools measure cross locations calculated from CCD frames. The signal processing filters fast errors such as vibration. The Nikon Model XY-6i claims a 4 nm repeatability and 7 nm nominal accuracy over a 225 mm x 225 mm area [76]. This tool is no longer produced since Nikon left the pattern placement metrology business. Leica is the only company currently offering a placement metrology tool. The Leica LMS IPRO specifies a 5 nm repeatability and a 10 nanometer nominal accuracy over a 130 mm x 130 mm area [66]. In practice, these tools have degraded accuracy because of difficulties of mark detection, are extremely slow, and are only practical for evaluating long spatial period errors.

1.3.1 Interference lithography

Interference lithography (IL) is the process of recording interference fringes [81, 87]. Reference [27] provides a good description of interference lithography and its history. Figure 1-4 shows a basic IL system. In this system, the split beams are conditioned before interfering on the substrate. The variable attenuator is adjusted to equalize the power of the beams and thus maximize fringe contrast. The spatial filters, by blocking undesired angular components of the beams, attenuate wavefront distortions. The focal length of the lens in the spatial filter is chosen to set the divergence of the beams, thereby defining the size of the region of interference for a given pinhole-to-substrate distance. The beams have a Gaussian intensity distribution and the spot size on the substrate should be large enough to provide the required dose uniformity, which defines the critical dimension (CD) control. A reasonable pinhole criterion for the spatial filters is to set the pinhole diameter to about 1.6 times the Gaussian waist diameter [27]. For this parameter, about 99% of the nominal power is transmitted.

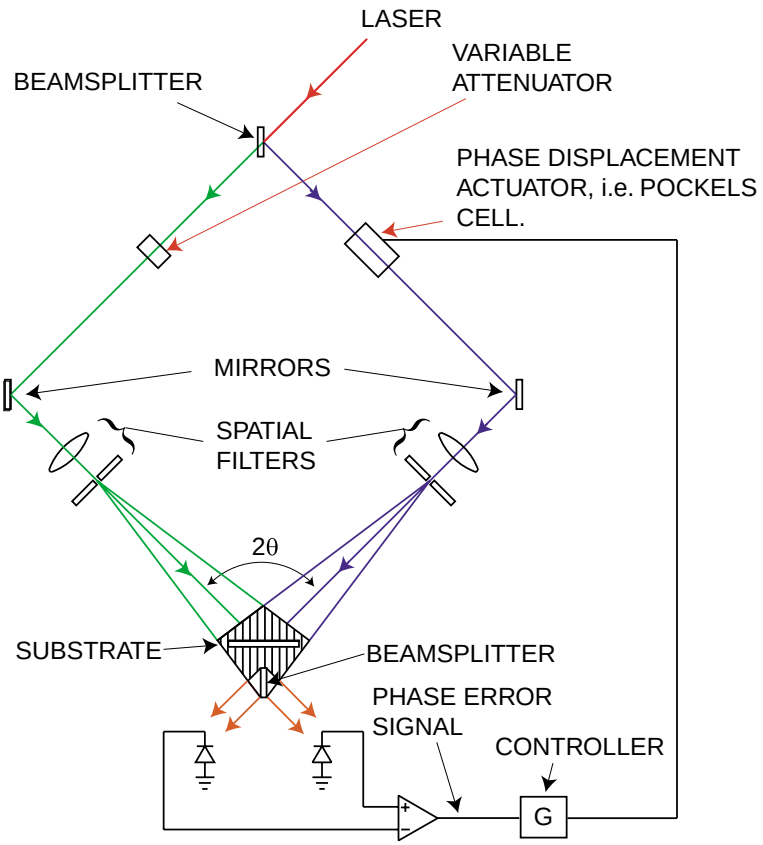

Figure 1-4: Interference lithography system

The distance from the spatial filter to the substrate defines the radius of the spherical wavefront. The shape of fringes produced by spherical waves has been studied in detail [27, 46, 25, 16] and they contain an inherent hyperbolic distortion. The distortion limits the pattern size that can be considered linear. The plot of the nonlinearity for a 200 nm nominal period interference image is shown in Figure 1-5. The nonlinearity was calculated using the relations derived by Ferrera [25]. The nonlinearity is reduced for large beam radii, which is the distance from the beam waist in the spatial filter to the substrate plane as indicated in the figure. Even for 1 m beam radii, the nonlinearity is more than 500 nanometers over only a 2 cm $\times$ 2 cm area. While it is desirable for the radii to be as large as possible (typically $>$ 1 m) for reduced hyperbolic distortions, instability due to air index variations, vibration, and thermal drift limits the maximum practical propagation distance. Lenses may be used to collimate the beam after the spatial filter and thus eliminate the hyperbolic distor-

tion. However, it is questionable whether it is practical to fabricate optics capable of producing large gratings with sub-nanometer fidelity. A beam splitter located near the plane of the substrate provides the interference signal for measuring fringe drift, which is mainly due to air index variations, vibration, and thermal drift of the optical setup. The differential signal from two photodiodes is the error signal that drives the controller for a phase displacement actuator. The phase displacement actuator is typically a mirror mounted to a piezo or a pockels cell - piezo mirror system. The period of the fringes is adjustable by changing the angle of interference θ according to Equation 1.10. IL is therefore maskless and can pattern arbitrary periods down to half the wavelength of the interference light. For some spectroscopy applications, the interference lithography and substrate profile have been configured for abberation compensation [45, 61].

An example of a grating produced by interference lithography is shown in Figure 1-6. The figure shows a grating after IL exposure and wet development but before the Ta_2O_5 etch mask interlayer and anti-reflection coating (ARC) is reactive ion etched. Details of the fabrication process can be found in Reference [85].

Interference lithography has many inherent advantages. First of all, the interference pattern produces highly coherent gratings. IL gratings are smoother than ruled gratings in that they are free of ghosts [87]. Secondly, the depth of focus is very large. Additionally, the topology of a spatial filter followed by no subsequent optics provides extremely low wavefront distortions. Other advantages include: built in metrology of the interfered pattern, a diffraction resolution that is $\approx$2x that of traditional on-axis optical projection lithography, and excellent image contrast even at high numerical apertures. SBIL builds upon these inherently good system properties.

Although many companies pattern gratings with interference lithography, none specify their products' accuracy directly. At best, residual chirp is specified and the lowest value that I found is 0.005 nm/period/cm available from Lasiris [101]. Assuming a 1 μm period grating and a linear chirp, the deviation from a linear grating will be 121 nm over their 44 mm grating aperture. In the Space Nanotechnology Lab at MIT, Juan Ferrera demonstrated 50 nm repeatability for 400 nm period gratings

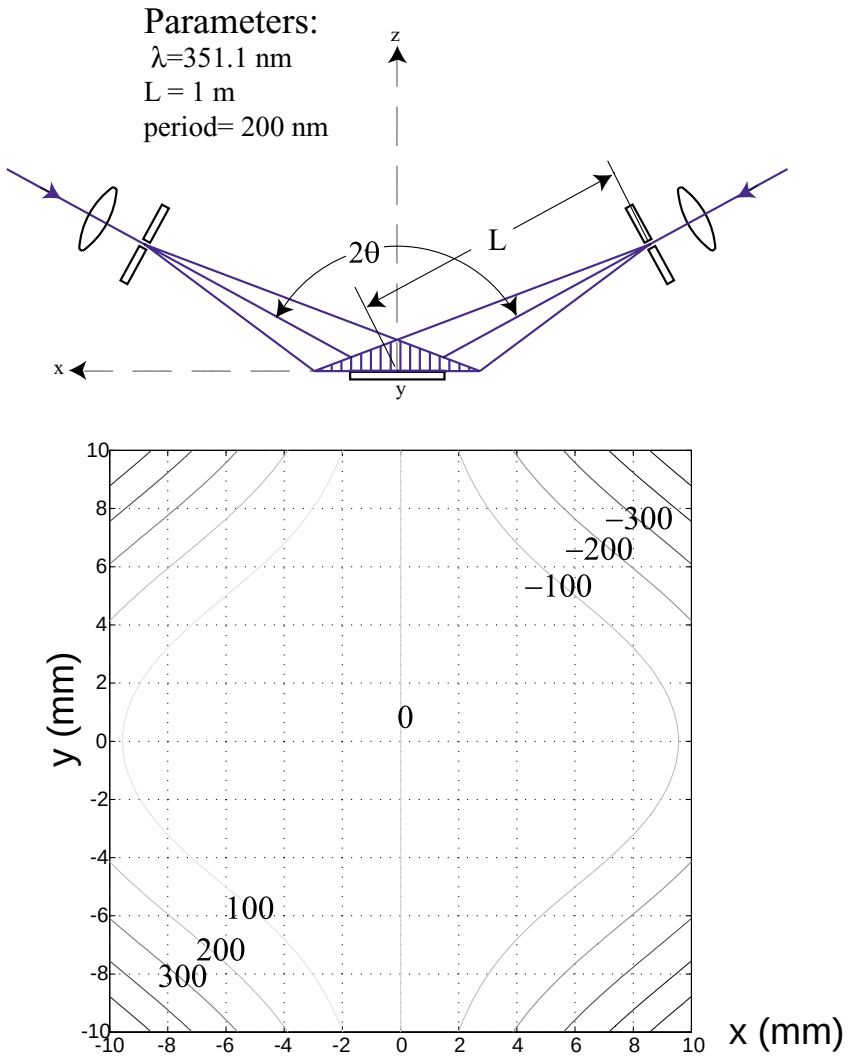

Figure 1-5: The lower plot is the nonlinearity in nanometers for an interference lithography image with spherical beam radii of 1 m and a nominal period of 200 nm. The upper schematic contains the parameters used in the calculation.

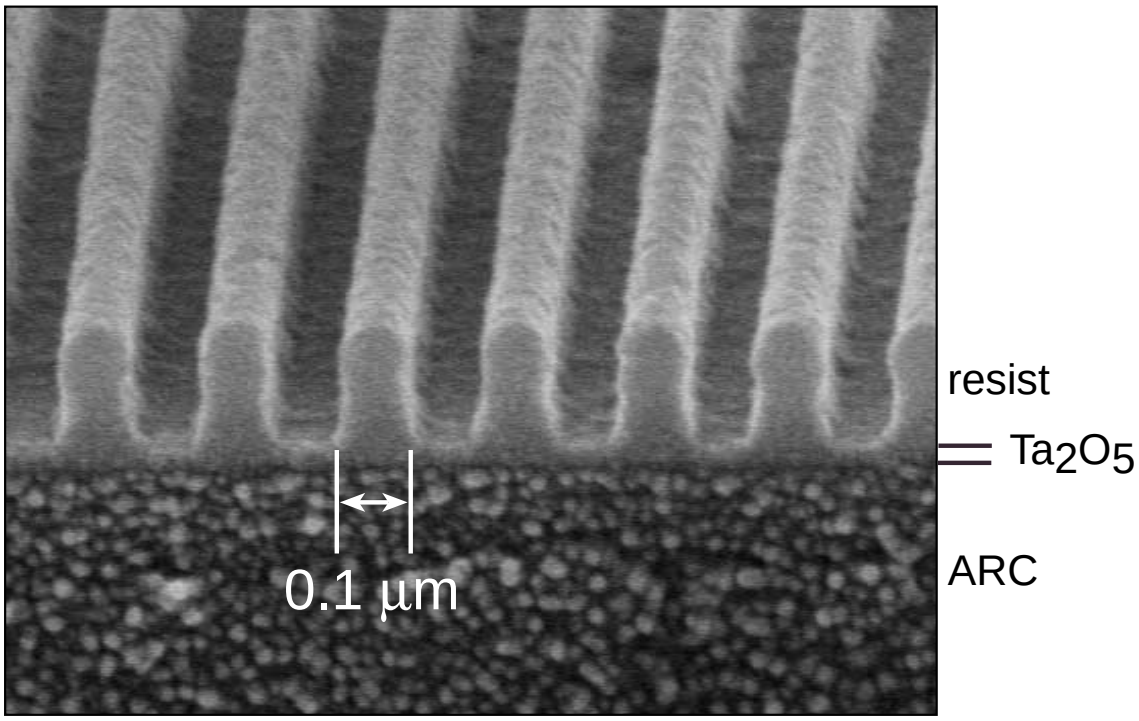

Figure 1-6: Grating produced by interference lithography in the Space Nanotechnology Laboratory

over 3 cm x 3 cm [27]. Thus, to my knowledge, holographically produced gratings have never been manufactured to sufficient repeatability for semiconductor metrology. Even if holographically produced gratings could be produced with sufficient repeatability, the large hyperbolic distortions would require correction with a look up table. Linear gratings are clearly preferable for metrology since they won't require these corrections that are sensitive to errors in the location of the hyperbolic origin [27].

1.4 SBIL concept

Figure 1-7 depicts the SBIL system concept. The optics closely resemble those of the basic IL system but the image is much smaller than the total desired patterning area. The grating image diameter is typically 200 μm - 2 mm ($1/e^2$ intensity diameter). Large gratings are fabricated by scanning the substrate at a constant velocity under the image. Beam pick-offs direct a fraction of each arm's power to the fringe locking system. The stage error and the lithography interferometer's phase error signals are

fed to the fringe locking controller.

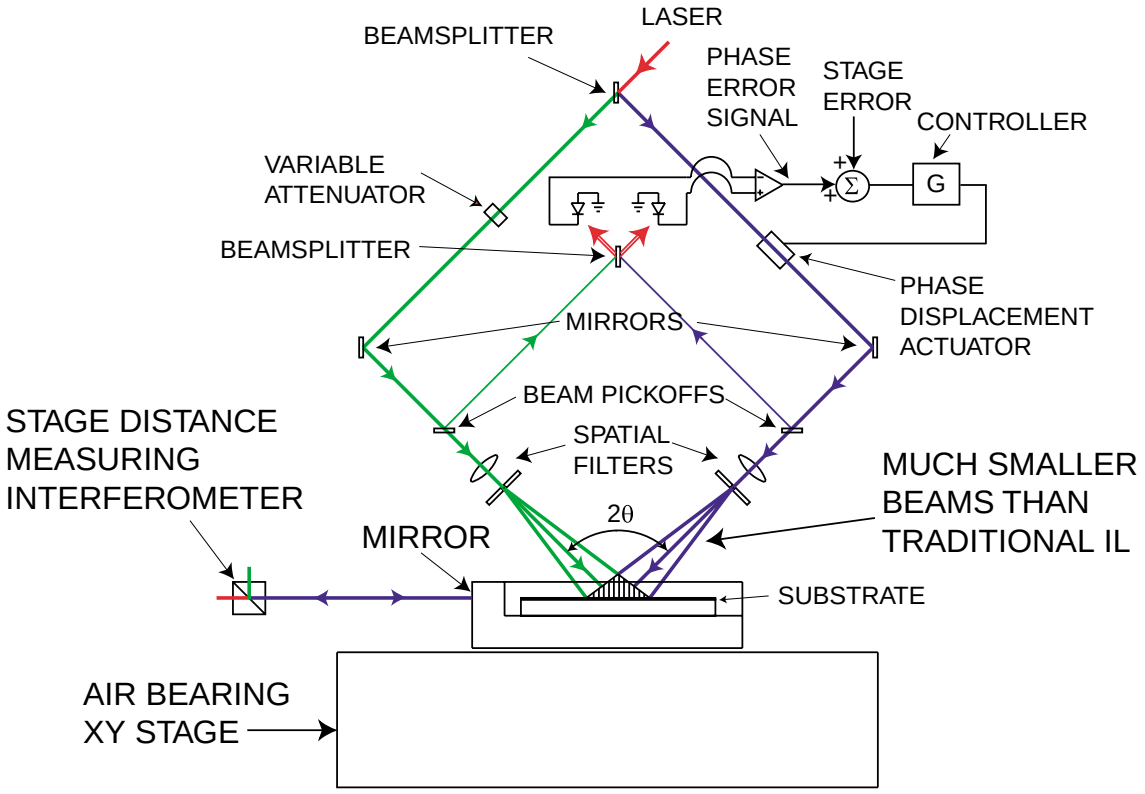

Figure 1-7: SBIL system concept

SBIL depends on accurate stage and fringe locking interferometry. Interferometers systems, if carefully designed and implemented, have sufficient stability for sub angstrom stability. Reference [31] demonstrated 15 pm stability over 6 minutes for an interferometer in vacuum. The long term stability of 150 pm over 10 hours was also demonstrated in that reference but the thermal stability of the components for the 5 mK temperature variation in that experiment probably accounts for the larger drift.

Figure 1-8 depicts how overlapping the scans achieve a uniform dose. The top left figure shows the image scanning in the y axis. Then the stage will be stepped over in x by an integer number of periods and scanned again. The grating image has a Gaussian intensity envelope as shown in the top left figure. Overlapping scans produce a uniform exposure dose as depicted in the lower figure.

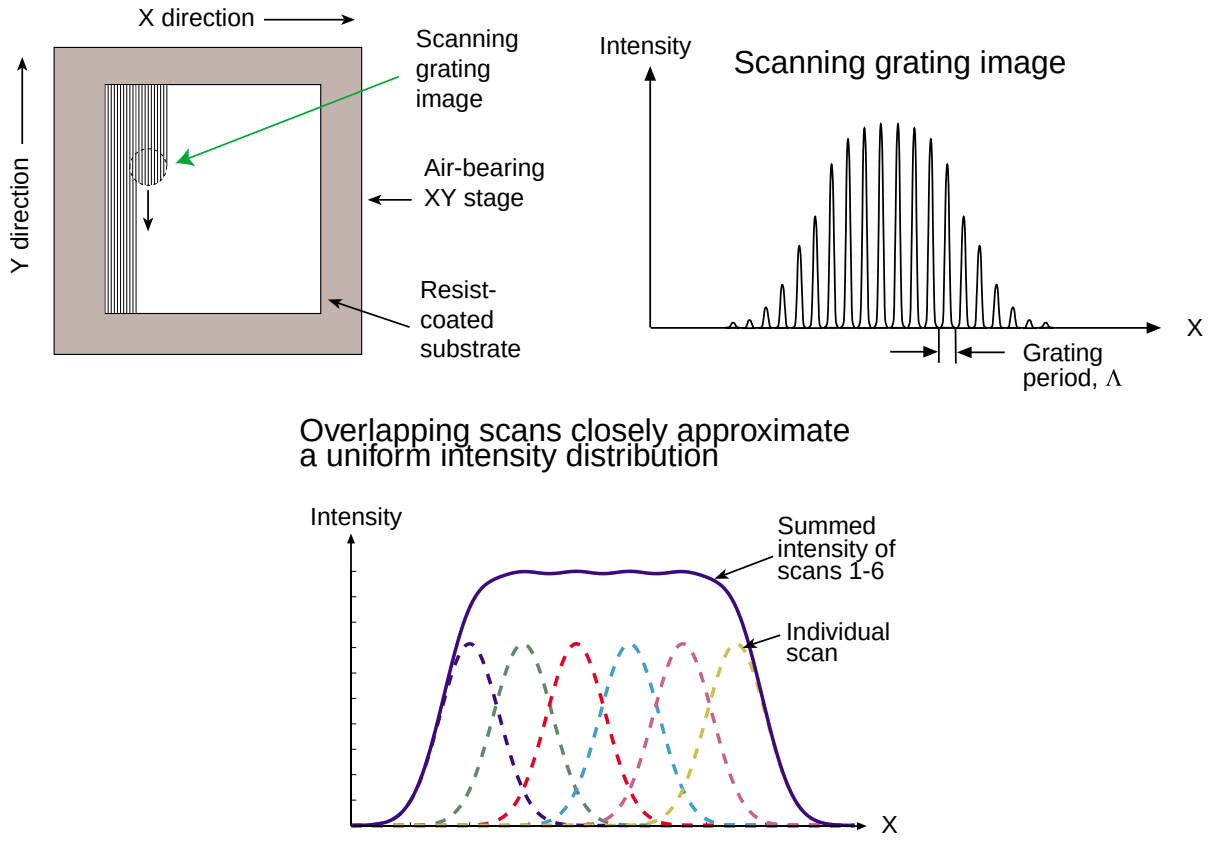

Figure 1-8: Image scanning method. The top left figure shows the image scanning in the y axis. The grating image has a Gaussian intensity envelope as shown in the top right figure. Overlapping scans achieve a uniform exposure dose as depicted in the lower figure.

1.5 The grating image

The introduction to SBIL would not be complete without a discussion on the grating image. In this section, I derive the image intensity for the interference of plane waves using fundamentals of optics [39], [115], [38]. Also, I consider the dose for a scanned image and the relationship between CD and dose uniformity.

Figure 1-9 shows the interference of plane waves with fields $\mathbf{E}_1$ and $\mathbf{E}_2$ given by

$$\mathbf{E}_1 = A_1 e^{j(\omega t + k\sin\theta\, x + k\cos\theta\, z - kL_1 + \phi_0/2)}\,\hat{\mathbf{y}} \tag{1.3}$$

and

$$\mathbf{E}_2 = A_2 e^{j(\omega t - k\sin\theta\, x + k\cos\theta\, z - kL_2 - \phi_0/2)}\,\hat{\mathbf{y}}. \tag{1.4}$$

The amplitudes of the electric field are A_1 and A_2. The lengths L_1 and L_2 are path length terms. The phase term ϕ_0 is a phase offset constant. The z axis bisects the interfering plane waves where the interference half angle is θ. The wave number, k, is

$$k = \frac{2\pi}{\lambda} \tag{1.5}$$

where λ is the wavelength of interfering light.

The waves interfere in the region where the plane waves overlap and the total field there is given by

$$\mathbf{E} = \mathbf{E}_1 + \mathbf{E}_2 \tag{1.6}$$

The time average intensity is given by

$$I = \frac{1}{2}\sqrt{\frac{\epsilon}{\mu}} Re\left[EE^*\right] = \frac{1}{2}\sqrt{\frac{\epsilon}{\mu}}\left[E_1E_1^* + E_2E_2^* + Re[2E_1{E_2}^*]\right]. \tag{1.7}$$

Applying Equations 1.3 through 1.7, the time average intensity is expressed as

$$I = \frac{1}{2}\sqrt{\frac{\epsilon}{\mu}}\left[A_1^2 + A_2^2 + 2A_1A_2\cos\left(2k\sin\theta x + k[L_2 - L_1] + \phi_0\right)\right]. \tag{1.8}$$

The phase of the fringes is a function of the position x and is defined as

$$\phi(x) = 2k\sin\theta x + k[L_2 - L_1] + \phi_0 = 2\pi\left(\frac{x}{\Lambda_0} + \frac{L_2 - L_1}{\lambda}\right) + \phi_0. \tag{1.9}$$

The nominal period, Λ_0, of the interference fringes is controlled by the angle θ, assuming the laser wavelength is constant, and is given by

$$\Lambda_0 = \frac{\lambda}{2\sin\theta}. \tag{1.10}$$

Also of note is the phase of the fringes can be shifted by 2π if the path length term, $L_2 - L_1$, changes by λ.

While for SBIL the wavefronts are designed to be very planar, the amplitude will have a Gaussian field distribution. Moreover, the field amplitudes A_1 and A_2 will

vary in x and y. If the beams are well aligned and balanced in power, A_1 for practical purposes will be equal to A_2. The amplitude of the electric field can be derived from the electric field profile of a Gaussian beam where

$$A = A_0 \exp\left(-\left(\frac{r}{w}\right)^2\right). \tag{1.11}$$

Here A_0 is a constant proportional to the field magnitude. The variable w is the radius of the Gaussian beam. The term r is the distance from the optical axis.

In the plane of the substrate the beams have some ellipticity due to the angle of incidence and possibly due to diffraction from a grating beam splitter. For simplicity, I will assume

$$r^2 = x^2 + y^2 \tag{1.12}$$

where the substrate is in the $x - y$ plane.

It is useful to express the intensity as a function of beam power since the power can be readily measured. The intensity of each beam can be written as

$$I_b(x, y) = \frac{2P}{\pi w^2} \exp\left(-2\frac{x^2 + y^2}{w^2}\right) \tag{1.13}$$

where P is the total power in the beam given by the integral of the intensity

$$P = \int_{-\infty}^{\infty} \int_{-\infty}^{\infty} I_b \, dx \, dy. \tag{1.14}$$

The integration of Equation 1.13 can be evaluated with the following identity obtained from Mathematica[1]

$$\int_{-\infty}^{\infty} e^{-\frac{x^2}{q}} \, dx = \sqrt{\pi q}. \tag{1.15}$$

The intensity in the write plane from Equation 1.8 expressed as a function of the

[1]Mathematica Version Number: 4.0.0.0, Wolfram Research, Inc., 100 Trade Center Drive Champaign, IL 61820, USA

power, assuming both beams have equal beam size, is

$$I(x,y) = \frac{2}{\pi w^2}\exp\left(-2\frac{x^2+y^2}{w^2}\right)\left[P_1 + P_2 + 2\sqrt{P_1 P_2}\cos\left(2\pi\left(\frac{x}{\Lambda_0} + \frac{L_2 - L_1}{\lambda}\right) + \phi_0\right)\right]. \tag{1.16}$$

It is desirable for both beams to be matched in power to provide the maximum contrast image. However, there will always be some mismatch, which causes a background dose. For SBIL, where the image is scanned, the dose from one stage scan is obtained by setting $y = vt$ and integrating Equation 1.16 with respect to time such as

$$D_{scan}(x) = \int_{-\infty}^{\infty} \frac{2}{\pi w^2}\exp\left(-2\frac{x^2+(vt)^2}{w^2}\right)\left[P_1+P_2+2\sqrt{P_1 P_2}\cos\left(2\pi\left(\frac{x}{\Lambda_0} + \frac{L_2 - L_1}{\lambda}\right) + \phi_0\right)\right]dt. \tag{1.17}$$

This equation evaluates to

$$D_{scan}(x) = \sqrt{\frac{2}{\pi}}\frac{1}{wv}\exp\left(-2\frac{x^2}{w^2}\right)\left[P_1 + P_2 + 2\sqrt{P_1 P_2}\cos\left(2\pi\left(\frac{x}{\Lambda_0} + \frac{L_2 - L_1}{\lambda}\right) + \phi_0\right)\right]. \tag{1.18}$$

The total dose is the sum of the dose from all scans. The step size between scans must be small enough such that the good dose uniformity is achieved. For instance, a step size equal to $0.9w$ produces a dose uniformity better than 1%. The linewidth uniformity is a function of the dose uniformity. In a simple model, the resist is highly nonlinear where it develops if the dose is above a clipping dose but doesn't develop if the dose is below the clipping dose. The linewidth, l, is calculated from the clipping dose, D_c, as

$$D_c = B_D + A_D\cos\left(\frac{\pi l}{\Lambda_0}\right) \tag{1.19}$$

where B_D is the exposure background dose, and A_D is the exposure dose amplitude. The effect of the dose nonuniformity caused by the finite step size used in SBIL changes B_D and A_D proportionally. In this case, let

$$D_c = B_D\left((1 + a\cos\left(\frac{\pi l}{\Lambda_0}\right)\right) \tag{1.20}$$

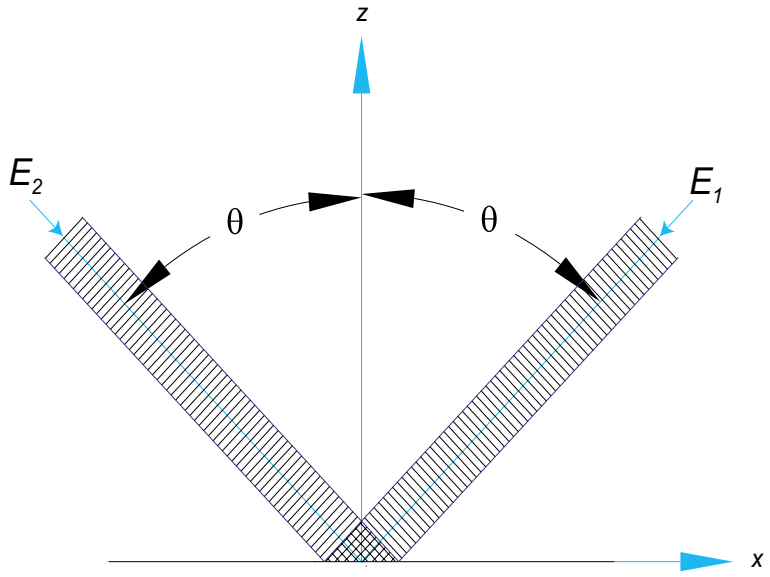

Figure 1-9: Interference of plane waves.

where a is a fixed contrast value ideally equal to one. When $B_D = D_c$ then l is equal to $\Lambda_0/2$ regardless of the value of a. Also, for small changes in dose the change in linewidth with respect to changes in B_D is calculated from Equation 1.20 as

$$\frac{\Delta l}{l} = \frac{2}{\Lambda}\frac{dl}{dB_D}\Delta B_D \approx \frac{2}{\pi a}\frac{\Delta B_D}{B_D} \tag{1.21}$$

Thus for a high contrast exposure where $a \approx 1$, the change in linewidth $\Delta l/l \approx 0.6\Delta B_D/B_D$. Or in other words, for the linewidth to change by 1% the background dose needs to change by 1.6%. The background dose varies due to changes in beam power in addition to the scan overlap. For a high contrast image, the background dose needs to be held within a few percent if the desired linewidth variations are to be a few percent.

Patterning of gratings using a scanned interference image has advantages that are discussed in the next section.

1.6 System advantages

In addition to the leveraged benefits of interference lithography, SBIL is advantageous for the following reasons

- SBIL is relatively insensitive to vibration because phase errors are averaged over the time of the exposure. On the other hand, focused beam tools such as ebeam lithography are very sensitive to vibration, where only a limited amount averaging is practical with multiple-pass printing [116]. The relatively long exposure time in SBIL naturally attenuates vibrations with a very fast cut off filter. The overlap of scans further averages placement errors.
- Distortion in the interference image is averaged by scanning and overlapping.
- Optics sensitive to vibration are mounted on a small, high resonant frequency metrology frame.
- The interference image can be shifted at high bandwidth, relaxing the requirement on stage control.
- SBIL is much faster than ebeam lithography, which must address each pixel. Also, ebeam lithography must trade off beam current, which is proportional to throughput, and resolution.
- In reading mode, the unobservable errors can be measured and studied across the full substrate area and at full stage scan speeds. No other tool has this capability. The measurements are invaluable for understanding error sources, which leads to improvements.
- Scanning the measurement axes in reading and writing mode can eliminate interferometer periodic errors.
- The image size is much smaller than the desired patterning area. Since the optical figure of components is always better for smaller areas, the figure requirements for SBIL are more easily attained. The alignment requirements are also reduced for the small beams.

- Unprecedented dose control can be achieved because many overlapping scans construct the exposed dose. Traditional interference lithography must expand the beam to be very large to achieve good dose control over very small areas.

- Fringe position is only critical in one degree of freedom – perpendicular to the grating. The system has slow velocities in the direction perpendicular to the grating lines. Disturbances tend to be less in the perpendicular scan direction.

- Slow velocities perpendicular to the grating essentially eliminate data age errors.

These many advantages contribute to SBIL's success as a ultra-high accuracy patterning and metrology tool.

1.7 Contributions and thesis structure

I designed, analyzed, and demonstrated the first patterning machine based on a scanning substrate and an interference image. The many error budget terms affecting nanometer scale patterning accuracy are categorized and analyzed. The models are shown to be consistent with the system performance. The system can pattern and measure large-area gratings with nanometer-level repeatability.

In Chapter 2, the novel system's topology is introduced. The design includes interference lithography optics, an X-Y air bearing stage, column referencing displacement interferometry, refractometry, a grating length-scale reference, a beam alignment system, and acousto-optic fringe locking. Supporting systems also include an environmental enclosure, a beam steering system, and vibration isolation with feedforward.

Then I categorize the SBIL error sources in Chapter 3. The SBIL interferometers and metrology definitions are described. The errors in lithography are recognized to be a function of the integrated intensity. The dose placement transfer functions are derived for continuous and discrete phase placement data.

In Chapter 4, I describe the rigid body error motions. The motion of the metrology optics, the stage, lithography beams, and heterodyne beams are analyzed. The most significant unobservable errors are shown to be Abbe errors.

In Chapter 5, I first analyze the environmental errors. Then I discuss an environmental enclosure with novel air paths. After that, I consider fundamental limits on index stability and temperature control. Based on temperature data, temperature-related air index variations and thermal expansion errors are consistent with errors observed in the SBIL system. Measurements of temperature, pressure, and humidity are presented.

In Chapter 6, I study the beam steering requirements for interference lithography. Plane and spherical wave interference are considered. The analysis leads to the +1/-1 order diffraction grating as the ideal beamsplitter for interference lithography because it can provide insensitivity to the spatial and temporal coherence of the laser. I also discuss the design and performance of a beam steering system implemented on the Nanoruler.

I controlled placement of fringe phase with a novel system of stage control and acousto-optic fringe locking. A new hardware and software architecture was required for the real-time control. The electronic and software architecture is the topic of Chapter 7. In Chapter 8, I explain the experimentally verified system dynamic performance that allows control of the fringe phase to the limits of quantization and sampling rate. The fringe-to-substrate dynamics are a function of stage and column motions. The impact of stage controller performance and vibration isolation feedforward performance are evaluated. Extremely high resonant frequency metrology frames were designed that provided unusual insensitivity to disturbances. The vibration errors are demonstrated to be sub angstrom (0 to 100 Hz).

The image-to-substrate motion during writing is comprised of "servo error", which is calculated from interferometric measurements, and unobservable error. The SBIL system contains a built-in metrology capability where it can measure directly the image-to-substrate motions, which includes the unobservable error. In this special metrology mode, measurements can be performed at all substrate locations and on the fly – a capability possessed by no other patterning machine. This feature is used to assess the system errors. On the fly metrology is further noted to be important because interferometric nonlinearity is removed. Chapter 9 analyzes the system

performance. The experimental results and models enhance the understanding of ultra-precision patterning.

Based on my work, it is concluded that the SBIL system should be capable of easily satisfying the nanometer level placement requirements. In my work I have demonstrated long term (1 hour) fringe placement stability of ± 1.4 nm, 3σ (0 to 1.4 Hz). Also, the short term placement stability is < 3 nm. The wafer mapping repeatability was shown to be 2.9 nm, 3σ while measuring a 100 mm substrate. The repeatability is consistent with error models. The remaining errors of significance are analyzed and improvements are suggested. I don't see any limiting error that will prevent achieving subnanometer writing and reading accuracy. My research is a major contribution toward nanometer accurate gratings.

The SBIL system is complicated in that there are many sources of error. The performance depends on many sub systems that are designed to suppress these errors. In writing this thesis, I tried to organize the sections in a sensible way. However, the topics are very interrelated and the reader will probably need to reread some sections after concepts are introduced in later sections. In fact, I recommend reading this thesis at least twice. Also, I recommend obtaining a color copy. A color .pdf file of the thesis should be available from the Space Nanotechnology Laboratory web site[2] or from MIT Document Services.

[2]http://snl.mit.edu/

Chapter 2

SBIL prototype: The Nanoruler

In designing the Nanoruler, I took the error sources and disturbances into account. The general design strategies for achieving our performance goals included:

- implementing passive designs that are insensitive to critical parameter variations
- minimizing disturbance sensitivity with feedback control
- reducing critical parameter variations.

For nanometer level placement, all three strategies are necessary. In fact, all three must be done very well. In this chapter, I review the Nanoruler design. The discussion here is an overview. Many aspects of the system are discussed deeper in other chapters.

Figure 2-1 shows the front of the system. The optical bench for the interference lithography optics is visible along with the X-Y air bearing stage. The interference lithography optics will be discussed in the next section. The chuck and the metrology block are critical metrology frames that are reviewed in Section 2.2.

The stage positioning requirement for SBIL can be relaxed because the stage error is corrected by a high bandwidth fringe locking system. The X-Y air bearing stage is the Microglide MG T300L motion system from Anorad[1]. The travel of this commercially available stage is 310 mm in X and 470 mm in Y. Both the flatness

[1]Anorad Corporation, Hauppauge, NY. http://www.anorad.com

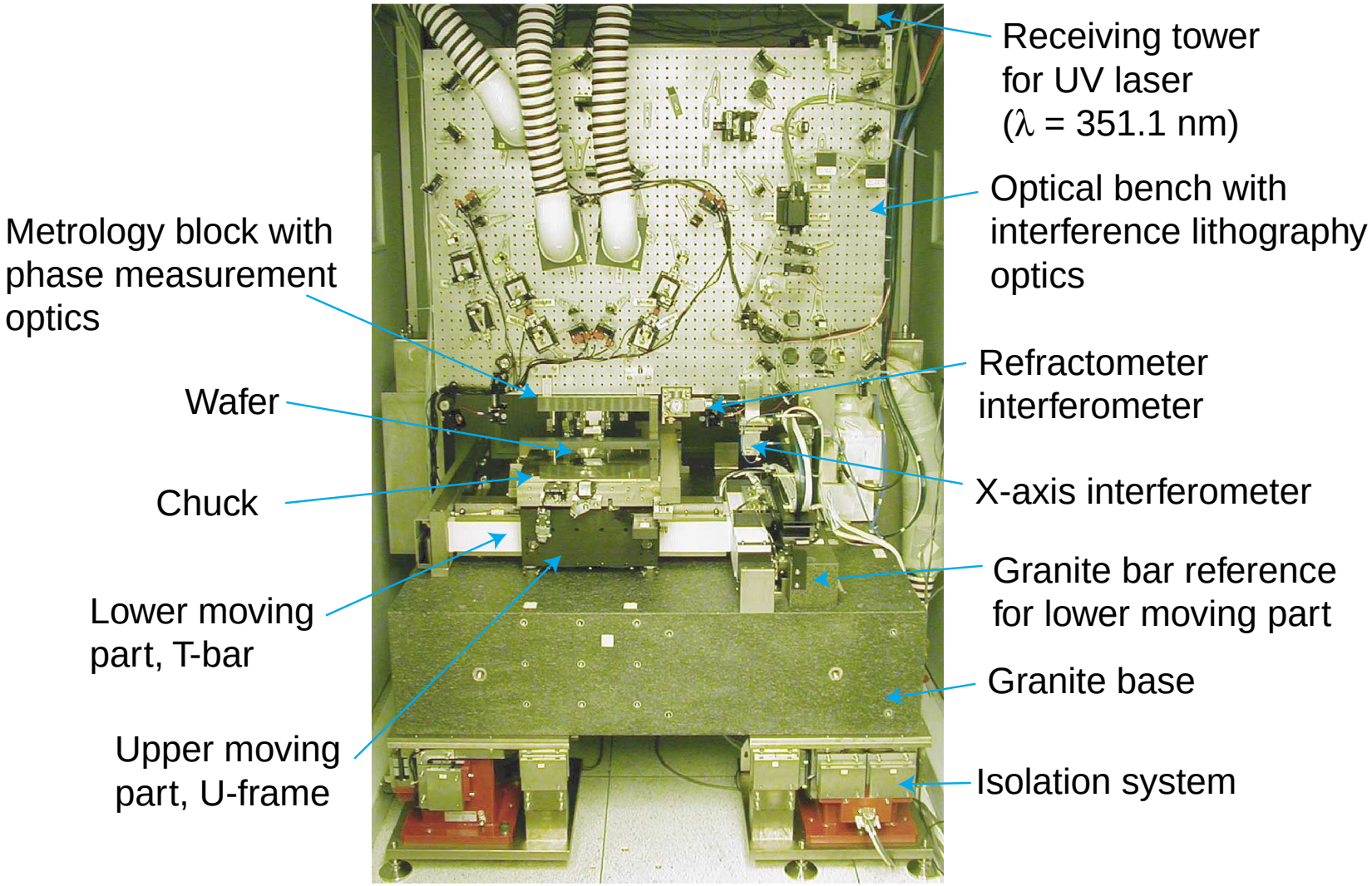

Figure 2-1: Front of system.

and straightness of the stage are specified as ± 0.1 μm per 10 mm and ± 1.5 μm per 310 mm. Specified pitch and yaw motions for the X and Y axis independently are ± 0.5 arc sec. Both the X and Y axis vertical air bearing pads[2] reference the granite surface. The lower moving part is an aluminum oxide T-bar constrained in X and yaw by air bearing pads referenced against a granite bar. The upper moving part is an aluminum U-shaped frame constrained in Y and yaw by air bearing pads referenced against a precision surface on the aluminum oxide T-bar. The air bearings are preloaded magnetically by use of magnets and iron rails. Anorad linear amplifiers housed in an Anorad 5U amplifier chassis drive the motors for the stage. The chassis also packages limit switch and air pressure fault electronics. The linear amplifiers (Anorad 69812) for the X and Y axis motors (Anorad LEB series) are hall effect commutated.

The signal processing and real time I/O platform that I developed is described in Chapter 7. This system controls the stage, fringe locking, and the isolation feed-forward. It contains a multiprocessor DSP board, analog and digital I/O, digital change of state inputs, and phase meters. A high bandwidth controller locks fringes in the reference frame of the substrate based on an error signal that incorporates stage position error, index corrections, and fringe drift measured from the lithography interferometer.

The isolation system is the TCN passive/active isolation system from IDE[3]. The stage position and accelerations for X and Y are supplied by analog inputs into the IDE controller. Motors on the isolation system output forces to counter-act the stage reaction forces and prevent the system from rocking. The relatively heavy stage ($\approx$60 kg moving in X and $\approx$100 kg moving in Y) required a non standard motor package to counter-act its large reaction forces. I packaged twenty four motors into the system to counter-act forces associated with shifts in the stage's center gravity and accelerations (up to 0.3 g).

[2]Specialty Components, Wallingford, CT. http://www.specialtycomponents.com
[3]Integrated Dynamics Engineering, http://www.ideworld.com

The displacement measuring interferometry (DMI)is based on products from Zygo. The Zygo electronics and laser are from the ZMI 2000 product line. The location of the refractometer interferometer and the X-axis interferometers are visible in Figure 2-1. The Y-axis interferometer head is visible in Figure 2-2. The DMI system employs heterodyne column referencing interferometry to measure x-axis and yaw displacements. The y-axis interferometer is not currently implemented with column referencing. The refractometer is based on the Zygo DPMI and it provides for correction of uniform index changes and vacuum wavelength changes of the helium neon laser.

Figure 2-2 shows the back of the system. The argon ion exposing laser (351.1 nm wavelength) is received by the tower shown and a few percent of its power is directed to beam steering optics located on the back of the optical bench. The laser is located about 10 meters from the SBIL system on a separate isolation system. An active beam steering system stabilizes the laser to the SBIL system. The beam steering system is discussed in Chapter 6. Locating the laser outside of the system allows the laser to be shared with multiple interference lithography stations and removes the laser heat load. The HeNe laser for the displacement measuring interferometer system is also visible from the rear of the system. This laser is contained within a well insulated box. Air is forced through this box and then routed away from thermally sensitive areas.

The SBIL tool is housed within an environmental enclosure. The enclosure is discussed in Section 5.2. It provides a stable temperature environment and a Class 10 cleanroom. The enclosure also provides relatively stable humidity and differential pressure. The entire enclosure is housed in a Class 1000 cleanroom.

The optical bench is vertically oriented to achieve the most open area for air flow. The air flow was assumed to be the most important issue rather than vibration of the bench. Temperature related air index variations and thermal expansion errors are in fact much larger than vibration errors in the system.

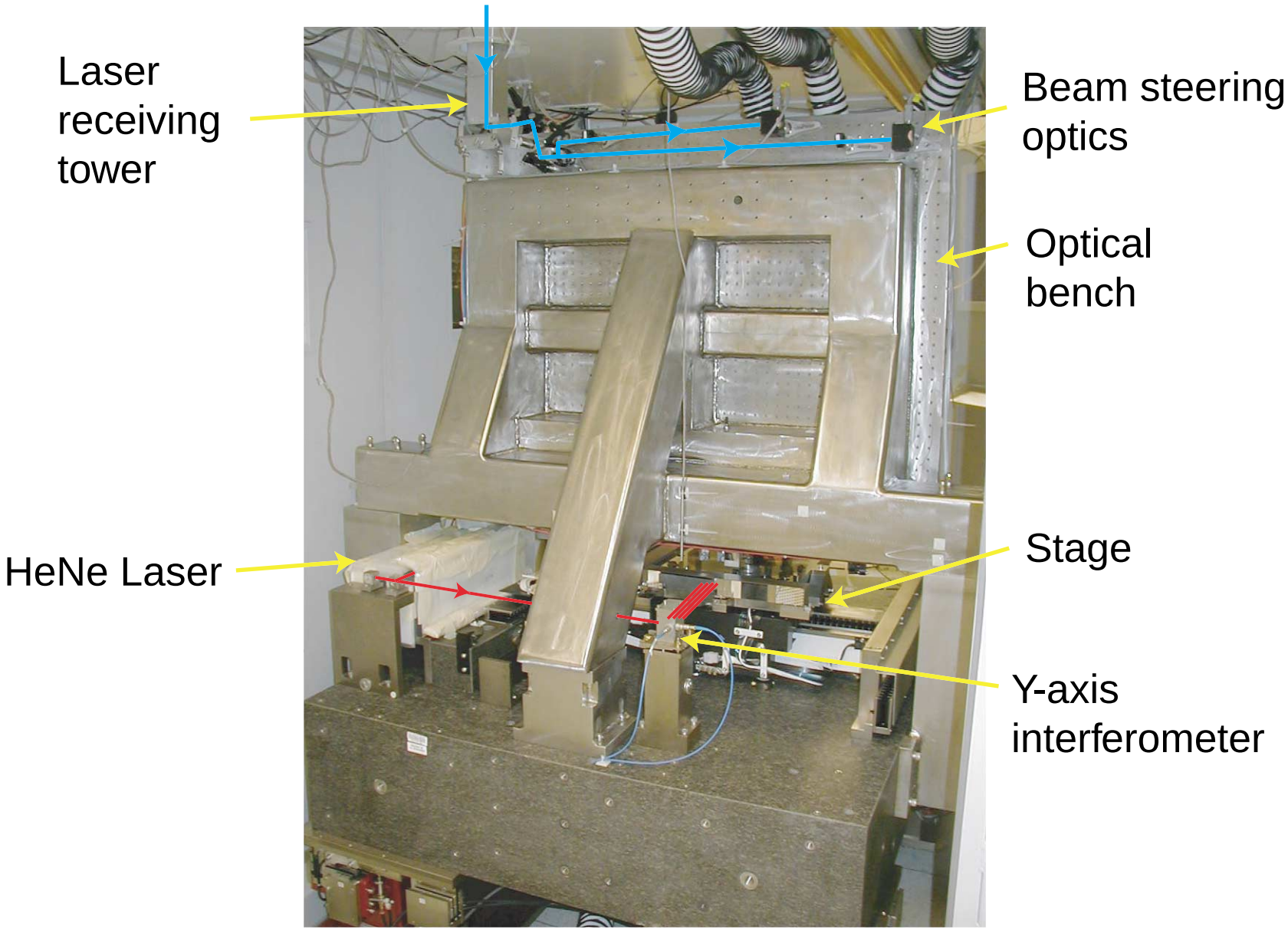

Figure 2-2: Back of system.

2.1 Optics

The interference lithography optics are located on the front of the optical bench. Figure 2-3 indicates the major components. In order to simplify the description of the optics, I have broken down the components according to beam conditioning and alignment functionality.

Figure 2-4 shows a simplified schematic of the optics used for beam conditioning. These optics control the polarization, beam size, wavefront curvature, and power. The polarizer is adjusted such that the beams will interfere with TE polarization for maximum contrast. The half wave plate is rotated to maximize the power transmission through the polarizer. The dose and dose uniformity are dependent on the beam power, beam size, stage scan velocity, and the step size between scans. The power at the write plane is adjusted by setting the power output of the Argon ion laser as well as the amplitude of the RF signals to the acoustic optic modulators. The beam size is controlled with appropriate transfer lenses along the beam path to maintain nominally 1 mm beam radii at the write plane and near 1 mm beam size over the propagation paths. The collimating assembly can also be designed with a magnification factor to control the beam size. In our system the collimating assembly has a nominal magnification of one. The +/-1 grating beam splitter is used instead of a glass beam splitter because it makes the system insensitive to the spatial and temporal coherence of the laser as discussed in Chapter 6. The pinhole in the collimating assembly spatial filters the wavefront distortion. This distortion is due to imperfections in the optics. Since the grating beam splitter provides insensitivity to the spatial coherence of the incoming laser beam, essentially only the grating and optics after the grating can contribute to distortions of the grating image. Even with perfect optics, the spatial filters are still necessary to filter out the zero order beam from the acoustic opto modulators and the laser beam profile deformation inherent in Bragg acousto-optic interaction [50]. The lens and beam pickoff after the pinhole need to have especially good figure since distortions introduced by these optics are not spatial filtered. The collimating lenses after the spatial filters are adjusted to

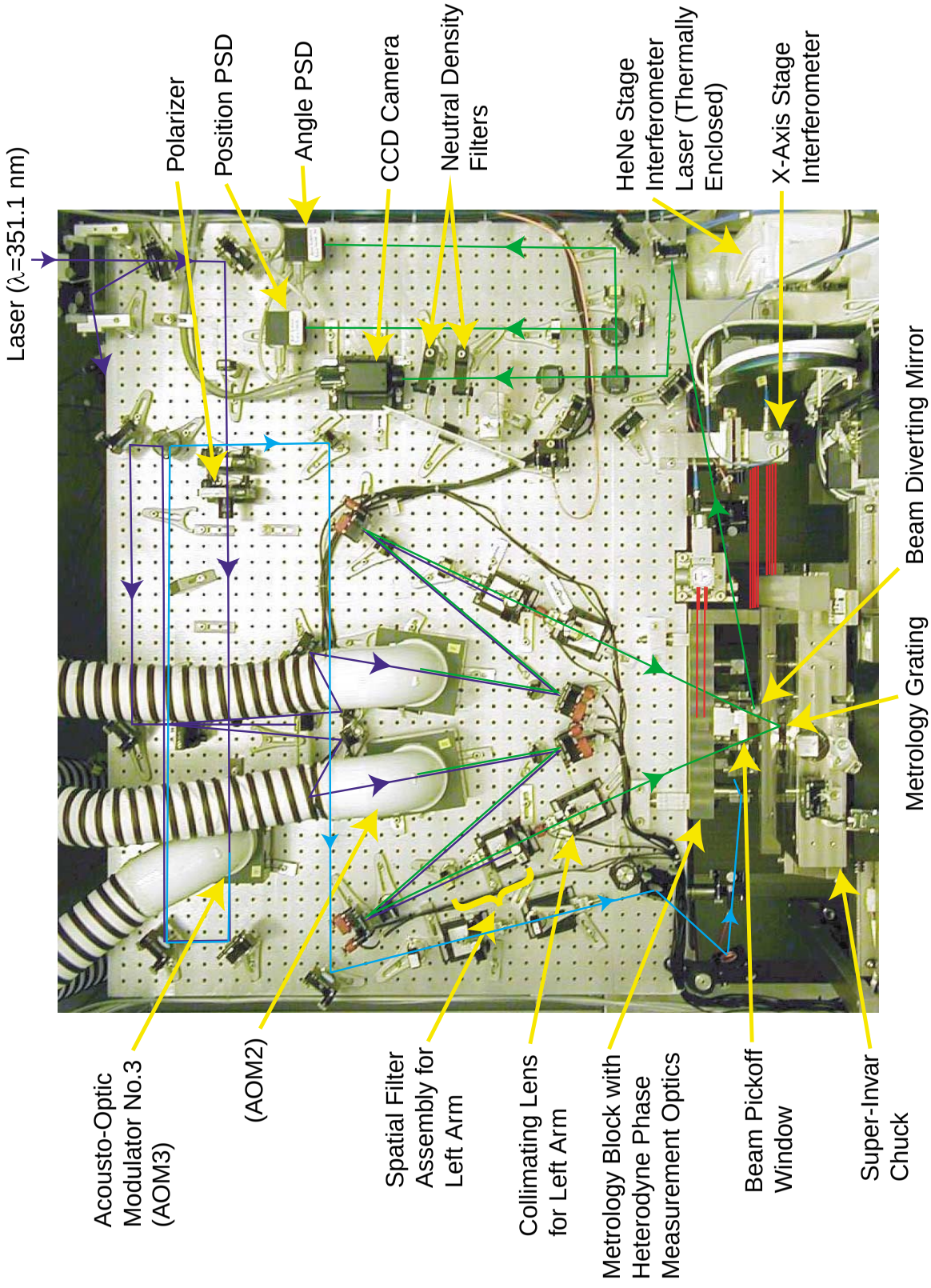

Figure 2-3: Front of system with the optics indicated.

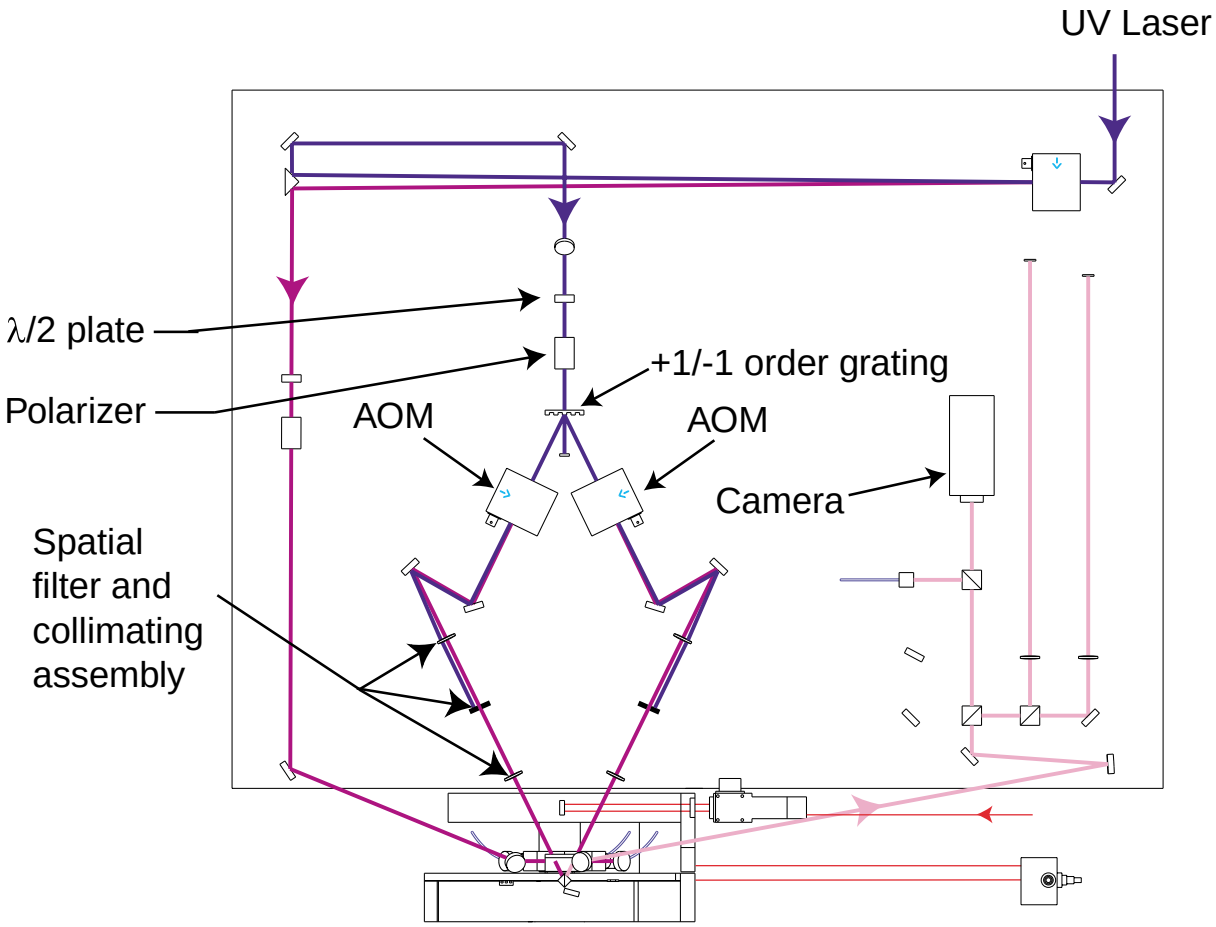

Figure 2-4: Simplified schematic highlighting optics used for beam conditioning.

minimize the wavefront curvature at the write plane. A phase shifting interferometry (PSI) system that observes the moire image at the camera provides feedback for adjusting the collimating lenses [15]. The PSI also reveals high spatial frequency distortions.

Figure 2-5 highlights the optics used for beam alignment. The system provides for alignment of the image period and rotation. The fringes are aligned vertical to the write plane through a precision aligned beam splitter cube. The left and right arms are shuttered individually by cutting power to AOM's. The right arm is reflected from the beam splitter and directed back to the optical bench. Lenses and position sensitive detectors (PSD's) sense the beam position in two degrees of freedom and the beam angle in two degrees of freedom. Similarly, the left arm is transmitted through the beam splitter and directed to the beam alignment detectors.

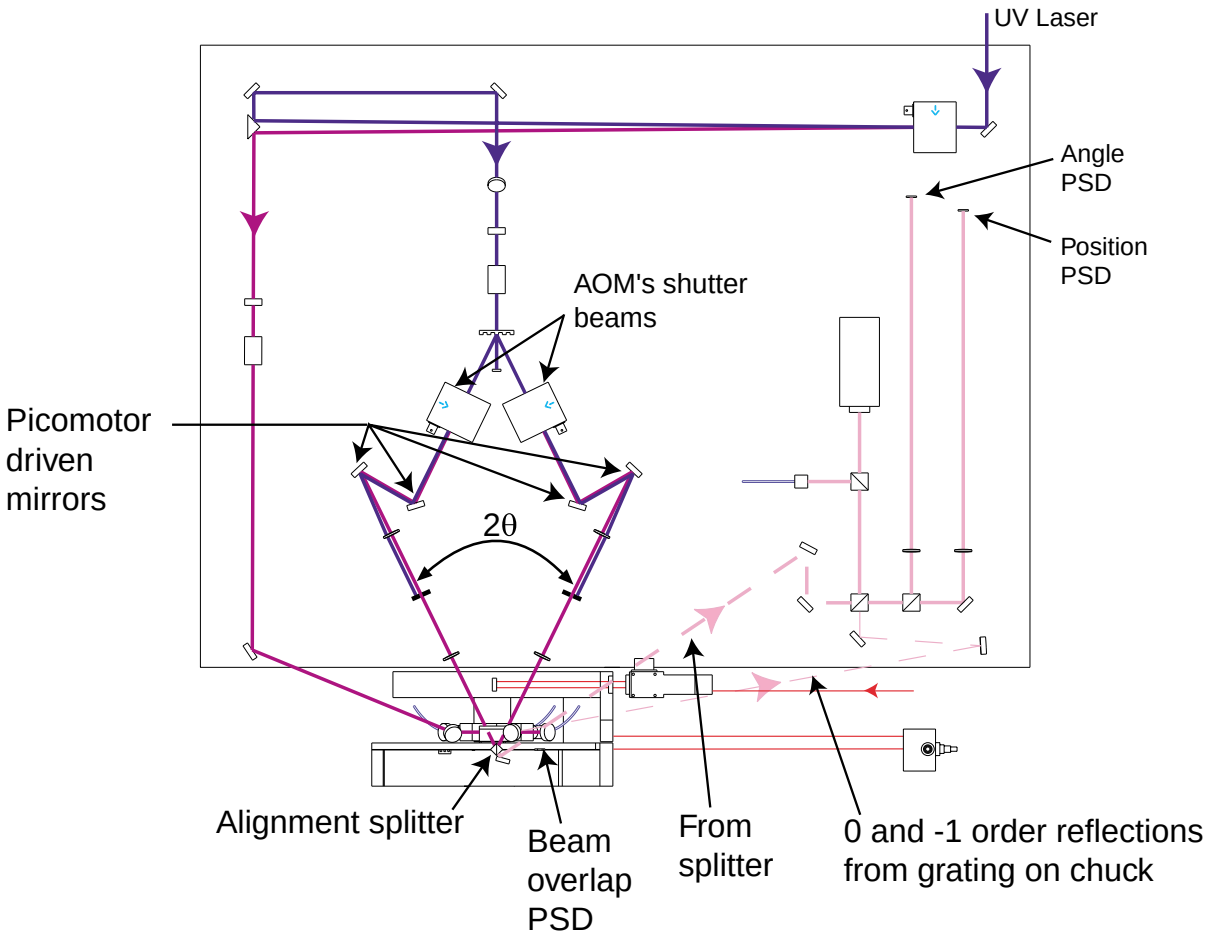

Figure 2-5: Simplified schematic highlighting components used for alignment.

The measurements provide feedback to drive picomotors that adjust the angle and position of the interfering beams. When the system is aligned, the left and right arms will fall on top of each other on the beam alignment detectors.

The period is measured separately by the concept [14] shown in Figure 2-6. As the beam splitter travels through the grating image, an interference signal is detected by the photodiode. In our case, the photodiode is the power signal provided by one of the alignment PSD's. The number of fringes, N, are counted and the period is calculated as

$$\Lambda = \frac{D}{N} \tag{2.1}$$

where D is the distance the stage moves. If the period is not the desired period, the beams are realigned to new places on the alignment detectors and the period

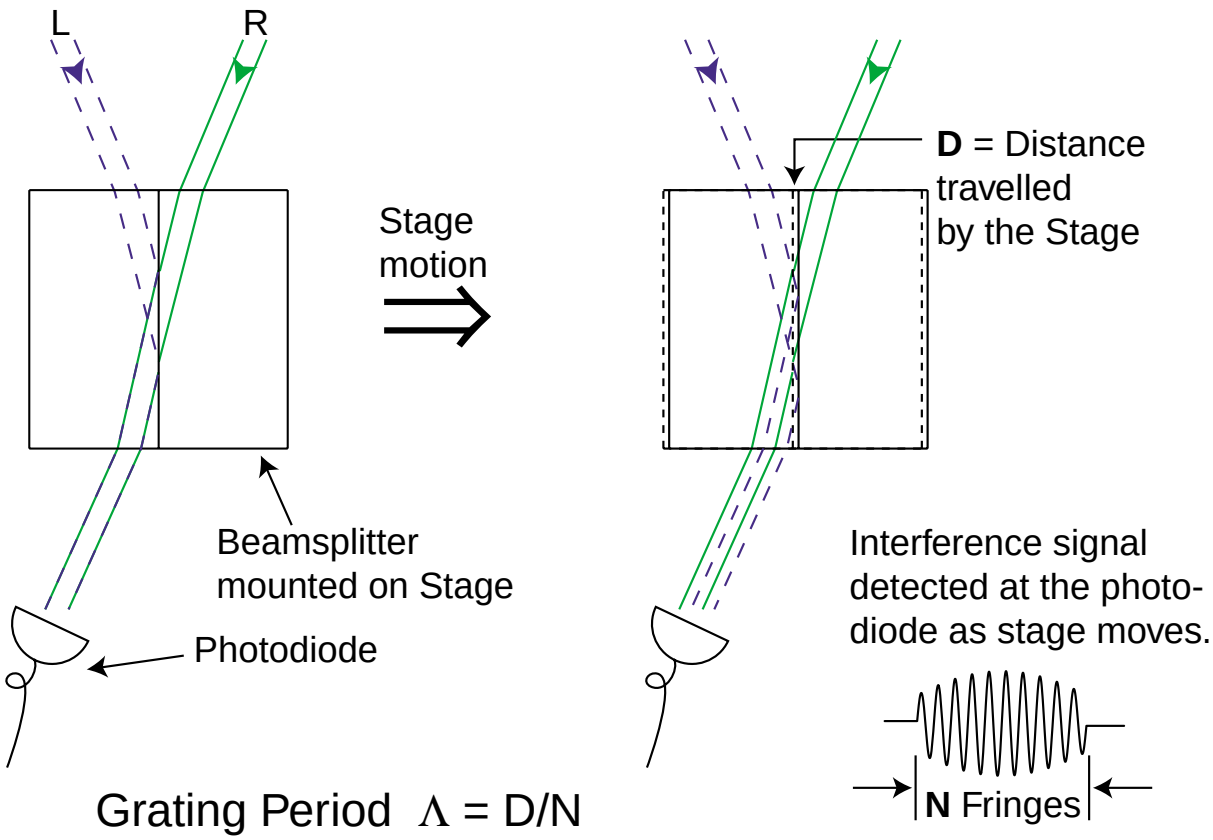

Figure 2-6: Period measurement concept. The grating period is calculated based on the distance the stage moves and the fringes counted.

reverified. The fringes can also be counted in reading mode via heterodyne detection. The heterodyne fringe locking and metrology interferometers are discussed in Section 3.1. In addition to aligning with respect to the beam splitter, a grating can be used as an alignment reference. Figure 2-5 indicates that the 0 and -1 order beams can be received by the alignment optics. Overlapping the 0 and -1 order beams from the grating aligns the system for the period of that grating.

Figure 2-7 shows the chuck with metrology references. The period measurement splitter is visible. There is also a beam overlap PSD that is used to ensure that the beams are overlapping in the write plane. The chuck is compatible with 100 mm, 150 mm, 200 mm, and 300 mm wafers. The reference grating is read to establish a repeatable length scale.

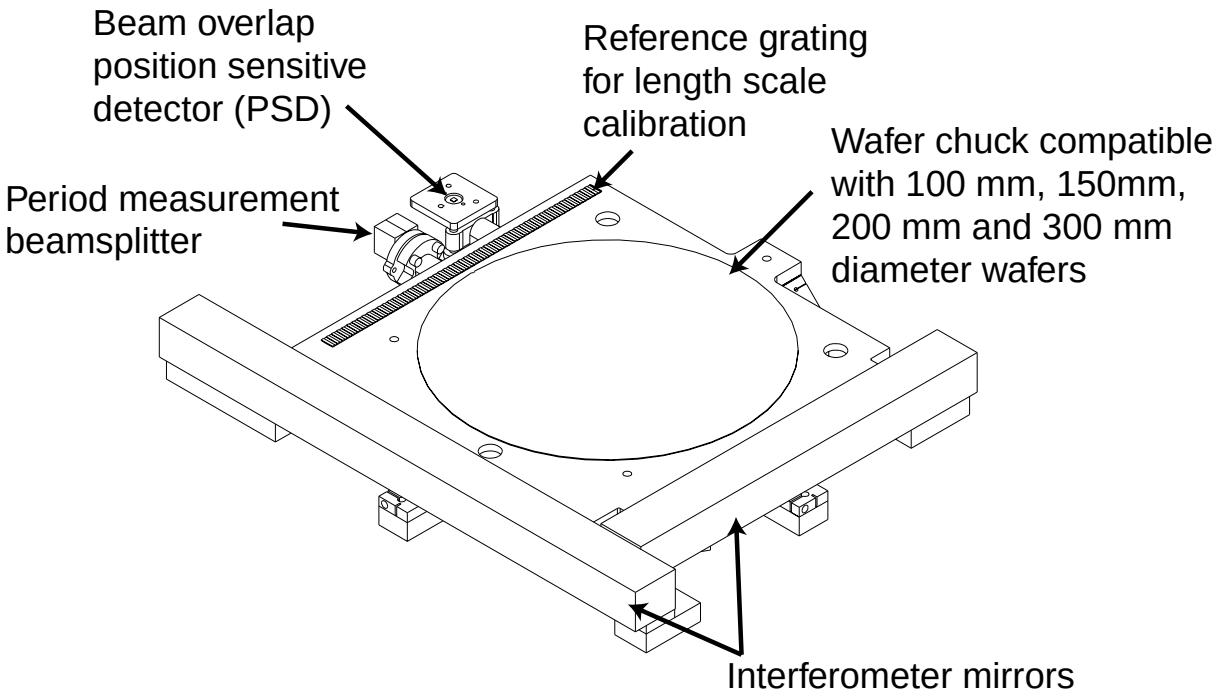

Figure 2-7: Chuck system with metrology references.

2.2 Metrology frames

The stability of the metrology block and the wafer chuck is critical to the performance of the SBIL system. Figure 2-8 shows these critical metrology frames. The metrology block is Zerodur with Super Invar inserts. The x-axis column mirror is rigidly bonded to the block. The metrology block houses the optics for the heterodyne phase detection optics. Many of the optical mounts are Super Invar. The critical optics on the metrology block are also symmetric where uniform temperature changes nominally do not cause thermal expansion errors.

The metrology block is flexure mounted to the optical bench. The optical bench has a much higher CTE than the metrology block and the flexures prevent the strain of the bench from transmitting to the metrology block. The flexures are designed such that the metrology block does not rotate for uniform temperature changes.

The refractometer cavity built into the metrology block is much more compact and is less sensitive to temperature than the commercially available refractometers [96, 99]. Also, the cavity is much closer to the x-axis beam paths than a commercial

etalon could possibly be packaged. The refractometer measurement compensates for index of air variations and vacuum wavelength changes of the laser.

The chuck has the most stringent mechanical requirements on the entire system. The thermal and vibration sensitivity is critical. The chuck can experience the highest level of vibration because of disturbances during scanning. Furthermore, the chuck has significant motion and is sensitive to temperature gradients. The chuck must also serve as a heat sink to spread out the heat from the UV laser and the stage motor coil that is located on the underside of the U-shaped frame.

The chuck was designed to provide critical metrology frame alignments. Figure 2-9 highlights the alignment and bonding features. The chuck design required some compromises because of time constraints. I would have preferred an all Zerodur design but the greater than six month lead time for such a part was unacceptable. Instead the main chuck body is Super Invar while the mirrors are Zerodur. The mirrors were bonded using alignment features built into the chuck. Some of these components were salvaged from Anorad mirror mounts provided with the stage. Other alignment schemes are possible that could reduce the weight of the assembly. However, the other alignment schemes would have required tooling that I did not have time to pursue. Most importantly, the weight and vibration performance of the chuck is more than acceptable. The chuck surface is precision polished electroless nickel plating flat to about one micron. With this specification, the chuck surface is expected to distort the substrate in-plane by more than a nanometer (see Section 9.8) compared to when clamped to a perfectly flat surface. But the distortions are repeatable. Sub nanometer repeatable substrate clamping was the requirement for the design at this stage of the SBIL effort.

The chuck was leveled flat to the plane of motion of the stage with leveling screws and feedback was provided by a Federal gauge. The total indicated run (TIR) was less than 2 μm. This flatness includes both the chuck surface flatness and the flatness of the stage motion. The chuck is bolted to three flexures that relieve the strain transmitted by the U-shaped aluminum stage. The flexures are configured such that the chuck does not rotate with uniform temperature changes. The leveling screws

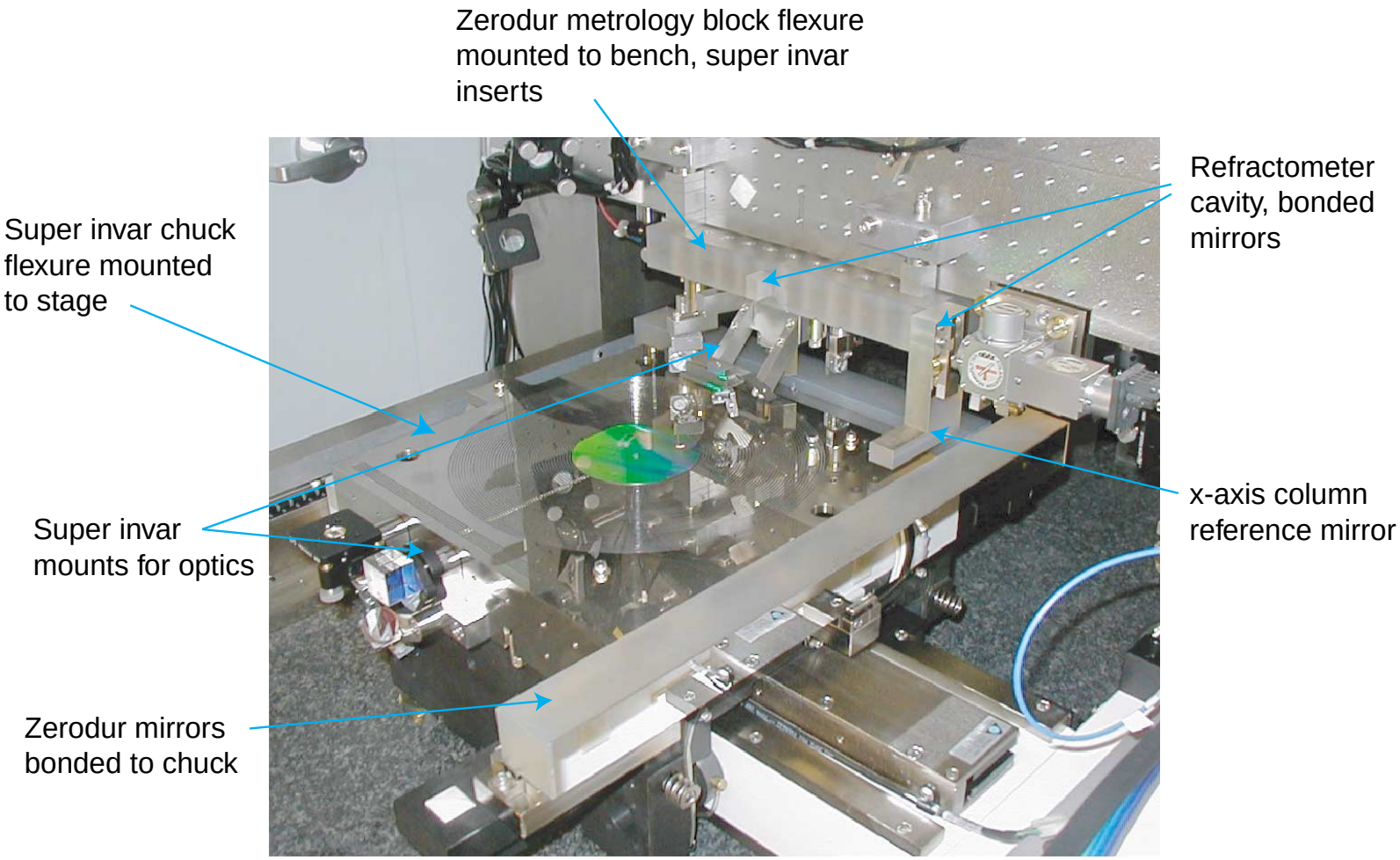

Figure 2-8: SBIL metrology frames.

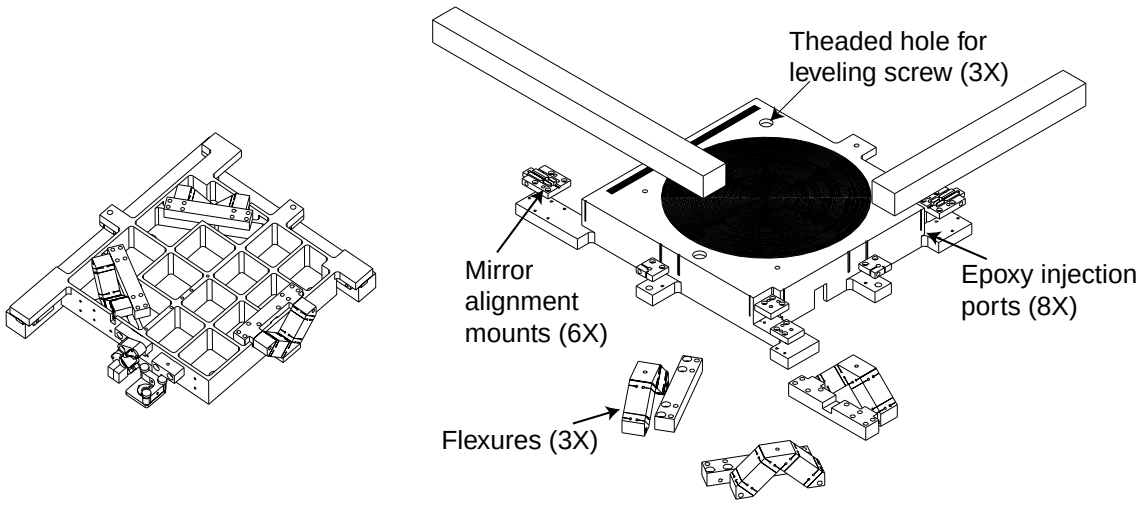

Figure 2-9: SBIL chuck assembly showing alignment and bonding features.

were removed after alignment. The x-axis interferometer mirror was aligned parallel to the mechanical y-motion of the stage by mechanically locking the x-axis and moving the stage against a Federal gauge for feedback. A Starrett Croblox was employed to align the mirrors' pitch and orthogonality. The mirrors were bonded with epoxy. The chuck contains built-in epoxy injection ports. Hot melt glue contained the epoxy within the mirror-chuck interface until it cured. The hot melt was easily cleaned afterward. After bonding, the mirrors were orthogonal to 2μrad and the pitch of the mirrors with respect to the write plane was orthogonal to 10 μrad according to the Croblox. The accuracy of the Croblox orthogonality was 5 μrad. However, the pitch measurement from the Croblox is sensitive to the Croblox placement on the chuck. Depending on the Croblox placement, the pitch may be off by 30 μrad.

The stability of the optical bench is also an issue. Its stability is important because of Abbe errors and requirements for period stability defined by the angle between the interfering beams. Ideally the bench would have the same CTE as the base. However, it was not practical to fabricate a granite bench because of the many tapped holes required. The bench material is 410 stainless steel with a CTE of 9.9 ppm/°C whereas the granite CTE is 8 ppm/°C. The bench is an all welded stainless steel structure. The bench-base structure is highly stable because of the relatively low mismatch of 2 ppm /°C between the granite and the bench. The bench and base also have long

thermal time constants that lead to better than expected stability during the time of writing, which may be only 10 minutes.

Resonances between the column mirror and the base limit the stage control. At several hundred Hz, resonances in the stage itself can also limit the stage control. It is reasonable to design the column mirror-to-base coupling for about 200 Hz. In practice, the resonance of the bench that limits the stage control is at 168 Hz. The system dynamics are considered in Chapter 8. The resonances of the optical bench also couple with the metrology block to increase the fringe locking error and the unobservable errors. The stainless steel bench is not well damped and large resonant Q factors will be obvious in data that will be presented. However, the bench resonances are at fast frequencies where the errors are significantly averaged over the time of the exposure.

Chapter 3

SBIL Errors

Many sources of error diminish the repeatability of our system. The system design is further complicated because many of the errors are interrelated. Considering the complexity of SBIL, it necessary for design purposes to budget the errors according to subsystems. Additionally, categorizing the errors according to basic physics aids in understanding the limitations of the system. The error budget summary by subsystem and physics is shown in Figure 3-1. There are two columns for the errors. The first one will predict the fringe stability for a small deadpath (< 7 cm) and a well thermally equilibrated system. Also, it does not include errors associated with clamping the substrate. The second error budget column is the worst case scenario accounting for errors when patterning a 300 mm wafer. The worst case scenario includes extra thermal expansion errors associated with moving the chuck through a temperature gradient and extra index errors due to the longer dead path and stage movement. The worst case errors also include terms associated with clamping the wafer. Appendix A contains the detailed breakdown by subsystem. I will elaborate further on the errors in the remainder of this thesis and I will not dwell on the values here. This section only introduces the major error sources and their physics.

The "spot-averaged" phase error can be categorized into five "subsystem" sources: displacement interferometer, fringe locking interferometer, metrology-block frame, substrate frame, and rigid body error motions. Within the spot, the period control and image distortion define the errors in the grating image.

Errors by Subsystems

Error Category	Error budget, static [±nm]	Error budget, worst case [±nm]
Displacement interferometer	1.66	4.88
Fringe locking interferometer	1.58	1.58
Metrology block frame	0.51	0.51
Substrate frame	0.40	2.83
Rigid body error motions	0.12	0.12
rss error	2.39	5.88

Errors by Physics

Error category	Error budget, static [±nm]	Error budget, worst case [±nm]
Thermal expansion	0.68	2.46
Air index	2.00	5.00
Periodic error	1.02	1.02
Electronic	0.22	0.22
Vibration	0.08	0.08
Substrate clamping distortion	0.00	1.41
Substrate thickness variation / fringe tilt	0.00	0.50
Control	0.40	0.40
rss error	2.39	5.88

Figure 3-1: Error budget summary. The upper table categorizes the errors by subsystems. The lower table categorizes the errors by physics.

Fundamentally, accurate fringe placement relies on accurate knowledge of three distances x_d, x_f, and x_s [58] as shown in Figure 3-2. The distance, x_d is the displacement between the stage and column reference mirrors. Errors in this measurement are displacement interferometer errors. Thermal motions, electronic inaccuracy, periodic errors, air index variations, and refractometer correction inaccuracy comprise the significant errors for the displacement interferometer. The distance x_f is the displacement of the fringe image at the substrate-interference image interface relative to the column reference. During writing, we shift the fringes with a high speed acousto-optic

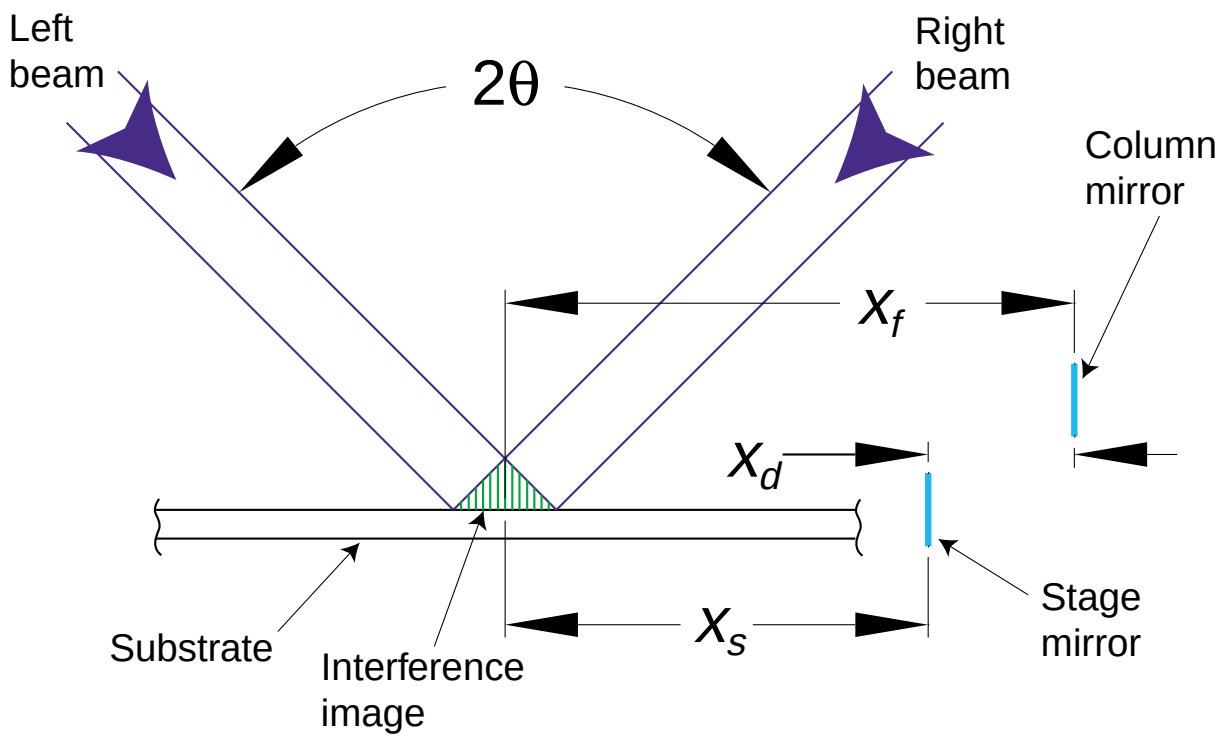

Figure 3-2: Definition of coordinate systems for error terms.

fringe locking system such that

$$x_d - x_f + x_o = NM\Lambda. \tag{3.1}$$

Here x_o is a constant depending on the location of the first scan and N is the integer scan number incremented from zero. The distance $M\Lambda$ is the step size between scans, where M is an integer and Λ is the period of the interference image. Inaccuracy in the fringe position, x_f, comprises errors from two subsystems. The first is the fringe locking error, which is due to inaccuracy in the fringe locking sensor signal and the controller's inability to lock out the total fringe locking error. The fringe locking control is discussed in Section 8.1. The inaccuracy in the fringe locking sensor signal is due to air index variations, periodic errors of the UV interferometers, and electronic inaccuracy. The metrology-block error category contains the remaining sources of errors in x_f. These errors are due to thermal and vibration motions of the sensor optics with respect to the column reference.

The position of a substrate location relative to the stage mirror is x_s. The substrate frame error contributes to inaccuracy in this position; during writing the substrate must accurately track the stage mirror for this error to be zero. Vibration and thermal motions contribute to the x_s error. Additionally, the substrate must be clamped during writing in substantially the same way that it will be used as a metrology reference, otherwise clamping distortions will limit the accuracy of the reference. Substrate non flatness and non vertical fringes also cause errors in this subsystem.

The rigid body error motions are due to motions of the chuck, the metrology block, the interferometer head, and the interferometer beams. Under most circumstances, the largest errors in this category are the Abbe errors. The Abbe errors cause a coupled inaccuracy in x_s and x_f. The analysis of rigid body motions is the subject of Chapter 4.

Another category of error is period control. Variations in λ and interference angle, θ, limit the period control. The period control goal was 1 nm of accumulated phase error across a 1 mm image radius or 1 ppm [59, 14]. The image distortion category is due to nonlinearity of the interference image. To some extent, the image nonlinearity can be averaged out by tightly overlapping adjacent scans but this approach limits throughput and dose contrast is sacrificed. Image distortion of about a nanometer within the $1/e^2$ Gaussian beam diameter was the original design goal.

The focus of this thesis is on accurate placement of the fringes with respect to the substrate. Similarly, the period control and image distortion are not the focus of this thesis. The image work is the subject of another PhD thesis [15].

The fundamental performance metric incorporating all the errors is the fringe-to-substrate phase placement repeatability. During writing, the placement repeatability cannot be measured directly. However, a good measurement of the placement repeatability can be obtained in reading mode. In reading mode, errors that were "unobservable" in writing mode are observable. Similarly, in reading mode the fringe-to-substrate phase is measured directly, whereas in writing mode only the residual fringe locking error is measurable. The distinction is extremely significant.

In reading mode, a wafer that was previously written by SBIL can be put back

into the system for phase measurement. Multiple wafers can undergo the write-read procedure and then the repeatability of the phase maps is a very good measure of the grating writing repeatability. In reading mode, the unobservable errors can be measured and studied across the full substrate area and at full stage scan speeds. No other tool has this capability. The unobservable errors are what limits the performance of our system. Similarly, the observable errors are corrected by a high speed fringe locking control system and I will show the residual servo error contributes sub nanometer phase placement error. Much of the SBIL system design is dedicated to achieving very small unobservable errors. The metrology system developed for SBIL allowed high speed measurement of the unobservable errors. These measurements helped to drive key refinements to the system. The interferometers that make up the metrology system are described in the next section.

3.1 SBIL interferometer systems

Figure 3-3 shows the fringe locking system [42] based on digital frequency synthesizers, acousto-optics, and heterodyne phase sensing. While heterodyne sensing of grating phase has been done by other researchers [103], the fringe locking and metrology system used in the SBIL is the first heterodyne system suitable for interference lithography where the fringe phase needs to be controlled. Furthermore, the design meets the associated requirements for patterning and metrology. The system has two modes – one for writing shown in Figure (a) and one for reading in Figure (b). In all, the UV interferometer system has three acousto-opto modulators and four phase meter axes. The electronic architecture is discussed in Chapter 7. In writing mode the nominal frequencies to the AOM's are 100, 100, and 120 MHz to AOM1, AOM2 and AOM3 respectively. This frequency choice produces the heterodyne frequency of 20 MHz on the phase meter axes. The 100 MHz offset is chosen because the diffraction efficiency for our AOM's is highest in the 100 MHz range. Diffraction efficiencies[1] of

[1]The diffraction efficiency from a volume grating is defined as the ratio of the power in the minus one order to the power in the zero order.

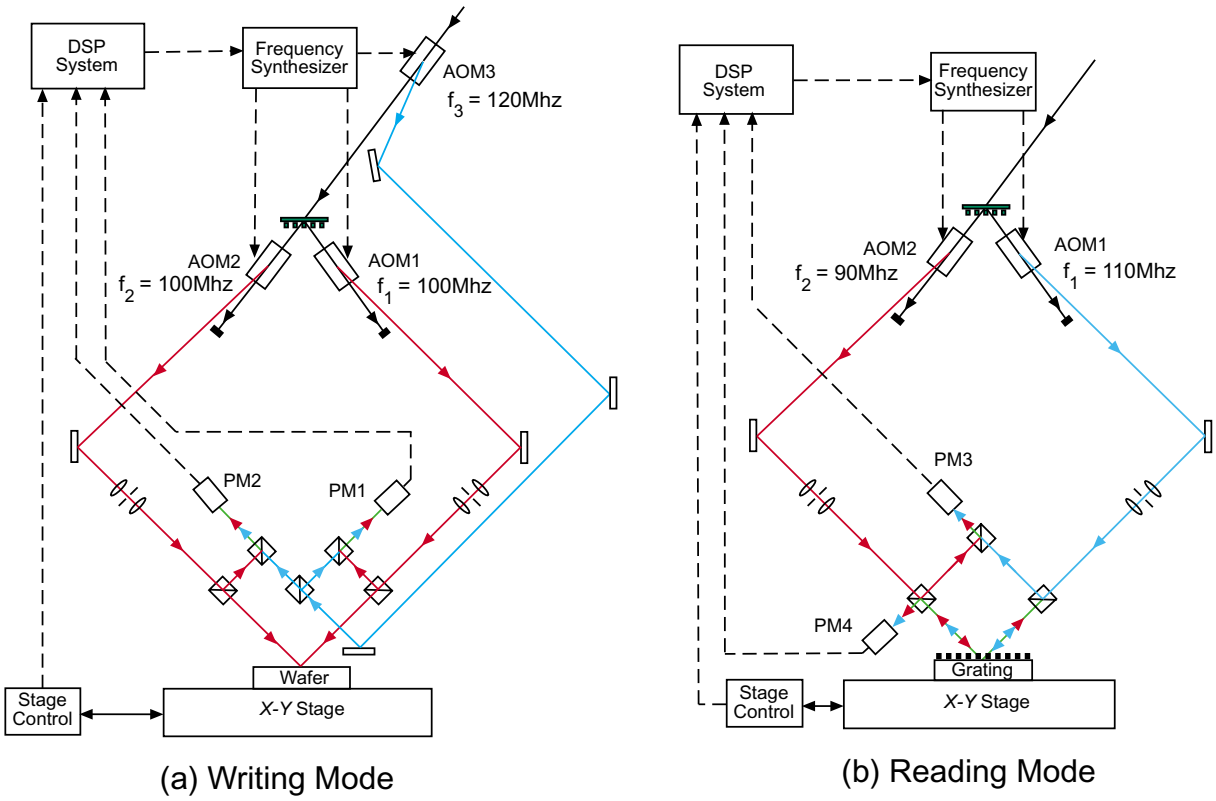

Figure 3-3: Fringe locking system for SBIL. Figure (a) shows simplified diagram for writing mode. The AOM configuration and phase meters relevant to this mode is shown. Figure (b) shows the system components relevant to reading mode.

$> 80\%$ are attained when our modulators are aligned to the Bragg condition [115, 67]. In writing mode, the fringes are designed to be stationary relative to the substrate. The relative phase between the right and left arms are sensed by the difference between phase meter 1 and phase meter 2. The metrology block interferometer phase is combined with the stage error signal to control the fringes. The frequency to AOM1 is updated in real time based on a fringe locking error signal. In reading mode, the nominal frequencies to the AOM's are 110 and 90 MHz to AOM1 and AOM2 respectively. The amplitude of the RF signal driving AOM3 is zero in reading mode. The amplitude of the RF signals to the AOM's in general are selected for the desired optical power in the arms of the interferometer.

There are several measurements that are key indicators of the system performance. These definitions will also be discussed further in other sections. However, I lay them out in advance to have a concise definition in one place.

The phase reading in radians for the metrology block interferometer is defined as

$$\phi_m = \frac{2\pi OPD_{right-left}}{\lambda_{il}}. \tag{3.2}$$

The vacuum wavelength of the interference lithography laser is λ_{il}. The optical path difference between the right and left arms of the lithography interferometer is $OPD_{right-left}$. In writing mode,

$$\phi_m = \frac{2\pi(PM1 - PM2)}{p}, \text{ writingmode.} \tag{3.3}$$

Here $PM1$ and $PM2$ are the digital readings for the phase meters shown and p is the phase meter counts per period. Every phase meter in our system has $p = 512$. This definition assumes the Zygo phase meters use the default configuration where measurement signal frequencies greater that the reference frequency of 20 MHz cause a phase increment. Conversely frequencies less than the reference frequency will cause a phase decrement. If f_3 was 80 MHz instead of 120 MHz this definition would need to have the opposite sign. In reading mode, the metrology block interferometer phase is

$$\phi_m = -\frac{2\pi PM3}{p}, \text{ readingmode.} \tag{3.4}$$

The fringe locking error signal converted to distance units in the writing plane is

$$x_{fle} = \frac{\phi_m \Lambda}{2\pi} - x_{die} \tag{3.5}$$

This is the error signal that the fringe locking controls toward zero by shifting the AOM frequency f_1. The displacement interferometer error perpendicular to the fringes is x_{die} and is given by

$$x_{die} = (\cos\alpha \ \ (x_r - x) + \sin\alpha \ \ (y_r - y)) \tag{3.6}$$

The subscript r refers to a reference position and the definition of the coordinate system follows from Figure 4-9. The position values for x and y are scaled from the

stage interferometer axes given the wavelength and resolution of the cards. The x axis measurement is also corrected by a refractometer measurement. Not including the refractometer correction (discussed in Section 9.2), the stage x measurement is

$$x = \frac{\lambda_{DMI,air} PM_x}{np}. \tag{3.7}$$

Here $\lambda_{DMI,air}$ is the wavelength of the displacement measurement interferometer in air, PM_x is the reading from the x axis phase meter, and the interference scale factor n equals four for our double pass interferometer. The stage y measurement is similarly obtained with the y axis phase meter.

The fringe locking error signal will be derived in Chapter 4 and its application will be discussed extensively in Section 8.1. The fringe locking controller can operate in both reading and writing modes. Locking the fringes in reading mode allows the fringe-to-substrate displacement to be assessed under conditions that very closely approximate the writing mode condition. The fringe-to-substrate motion, which can only be assessed in reading mode, is measured as

$$x_4 = \frac{\phi_4 \Lambda}{2\pi}. \tag{3.8}$$

Since the interference beams are combined at the substrate, this measurement of the fringe-to-substrate stability contains very few sources of error. The unobservable error is obtained by removing any residual fringe locking error from x_4 and is given by

$$x_{ue} = x_4 + x_{fle}. \tag{3.9}$$

The unobservable error is the inaccuracy in the signals used to control the fringes.

When the substrate is scanned in reading mode, phase measurement of the grating is observed in x_4. At times, it is of interest to measure the nonlinearity of the grating. The definition of the grating nonlinearity is

$$x_{nl} = x_4 + x_{fle} + \cos\alpha \ \ (x_r - x_o) + \sin\alpha \ \ (y_r - y_o) \tag{3.10}$$

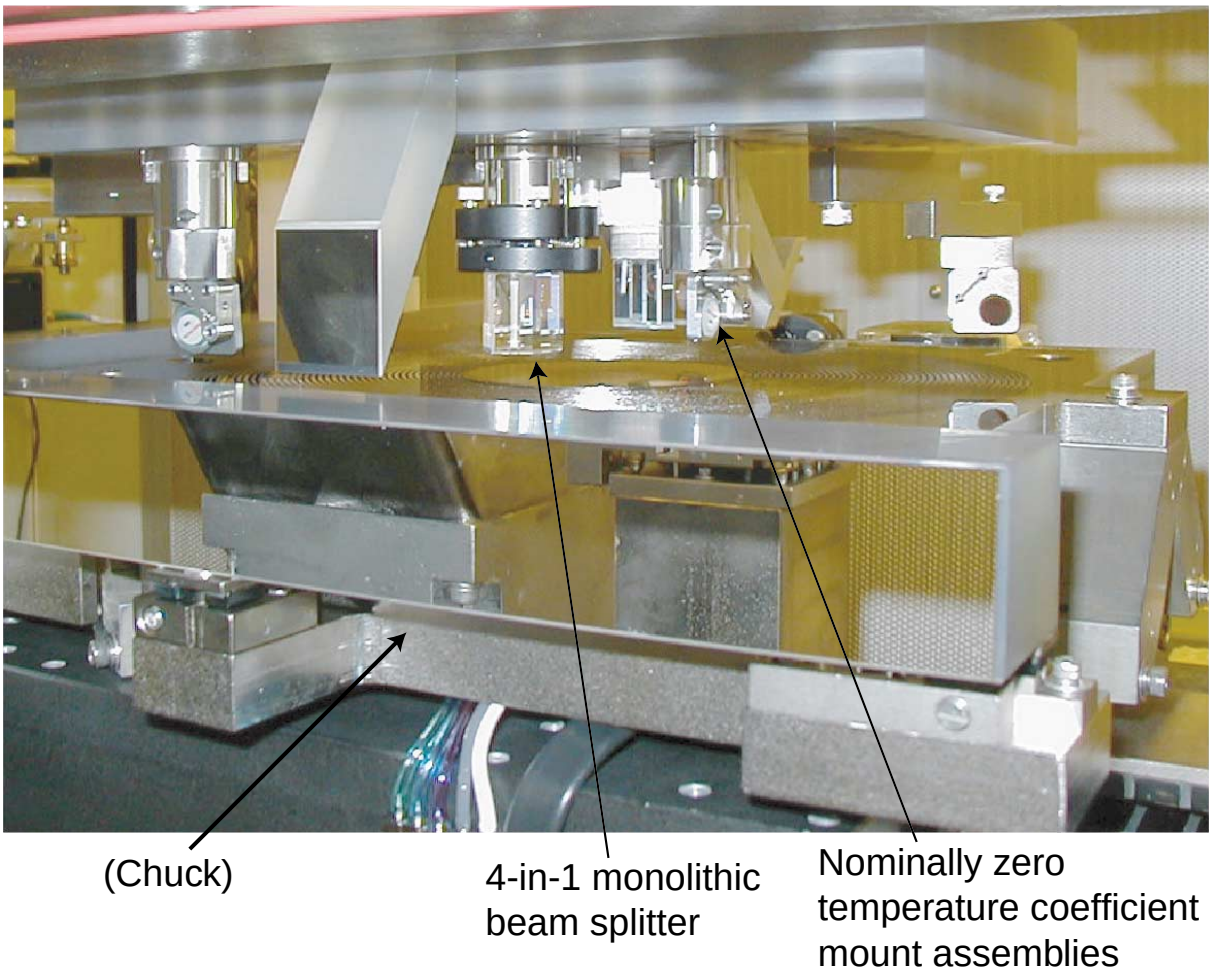

Figure 3-4: Photograph underneath the optical bench showing optics on the metrology block.

where the starting position is given by x_o and y_o. The period Λ and the fringe angle α must be precisely calculated to determine x_{nl}. This definition and the others given in this section will be used and elaborated on throughout this thesis.

Figure 3-4 contains a photograph of the optical hardware on the metrology block. The beam splitters for the phase sensing are integrated into one 4-in-1 monolithic beam splitter. The optical paths after the pickoff are nominally symmetric. A sectional schematic of the optics is shown in Figure 3-5. The phase sensing optics and stage interferometer beam paths are visible. The beams from AOM1 and AOM2 have nearly identical beam paths in reading mode and writing mode. In reading mode, the beams have only $0.5''$ of extra travel within the beam splitter for each arm. In writing

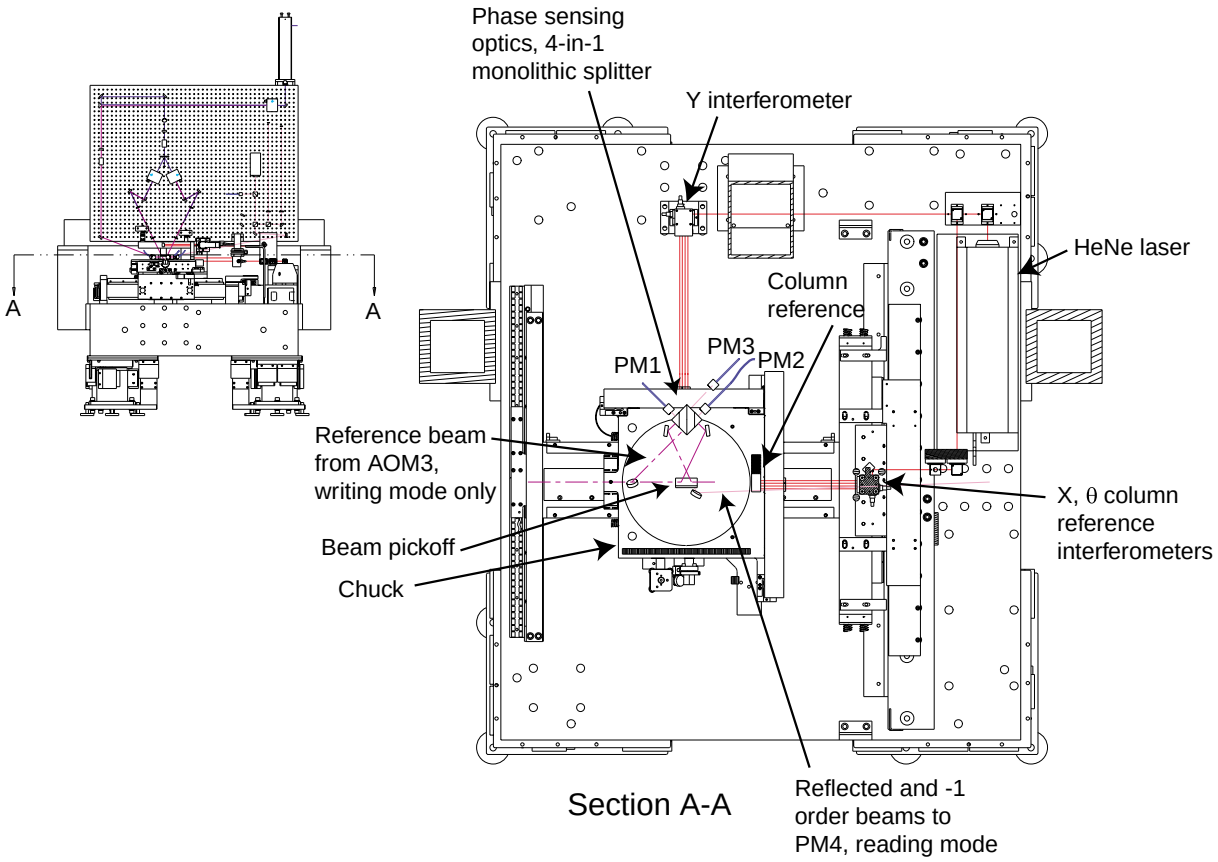

Figure 3-5: A sectional view of the system looking normal to the write plane. The phase sensing optics and stage interferometer beam paths are visible.

mode, after the reference beam from AOM3 is split in the phase sensing optics there is only 0.5″ of travel within the beam splitter before combining with the measurement beams. Since the different paths for reading and writing mode are small, balanced, and in glass, the reading mode ϕ_m should be an extremely good estimate of the writing mode ϕ_m. Assuming the system is properly aligned, the reading mode measurements and the writing fringe placement are separated essentially by the small electronic errors. Therefore, the stability and repeatability assessed by reading gratings should be a very accurate estimate of the fringe placement stability and repeatability when writing gratings.

3.2 Printed error

A benefit of SBIL over other patterning techniques such as electron beam lithography or scanned laser writing is the relatively long integration time for the intensity. The long integration reduces sensitivity to high frequency errors. An objective of this section is to quantify the sensitivity to errors as a function of frequency. Also, the filter design for estimating the printed error and dose amplitude attenuation from phase error data is derived. The natural filtering of errors due to scanned beams significantly improves the performance.

The dose for a lithographic exposure is written as

$$D(x,y) = \int_{-\infty}^{\infty} I(x,y,t)dt. \tag{3.11}$$

where D is the dose and I is the intensity. The coordinates x and y define positions on the substrate. For SBIL, where we are exposing gratings, the intensity can be expressed as

$$I(x,y,t) = B(x,y,t) + A(x,y,t)\sin\left(\frac{2\pi x}{\Lambda} + \phi_e(t)\right). \tag{3.12}$$

The fringes with period Λ are defined to be perpendicular to the x axis for this analysis. The intensity phase error as a function of time is $\phi_e(t)$ and under ideal conditions would always be zero. The background intensity, B, and the intensity amplitude, A, is a function of intensity profile of the interference image and the location of the substrate. For perfect contrast fringes A would equal B. Otherwise A is less than B. The dose is rewritten as

$$D(x,y) = \int_{-\infty}^{\infty} \left(B(x,y,t) + \sin\left(\frac{2\pi x}{\Lambda}\right) A(x,y,t)\cos\phi_e(t) + \cos\left(\frac{2\pi x}{\Lambda}\right) A(x,y,t)\sin\phi_e(t)\right) dt, \tag{3.13}$$

which we desire to be written in the form

$$D(x,y) = B_D(x,y) + A_D(x,y)\sin\left(\frac{2\pi x}{\Lambda} + \Phi_e(x,y)\right) \tag{3.14}$$

Using the identity

$$E\sin X + F\cos X = A_D\sin\left(X + \Phi_e\right), \tag{3.15}$$

where

$$A_D = \pm\sqrt{E^2 + F^2} \tag{3.16}$$

and

$$\Phi_e = \text{atan}\frac{F}{E} \tag{3.17}$$

the dose amplitude and dose phase error is rewritten as

$$A_D(x,y) = \sqrt{\left(\int_{-\infty}^{\infty} A(x,y,t)\cos\phi_e(t)\,dt\right)^2 + \left(\int_{-\infty}^{\infty} A(x,y,t)\sin\phi_e(t)\,dt\right)^2} \tag{3.18}$$

and

$$\Phi_e(x,y) = \text{atan}\frac{\int_{-\infty}^{\infty} A(x,y,t)\sin\phi_e(t)\,dt}{\int_{-\infty}^{\infty} A(x,y,t)\cos\phi_e(t)\,dt}. \tag{3.19}$$

I have chosen for A_D to be positive, which also requires A to be positive. If the phase error magnitude is small such that $\sin\phi_e \approx \phi_e$ and $\cos\phi_e \approx 1 - \frac{\phi_e^2}{2}$, the dose amplitude and dose phase error can be simplified as

$$A_D(x,y) \approx \sqrt{\left(\int_{-\infty}^{\infty} A(x,y,t)\left(1 - \frac{\phi_e(t)^2}{2}\right)\,dt\right)^2 + \left(\int_{-\infty}^{\infty} A(x,y,t)\phi_e(t)\,dt\right)^2} \tag{3.20}$$

and

$$\Phi_e(x,y) \approx \frac{\int_{-\infty}^{\infty} A(x,y,t)\phi_e(t)\,dt}{\int_{-\infty}^{\infty} A(x,y,t)\,dt}. \tag{3.21}$$

The dose phase error is thus the amplitude weighted moving average. The dose

amplitude can be further approximated as

$$A_D(x,y) \approx \left[\left(\int_{-\infty}^{\infty} A(x,y,t)\,dt \right)^2 - \right.$$
$$\left. \int_{-\infty}^{\infty} A(x,y,t)\,dt \int_{-\infty}^{\infty} A(x,y,t)\phi_e(t)^2\,dt + \left(\int_{-\infty}^{\infty} A(x,y,t)\phi_e(t)\,dt \right)^2 \right]^{\frac{1}{2}}. \quad (3.22)$$

The dose amplitude normalized is

$$\frac{A_D(x,y)}{A_{D,0}(x,y)} \approx \sqrt{1 - \Phi_{e,rsq}(x,y)^2 + \Phi_e(x,y)^2} \quad (3.23)$$

where I define the nominal dose amplitude when $\phi_e(t) = 0$ as

$$A_{D,0}(x,y) = \int_{-\infty}^{\infty} A(x,y,t)\,dt. \quad (3.24)$$

The amplitude weighted root square phase error is given by

$$\Phi_{e,rsq}(x,y) = \sqrt{\frac{\int_{-\infty}^{\infty} A(x,y,t)\phi_e(t)^2\,dt}{\int_{-\infty}^{\infty} A(x,y,t)\,dt}}. \quad (3.25)$$

Finally, the normalized dose amplitude error is defined as

$$e_A = \frac{A_D(x,y)}{A_{D,0}(x,y)} - 1, \quad (3.26)$$

which is the normalized drop in dose amplitude due to phase jitter. When the rms phase jitter is much less than one

$$e_A \approx \left(\Phi_e(x,y)^2 - \Phi_{e,rsq}(x,y)^2 \right)/2. \quad (3.27)$$

The normalized dose amplitude error is always negative since jitter always reduces the dose amplitude.

In summary, the dose phase error Φ_e is described by the amplitude weighted moving average and the reduction in dose amplitude depends on the difference between the square of the amplitude root square phase error $\Phi_{e,rsq}$ and the square of the dose

phase error. Incidentally, the change in dose amplitude has little effect on the printed pattern for the correct background dose, B_D, when printing one-to-one line-space ratios. The clipping behavior of resists makes the developed pattern insensitive to variations in the dose amplitude. However, for non ideal dose background and/or non ideal clipping behavior, changes in dose amplitude will cause linewidth variations.

The effect of intensity integration has such a significant effect that it deserves careful consideration. The filtration leads to important conclusions about whether high frequency errors can be ignored. I consider the effect for top hat and Gaussian laser profiles in the next sections.

3.2.1 Top hat laser profile approximation

If the intensity profile of the laser beam is approximated as a top hat function and if we are only interested in characterizing the error along the scan axis, which is defined as the y axis, then the intensity amplitude is

$$A(y) = A_o \left[1(y/v + \tau/2) - 1(y/v - \tau/2)\right]. \tag{3.28}$$

Here the center of the spot is represented as moving in time with its center located at $y = vt$. The function "$1(x)$" is the step function where $1(x) = 0$ for $x < 0$ and $1(x) = 1$ for $x >= 0$. The integration length is $v\tau$ for the image moving at a constant velocity relative to the substrate. The choice of integration limits neglects the effect of overlapping multiple scans. This choice conservatively reduces the integration time and simplifies the phase error as the moving average given by

$$\Phi_e(y) = \frac{1}{\tau} \int_{y/v-\tau/2}^{y/v+\tau/2} \phi_e(t) dt. \tag{3.29}$$

Although the effect of overlapping scans can be incorporated into the integral by modifying the integration limits, the back and forth motion of the stage leads to varying filter behavior depending on the position on the substrate. Thus, to simplify the filter and conservatively approximate the phase error, the integration limits approximate that most of dose is exposed by a single scan. Furthermore for

top hat laser profile approximation, the amplitude weighted root square phase is simply the time averaged root square of the phase error given by

$$\Phi_{e,rsq}(y) = \sqrt{\frac{1}{\tau}\int_{y/v-\tau/2}^{y/v+\tau/2} \phi_e(t)^2\, dt}. \tag{3.30}$$

The moving average as a performance criterion is an established practice in lithography [91] and is a reasonable choice for a slit illumination. However, for SBIL, the beams are best modeled as Gaussian and therefore the top hat amplitude function leads to an inaccurate placement accuracy prediction. Nevertheless, because of its intuitive simplicity, the top hat approximation and its applicability is worth understanding. Furthermore, the advantage of Gaussian illumination will be better appreciated.

The moving average $y(t)$ of a continuous time signal $x(t)$ is given by

$$y(t) = \frac{1}{\tau}\int_{t-\tau/2}^{t+\tau/2} x(t)dt. \tag{3.31}$$

Here τ is the integration time. The Laplace transform [28] of $y(t)$ is given by

$$Y(s) = X(s)\frac{e^{s\tau/2} - e^{-s\tau/2}}{s\tau}. \tag{3.32}$$

The moving average transfer function is a sinc function given by

$$M_a(j\omega) = \frac{e^{j\omega\tau/2} - e^{-j\omega\tau/2}}{j\omega\tau} = \frac{2\sin\left(\frac{\omega\tau}{2}\right)}{\omega\tau}. \tag{3.33}$$

Figure 3-6 shows the gain and phase of M_a plotted versus the normalized frequency f_n where

$$f_n = \frac{\omega\tau}{2\pi}. \tag{3.34}$$

The moving average transfer function is real and hence the phase is either 0^o or 180^o.

The envelope, $\frac{2}{\omega\tau}$, is also plotted and is useful to keep in mind as the minimum moving average attenuation. That is, the attenuation is inversely proportional to the frequency. From the figure one can see that the transfer function is null at integer

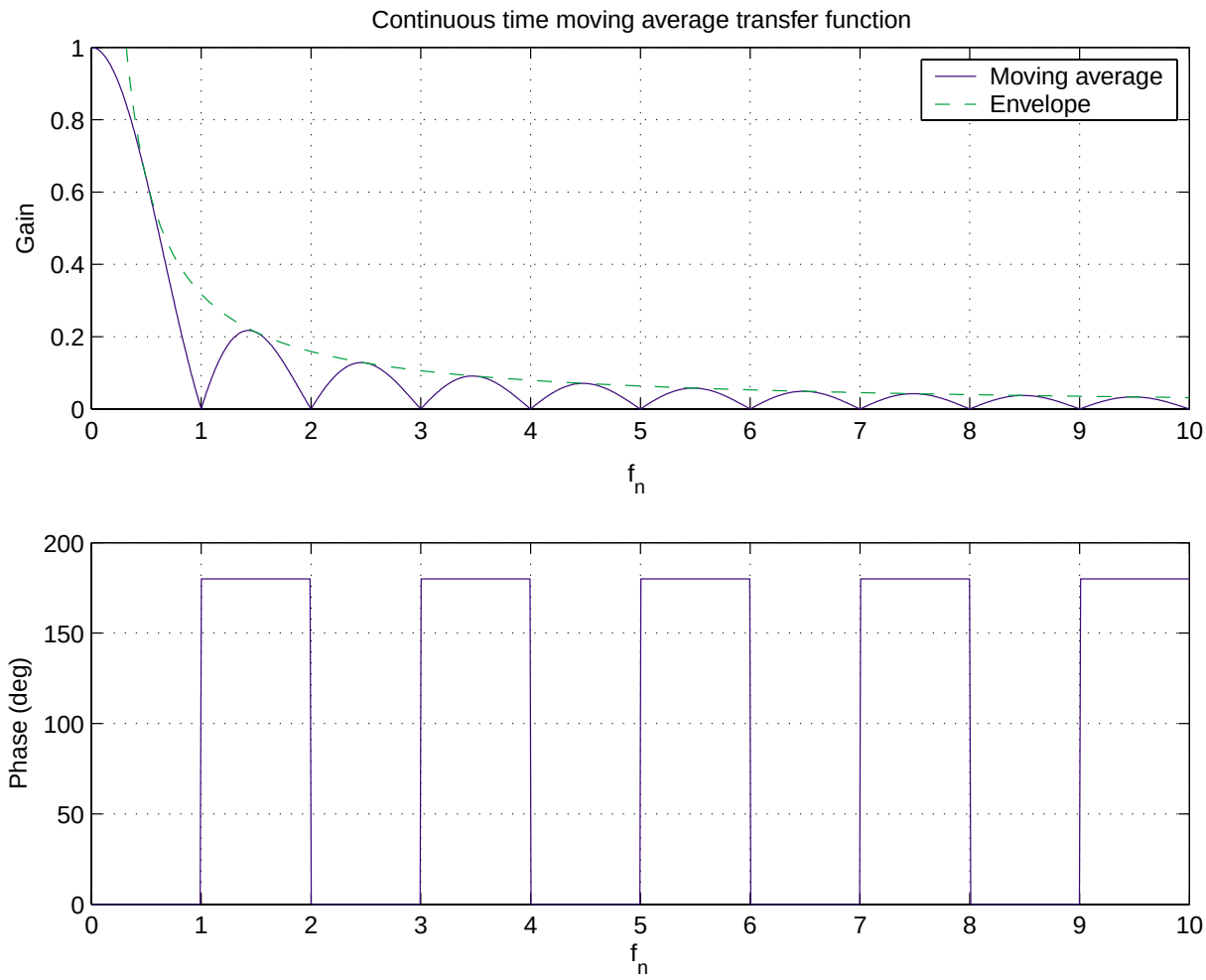

Figure 3-6: Continuous time, moving average transfer function. The envelope is shown in dashed lines.

multiples of the integration frequency, which is intuitively obvious. Furthermore, the moving average attenuation of high frequency disturbances is a significant effect that must be considered when calculating the placement accuracy from raw phase data.

The continuous time moving average is inevitably estimated by taking the moving average of discrete time data. The discretization tends to overestimate the error for frequencies close to Nyquist. The discrete time moving average calculated from $N+1$ points is given by

$$y_a[k - N/2] = \frac{1}{N+1} \sum_{i=0}^{N} x[k-i]. \tag{3.35}$$

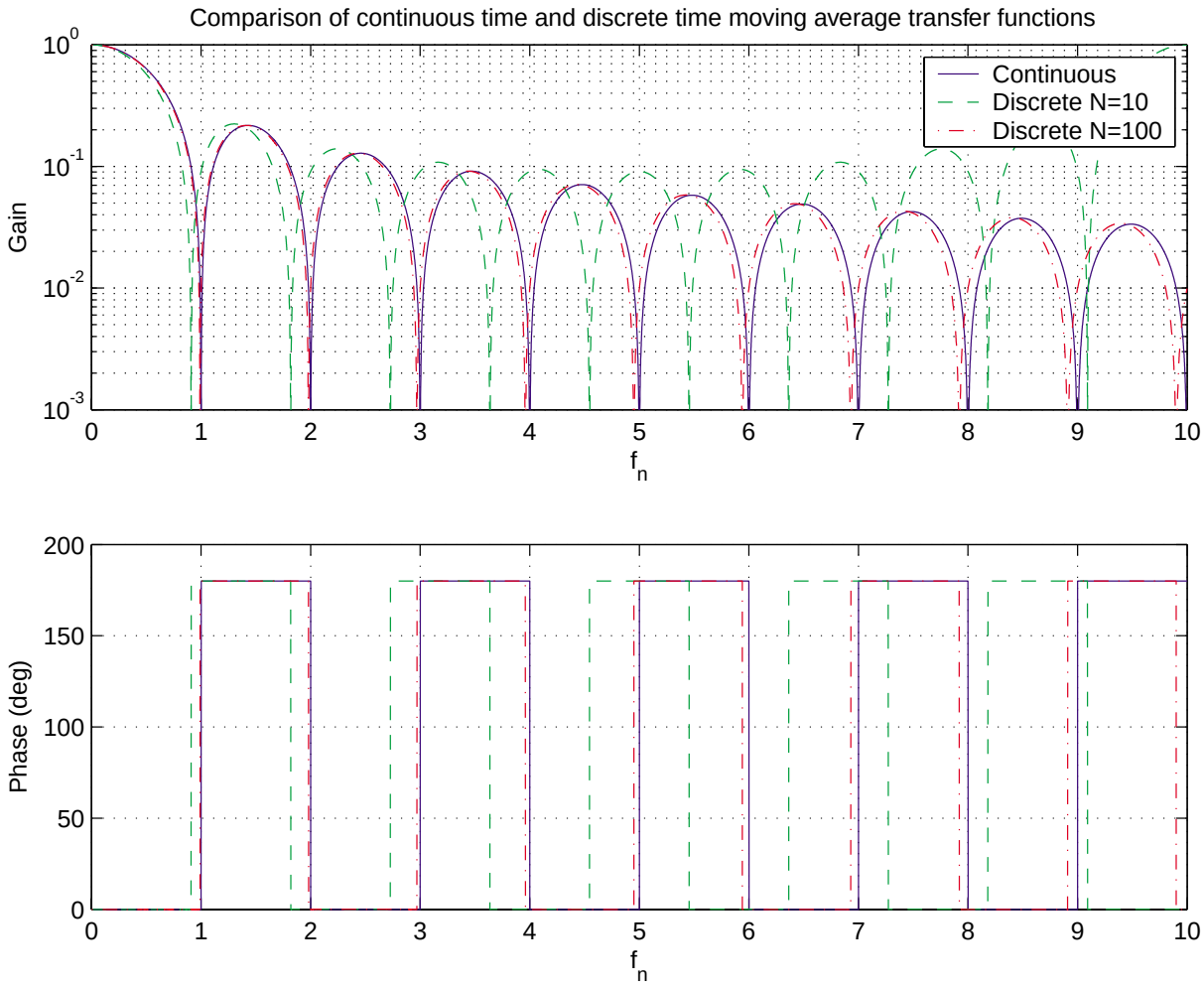

Figure 3-7: Comparison of continuous time and discrete time moving average transfer functions plotted for f_n between 0 and 10. Discrete time functions are shown for $N = 10$ and $N = 100$.

Here y_a is the discrete time moving average of the data x, which is sampled at discrete intervals of time. The integer k is the time index. This formulation requires that N be even and produces a transfer function that is free of linear phase delay. The discrete time moving average transfer function, $M_a[z]$, is then given by

$$M_a[z] = \frac{1}{N+1} \frac{\sum_{i=0}^{N} z^i}{z^{N/2}}. \tag{3.36}$$

The frequency response is readily calculated by substituting $z = e^{j\omega T_s}$ where T_s is the sample time. If we define the normalized frequency as

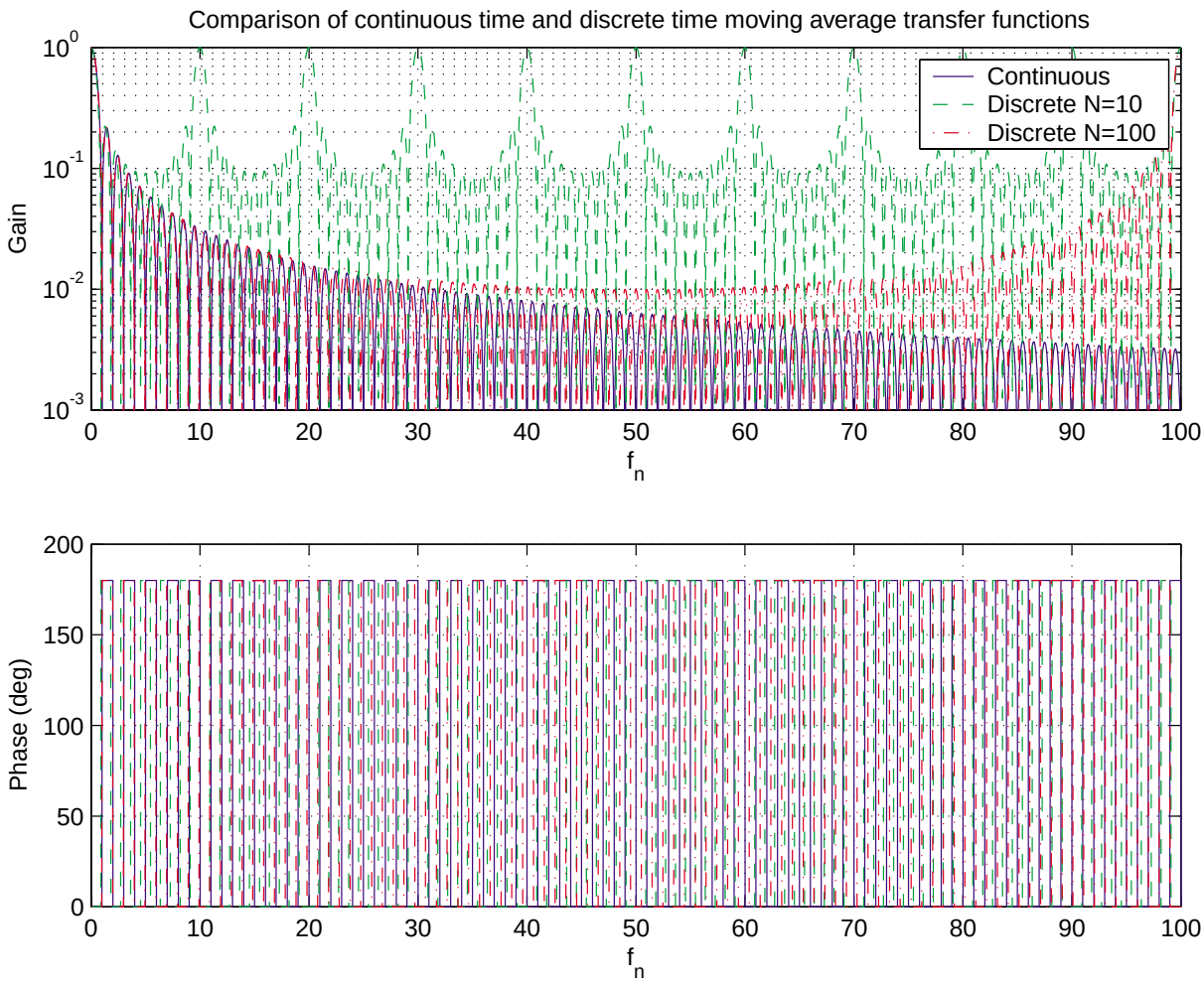

Figure 3-8: Comparison of continuous time and discrete time moving average transfer functions plotted for f_n between 0 and 100. Discrete time functions are shown for $N = 10$ and $N = 100$.

$$f_n = \frac{\omega\tau}{2\pi} \tag{3.37}$$

and let

$$\tau = NT_s \tag{3.38}$$

then

$$z = \exp\left(\frac{j2\pi f_n}{N}\right). \tag{3.39}$$

Figure 3-7 shows the comparison of continuous and discrete time moving average

transfer functions plotted versus f_n. The transfer function for $N = 100$ shows a good approximation to the continuous time version for the range of f_n shown. Discrepancy between the continuous and discrete moving averages gets worse as the frequency approaches Nyquist. The Nyquist frequency occurs at

$$f_n = \frac{N}{2} \tag{3.40}$$

so $N = 100$ corresponds to Nyquist at $f_n = 50$ and $N = 10$ corresponds to Nyquist at $f_n = 5$. If the signal is band limited no aliasing will occur and the effect above Nyquist is not a concern. Below Nyquist, there is clear deviation of the position of the lobes for the $N = 10$ case, especially near Nyquist. The envelope of the discrete time case over estimates the moving average, especially near Nyquist. This is also seem in Figure 3-8. Although the lobes for the discrete time case do not match the continuous time near Nyquist, in many cases the noise power of interest is located significantly below Nyquist so the discrete time estimation is valid. When there is significant noise close to Nyquist, the discrete time estimation is likely to estimate a larger moving average. However, the form that I used for the discrete time moving average has shortcomings that can be solved by designing a longer filter with a frequency response closer to that of the ideal continuous time version. More importantly, even the continuous time moving average really does not adequately describe SBIL writing because the Gaussian intensity profile needs to be considered.

3.2.2 Gaussian laser profile

For a laser beam with a Gaussian intensity profile, the intensity amplitude along the scan direction can be written as

$$A(y) = A_o \exp\left(\frac{-2(y - vt)^2}{w_o^2}\right). \tag{3.41}$$

Here the Gaussian beam has a $1/e^2$ intensity radius of w_o and the center of the spot moving in time with its center located at $y = vt$. For a sinusoidal intensity phase

error of amplitude ϵ given as

$$\phi_e(t) = \epsilon \cos(\omega t + \phi_o) \tag{3.42}$$

applied to Equation 3.21 the dose phase error is given by

$$\Phi_e(y) \approx \frac{\int_{-\infty}^{\infty} A_o \exp\left(\frac{-2(y-vt)^2}{w_o^2}\right) \epsilon \cos(\omega t + \phi_o)\, dt}{\int_{-\infty}^{\infty} A_o \exp\left(\frac{-2(y-vt)^2}{w_o^2}\right) dt}. \tag{3.43}$$

This can be evaluated using Equation 1.15 and another identity obtained from Mathematica given by

$$\int_{-\infty}^{\infty} e^{-\frac{x^2}{q}} \cos\left(ax + b\right)\, dx = \sqrt{\pi q} e^{-\frac{a^2 q}{4}} \cos b. \tag{3.44}$$

The dose phase error evaluates to

$$\Phi_e(y) \approx \epsilon \exp\left[-\frac{1}{8}\left(\frac{\omega w_o}{v}\right)^2\right] \cos\left(\frac{\omega y}{v} + \phi_o\right). \tag{3.45}$$

Since the center of the spot is located at $y = vt$ the intensity phase error and the dose phase error are always in phase and the dose phase error transfer function is given by

$$M_G(s) = \frac{\Phi_e(s)}{\phi_e(s)} = \exp\left[\frac{1}{8}\left(\frac{s w_o}{v}\right)^2\right]. \tag{3.46}$$

When

$$\tau = K_{Gaus} \frac{2 w_o}{v} \tag{3.47}$$

where

$$K_{Gaus} = \sqrt{-\frac{\pi^2}{32 \ln\left(\frac{2}{\pi}\right)}} \approx 0.83 \tag{3.48}$$

then

$$M_G(f_n) = \exp\left(4 \ln \frac{2}{\pi} f_n^2\right). \tag{3.49}$$

I have plotted $M_G(f_n)$ along with the continuous time moving average on Figure 3-9. The choice for τ and K_{Gaus} makes the transfer functions equal at the normalized

frequency $f_n = 1/2$. One can see that the moving average and Gaussian transfer functions are very similar for $f_n < 1$. However, at high frequency the lobes are not present and the Gaussian transfer function exhibits a very fast cut off. The fast cut off makes SBIL extremely insensitive to high frequency phase instability.

Sometimes it is more convenient to work with the normalized Gaussian frequency that I define as

$$f_G = \frac{fd}{v}. \tag{3.50}$$

where d is the $1/e^2$ intensity diameter. Then equation 3.49 becomes

$$M_G(f_G) = \exp\left(-\frac{\pi^2}{8} f_G^2\right). \tag{3.51}$$

When $f_G = 1$, then $M_G = 0.29$ provides modest attenuation. However, when $f_G = 2$, then $M_G = 0.007$ provides significant attenuation. The gaussian filter cuts off extremely fast at higher f_G. For example, the attenuation at $f_G = 10$ is 3×10^{-54}! For practical purposes if the rms errors are small enough to provide acceptable contrast, errors occuring where $f_G > 2$ can be ignored.

The discrete time filter equation for the Gaussian dose error is

$$\Phi_{e,G}[k - N/2] = \frac{\sum_{i=0}^{N} \exp\left(-2\left(\frac{w_c 2}{w_o N}\right)^2 (i - N/2)^2\right) \phi_e[k-i]}{\sum_{i=0}^{N} \exp\left(-2\left(\frac{w_c 2}{w_o N}\right)^2 (i - N/2)^2\right)}. \tag{3.52}$$

This is the discrete approximation of the amplitude weighted moving average given by Equation 3.21. The Gaussian dose error transfer function

$$M_G[z] = \frac{\sum_{i=0}^{N} \exp\left(-2\left(\frac{w_c 2}{w_o N}\right)^2 (i - N/2)^2\right) z^i}{z^{N/2} \sum_{i=0}^{N} \exp\left(-2\left(\frac{w_c 2}{w_o N}\right)^2 (i - N/2)^2\right)}, \tag{3.53}$$

Here w_c/w_o is a design parameter that defines how far out on the tail of the Gaussian the filter coefficients extend. The variable w_c can also be written as

$$w_c = \frac{vT_s N}{2}. \tag{3.54}$$

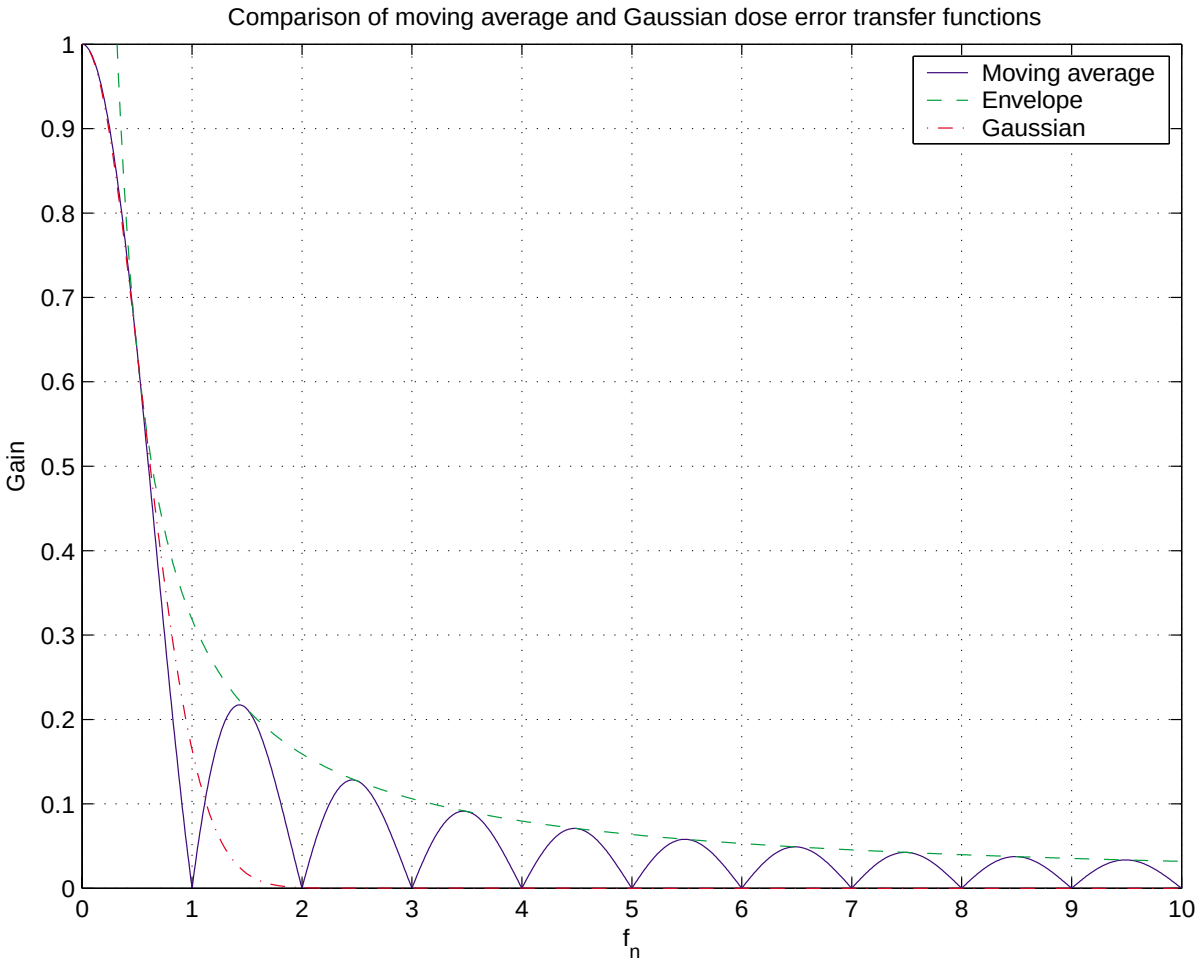

Figure 3-9: Comparison of continuous time moving average and continuous time Gaussian transfer functions. The moving average and its envelope are shown in the continuous and dashed lines respectively. The dash-dot line is the Gaussian transfer function.

If w_c/w_o is too small, the filter response will show significant side lobes. For the desired filter behavior, $w_c/w_o = 2$ is adequate. For this case the smallest filter coefficient will be 3.3×10^{-4} the largest. Because this produces coefficients that extend sufficiently out on the tail of the Gaussian, the side lobes are insignificant and the results are accurate. Also, the length of the filter is reasonable where the time required to fill the filter is the time it takes the stage to travel two Gaussian beam diameters.

Figure 3-10 shows the comparison of the transfer functions for the discrete time and continuous Gaussian dose error filters. The discrete time case is shown for N=10

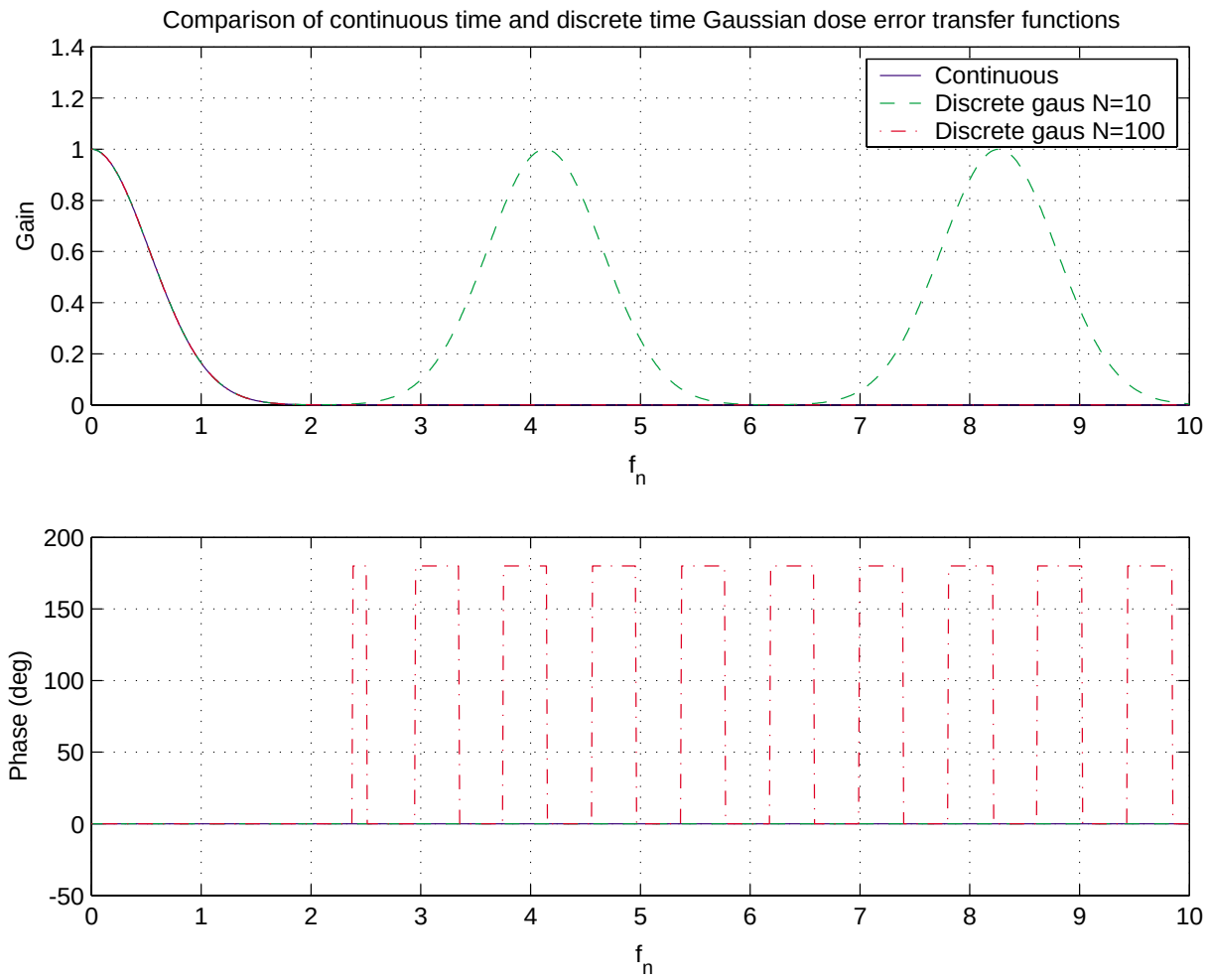

Figure 3-10: Comparison of continuous time Gaussian dose transfer functions with discrete time versions.

and $N = 100$. For the discrete time cases, the plot corresponds to

$$z = \exp\left(\frac{j2\pi w_c f_n}{K_{Gaus} w_o N}\right), \tag{3.55}$$

which follows from definitions given in Equations 3.37, 3.47, and 3.54.

The plot shows very good correspondence between the continuous time and discrete time cases even very close to Nyquist frequency. The Nyquist frequency occurs at $f_n = K_{Gaus} w_o N/(2w_c)$. For $N = 10$ Nyquist occurs at $f_n = 2.1$ and for $N = 100$ Nyquist occurs at $f_n = 21$. The very good correspondence shown between the discrete and continuous time transfer functions allows accurate estimation of the dose error

from discrete time data.

The filtering property of the exposure is a significant effect that must be considered when evaluating the performance of the SBIL system. It is also a property that can be exploited. By scanning the stage slower and reducing the laser power, the integration frequency is lowered resulting in greater averaging and hence attenuation of the high frequency disturbances. Scanning slower also decreases the reaction forces, substrate heating, and the motor thermal loads.

Chapter 4

Rigid body error motions

In this chapter, I consider the relative rigid body motions of the metrology block, the stage, and the interferometer. All parts are assumed infinitely rigid and stable. Also, I consider motions of the displacement measuring interferometer (DMI) and interference lithography beams.

First I look at motions of individual assemblies while assuming all others are stable and perfectly aligned. Then I consider the most significant coupled error motions. The coordinates X, Y, Z are a coordinate frame referenced to the machine base. I show this coordinate system in several figures with different origins. The coordinate system is used only as a stable reference for orientation.

4.1 Metrology block error motions

The coordinates Xm, Ym, Zm describe the motion of the metrology block assembly. These coordinates are always [0,0,0] if the metrology block does not move relative to the base. Pure rotations (without any translations) of the metrology block θ_{Xm}, θ_{Ym}, and θ_{Zm} are defined to occur about the nominal intersection of the interference lithography beams, which occurs in the write plane. When $[\theta_{Xm}, \theta_{Ym}, \theta_{Zm}] = [0, 0, 0]$ the axes Xm, Ym, and Zm are parallel to the X, Y, and Z axes respectively.

Figure 4-1 shows a model of the metrology block optics. The figure shows a pickoff that directs beams from the left and right arms of the interference lithography system

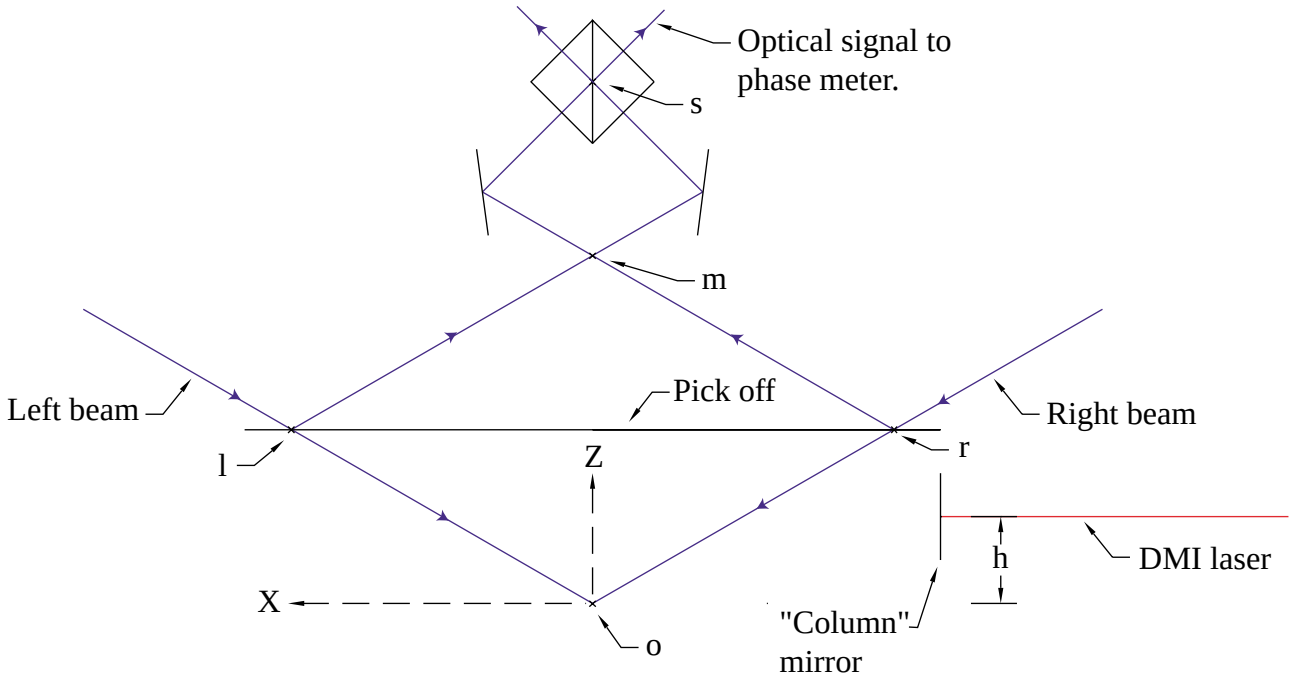

Figure 4-1: Metrology block assembly.

to an optical assembly that recombines the beams to produce a phase signal. The beams are recombined with a beam splitter. The column mirror for the x axis DMI is also attached to the metrology block assembly. Rigid body error motions of the metrology block consider errors when the whole metrology block assembly moves as a rigid body. Thus, the components moving together are the pick off, the directing mirrors after the pickoff, the beam splitter, and the stage column reference mirror. In the figure, the optics of the metrology block are shown folded up so all the optical paths lie in a plane. This reflected image of the metrology block gives identical results as for the real configuration where the pickoff is angled. I elaborate more on the mirror symmetry of the folded and unfolded optical systems in the next sections.

4.1.1 Metrology block translations

For displacement of the metrology block in the Xm direction, consider Figure 4-2. Here the nominal beams into the metrology block optical assembly are shown in solid

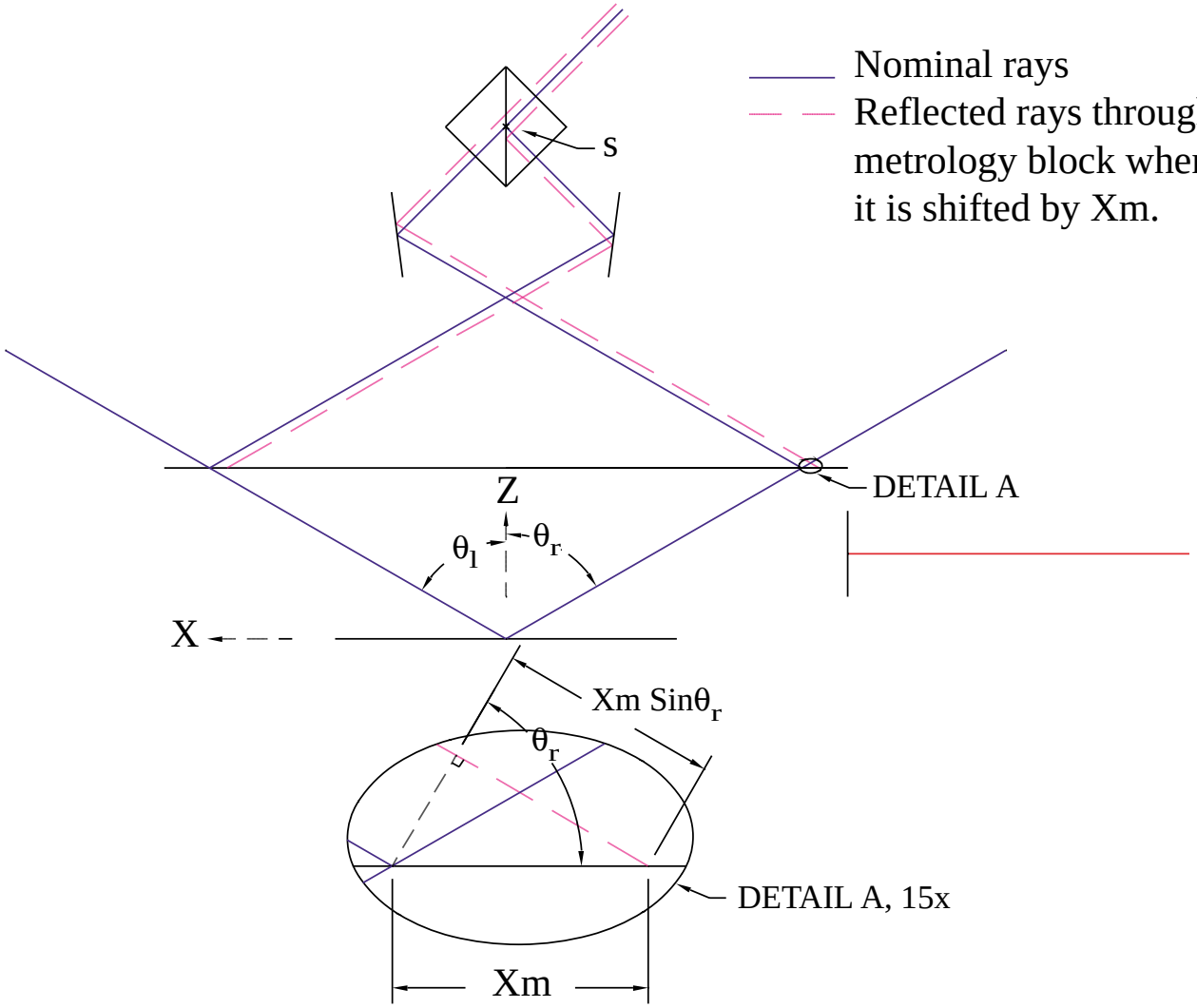

Figure 4-2: Metrology block assembly showing nominal rays and rays reflected from the pickoff when the metrology block assembly is shifted by Xm.

lines. The dashed lines are the reflected ray positions when the metrology block is shifted by Xm in the positive X direction. The optical path difference of the right arm minus the left arm due to the position shift is

$$OPD_{right-left} = n_{air} Xm \left(\sin\theta_r + \sin\theta_l\right) = n_{air} Xm 2 \sin\theta \cos\epsilon \tag{4.1}$$

where θ is the half angle given by

$$\theta = \frac{\theta_l + \theta_r}{2} \tag{4.2}$$

and ϵ is the rotation of the interference half-angle plane from the Z axis about the positive θ_Y (rotation about the Y axis) direction. The variable ϵ is given by

$$\epsilon = \frac{\theta_l - \theta_r}{2}. \tag{4.3}$$

The variable n_{air} is the index of air. The phase reading in radians for the metrology block interferometer is given by

$$\phi_m = \frac{2\pi OPD_{right-left}}{\lambda_{il}}. \tag{4.4}$$

The vacuum wavelength of the interference light is λ_{il}. In practice, the phase reading also includes phase errors induced above the pickoff by index variations and vibrations or otherwise. We want the phase measurement signal to include these too. In this section on error motions, I am dropping any terms associated with disturbance above the pickoff. Using Equation 4.1 and the period of the fringes, the phase reading is

$$\phi_m = \frac{2\pi n_{air} Xm 2 \sin\theta \cos\epsilon}{\lambda_{il}} = \frac{2\pi Xm}{\Lambda_{Xm}}. \tag{4.5}$$

Here Λ_{Xm} is the period of the interference fringes measured along the Xm axis of motion.

The translation of the metrology block also causes an optical path difference in

the DMI. The stage interferometer phase in radians for the x axis is given by

$$\phi_x = \frac{2\pi n_{air}(Xs - Xm)n}{\lambda_{DMI}}. \tag{4.6}$$

The variable Xs is the stage position along the stage X axis, λ_{DMI} is the vacuum wavelength of the DMI, and n equals 4 for our double pass interferometer. For now I am assuming the column beams of the DMI are parallel to the stage beams. The error signal, ϕ_{fle}, to the fringe locking control system is

$$\phi_{fle} = \phi_m - K_s\left(\phi_r - \phi_x\right). \tag{4.7}$$

Here ϕ_r is a reference phase, which for SBIL writing would be constant during a scan if the fringes are aligned parallel to the Ys axis. The error signal when the fringes are not exactly aligned to Ys will be considered in Section 4.3. Setting the scale factor to

$$K_s = \frac{\lambda_{DMI}}{n\Lambda_{Xm}}, \tag{4.8}$$

produces

$$\phi_{fle} = \frac{2\pi Xs}{\Lambda_{Xm}} - K_s\phi_r, \tag{4.9}$$

which has no Xm term. Thus translations of the metrology block in the Xm direction do not induce erroneous fringe shifts.

The exact optical configuration (i.e. number of mirrors and there orientation) in the metrology block assembly in general is unimportant as far as phase changes due to translation are concerned. To see this, lets make the metrology optics a "black box" as shown in Figure 4-3. In here the left and right arms of the interferometer reflect from some unknown number of mirrors and pass through unknown pieces of glass before being combined by a beam splitter. The nominal ray positions before the black box is shifted is shown as the solid line. The ray positions when the optics are shifted by Xm are shown as the dashed lines. If the phase fronts going into and leaving the black box are flat then the OPD due to a position shift Xm is given by Equation 4.1. The detailed optical path differences are shown in Detail A and Detail

B. The right arm gets lengthened by $Xm \sin\theta_r$ and the left arm get shortened by $Xm \sin\theta_l$. This result is completely general with the only requirement being that the surfaces in the metrology system be flat and that the incoming beams have flat wavefronts. Non flat surfaces and non flat incoming beams will contribute errors. However, these errors are expected to be small because the beams are expected to "walk" along the optics a very small distance compared to the spot size. Furthermore, we use high quality optics and the incoming beams are required to be very flat for SBIL. Non flatness of the correct symmetry will also not produce errors.

Equation 4.1 also applies to the beam splitter on the chuck that is used for period measurement. By scanning the stage in the Xs direction, which is very parallel to the column beam direction, we can obtain a very accurate measurement of Λ_{Xm}. This result fits into the calculation of K_s in Equation 4.8.

Translations Ym and Zm of the metrology block do not change the phase of the optical signal if the interference fringes are aligned along the $Ym - Zm$ plane. This will never be exactly true so alignment requirements are imposed by small motions. For instance, if these motions are 100 nm due to vibration, thermal expansion or otherwise, alignment of 100 μrad will produce an error of 0.01 nm. Since these alignment and displacement stability requirements are achieved, correcting for Ym and Zm motions is unnecessary in our system. The good alignment of the fringes in the $Ym - Zm$ plane are a consequence of the SBIL beam alignment system and a carefully aligned reference beam splitter.

4.1.2 Metrology block rotations

For metrology block rotation θ_{Ym}, consider Figure 4-4. Here the rays and optical components of the unrotated metrology block assembly are shown in solid lines. The rays and optical components for the assembly rotated by θ_{Ym} about point o are shown in dashed lines. Point o is the intersection of the rays, which lie in the nominal write plane. I have shown crosses for illustration purposes at point m, l, and r. I have included the crosses with the rotated version of the metrology block assembly where the crosses moved with the assembly. The selection of rotation about point o is a

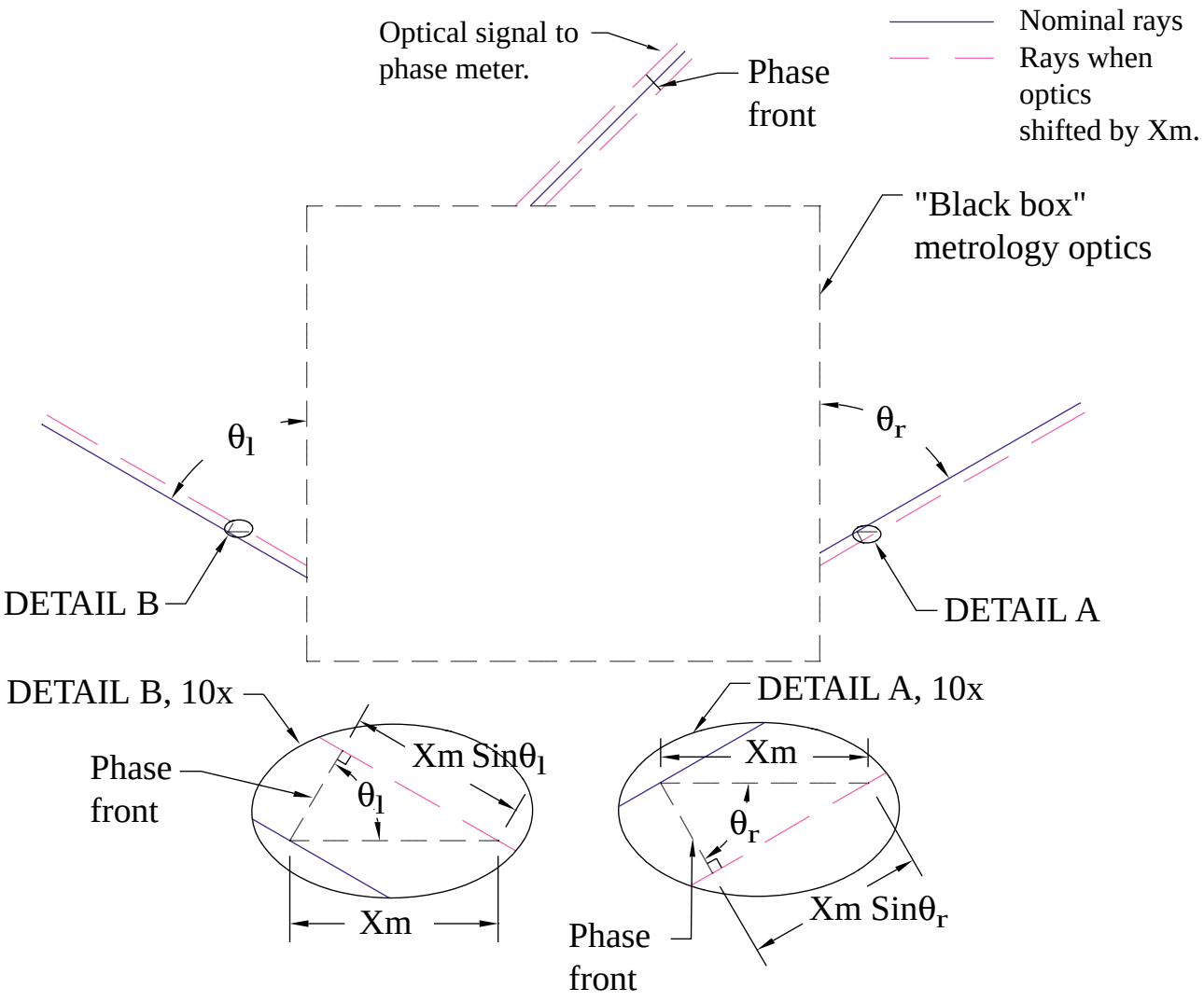

Figure 4-3: "Black box" metrology optics block assembly showing nominal rays and rays when the metrology block assembly is shifted by Xm.

very convenient choice. In this case the intersection of the rays after reflection off the pickoff, at point m', coincides with the cross that was at point m for the unrotated assembly. Since the reflected rays from l' to m' and r' to m' are the mirror image of l' to o and r' to o, there is no optical path difference in the reflected rays up to m'.

Now consider Figure 4-5. Here I am showing just the portion of the assembly after point m. The solid lines are the rays through the assembly for the unrotated block. The dashed lines are the rays when the block is rotated by θ_{Ym} about point o. The interfering rays have a half angle of θ_{Ym} if the beams were originally perfectly aligned. Any angle between the rays produces a linear fringe pattern at the detector. The phase of the power signal has the same phase as the intensity in the center of the overlap region (see Section 4.6 for verification). This center is located at point s. The optical path difference of the right minus the left due to the rotation θ_{Ym} is

$$OPD_{\theta_{Ym}} = (\bar{ms}_r - \bar{ms}_l)\left(\frac{1}{\cos\theta_{Ym}} - 1\right). \tag{4.10}$$

Here $\bar{ms}_r$ and $\bar{ms}_l$ are the optical path distances from point m to point s for the right and left arms respectively. Thus the optical path difference at the metrology block phase meter is a cosine type error proportional to the misbalanced path lengths in the interferometer. For $\theta_{Ym} \approx 0$,

$$OPD_{\theta_{Ym}} \approx (\bar{ms}_r - \bar{ms}_l)\frac{{\theta_{Ym}}^2}{2}. \tag{4.11}$$

If the beams are not nominally perfectly aligned coming out of the splitter the optical path difference due to θ_{Ym} is

$$OPD_{\theta_{Ym}} \approx (\bar{ms}_r - \bar{ms}_l)\frac{(\theta_{Ym} + \alpha_m)^2 - \alpha_m^2}{2} = (\bar{ms}_r - \bar{ms}_l)\frac{\theta_{Ym}^2 + 2\alpha_m\theta_{Ym}}{2}. \tag{4.12}$$

which is further approximated as

$$OPD_{\theta_{Ym}} \approx (\bar{ms}_r - \bar{ms}_l)\,\alpha_m\theta_{Ym} \tag{4.13}$$

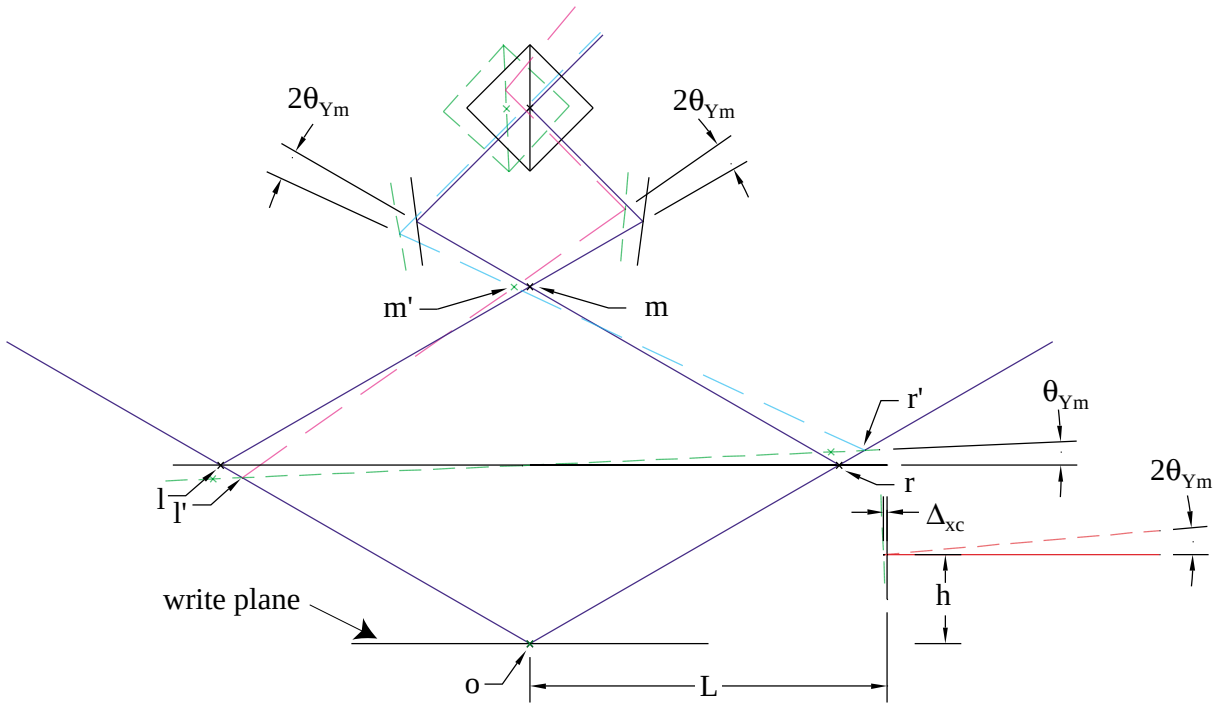

Figure 4-4: Metrology block assembly showing rays and components before and after rotation of assembly about point o by θ_{Ym}.

when α_m is much greater than θ_{Ym}. The variable α_m is the nominal "misaligned" half angle of the interfering beams that are combined in the splitter. Equation 4.13 is similar to the alignment requirement derived in [71] for another interferometer. This type of an alignment requirement is a recurring property of interferometers. As an example, for a path length misbalance of 1 cm and $\alpha_m = 100$ μrad, $\theta_{Ym} = 1$ μrad, the OPD_{Ym} is 10^{-12} meters. Thus the effect of rotation about point o on the phase meter signal is negligible. The test point signal of the Zygo interferometer cards provides feedback for alignment. By maximizing the interferometer signal strength, better alignment tolerance for α_m is achieved. Normally pathlength misbalance within the metrology block optics would cause errors due to index of air changes. In our system, the refractometer is calibrated to correct for the pathlength misbalance in the metrology block optics.

The Abbe offset of the column reference mirror has a relatively large effect on the stage interferometer's accuracy. The displacement of the point on the mirror where

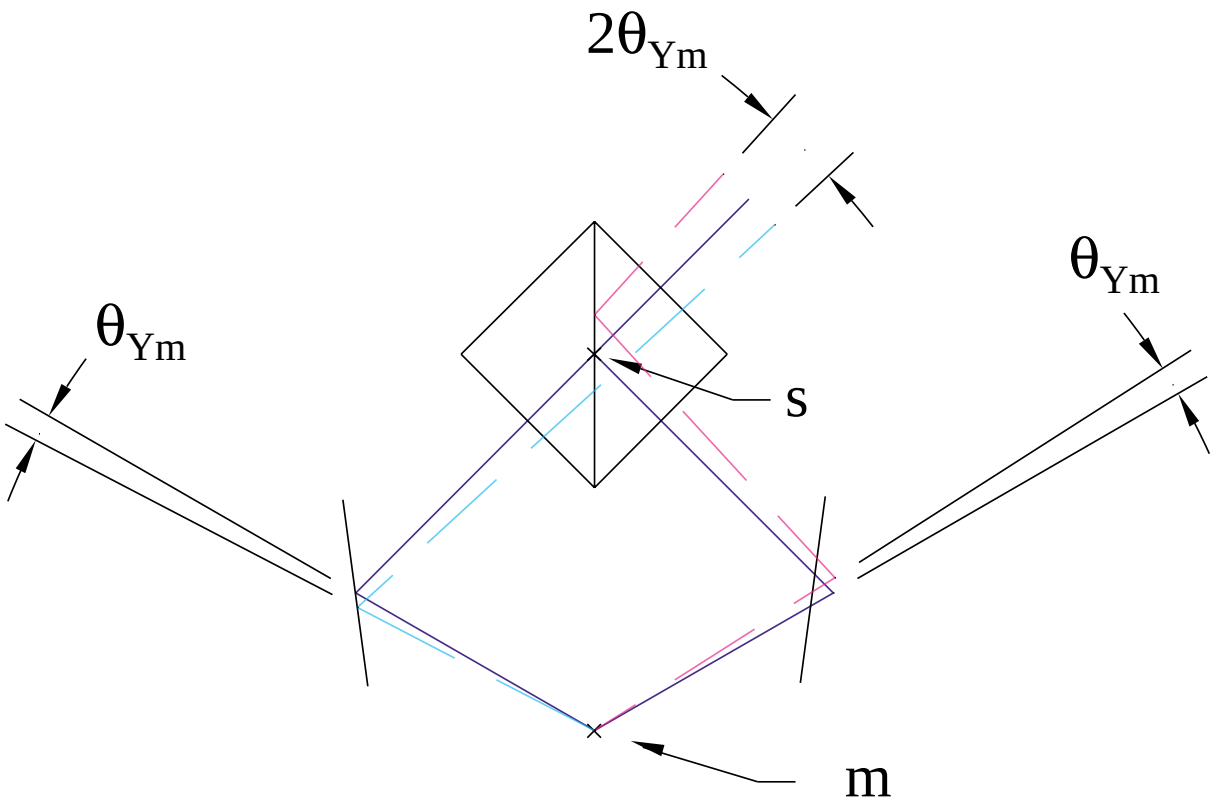

Figure 4-5: Portion of the metrology block assembly showing rays through the metrology block before and after rotation of assembly about point o by θ_{Ym}. The solid lines are the rays for the unrotated block. The dashed lines are the rays when the block is rotated by θ_{Ym} about point o.

the intersection occurs as shown in Figure 4-4 is

$$\Delta_{xc}, \theta_{Ym} = h \tan \theta_{Ym} + L \left(1 - \frac{1}{\cos \theta_{Ym}}\right). \tag{4.14}$$

For $\theta_{Ym} \approx 0$, this relation is approximated by Taylor series expansion to

$$\Delta_{xc}, \theta_{Ym} \approx h\, \theta_{Ym} - L\frac{\theta_{Ym}^2}{2}. \tag{4.15}$$

The left term is a sine term proportional to h the right term is a cosine type error proportional to L. For our system, L is 0.17 m and assuming $\theta_{Ym} = 1$ μrad the cosine error term contributes a negligible 8.5×10^{-14} m. The sine term unfortunately

is not likely to be negligible. The beam spacing of the column reference interferometer sets h and for our interferometer, $h = 1.9$ cm. Thus the error for only 0.1 μrad of the metrology block rocking in θ_{Ym} is 1.9 nm. We use the commercially available interferometer: Zygo #6191-0615-01, Special Column Reference Interferometer. This is a version of the #6191-0615-01 modified with a fold mirror to change the side of the entrance beam. I discuss this interferometer in detail in Section 4.4. Another interferometer design is not likely to reduce h by much for practical reasons. The laser beams are 3 mm in diameter and sufficient spacing is required to prevent mixing. Also, roll off (non flatness) near the edges of mirrors is a characteristic of polishing processes and the flatness requirement will set a practical limit on closer beam spacing. In section 4.5, I discuss that this "pitch" error depends of the motion of the metrology block relative to the interferometer head.

The pitch also causes a cosine type error in the stage interferometer [118]. The apparent lengthening of the column reference path due to θ_{Ym} is given by

$$\Delta_{xc}, col = \frac{L_c}{2}\left(\frac{1}{\cos(2\theta_{Ym})} - 1\right). \tag{4.16}$$

Here L_c is the length of the column reference path. The pitching of the stage mirror causes the measurement beam to translate at the interferometer output without changing angular orientation in a double pass interferometer. This property makes the double pass interferometer signal power relatively insensitive to alignment compared to a single pass interferometer that uses a plane mirror target (i.e. Michelson interferometer). When θ_{Ym} is much less than one, Equation 4.16 simplifies to

$$\Delta_{xc}, col = L_c\theta_{Ym}^2. \tag{4.17}$$

When the column reference mirror has some mean misalignment α_c, this equation is modified to be

$$\Delta_{xc}, col \approx L_c\left((\theta_{Ym} + \alpha_c)^2 - \alpha_c^2\right). \tag{4.18}$$

Again this cosine error is negligible. For our system $L_c = 0.26$m, so for very bad

alignment and angle stability specifications of $\alpha_c = 1$ mrad and $\theta_{Ym} = 0.1$ μrad the error contribution is only 0.05 nm. While these angular variations and alignments are much worse than what I believe is actually achieved, this example serves to convince that the cosine error term can be ignored.

Another rotation to consider is θ_{Zm}. To help picture what happens when the pickoff is angled like in the real SBIL system, let's consider Figure 4-6. Here the pickoff is shown in its initial state along with the partial beam paths. Figure 4-7 shows the same pick off but rotated by $-10°$ in θ_{Zm}. The ray trace of the beam paths is geometrically accurate. I rotated the cross at point m with the pickoff as a rigid body. The important point as seen in the figure is that the intersection point rotates with the metrology block for rotations of the metrology about point o. An alternative way of looking at the problem, is to mirror flip the metrology block down such that point m in Figure 4-4 coincides with point o. From here the problem reduces to calculation of the optical path difference after point m. The problem is similar to that shown in Figure 4-5 but the rays will sweep a cone. The result of rotation by θ_{Zm} is a cosine type error that is dependent on the period that is being written. The optical path difference sensed by the metrology block optics due to the θ_{Zm} rotation is given by

$$OPD_{\theta_{Zm}} = (\bar{ms}_r - \bar{ms}_l)\left(\frac{1}{\cos\gamma} - 1\right). \tag{4.19}$$

Here γ is the angle formed between the nominal beams and the beams when the metrology block is rotated by θ_{Zm}. Rotation of the block by θ_{Zm} rotates the beams through a cone with its vertex at point m. Using the dot product [4] to calculate the angle between the nominal and rotated beams $\cos\gamma$ is calculated as

$$\cos\gamma = \frac{\mathbf{a} \bullet \mathbf{b}}{|\mathbf{a}||\mathbf{b}|}. \tag{4.20}$$

The vector $\mathbf{a}$ is given by

$$\mathbf{a} = [\sin\theta, 0, \cos\theta] \tag{4.21}$$

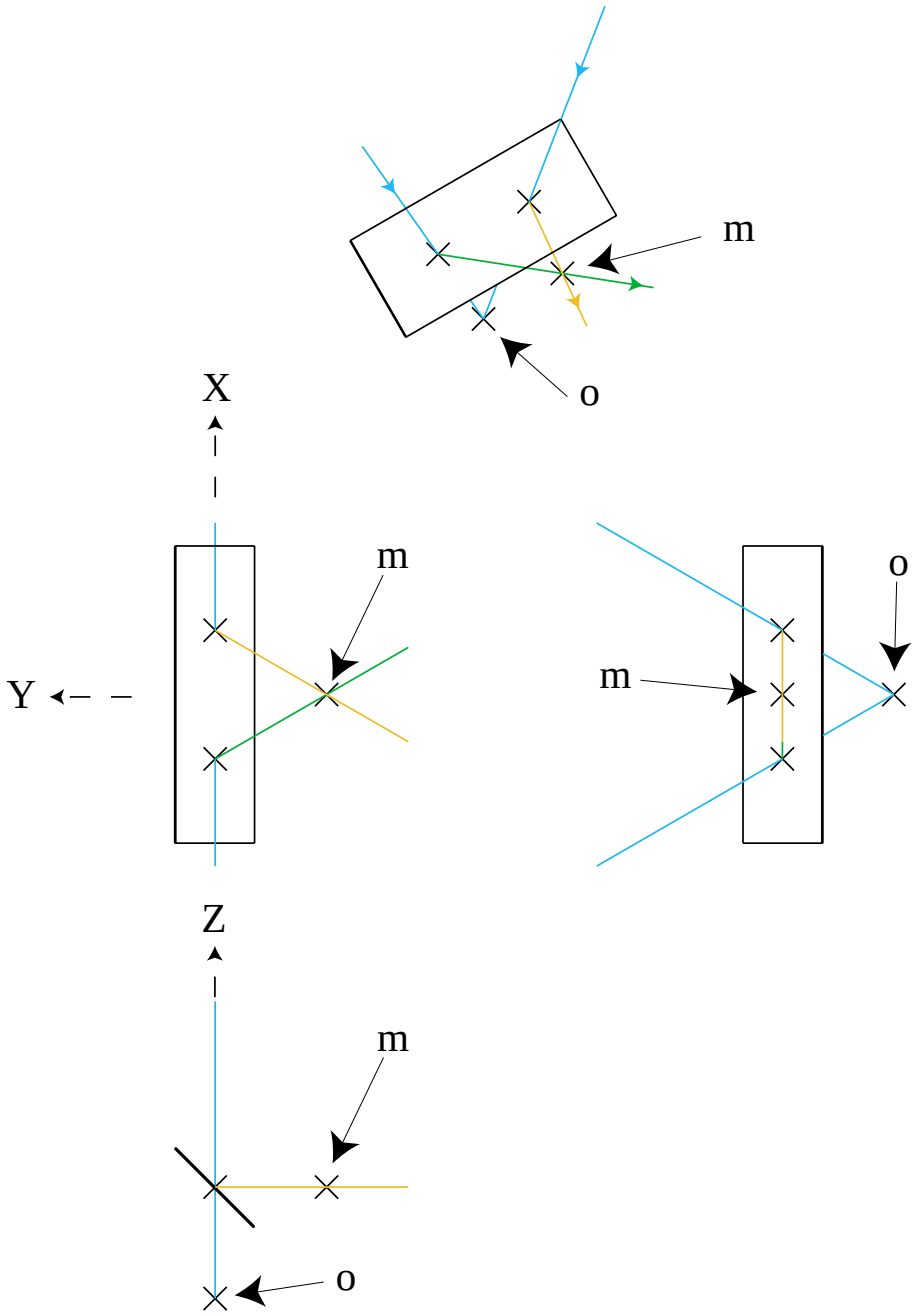

Figure 4-6: Pick off and laser beam paths for the metrology block pickoff. The top figure shows the isometric view and the bottom three figures show orthogonal views. The intersection point o lies nominally in the write plane. The mirrored intersection point is point m.

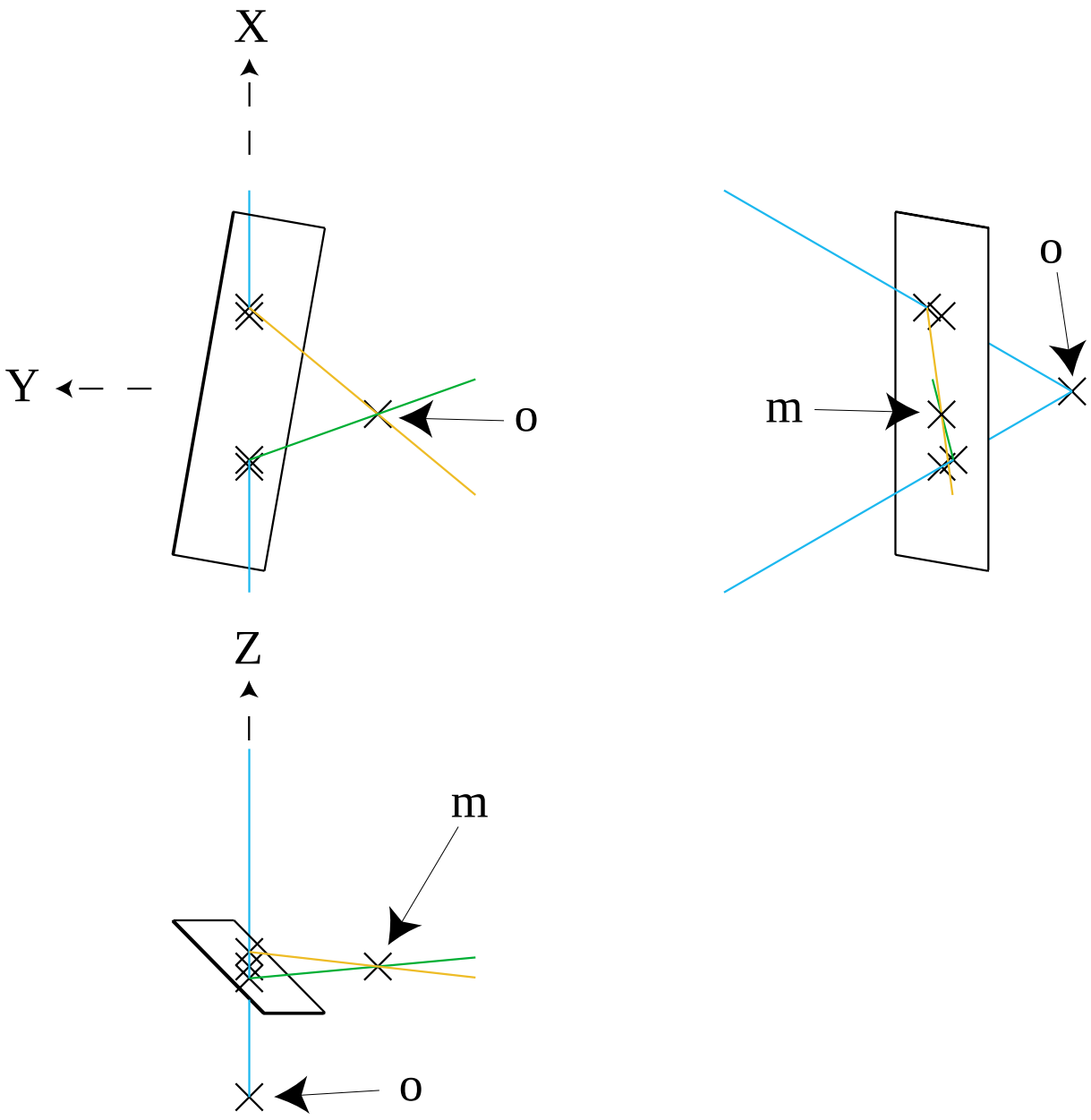

Figure 4-7: Orthogonal views for the pick off and the laser beam paths for the metrology block pickoff when θ_{Zm} is exaggerated at $-10°$.

and the vector $\mathbf{b}$ is given by

$$\mathbf{b} = [\sin\theta\cos\theta_{Zm}, \sin\theta\sin\theta_{Zm}, \cos\theta]\,. \tag{4.22}$$

The angle θ is the interference half angle, which defines the period. The optical path difference after applying Equations 4.19-4.22 and Taylor series expanding is then approximated as

$$OPD_{\theta_{Zm}} \approx (\bar{ms}_r - \bar{ms}_l)\,\frac{1}{8}\left(\frac{\lambda_{il}}{n_{air}\Lambda}\right)^2 \theta_{Zm}^2. \tag{4.23}$$

The term $\lambda_{il}/(n_{air}\Lambda)$ can be 2 at the largest. Comparing Equation 4.23 to Equation 4.11, the OPD sensitivity due to θ_{Zm} will be less than that of θ_{Ym}. Both cosine error terms will be negligible.

The Abbe offset associated with θ_{Zm} is an important consideration. If point o does not have the same Y coordinate as the effective column reference beam location then an Abbe offset exists. If the point o is offset in the positive Y direction by a distance Δ_{yc} from the column beam location on the column reference mirror then the column reference path is lengthened by

$$\Delta_{xc}, \theta_{Zm} = L\cos\theta_{Zm}\,(1 - \cos\theta_{Zm}) + \Delta_{yc}\sin\theta_{Zm}. \tag{4.24}$$

For $\theta_{Zm} \approx 0$, this relation is approximated by Taylor series expansion to

$$\Delta_{xc}, \theta_{Zm} \approx L\frac{\theta_{Zm}^2}{2} + \Delta_{yc}\,\theta_{Zm}. \tag{4.25}$$

.

The cosine error proportional to L is negligible. The sine error term proportional to Δ_{yc} is expected to be small. By design Δ_{yc} is zero in our system but considering part and alignment tolerance I expect that Δ_{yc} is less than 1 mm. Thus for $\theta_{Zm} = 0.1$ μrad, the error contribution is expected to be less than 0.1 nm. It would be possible to better position point o on our system to further reduce the sensitivity to θ_{Zm}. In section 4.5 I will consider error correction.

The rotation of the column mirror in θ_{Zm} will also produce another cosine error in the stage interferometer similar to that in Equation 4.18 for θ_{Ym}. This term can be safely neglected for the expected angle and alignment parameters.

4.2 Lithography beam instability

The lithography beams have some small angular and position instability. The magnitude of this instability is mainly limited by the beam steering performance discussed in Chapter 6. For discussion purposes, the beams are stable to several μrad in position and 10 microns in position. Because we use a grating beam splitter, the grating image period is insensitive to angle variations of the incoming beam. Also, the overlap of the beams on the substrate is nominally preserved if the incoming beam are unstable in position. In addition to the beam steering performance limitation, there are additional optical paths in the SBIL system where the beams can be disturbed. The magnitude of the additional disturbance is expected to be much smaller than the beam steering performance. However, the fringe period and the beam overlap may change due to these disturbances. The effect of angle instability on the beam period is discussed in Chapter 6. Here I discuss the effect on the phase measurement.

In Figure 4-8, I show the metrology block optics and beam paths for the nominal beams and beams deviated in angle. The right beam is deviated by α_r and the left beam is deviated by α_l. In the figure I am considering the case where the beams are perfectly overlapped at the substrate. The center of the grating image is at point o. The reflected image of point o is at m. To calculate the optical path difference I first unfold the beam paths as shown in the lower left figure. Detail A shows the distances for calculating the OPD. There are two point m's in the detail, one from unfolding the left side and one from unfolding the right side. The phase of the power signal is the phase of the intensity at the center of the interference image, which will have the phase of the intensity at the location of point q. The ray from the right beam was extended to intersect the left beam. The intersection is point q. The change in OPD of the left arm minus the right arm due to the beam instability is given by

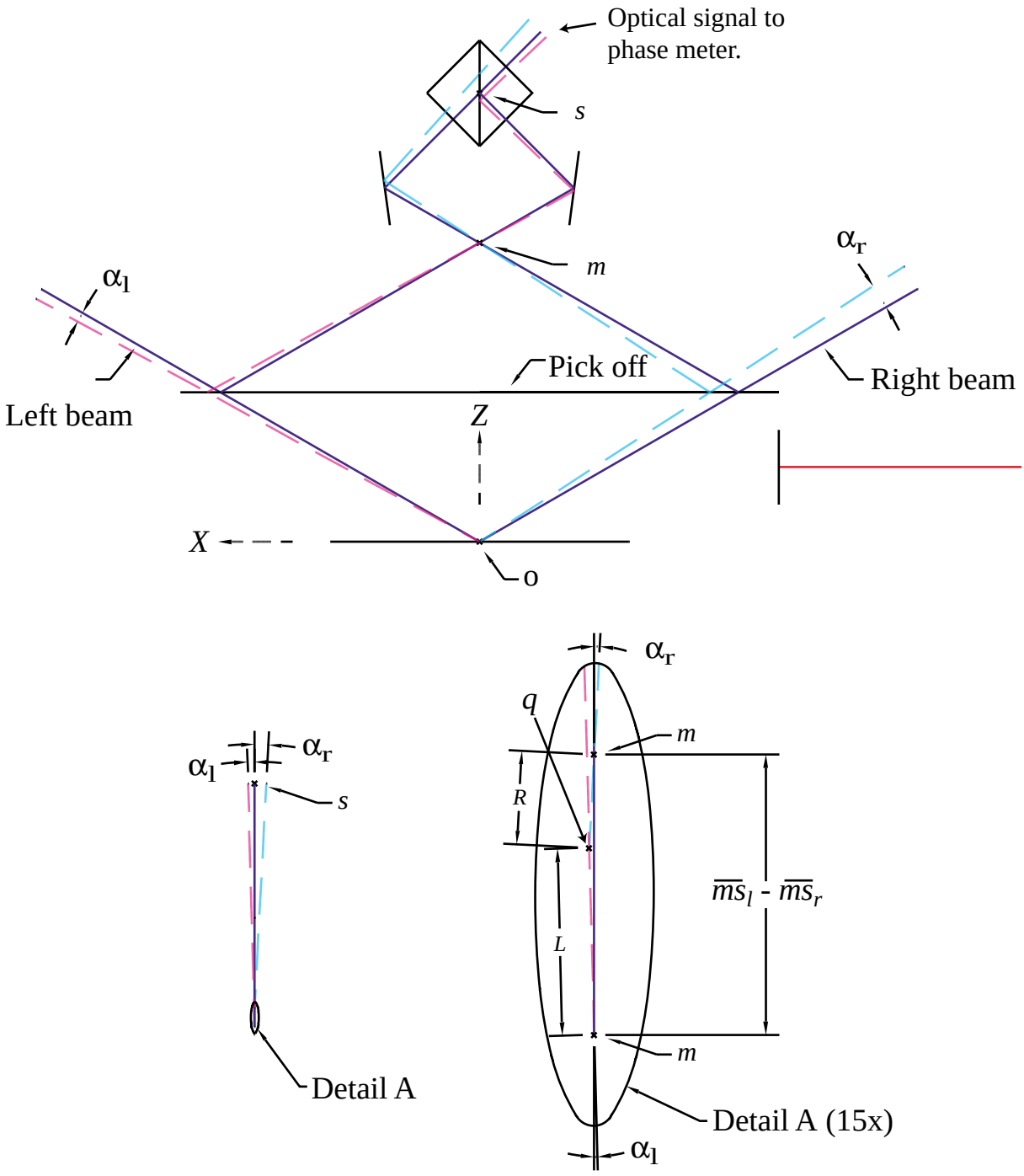

Figure 4-8: Metrology block optics and ray paths for the nominal beams and beams with angular instability. The lower left corner figure shows unfolded beam paths of rays after point m. The lower right figure shows the detailed paths for calculating the optical path difference.

$$OPD(\alpha_r, \alpha_l) = L + R - (m\bar{i}s_l - m\bar{i}s_r)\,. \tag{4.26}$$

The distances L and R, are shown in the figure. I will assume the air index is one and will not explicitly include it in the optical path distance calculation. The path length misbalance, $(m\bar{i}s_l - m\bar{i}s_r)$, is also shown. The distances are calculated using basic trigonometry and the OPD becomes

$$OPD(\alpha_r, \alpha_l) = (m\bar{i}s_l - m\bar{i}s_r)\left(\frac{\sin\alpha_l + \sin\alpha_r}{\sin(\alpha_l + \alpha_r)} - 1\right) \tag{4.27}$$

For α_l and α_r very small, the OPD can be approximated by Taylor series expansion to obtain

$$OPD(\alpha_r, \alpha_l) \approx (m\bar{i}s_l - m\bar{i}s_r)\,\frac{\alpha_l\alpha_r}{2}. \tag{4.28}$$

This equation shows that the phase measurement is insensitive to the angular stability of the beams. Even for the unrealistic case of a path length misbalance of 1 cm and angular instabilities of 100 μrad, the error is only 0.05 nm. This error can be safely ignored. For consideration of angle instability out of the plane of the figure, the calculation for errors is similar.

The lithography beams are unstable in position as well as in angle. The position instability of the beams is on the order of ± 10 μm. The effect of this position instability leads to small dose fluctuations for the exposure. For the assumption of plane waves, translation of the beams perpendicular to the axis of propagation have negligible effect on the phase.

4.3 Stage Motions

The coordinates Xs, Ys, Zs describe the motion of the stage assembly. These coordinates are [0,0,0] at the homed location, where the limit switches are located. These coordinates do not change if the stage does not move relative the machine base. Pure rotations of the stage $[\theta_{Xs}, \theta_{Ys}, \theta_{Zs}]$ are defined to occur about the nominal intersec-

tion of the interference lithography beams.

Figure 4-9 shows the stage metrology for the SBIL system. The chuck and interferometer heads are shown. The model of interferometer used for both axes is a linear-angular model. The interferometers produce four beams that reflect from the stage mirror and four beams that reflect from the column mirror. The stage measurement beams for the linear axes are the two closest to the entrance side of the interferometer. The x and y interferometers are different "left" and "right" versions where the side of the entrance beam is flipped and the optics are mirror symmetric. The remaining two beams are for yaw measurement. The two linear measurement beams are effectively measuring the average displacement of each beam. I have drawn an "x" at the effective linear measurement point on each mirror. Point p is the intersection of the x measurement axis with the x coordinate where the y measurement axis crosses it. Point o is the center of the grating image in the write plane. The offset Δ_x, Δ_y and Δ_z are also shown and are described in the next section.

First, I consider the stage displacement error motions. The error of interest is displacement perpendicular to the grating image. The grating image is aligned very parallel to the Ys axis but may have some angle α to the Ys axis as shown. After implementing high quality optics and an alignment system, the angle of the fringes is typically very small, i.e. $\alpha < 100\mu$rad. The angle of the fringes can be measured to sub μrad levels. Given that the spot is on the order of a millimeter in radius, the scan direction should be aligned to the image to better than 1 μrad to prevent more than 1 nm of "smearing". Similarly, the smearing produces a small contrast loss if α is known to a μrad and the stage scans along this angle. The stage yaw as it moves (which is largely repeatable) also leads to smearing. The measured stage yaw using an autocollimator is 1.9 μrad TIR for y axis motion and 1.5 μrad TIR for x axis motion so in our system there is a small amount of smearing dominated by the stage yaw motion. Removal of this smearing would require either a straighter stage, rotation of the fringes during stage scan, or controlling stage rotation. Since the smearing is small and is largely a small contrast loss in our system, it is not a concern. Stage yaw over displacements with spatial periods less than the size of the spot are expected to

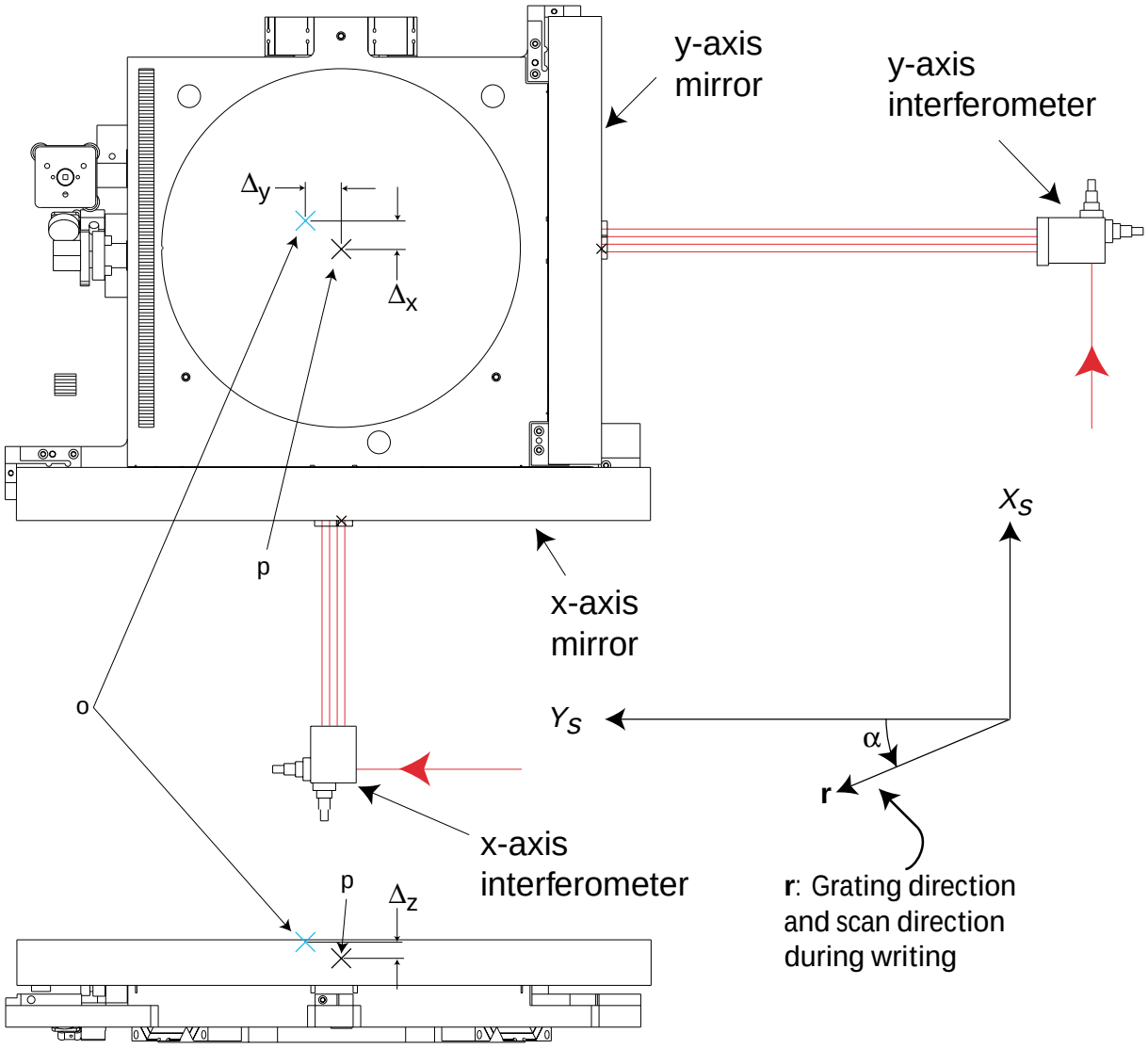

Figure 4-9: SBIL stage metrology showing interferometers, chuck, and Abbe offset definitions.

be less than 0.1 μrad over the sub 100 Hz frequency range of interest and will lead to negligible phase errors. Furthermore, any phase errors due to stage yaw as a function of position are largely repeatable and can be corrected.

The revised version of Equation 4.7 considering the angle of the fringes is given by

$$\phi_{fle} = \phi_m - K_s \left[\cos\alpha \ \ (\phi_{rx} - \phi_x) + \sin\alpha \ \ (\phi_{ry} - \phi_y)\right]. \tag{4.29}$$

Here ϕ_{rx} and ϕ_{ry} are reference phases for the x and y axes, respectively. During the constant velocity portion of the scan, these reference phases vary according to

$$\phi_{rx}(t) = \phi_{rx}(0) + \frac{2\pi n_{air} \sin\alpha \, vt}{\lambda_{DMI}} \tag{4.30}$$

and

$$\phi_{ry}(t) = \phi_{ry}(0) + \frac{2\pi n_{air} \cos\alpha \, vt}{\lambda_{DMI}} \tag{4.31}$$

where $\phi_{rx}(0)$ and $\phi_{ry}(0)$ are the phases at the beginning of the constant velocity portion of the scan. The variable v is the stage velocity and t is the time. Both the stage controls and the fringe locking controls are designed to keep ϕ_{fle} as small as possible. The variable ϕ_y is given by

$$\phi_y = \frac{2\pi n_{air} \, nYs}{\lambda_{DMI}}. \tag{4.32}$$

Note that the y axis phase measurement does not have a Ym term. This is because the column reference beams are blocked at the interferometer head in the current implementation. Although the metrology block has a column reference mirror for the y axis and the y axis interferometer head has column reference beams, I chose not to implement this functionality. The column dynamics for the y axis would lead to a lower bandwidth controller, higher stage vibrations, and less smooth scanning. Moreover, the high frequency disturbance in the y direction can couple into the x axis. Furthermore, since pure y axis errors hardly contribute to the writing errors and the additional errors due to granite expansion and the extra dead path are very

tolerable, the y axis column reference was never implemented.

The scale factor K_s is also redefined as

$$K_s = \frac{\lambda_{DMI}}{n\Lambda n_{air}}, \tag{4.33}$$

where Λ is the period of the fringes measured perpendicular to them and is very close to Λ_{Xm} for small α. There is a negligible cosine error if the fringes are measured along X_m and not perpendicular to them. The stage error correction for the y axis is not usually significant. However, for fast accelerations and velocities and minimal "settling time", the y axis stage error may be in the micron range. For one micron of stage error and $\alpha = 100$ μrad the correction amounts to 0.1 nm of fringe motion on the substrate. Thus, under expected circumstances removing the y axis error from the fringe locking error signal would be acceptable.

The last stage translation to consider is stage motion Zs. The nonrepeatable Zs motion is expected to be significantly less than 100 nm. Thus for a fringe tilt of 100 μrad with the Zs axis, the error associated with this motion is expected to be 0.01 nm and is negligible. The substrate thickness variation of 10 μm causes a significant 1 nm of error for 100 μrad of fringe tilt, however. This type of error will not be readable if the substrate is read while located in the same position where it was written. The fringe tilt is set by the beam splitter alignment since the beams are aligned to overlap through the spitter. The current beam splitter alignment is 50 ± 50 μrad. The alignment and uncertainty will eventually need to be improved to about 10 μrad for substrates with 10 μm of thickness variation (or 10 μm of non flatness for thick substrates) when allotting 0.1 nm to the error budget.

4.3.1 Stage rotations

Stage rotations lead to Abbe errors and cosine errors if the grating image is not co-located with the intersection of the interferometer beams. Referring to Figure 4-9, the Abbe offset Δ_x (shown positive) is the offset in the X direction of the grating image from the y measurement axis. The Abbe offset Δ_y (shown positive) is the offset in

the Y direction of the grating image from the x measurement axis. The Abbe offset Δ_z (shown positive) is the offset in the Z direction of the grating image from the x measurement axis.

The cosine terms and cross coupling terms are negligible for the expected stage rotations and alignment tolerances. As a consequence, the fringe placement error is not sensitive to Δ_x. For rotation of the stage about the grating image point p, the stage measurement path is lengthened by

$$\Delta_{xs} \approx \Delta_y \, \theta_{Zs} - \Delta_z \, \theta_{Ys}. \tag{4.34}$$

The offset Δ_z will depend on the height of the substrate and alignment. Also, Δ_z may change with the position of the stage. This would happen if the substrate is not flat and level or if the stage did not travel in a flat plane. Also if the interferometer was aligned to a mirror that had a pitch that was not orthogonal to the plane of motion, then Δ_z would change with the stage position.

The pitch of the stage interferometer mirror on the SBIL system is about 50 μrad. Thus for $\pm$150 mm of travel, the Abbe offset variation due to this effect is 8 microns. The interferometer system was aligned for Δ_z to be as small as possible for 650 micron wafers. This was done by first visually aligning the center of a pinhole on a stable stand to the edge of a 150 mm diameter wafer that was on the chuck. The surface of the chuck was previously leveled to the plane of motion to better than 2 microns TIR (the granite flatness is 1.3 μm TIR and is part of this error). The pinhole was then moved to verify the height of the stage interferometer beams. I expect the beams are aligned to the plane of the substrate to about $\pm$ 200 microns. The range of thickness for substrates in the SBIL system is expect to be $\pm$200 microns. Thus Δ_z is expected to be $\pm$400 microns. For θ_{Ys} of one μrad, the Abbe error is 0.40 nm. However, the nonrepeatable θ_{Ys} over the frequency range of interest is smaller. For 0.05 μrad, the error is 0.02 nm.

The offset Δ_y is designed to be nominally zero but it depends on the alignment of the lithography beams. I expect this offset to be less than 1 mm and can be reduced

by better alignment. For θ_{Zs} of one μrad, the associated Abbe error is expected to be less than 1 nm. Again, the nonrepeatable angle stability over the frequency range of interest is smaller. For 0.05 μrad, the error is 0.05 nm.

4.4 Interferometer head motions

The coordinates Xix, Yix, Zix describe the motion of the x axis interferometer. These coordinates are always [0,0,0] if the interferometer does not move relative to the base. Pure rotations of the interferometer $[\theta_{Xix}, \theta_{Yix}, \theta_{Zix}]$ are defined to occur about the centroided location of the spots in the polarization beam splitter interface plane.

As already mentioned, we use a commercially available interferometer head available from Zygo Corporation. Unfortunately, the Zygo documentation has confusing and inaccurate drawings of the interferometer topology. I even received nonsensical descriptions of the interferometer from Zygo employees. After piecing together several sets of information including observations of the interferometer head itself, the Zygo documentation, and information from Zygo employees, I believe the topology of the optics is that depicted in Figure 4-10. Since some of the optics are not easily visible, I made some assumptions about some of the component sizes and exact component placement. The interferometer head is provided in an electroless nickel plated magnetic stainless steel housing. The interferometer is a double pass design with column referenced linear and angle axes. The entrance beam reflects from the right angle prism into the polarizing beam splitter (PBS). The entrance beam is a two frequency laser beam where the different frequencies are orthogonally polarized. The frequency split is nominally 20 MHz. The light with frequency f_1 passes through to the stage. Frequency f_2 reflects from the PBS and is diverted to column reference mirror after reflecting from the column diverting mirror. The column diverting mirror is separated from the PBS by a spacer that sets the spacing between the column and stage beams, h_i, to nominally 0.75 in. I was informed that the spacer is made of super Invar and the space in the cavity between the PBS, the column diverting mirror, and the $\lambda/4$ plate is air. The glass where optical transmission occurs is either BK-7 or quartz. The

materials list also includes Zerodur and I suspect the column diverting mirror may be Zerodur. After reflection from the column and stage mirrors, the beams return to the PBS with polarization orthogonal to the outgoing polarization because they have passed through the $\lambda/4$ plate twice. Both the stage and column beams then reflect from the retroreflector and pass through to the stage and column for a second pass. When the beams return to the PBS they pass through to the right angle prism and to the non polarizing beam splitter (NPBS). The beam transmitting through the NPBS and out of the interferometer is the linear axis. The linear axis beam then passes through the fiber assembly (not shown), which has a polarizer rotated at 45^o to the polarizations. This polarizer is sometimes called the "analyzer" and it produces the interference signal from the orthogonally polarized beams. The fiber assembly also contains a lens and a standard fiber optic connector. The beam reflected from the NPBS enters the angular interferometer portion. Before striking the polarization beam splitter, the $\lambda/2$ plate rotates the polarizations by 90^o. Now f_1 passes to the column and f_2 passes to the stage. The beams double pass to the reference mirrors and are recombined to form the angle axis. The angle axis beam then passes to a fiber optic assembly.

The interferometer signals are insensitive to translations of the interferometer head in Xix, Yix, and Zix. The Y_{ix}, and Z_{ix} motions have the effect of changing the Abbe offsets but if these motions are in the 100 nm range at worst, the effect is negligible. Non flatness of the optics in the interferometer head and the interferometer mirrors can also produce errors if the laser hits different locations on the optics. However, these errors are expected to be negligible since the beam is expected to move only a small distance compared to its diameter and the optics are flat to sub wave levels over areas much larger than the size of the beam. The interferometer signals are also insensitive to the entering beam orientation and translation. Changes in the entering beam orientation produces a cosine error proportional to the dead path of the interferometer. These cosine terms are negligible.

I define pure rotations of the interferometer $[\theta_{Xix}, \theta_{Yix}, \theta_{Zix}]$ as rotations about the centroided location of the two linear axis spots in the polarization beam splitter

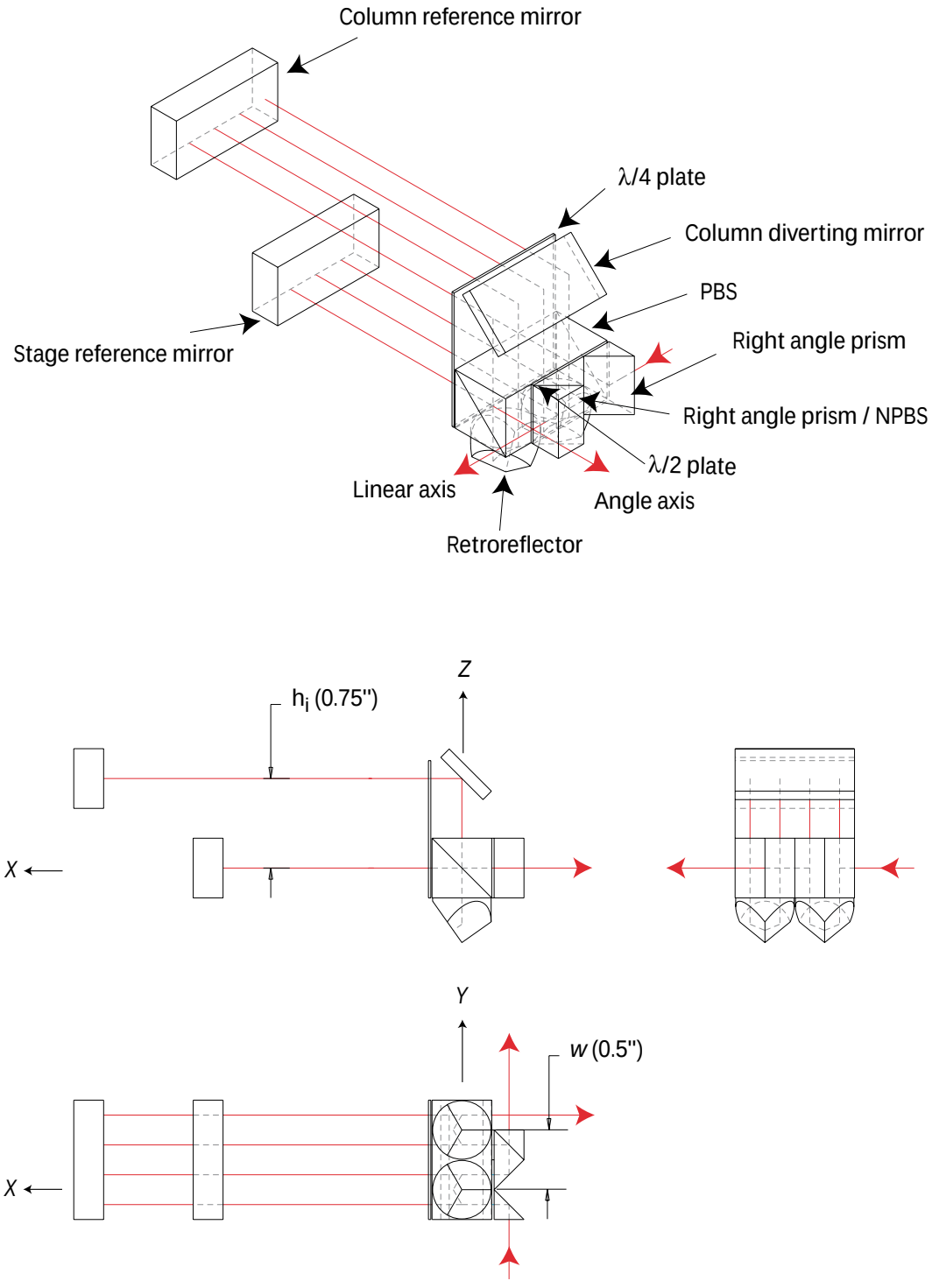

Figure 4-10: Presumed configuration of optics in Zygo 6191-0605-01, Special Column Reference Interferometer, Left Angled Version.

interface plane. Rotation of the interferometer head by θ_{Xix} will change the Abbe offset and the orientation of the angle measurement axis. The change in Abbe offset is expected to be small compared to the average Abbe offset so the effect of instability in θ_{Xix} is expected to be negligible. Moreover, a one μrad instability in θ_{Xix} will change the Abbe offset by a negligible 19 nm.

The interferometer is also insensitive to θ_{Zix}. Rotation by θ_{Zix} produces a cosine error proportional to the dead path of the interferometer. This error is negligible. However, rotation of the interferometer in θ_{Yix} produces a significant error. Figure 4-11 shows the ray trace of the column reference interferometer for the nominal configuration and the case when the interferometer head is pitched by θ_{Yix}. Pitching the interferometer causes a relative path length difference between the column and stage beam paths. The relative column path lengthening due to θ_{Yix} is given by

$$\Delta_{xc}, \theta_{Yix} = a - h_i - b \approx -h_i \, \theta_{Yix}. \tag{4.35}$$

The distance a as shown in the figure is the distance from the entering beam intersection with the PBS interface to the reflecting point at the column diverting mirror. The distance b is the distance along the nominal horizontal beam path from the column diverting mirror to the rotated ray's intersection with the column diverting mirror as shown. Note that the stage beams and column beams do not change orientation due to the interferometer pitch motion. Also, the beam paths for the stage and column beams below the beam splitter interface (on the retroreflector side) are the same. Furthermore, the pitch does not affect the overlap of the beams at the receiver since the stage and column beams move together. In the approximation I neglect all second order terms. Most importantly, the system is highly sensitive to θ_{Yix} because of the large Abbe offset. Pitch of the interferometer head by only 0.1 μrad will produce a 1.9 nm measurement error.

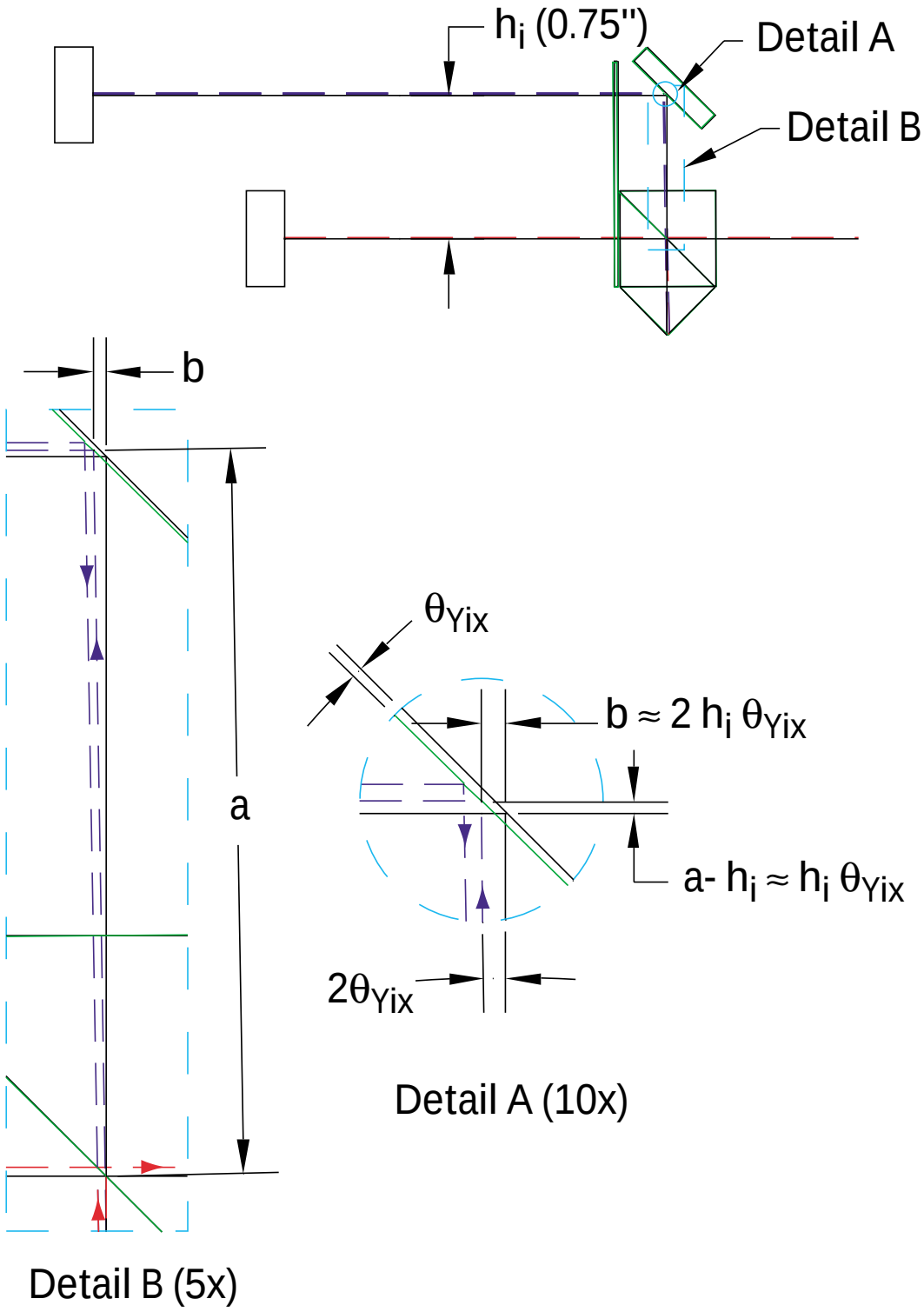

Figure 4-11: Ray trace of column reference interferometer showing components and beam paths for nominal configuration and the case when the interferometer head is pitched by θ_{Yix} (clockwise). The nominal beams are shown in black solid lines. The beams for the pitched configuration are dashed.

4.5 Coupled motions

In this section, I combine the rigid body error motions to consider the differential motions. When I neglect all cosine errors, the error in the position measurement is given by Abbe error terms,

$$e_{Abbe} = -h\,\theta_{Ym} + h_i\,\theta_{Yix} - \Delta_z\,\theta_{Ys} + \Delta_y\,\theta_{Zs} - \Delta_{yc}\theta_{Zm}. \tag{4.36}$$

Here I have subtracted the column path lengthening error terms from the stage path lengthening terms of the previous sections. As long as the column and stage beams of the DMI are parallel then

$$h_i = h + \Delta_z. \tag{4.37}$$

Now

$$e_{Abbe} \approx h_i(\theta_{Yix} - \theta_{Ym}) + \Delta_z(\theta_{Ym} - \theta_{Ys}) + \Delta_y\,\theta_{Zs} - \Delta_{yc}\theta_{Zm}. \tag{4.38}$$

Also, if the interferometer is not rotated significantly about the X axis then the column beams are above the stage beams where

$$\Delta_{yc} = \Delta_y \tag{4.39}$$

and

$$e_{Abbe} \approx h_i(\theta_{Yix} - \theta_{Ym}) + \Delta_z(\theta_{Ym} - \theta_{Ys}) + \Delta_y(\theta_{Zs} - \theta_{Zm}). \tag{4.40}$$

Equation 4.40 contains the important design information for measurement and error correction. The first term is the Abbe error proportional to the separation of the stage and column beams ($0.75''$) times the differential pitch motion of the interferometer head and the metrology block. The second term is the Abbe offset error due to vertical offset of the write point from the x axis stage beams. It is proportional to the differential pitch motion of the metrology block and the stage. The third term is the Abbe offset error due to horizontal offset of the write point from the x axis stage beams. It is proportional to the differential yaw motion of the metrology block and

the stage. This offset is the easiest to realign. Since we are already measuring the differential yaw motion, I did derive coefficients for yaw correction by least squares fitting to the yaw data. But the coefficients turned out to be nonsensical and not repeatable. Therefore, the yaw Abbe error is believed to very much smaller than the remaining errors. Inaccuracy of the yaw measurement also would produce the nonsensical coefficients.

For a 0.1 nm error budget term, the pitch of the metrology block relative to the interferometer head must be stable to 5 nrad. Without a direct measurement, I am hesitant to claim this level of mechanical stability. However, vibration measurements discussed in Section 8.2 and shown in Figure 8-32 indicate the pitch of the bench and the pitch of the metrology block are indeed small – at the 5 nrad level. Although the interferometer head might have some additional pitch motion, it is plausible that the pitch vibrations in the frequency range of interest may indeed be 5 nrad or better. Also, the calculated thermal coefficient for the metrology block pitch is small enough to cause only 5 nrad instability if the temperature is stable to 5 mK. Mounting the interferometer head to the optical bench provides a small structural loop to the metrology block. This topology was essential to attain these stabilities.

The thermal and vibration sensitivities of the metrology-block-to-interferometer-head motions could be improved if necessary. Alternatively, the relative pitch of the interferometer head and the metrology block could be measured and the error corrected. Another axis of interferometry that is stable with respect to the linear axis of measurement could be implemented. A monolithic interferometer head assembly could be built by bonding two linear axis interferometers together. The additional linear axis would have both the column and stage beams referencing the metrology block. This monolithic assembly might be constructed by removing the housings from a Zygo linear-angular interferometer and a Zygo linear interferometer and then bonding them to a stable base. If both linear interferometers have the same temperature coefficient, column separation, and built-in dead path then subtracting the pitch interferometer measurement from the linear measurement will not only correct for the pitch error, but it will also compensate for the temperature sensitivity and

the built-in dead path error (if the interferometers are in air). The problem with adding another axis of measurement is that additional noise will be added. Since angle motion axes cannot be scanned as discussed in Section 9.4.1, angle measurements may be doomed for inaccuracy because of the periodic interferometric errors. An all optical pitch error subtraction should be devised by sending the linear axis beams (the analyzer and fiber assembly would need to be removed from the linear interferometer) at the correct polarization through the second interferometer head. It would be prudent to enclose the pitch axis beams and both the x axis and pitch interferometers in vacuum to eliminate air index variations within the interferometer heads. At some point, enclosing the stage x axis beams in vacuum may be necessary because of index variations. Bellows or another form of sliding vacuum containment would be necessary. For this case, the x interferometer might be attached directly to a longer version metrology block. The interferometer would be a special version contained in vacuum with the column beams blocked off. For this topology, the vibration and thermal sensitivity of the larger metrology block will be critical. Also, differential sets of capacitance gauges can be considered instead of interferometry if the pitch motion correction turns out to be necessary.

The Δ_z term is expected to be much smaller than the pitch term. If Δ_z is ± 400 microns then the metrology block to stage pitch must be less than 0.25 μrad to have less than an angstrom of error. This level of stability is believed to be achieved already.

4.6 Optical power signal

In this section, I calculate the optical power produced by misaligned beams. The phase is found to have the same phase as the intensity in the center of the overlap region.

Equation 1.8 gives the time average intensity for interfering plane waves. Although this intensity was derived for the interference image used for writing, it still applies to the case when the half angle θ between the interfering beams is small. The phase meter

senses the zero crossing of an AC filtered power signal so only the term proportional to $A_1 A_2$ affects the phase measurement if the beam power fluctuations are slow. The Zygo phase meter is designed for a frequency range of 20 ± 13.3 MHz [18] and should be insensitive to power fluctuations outside of this band. If the interfering beams are Gaussian then the electric field amplitude can be written as

$$A_1 = A \exp\left(-\left(\frac{r_1}{w}\right)^2\right) \tag{4.41}$$

and

$$A_2 = B \exp\left(-\left(\frac{r_2}{w}\right)^2\right) \tag{4.42}$$

where for non overlapping beams r_1 and r_2 can be written as

$$r_1 = \sqrt{(x - \Delta_x)^2 + (y - \Delta_y)^2} \tag{4.43}$$

$$r_2 = \sqrt{(x + \Delta_x)^2 + (y + \Delta_y)^2}. \tag{4.44}$$

These definitions of r_1 and r_2 describe beams with an overlap region centered at $[x, y] = [0, 0]$. The Gaussian power center of the right beam (designated with subscript 1) is offset at $[x, y] = [\Delta_x, \Delta_y]$. The left (subscript 2) beam's power center is at $[x, y] = [-\Delta_x, -\Delta_y]$. The time average signal intensity is now proportional to

$$I_s = 2AB \exp\left(-\frac{2(\Delta_x^2 + \Delta_y^2)}{w^2}\right) \exp\left(-\frac{2y^2}{w^2}\right) \exp\left(-\frac{2x^2}{w^2}\right) \cos\left(2k \sin\theta x + k[L_2 - L_1] + \phi_0\right). \tag{4.45}$$

The power signal is the integral of the intensity and is given by

$$P_s = \int_{-\infty}^{\infty} \int_{-\infty}^{\infty} I_s \, dx \, dy. \tag{4.46}$$

The power signal can be evaluated using the identities already given in Equation 1.15 and Equation 3.44. After evaluation P_s is given by

$$P_s = AB\pi w^2 \exp\left(-2\left(\frac{\Delta_x^2+\Delta_y^2}{w^2}\right)\right)\exp\left(-\frac{(k\sin\theta w)^2}{2}\right)\cos\left(k[L_2-L_1]+\phi_0\right). \tag{4.47}$$

This can be written in a more useful form using the following relations

$$P_1 = A^2\frac{\pi w^2}{2}, \tag{4.48}$$

$$P_2 = B^2\frac{\pi w^2}{2}, \tag{4.49}$$

$$\Delta_d^2 = 4(\Delta_x^2+\Delta_y^2), \tag{4.50}$$

and

$$d = 2w. \tag{4.51}$$

The integrated intensity of the beams gives the powers P_1 and P_2 of the right and left arms respectively. The separation between beam centers is Δ_d and the beam diameters are d. In this case, the optical signal power is given by

$$P_s = 2\sqrt{P_1P_2}\exp\left(-2\left(\frac{\Delta_d^2}{d^2}\right)\right)\exp\left(-\frac{\pi^2d^2}{8\Lambda^2}\right)\cos\left(k[L_2-L_1]+\phi_0\right). \tag{4.52}$$

This equation has several applications. First of all, it indicates that the phase of the power signal has the same phase as the intensity in the center of the overlap region where $x = 0$. The power signal loss due to angular and position misalignment can also be calculated. Table 4.1 shows some useful values for understanding the sensitivity of the power signal to alignment.

Power loss (%)	Δ_d/d	Λ/d	$\theta\,(\mu\text{rad})$
10	0.23	3.4	26
50	0.59	1.3	66

Table 4.1: Beam alignment parameters for different optical power loss.

For a power loss of less than 10% the beam separation cannot be more than 23% of the spot diameter. Also, if the period of the image is 3.4× the diameter, there is an additional 10% loss. The misalignment half angle shown corresponds to a 2 mm beam diameter and λ=351nm. For these parameters, a fringe period of 3.4× the spot diameter corresponds to a 26 μrad misalignment. Equation 4.52 can also be used to calculate the interferometric alignment from the measured phase meter power in some cases. In practical applications, the interferometric dead path affects the optical power signal too because the interfering beams will have different wavefront curvature. Other wavefront errors can also reduce the power signal.

Chapter 5

Environment

The environmental parameters of temperature, pressure, humidity, particle contamination, and acoustics significantly affect the repeatability of the SBIL system. Since the clean room where the SBIL system is installed has unacceptable levels of environmental disturbance, an environmental enclosure needed to be specified and installed.

In this chapter, I derive the environmental specifications for the enclosure. Then I will review the enclosure topology. Fundamental limits on index and temperature stability are highlighted. The system was instrumented with a variety of sensors to characterize the level of environmental disturbance. I present the measurements and show the expected errors are consistent with observations.

5.1 Environmental specifications

The stability and accuracy of interferometry is sensitive to the index of air. Edlen published formulas accurate to ±50 ppb for the refractive index of air as a function of temperature, pressure, humidity, and CO_2 concentration. Birch and Downs [8, 9] later revised the Edlen equations with the stated accuracy of ±30 ppb 3σ. Most of the uncertainty was attributed to measurement uncertainty in the temperature, pressure, and humidity.

In this section, I focus on stability considerations. The problem of the accuracy of the length scale is addressed in Section 9.2. Using the revised form of the Edlen

Equation [9], I tabulated the sensitivity of the index to temperature, pressure, humidity, and CO_2 in Figure 5-1 for the HeNe and UV wavelengths used in the system. With the exception of humidity, the sensitivities are very close to what is calculated if one assumes the refractivity varies proportionally to the density of air. The nominal operating parameters shown are those of standard laboratory conditions. The requirements for stability to 7 ppb or about 1 nm over 150 mm are also shown for the HeNe wavelength. The stability requirements are about 8 mK for temperature, 3 Pa for pressure, and 0.8% relative humidity. The CO_2 concentration stability requirement is 48 ppm but this concentration is not expected to change significantly [20]. Since the SBIL system includes a refractometer, any uniform index fluctuations can be corrected. However, non uniform index fluctuations cause errors. To help minimize the errors due to nonuniformity, the refractometer was placed as close as practical to the stage beam paths while the x axis is column referenced.

The environmental control was specified for ± 5 mK temperature, 0.8% relative humidity, and 16 Pa/m pressure gradient to guarantee no more than a nanometer of error to each index variable. The temperature control was specified to ± 5 mK only in a critical volume whereas the rest of the enclosed volume was specified to ± 25 mK. The critical volume included the entire area swept be the chuck and extended from the bottom of the chuck to the top of the metrology block. Also, all the interferometers and their beams were specified to be in the critical volume.

The thermal expansion of the assemblies in the system also cause errors. Figure 5-2 contains the estimated temperature coefficients for the critical assemblies. The error for 5 mK of temperature control is also shown. The interferometer coefficients are the specified values from the Zygo manual. The metrology block coefficient was calculated assuming the rule of mixtures [32] and the known percentage of Zerodur, Super Invar, and epoxy in the assembly. After calculating a composite CTE of 0.25 ppm/°C, the expansion length of 0.17 was assumed to obtain the 40 nm/°C coefficient. This length is the distance from the x axis column reference mirror to the center line of the metrology block interferometer optics. The metrology block pitch and beam splitter mount coefficients were calculated based on the materials and geometries in

Nominal Conditions
T = 20 [C]
P = 1.02e5 [Pa]
RH = 40%
CO2 frac = 365 [ppm]

Index and sensitivity parameters

Interferometer parameters	Units	HeNe	Ar+
Nominal air index, n	NA	1.000272	1.000281
Vacuum wavelength	nm	632.9915	351.1
Index temperature sensitivity (dn/dT)	1/C	-9.30E-07	-9.62E-07
Index pressure sensitivity (dn/dP)	1/Pa	2.68E-09	2.78E-09
Index pressure sensitivity (dn/dP), adiabatic	1/Pa	1.91E-09	1.98E-09
Index humidity sensitivity (dn/d%RH)	1/(%RH @	-8.50E-07	-7.97E-07
Index CO2 sensitivity (dn/dCO2)	1/[CO2 frac	0.000147	0.000152

Change for 7 ppb stability

Units	Change
mK	-7.5
Pa	2.6
Pa	3.7
%RH	-0.82%
ppm	48

Figure 5-1: The calculated index and index sensitivity from Edlen's equations (lower left table). The nominal parameters (upper table) and the requirements for 7 ppb stability (lewer right table) are also shown.

those assemblies. Expansions due to temperature gradients are not accounted for in these coefficients. Changes in temperature gradients will produce additional errors. The chuck coefficient took into account the Zerodur interferometer mirror, the 130 μm thickness of epoxy to bond the mirror, and the 33 cm long length of Super Invar. This length would reach from the far edge of a 300 mm wafer to the back edge of the Zerodur mirror. I assumed a 0.6 ppm/°C CTE for all the Super Invar components, which is a worst case assumption. Super Invar will have a CTE of 0.3 ppm/°C only after very specific heat treatment [5]. Since the CTE of Super Invar is sensitive to the heat treatment and cycling of temperature, I assume the higher value. This assumption is especially valid since the nickel plating required a baking step to ensure good adhesion and the Super Invar material was provided in a forged condition. I did attempt to get the part heat treated. But after considering the time and the risk of warping the machined part, the treatment was not performed. The metrology block and the chuck are flexure mounted such that the expansion of the optical bench and the stage can be neglected.

Other important but less critical components for temperature control include the optics and beam paths starting at the grating beam splitter and the stage. Any

Part	Temperature coefficient (nm/C)	Error for $\Delta T = 5mK$
X axis interferometer	30	0.15
Refractometer interferometer	10	0.05
Metrology block expansion	40	0.20
Metrology block pitch	20	0.10
Beam splitter mount	100	0.50
Chuck	200	1.0
Root sum square	230	1.15
Sum	400	2

Figure 5-2: Estimated temperature coefficients of critical components and the error for 5 mK of temperature change.

index disturbance in these paths will possibly distort the wavefront of the beams and add additional disturbance that must be locked out. The angle stability of several components outside the critical zone is also a concern. Sub-micro radian angle stability between the interfering beams is required for period control. Also, the metrology block, the chuck, and the x axis interferometer should be stable in angle because of Abbe errors.

Overall, the sensitivity to temperature is similar for the thermal expansion error source and the index of air source. However, each source has a different frequency response. The part expansion is low pass filtered by the built in time constant of the components. Depending on the critical component the time constant can range from about a minute to about ten minutes. Meanwhile, the air index errors can occur on much faster time scales. The refractometer provides insensitivity to slow, uniform temperature changes for the index errors.

The enclosure was specified as a Class 10 clean room to reduce the particles. At this level, opening the doors and human operators definitely limit the cleanliness. Particle contamination of the optics is a problem because the particles cause scattering of the light. If the particles contaminate the optics after the spatial filter, the wavefront quality is affected. Particles can also get trapped in between the wafer and the vacuum chuck. These particles will distort the wafer and cause errors due to

in-plane strain.

The compressibility of the materials is another error consideration. I define the compressibility as

$$C = \frac{\Delta L}{L \Delta P} \tag{5.1}$$

where ΔL is the change of the material length L due to change in pressure ΔP. Reference [88] directly measures the compressibility of a 280 mm long Zerodur rod. For $\Delta P = 1.000212 \times 10^5$ Pa and $\Delta L = 161 \pm 2$ nm, the compressibility evaluates to 5.7×10^{-3} ppb/Pa. In the absence of direct measurements, the compressibility can be calculated from

$$C = (1 - 2\nu)/E \tag{5.2}$$

where ν is the Poisson ratio and E is the Young's modulus. For Zerodur, $E = 9.02 \times 10^{10}$ Pa and $\nu = 0.243$. Using Equation 5.2, the compressibility evaluates to the directly measured compressibility of 5.7×10^{-3} ppb/Pa. Since the pressure due to weather can vary by 2000 Pa, the pressure at the time of writing and the substrate material will significantly affect the length scale of the grating. For instance, a Zerodur substrate 0.3 m long will compress by 3.4 nm for 2000 Pa pressure change.

During writing, pressure variations of 25 Pa/hr are not uncommon. Conservatively assuming 100 Pa pressure change and the length of 17 cm for the metrology block, the compression error will be 0.097 nm. Using Equation 5.2, I calculated the compressibility for Super Invar to be 3.8×10^{-3} ppb/Pa. The chuck compression error is expected to be 0.17 nm for 100 Pa pressure change taking into account the Zerodur mirror and the length of Super Invar out to the furthest edge of a 300 mm wafer. For thin substrates and a vacuum chuck, the substrate can be assumed to compress with the chuck. The compression errors during writing are small for now and the metrology block and chuck compression even somewhat cancel each other depending on the write location on the chuck. On the other hand, the compressibility of the substrate will definitely need to be accounted for when writing length scales with subnanometer repeatability. All the compressibility errors could be compensated by measuring the pressure and correcting for the error. For my work, demonstrating linearity was the

first objective and the compressibility was not corrected.

5.2 Enclosure description

In this section, I review the enclosure topology. The environmental enclosure was designed and built by TAC-Control Solutions Inc[1] (CSI). While they promised a turnkey system within three to four months of issuing the PO, the system was delivered after more than 15 months. The system failed factory acceptance tests several times and unfortunately there were many time consuming problems along the way. At the time of this writing (23 months since issuing the PO) the environmental control of the SBIL system had not achieved the specifications for temperature. Furthermore, the humidity control had adverse effects on the temperature control and was better left off. In hindsight, I can say the company greatly exaggerated their skills and abilities and the references we obtained prior to placing the order had purchased systems with significantly different requirements. Doing business with TAC-Control Solutions Inc was a mistake. I write this as a service to others who may be in the market for environmental control.

Since the specifications for the environmental control were based on conservative models, the fringe placement stability and the reading repeatability met nanometer level performance goals. I suspect the critical temperature control specification will eventually be met and the errors will be reduced significantly from what I am reporting.

Figure 5-3 shows the outside of the enclosure. The system consists of two air handlers, labeled A and B. The location of one end of a differential pressure sensor that I discuss later is noted. Nearly 360° access to the SBIL tool is possible because the air handlers are detachable and sets of double doors open on each side of the system. The nearly ideal accessibility was intended to allow future retrofits.

Figure 5-4 is a photograph from the other side of the system with the double doors open. The grills for the air outlets and returns are obvious on the face of the air

[1] 1770 Mason-Morrow Rd., Lebanon, Ohio

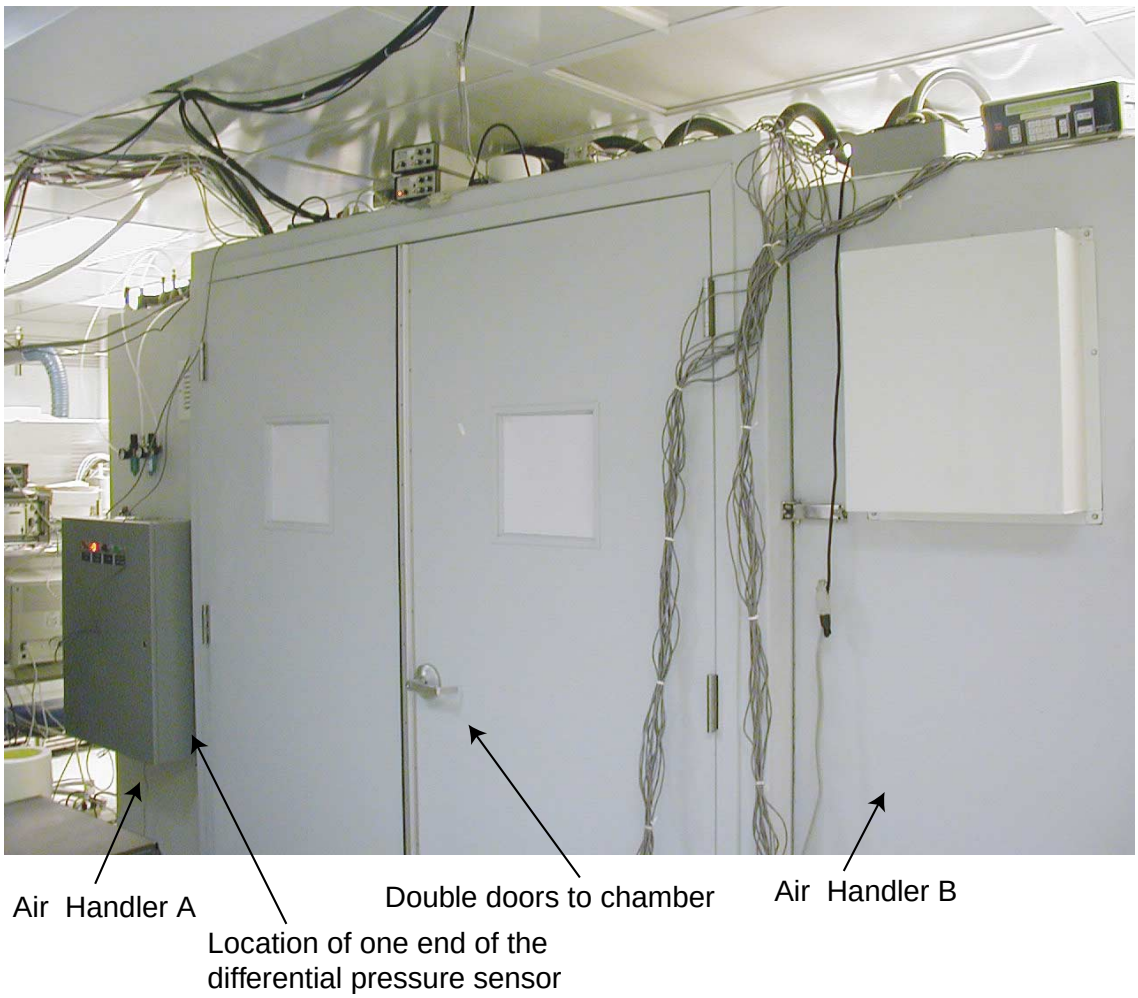

Figure 5-3: Environmental enclosure showing the two air handlers and the doors to the main chamber

handlers. The air passes through ULPA filters in the center of each air handler with a face velocity of 60 fpm. The air volume flow of 700 cfpm for each air handler circulates the full room air volume in 11 seconds. The air returns through the grills located at the top and bottom of the units. The returns have adjustable dampers for controlling the top-to-bottom air flow ratio and the positive pressure in the enclosure. The positive pressure prevents particle contaminated air from leaking into the controlled environment. The arrows show the expected air flow paths. About one third of the air returns through the top returns. This air is cooled by a chill coil to remove humidity and heat. The chill coil temperature is regulated by controlling a three way valve that sets the mix ratio of water from a chiller (Neslab HX-300) and water

that is recirculated. After passing the chill coils, the air is reheated by electrical coils to a controlled temperature. Then the reheated air and the lower return air mixes and is forced by a fan through an acoustic silencer. Finally the conditioned air flows out through the ULPA filter. Thermistors[2] are located after the chill coil, after the reheat, and after the fan on each air handler. Also, two thermistors are located inside the chamber. Only the chamber thermistors and the thermistors after the fans were implemented in the reheat control loop. Also, the three way valve for the chilled water was left open such that all water circulated back to the chiller. The tuning of the control system was the responsibility of the vendor.

It is critical for the two chamber temperature setpoints to be matched and stable to each other. For an overall temperature uniformity specification of ± 5 mK, the chamber setpoints should be matched to about 1 mK. We had an independent, movable thermistor, for verifying the setpoint calibration. A single air handler system using a similar sensor topology is described in reference [63].

5.3 Limits on index stability and temperature control

The air handler topology was chosen because it ensures that minimal heat sources exist between the critical volume and the controlled air that flows out of the ULPA filters. The vertical optical bench design provides the very open landscape for the air flow. The horizontal air flow also has the benefit of avoiding gravity induced temperature gradients. Vertically blown air experiences natural temperature gradients. The adiabatic expansion of air for an ideal gas [75] has the pressure-temperature relationship given by

$$T_2 = T_1 \left(\frac{P_2}{P_1} \right)^{\frac{\gamma - 1}{\gamma}} . \tag{5.3}$$

[2]Deban Air010 thermistors. The thermistor signal conditioners are Deban 1442.

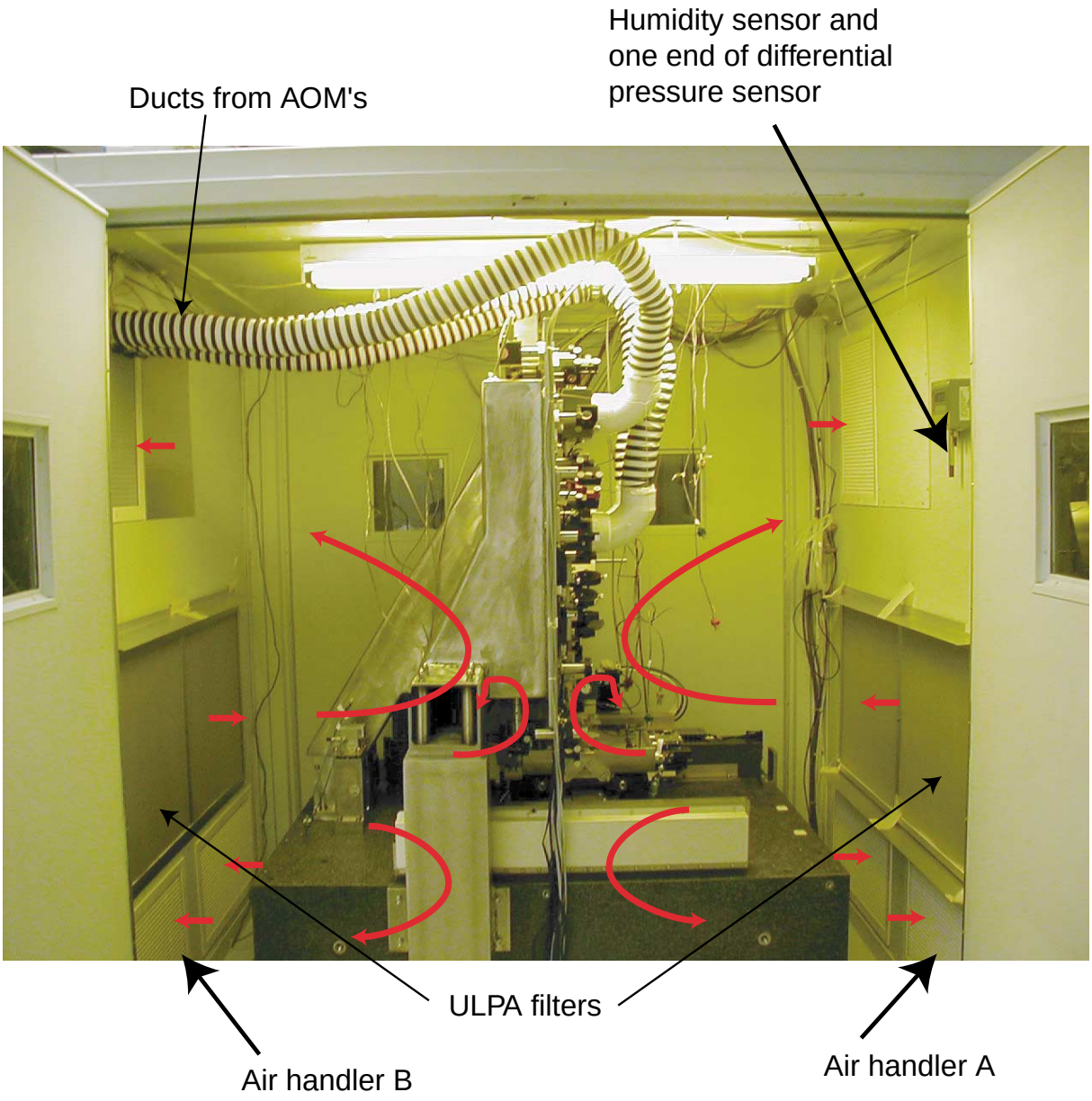

Figure 5-4: Inside the main chamber. The grills for the air outlets and returns are obvious on the face of the air handlers. On each air handler, the air outlets through an ULPA filter located midway up the face. The air returns through the grills located at the top and bottom of the units. The arrows show the expected air flow paths.

Here γ is the specific heat ratio, which for air is 1.4. The pressure as a function of height, h, is

$$P_2 = P_1 - \rho g h. \tag{5.4}$$

For standard air at 20 °C, the density ρ of 1.2 kg/m^3 [75] results in a vertical pressure gradient of 12 Pa/m. The vertical temperature gradient for air moving vertically at height h=0 is

$$\frac{dT_2}{dh} = -\frac{T_1 \rho g(\gamma - 1)}{P_1 \gamma}. \tag{5.5}$$

At the standard conditions of $P_1 = 1.01 \times 10^5$ Pa and $T_1 = 293.15$ °C, the vertical temperature gradient is -.0098 °C/m. This temperature gradient is known as the adiabatic lapse rate [49] for air. It is the temperature gradient experienced by a parcel of air moving vertically without heat leaving or entering it. However, if the air is still, then molecular gas theory [79] can be used to calculate the expected temperature gradient. The kinetic energy per mol of gas is

$$\frac{1}{2} N_o m \overline{u}^2 = \frac{3}{2} RT \tag{5.6}$$

Here N_o is Avogadro's number, m is the mass of a molecule, and $\overline{u}$ is the root mean square speed of the molecule. Since the kinetic and potential energy, mgh, must be conserved, the vertical temperature gradient is calculated as

$$\frac{dT}{dh} = -\frac{2 N_o m g}{3R} \tag{5.7}$$

The variable R is the universal gas constant (8.314 J/mol/K). For air, I will approximate the mass per mol as that of nitrogen (N_2 molecule), where $N_o m$ is 0.028 kg/mol. The vertical temperature gradient in still air is expected to be -.022 °C/m. The actual gradient in the absence of heat sources is expected to be somewhere in between the adiabatic lapse rate and the molecular gas calculation depending on air flow boundary conditions. Regardless, the vertical temperature gradient between -10 and -22 mK per meter is consistent with what I have observed in our enclosure and is a significant consideration for nanometer level stability and accuracy. Moreover, if the

air was designed to flow from top to bottom instead of horizontally, I would expect as the air flowed past the optical bench, the air would form undesirable temperature gradients that would lead to nonuniform temperature and instability in the critical zone.

There also may be index nonuniformity not associated with temperature gradients that need to be addressed. I have yet to see a satisfactory analysis of "turbulence" for a lithography stage. This is probably because good temperature control alone is satisfactory for nanometer errors. What some people call turbulence has nothing to do with the Reynold's number but is associated with poorly temperature controlled air. Bobroff [10] performs some experiments on air turbulence but provides no information on the air temperature distribution other than the temperature range at single point. The non uniform air index variations induced by temperature are not adequately described by single point measurements.

However, there is probably a limit to index uniformity even if the air handler could output laminar, temperature gradient free air. Hufnagel in Chapter 6 of reference [111] cites the Kolmogorov theory of turbulence. To paraphrase Hufnagel, "Key to this model is the hypothesis that the kinetic energy of larger eddies is redistributed without loss to smaller and smaller eddies until finally dissipated by viscosity." This seems like a reasonable hypothesis. But I cannot show that if eddies were to develop for the scenarios of interest that there would be the possibility for subnanometer errors. These eddies might develop for instance as the air separates from the surface of the stage interferometer mirror. For an eddie, the radial pressure gradient is given by

$$\frac{dP}{dr} = \rho\omega^2 r \tag{5.8}$$

where ω is the rotation rate in radians per second, ρ is the fluid density, and r is the radial distance. Integrating this equation one obtains

$$P_R = \int_0^R \rho\omega^2 r\, dr = \frac{\rho\omega^2 R^2}{2} = \frac{\rho v_R^2}{2}. \tag{5.9}$$

The velocity v_R is the velocity at radius R. This relation for the pressure increase is

also equal to the pressure increase of a stagnation point derived from the Bernoulli equation. In this case, $\Delta P = \rho v^2/2$ where v is the upstream velocity of the fluid. Taking $v_R = 60$ fpm and using the density of standard air, the pressure increase is a mere 0.06 Pa. This is too small to be of concern for even 0.1 nm level error budgets. Since the air would need to have unrealistic velocity distributions for pressure to cause significant errors, I believe the "turbulence" has to be associated with temperature gradients.

Another possible source of air temperature nonuniformity is viscous losses of the flowing air. If all the energy of the pressure drop is dissipated into the air, the temperature rise is calculated as

$$\frac{\Delta T}{\Delta P} = \frac{1}{\rho\alpha} \tag{5.10}$$

where ρ is the density, and α is the heat capacity. For standard air, $1/(\rho\alpha)$ equals 770 μK/Pa. Because the entire differential pressure in the enclosure was measured to be about 10 Pa, the viscous heating can account for about 8 mK. However, the air in the critical volume is expected to have a small fraction of the total pressure drop since that space is very open; most of the pressure drop occurs in the dampers.

Managing the power sources and containing them is essential to a temperature controlled environment. The temperature rise, ΔT of an airstream due to a power source is given by

$$\Delta T = \frac{\mathcal{P}}{Q\rho\alpha}. \tag{5.11}$$

Here $\mathcal{P}$ is the power and Q is the volume flow rate. In more convenient units, $\rho\alpha$ equals 0.61 W/cfm/°C for standard air. The air out of the ULPA filters has a velocity of approximately 60 feet per minute and at this speed the air will remove 0.18 W/ft^2 if after passing a heat source the air heats by 5 mK. But even 0.1 W in the wrong place can cause nanometer level errors.

The heat sources in the system are depicted in Figure 5-5. The powers shown are maximum values used for design purposes. The x axis motor coil is mounted to the aluminum u-shaped cross slide. It is critical for the power dissipated in this motor to be small. Since the stage scans in the long y axis direction, the x axis duty cycle

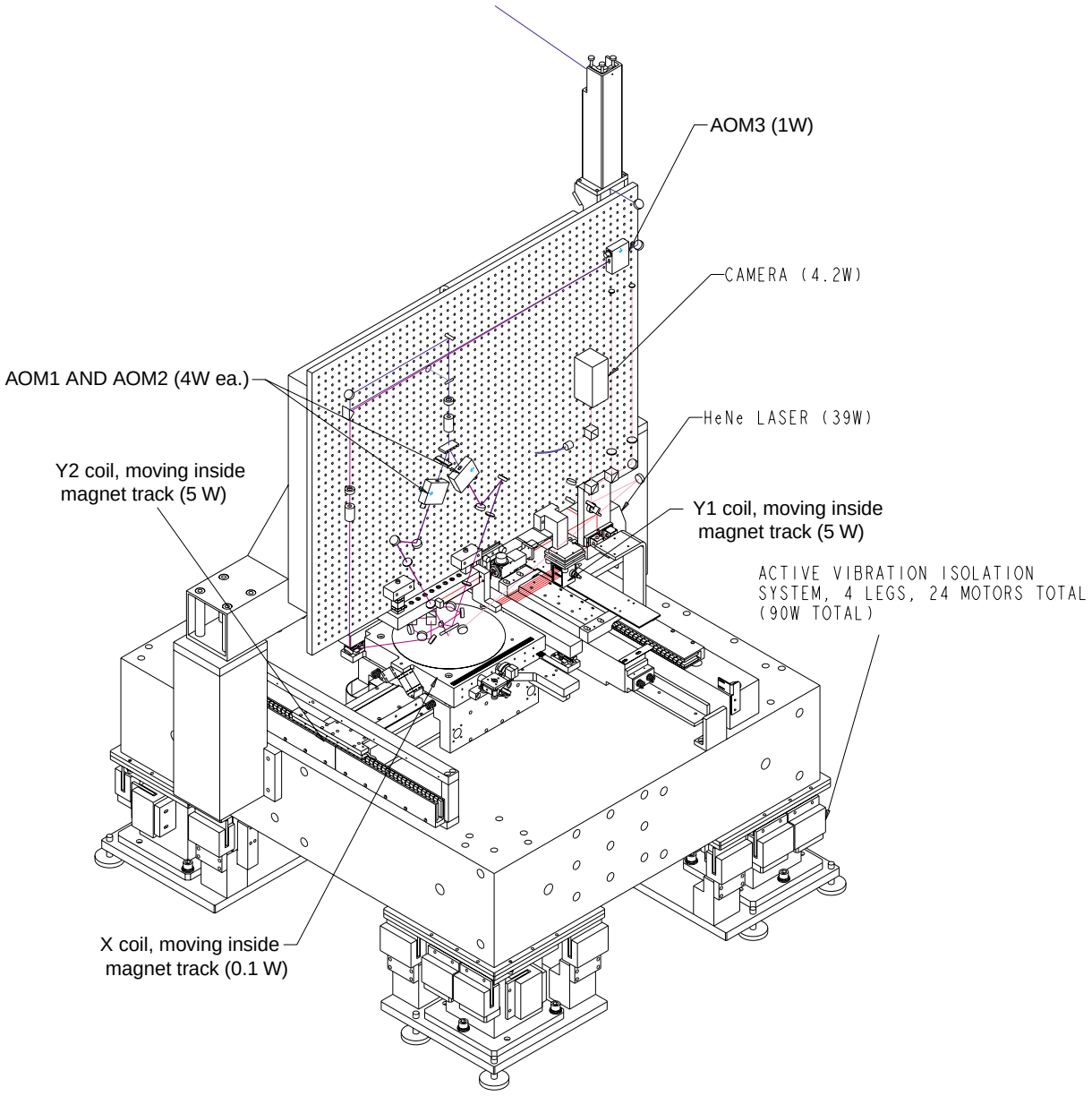

Figure 5-5: Major heat sources in the SBIL system. The powers shown are maximum.

is small for typical SBIL routines. With this scan strategy, reasonable throughput is possible with acceptable power dissipation in the x axis. Meanwhile, there are two y axis motors that can dissipate significant power. Although the airflow will tend to force most of the heat away from the x axis interferometer, there is some sensitivity to the Y1 motor heating. The x axis interferometer head is located as close as possible to the stage but it is still just barely fully on the inside of the Y1 motor coil. The y motor heating currently limits the stage speeds for the SBIL routines of interest. The laser with a power dissipation of 39 W, needed to be enclosed in a box that was well insulated. Air was pulled through a very insulated duct that had a fan attached to the end of it. This end of the duct was fed directly to the return of air handler B. The AOM's were also enclosed, ducted, and attached to fans fed directly to air handler B. The ducts for the AOM's are visible in Figure 5-4. Since the AOM's are far from the critical zone and dissipate less power, they did not require the thick insulation used for the laser. The AOM's operate with maximum diffraction efficiency when their RF power is below 4 W of power. The typical power for AOM1 and AOM2 ranges from 1-3 Watts. AOM3 typically is operated below 1 W of power. The camera depicted in the figure is currently unenclosed and is off during most work.

The air flow has a dead-spot located approximately in the center of the critical volume. The dead-spot is acceptable since the chuck and the aluminum u-shaped stage serve as very good heat sinks and efficiently spread out the heat dissipated by the x axis motor and the lithography laser. Even though air flow without the dead-spot in the center of the critical volume could have been achieved by pushing air out of one air handler and pulling it out the other side, this option would make the y axis motor heat more of problem – the air past the y motors would not be blowing away from the critical volume. Furthermore, packaging the return ducts would have been problematic for this configuration because of the limited space available in our clean room.

The motors have both static and dynamic dissipation components. The static dissipation is due to the motor offset currents and forces. The forces are primarily associated with non-ideal magnetic preloading of the stage. When the stage x axis

is moved by hand, this non-ideal behavior is easily felt. We believe that bolts in the steel plates used for preloading cause these forces. The y axis preloading is designed with bolts further away from the magnets and the preloading is not felt. Since turning the stage control on produces no temperature rise observable at any of the sensors to be discussed, I will ignore the static motor dissipation.

The temperature rise in the critical area can be conservatively calculated based on the x motor power. Only a ball park estimate is required and I will simply assume a cross sectional area of 1 ft^2 and the air velocity of 60 fpm. A power dissipation of 180 mW on the x axis motor should result in a noticeable heat rise on the order of 5 mK. The x axis motor normally has such a small duty cycle that the dissipation on this motor is usually much less. The laser dissipates power in the critical volume too. In reading, I was unable to observe any increase in error when the laser power on a stationary grating was adjusted from 4 mW to 40 mW. Typical powers used for writing were 30 mW. The lithography laser power during writing is not believed to be a problem since the beams must always be moving and the heat capacity of the substrate limits the heating.

The x axis motor power is estimated from the 60 kg moving mass, the motor force constant of 57 N/A_{rms}, motor resistance of 5.2 ohms, and the stage profile. I only consider ohmic losses in the motors and ignore losses to eddie currents. The stage profiling ramps up the acceleration at a constant jerk rate up to the maximum acceleration if the step size is large enough. For small steps, the maximum and acceleration and maximum velocities are never reached. For the jerk rate of 4.9 m/s^3, scan length of 36 cm, x axis step size of 800 μm, scan velocity of 100 mm/s, and maximum acceleration of 0.05 g, the time average power dissipated on the x axis is only 4 mW. Meanwhile, the y axis motors dissipate 80 mW each. The y axis motors are identical to the x axis motor and the assumed y axis moving mass is 100 kg. No noticeable temperature rise is observed for these parameters where the time to pattern a 300 mm wafer is 27 minutes. In the next section, I also will consider other profiles and evaluate the temperature gradients in the system.

Heat sources, viscous losses, and gravity gradients do impose limits to temperature

control and gradients. However, the limit is believed to be below a milli-Kelvin for small volumes with little heat dissipation such as the the SBIL critical volume.

5.4 Temperature measurements

The temperature specification required the critical volume to have a stability and uniformity of ±.005 mK. The critical volume covers the entire area swept by the chuck and extends from the bottom of the chuck to the top of the metrology block. Figure 5-6 shows the locations of the temperature sensors to be discussed. There are four rear sensors labeled 1-4, four front sensors labeled 5-8, four vertical sensors 6, 10, 0, and 11, and a sensor placed close to the x axis interferometer labeled 9. Sensors 1-9 are located in the critical volume within 3 inches of the write plane. The vertical sensors are spaced an average of 12 inches apart. The drawing also shows the location of control sensors used for feedback labeled as T_A and T_B. The control sensors are in the critical volume.

The temperature sensors are Instrulab[3] Model 405 sensors. These are two-wire thermistors with a time constant of 10 seconds. The sensors are quoted with an accuracy of ±0.02 °C for a calibration over ±5 °C. The stability is not specified. The electronic system that provides a digital temperature read out is Instrulab Model 3312A. The electronic system is quoted to have an accuracy of ±.01 °C with a resolution of 1 mK. The sensor system belonged to CSI and was installed as part of the acceptance test procedure. The sensors were calibrated by CSI in a water stirred bath[4] and originally matched with each other to the noise floor of the sensor/bath system such that all sensors read within 3 mK of each other. A better bath or a calibration service might be employed to better calibrate sensors in the future. For instance, Harvey [37] constructed a bath with ±70μK stability with gradients of 50 μK within the bath. Since the temperature data that I will show has gradients far exceeding 3 mK, the sensor calibration was not the limitation at this point in the

[3]http://www.instrulab.com
[4]Hart Scientific

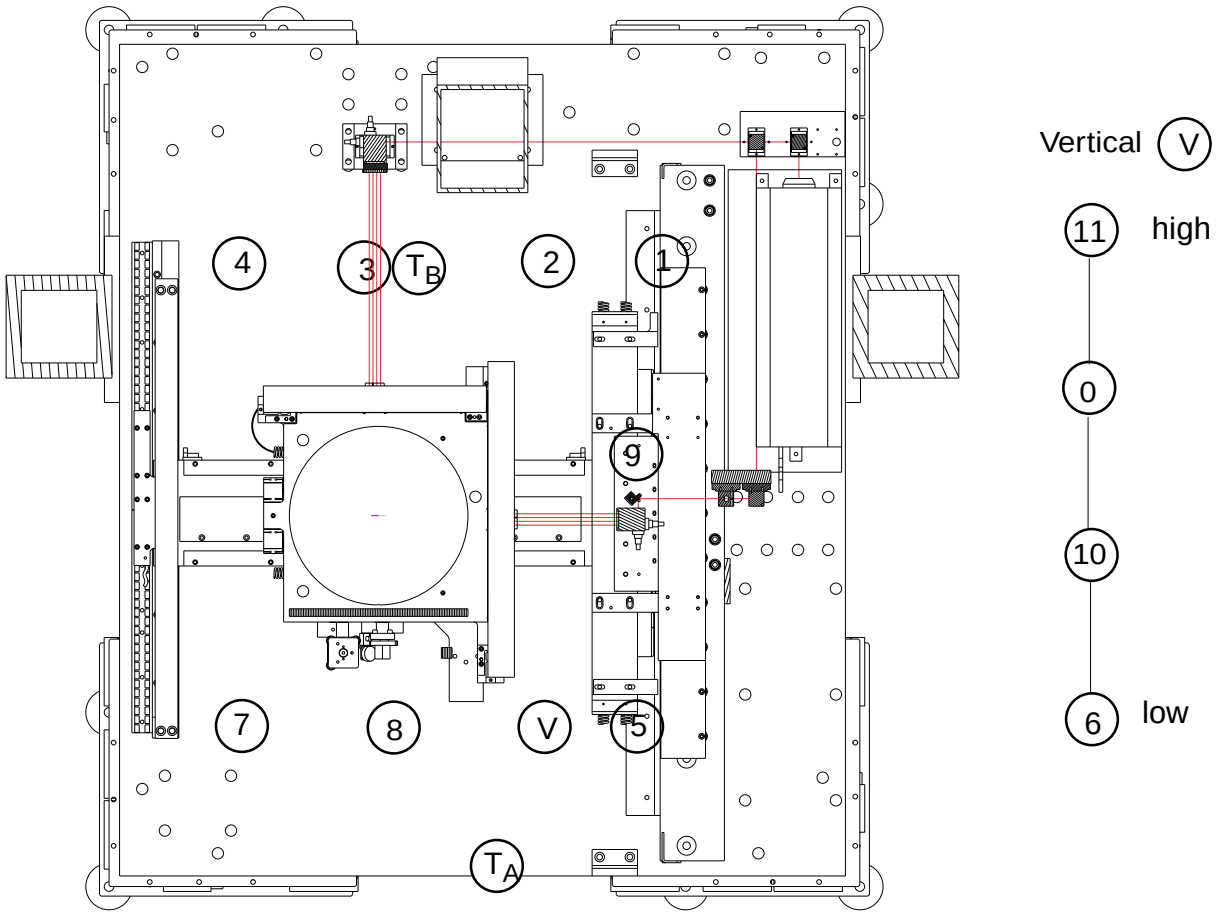

Figure 5-6: Location of the twelve data and two control thermistors. The four rear sensors are labeled 1-4. Four front sensors are labeled 5-8. Sensor 9 is placed to monitor the temperature near the x axis interferometer. Sensors 1-9 are located in the critical volume, within 3 inches of the write plane. The vertical sensors, 6, 10, 0, and 11 have an average spacing of 12 inches. The control sensors used for feedback are labeled T_A and T_B

work.

The self heating of the thermistors in still air was estimated to be less than 1 mK. Thus, the measurements should be insensitive to the air velocity at better than the 1 mK level. The long term stability of the sensor system has not been rigorously characterized. However, I believe the sensor system is stable to better than ± 2 mK based on data that I will discuss. In general, thermistors are suitable for precision temperature measurements since they have been demonstrated to have sub mK relative stability over five years [64, 65] using commercial two-wire instrumentation. Separate observations by Edwards [19] showed thermistors stable to 0.1 mK per 100 days.

The sensors must be stable and calibrated to be able to assess temperature gradients. I estimate the long term relative stability of the temperature control and sensor system by comparing the temperature change after more than month for a well equilibrated system that had all heat sources off. The change in average temperature reading after 33 days is shown in Tables 5.1, 5.2, and 5.3 for the rear, front, and vertical sensors respectively. Each average temperature reading is calculated by averaging data over more than 6 hours. The rear sensor stability is the best estimate of the measurement system long term stability. The rear sensors were solidly tie wrapped to the optical bench (insulation was placed between the sensor stem and the bench to ensure the sensor was reading the air temperature) and the setpoint on air handler B was not changed over this time period. Furthermore, air handler B generally has better performance as measured by T_B. The rear sensor stability is within 1 mK. This stability is affected by T_B stability too. Thus the T_B sensor and the rear sensors have mK level relative stability. Sensors 5-8 block access to the optics and may not have been in the exact same place in both sets of data. The vertical string of sensors sensors were removed and then returned. These sensors may not be in the same place by an amount on the order of a foot. Also, the setpoint on the air handler A is known to have been adjusted. The movement of the sensors and the setpoint adjustment prevents rigorous determination of the front and vertical sensor stability. However, based on the rear sensor stability of 1 mK and the fact that all the sensors were the same type, the larger instability of the front and vertical sensors are very likely due to the sensor movement and the setpoint adjustment. Therefore, the relative stability of the sensors is believed to be $\pm$ 1 mK. Since when the sensors were calibrated in the fluid bath they read within 3 mK of each other, the sensor matching is probably accurate to $\pm$ 2 mK.

Figure 5-7 shows the temperatures of the front sensors of the system during use. The data shown is the moving average temperature over one minute. The spikes in temperature correspond to the chamber door opening. Sensor 7 reacts with the largest temperature disturbance since this sensor was closest to the opened door. The magnitude of the spike in temperature is dependent on the time that the door is left

Sensor Number	Stability (mK)
1	0.3
2	-0.8
3	-1.0
4	-0.9

Table 5.1: Long term rear sensor stability, the change in average temperature reading after 33 days.

Sensor Number	Stability (mK)
5	-2.1
6	-6.3
8	-2.4
7	-1.5
9	-2.0

Table 5.2: Long term front sensor stability, the change in average temperature reading after 33 days.

Sensor Number	Stability (mK)
6	-6.3
10	2.8
0	9.3
11	13.9

Table 5.3: Long term vertical sensor stability, the change in average temperature reading after 33 days.

open, how wide it is opened, and the temperature of the main clean room at the time the door is opened. It takes the air temperature about 10 minutes to recover to 5 mK of the equilibrium temperature after closing the door for the data shown. Figure 5-8 shows the same data but with an enlarged temperature scale. The vertical lines denote the time when a SBIL routine was starteded. During this SBIL routine a 100 mm wafer was exposed with the following parameters: v=55mm/s, a = 0.49 m/s^2, jerk = 4.9 m/s^3 scans=129, scan length = 250 mm, step size = 0.857 mm, and α = 0.5 μrad. This SBIL routine takes about 10 minutes to complete. The estimated x motor power is 3 mW and the y motor power is 31 mW during writing. As can be seen from the figure, the temperature rise during the duration of the SBIL routine is unnoticable. The effect of the system still equilibrating is observable at the 5 mK level on sensor 5, however. Sensor 9 is the best choice for observing the motor related heating.

The difference between the maximum and minimum temperatures during each minute is plotted in Figure 5-9. During thermal equilibrium the stability is 14 mK peak to valley for the worst sensor (maximum -minimum temperatures taken between time=20 and time = 90 seconds). The humidity control needed to be off to attain this stability. The temperature measurements are low pass filtered because of the 10 second time constant of the thermistors. The magnitude of the temperature stability without the low pass filtering is not known at this time. The front sensors also show a significant nonuniformity of about 15 mK. The total range for the front sensors, maximum of sensors 5-9 minus the minimum for these sensors is 29 mK. The temperature gradient is also the greatest in between sensors 5 and 6, which is particularly troublesome because this air passes into the x axis interferometer beam paths.

Figure 5-10 shows the temperature of the rear sensors taken at the same time. The rear sensors are much less affected by the door opening, which is expected because the door that was opened was located toward the front of the system. The rear sensors also show unnoticeable change due to the SBIL routines. Figure 5-11 shows the maximum minus the minimum temperatures over a minute. The rear sensors show better stability and uniformity than the front sensors. The stability at a particular

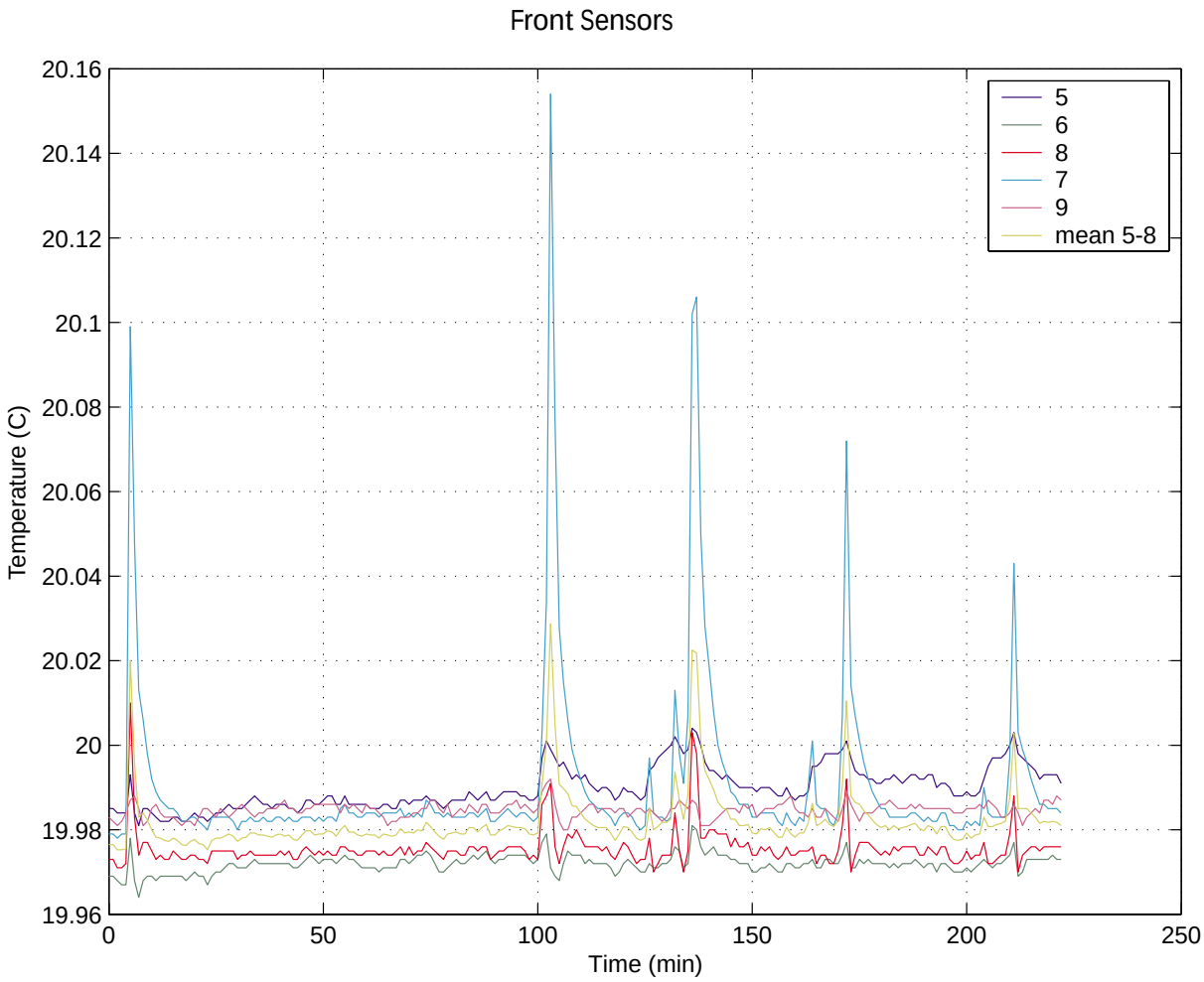

Figure 5-7: Front sensor temperatures averaged over a minute. The spikes in temperature correspond to the opening of the environmental chamber door.

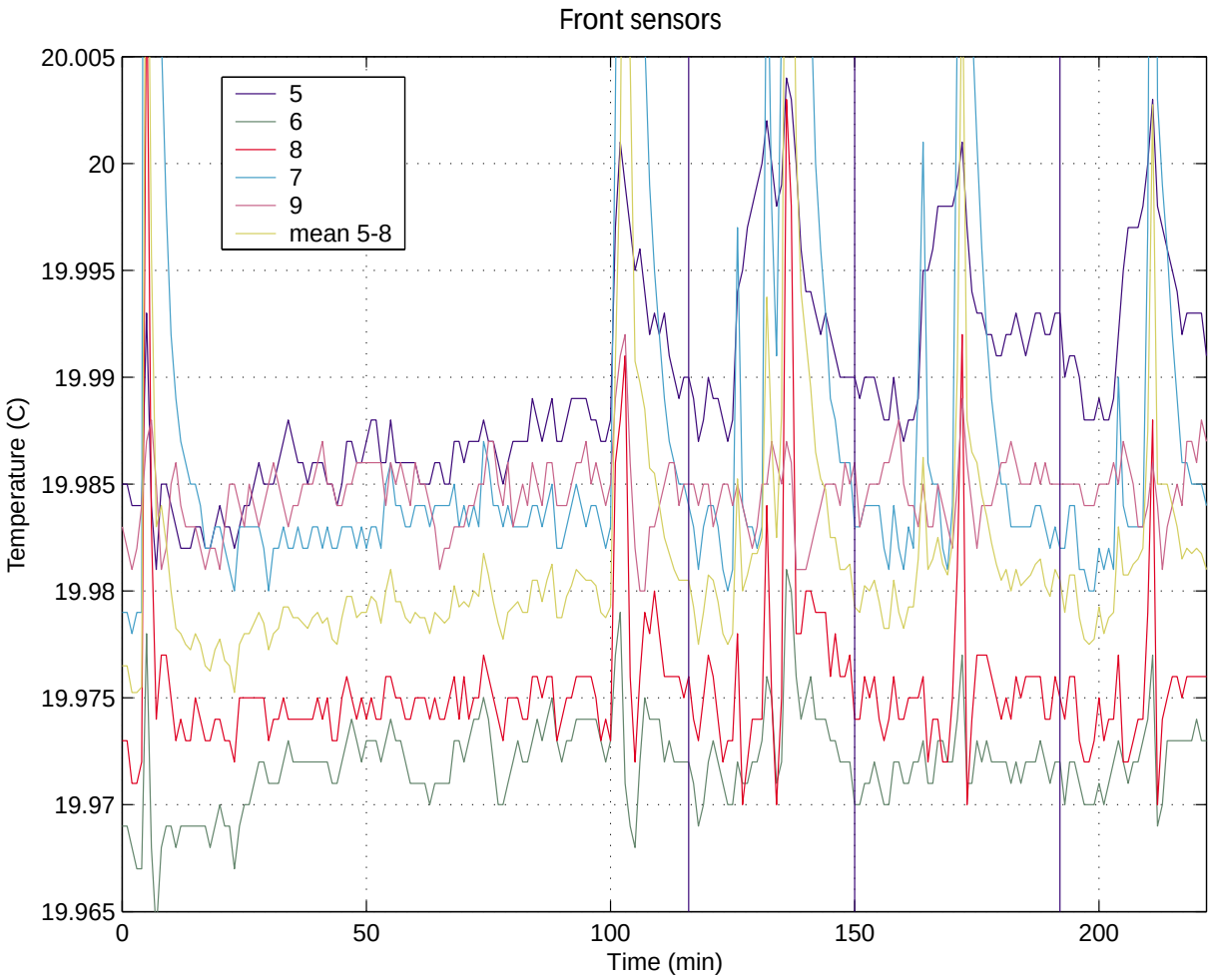

Figure 5-8: Front sensor temperatures with an enlarged temperature scale. The vertical lines denote the time when a SBIL routine was started.

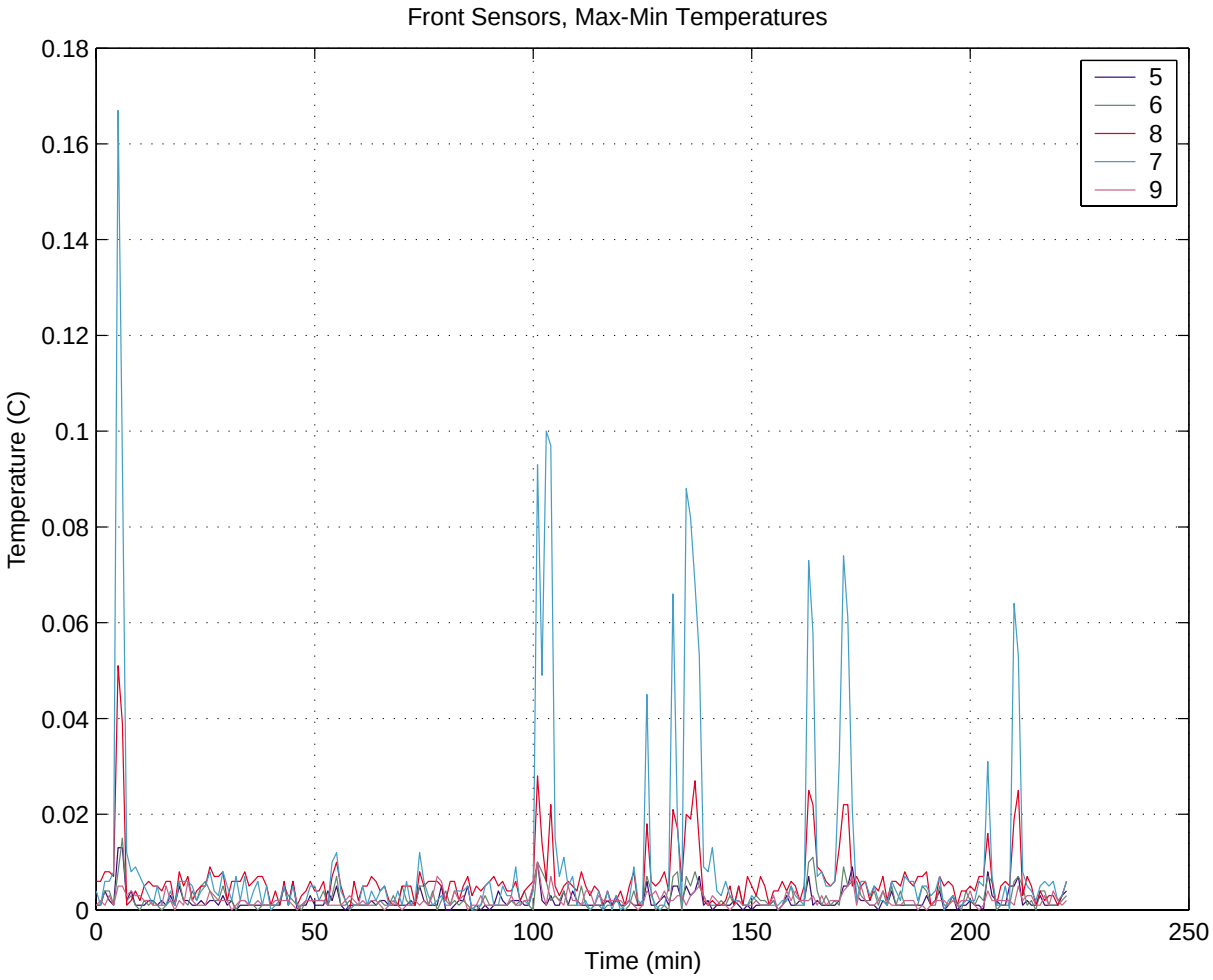

Figure 5-9: The difference between maximum and minimum temperatures occuring during a one minute time frame, front sensors.

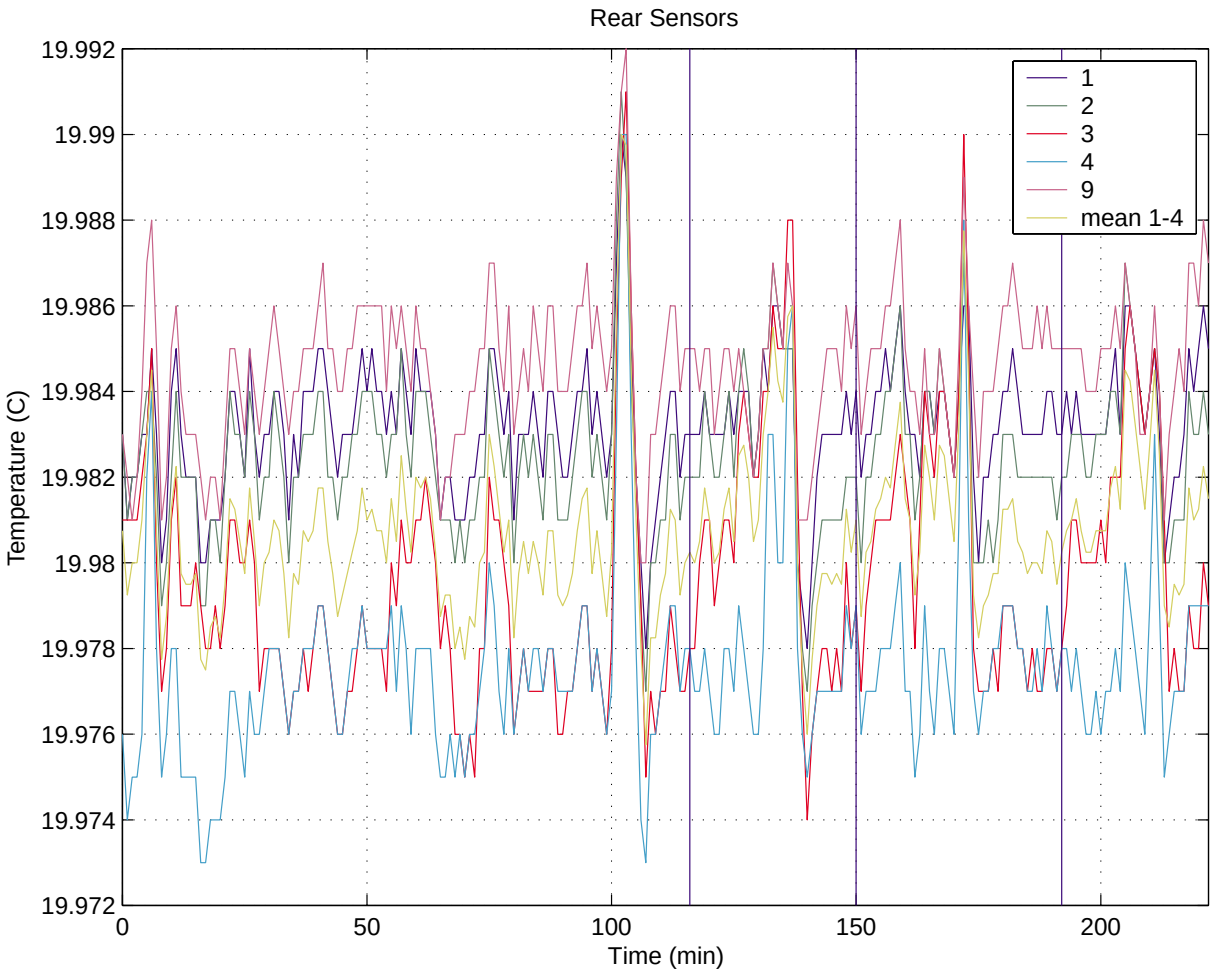

Figure 5-10: Rear sensor temperatures averaged over a minute. The vertical lines denote the time when a SBIL routine was performed.

sensor is 9 mK in the worst case (maximum minus the minimum temperature from time = 20 minutes to time = 90 minutes). The total range of temperature for sensors 1-4 is 14 mK.

Figure 5-12 shows the temperatures of the vertically located sensors. These sensors are toward the front of the system and are sensitive to the door opening. Figure 5-13 displays the same data with a zoomed temperature scale. In equilibrium, the vertical sensors show a temperature gradient where the air is cooler at higher points – for the series 10-0-11. Sensor 6 is directly in the flow from the air handler and is affected by the non-uniformity of that air stream. The average gradient between sensor 10 and 11 is 10 mK over 24 inches or 16 mK per meter, which is consistent with the

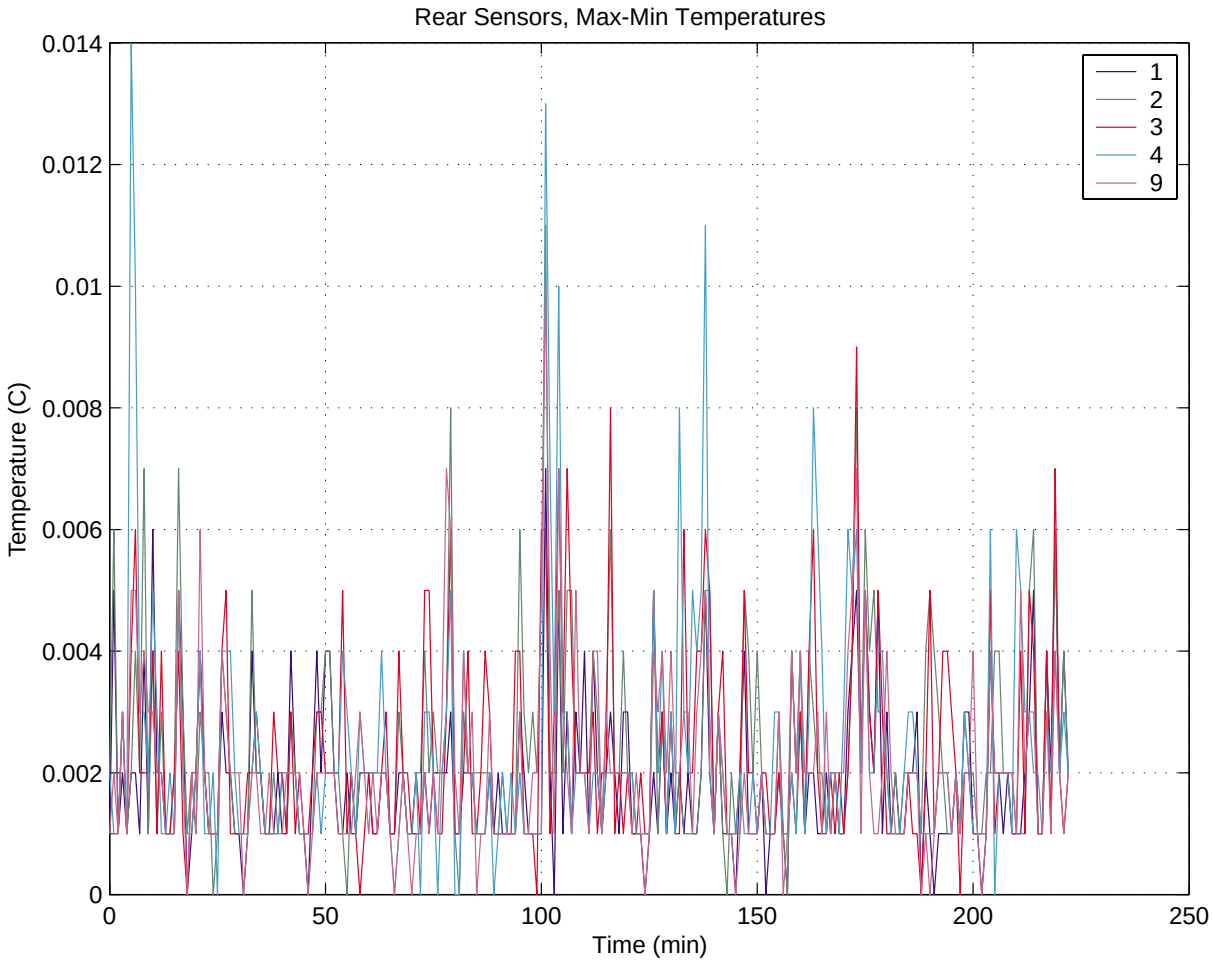

Figure 5-11: The difference between maximum and minimum temperatures occuring during a one minute time frame, rear sensors.

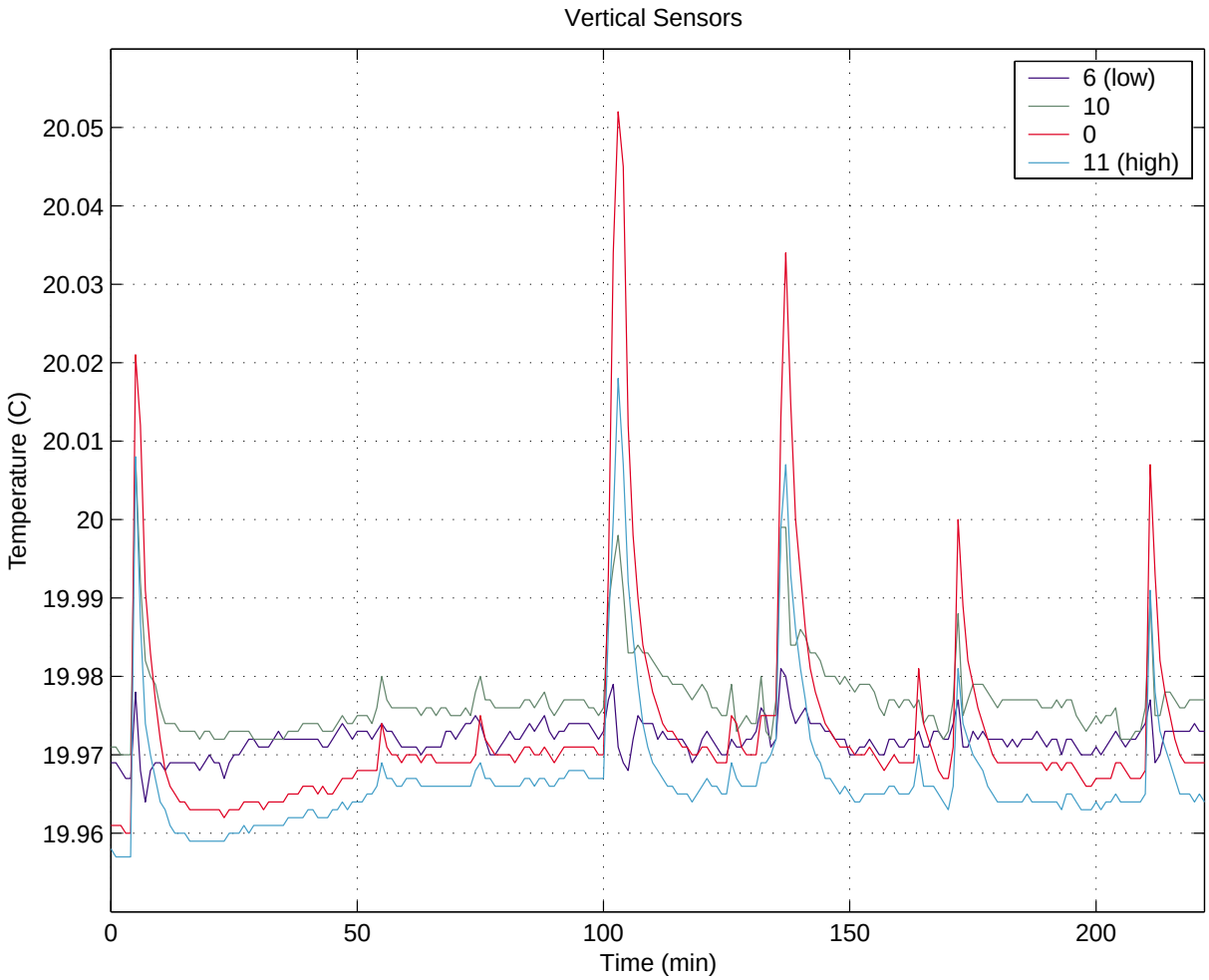

Figure 5-12: Vertical sensor temperatures. The spikes in temperature correspond to the opening of the environmental chamber door.

vertical gradient that I discussed earlier. Figure 5-14 shows the difference between the maximum and minimum temperature during a minute.

Figure 5-15 shows the front sensor temperatures during various experiments. Numbered vertical lines mark the start of the events indicated. At line 1, the stage performed a SBIL routine with the following parameters: v = 50mm/s, a = 0.05 g, jerk = 4.9 m/s^3, scans =379, scan length = 360 mm, and step = 0.8 mm. This routine would be suitable for patterning an entire 300 mm wafer. The approximate time for this routine is 49 minutes. There is a noticeable instability during the routine. The power dissipation of 2 mW in the x motor and 17 mW in each y motor is too small to explain this instability. Instead, it is attributed to the non-uniform airflow from air

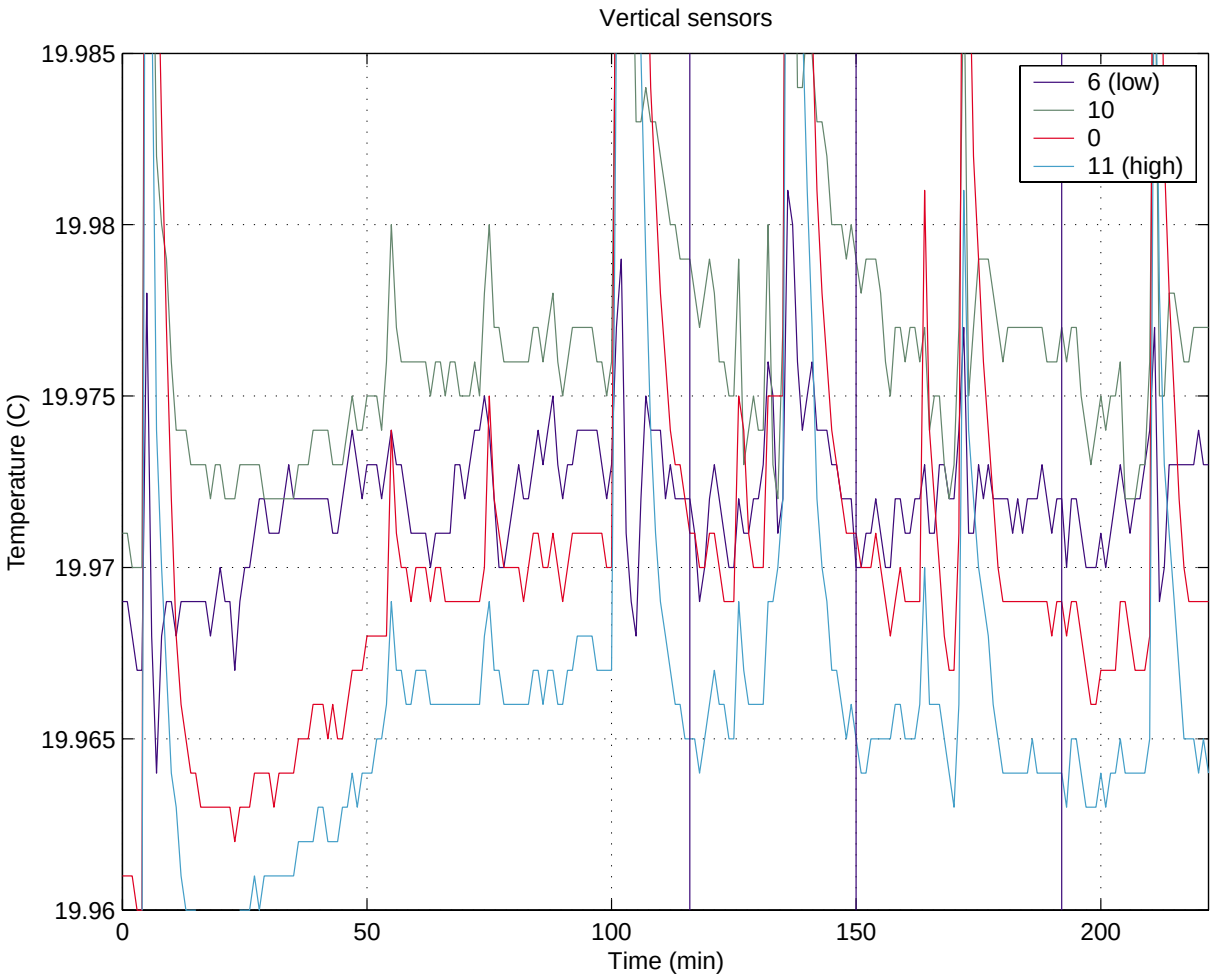

Figure 5-13: Vertical sensor temperatures with a zoomed temperature scale. The vertical lines denote the time when a SBIL routine was performed.

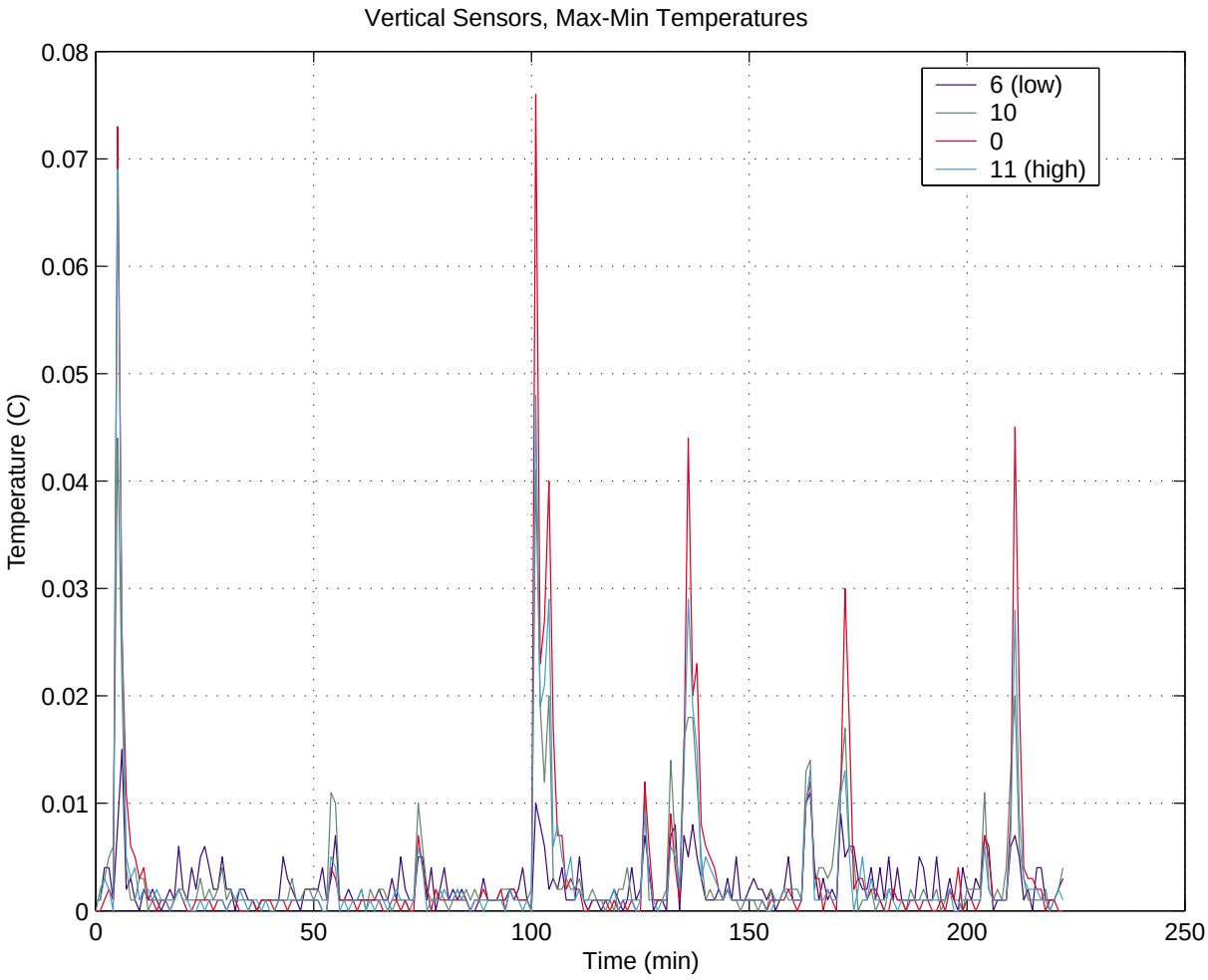

Figure 5-14: The difference between maximum and minimum temperatures occuring during a one minute time frame, vertical sensors.

handler-A diverting due the stage position. At line 3, the stage was moved into the corner of the system toward air handler A and the Y1 motor. Sensors 5-8 are clearly sensitive to the stage position. Sensor 5 increases in temperature by more than 10 mK, while sensors 6 and 8 drop by about 5 mK. This effect is highly repeatable and is definitely not due to any heat source since a separate test confirmed the response does not change when every electronic device in the system was unplugged. At line 4, the stage was moved back to the center of travel and sensors 5-8 quickly return. At line 5, a SBIL routine identical to the previous one started but with the scan velocity of 100mm/s. There is no noticeable temperature rise with the estimated 4 mW in the x motor and 81 mW in each y motor. The sensors actually appear more

stable with the faster routine. The sensor time response and the time response of air diverting probably favors the faster scanning. At line 7, a SBIL routine initiated with a = 0.25 g, jerk = 2.45 m/s^3, v = 300mm/s, and a scan length of 0.42m. There is clearly a temperature rise at sensor 5 and 9 of about 10 mK. The expected x axis and y axis powers are 44 mW and 2.5 W respectively. The significant temperature rise is attributed to the Y1 motor power. The temperature falling before finishing the routine is likely because of the extra air flow for the Y1 motor when the stage moves away from it. At line 8 the stage returned to the center and the power to the system was cut. The very slow change in temperature of 4 mK for sensors 5 and 9 might be attributed to the system not being at thermal equilibrium when the experiments began. Moreover, previous to taking this data, lights were on and the tool temp A sensor had been moved. This equilibration affects the data on very long time scales and does not detract from the conclusions made regarding the motor heating effects and the stage position effects. Also, the humidity control was on during these experiments, which contributes temperature fluctuations at short time scales. The humidity control especially affects the difference between the maximum and the minimum temperatures over a minute.

To verify that the temperature rise is due to the y axis motor power, the system was scanned at a =0.25 g, v = 300mm/s, and a scan length of 0.42m with no x axis step over. Figure 5-16 shows the data where the scanning began at the first vertical line. The scanning ran for about 29 minutes where the end is designated by the second vertical line. The power dissipated in each y axis motor is expected to be 2.7 W. After about 13 minutes, the temperature rise at sensor 5 and 9 are similar to those shown in Figure 5-15. Therefore, the temperature rises in the region of sensors 5 and 9 are primarily attributed to the y axis motor. Furthermore, the x axis motor dissipation for the SBIL routine is not the limiting air temperature stability, at least for the measurement points considered.

The stage can be slowed to what ever speed necessary to prevent significant heating. Furthermore, the 100 mm/s SBIL profile provides more than adequate speed for research purposes. These experiments also revealed that the temperature gradients

leads to significant instability when the stage is moving.

The nonuniform temperature air will cause temperature changes of the chuck that are dependent on the stage position. Figure 5-17 shows the chuck temperature and the temperature near the T_A sensor. The sensor measuring the temperature of the chuck was located within one of the light weighting cavities. This sensor was really measuring the air in that cavity since the sensor housing did not actually contact the chuck. The temperature of the chuck may be even more stable than the measurement over the short time scales. The stage was moved to the rear corner of the system that is closest to the laser at the time denoted by the vertical line. From this data, it is clear that the chuck temperature will be a function of the stage position. The temperature jump of 0.01 °C is significant since the chuck expansion will produce 2 nm of error for the largest substrates. Furthermore, the chuck responds with a time constant on the order of less than 10 minutes, which is less than the time typically required to pattern a substrate. Additionally, the temperature rise may be associated with the laser heating and air flow past the laser being partly blocked by the stage. The higher chuck temperature than the air temperature measured at other places in the critical volume supports this hypothesis.

Operating the stage in the smallest range of travel will help the chuck stability. Also, since the stage is moving back and forth the chuck will tend to average the temperature along the scans. However, if the chuck is allowed to equilibrate to a temperature different than the average "scan temperature", which is certain to happen without care, the chuck expansion during the writing is likely to be a significant error. Therefore, the non uniform air temperature is extremely problematic for the chuck the stability.

The data does show that the chuck temperature is much more stable than the air temperature. Over the time from 0 to 80 minutes the system was essentially in equilibrium. The minute averaged chuck temperature varies by 3 mK peak-to-valley whereas the air temperature by Tool Temp A sensor varies by 11 mK. Furthermore, the max-min temperature during a minute is 2 mK for the chuck versus 7 mK for the air temperature by the control sensor.

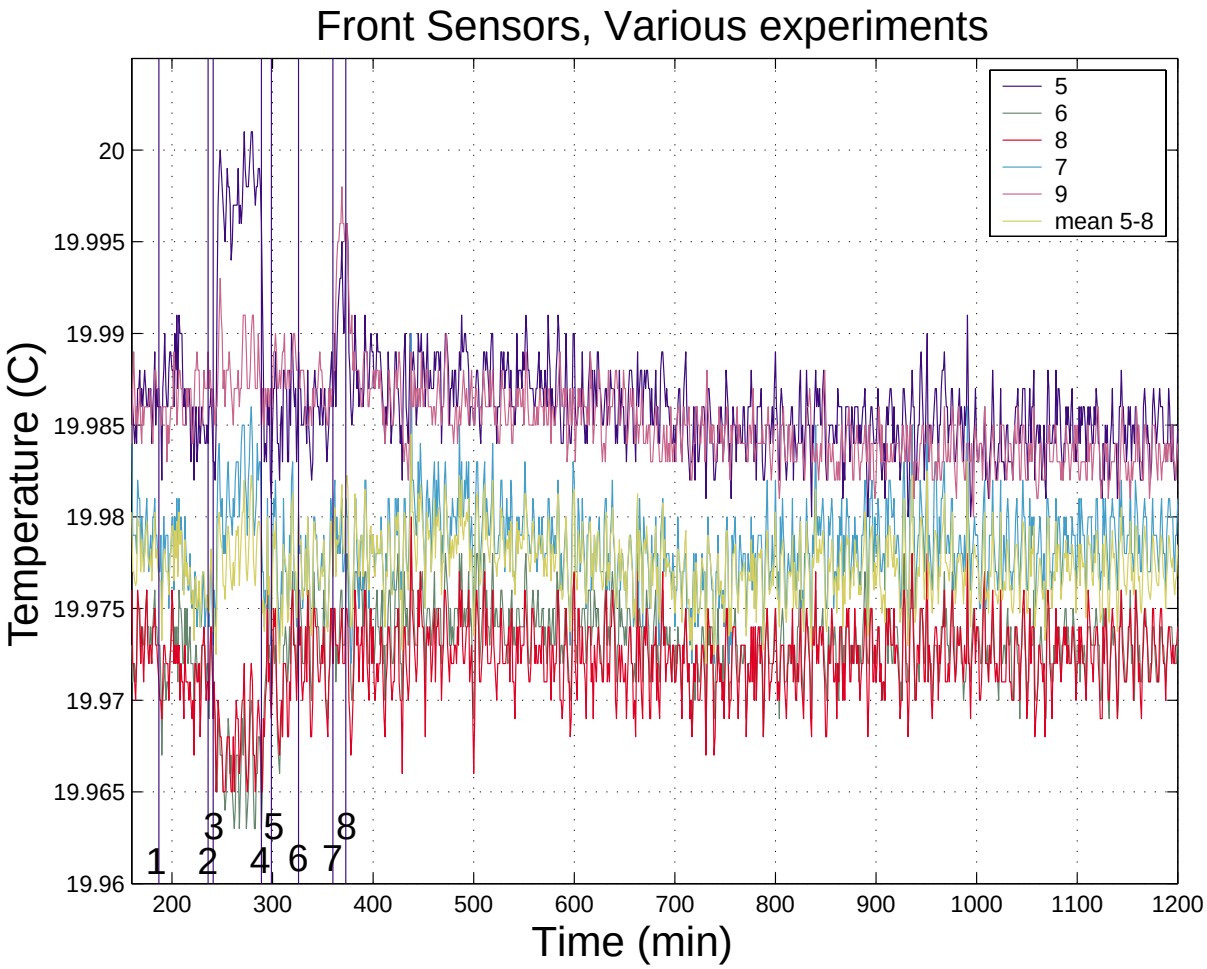

1) Start 50 mm/s SBIL routine (49 minutes), Px = 2 mW, Py = 17 mW
2) End SBIL routine, stage returns to center
3) Stage moves to front, right corner
4) Stage returns to center
5) Start 100 mm/s SBIL routine (27 minutes), Px = 4 mW, Py = 81 mW
6) End SBIL routine, stage returns to center
7) Start 300 mm/s SBIL routine (13 minutes), Px = 44 mW, Py = 2.5 W
8) End SBIL routine, stage returns to center, all power off

Figure 5-15: Front sensor temperatures during various experiments. The motor powers for the SBIL routines are noted. A brief description of the experimental events is shown and marked with the vertical lines.

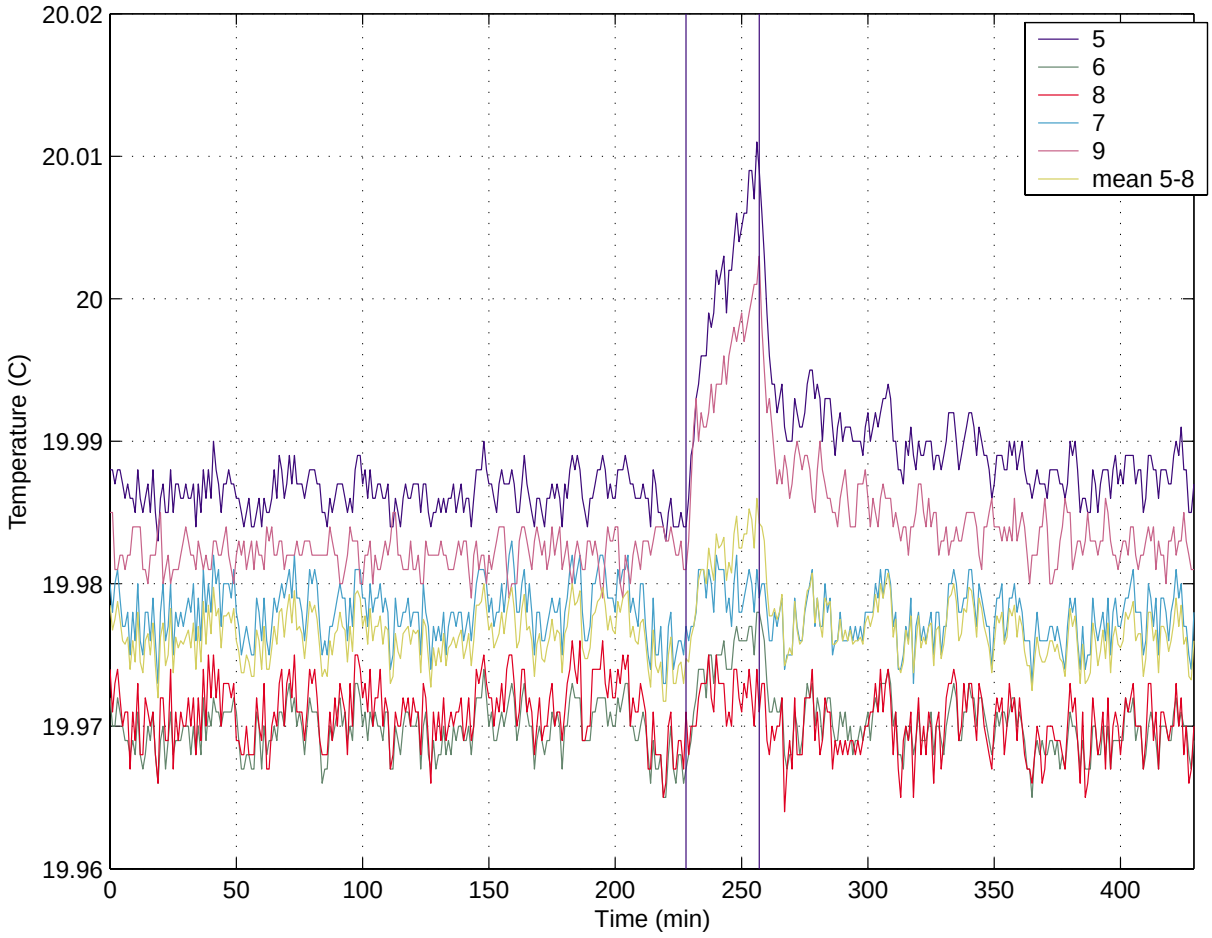

Figure 5-16: Front sensor temperatures during a test of the y axis motor dissipation. The first vertical line marks the start of y axis scanning. The second vertical line marks the end of scanning.

Figure 5-18 shows the rear sensor temperatures during the same experiment. Sensor 9 temperature moves by about 2 mK. The response at this sensor is expected if the stage is blocking air flow past the laser.

Based on the data collected, the temperature stability in the front side critical volume is ±7 mK if the humidity control is off. The rear side critical volume stability is ±5 mK. This conclusion ignores the filtering of high frequency temperature fluctuations due to the 10 second time constant of the sensors. The uniformity of the air in the critical volume is about 29 mK peak to valley under usual circumstances. If the stage is moved into the corner, the uniformity in the critical volume is worse than 40 mK. The fact that the stage position affects the temperature measurements

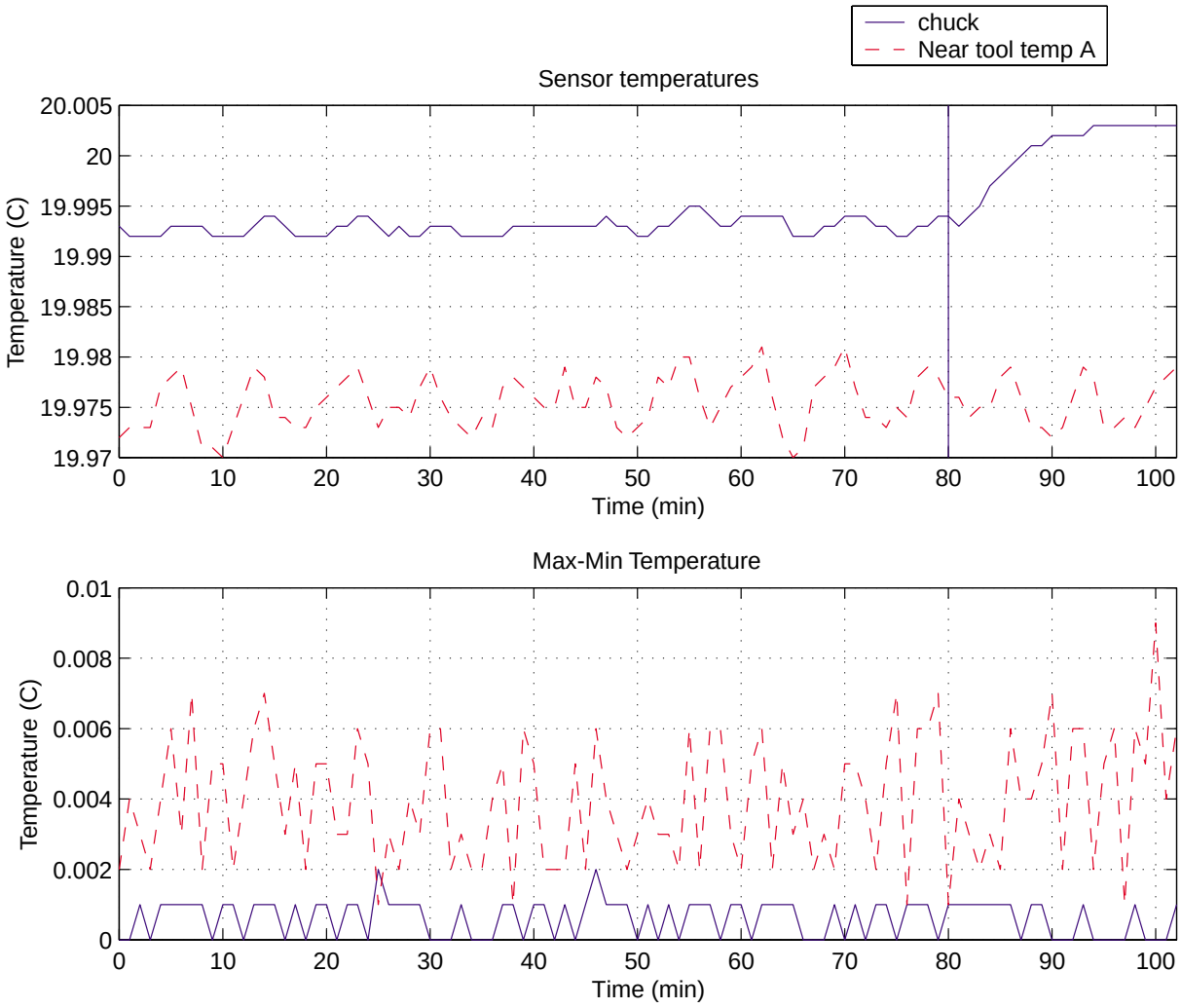

Figure 5-17: Temperature measurements testing the affect of stage position on the chuck temperature. A diagnostic sensor was placed close to Tool Temp A sensor and another sensor was placed within one of the cavities of the chuck. The vertical line denotes the time when the stage was moved. The top plot shows the minute-average temperatures and the bottom plot shows the maximum minus the minimum temperature during a minute.

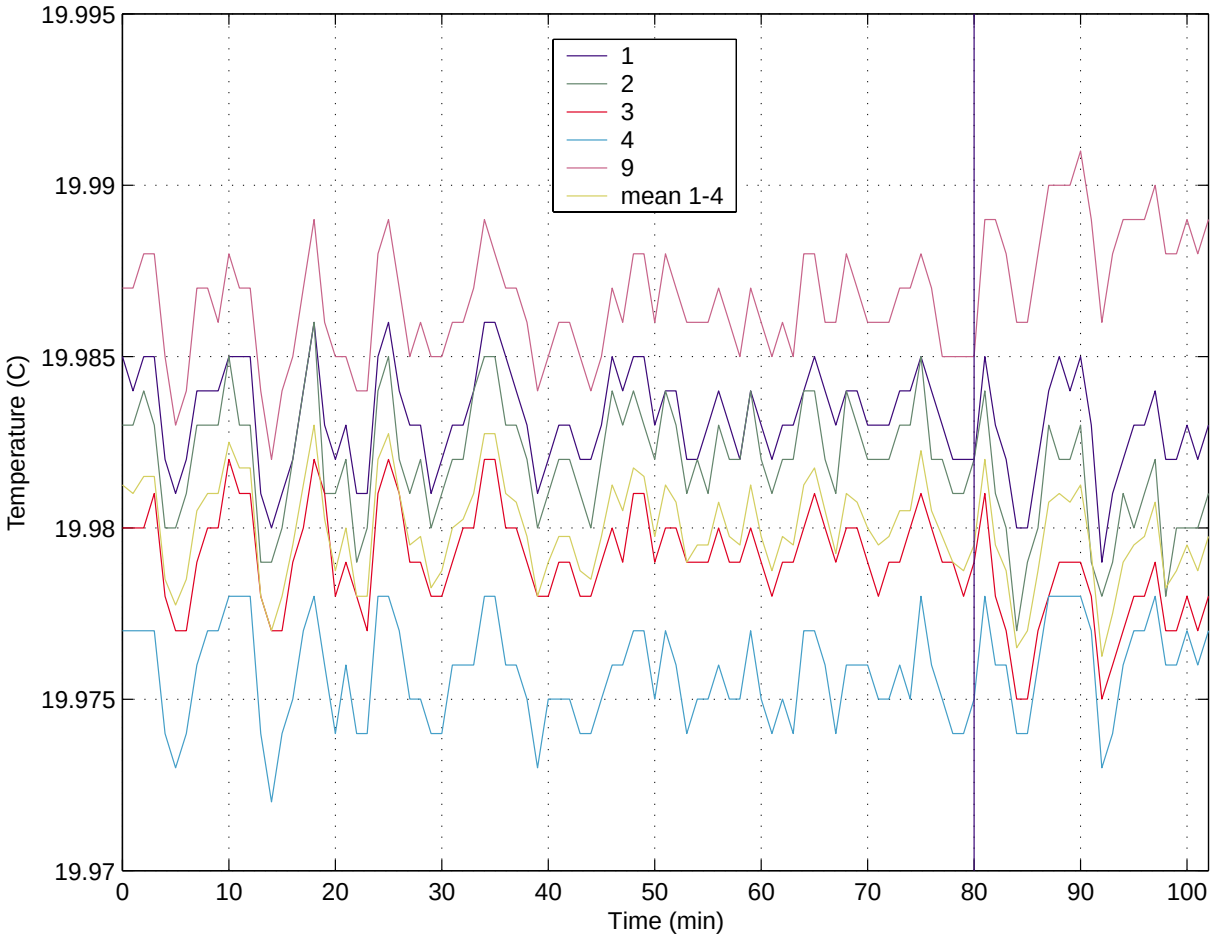

Figure 5-18: Temperature measurements of the rear sensors when testing the affect of stage position on the chuck temperature. The vertical line denotes the time when the stage was moved.

supports the assertion that the air blowing out of the ULPA filters is non-uniform. Non-uniform air in the beam path creates errors that are uncorrectable by the refractometer. The non-uniform temperature air will also lead to thermal expansion errors that depend on the stage position.

5.5 Humidity measurements

The humidity in the system is regulated by the lowest temperature chill coil. Figure 5-19 shows the temperature of the air leaving the chill coils. Chill coil A is much warmer than chill coil B and is expected to have no effect on the humidity regulation.

Chill coil B has a temperature around 5.5 °C. The relative humidity calculated using a dew point of 5.5 °C for air with a temperature of 20 °C is 38.7%. This corresponds well with measured humidity range from 38.62% to 39.04% seen in Figure 5-20. The humidity sensor[5] has a response time of 15 seconds and an expected accuracy of about ± 2% while the stability of the sensor is not specified. The stability was to be verified with another humidity meter. The slightly higher measured humidity may be associated with the inaccuracy but the humidity is in fact expected to be higher than that calculated from chill coil calculation because of the small amount of high-moisture (40% RH to 55% RH) content makeup air. The humidity sensor is located on the air handler A side of the room and all the make up air was taken through a grill in air handler A. The humidity uniformity across the room is expected to be uniform to at least the tenths of a percent level. The humidity varies by 0.4% peak to valley over a half hour. Slow humidity variations should be largely uniform across the chamber and can be corrected by the refractometer. It is not clear to what extent the humidity variations that occur over tens of seconds will be uniform and thus correctable by the refractometer. The humidity uniformity was never verified with multi-point measurements. The sensor noise contribution is also not known. In the worst case, the humidity variation over the tens of second time frame is 0.25% peak to valley. The humidity contribution to the air index related errors is expected to be below ± 0.2 nm. The humidity stability is thus very good by virtue of the chill coils being maintained at a reasonably constant temperature.

5.6 Pressure measurements

The pressure gradients affect the linearity of the interferometric measurements if they are stable. Instability in the pressure gradient produces uncorrectable errors. To measure the magnitude of pressure fluctuations, the enclosure is equipped with a differential pressure sensor[6]. This sensor measures the pressure difference between the

[5]Vaisala HMP231, wall mounted humidity and temperature transmitter.
[6]Modus T30-001, Modus Instruments Inc.

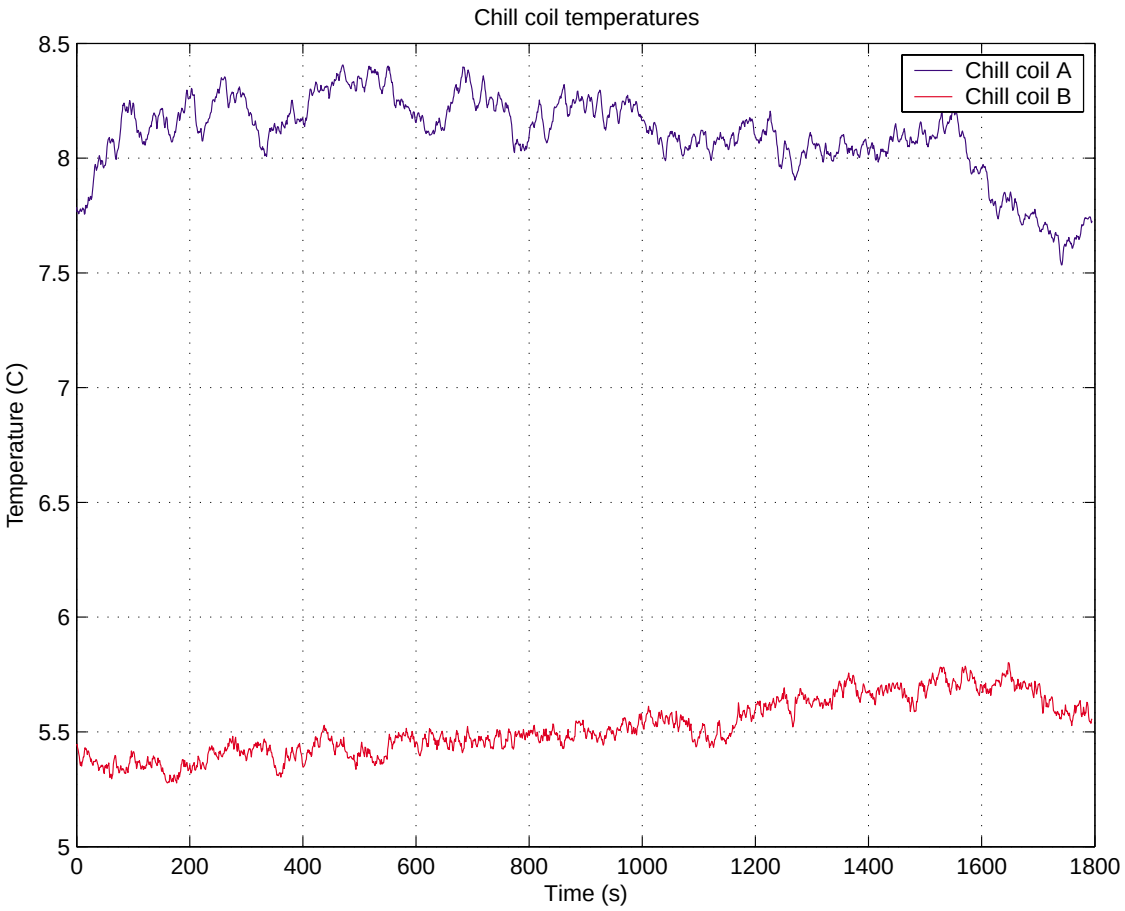

Figure 5-19: Temperature of air leaving the chill coils.

two locations indicated in Figure 5-3 and Figure 5-4. If the air handling equipment induced any significant pressure fluctuations, it would show up in this measurement. The air path length between the differential points is greater than one meter long. Figure 5-21 shows the differential pressure measured by this sensor over 30 minutes. Most of the pressure fluctuations in this data are very likely acoustic. Acoustic measurements will be discussed in Section 8.3. Figure 8-36 shows acoustic data where the 3σ pressure is 0.9 Pa between 0 and 800 Hz. Assuming the pressure varies by ± 0.5 Pa over 1 meter, the gradient is ± 0.5 Pa/m.

Figure 5-22 shows the differential pressure when the clean room doors were opening and closing. The largest spike corresponds to the opening of the two sets of clean room doors at nearly the same time. Opening both sets of clean room doors drops the pressure in the clean room by about 30 Pa, as measured by another differen-

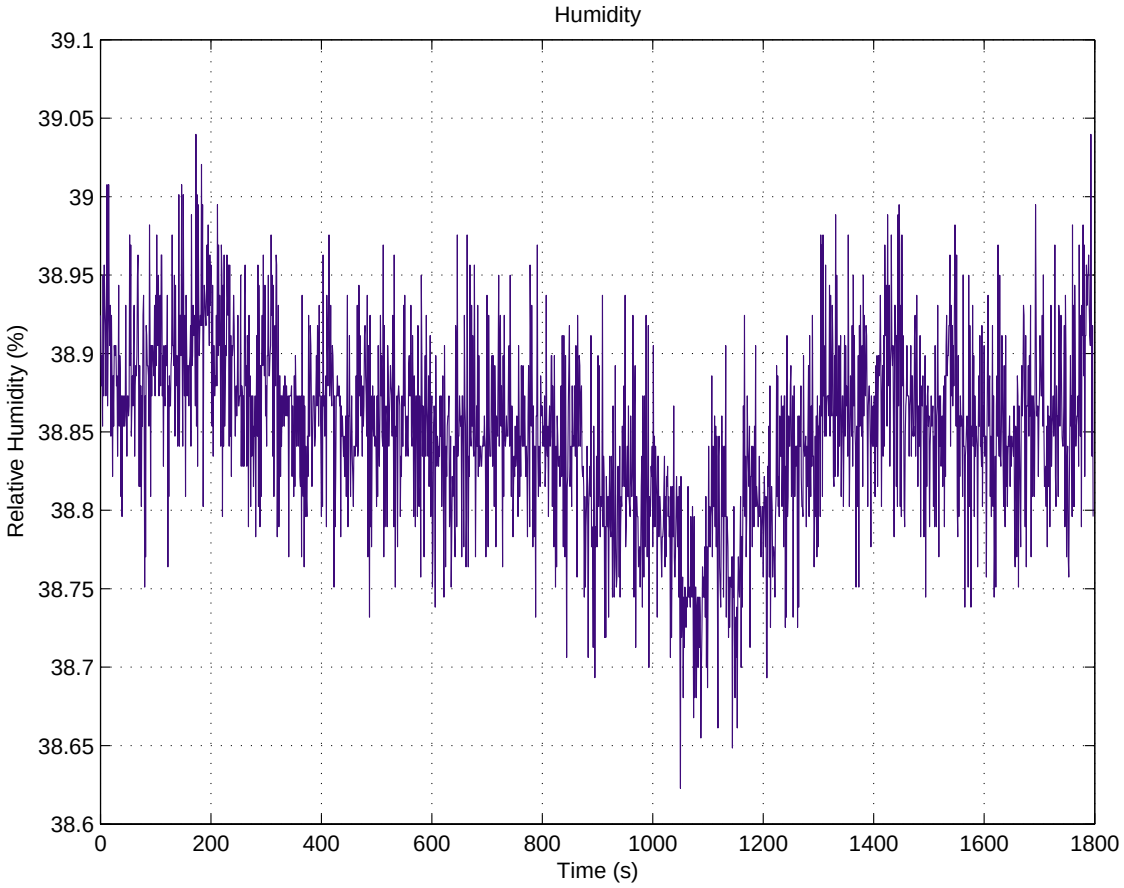

Figure 5-20: Relative humidity without any humidity control. The chill coils are controlled to a constant temperature and the makeup air is expected to be a small fraction of the total air flow, making the relative humidity much more stable than the outer room humidity. Over one half hour the humidity varies by 0.4% peak to valley.

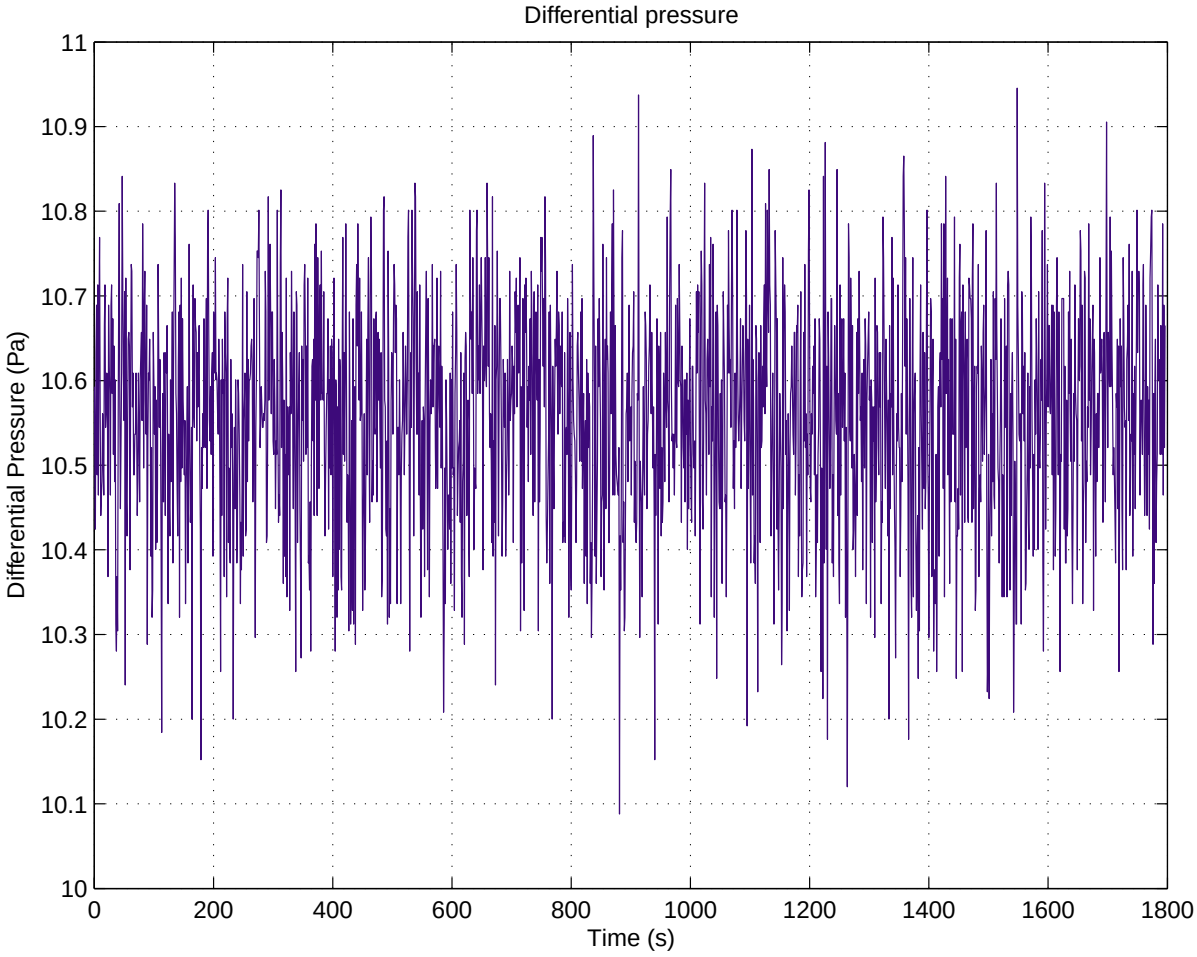

Figure 5-21: Differential pressure

tial pressure sensor installed in our clean room. In the extreme case, the maximum differential pressure change sensed by the enclosure sensor is only about 1 Pa. Conservatively, the pressure gradient cause by this extreme case is 1 Pa/m. Even with large changes in the clean room pressure, the pressure gradient in the SBIL system is not significant.

Although I haven't measured the differential pressure along the interferometric beam paths, a conservative estimate of this pressure gradient due to the viscous pressure drop of the moving air is found by dividing the entire enclosure differential pressure by the path the air travels. This linear assumption of pressure gradient with path length is conservative because the interferometric beam path is very open and most of the pressure drop probably occurs in the dampers of the air handler return. Since the linear path is at least 4 meters, the expected pressure gradient is expected to be less than about 10.6 Pa over 4 meters or 2.7 Pa/m. The specification of 16 Pa/m is therefore expected to easily be met. Furthermore, this specification arguably is conservative because the pressure gradient error may be largely repeatable if the pressure gradient is constant.

The errors due to acoustic pressure and the pressure gradients are expected to be less than $\pm$ 0.2 nm.

5.7 Conclusions

The low frequency unobservable error derived from the power spectral density of Figure 8-37 from 0 to 100 Hz with the 60 Hz error removed is 0.75 nm 1σ. The data was 56 seconds long and the stage was positioned such that the nominal deadpath in the x axis interferometer was 7.2 cm. The majority of this error is likely due to index fluctuations – the vibration errors are much smaller and the thermal expansion errors are only significant at very low frequencies, approximately below 0.04 Hz as discussed in Section 9.2. To further support the assertion that most of the error is index related, shutting down the air handlers noticably reduces the errors between 2 and 100 Hz. Since vibrations are too small to explain the extra error with the air handlers on, the

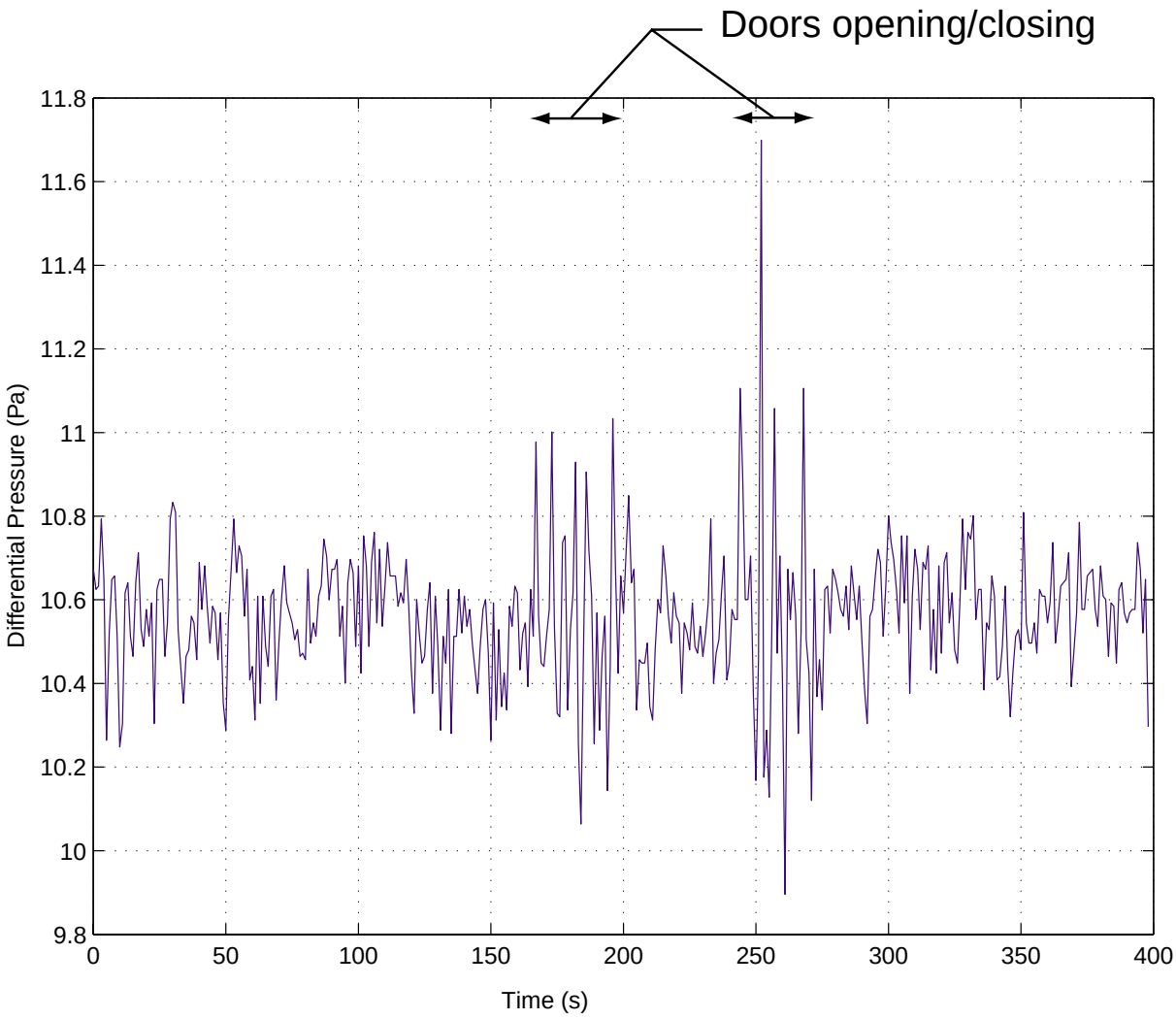

Figure 5-22: Differential pressure during times when the clean room doors were opening and closing. The clean room has two sets of doors and the largest spike corresponds to the opening of both doors at nearly the same time.

air index is hypothesized to have parcels of different temperature air that increase the frequency of the error as the air speed increases. At low frequency with the air handlers on, errors decrease at frequencies below 2 Hz due to improvements in the temperature control. Additional strong evidence indicating that the errors below 100 Hz are dominated by air index nonuniformity comes from Section 9.2. There, I show that the errors over two minutes increase with increasing deadpath despite the refractometer correction.

While it is impossible to accurately predict the index error based on the tempera-

ture data discussed, the error observed does appear consistent with the temperature instability and gradients in the system. The accurate prediction cannot be made with the data discussed because temperature data at many spaces along the beam paths are required with sensors having time constants of several milliseconds. Measurements on spatial scales smaller than the interferometer beam spacing of 0.75 inches would be ideal.

In the absence of those measurements, the temperature nonuniformity between sensor 5 and 6 indicates the air could very well be responsible for most of the error observed. These sensors measure air that is blown directly into the interferometer beam path. Their temperature range is 29 mK when the stage is nominally centered. The measurements are low pass filtered by the 10 second time constant of the thermistors and the actual range is expected to be larger. The sensors, which are spaced less than a foot apart, also have a stable gradient of 15 mK for the stationary stage in the center of travel. The measured stability at a single thermistor is ± 7 mK. The air in the beam paths is expected to be very non uniform since the air with large gradients must mix as it makes a turn at the stage and into the x interferometer beam path. The close spacing of the reference and measurement interferometer beams provides some insensitivity to the inhomogeneity on large spacial scales. But even when the stage is positioned to have zero deadpath, index related errors still exist. Furthermore, within the x axis and refractometer interferometers nominally unbalanced measurement and reference arms respond to temperature fluctuations at different rates than the unenclosed beams. Even if only the 7.2 mm of deadpath is considered and the temperature fluctuation of ± 7 mK is assumed, then ± 0.44 nm of error is expected. The additional observed error could very well be due to the actual temperature control being worse because of high frequency fluctuations. Index instability across the balanced path sections of the interferometers also cause errors.

Correcting the temperature nonuniformity and improving the stability will likely lead to significantly improved system stability. The obvious place for improvement is to track down the source of the large temperature gradient observed between sensor 5 and 6. Removing this gradient will likely lead to improved the overall stability of the

A side temperature control since the T_A sensor reading won't be as noisy. In general, temperature gradients and control can be improved throughout this system. Since the heat sources can be contained and minimized, it may be possible to improve the temperature stability and gradients by an order of magnitude.

Enclosing the beam paths and x axis interferometer in vacuum is however guaranteed to fix index non uniformity problems. A bellows or a sliding vacuum tube could be retrofitted to the system. A more compact metrology block optic design or one contained in vacuum will probably also be important. The enclosed beam paths may be required to achieve angstrom level error budget terms.

Two-wavelength interferometers might be considered to eliminate air-index errors [54, 43]. However, these interferometers have not been demonstrated with the necessary stability and they may introduce noise that is greater than the stability that we are already achieving. Also, humidity fluctuations may necessitate three wavelength interferometers [11], which have never been demonstrated. Designing low temperature coefficients for these complex multi-wavelength interferometers may be problematic.

The thermal expansion of parts is the largest error source on long time scales. A lower CTE chuck will allow a more lenient specification on the remaining temperature gradients. The chuck has the worst thermal coefficient among the critical components. Use of a better material, such as Zerodur, Expansion Class 0, would improve this component. Since the chuck must move throughout the space it is sensitive to the temperature gradients. To some extent it should be possible to correct for the chuck expansion by measuring the temperature of the chuck and applying a correction. The beam splitter mount on the metrology block is the next worst component and although it doesn't have the worst temperature coefficient, it will have the fastest time constant. The chuck and the beam splitter mount could be designed for improved temperature sensitivity.

Although the index errors and thermal expansion errors are the largest errors remaining in the system (not including the particle defects discussed in Chapter 9), there are many areas for improvement.

Chapter 6

Beam steering and beam splitting for interference lithography

The stability of a laser beam's position and angle affects the accuracy and dose uniformity of interferometrically produced patterns. We consider the beam stability requirements for the cases of interference by plane and spherical waves. Interferometers using beamsplitter cubes and diffraction gratings are among the analyzed topologies. The limitations of spatial filtering to remove angular variations are also discussed. We present a beam steering system that uses position sensing detectors, tip-tilt actuators, and digital control to lock the beam position and angle at the interference lithography system. The prototype's performance and limitations of the approach are discussed. This beam steering system allows us to locate the laser far (≈10 m) from the sensor assembly, thereby reducing the thermal and mechanical disturbances at the lithography station and allowing sharing of the laser between different lithography tools. We demonstrate the beam steering error of our system is acceptable for production of nanometer accuracy fiducials. The analysis of grating interferometers leads to the +1/-1 order diffraction grating as the ideal beamsplitter for interference lithography because it can provide insensitivity to the spatial and temporal coherence of the laser. Parts of this chapter follow closely from Reference [59].

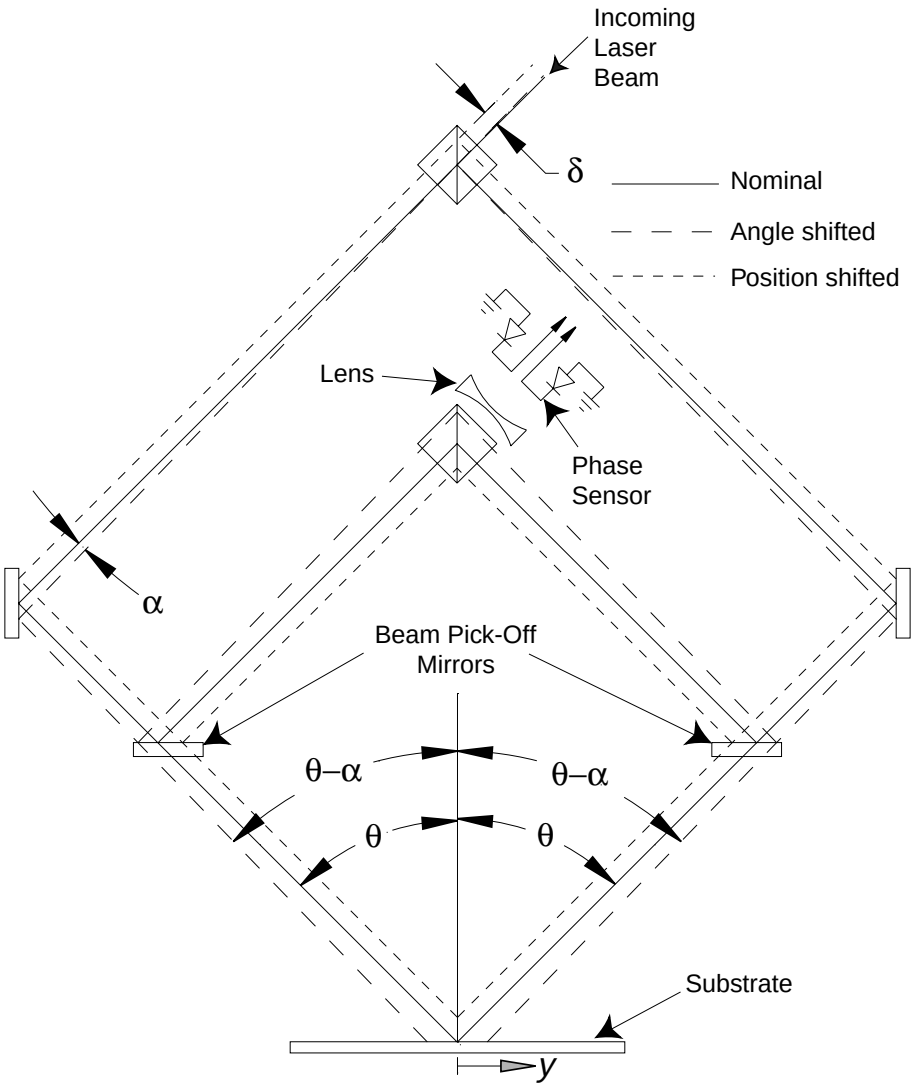

Figure 6-1: Ray trace of interference lithography optics showing paths when the incoming beam is unstable in angle and position.

6.1 Beam Stability Requirements for Plane Wave Interference

Figure 6-1 shows the ray trace of basic interference lithography optics for a nominal incoming beam, a ray deviated by the angle α, and a beam offset by distance δ. The beamsplitters in this system are reflective. The phase sensor is schematically shown.

For the case of plane waves, the interference results in a fringe pattern with a period given by Equation 1.10. When the incoming beam is unstable in angle by α,

the phase at the center of the interference pattern does not shift if the path length on each side of the interferometer is matched. However, the period change due to the change in half angle causes a phase shift that increases toward the edges of the exposed pattern. At the distance, y, from the bisector plane, the phase error, ϕ_e, is given by

$$\phi_e = 2\pi q = \frac{4\pi y}{\lambda}\left[\sin\theta - \sin(\theta - \alpha)\right] \approx \frac{4\pi y}{\lambda}\alpha\cos\theta. \tag{6.1}$$

The symbol q denotes the spatial error normalized by the period, i.e. for 0.1 nm error and a 200 nm period, then $q = 1/2000$. The approximated expression is valid for $\alpha << 1$. Solving for α as a function of Λ_0, we find

$$\alpha = \sin^{-1}\left(\frac{\lambda}{2\Lambda_0}\right) - \sin^{-1}\left(\frac{\lambda}{2\Lambda_0} - \frac{q\lambda}{2y}\right) \approx \frac{q\lambda}{2y\cos\theta} = \frac{q}{y\sqrt{\frac{4}{\lambda^2} - \frac{1}{\Lambda_0^2}}}. \tag{6.2}$$

Figure 6-2 shows α plotted when $q = 1/2000$, $y = 1$ mm, and $\lambda = 351.1$ nm. The dotted line indicates the large period asymptote, which is $\alpha = \frac{q\lambda}{2y}$. The plot shows that for the same fractional interpolation of period, the largest allowable angular instability occurs for the smallest periods. However, the required angular stability is severe even at $\Lambda_0 = 200$ nm where it amounts to about 0.18 μrad. While this reflective beamsplitter configuration is very sensitive to *angular* stability, beam *position* stability does not affect either the fringe period or phase.

When collimating optics are used in each arm, the beam will have a transfer function where both the beam's position and angular instabilities affect the angles of the beams impinging on the substrate. Therefore, appropriate magnification factors can be applied to the analysis above to determine the allowable magnitudes of these instabilities. However, for a basic configuration with a magnification factor of one, the allowable angular instability is a severe requirement.

It is of interest to note that the intensity profiles on the wafer shift with position and angle changes, which leads to contrast loss at the edges of the interference pattern. Therefore, beam position shifts in the wafer plane should be maintained to a small fraction of the beam width. For example, a 1 mm beam radius and a 1% radius shift requires position stability of better than 10 μm.

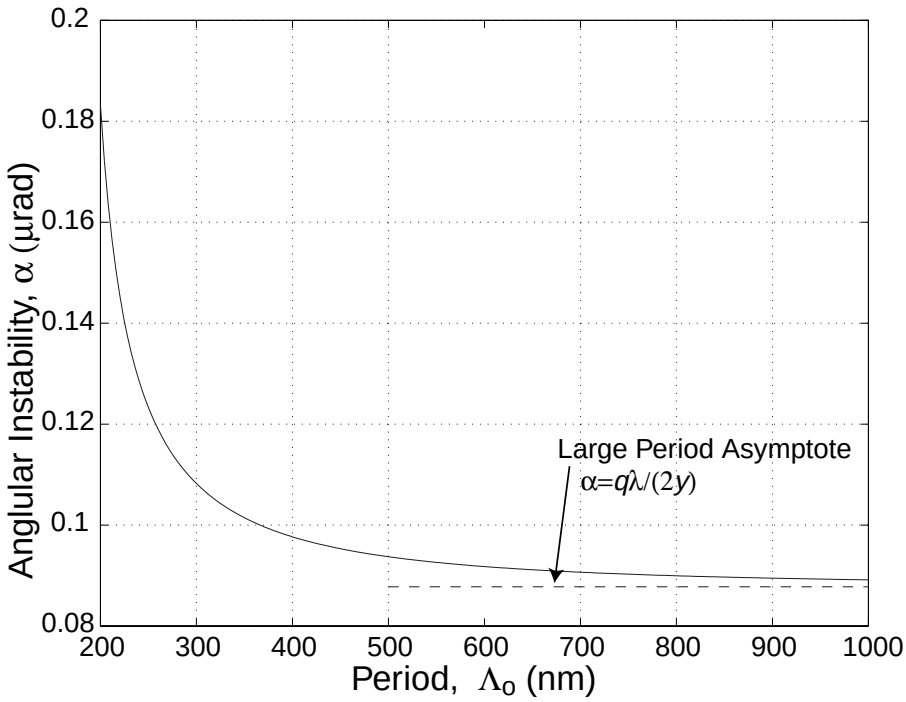

Figure 6-2: Allowable angular instability for $q = 1/2000$. The dotted line indicates the large period asymptote.

As we discuss in Section 6.4, we have found that after propagating a beam to the interference lithography system over about 10 meters with many mirror bounces, the beam angular instability is greater than the sub microradian requirement even with an active beam steering system. The sources of this instability include rocking of the isolation tables of the laser and the lithography stations, air index gradients, vibration of the optical components, and thermal drifts. Therefore, we analyzed other optical topologies that may be less sensitive to the instabilities of the incoming beam.

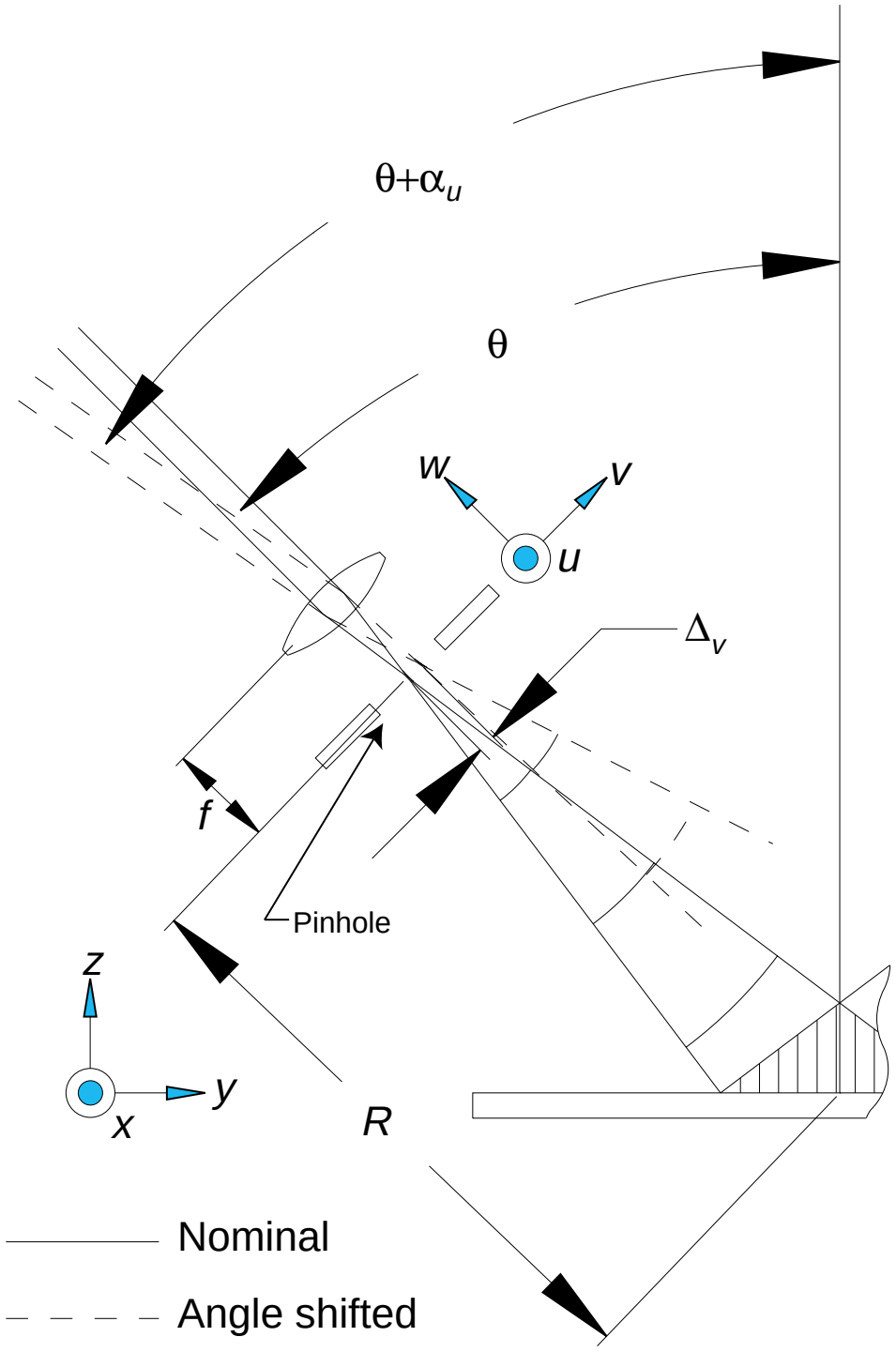

Figure 6-3: Interference of spherical waves showing the shift in waist position due to an angle shift of the incoming beam (partial view).

6.2 Beam Stability for Spherical Wave Interference

The shape of the interference fringes produced by spherical waves has been studied in detail.[46, 25, 27] The phase errors due to beam instability follow from the effect of the beam waist being focused to a shifted position due to angle changes. Figure 6-3 illustrates the shift in the position of the beam waist. The normalized spatial error due to this position shift is given by

$$q = \frac{R}{\lambda}\left(\sqrt{X^2+\cos^2\theta+(\sin\theta-Y)^2}-\sqrt{X^2+\cos^2\theta+(\sin\theta+Y)^2}-\right.$$
$$\sqrt{(X-U)^2+(\sin\theta-V\,\cos\theta-Y)^2+(\cos\theta+V\,\sin\theta)^2}+$$
$$\left.\sqrt{(X-U)^2+(\sin\theta-V\,\cos\theta+Y)^2+(\cos\theta+V\,\sin\theta)^2}\right). \qquad (6.3)$$

Here we have used the normalized variables $X = x/R$, $Y = y/R$, $V = \Delta_v/R$, and $U = \Delta_u/R$ where R is the distance from the pinhole to the center of the interference pattern on the substrate. Symbols Δ_v and Δ_u denote the transverse beam displacements in the pinhole plane due to change in beam angle. For $V << 1$, $U << 1$, and series expanding with respect to V, this equation reduces to

$$q = -\frac{R}{\lambda}Y\,\cos\theta\left(\frac{1}{\sqrt{1+X^2+Y^2-2\,Y\,\sin\theta}}+\frac{1}{\sqrt{1+X^2+Y^2+2\,Y\,\sin\theta}}\right)V+O(V)^2 \qquad (6.4)$$

For a spot size of radius $\rho = \sqrt{x^2+y^2}$, the maximum phase error occurs for $x = 0$ and $y = \rho$. Since $V = \alpha_u f/R$, where f is the focal length, the maximum allowed deviation in beam angle from Equation (6.4) for $\rho/R << 1$ is approximated as

$$|\alpha_u| \approx \frac{q\lambda R}{2f\rho\,\cos\theta}. \qquad (6.5)$$

By combining the approximation given in Equation (6.2) with Equation (6.5),

the relationship between the allowable angular stability for spherical waves and plane waves when $\alpha << 1$ becomes $\alpha_{u,spherical} = \frac{R}{f}\alpha_{u,plane}$. Thus for large R/f, the allowable angular instability is much greater for the expanded spherical waves.

Now we consider the effect of deflection, U. For $V << 1$, $U << 1$, and series expanding with respect to U, Equation (6.3) reduces to

$$q = \frac{R}{\lambda} X \left(\frac{1}{\sqrt{1 + X^2 + Y^2 - 2\,Y\,\sin\theta}} - \frac{1}{\sqrt{1 + X^2 + Y^2 + 2\,Y\,\sin\theta}} \right) U + O(U)^2. \tag{6.6}$$

For a spot size of radius ρ, $\rho/R << 1$, and $U = -\alpha_v f/R$, the allowable angular instability is approximated as

$$|\alpha_v| = \frac{q\lambda R^2}{\sin(2\phi) f \rho^2 \sin\theta}. \tag{6.7}$$

Here ϕ and ρ are polar coordinates in the x, y plane. Because the phase error associated with α_v is given by an odd function of ϕ, the effect of α_v for SBIL, where the beam is scanned along the direction of the grating, will largely result in a contrast loss and not a phase error.

Spatial filtering can also be considered as a means to relax the requirement on the beam angle. The lens of the spatial filter focuses components shifted in angle off the optical axis and if these components are large enough they can be blocked by the pinhole. The lens focuses the beam to a waist with radius, ω_0, given by[27]

$$\omega_0 = \frac{\lambda f}{\pi \omega_L}. \tag{6.8}$$

Here ω_L is the beam radius at the lens. For a pinhole of radius $\omega_p = \kappa\omega_0$, where κ denotes the fractional size, the components that can be blocked by the pinhole have an angular deviation greater than

$$\alpha_{blocked} = \frac{\kappa\lambda}{\pi\omega_L}. \tag{6.9}$$

To guarantee the pinhole will block angular deviations that can cause a normalized spatial error q, $\alpha_{blocked}$ from Equation (6.9) is set less than α_u from Equation (6.5) and the requirement for κ is given as

$$\kappa < \frac{\pi q \omega_L R}{2\cos(\theta)\rho f} = \frac{\pi q}{2\cos(\theta)}. \tag{6.10}$$

For $q = 1/2000$ and $\Lambda_0 = 200$ nm, we find $\kappa < 0.0016$. This corresponds to a power transmission of only 5.1×10^{-6}! Thus, brute-force spatial filtering to stabilize the beam angle is not an attractive option for a practical system. However, more sophisticated spatial filtering, such as through single mode wave guides, may prove more attractive.

6.3 Beam Stability Requirements in a Grating Interferometer

Grating interferometers can be insensitive to the spatial coherence of the incoming laser beam. In fact, Reference [44] shows that it is possible to form stable fringes in a specific grating interferometer regardless of both the spatial or temporal coherence of the laser. We first consider the simple grating interferometer shown in Figure 6-4. For a grating beamsplitter with 0 and -1 orders sharing equal angles with the grating normal, each beam rotates by exactly the same amount and in the same direction for small angular deviations of the incoming beam. For this case, the allowable angular deviation for an allotted q is given by

$$\alpha = \cos^{-1}\left(1 - \frac{q\Lambda_0}{y}\right) \approx \sqrt{\frac{2q\Lambda_0}{y}}. \tag{6.11}$$

The approximation assumes $\alpha << 1$. When $q = 1/2000$, $y = 1$ mm, and $\Lambda_0 = 200$ nm, we find that $\alpha = 0.45$ mrad. Thus, the grating-based interferometer allows for a relatively generous tolerance on angular stability.

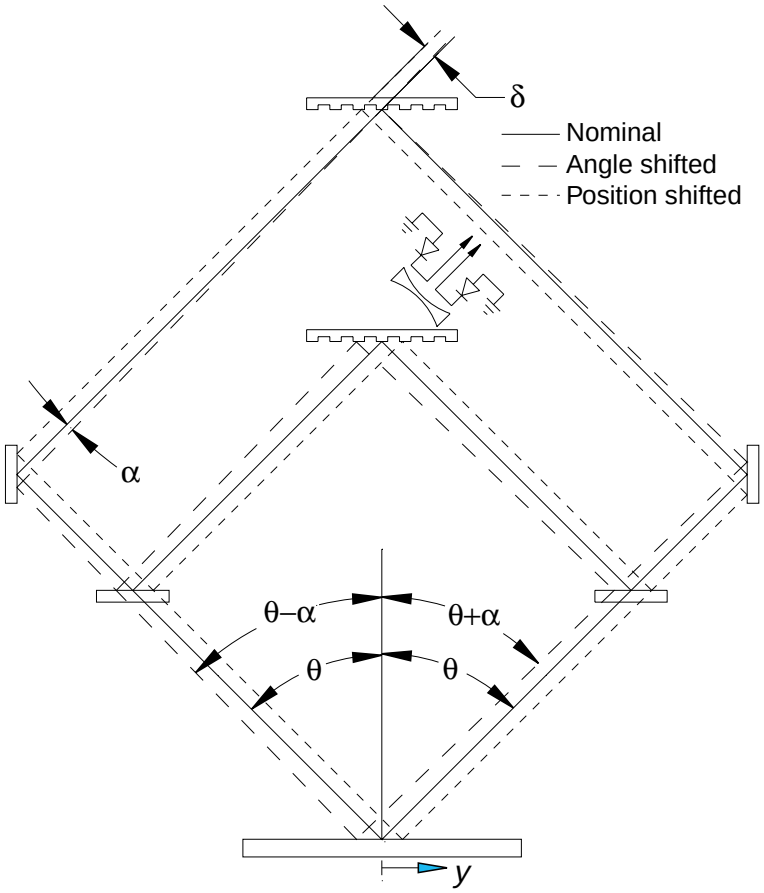

Figure 6-4: Ray trace of interference in a grating-based interferometer.

6.4 Beam Steering System

Beam steering has been implemented by many other groups [34, 89]. Figure 6-5 shows the schematic of our system. The actuation consists of two Physik Instrumente GmbH S-330.10 tip-tilt actuators. The sensor system is based on two On-Trak Photonics, Inc. UV2L2 dual axes position sensing detectors. With our nominal laser power of 1.7 mW to each detector, the noise equivalent position is estimated as 12 nm after considering Johnson, shot, and dark current noise of the detector and an estimate of the amplifier noise.

Optics denoted by focal lengths f_1 and f_2 are positioned to decouple position and angle. We set $L_2 = f_2$ such that the angular variations, α, are transformed into position variations equal to αf_2 on the tilt detector. L_0 and L_1 are set such that

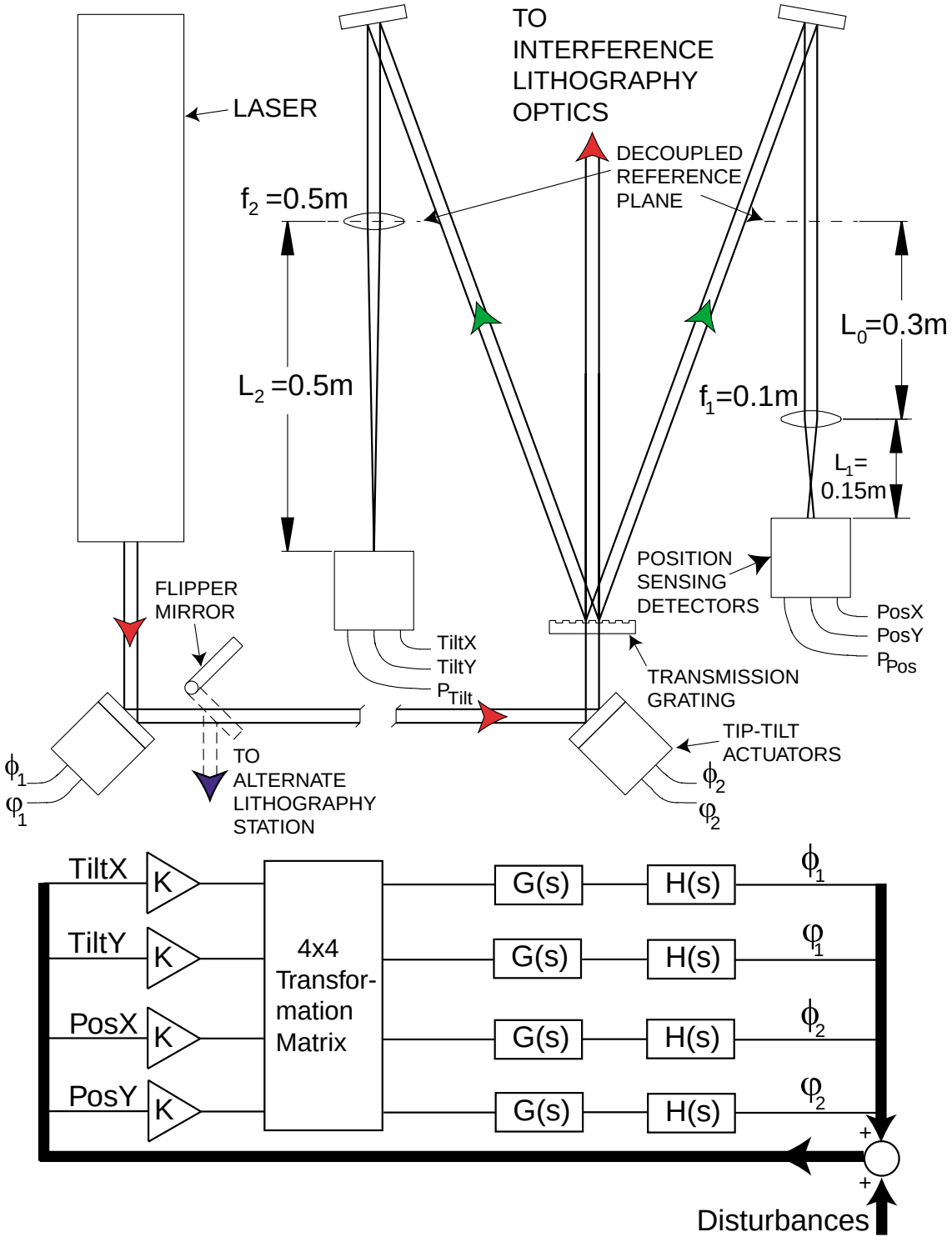

Figure 6-5: Beam steering system for stabilizing beam position and angle.

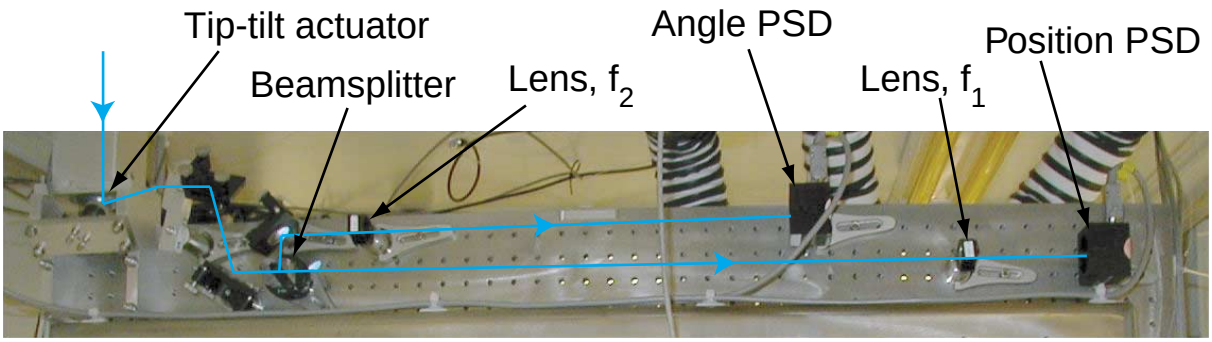

Figure 6-6: Beam steering optics on the SBIL system.

only translation in the reference plane can be sensed on the position detector. The requirement for this decoupling is given by $L_0 = L_1 / \left(\frac{L_1}{f_1} - 1\right)$. For this condition, the magnification, M, of the position on the translation sensor relative to the position on the reference plane is given by $M = 1 - \frac{L_1}{f_1}$ or equivalently $M = \frac{L_1}{L_0}$. The system in the schematic uses a grating to pick off the beams for the position and angle detectors. In a later version of the system, the grating pickoff was replaced with a glass pickoff for packaging reasons. The photograph of the experimental system currently implemented on the SBIL system is shown in Figure 6-6.

The digital control hardware and beam steering software was purchased from Adaptive Optics Associates, Inc. It consists of a RadiSys Spirit-32 E88 digital signal processing and input/output system. A TMS320C32 performs the processing with the control loop running at 2 kHz. Input consists of 12 bit analog to digital conversion with second order anti-alias Butterworth filters. The output consists of 12 bit digital to analog conversion with one pole smoothing filters.

After considering the beam transfer functions, the detector sensitivities, intermediate amplifier gains, and the 12-bit analog to digital converters, the position and angle resolutions of our sensor system are 0.98 μm and 0.17 μrad, respectively. The actuator furthest from the sensor assembly produces position and angle resolutions on the reference plane of 11 μm and 0.98 μrad, respectively. Meanwhile, the actuator closest to the sensor assembly produces position and angle resolutions on the reference plane of 0.65 μm and 0.98 μrad, respectively. These resolutions can be reduced by further amplifying the signals entering and leaving the I/O system. However, this

results in lost dynamic range, which makes it more difficult to obtain an accurate decoupling matrix in the presence of disturbances.

The amplifier and piezo actuators have a transfer function that closely resembles an RC circuit for frequency ranges of <500 Hz. The pole was found experimentally to be at 120 Hz. The Laplace transform of the modeled plant, $H(s)$ is given by

$$H(s) = \frac{K_H}{s/(2\pi 120) + 1}. \tag{6.12}$$

Here, K_H, is the voltage-to-angle gain of the piezo system and s is the Laplace transform variable equal to $j\omega$, where ω is the frequency in radians per second. The digital control system is approximated as a continuous time controller with a delay. We implemented the controller with the continuous time equivalent Laplace transform, $G(s)$, given by

$$G(s) = \frac{K_G[s/(2\pi 200) + 1]e^{-s\,2000}}{s\,[s/(2\pi 400) + 1]}. \tag{6.13}$$

The controller is composed of gain K_G, an integrator, and a lead compensator with the zero at 200 Hz and the pole at 400 Hz. The gain is adjusted for open loop cross over at 110 Hz. The top and middle plots of Figure 6-7 show the open loop transfer function of the system. The solid line shows the experimental data and the dashed line is given by the model. The model shows good enough agreement for design purposes. The bottom plot shows the disturbance transmissibility given by $|1/(1 + KGH)|$. The constant, K, is the input scaling as shown in Figure 6-5. The experimental model and the model data is derived from the data plotted for the open loop transfer function. The data in the table of Figure 6-7 shows the controller performs approximately as expected. The 4^{th} column contains the expected standard deviations given the disturbances represented by experimentally determined power spectrums with the control off and the disturbance rejection of our model. The table lists the standard deviations of each control axis for various frequency bands. We are achieving beam stability of better than 1 μrad for angle and about 4 μm for position (both 1σ from 0 to 88 Hz). The discrepancy between the modeled and actual performance for the control can largely be attributed to an inaccurate decoupling matrix and quantization noise.

Although we attempted to reduce the quantization noise by amplifying the input and output signals of our I/O system, we found it increasingly difficult to calibrate our transformation matrix because of lost dynamic range. Furthermore, we also implemented higher order controllers with better expected disturbance rejection but the poor decoupling limited the performance. To boost the performance of our system further, we could apply a more reliable decoupling algorithm and/or adaptive controls along with intermediate amplifiers for the actuators and sensors. A better system would have used 16 bit A/D and D/A converters. Also, it would be desirable to have a faster controller loop rate than 2 Khz. For the data discussed in this section, the tilt sensor signals were amplified by 5.6× with an amplifier placed between the On-track amplifier and the A/D board. Removing this amplifier reduces the performance of the system by about three to four fold. Since the performance of our system was sufficient for a grating-based interferometer, we did not pursue this issue further. In fact, the intermediate amplifier for the tilt sensors was later removed because recalibrating the decoupling matrix was too unreliable for general users and the performance was still adequate without it.

6.5 Analysis of a +1/-1 order grating interferometer for interference lithography

This section analyzes the grating interferometer in Figure 6-8. Here, a grating splits the incoming beam into $+1/-1$ orders. The half angle between the beams is θ and it is preserved with small angle fluctuations of the incoming beam. Furthermore, this interferometer is designed to produce a fringe pattern on the substrate with nominally half the period of the beamsplitter grating. This is a condition that happens to make the interferometer insensitive to wavelength variations. I will explicitly show that this interferometer produces fringes with period that is insensitive to the angle and wavelength of the incoming laser beam. The analysis assumes the interference of plane waves.

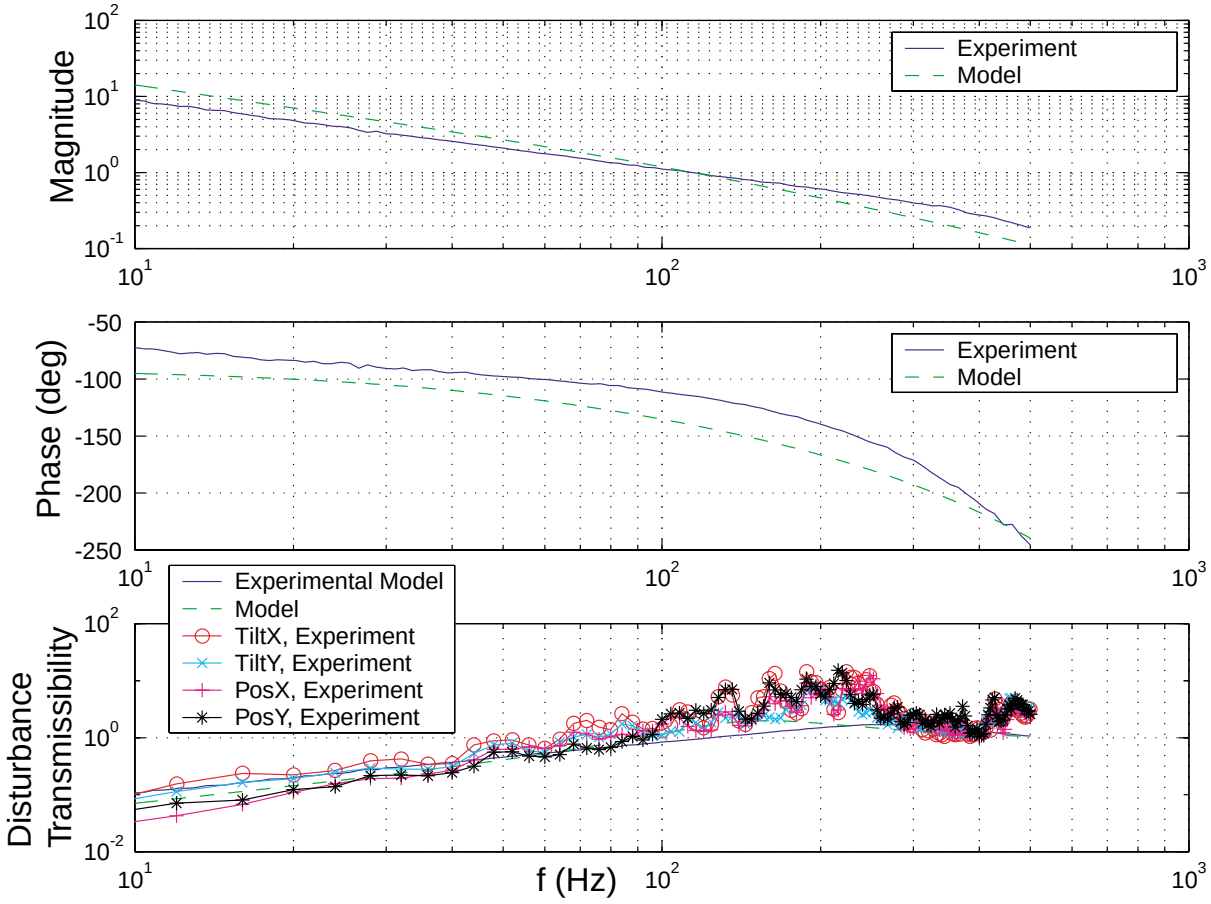

Control variable, frequency band	Control off	Control on	On, modeled
TiltX σ (μrad), 0<f<1600 Hz	28	1.0	0.57
TiltX σ (μrad), 0<f<88 Hz	28	0.65	0.41
TiltX σ (μrad), 88<f<1600 Hz	0.34	0.76	0.40
TiltY σ (μrad), 0<f<1600 Hz	8.0	1.3	0.54
TiltY σ (μrad), 0<f<88 Hz	7.9	0.89	0.24
TiltY σ (μrad), 88<f<1600 Hz	0.41	0.90	0.49
PosX σ (μm), 0<f<1600 Hz	96	6.6	4.0
PosX σ (μm), 0<f<88 Hz	96	4.5	2.8
PosX σ (μm), 88<f<1600 Hz	2.5	4.8	2.9
PosY σ (μm), 0<f<1600 Hz	84	6.0	3.1
PosY σ (μm), 0<f<88 Hz	84	3.9	2.4
PosY σ (μm), 88<f<1600 Hz	1.7	4.6	2.0

Figure 6-7: Top Plot: Magnitude of the open loop transfer function. Middle Plot: Phase of the open loop transfer function. Bottom Plot: Modeled and experimental disturbance transmissibilities. Table: Comparison of beam angle and position stabilities over different frequency bands.

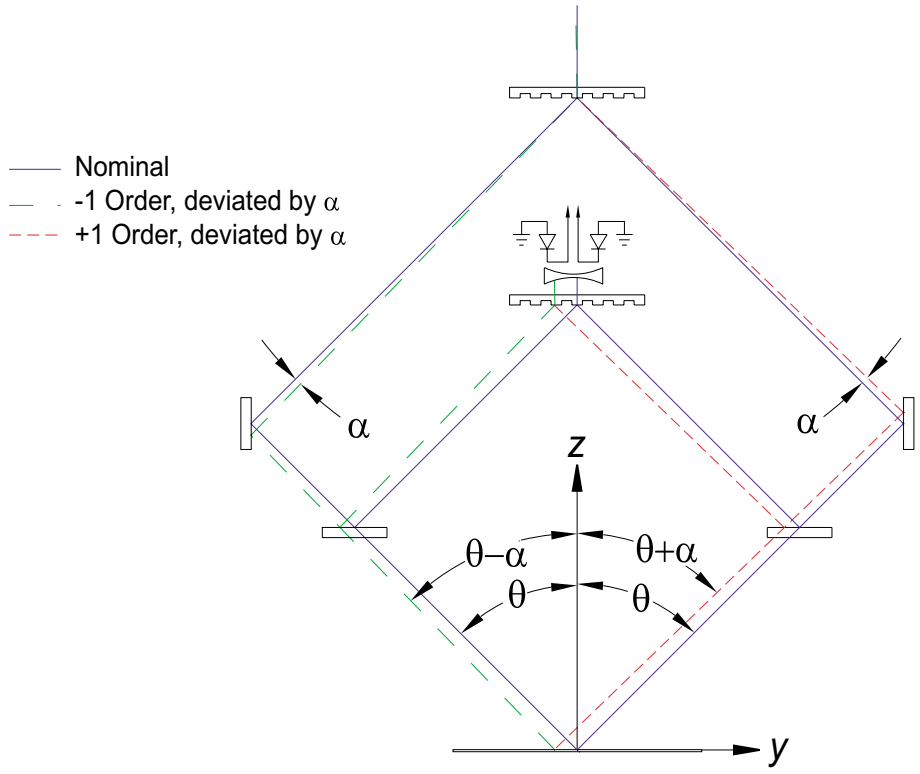

Figure 6-8: A grating interferometer using diffracted +1/-1 orders.

6.5.1 Analysis

In section 6.3, I showed a grating interferometer can be much less sensitive to angular variations of the incoming beam compared to an interferometer based on a reflective beam-splitter. I assumed a 0/-1 order beam splitter and the condition that incoming beam is aligned such that the 0 and -1 order beams have equal angles to the grating normal. For this condition, the split beams rotate by the same amount and in the same direction, thereby preserving the half angle between the beams interfering on the substrate. The angular instability results in a benign cosine error.

The condition of half angle preservation with rotation of the incoming laser beam also holds for a $+1/-1$ order beam splitter when the incoming beam is normal to the grating. The relationship between the rotation of the incoming beam and the rotation of the diffracted orders is derived from the grating equation. Following the geometry in Figure 6-9, the relationship between the diffracted and incident beams

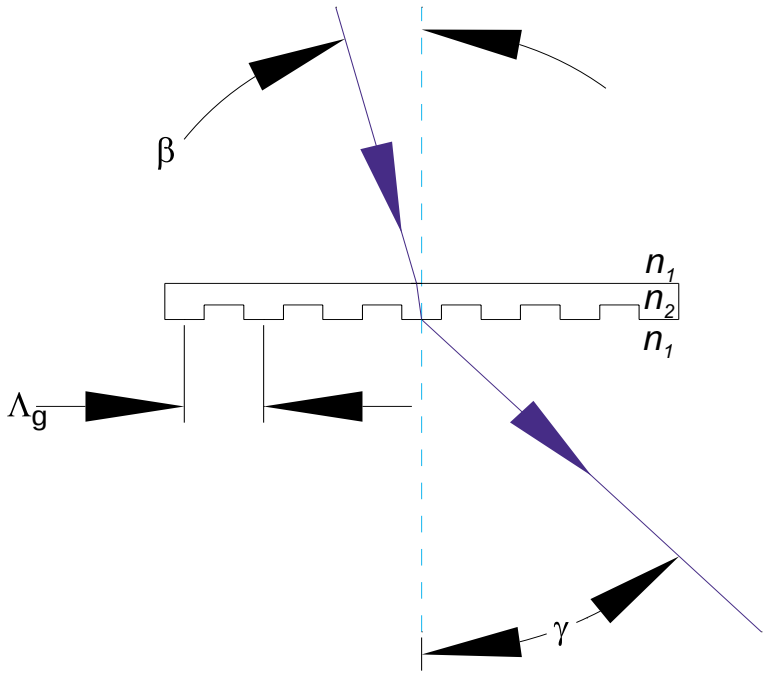

Figure 6-9: Diffraction by a grating.

is given by

$$\sin\gamma - \sin\beta = \frac{m\lambda}{\Lambda_g}. \tag{6.14}$$

Here β is the angle between the incoming beam and the grating normal, γ is the angle of the diffracted order from the grating normal, m is the diffracted order, λ is the wavelength of the light in the medium with index n_1, and Λ_g is the grating period. From Equation (6.14) I find that

$$\frac{d\gamma}{d\beta} = \frac{\cos\beta}{\sqrt{1-(m\lambda/\Lambda_g + \sin\beta)^2}} \approx \frac{\Delta\gamma}{\Delta\beta}. \tag{6.15}$$

For β nominally equal to 0°, the positive and negative symmetric orders have equal deflections for small $\Delta\beta$. In other words,

$$\left.\frac{d\gamma}{d\beta}\right|_m = \left.\frac{d\gamma}{d\beta}\right|_{-m} = \frac{1}{\sqrt{1-(m\lambda/\Lambda_g)^2}}. \tag{6.16}$$

Moreover, this condition of equal deflections for the positive and negative orders is

intuitively obvious from inspection of the symmetry. The ratio of $\Delta\gamma$ to $\Delta\beta$ ranges from one for small $m\lambda/\Lambda_g$ to infinity for $m\lambda/\Lambda_g = 1$, which occurs when the $\gamma = 90°$. As a practical example, when $m\lambda/\Lambda_g = 1/2$, $\Delta\gamma$ is amplified by just $1.15 \times \Delta\beta$. Taking advantage of the result derived in Equation 6.11, the allowable β instability that causes a fringe placement error, e, due to period shift in a spot of radius, r, is given by

$$\beta = \frac{d\beta}{d\gamma}\sqrt{\frac{2e}{r}}. \tag{6.17}$$

For $e = 0.1$ nm, $m\lambda/\Lambda_g = 1/2$, and $r = 1$ mm, the allowable β instability equals 0.39 mrad, which is much larger than the several μrad beam steering control demonstrated.

6.5.2 "Achromatic" configuration

Changes in the wavelength of light cause period fluctuations in the interference pattern. These changes are due to the vacuum wavelength stability of the laser and index fluctuations in the air. However, use of a grating as a beam splitter can compensate for these fluctuations by automatically adjusting the angle of interference to stabilize the exposed period.

From Equation 1.10, the derivative of the period with respect to the wavelength is

$$\frac{d\Lambda_0}{d\lambda} = \frac{1}{2\sin\theta}\left(1 - \frac{\lambda}{\tan\theta}\frac{d\theta}{d\lambda}\right) \tag{6.18}$$

Setting $d\Lambda_0/d\lambda = 0$ provides the condition for period stability that is sensitive to only high order terms of $\Delta\lambda$. This condition produces an interferometer that is achromatic to first order. For interfered beams produced by $+1$ and -1 orders from a grating beam splitter and where $\beta = 0°$

$$\frac{d\theta}{d\lambda} = \left.\frac{d\gamma}{d\lambda}\right|_{m=1}. \tag{6.19}$$

From Equation 6.14, it is found that

$$\left.\frac{d\gamma}{d\lambda}\right|_{m=1} = \frac{1}{\Lambda_g\cos\gamma} \tag{6.20}$$

With $\gamma = \theta$, I solve Equation 1.10 and Equations 6.18 – 6.20 to get the requirement

$$\Lambda_0 = \frac{\Lambda_g}{2}. \tag{6.21}$$

Thus, when the written period is half the period of the beam-splitter period, the written fringes are insensitive to $\Delta\lambda$. This first order achromatic interferometer is a significant improvement for SBIL. When using a reflective splitter, if the index of air changes by 1 part in 10^6 then the error will be 1 nm across a 1mm spot.

While Equation 6.21 defines the ideal grating period for the beam splitter, it is not practical to replace the beam splitter for every different period written. In general, the normalized sensitivity to wavelength changes is given by

$$\frac{\Delta\Lambda_0}{\Lambda_0} = \frac{d\Lambda_0}{d\lambda}\frac{\Delta\lambda}{\Lambda_0}. \tag{6.22}$$

This is solved by first modifying Equation 6.18 to obtain

$$\frac{d\Lambda_0}{d\lambda} = \frac{1}{2\sin\theta}\left(1 - \frac{\lambda}{\Lambda_g \sin\theta}\right). \tag{6.23}$$

After combining this equation with Equation 1.10, the normalized sensitivity is given by

$$\frac{\Delta\Lambda_0}{\Lambda_0} = \frac{\Delta\lambda}{\lambda}\left(1 - \frac{2\Lambda_0}{\Lambda_g}\right). \tag{6.24}$$

This relation shows that when $\Lambda_0 = \Lambda_g$ then $\Delta\Lambda_0/\Lambda_0 = \Delta\lambda/\lambda$. Moreover, as long as the grating period, Λ_g, is greater than the image period,Λ_0, the grating beam splitter will produce an interferometer less sensitive to wavelength changes than a reflective beam splitter based system. In the best case defined by Equation 6.21, the grating beam splitter system is insensitive to wavelength changes.

6.5.3 Effect of grating beam-splitter strain

One drawback of using a grating interferometer is that the period of the exposed grating will vary as the beam-splitter grating thermally expands – or strains by some

other mechanism. The change in γ due to the period change of the beam splitter is given by

$$\Delta\gamma = \frac{d\gamma}{d\Lambda_g}(\Delta\Lambda_g) = \frac{m\lambda}{\Lambda_g\sqrt{1-\left(\frac{m\lambda}{\Lambda_g}\right)^2}}\frac{(\Delta\Lambda_g)}{\Lambda_g}. \tag{6.25}$$

After combining this equation with Equation 6.1 while substituting $\Delta\gamma$ for α, the allowable period strain is given by

$$\frac{(\Delta\Lambda_g)}{\Lambda_g} = \frac{e}{2\,|m|\,r}. \tag{6.26}$$

For e =0.1nm, $r = 1$ mm, and $|m| = 1$, the allowable grating beam-splitter strain is 5×10^{-8}. If the grating is held in a stiff aluminum mount with CTE=2×10^{-5}/K then a temperature change of just 2.5 mK will produce this significant strain. However, if the CTE of fused silica (7.5×10^{-7}/K) is used, the temperature change causing the 0.1nm error will be a manageable 67 mK. In our system, the grating is fused silica while the grating is cantilevered from an aluminum mount to provide an estimated strain relief of 10 $\times$ from the aluminum frame. Since the temperature variations at the grating splitter are expected to be less than 25 mK, the grating beam splitter strain is negligible for our environmentally controlled conditions.

6.6 Conclusions

Our goals for writing subnanometer distortion gratings limit the amount of beam instability that we can tolerate in our interference lithography system. For the interference of plane waves, the beam stability requirements are severe for angle, where we require 0.2 μrad stability. A spherical wave interferometer can have a much relaxed angular requirement if the ratio of the spherical radius to the focal length of the spatial filter is large. However, for SBIL we desire to use small beams and therefore we cannot achieve $\frac{R}{f}$ values much greater than one. Alternatively, a grating interferometer can have a much relaxed beam stability requirement. The "achromatic" grating interferometer that we considered is insensitive to position and allows a 0.39 mrad

instability. Furthermore, to maintain good contrast we desire the beam to be stable to better than about 10 μm in position. Our beam steering system locks the beam to approximately 1 μrad and 4 μm (both 1σ). Therefore, we have achieved beam steering requirements for subnanometer distortion goals with a grating interferometer.

The +1/-1 order grating beamsplitter is ideal for interference lithography because it produces fringes with period that is insensitive to the angle and wavelength of the incoming laser beam. This interferometer requires the following conditions: nominal incoming beam angle $\beta \approx 0$ rad, $\theta = \gamma$, $\Lambda_g/2 = \Lambda_0$, and interference of plane waves. The phase error due to angle variations is accurately determined by considering the period change on the substrate.

Chapter 7

Electronic and Software architecture

Figure 7-1 depicts the control architecture. The system contains a VME-based real time control platform and a PC for Labview-based I/O. The signals to the boards are depicted. The realtime control platform is shown in further detail in Figure 7-2.

The Ixthos[1] IXC6 Quad DSP board performs the signal processing. This board by certain metrics was the fastest VME-based processing system that I found back in the Fall of 1998. The board is capable of up to 4 GFLOPS of processing power, uses the latest PCI bus architecture, and contains two PMC slots – the fastest industry standard mezzanine card interface. The board includes four Texas instruments C6701 digital signal processors running at 167 MHz. The DSP's are programmed using the Code Composer development tools from TI and the IXCTools communication utilities provided by Ixthos. The Motorola MPC 8240 Power PC on the board is programmed under the Tornado II/VxWorks environment from Wind River Systems Inc. Both development environments include C/C++ compilers.

In hindsight, the vendors selling processor boards really do not provide enough information to select the best one for an application such as SBIL. For the our application, the time for single address PCI writes is important. Also, the time for single

[1]Ixthos, Inc., Leesburg, VA. This company is now owned by DY4 Inc.

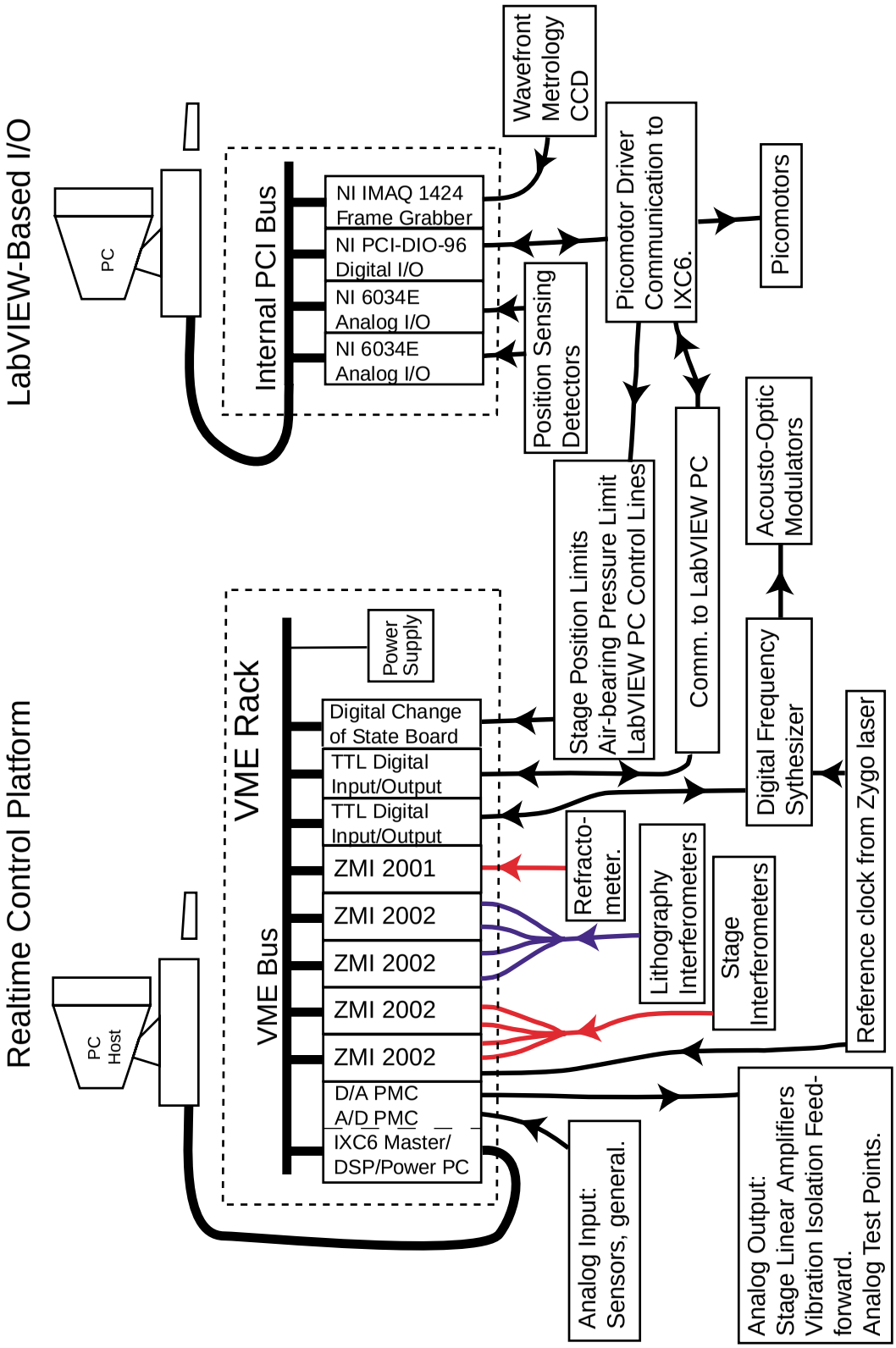

Figure 7-1: Control architecture.

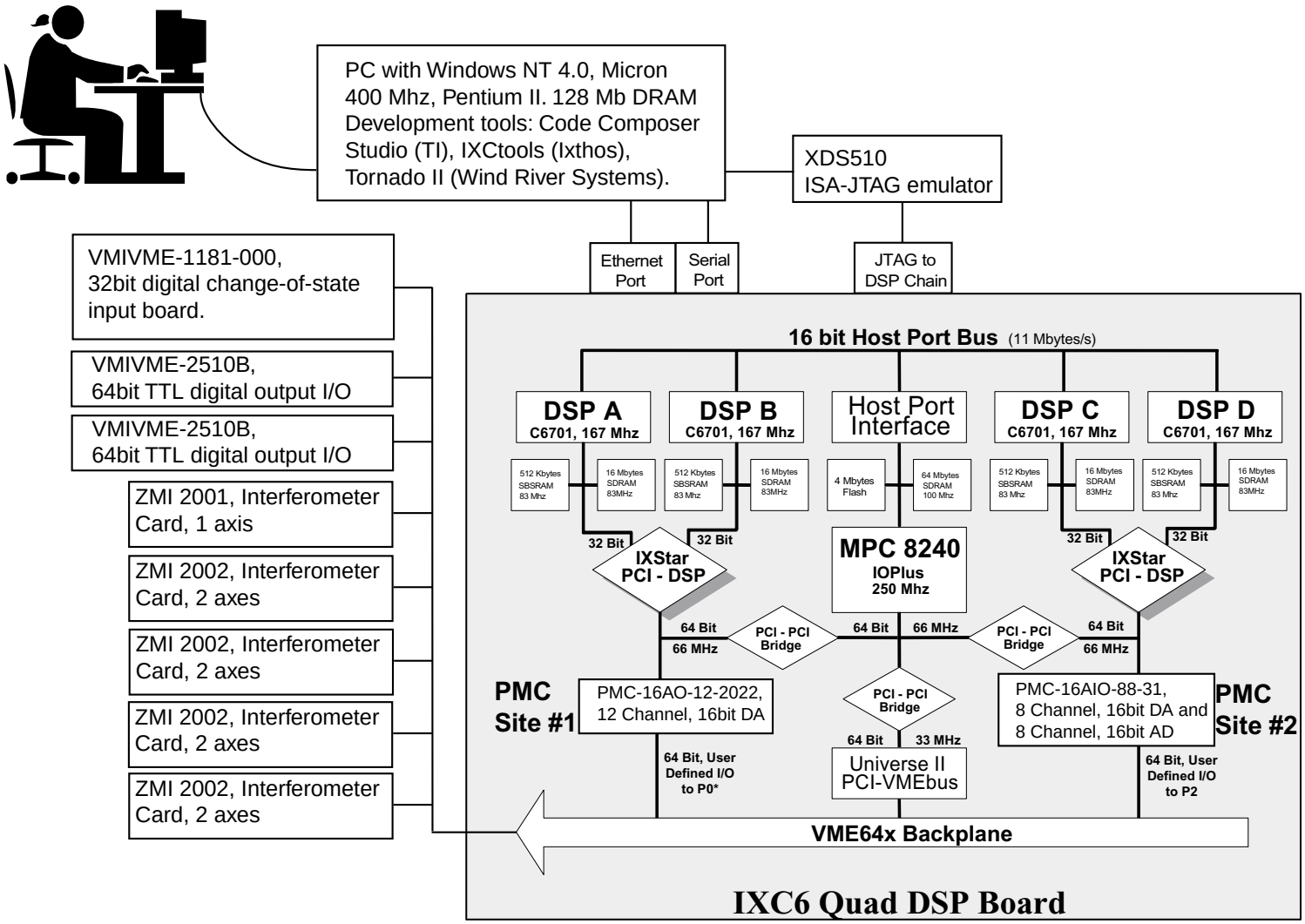

Figure 7-2: Real time control platform

address VME reads and writes is important. Even today, most vendors don't publish this information, which is necessary to predict the speed of applications requiring extensive I/O. Furthermore, the raw bus clock speed is not a good indication of the time for single address I/O. The single address I/O time has significant overhead associated with handshaking and interface chip set up. Obtaining specifications on single address I/O is the only reliable way to gauge its time. The timer period for the realtime control loop for all the data that I discuss in the thesis was programmed to 100 μsec. The VME and PCI I/O accounted for about half of this time. The time for reading and writing to the VME bus is about 1.6 μsec per single address operation whereas the time for PCI operations was 1.5 μsec per single address operation. The processing can consume almost all of the remaining time in the control loop depending on how many channels are downsampled. I do not consider the code optimized by any means and both the I/O functions and the processing code can probably be further streamlined. Most importantly, the 10 KHz sampling rate appears to be adequate based on the performance of the system.

For the future, I don't see general purpose processors competing for applications with similar processing requirements such as SBIL. Currently, the best general purpose processors far exceed the best Texas Instruments DSP's in terms of processing power and cache memory. A benchmark [24] by Berkeley Design Technology Inc confirms that the general purpose Pentium III processor exceeds the C67xx even for traditional DSP tasks of fast Fourier transform and finite impulse response filters. The general purpose processors also tend to have much larger cache memory, which allows larger programs to run at full clock speed. Furthermore, Texas Instruments has made little improvement in its floating point processors over the past four years, while the multipurpose processors have shown significant gains. The DSP's seem destined for applications that are cost or power sensitive.

The analog and digital I/O boards in the realtime system are commercially available. The VMI digital I/O boards are available from VMIC, Inc. The D/A and A/D boards are available from General Standards Inc. The data acquisition boards for the Labview-based system are available form National Instruments Inc.

In the rest of this chapter, I discuss the fringe locking electronics and the software.

7.1 Fringe locking electronics

The SBIL prototype uses a novel acousto optic fringe locking system. A key element of the system is a direct digital frequency synthesizer that is controlled in real-time to shift the fringe phase at high speed. The phase reading is obtained digitally by Zygo phase meters (ZMI 2000 cards). A photograph of the electronic systems is shown in Figure 7-3. The figure points out the TTL Digital IO and phase meters that are housed in the VME rack. The Intraaction[2] Model MFE-1054C32 synthesizer and the signal lines are also shown. One VMEVMI-2510B with 64 digital IO channels communicates with the frequency synthesizer system. Four phase meter axes are used, two for reading mode and two for writing mode. The synthesizer has three output channels that interface to acousto-optic modulators. The frequency synthesizer system was designed and built by Intraaction. We were the first customer for the Model MFE synthesizer and Figure 7-4 shows the partially assembled system that I tested at their site. The system is designed to provide three channels of digitally programmable frequency and amplitude with a power output of up to 5 W of RF in each channel. The direct digital frequency synthesizers [2] are based on the Analog Devices AD9852 "CMOS 300 MHz Complete-DDS" [1]. The AD9852 is an extremely high resolution synthesizer based on direct digital synthesis (DDS) with a built-in digital to analog converter. The PCB board contains three AD9852 chips, ROM, a microcontroller, a display, FPGA-based "glue logic", and low pass filters. The functions of the microcontroller include loading the FPGA program from ROM on power up and servicing the display. During operation, the data at the TTL inputs is passed directly by the FPGA to the synthesizer chips. The AD9852 has 48 bit frequency tuning word and a 12 bit amplitude tuning word. The output of each channel has a low pass filter to attenuate the aliased output spectrum above roughly 150 MHz. The outputs from the PCB are provided to the front panel of the MFE for the purpose of observing them on

[2]Intraaction Corp. Bellwood, Il

a scope or spectrum analyzer. The outputs are also supplied to amplifiers that boost the power. The amplifiers provide approximately five watts of power to the AOM's if the AD9852 is operating at full scale amplitude. The Intraaction SDM-1052B8 acoustic optic modulators are designed to have a 50 ohm input impedance.

The AD9852 clock signal can either be programmed to be derived from an internal clock or an external clock. In our system, the 20 MHz reference signal from the Zygo laser provides the external clock signal. A programmable PLL-based reference clock multiplier multiplies the reference clock by 15 to set the DDS clock speed at 300MHz. For SBIL, I only use the upper 32 bits of the frequency word to provide a resolution of $300/(2^{32}-1)$ MHz or 0.07 Hz. Even though I am not using the lower 16 bits, this frequency resolution limits the phase control resolution to a remarkable 7×10^{-5} periods if the control loop rate is 10 KHz. Deriving the DDS clock signal from the phase meter reference signal ensures accurate control of optical frequency shifts with respect to the phase measurement reference signal. While the error signal derived from the UV phase axes is a differential measurement and is largely insensitive to the synthesizer clock signal, synchronization issues and the finite measurement range of the phase meters impose a stability requirement on synthesizer clock signal with respect to the Zygo reference signal. All the phase meters use the same Zygo reference signal, which is output from the laser head. The reference signal is provided as a fiber optic input signal to one of the cards. The reference signal is then daisy chained to all the other cards using a special cables available from Zygo. The reference daisy chaining ensures the best synchronization of the axes. The phase meter data is triggered by a programmable output clock associated with one of the Zygo axes. This output clock signal is daisy chained to all the other axes and triggers the position data latch. The clock signal also triggers the real-time control loop interrupt. All these timing considerations ensure stable frequency generation, the best axis to axis synchronization, and the lowest latency.

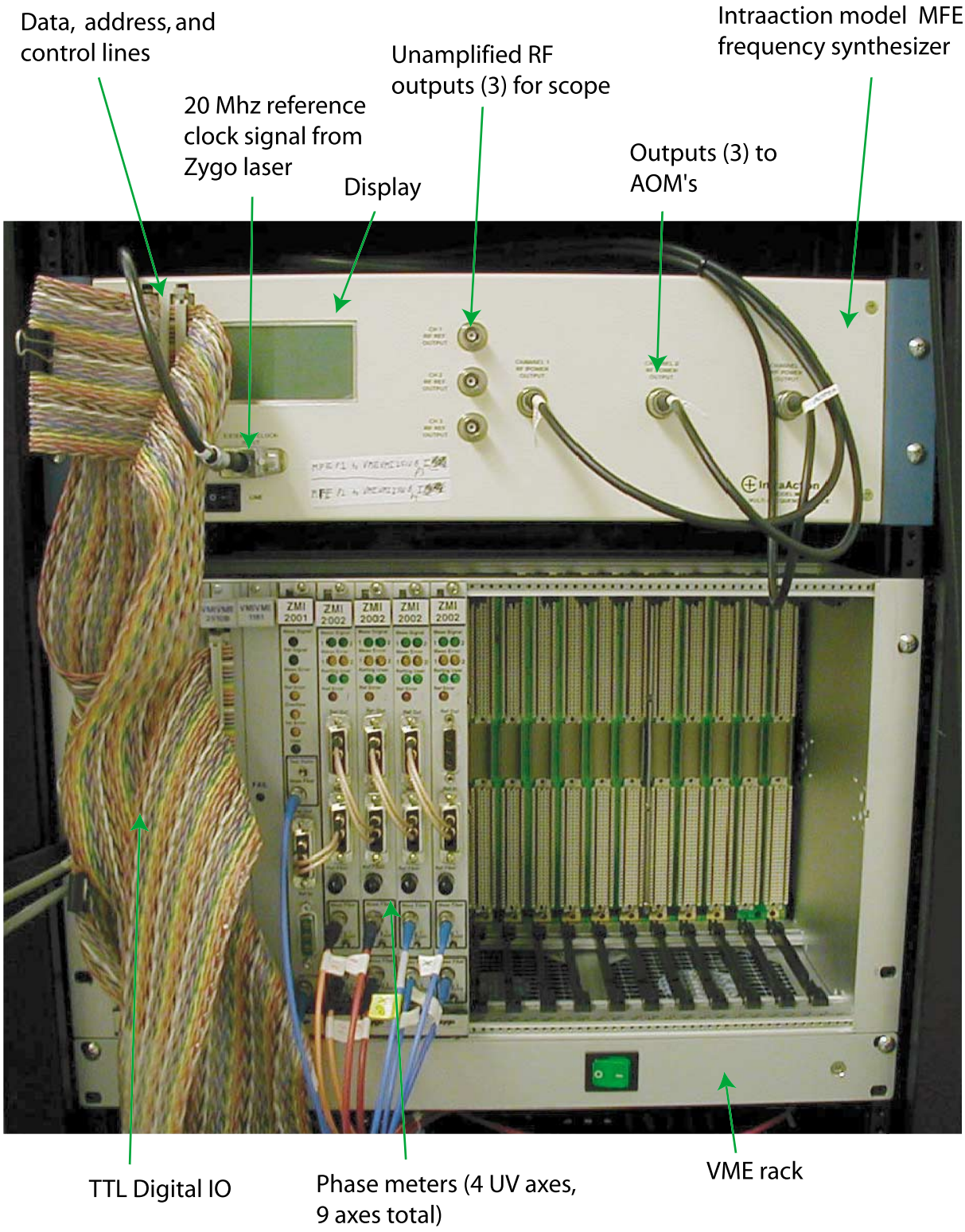

Figure 7-3: Photograph of the frequency synthesizer and the VME based systems.

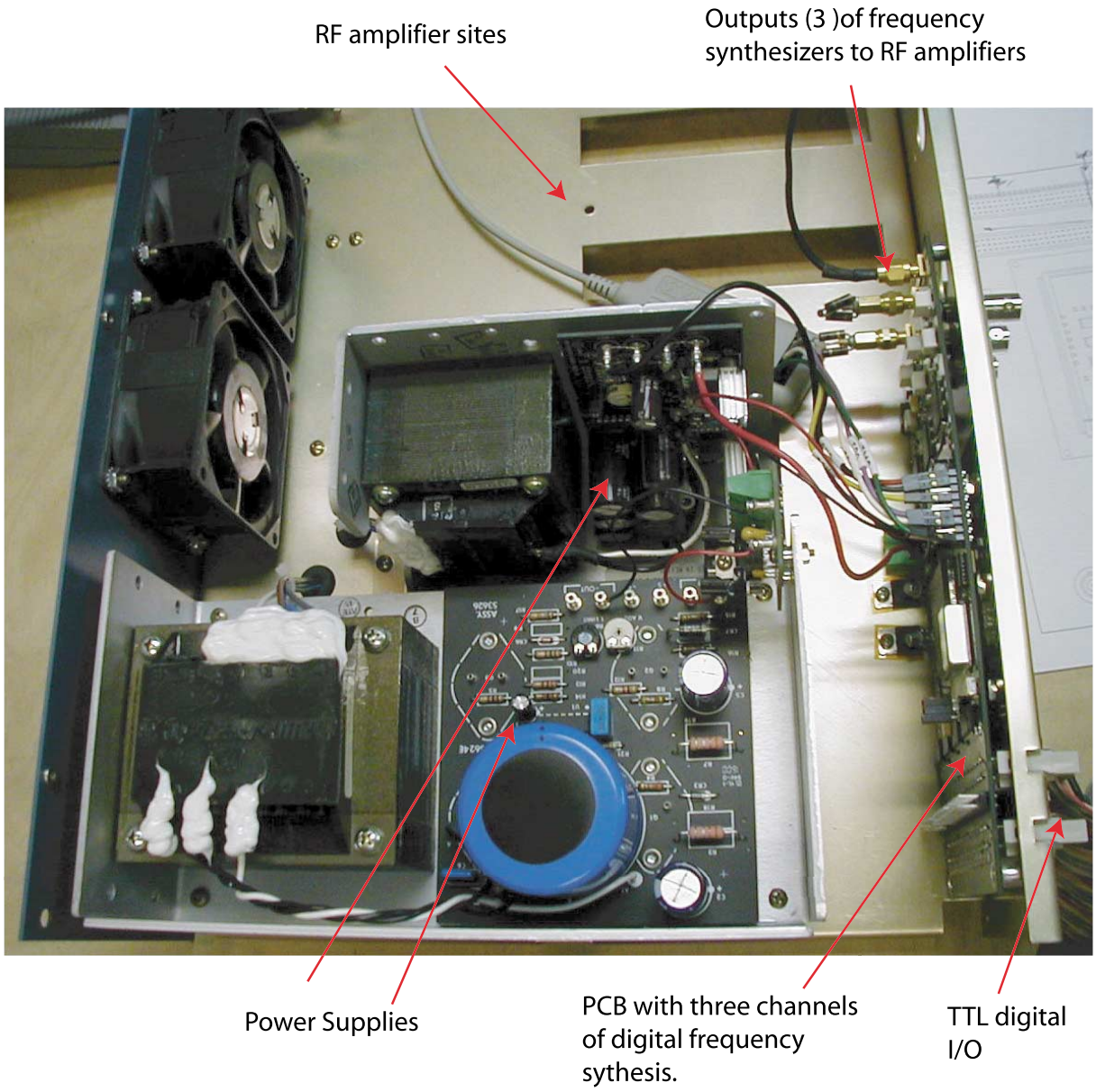

Figure 7-4: Photograph of partially assembled Intraaction Model MFE frequency synthesizer. The unit houses a printed circuit board hosting the three digital frequency synthesizers. Power supplies and RF amplifiers are also contained within the unit.

7.2 Software

Only the DSP's contain software that I wrote. The PowerPC does have the VxWorks operating system and performs some communication functionality but this is transparently provided by the use of standard functions provided with the IXCTools. The PowerPC was abandoned for any real-time functionality after I developed code that tested the I/O performance. It was found that I/O originating from the PowerPC to the VME bus was slower than on the DSP's.

Three DSP's contain programs for SBIL. One DSP contains all the real time functionality. A second DSP acts as an interface DSP, where commands for the real-time DSP are generated and stored in a FIFO buffer. The real-time DSP acquires these commands from a shared memory location. The basic programming strategy is to provide the leanest real-time program, while off loading as much processing and memory requirements as possible to the interface program. The compiled program for the real time DSP fits within the 128 KB cache memory of the C6701 DSP. The software architecture is scalable since the modifications to the interface program don't affect the real-time performance. Complex sequences of operations can be readily added. The third DSP is the data retrieval DSP that uses Texas Instrument's real-time data exchange functionality to bring data into Matlab.

The real-time DSP contains two interrupt loops as well as a non real-time "while" loop that executes only if the interrupt loops are not executing. The first interrupt loop is triggered by a programmable clock on one of the Zygo boards. This loop is the core of the SBIL control and it performs the following activities: read of all interferometer axes, stage profiling, fringe locking control, refractometer corrections, isolation feedforward calculations and output, stage x and y axis control and output, data collection, command status and acquisition, downsampling and data uploading to the data retrieval DSP, interferometer axis command bit reset, and interrupt resetting. The second interrupt routine is triggered off the VME 1181 change-of-state board. It monitors error conditions, limits, interferometer signal drop outs, and communication signals. This loop also performs quick position reset of the stage in-

terferometer axes after homing against limits and it also resets the refractometer axis on x axis homing. The "while" loop acts as a command interpreter. Since it is not practical to sample data at the full loop rate for data longer than a few seconds, data can be downsampled in real time. For all the data in this thesis, if I state that the data is sampled at any rate other than 10 KHz, then the data was downsampled. The downsampling algorithm first low pass filters selected data using an FIR filter with a Hamming Window. The corner frequency of the low pass filter is placed at the new Nyquist frequency. The program automatically calculates the FIR filter coefficients based on the downsampling ratio using well known design procedures [78, 82].

The interface DSP primarily is used to generate and store commands into a FIFO buffer. It also performs hardware configuration on startup and shutdown. Standard functions provided by Ixthos reconfigure hardware and release resources that are obtained from the PowerPC.

The Labview-based I/O system performs beam alignment, period measurement, and phase shifting metrology. Since the realtime and Labview platforms are separate, parallel software development was possible.

Chapter 8

System Dynamics and Controls

It is critical to shift the fringes at high bandwidth to lock them to the substrate. In this chapter, I discuss the fringe locking control and the fringe disturbances. The fringe locking control performance is shown to be limited by latency and quantization noise. Also in this chapter, I analyze the vibrations in the system. Acoustic and isolator transmitted vibrations are considered. Lastly, the stage control and the impact of stage controller performance on the unobservable error is discussed.

8.1 Fringe locking

A detailed model incorporating all dynamics necessary to predict and design the fringe locking control system performance is discussed in this section. Figure 3-3 shows the simplified diagram of the components of the fringe locking system. The disturbance rejection performance of this high speed electro-acoustic-optic system is limited only by quantization and latency. I derived a very good model of the system dynamics as indicated by the very good correspondence between the experimental and modeled loop transmissions in Figure 8-1. The model is based on the system shown in Figure 8-2. The model takes into account the dynamics of the controller $G(z)$, the frequency synthesizer $H(z)$, and the Zygo digital filter $P(z_z)$. The disagreement at the low frequency data points is attributed to quantization noise and this topic will be addressed further.

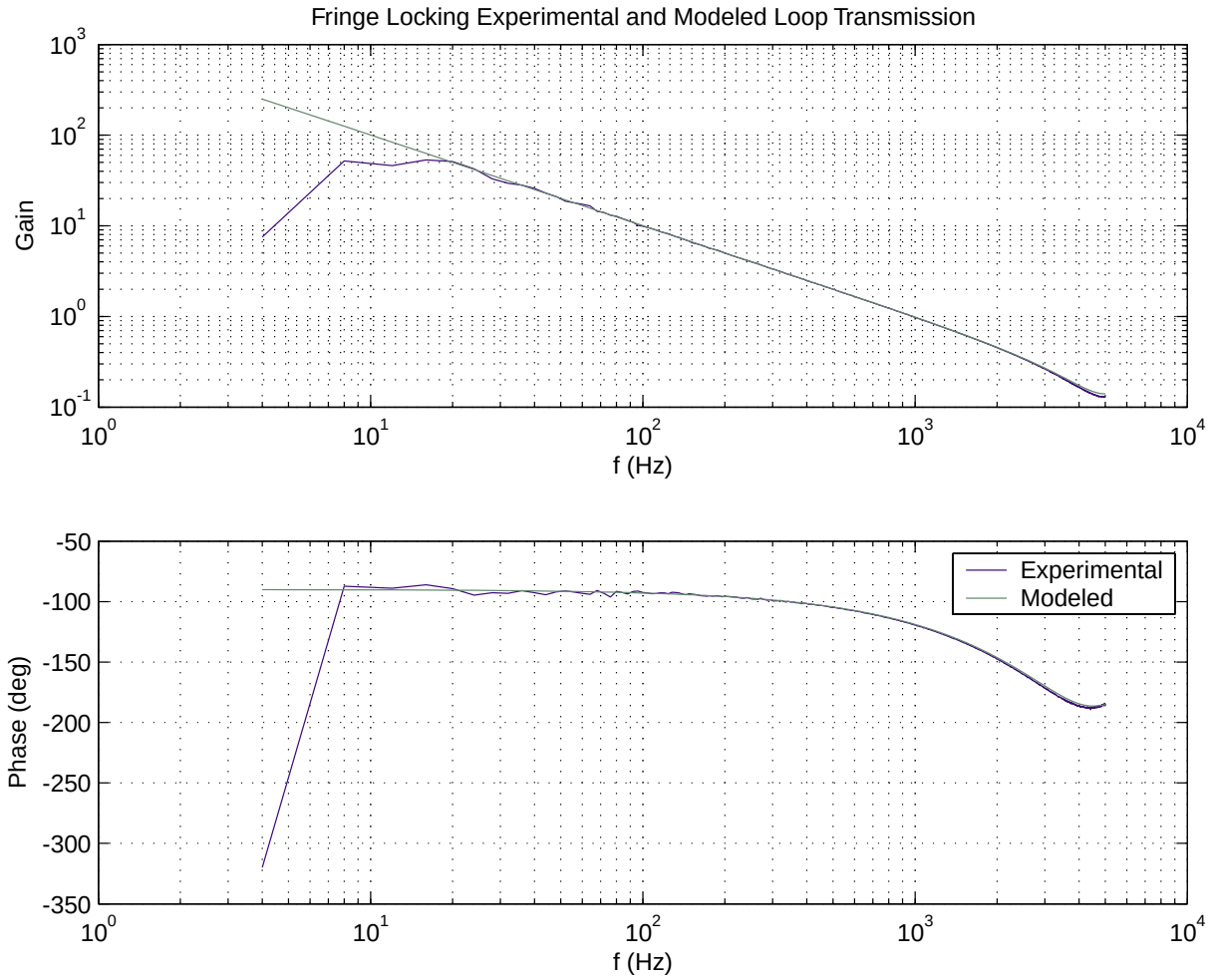

Figure 8-1: Experimental and modeled loop transmission for the fringe locking controller. The sampling rate is 10 KHz. The controller is proportional and the Zygo digital filter is programmed for 128 KHz bandwidth.

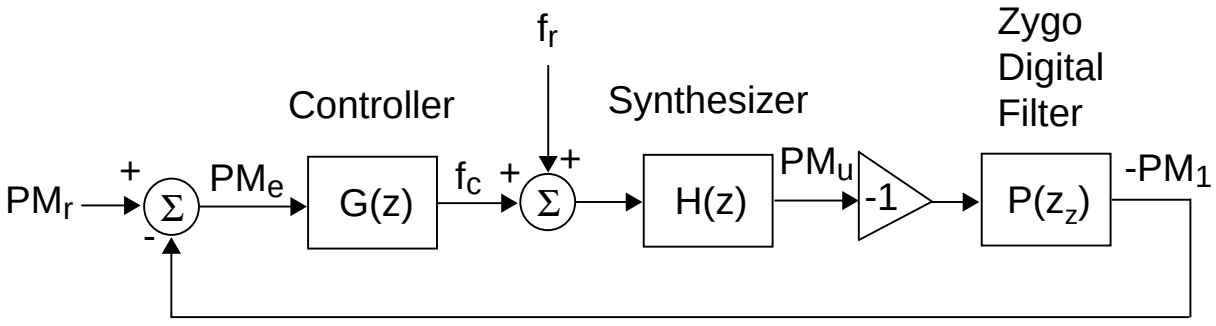

Figure 8-2: Control system block diagram for fringe locking.

In the block diagram, the signal, PM_{fle} is the error signal to the fringe locking controller in phase meter units given by

$$PM_{fle} = PM_r + PM_1. \tag{8.1}$$

The phase meter signal PM_1 is the measurement from phase meter 1 (PM1) in Figure 3-3. The phase meter reference PM_r is given by

$$PM_r = -PM_2 - \frac{\lambda_{DMI,air}}{n\Lambda}(\cos\alpha(PM_{x,ref} - PM_x) + \sin\alpha(PM_{y,ref} - PM_y)). \tag{8.2}$$

This equation assumes all axes of phase measurement have the same resolution (as a fraction of a period). In our system the phase resolution is $2\pi/512$. The variable $\lambda_{DMI,air}$ is the wavelength of the displacement measuring interferometer in air, $n = 4$ for our double pass interferometer, Λ is the period of the fringes, and α is the angle of the fringes with the y axis as previously discussed. The phase meter readings from the stage x and y axes are PM_x and PM_y respectively. The reference position of the substrate in x and y are $PM_{x,ref}$ and $PM_{y,ref}$ respectively. A plot with the frequency response of all components of the model is shown in Figure 8-3. The blue line shows the experimental loop transmission and the yellow line shows the sum of the components. These lines are the same data as in Figure 8-1.

The green line that is difficult to see shows an artifact of the technique used to obtain the experimental loop transmission. Figure 8-4 shows the enlarged plot of the Chan 2/ Chan 1 same data transfer function. This component is obtained by first outputting the same exact data to two DAC channels that are then sampled by a dynamic signal analyzer (HP 35670A). The signal analyzer FFT's both channels and then divides the complex coefficients to obtain the transfer function of channel 2 over channel 1. The data supplied to the DAC is white noise from a random number generator. There is some error inherent in this procedure. The most significant being the input and output gains of the analog channels and the channel to channel timing delay of the data writing and the DAC. The reason for using the signal analyzer for obtaining the transfer function, although it contributes errors, is convenience. Very

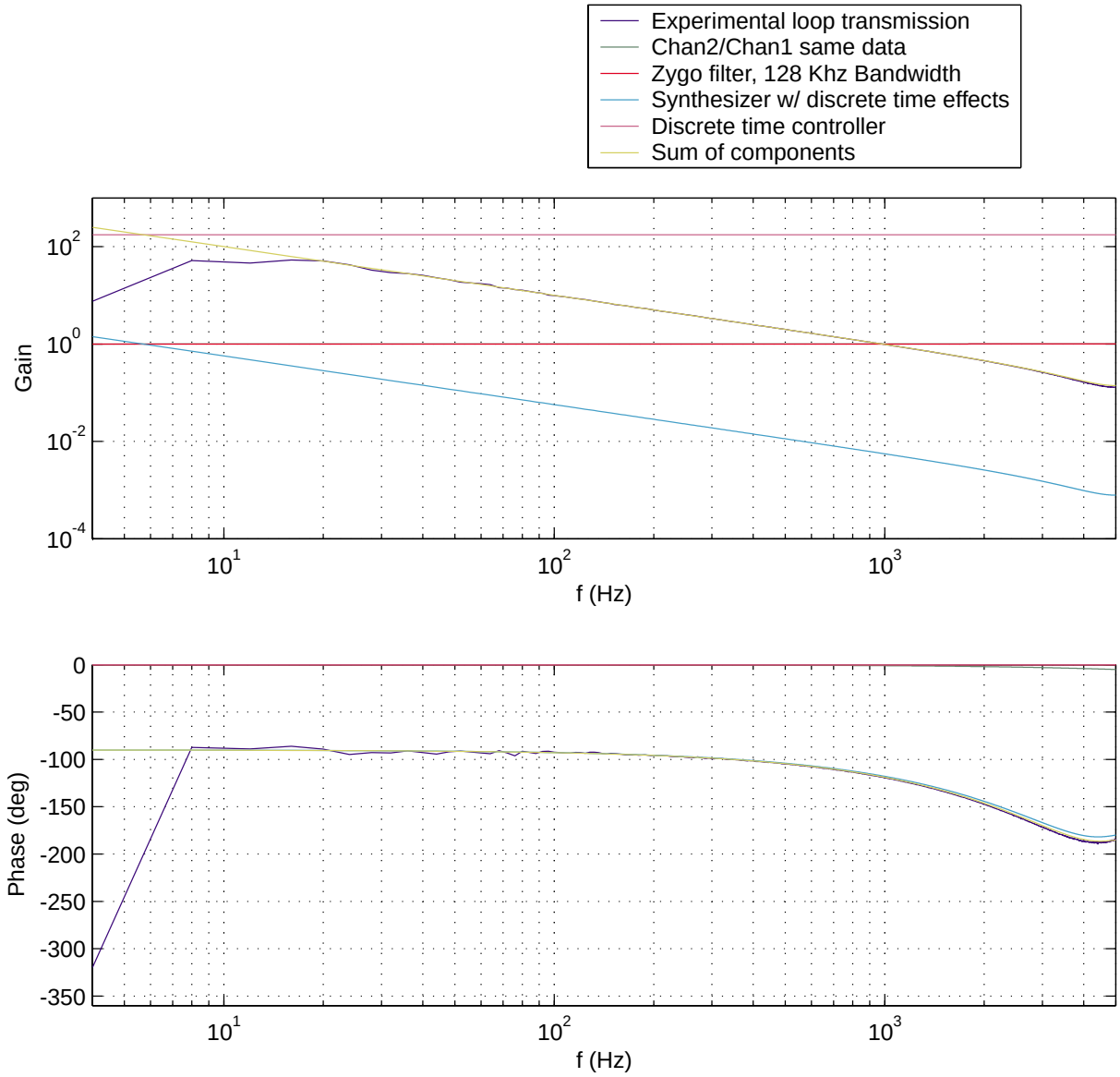

Figure 8-3: Experimental data and components of fringe locking model. The system uses proportional control and a 128 KHz bandwidth Zygo digital filter.

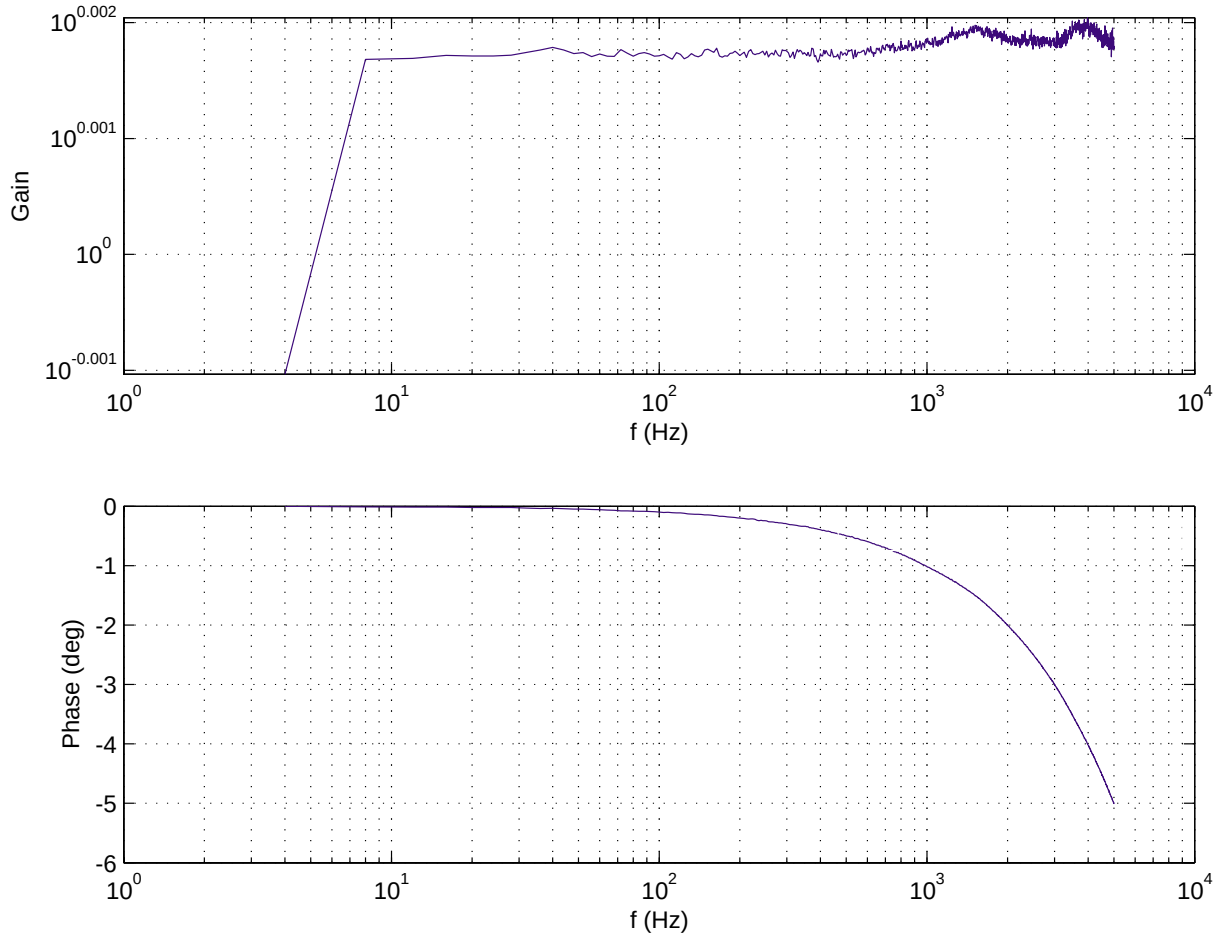

Figure 8-4: Frequency response of Chan2/Chan1, outputting same data to both DAC channels.

long sequences of data can be analyzed and averaged very conveniently. Furthermore, for all but the most detailed work, the errors are negligible. As seen from the plot, the gain is within 0.5% of unity. The phase of -5^o at 5 KHz corresponds to a delay of 2.8 μsec (=$5^o/360^o$/5000 Hz). Since the DAC data is supplied over the PCI bus with a delay between channel 1 and channel 2 on the order of 1.5 μsec and the DAC card outputs asynchronously at 400 KHz, the measured channel to channel delay of 2.8 μsec is within expectations. The small gain and phase distortion demonstrated is used to obtain a better match between the modeled and experimental data. Because the correction is small, under most circumstances it would be neglected.

The loop transmission is obtained by digitally adding white noise into the PM_r signal. Then PM_{fle} and PM_1 are output by DAC to Channel 1 and Channel 2 inputs

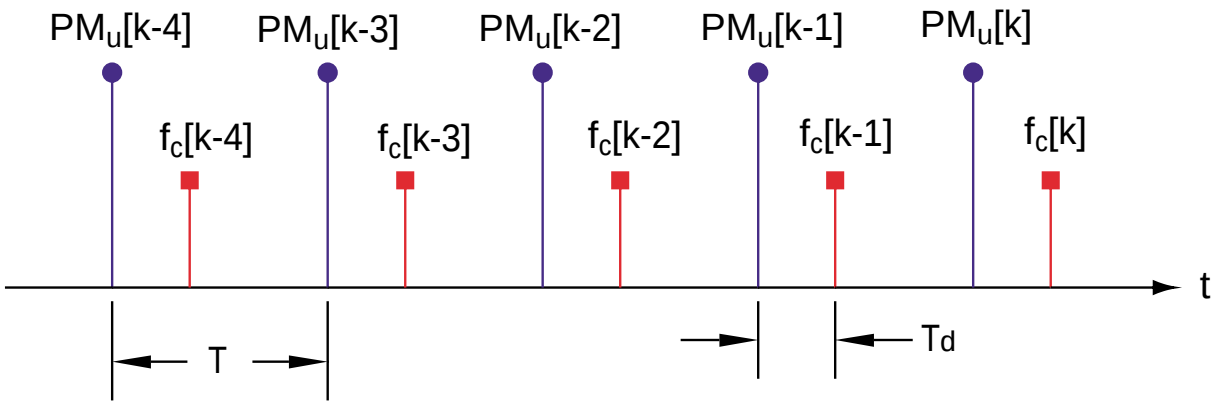

Figure 8-5: Timing diagram for the frequency synthesizer control. The unfiltered phase meter signal PM_u is sampled with a period T. The output of frequency correction, f_c is delayed from the phase meter sampling by T_d.

of the dynamic signal analyzer.

The controller used to obtain Figure 8-2 is simply a proportional controller where

$$G(z) = 176. \tag{8.3}$$

The controller output frequency correction f_c is in units of the frequency synthesizer digital data and corresponds to 0.07 Hz per least significant bit. The gain was adjusted to establish unity loop transmission crossover with about 60^o of phase margin. The cross over frequency is about 1 KHz.

The -1 gain block shown in Figure 8-2 is associated with the phase meter. Phase meter 1 decrements if f_1 increases. If f_3 was 80 MHz instead of 120 MHz, PM_1 would increase with increasing f_1 and the sign of the controller gain would need to be negative for stability.

The reference frequency f_r equals 0x55555555. This digital frequency corresponds to 100 MHz. The frequency updated to the synthesizer is the sum of f_c and f_r.

The timing diagram for the frequency synthesizer control is shown in Figure 8-5. The unfiltered phase meter signal PM_u is sampled with a period T. The output of frequency correction, f_c, is delayed from the phase meter sampling by T_d. The

difference equation for the phase meter output is given by

$$PM_u[k] = PM_u[k-1] + K_s(T - T_d)f_c[k-1] + K_s T_d f_c[k-2]. \tag{8.4}$$

Here K_s is the constant derived from the phase meter and frequency integration relationship for continuous time given by

$$PM_u = K_s \int f_c \, dt \tag{8.5}$$

The value of K_s is $512 \times 300 \times 10^6$Hz/0xffffffff or about 36. The 512 factor is the phase meter counts per period and the remaining terms equal the frequency resolution of the synthesizer. Equation 8.4 states that the phase meter value at time index k is equal to the previous phase meter value plus the integration of frequency $f_c[k-1]$ over a time duration of $T - T_d$ plus the integration of frequency $f_c[k-2]$ over a time duration of T_d. This difference equation assumes an ideal synthesizer with an instant and phase continuous update of f_c according to the timing diagram of Figure 8-5.

The transfer function $H(z)$ derived from Equation 8.4 is given by

$$H(z) = \frac{K_s((T - T_d)z + T_d)}{z^2 - z}. \tag{8.6}$$

The sampling time T is programmed into the control system. It must be long enough for the real-time control loop to complete execution. The frequency update delay T_d is limited by the time for servicing an interrupt, read of all the necessary data, calculation of the update frequency, output of the frequency to the synthesizer, FPGA pass of data from the MFE inputs to the AD9852 frequency synthesizer chip, AD9852 execution time, and the AOM acoustic propagation delay. In the plot of Figure 8-3, T is 100 μsec and T_d was the measured value of 28 μsec. An oscilloscope and a timing diagnostic signal sent to an available digital output was used to measure T_d. This delay was adjusted to include the frequency synthesizer update time and the acoustic propagation delay. The frequency synthesizer was measured to update in less than 0.4 μsec from the time new digital data was supplied. Also, the acoustic propagation

delay [67] is expected to be less than 0.5 μsec since the velocity of sound in fused silica is 5960 m/s and the entire beam is less than 3 mm from the transducer. Therefore, the overwhelming source of the delay is associated with the data acquisition and processing.

Taking into account the data acquisition, the synthesizer, and the controller produces a model with very good correspondence to the measured data even at frequencies close to Nyquist. The Zygo filter that has a bandwidth of 128 kHz has negligible effect for the range plotted. The only experimentally derived parameter of the model is T_d, but even this really is deterministic. All the other parameters were completely determined by programming.

Figure 8-6 shows the calculated transfer functions of two Zygo digital filters plotted from 100 Hz to 20 MHz. These filters can be programmed into the ZMI 2002 boards. The position transfer function for the filter is given by

$$P(z) = \frac{-X_p z_Z + X_p - X_v}{-z_Z^4 + 2z_Z^3 - z_Z^2 - X_p z_Z + X_p - X_v} \tag{8.7}$$

This transfer function is adapted from the ZMI 2002 manual [119]. The variables are defined as

$$X_p = 2^{K_p}, \tag{8.8}$$

$$X_v = 2^{K_v}, \tag{8.9}$$

$$\text{and } z_Z = e^{\omega T_z}. \tag{8.10}$$

The filter is implemented by programming a register to assign desired values to K_p and K_v. The time T_z corresponds to the internal sampling rate of the card of 1/(40 MHz). The filter plotted with the -3 dB bandwidth of 15 KHz uses $K_p = -9$ and $K_v = -20$. The filter with the -3 dB bandwidth of 128 KHz uses $K_p = -6$ and $K_v = -14$. The 128 KHz filter is used to obtain the experimental transfer function in Figure 8-3. The gain is essentially unity over the frequency range in that plot. For the filtered frequency range, the gain rolls off at about decade per decade. The

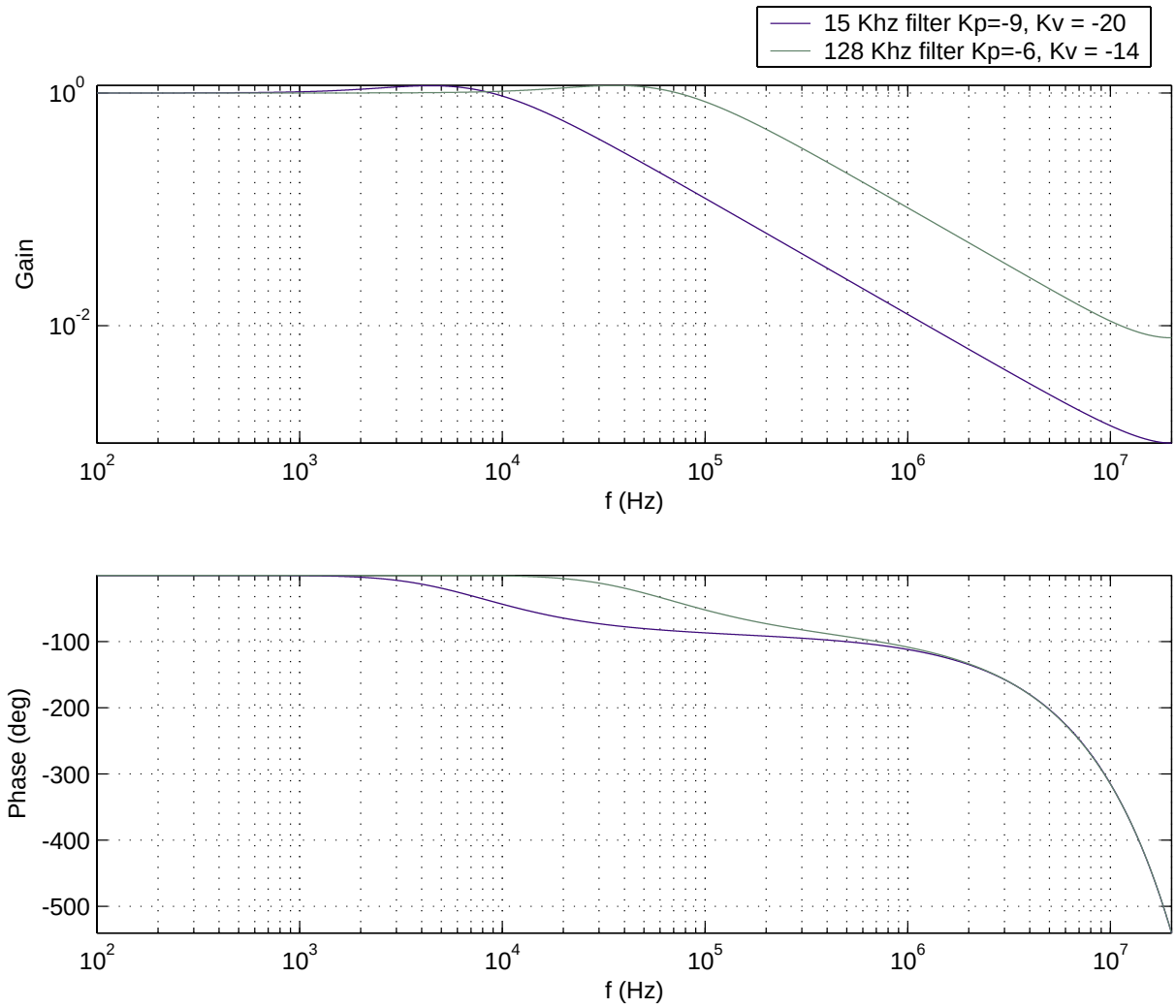

Figure 8-6: Position transfer function for two Zygo digital filters. The filters have -3 dB bandwidths of 15 KHz and 128 KHz.

15 KHz filter is the lowest bandwidth filter available on the board and is the filter that was ultimately chosen to provide the best rejection of aliased signals. Although aliasing will occur for phase noise above 5 KHz when using a controller loop rate of 10KHz, the filter is believed to be adequate because under most circumstances not much noise is expected within the aliased range where the filter also has poor attenuation. Additionally, aliasing up to about 9,900 Hz will introduce noise at a high enough frequency that it won't print even if the fringe locking controller locks it out. Actually, the aliased range of significance is only between 9,900 Hz and 10,100 Hz.

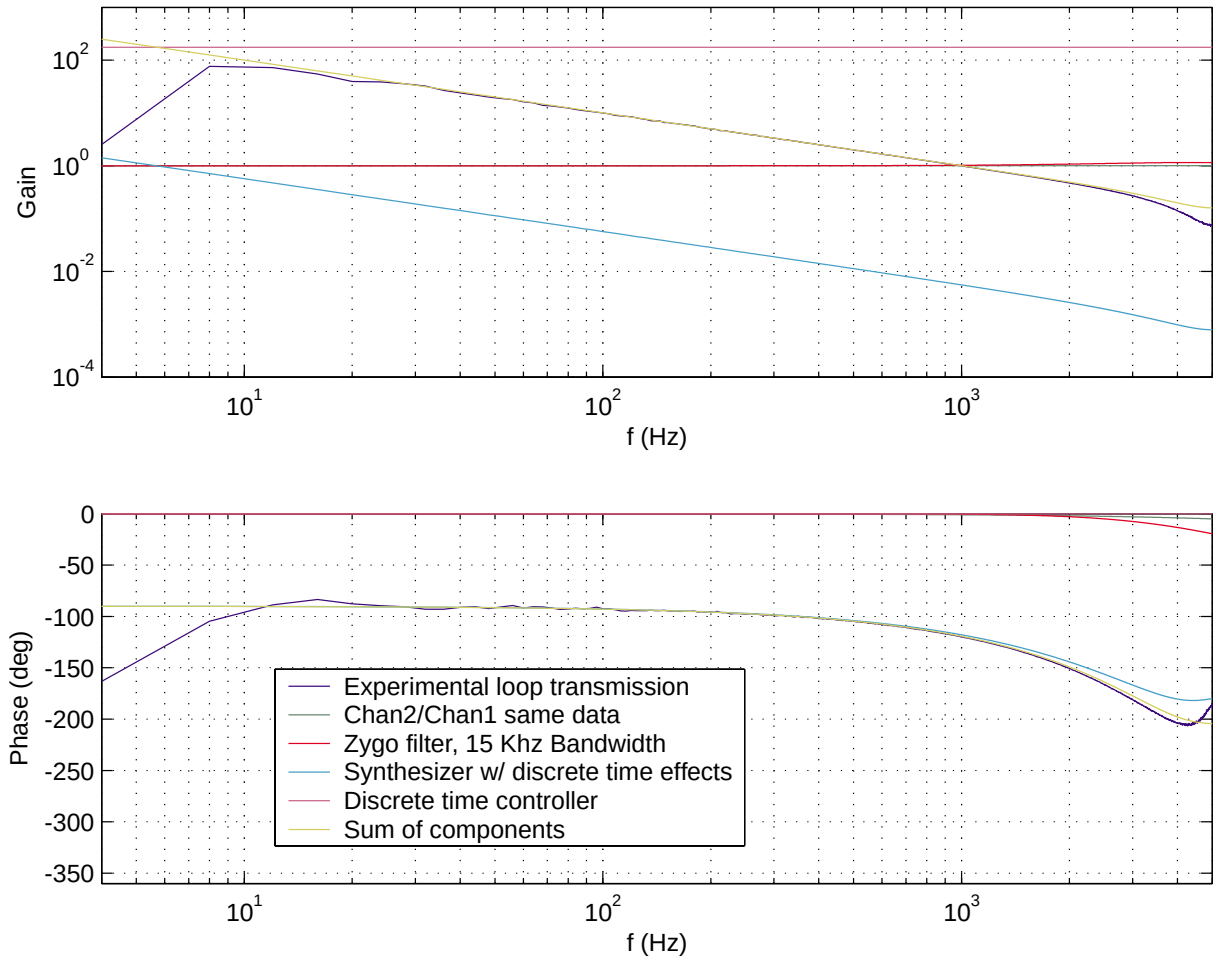

Figure 8-7: Experimental data and components of fringe locking model. This system uses proportional control and a 15 KHz bandwidth Zygo digital filter.

Figure 8-7 shows the experimental data and component models for a system that uses the 15 KHz bandwidth Zygo digital filter. Near Nyquist frequency there is an unmodeled multi-rate sampling effect. In the controller design, I address this discrepancy by incorporating a small correction to a frequency response based model. I will discuss the design of a higher bandwidth controller in the next section.

8.1.1 Control system design

The sampling and latency limit the performance of the control system. For proportional control, a 60° phase margin criteria, and a sampling rate of 10 KHz a cross over frequency of 1 KHz was obtained with the control system. The resulting disturbance

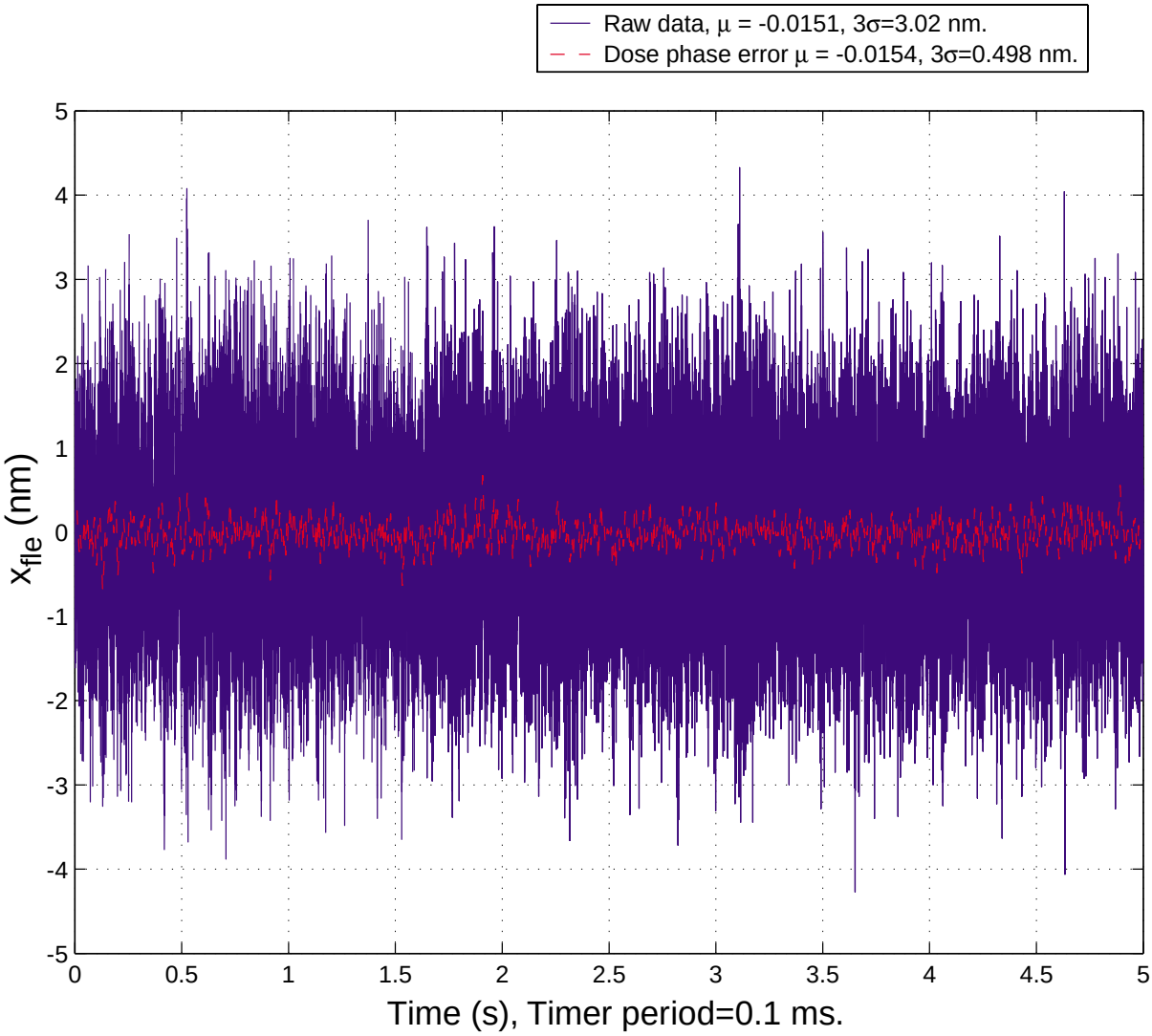

Figure 8-8: Fringe locking error signal with proportional control.

rejection obtained is adequate for subnanometer dose phase error in our system. Figure 8-8 shows the fringe locking error signal using proportional control. The 3σ raw error is 3 nm. The error relevant to the dose phase obtained after passing the data through a Gaussian filter with $d/v = .01$ sec is 0.5 nm, 3σ. Thus, most of the fringe locking error is at a high enough frequency that it does not entirely print.

Fringe locking error data without control is shown in Figure 8-9. The 3σ error over five seconds is 31 nm. Most of the error over this time scale is due to the stage error. There is also long term drift, which is much larger as indicated by the 1250 nm offset to the data. The long term drift is largely due to the lowest 16 bits on the

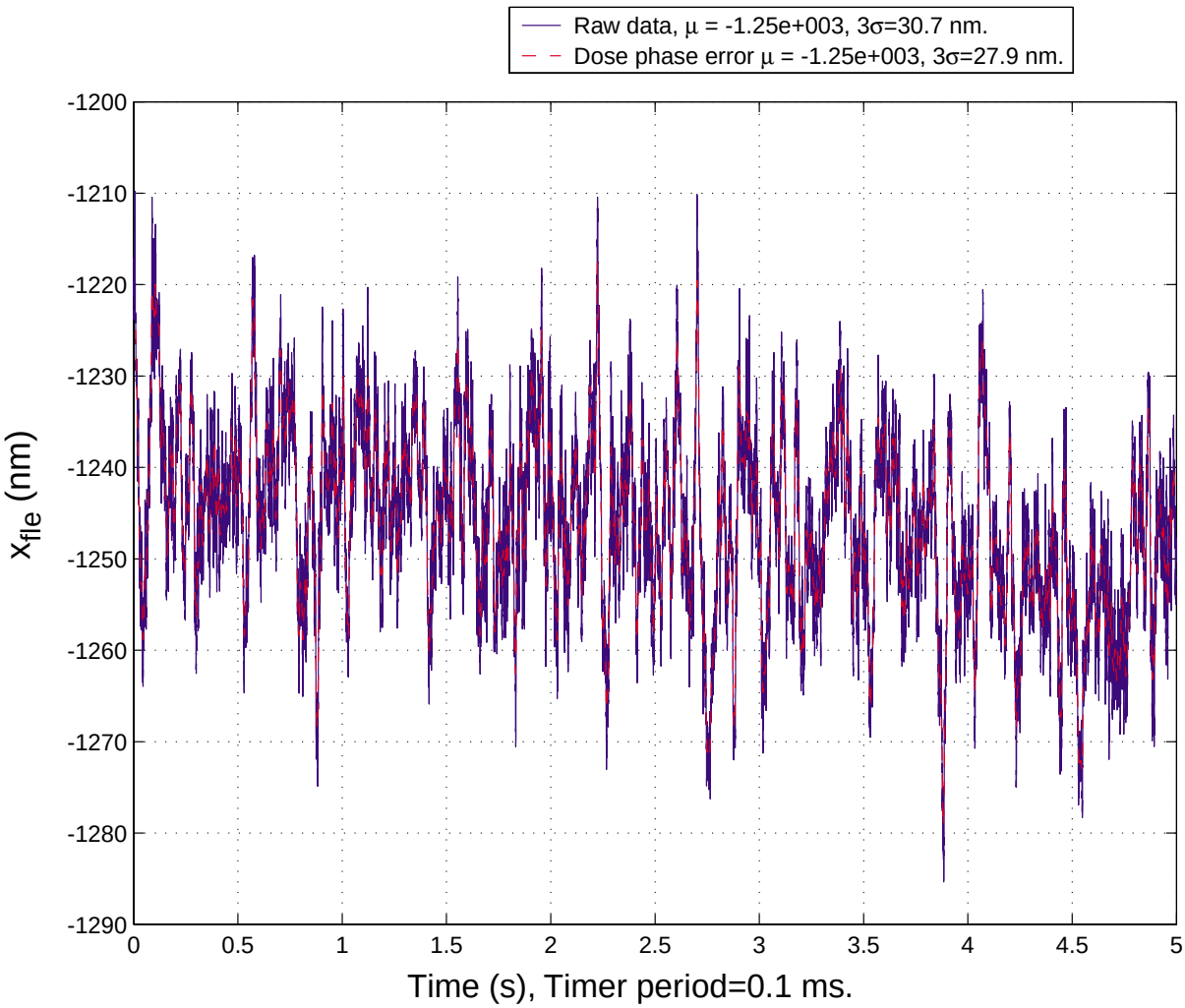

Figure 8-9: Fringe locking error signal with no control.

frequency synthesizer not being set.

I implemented a lead compensated controller to provide further disturbance rejection and to test the limits of the control bandwidth. Figure 8-10 shows the fringe locking error with the higher order controller whose frequency response is in Figure 8-11. The controller design will be discussed after reviewing this data. The data shows some broadband improvement by a factor of 1.2 and improvement for the Gaussian filtered data by a factor of 1.4. The DC gain of the open loop system is 1.6× higher than the proportional control system. The low frequency gain appears to be saturating because the Gaussian filtered data was predicted to improve by a factor of 1.6. This saturation may be the result of quantization noise.

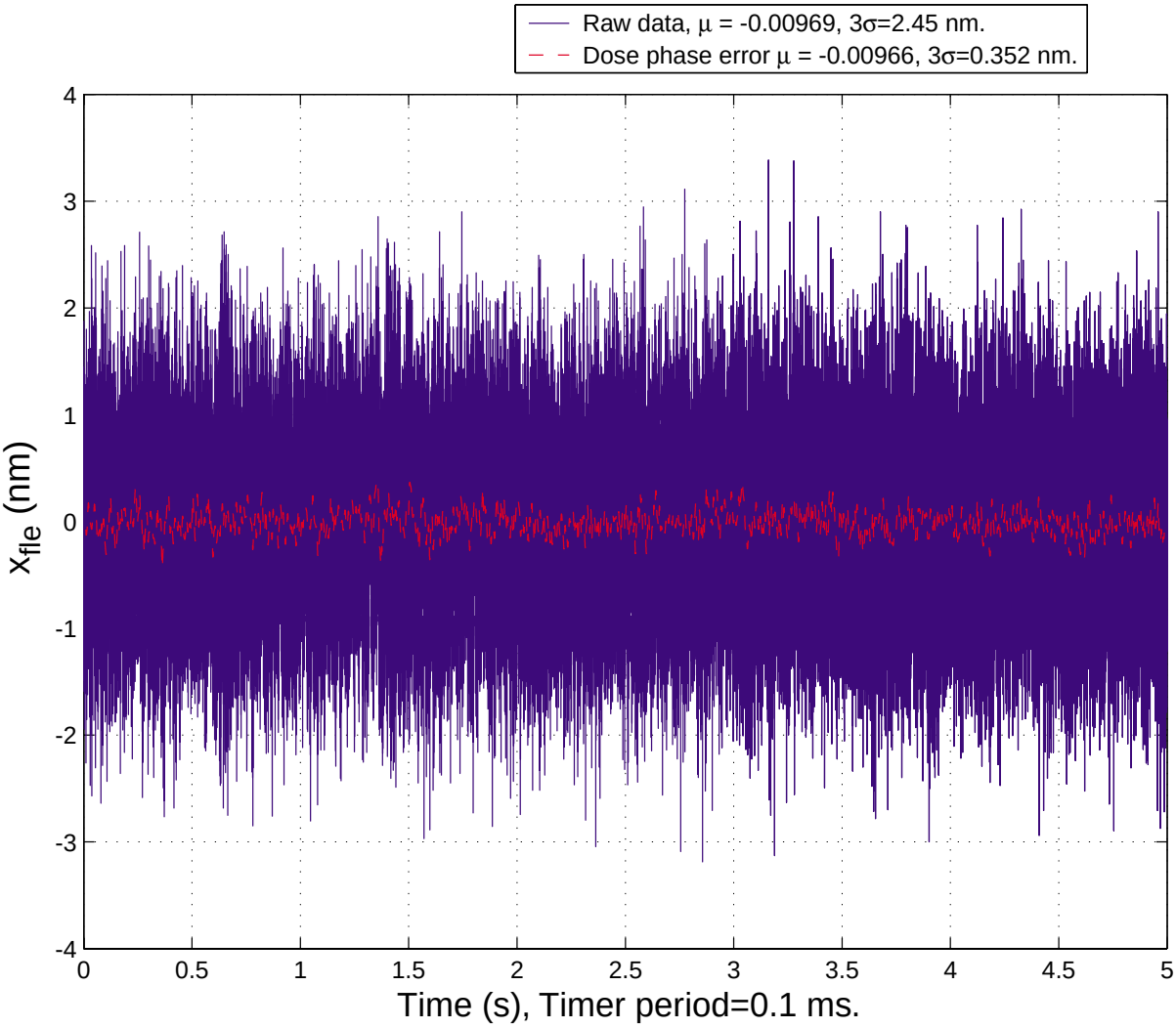

Figure 8-10: Fringe locking error signal with lead compensation.

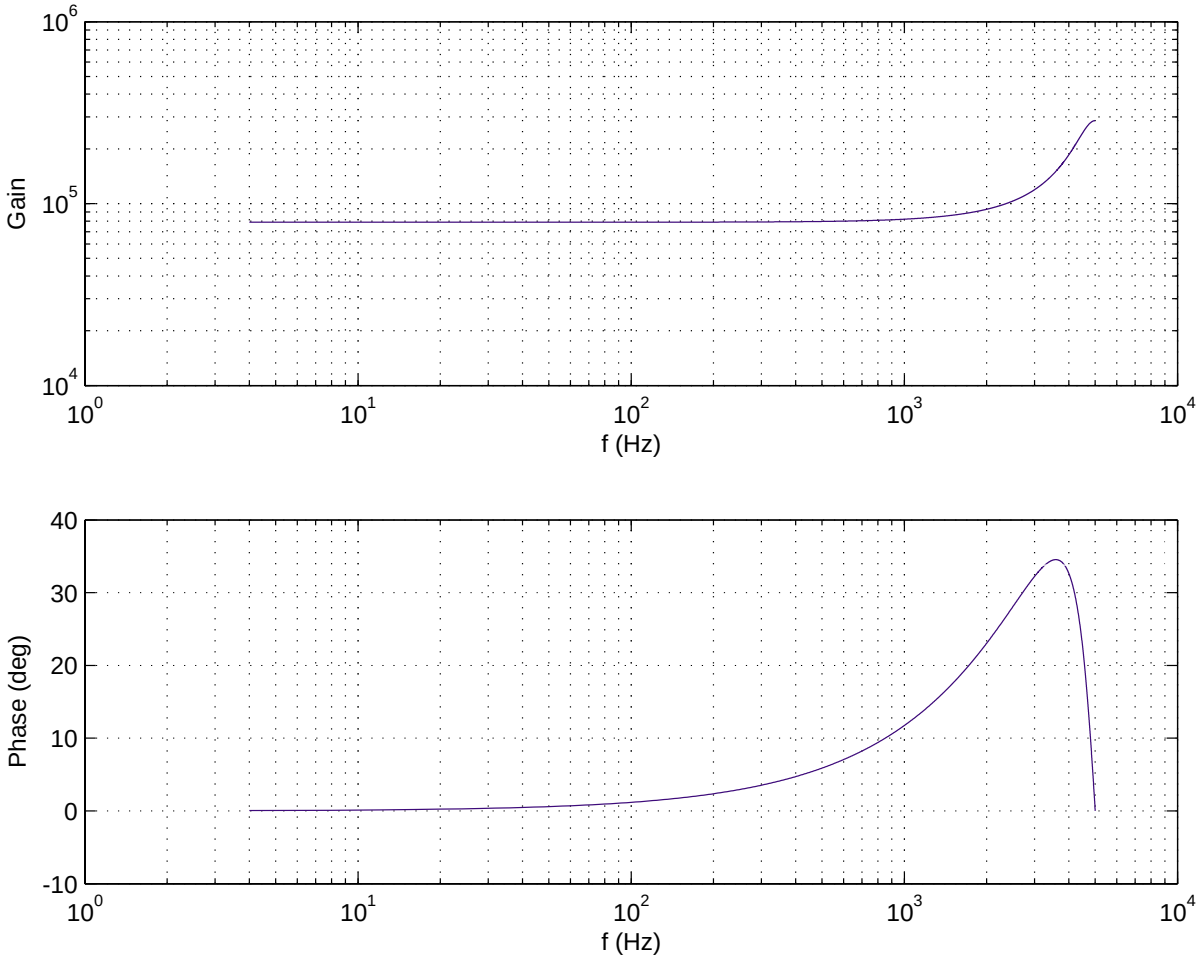

Figure 8-11: Frequency response of lead controller.

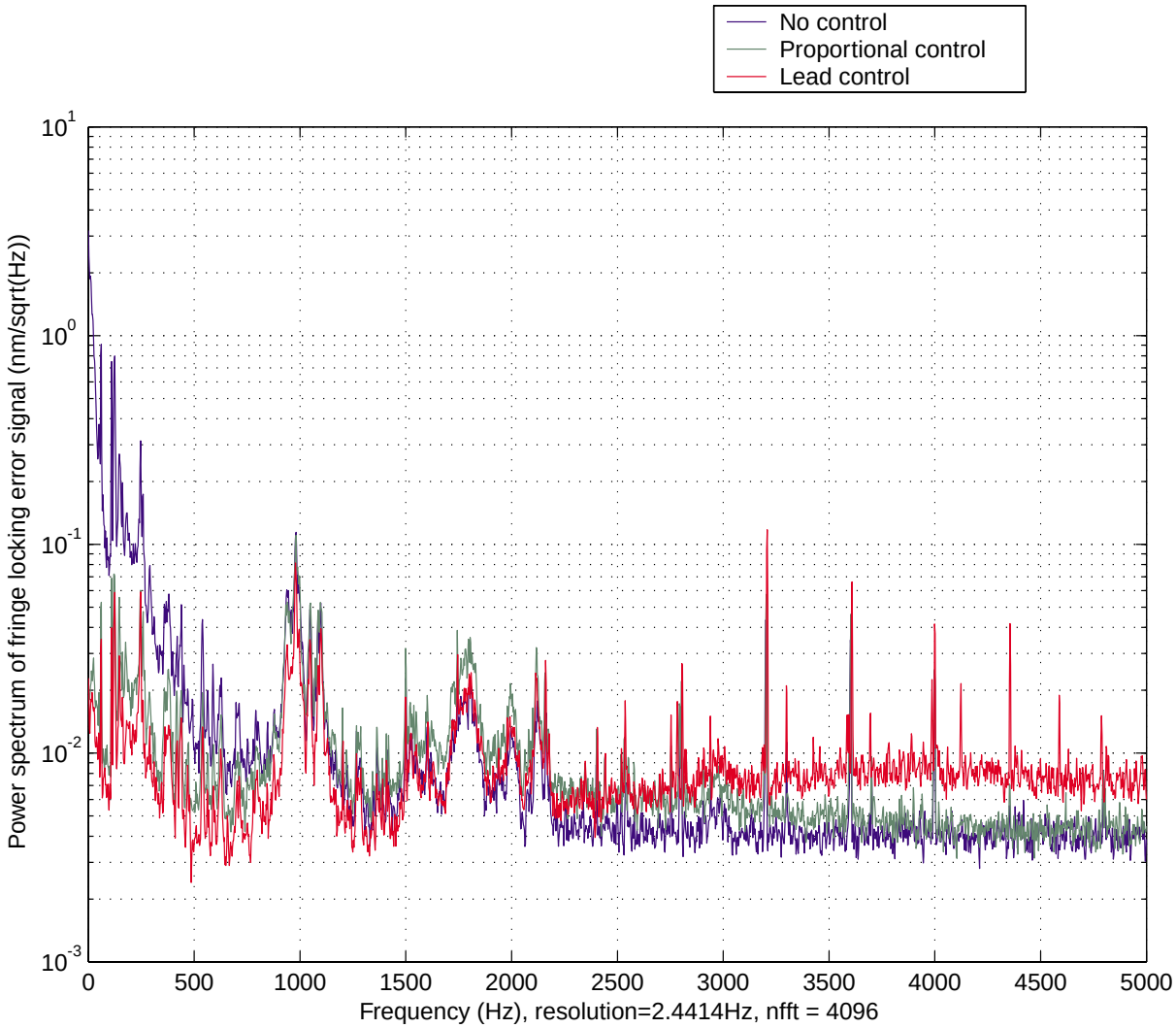

Figure 8-12: Power spectral density of the fringe locking error signal without fringe locking control, with proportional control, and with lead control.

Figure 8-12 shows the power spectrum of the data with no control, proportional control, and with lead control. The lead controller shows improved rejection at frequencies below 2 KHz and a tolerable amplification for disturbances above 2 kHz.

The limitation with proportional control can be seen from the discrete time root locus plot [29] shown in Figure 8-13. This root locus includes the synthesizer plant from Equation 8.6 where T=100 μs and T_d=28 μs. At high gains, the dominant poles quickly tend toward low damping. If a zero is placed to left of the $z = 0$ pole, the dominant poles are brought back toward the real axis at high gains. Furthermore, the dominant poles are forced to loop within a tighter circle about $z = 0$ and are

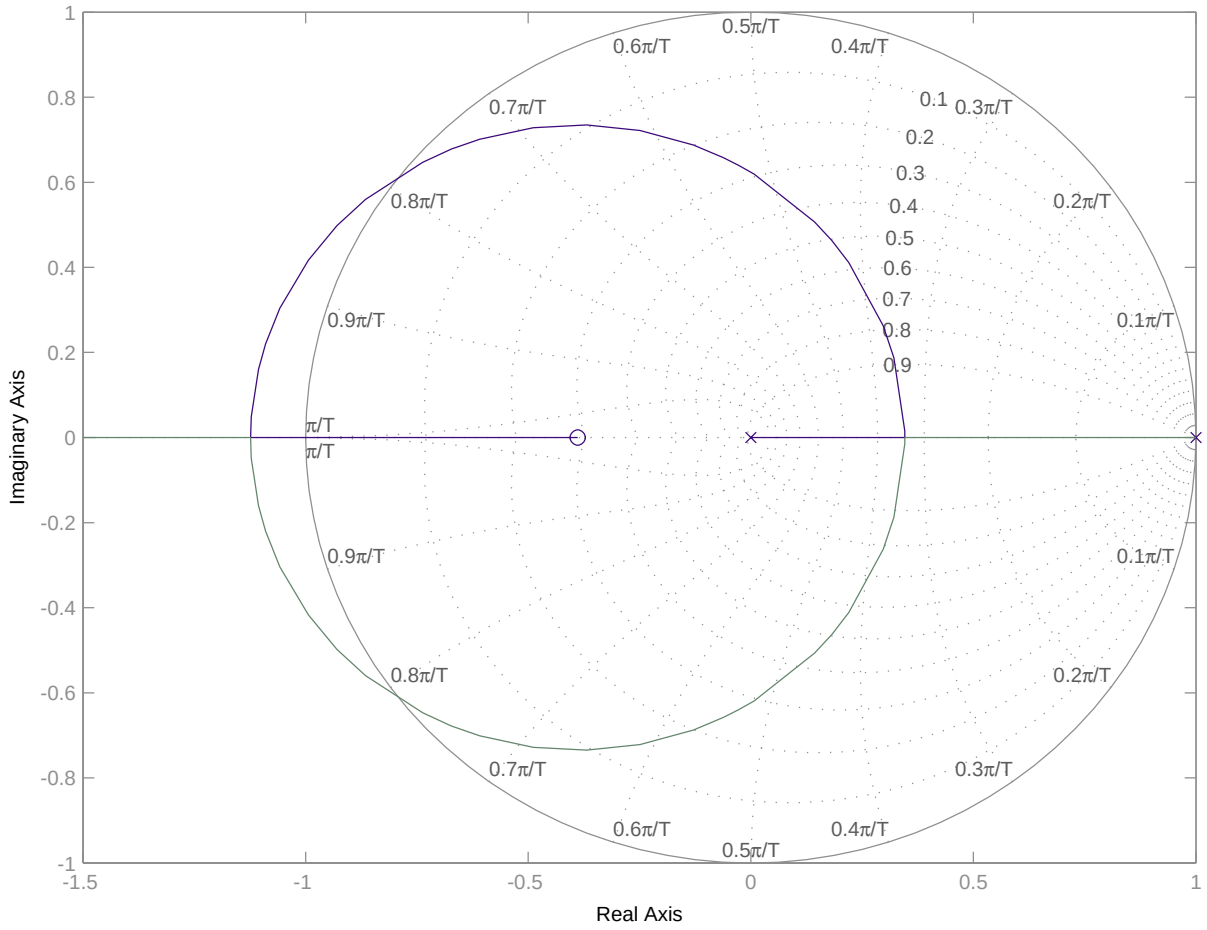

Figure 8-13: Root locus of plant with proportional control.

better damped. Since it is physically impossible to implement a controller with more zeros than poles, a pole must also added. Figure 8-14 shows the root locus plot using a "lead" controller. The transfer function for the controller is given by

$$G(z) = K\frac{z + 0.05}{z + 0.6}. \tag{8.11}$$

The pole location, $z = -0.6$, was selected to provide 60° of phase margin when the DC gain was 1.6× higher than that previously used for the proportional controller. At this gain, $K = 428$. This factor of 1.6 though seemingly arbitrary, was found to produce tolerable amount of high frequency noise amplification. The frequency response of the controller is shown in Figure 8-11.

Figure 8-15 shows the experimental loop transmission and the modeled compo-

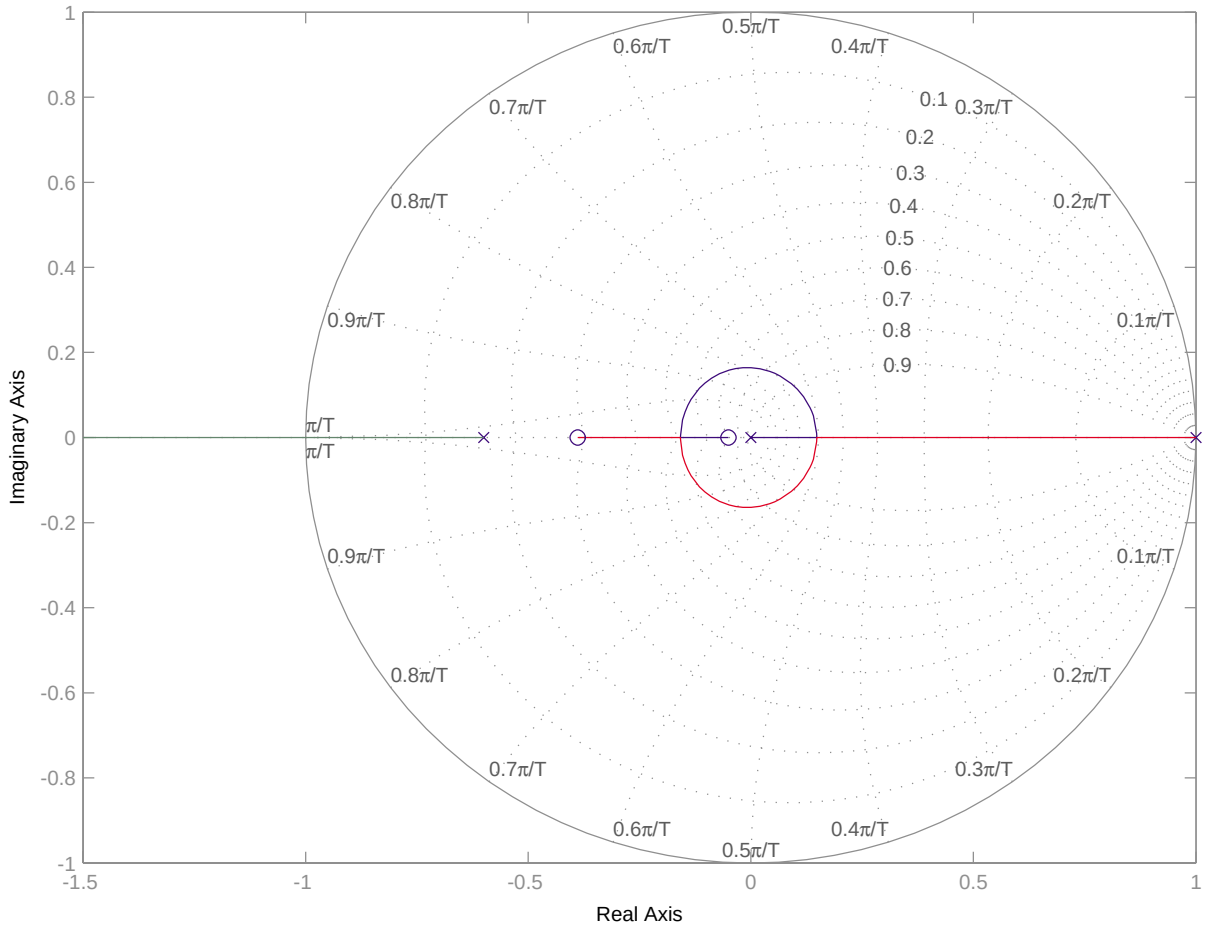

Figure 8-14: Root locus of plant with lead control.

nents for this higher order controller. The lack of correspondence at high frequency is essentially identical to the lack of correspondence seen with proportional control indicating the unmodeled multi-rate sampling effect is linear. The disturbance rejection can be predicted using the frequency response based plant derived from the experimental data. Using the plant derived from the data of Figure 8-7 and the lead controller transfer function, I have plotted the designed and experimental disturbance transmissibility in Figure 8-16. Since the open loop data has very little noise, the disturbance transmissibility, DT(z), is accurately calculated as

$$DT(z) = \frac{1}{1 + G_{ol}(z)}. \tag{8.12}$$

Here G_{ol} is the loop transmission. The disturbance transmissibility based on the

ratio of power spectral densities with the control on over the control off uses the data from Figure 8-12. The measured disturbance transmissibility very closely follows the designed disturbance transmissibility. The designed disturbance transmissibility is centered within the noise between 10 Hz and Nyquist frequency. There is some unpredicted high frequency noise for the lead controller, however. This noise might be the result of unmodeled timing jitter. This high frequency noise increases quickly with higher gains. The experimental disturbance transmissibility shows a floor at frequencies below 10 Hz probably due to quantization noise. The data when the control is on that is used to calculate the disturbance transmissibility is close to the level of the quantization noise floor in the sub 10 Hz frequency range. When the fringes are controlled, the spectral density is about 0.010 nm/rtHz in the sub 10 Hz range. This is only 2.5 times higher than the 0.0040 nm/rtHz noise floor observed at high frequencies. The noise floor at high frequency is consistent with a model discussed in reference [78] for uniformly distributed white noise. For this model the quantization noise spectral density is predicted as

$$\sqrt{\frac{\Delta^2 T}{24}}. \tag{8.13}$$

The effective quantization Δ for x_{fle} is 0.84 nm and the sampling time T of 100 μs predicts the quantization spectral density of 0.0034 nm/rtHz. This model is consistent with the observed high frequency noise floor. While this simple model does not precisely predict the *control* noise floor at low frequencies, it does illustrate that the control noise floor is close to the quantization noise level.

Figure 8-17 shows the frequency responses of the plant, controller, plant and controller, disturbance transmissibility, and closed loop systems. The closed loop -3 dB bandwidth is equal to the Nyquist frequency of 5 kHz. The cross over frequency at 1740 Hz, though not rigorously optimized, approaches the limits of the control bandwidth. Most importantly, the disturbance rejection is sufficient for sub-nanometer error budgets associated with the fringe locking error.

The residual fringe locking error does not limit the SBIL error. Rather the inac-

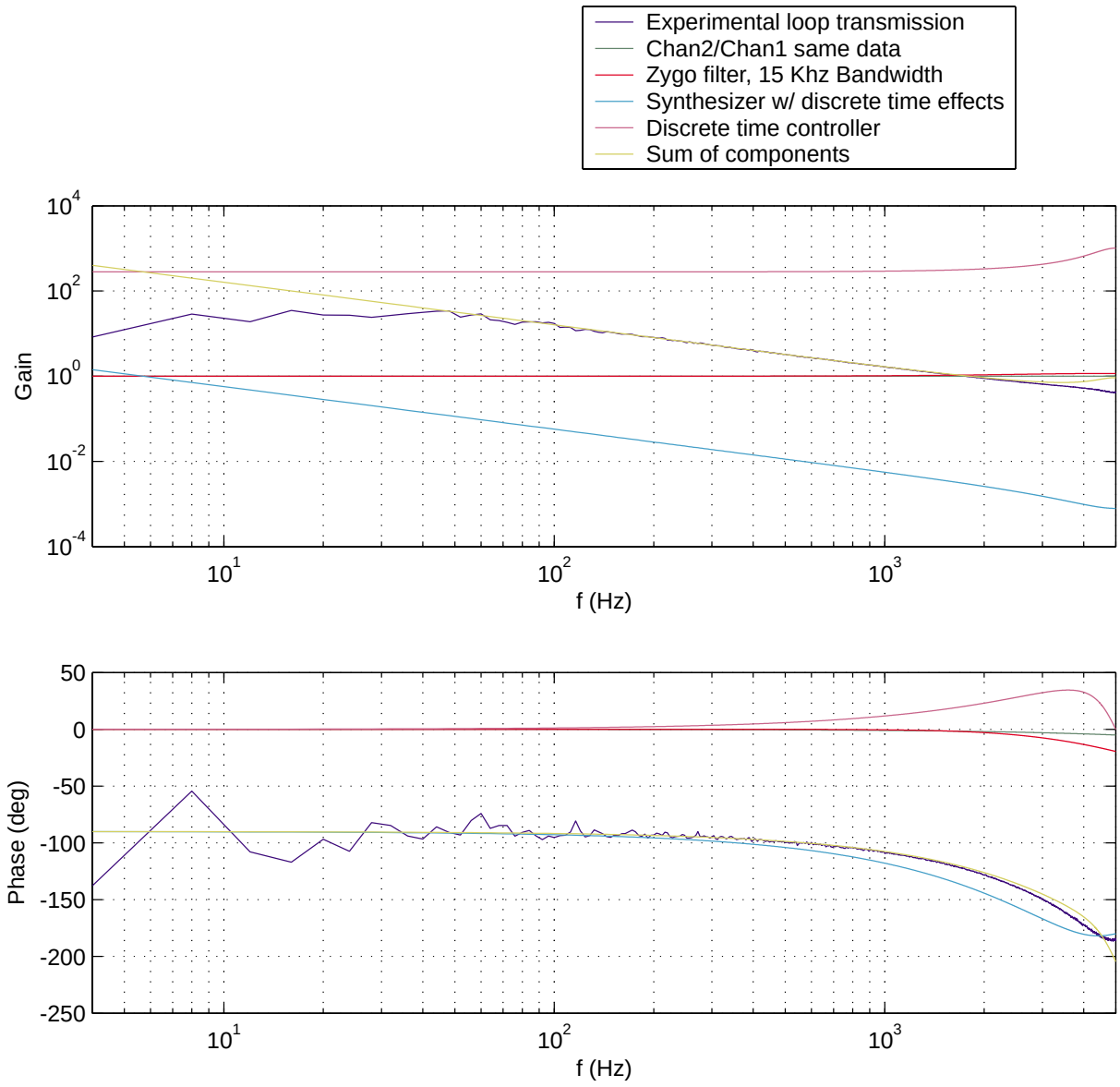

Figure 8-15: Experimental data and components of fringe locking model. This system uses a lead controller and a 15 KHz bandwidth Zygo digital filter.

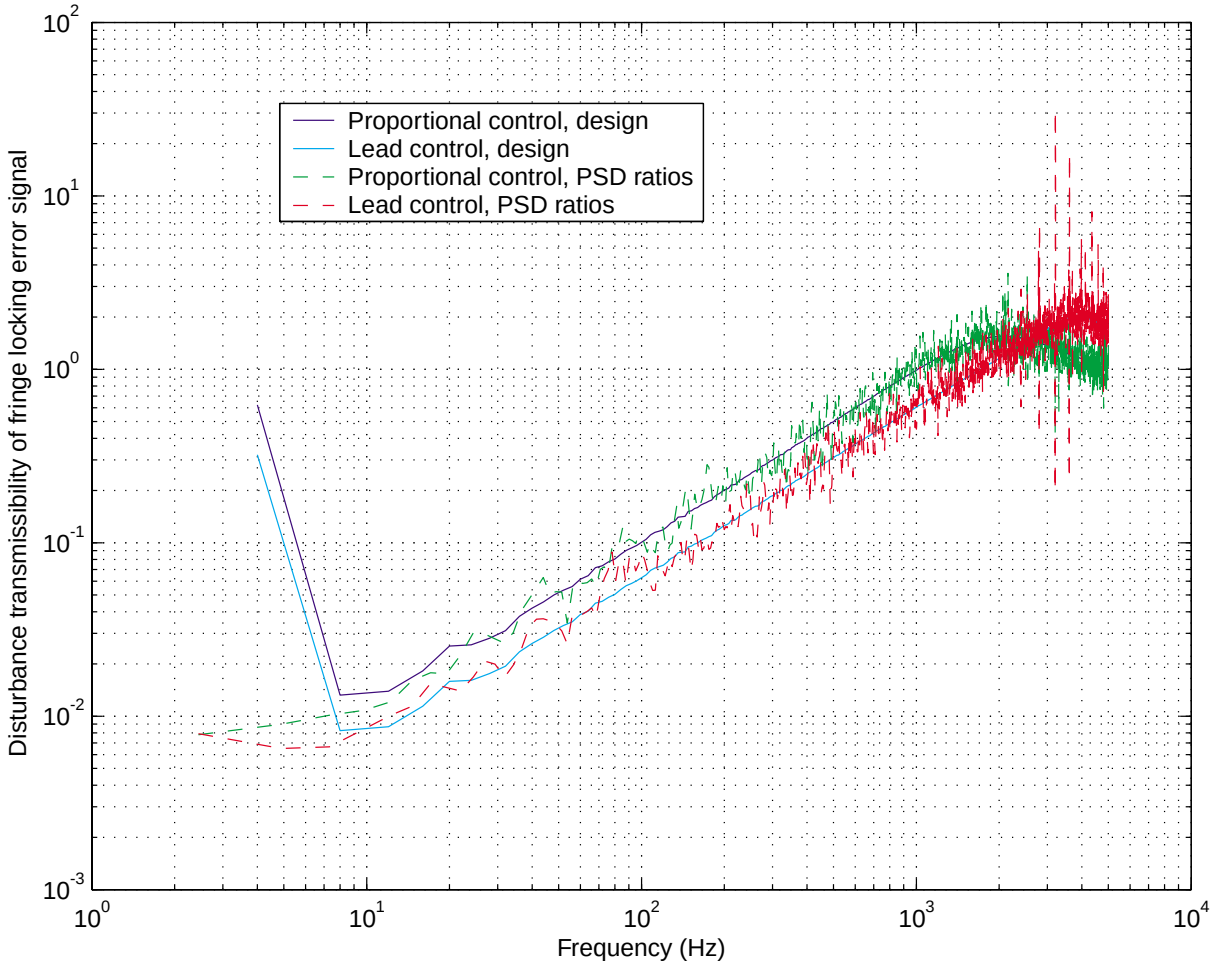

Figure 8-16: Plots of the predicted disturbance transmissibility derived from loop transmission data for two different controllers and disturbance transmissibility derived from ratios of power spectral densities.

curacy of the fringe locking signal limits the performance of the system. Figure 8-18 shows the ratio x_{fle}/x_{ue}. Note that this is a high frequency resolution plot that covers the range from 0 to 700 Hz. The noise at higher frequencies is not much of a concern because it essentially does not print. The fringe locking error signal is much smaller than the unobservable error over the frequency range of most interest. Moreover, even if the fringe locking error was zero, there would be negligible improvement for Gaussian filtered x_4 data with integration times of interest (i.e. $d/v > .01$ s). At high frequencies there are some notable frequency bands where the residual fringe locking exceeds the unobservable error as shown in Figure 8-19. However, these errors are small and they won't print anyway. If the stage is scanned at a high enough speed,

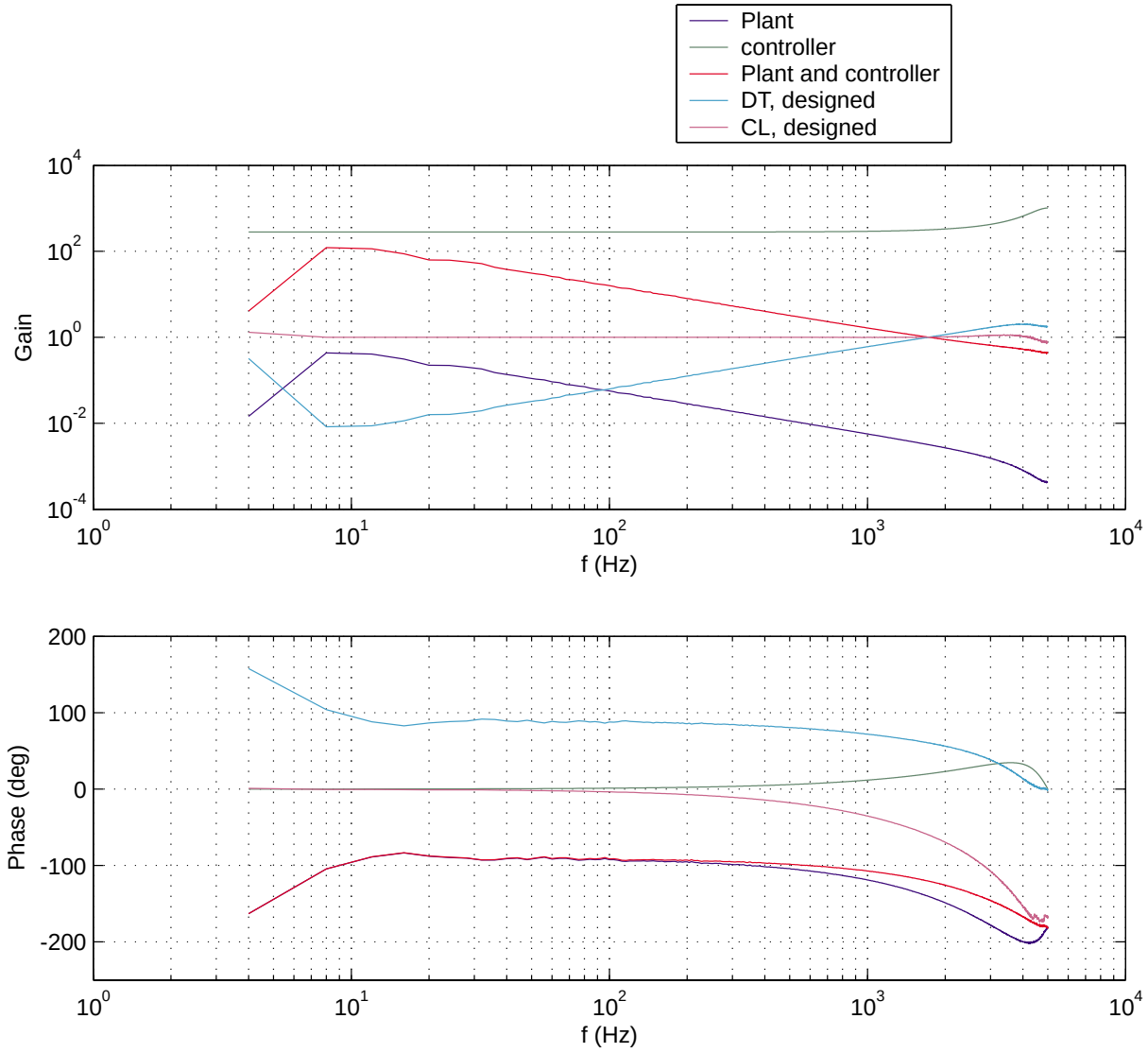

Figure 8-17: Frequency responses of the system. The graph shows the open loop plant, controller, plant and controller, disturbance transmissibility and closed loop systems.

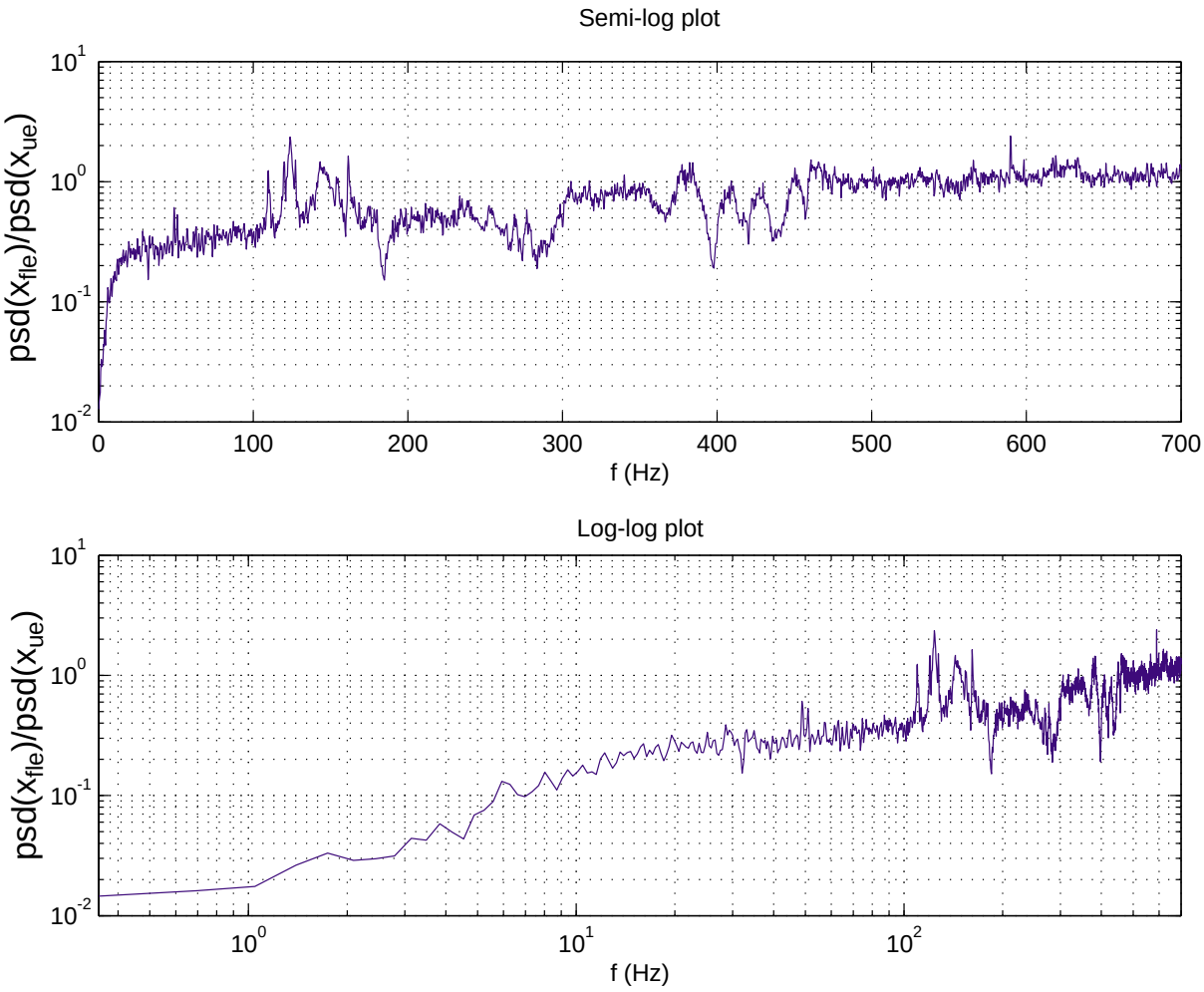

Figure 8-18: Plot of the ratio power spectral densities psd(x_{fle})/psd(x_{ue}) when the fringe locking control is on. The same data is shown on semi-log and log-log plots.

additional low frequency gain may be justified. But in Chapter 9, the fringe locking error is shown to be much smaller than the noise at the stage speeds of interest.

The question of whether there is optimal controller gain based on the noise and disturbance power spectrums is a worthy question. In all the data that I have taken x_4 was always more than x_{ue}. Thus, if the fringe locking error was zero the x_4 error would improve. The improvement is mainly at the higher frequency range however.

If disturbance-to-noise ratios are greater than one, the optimal control performance is obtained with the highest gains possible. This point can be argued rigorously. First, some basic stochastics must be understood. A review of basic stochastics can be found in [78, 72]. A signal can be described by its autocorrelation function,

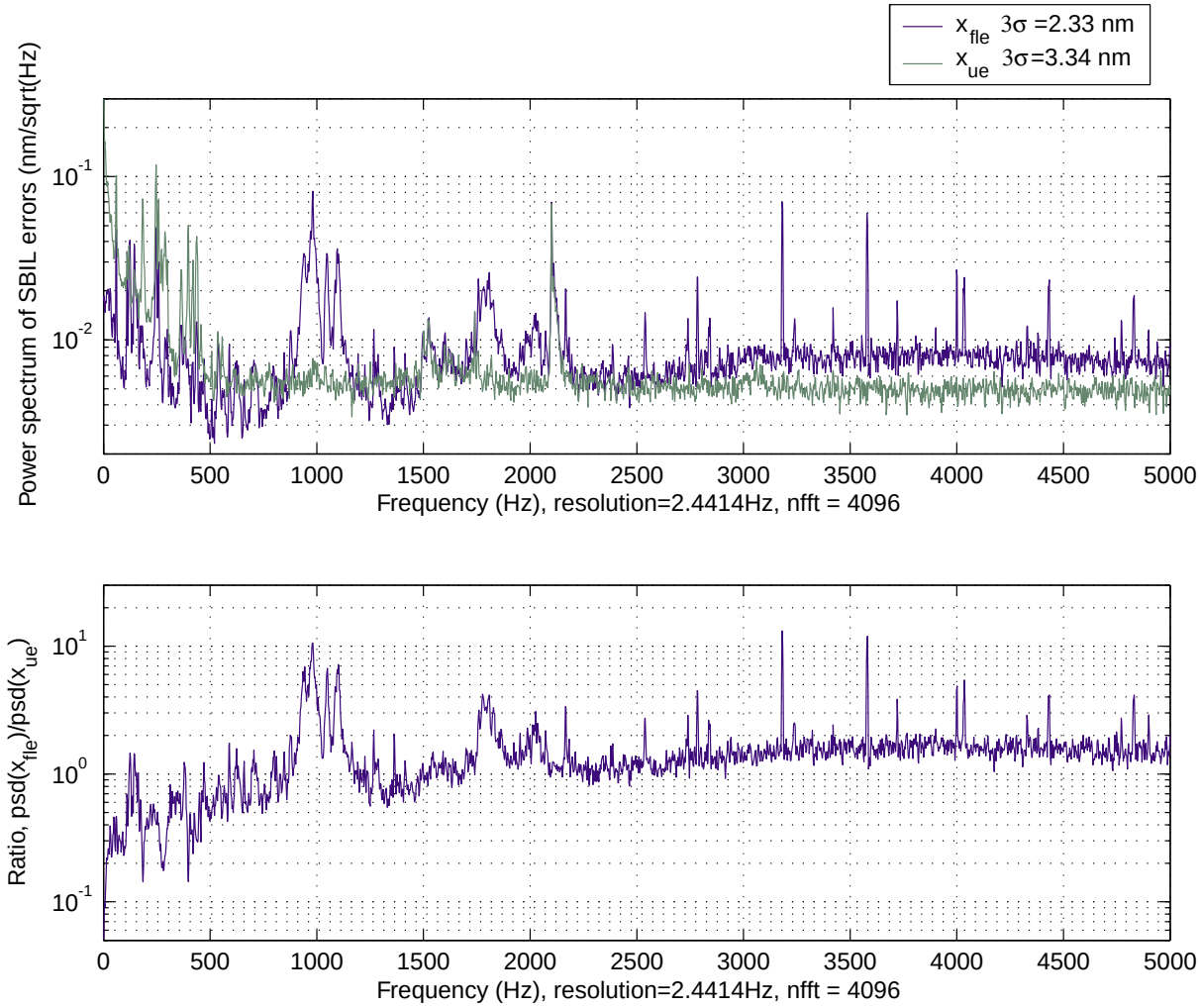

Figure 8-19: The top plot contains the power spectrums of x_{fle} and x_{ue} when the fringe locking is on. The bottom plot is the ratio of these errors.

which is given by

$$R_x(\tau) = \lim_{T\to\infty} \int_{-T}^{T} x(t)\, x(t-\tau) \mathrm{d}t. \tag{8.14}$$

If τ=0, the autocorrelation function reduces to the mean squared of the waveform or the variance. The Fourier transform of the autocorrelation function is the spectral density of the waveform and is given by

$$S_x(\omega) = \int_{-\infty}^{\infty} R_x(\tau) e^{-j\omega\tau}\, d\tau. \tag{8.15}$$

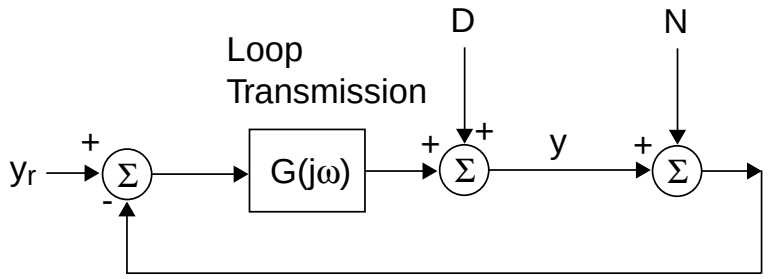

Figure 8-20: Block diagram for a generic control system.

If the signal is modeled as a random waveform $x(t)$ with a spectral density $S_x(\omega)$, the spectral density of the output waveform, y(t), assuming a linear plant, is given by

$$S_y(\omega) = |G(j\omega)|^2 \, S_x(\omega). \tag{8.16}$$

Thus, the spectral density of the output waveform can be modeled if the spectral density of the input waveform and the plant transfer function is known. The variance of the signal is calculated by taking the inverse Fourier transform to obtain the autocorrelation function at τ=0. The variance is given by

$$\sigma_y^2 = \frac{1}{2\pi} \int_{-\infty}^{\infty} S_y(\omega) \, d\omega. \tag{8.17}$$

Here σ_y is the standard deviation of y.

Figure 8-20 shows the block diagram of the fundamental control problem, where there is a closed loop system with a loop transmission $G(j\omega)$. The variable y is the parameter to be controlled in the presence of disturbance, D, and noise, N.

Let's assume the reference input, y_r, is a constant and for convenience let's further assume $y_r = 0$. Then the Laplace transform of y is given by

$$Y(s) = \frac{D(s) - G(s)N(s)}{1 + G(s)} \tag{8.18}$$

Assuming that the disturbance and noise are uncorrelated, then the spectral density

of y is given by

$$S_y(\omega) = S_D(\omega)\left|\frac{1}{1+G(j\omega)}\right|^2 + S_N(\omega)\left|\frac{G(j\omega)}{1+G(j\omega)}\right|^2. \tag{8.19}$$

Furthermore, I define

$$k(\omega)^2 = \frac{S_D(\omega)}{S_N(\omega)} \text{ and} \tag{8.20}$$

$$G(j\omega) = g(\omega)e^{j\theta(\omega)}. \tag{8.21}$$

Now S_y is rewritten as

$$S_y = S_N\frac{k^2+g^2}{1+2g\cos\theta+g^2}. \tag{8.22}$$

The fact that the variables are a function of ω is implied. I want to answer what the optimal gain g is given k and θ. The optimal gain will minimize S_y. Taking the derivative of S_y with respect to g and setting the result to zero will produce the solution for the gain that provides the maximum S_y, which is not the solution we want. The gain for minimum S_y is infinity when

$$\frac{k^2+g^2}{1+2g\cos\theta+g^2} - 1 > 0 \tag{8.23}$$

for $0 < g < \infty$. In other words, if S_y for all g is greater than the case when $g = \infty$ then $g = \infty$ is optimal. Putting everything over a common denominator this condition becomes

$$\frac{k^2-1-2\cos\theta g}{1+2g\cos\theta+g^2} > 0. \tag{8.24}$$

The denominator is guaranteed to always be greater than zero except for the unstable case when $\cos\theta = -1$ and $g = 1$. For this unstable case, which cannot be allowed to

occur, the denominator equals zero. The condition is now reduced to

$$k^2 - 1 > 2g\cos\theta. \tag{8.25}$$

Since $\cos\theta$ will be negative for the range of phase occuring in the system, the final condition for the optimal gain to be ∞ is

$$k^2 > 1. \tag{8.26}$$

Or in other words, if $S_D > S_N$ the optimal g is ∞. The optimal gain for $k < 1$ can be confirmed too. The optimal gain is 0 when

$$\frac{k^2 + g^2}{1 + 2g\cos\theta + g^2} - k^2 > 0 \tag{8.27}$$

for $0 < g < \infty$. In other words, if S_y for all g is greater than the case when $g = 0$ then $g = 0$ is optimal. This expression can be reduced to the condition

$$\frac{1}{k^2} - 1 > \frac{2\cos\theta}{g}. \tag{8.28}$$

Again $\cos\theta$ will be negative for the range of phase occuring in the system. Thus the condition for the optimal gain to be zero is

$$k^2 < 1. \tag{8.29}$$

These conditions are intuitive. It is also of interest to consider the diminishing returns of extra gain. The performance at the low frequencies (< 100 Hz) is critical to the writing performance. At these frequencies $\theta = -90^\circ$ and the spectral density is

$$S_y = S_N \frac{k^2 + g^2}{1 + g^2}. \tag{8.30}$$

From this relation, the diminishing return when g is greater than k can be clarified.

At high gains, such as in the 0 to 100 Hz range for our fringe locking system,

$$S_y \approx S_N \left(\frac{k^2}{g^2} + 1 \right) \tag{8.31}$$

and if $g = 2k$, the output square root power is within 11% of optimal. Another point worth mentioning is that if $k = 1$, then S_y is insensitive to the gain.

At the high frequencies, there is no benefit for my application by being precise about the optimal gain with optimal control techniques such as LQG control. The high frequency noise essentially does not print in writing mode. Furthermore, the loop transmission crosses over where the noise and disturbances are the lowest; the amplification due to the phase drop off is not a concern because the noise level at the high frequencies is so small.

At low frequencies, the residual fringe locking error is so much smaller than the noise that very little improvement can be obtained for fringe stability at the substrate-fringe interface even if the fringe locking error signal was zero. Improved system performance relies on achieving lower noise signals.

It is useful to know k for design purposes. This can be measured with the fringe locking control off by assuming the noise is x_{ue} and the disturbance is $x_4 - x_{ue} = x_{fle}$. This assumption is not entirely accurate for reasons such as electronic noise in PM_3 and PM_4 but it is expected to be accurate at the sub-nanometer level. I have plotted the experimentally determined disturbance-to-noise ratio in the lower plot of Figure 8-21. The upper plot shows the data used to calculate the D/N ratio. The data shows that the noise is hardly ever greater than the disturbance. For design purposes, k can be assumed to be greater or equal to one. The controller has higher gain than k in most portions of the power spectrum and in all areas of concern. A higher frequency resolution plot is shown in Figure 8-22. The peak at around 8 Hz is associated with the stage error. Figure 8-23 compares the power spectrums for the components of the fringe locking error x_3 and x_{die}. The 8 Hz peak is seen in the x_{die} data. The data for the higher resolution plots has a duration of 35 seconds. Over this time scale, the x_3 error is the larger component of the fringe locking error. The power spectrum for x_{ue}

is also shown for comparison purposes. Most of the resonances observed in x_{ue} are also observed in both x_3 and x_{die}. Errors in both of the components, indicates translation of the metrology block. The parts on the metrology block will deflect in response to the accelerations of their base. The deflections lead to unobservable errors. Also, unobservable pitch errors of the metrology block/and or the x-axis interferometer may partly explain the unobservable components of the resonances. For the sake of completeness, the components of the fringe locking error are compared to x_{ue} of the full sampling band in Figure 8-24. When there is observable error in x_3 that is not in x_{die}, this error is due to disturbance of the UV interferometer phase prior to the metrology block. For instance, the large KHz vibrations in x_3 are likely due to relative vibrations of the many optical mounts on the bench.

So far I have shown frequency responses obtained by injecting white noise into the fringe locking error signal. This produces the expected frequency responses from about 20 Hz to Nyquist frequency. Since the stability of the controller is highly affected by the dynamics near the cross over frequency, it is important to have meaningful data at the high frequency range. However, it is also of interest to verify that the controller is working as expected at low frequency. Figure 8-25 shows the frequency response of the experimental and modeled system for a disturbance injection designed to provide very clean low frequency data. The disturbance injection for the experimental system was white noise that was filtered with a two pole Butterworth filter. The poles were located at 20 Hz. The modeled data very closely matches the experimental data, even at low frequencies. There is an increase in noise at the high frequency data due to limited disturbance injection there. Similarly, for frequency ranges where the disturbance is at the level of quantization, the experimental data will not accurately describe the linear control dynamics.

It is important to verify the low frequency performance because of the additional disturbances present during the scanning. The high gains at low frequency ensure the fringe locking error remains small even during scans.

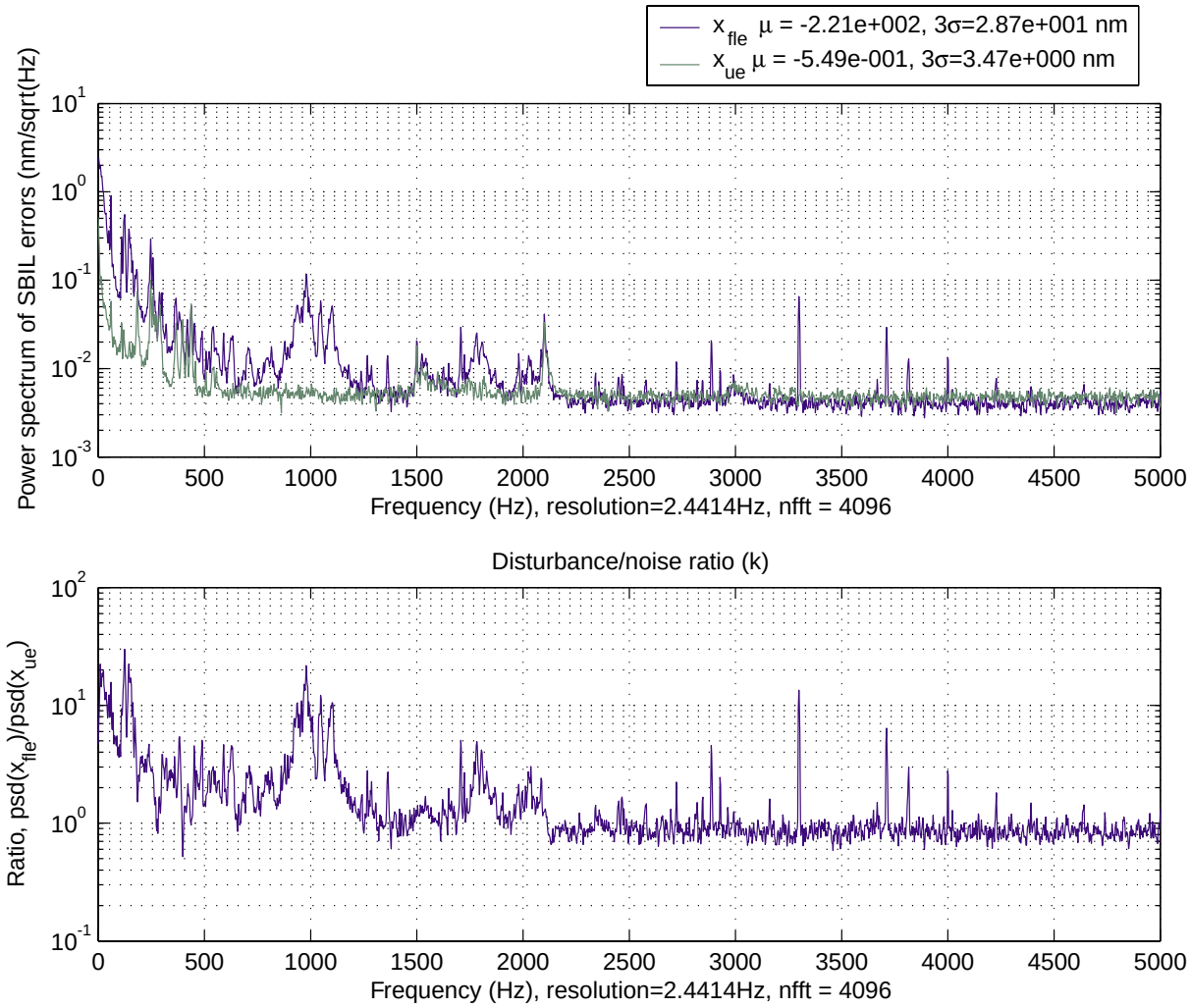

Figure 8-21: The top plot shows the power spectrum of x_{fle} and x_{ue} taken when the fringe locking control was off. The bottom plot shows the ratio of these power spectrums , which is the disturbance-noise ratio.

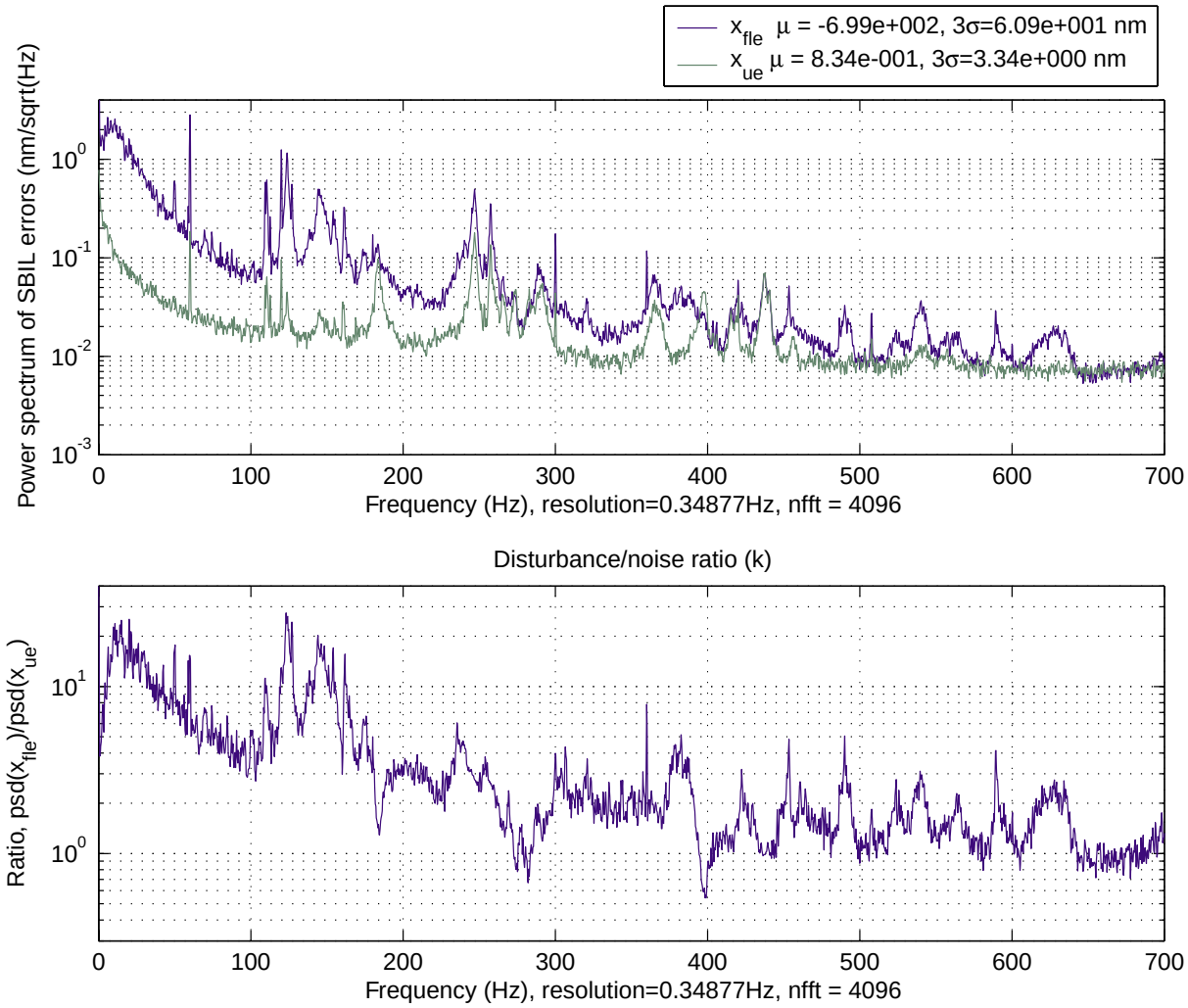

Figure 8-22: A higher resolution plot of the disturbance and noise power spectrums and their ratio. This data is taken with the fringe locking control off.

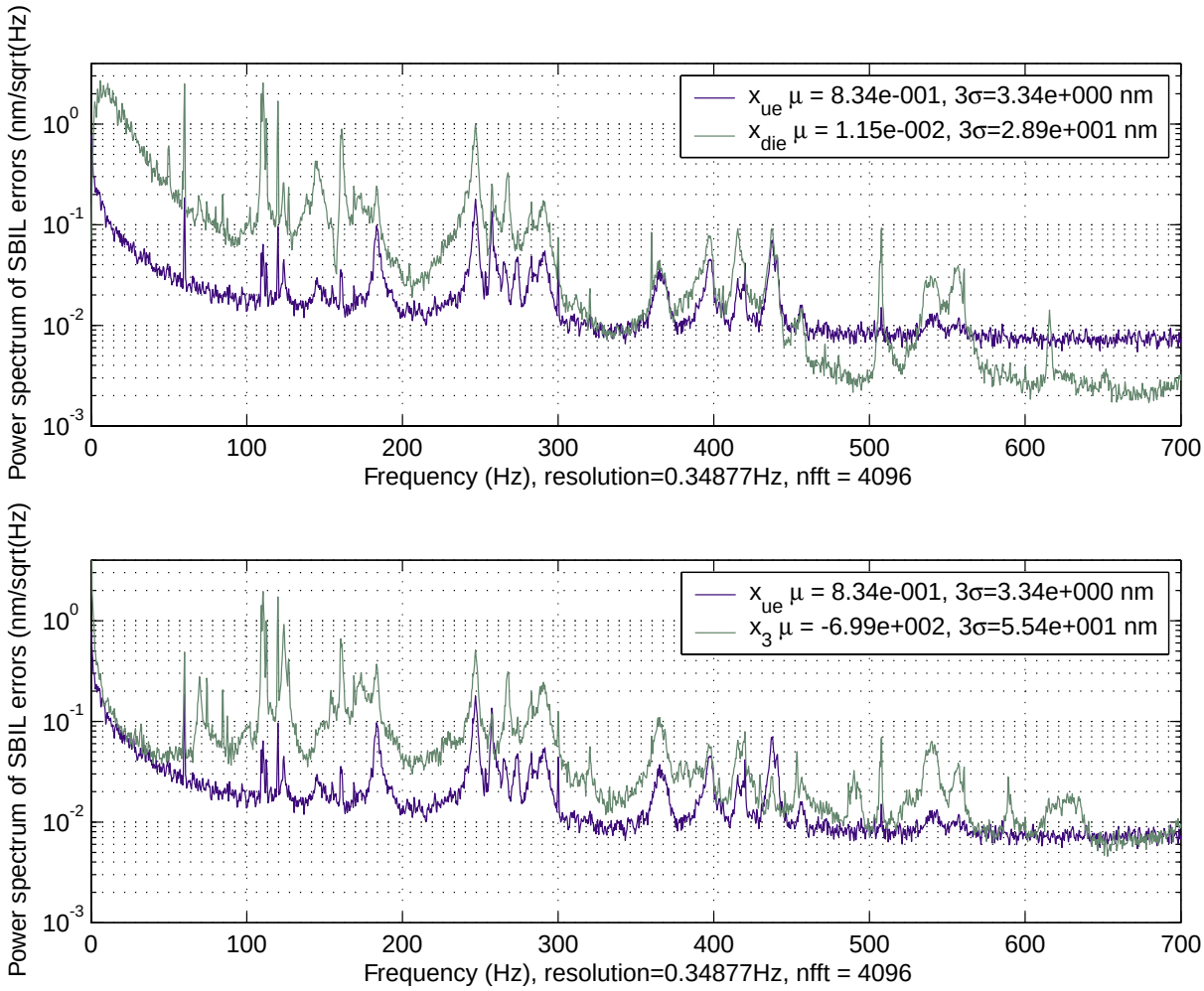

Figure 8-23: Plots comparing the components of the fringe locking error to x_{ue} from 0 to 700 Hz. This data is taken with the fringe locking control off.

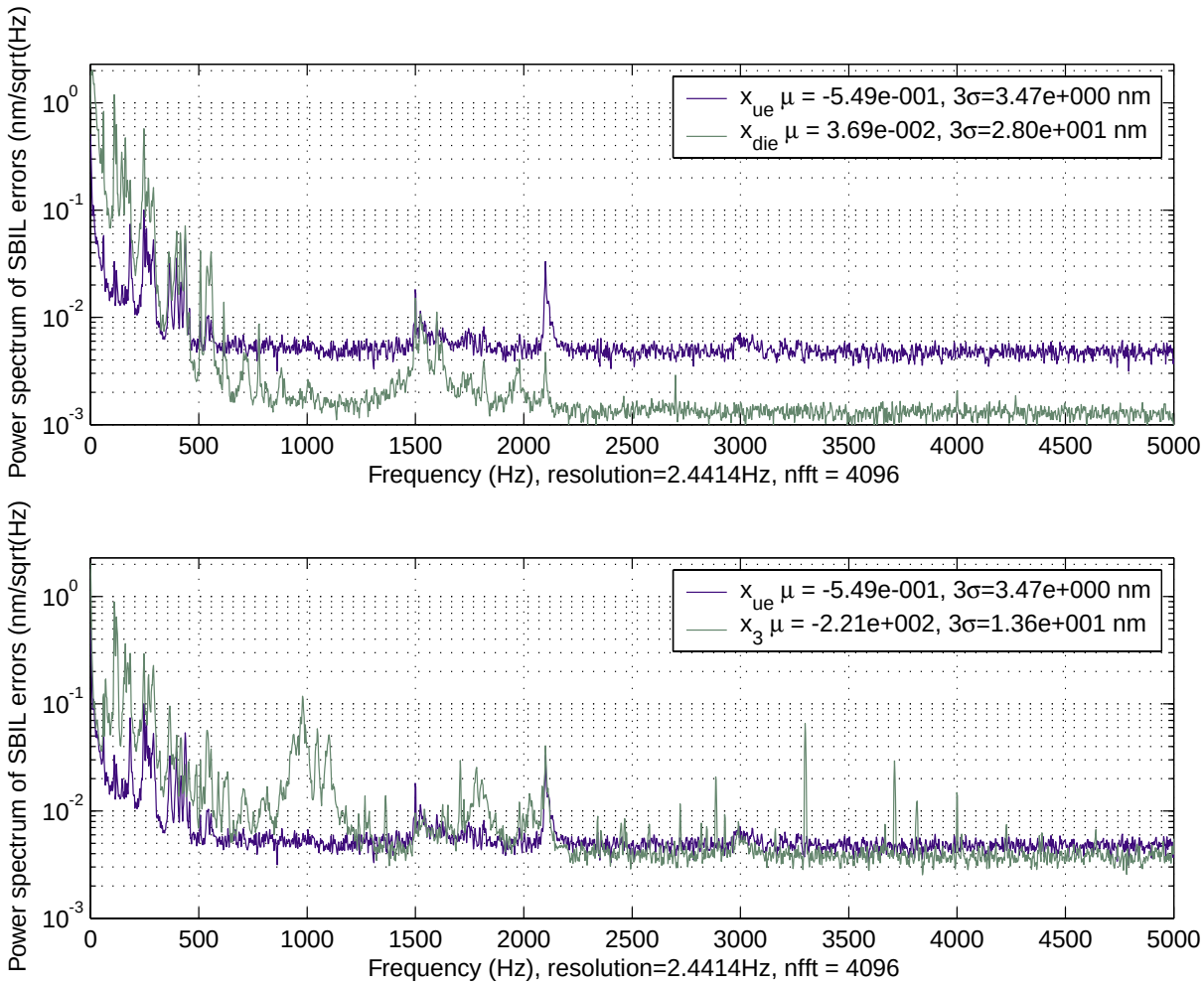

Figure 8-24: Plots comparing the components of the fringe locking error to x_{ue}. from 0 to 5000 Hz. This data is taken with the fringe locking control off.

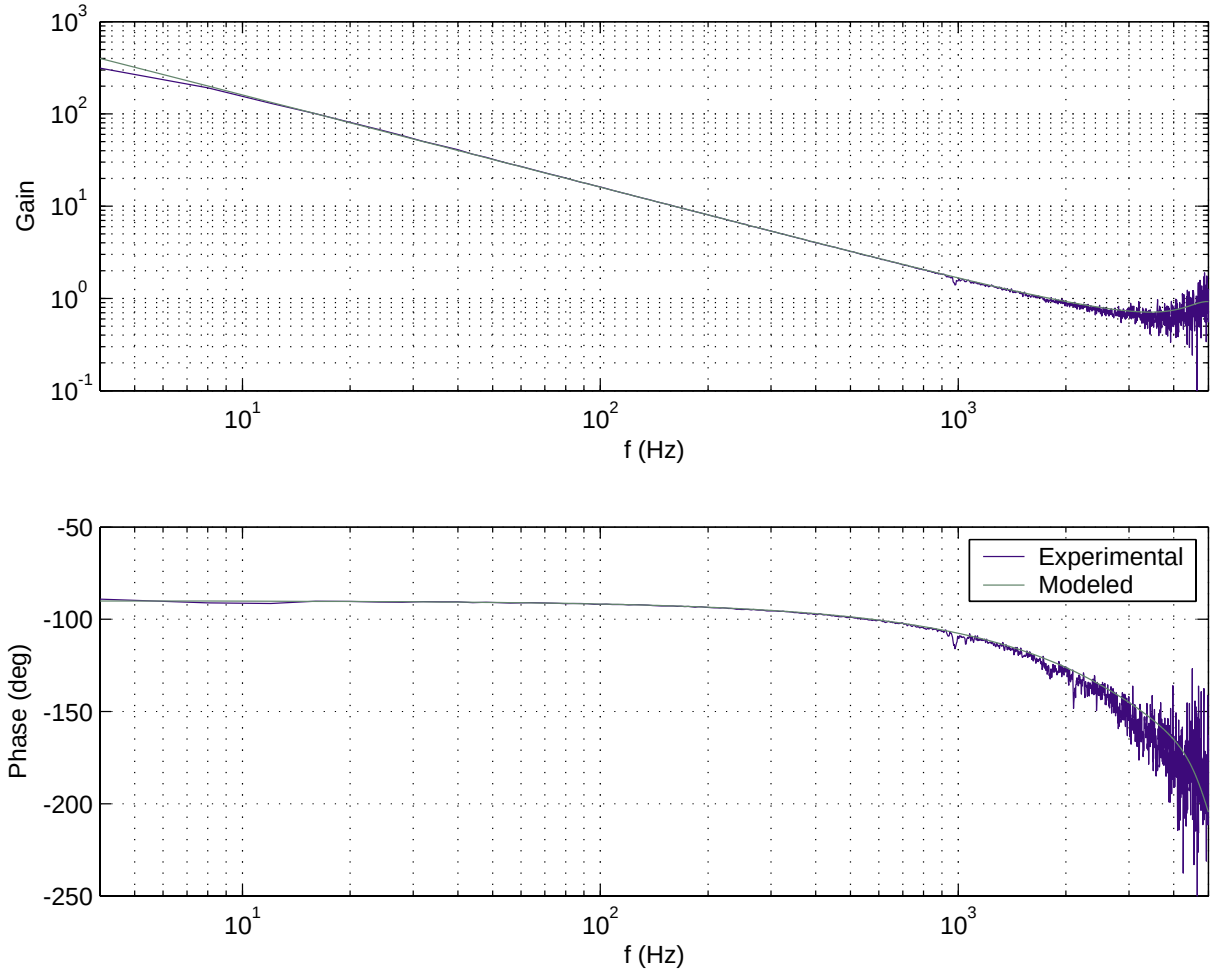

Figure 8-25: Experimental and modeled loop transmissions. The disturbance injection for the experimental data was filtered white noise. The system uses a lead controller and the 15 KHz Zygo digital filter.

8.2 Vibrations

In this section, the vibration errors are derived. The experimentally derived vibration sensitivity is applied to measured vibration levels for the estimation of the very small low frequency vibration errors.

The analysis of vibrations for lithography is greatly simplified if the substrate and metrology frames can be assumed to have resonant frequencies much greater the v/d. To first order the coupling of the optics to the metrology frames can be described by some resonant frequency [60, 109]. I assume the optics are attached to the metrology frame by a spring and dashpot according to Figure 8-26. The transfer function for

this system is given by

$$\frac{X_2(s)}{X_1(s)} = -\frac{s^2}{s^2 + 2\zeta\omega_n s + w_n^2} \tag{8.32}$$

where the natural frequency and damping factor designated ω_n and ζ are

$$\omega_n = \sqrt{\frac{k}{m}}, \quad \text{and} \tag{8.33}$$

$$\zeta = \frac{b}{2\sqrt{km}}. \tag{8.34}$$

For the stage induced payload motions it is more convenient to work with the acceleration of the metrology frame where

$$A_1(s) = s^2 X_1(s). \tag{8.35}$$

Equation 8.32 is now modified to get

$$\frac{X_2(s)}{A_1(s)} = -\frac{1}{s^2 + 2\zeta\omega_n s + \omega_n^2} \tag{8.36}$$

which is simplified for $\omega << \omega_n$ as

$$\left|\frac{X_2(s)}{A_1(s)}\right| \approx \frac{1}{\omega_n^2}. \tag{8.37}$$

The assumption of $\omega << \omega_n$ is valid for considering that the substrate frame, metrology frame, and their optics since they are found to have resonant frequencies much faster than the frequencies of interest (0 Hz to $\approx$ 100 Hz) for printed error.

The stage x error is compared to vibrations measured with geophones[1] on the metrology block and the stage in Figure 8-27. The correspondence of the x error to the metrology block measurement is very good for most of the data. There is some lack of correspondence at around 400 Hz that may be due to the placement sensitivity

[1]Model HS-1 available from Geo Space Corporation, Houston, TX.

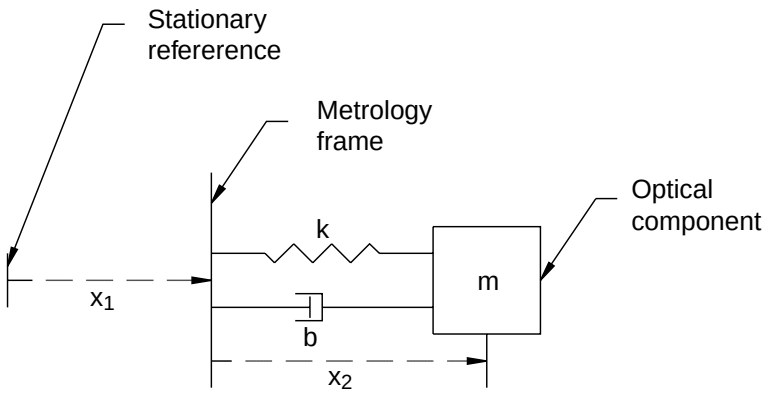

Figure 8-26: Model of optical component-to-metrology frame resonant structure

of the geophone on the metrology block in the presence of rotational motions. Since the characteristic vibrations between about 350 Hz and 450 Hz are in both the x_3 data and the x_{die} data as seen in Figure 8-23, it is safe to assume the metrology block is translating here. Most importantly, the data shows that the stage vibrations are much lower than the metrology block vibrations. Thus most of the stage x error at high frequency is due to the metrology block vibrations.

Comparison of the x_{ue} data and the stage error leads to the estimate of the effective resonant frequency of the metrology frame. This estimate is important since it is used to estimate the vibration error contribution of the metrology frame between 0 and 100 Hz. Figure 8-28 contains the stage acceleration error power spectrum computed from the position error data and x_{ue} power spectrum. The data was taken simultaneously. The units for the stage acceleration are mg/rtHz and the units for x_{ue} are nm/rtHz. Most of the resonant peaks are very well matched. The vibration sensitivity is estimated to be 1 nm per mg, which corresponds to an effective natural frequency of 500 Hz. Since the metrology block and column mirror was conservatively estimated to have better than 1000 Hz resonant frequency, the optical mounts on the metrology block are largely responsible for the worse performance. The optical mounts can be improved. The shape of the vibration modes is also a factor where each of the many components on the metrology block contributes to the deflection. Furthermore, the calculation is intended to be an estimate of the sensitivity to vibration rather

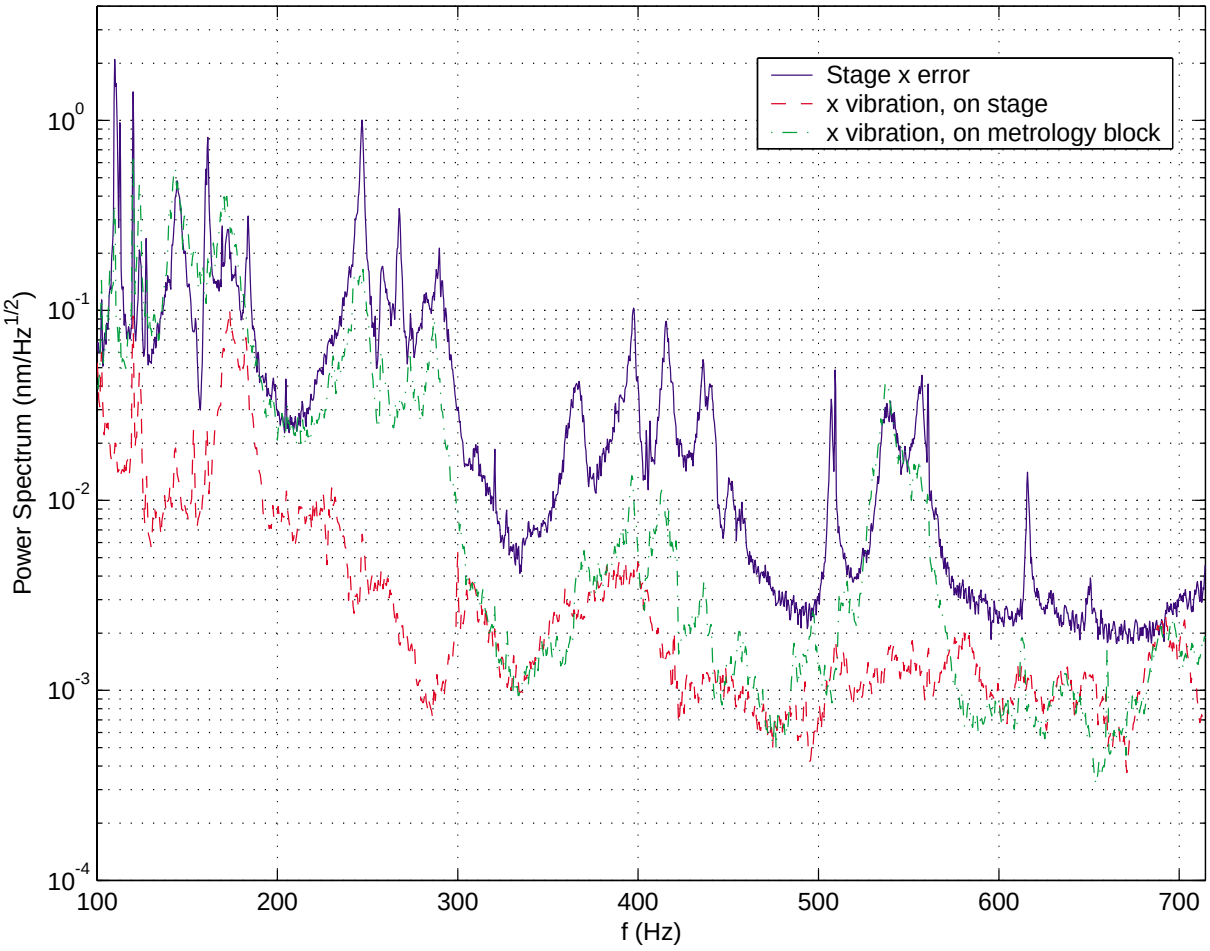

Figure 8-27: Power spectrum of the stage x error and vibrations measured on the stage and on the metrology block.

than a precise calculation of the first eigenvalue of the rather complicated system of components. Most importantly, the x metrology block accelerations appear to capture the vibration errors at high frequency very well. There are small discrepancies, such as at about 184 Hz. The discrepancy is probably due to the nature of the eigenmode, where vibrations in y, z, and/or rotations couple into error motions.

The vibrations measured with geophones on the granite and on the metrology block are shown in Figure 8-29, Figure 8-30, and Figure 8-31 for x, y, and z vibrations respectively. The top plots range from 1 to 800 Hz. The bottom plots range from 1 to 100 Hz. The units are g/rtHz. The noise floor of the DSA when its inputs are shunted with resistance to match the geophone resistance is also plotted. This a good measure of the sensor and data acquisition noise except for the EMI noise, which mainly occurs

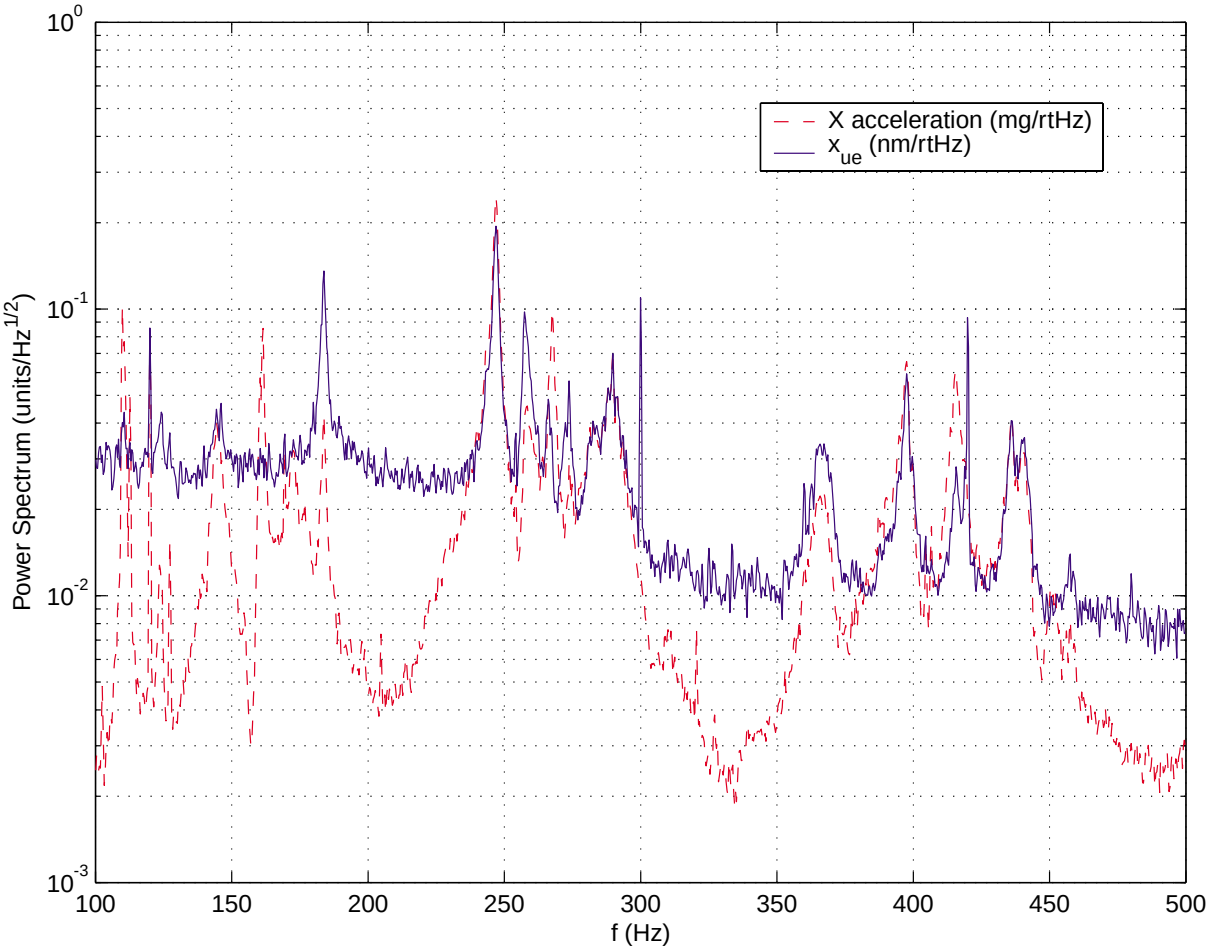

Figure 8-28: Power spectrum of the stage x acceleration error when the amplifier is off (stage freely floating) compared to x_{ue}.

at 60 Hz and its harmonics. The noise floor of the sensor system adequate for most of the data. The metrology block shows more vibrations than the granite at high frequencies because of resonances in the optical bench and its attachment to the granite. The integral of the power spectrum over different frequency bands are shown in the legends. Much more vibration is present from 100 to 800 Hz than below 100 Hz. The vibrations of concern are those between 0 and 100 Hz. If we assume 60 μg, 3σ accelerations of the metrology block over this frequency band and 1 nm/mg sensitivity, the vibration errors of the metrology block are estimated as 0.06 nm 3σ. The vibration power spectrums were adjusted to take into account the frequency response of the geophone. I used the published geophone natural frequency of 4.5 Hz and the damping constant of the geophone calculated from the published internal

damping and the shunt resistance. This technique allows the geophone to be used for measurements somewhat below its resonant frequency. The geophone data can be meaningfully stretched to about 1 Hz before the signal to noise ratio is inadequate.

The vibration levels for the metrology block are very adequate for sub nanometer error budgets. At low frequencies, perhaps up to 40 Hz depending on the tuning, the vibration could be improved further with active vibration isolation. However, the vibrations levels are already too low for the active feedback system to be significant for this application. I stopped development of the closed loop active system when I observed no obvious increase in x_{ue} after shaking the system at much higher than ambient disturbances. The IDE system provided for the disturbance injection. The stage motions induce extra disturbances that would be helped by the active system. However, the feedforward alone provided the necessary disturbance rejection. The feedforward performance is studied in Section 9.3.

The relative pitch vibrations between the metrology block and the x axis interferometer head is another source of unobservable error. Figure 8-32 compares the inertial pitch motions measured on the metrology block and the bench to x_{ue}. The pitch of the metrology block and the bench were measured with geophones vertically oriented and wired in series with opposing poles. The voltage measurements provided by the geophones were converted to differential vertical vibration. This measurement was divided by the separation distance between the geophones to obtain the angular motion. In the figure, I multiplied the angular measurement by h_i, the separation between the interferometer beams of 0.75 inches, to get the relevant Abbe error motion in nanometers. The Abbe error motion is really due to the $differential$ pitch motion of the metrology block and the interferometer head, whereas the data in the Figure is the pitch motion relative to the inertial reference frame. A more direct measurement of the metrology block-to-interferometer head pitch really needs to be measured to make a firm conclusion. But based on the measured pitch motions, the differential motion between the metrology block and the bench, which is less than the sum of the inertial motions because the components can be moving together, does not account as a major source of vibration error. The calculated metrology block pitch error only

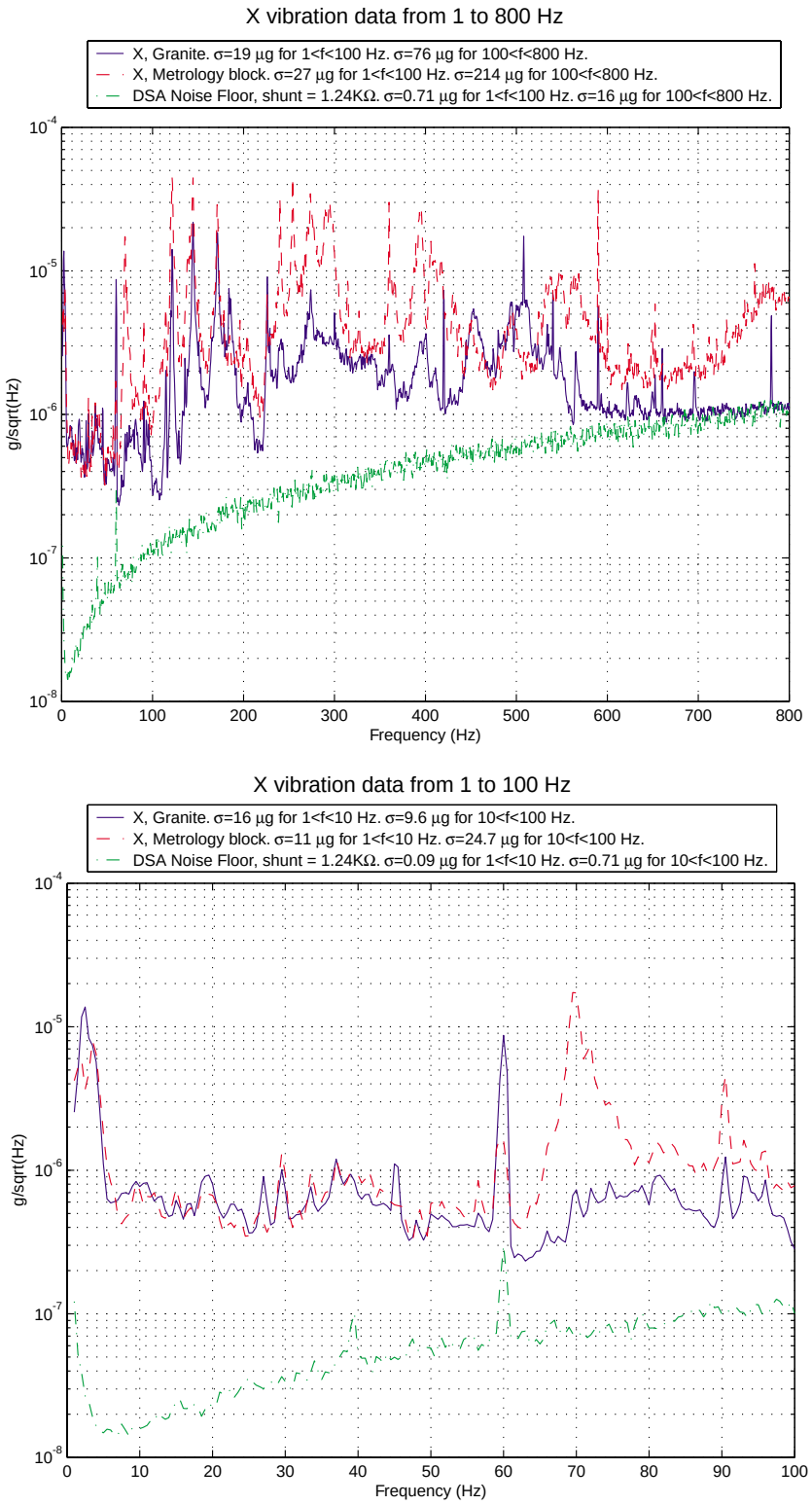

Figure 8-29: Power spectrum of x accelerations measured on the granite and the metrology block. The estimated measurement noise floor is also shown. The top plot ranges from 1 to 800 Hz. The bottom plot ranges from 1 to 100 Hz.

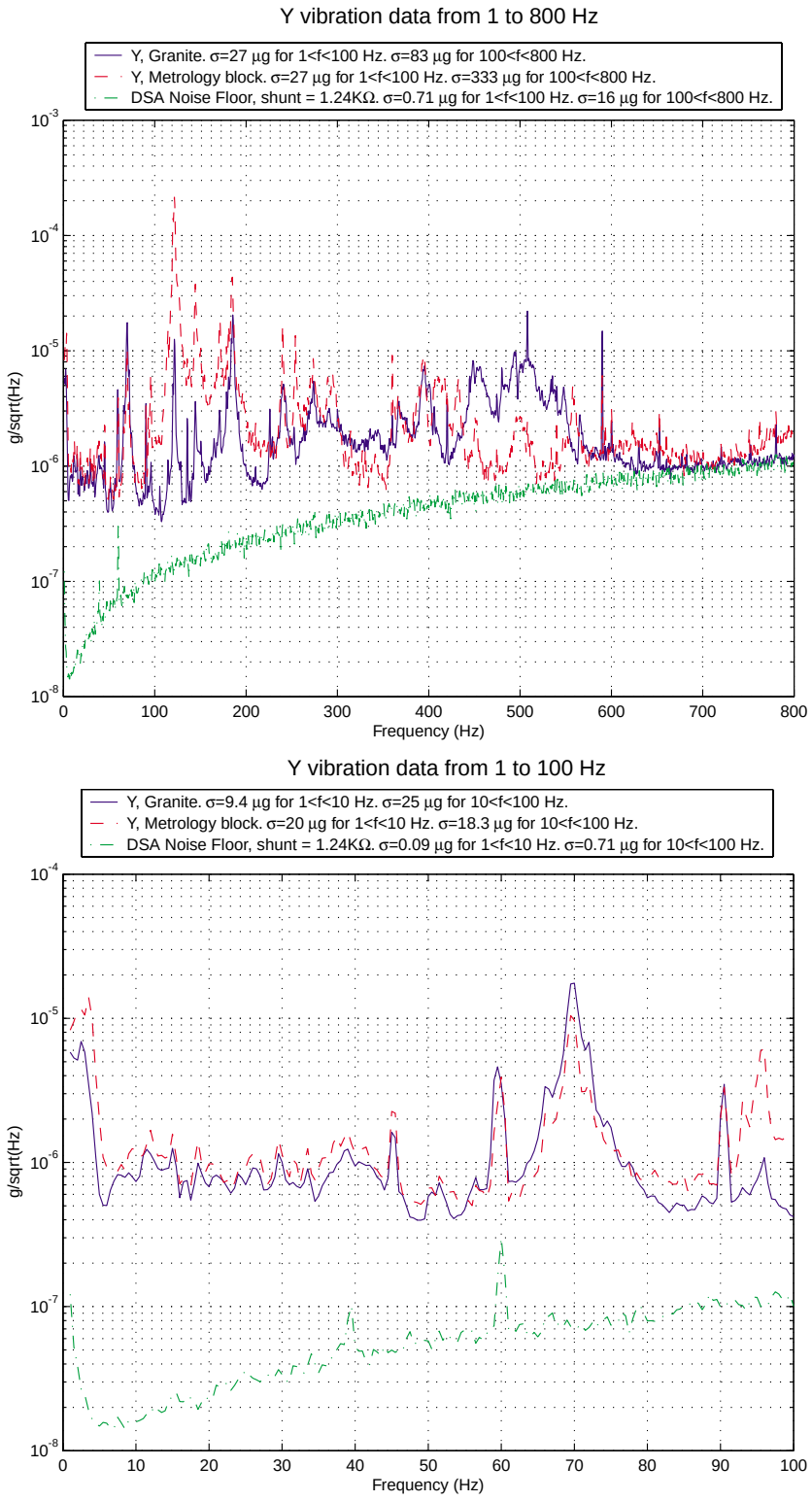

Figure 8-30: Power spectrum of y accelerations measured on the granite and the metrology block. The estimated measurement noise floor is also shown. The top plot ranges from 1 to 800 Hz. The bottom plot ranges from 1 to 100 Hz.

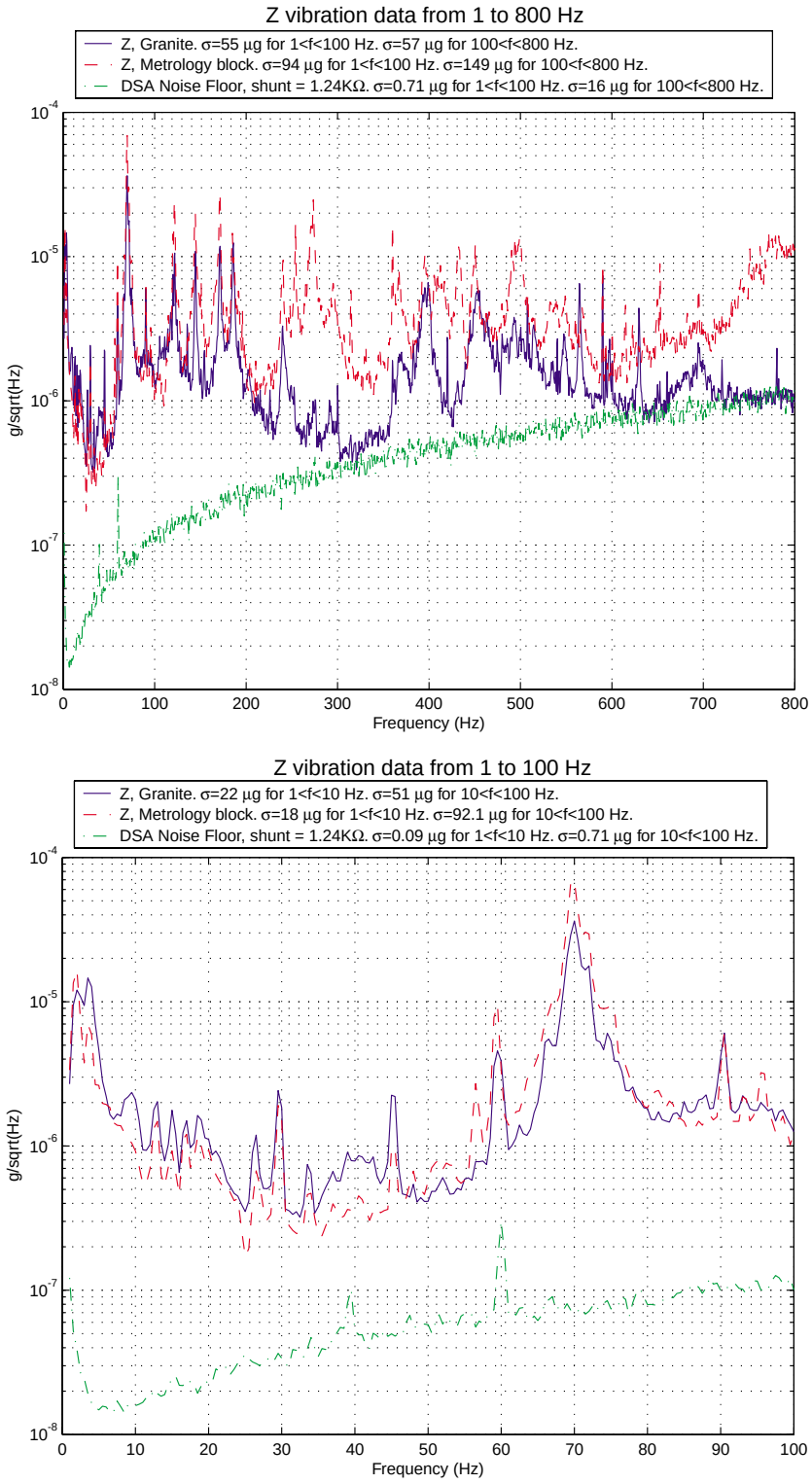

Figure 8-31: Power spectrum of z accelerations measured on the granite and the metrology block. The estimated measurement noise floor is also shown. The top plot ranges from 1 to 800 Hz. The bottom plot ranges from 1 to 100 Hz.

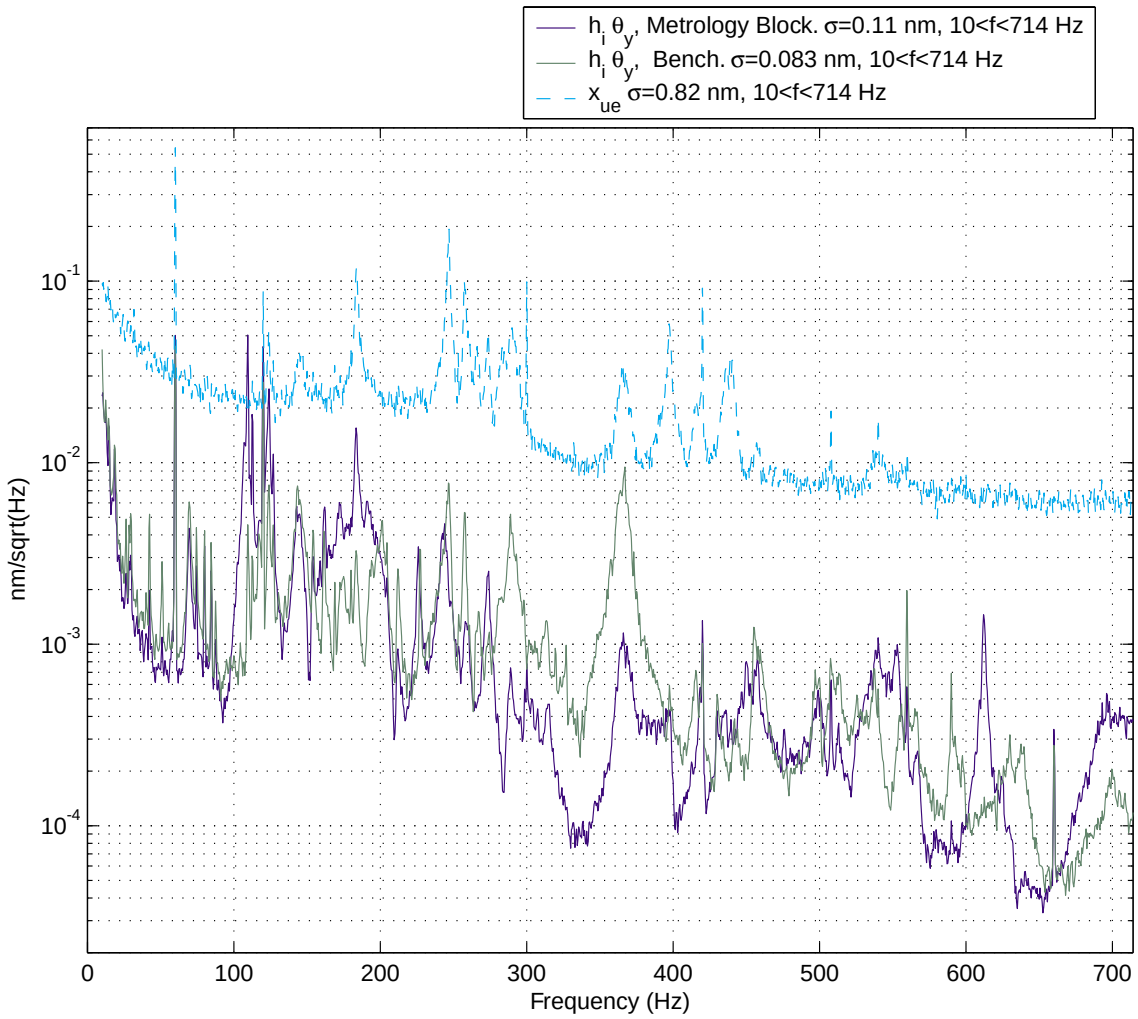

Figure 8-32: Comparison of pitch motions measured on the metrology block and the bench to x_{ue}.

approaches x_{ue} in the 120 Hz range.

The geophones were unsuitable for measuring the x axis interferometer head pitch motions because of there size. The geophone based pitch measurement is not expected to be very accurate either because relatively large vertical vibration signals need to be subtracted. Furthermore, the measurement is sensitive to mismatching of the geophone gains and the positioning. However, this data gives an early indication that the pitch errors are not expected to be large based on the metrology block or bench pitch.

The vibrations of the chuck between the interferometer mirror and the write location are another important vibration consideration. The substrate frame is evaluated

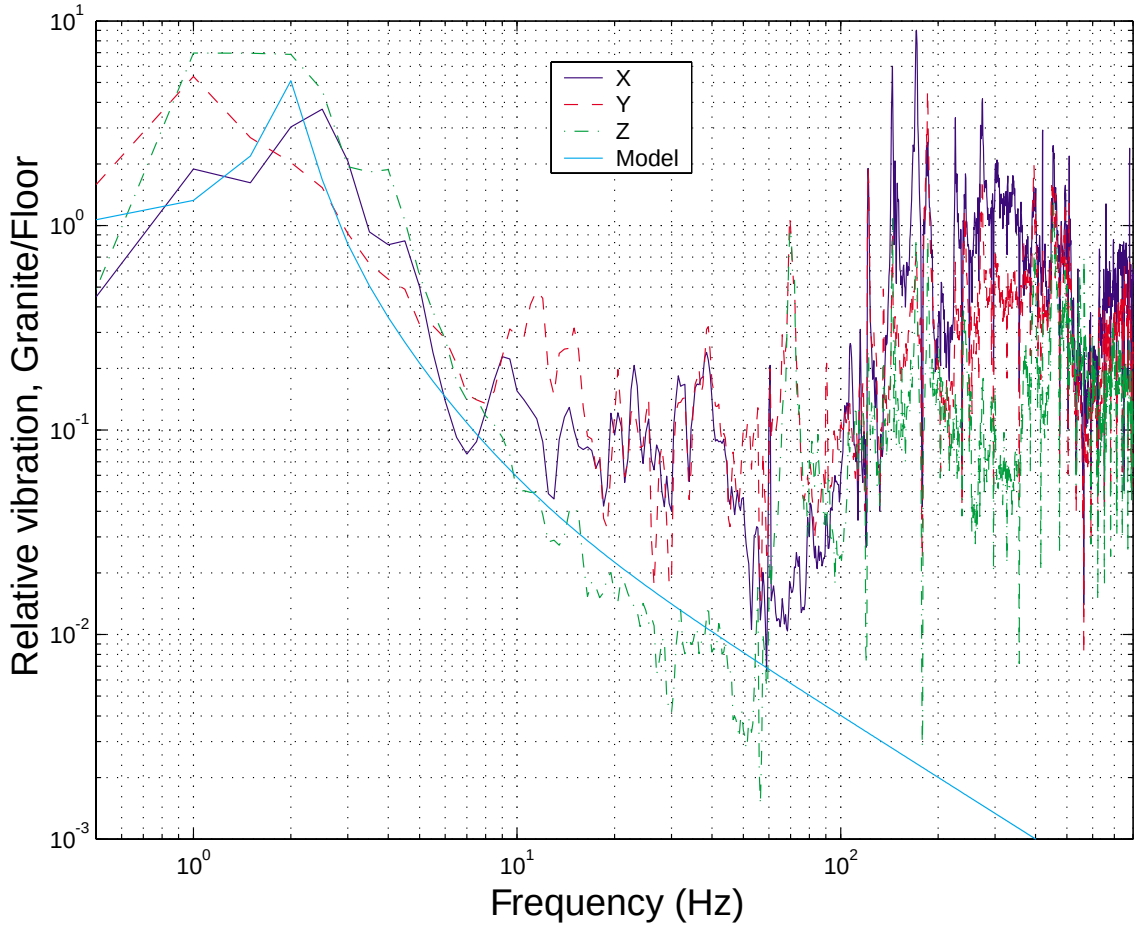

Figure 8-33: Relative vibration levels of the granite versus the floor.

in Section 9.3 and is shown to have an effective resonant frequency of about 2300 Hz for y axis acceleration. The extremely good vibration sensitivity of the chuck is important because the chuck can experience relatively high vibration levels during scanning. The stage performance is evaluated in the next section with further scanning evaluation in Section 9.3.

Figure 8-33 compares the vibration levels on the granite versus those on the floor. The plot is the ratio of the power spectrums of granite-to-floor vibration. At low frequencies, the plot represents the floor-to-payload vibration transmissibility . The modeled transmissibility is given by

$$\frac{X_1(s)}{X_0(s)} = \frac{2\zeta s + \omega_n^2}{s^2 + 2\zeta s + \omega_n^2} \tag{8.38}$$

where X_1 is the payload motion with respect to the inertial reference frame and X_0 is the floor motion with respect to the inertial reference frame. The modeled isolation natural frequency, ω_n, is at 2 Hz with the damping factor ζ of 0.1. The damping on the IDE isolators is provided primarily by eddie current damping of the motors. The motor coils are laminated with a weakly magnetic steel to increase the damping. The system does not contain pneumatic based damping. The model shows good correspondence with the z vibrations up to about 50 Hz and good correspondence with x and y vibrations up to about 10 Hz. At frequencies greater than about 50 Hz for z and 10 Hz for x and y, the acoustically induced vibrations exceed the floor vibrations that are transmitted through the vibration isolation system. Since the measured z floor vibrations are higher than the x and y floor motions, the z relative vibrations do not become dominated by acoustics until a higher frequency. Acoustics is the subject of the next section.

8.3 Acoustics and the effect of shutting down the air handlers

Above about 10-50 Hz the measured vibrations on the payload and stage are largely from acoustic disturbance. Figure 8-34 shows the ratio of power spectrums for vibration with the air handler on/off. The x direction metrology block and x direction stage vibrations are shown to depend on acoustic pressure. The stage control was off during the measurements. Up to about 200 Hz, the vibrations for the stage are essentially proportional to the sound pressure level. Between about 65 Hz and 200 Hz, the metrology block vibrations are proportional to the sound pressure level. The wavelength of sound at 200 Hz is 1.7 m, which is on the order of the dimensions of the isolated system. The effect of the sound below 200 Hz is mainly to shake the system uniformly. When the wavelength of sound is much greater than the dimensions of the object, the object can be assumed to have little influence on the shape of the sound field. Beyond about 200 Hz, the sound and vibration interactions get more

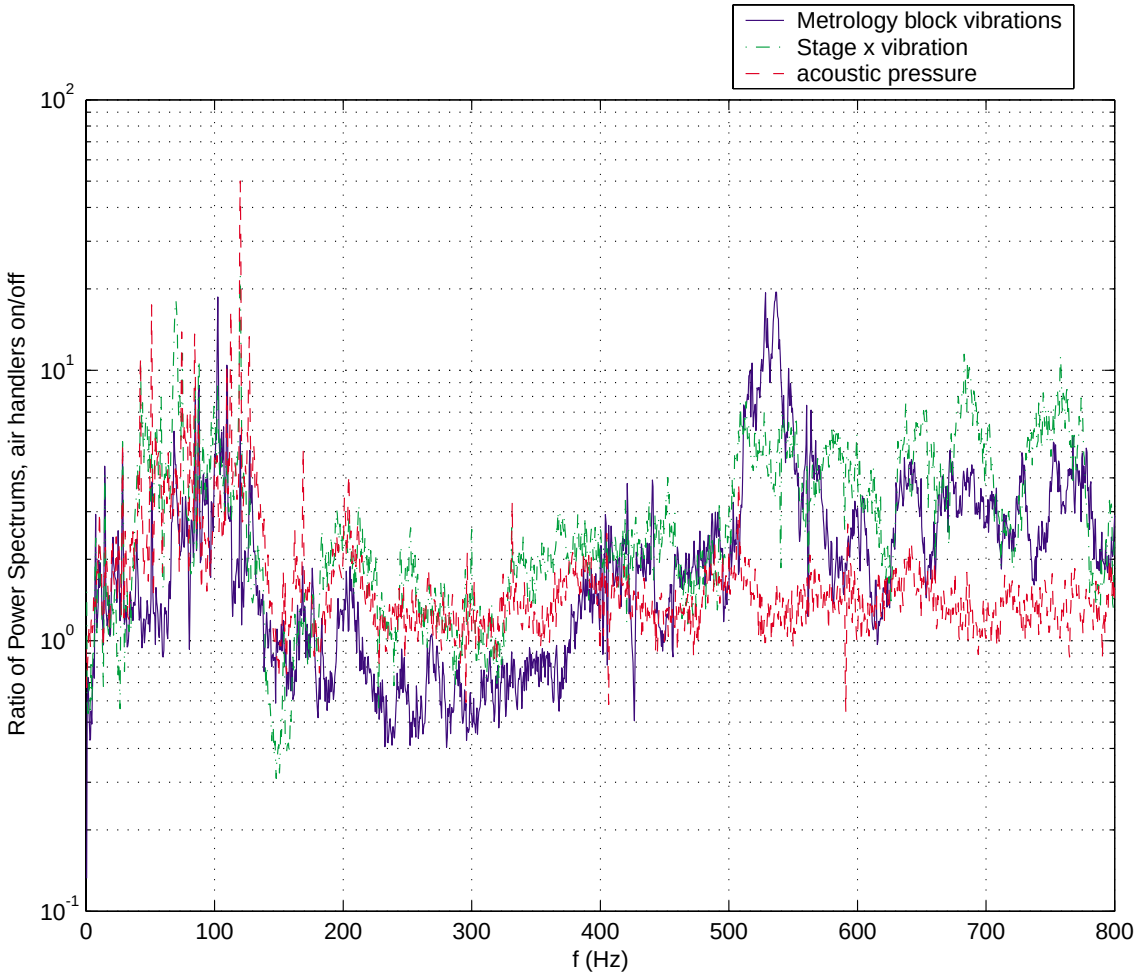

Figure 8-34: Ratio of power spectrums of vibrations and acoustic pressures with the air handlers on/off. The x direction metrology block and x direction stage vibrations are shown to depend on acoustic pressure.

complex because of diffraction and acoustic resonances. The sound measurement will also depend on the positioning of the microphone. The apparently large increase in vibration compared to pressure after 500 Hz is probably to due acoustic resonances in the space between the optical bench and the granite. The stage was also located in this space. Additionally, the increase in pressure due to the air handlers has an unusual boundary condition compared to the ambient sound, which is transmitted through the enclosure. The sound emitted by each air handler is radiated through the 12" diameter duct feeding into the ULPA filter and for the frequencies of interest, will diffract from this duct. Similarly, the sound due to the air handler is expected to have different sound field distribution than the ambient sound.

Figure 8-35 shows sound pressure level (SPL) [57] measurements. The cleanroom average is the average of several data sets taken in the cleanroom before the enclosure was installed. The locations were within the footprint of where the enclosure is now standing. The cleanroom is a very noisy environment. The "noise floor", dummy mic data set is the noise floor of the acoustic measurement system. The dummy mic has an impedance close to the actual microphone and this data verifies that the microphone electronics and data acquisition system have a very small noise level compared to the acoustics. The SPL inside the enclosure with and without the air handlers running is also shown. The enclosure provides some attenuation of noise from the surrounding cleanroom. Meanwhile, the air handling equipment contributes significant noise. The noise of most concern is in the 31 Hz and the 63 Hz octave band centers. Below the 31 Hz octave band, the vibrations are dominated by transmission through the isolators. Above the 63 Hz octave band, the vibration errors don't print or are filtered out.

Figure 8-36 shows the power spectral density of sound pressure inside the SBIL enclosure with and without the air handlers running. The air handlers contribute additional noise especially between the lowest frequency measured of 10 Hz up to 150 Hz. Also of note is the sound pressure level of 0.29 Pa 1σ between 10 and 800 Hz accounts for the noise level of the differential pressure measurement shown in Figure 5-21. The frequency response of the differential pressure sensor used in that data is not specified.

A high density thick base provides insensitivity to sound pressure induced vibrations. The base accelerations due to sound pressure can be estimated by

$$\frac{A(s)}{P(s)} = \frac{1}{\rho h} D(s) Q(s) \tag{8.39}$$

Here A and P are the Laplace transforms for the base accelerations and the acoustic pressure respectively. The density of the base is ρ while h is its thickness. The variable D is the diffraction factor, which in the worst case will be 2 for perfect reflection of the sound field from the base. The variable Q is due to mechanical resonance in the payload ranging from 1 to perhaps 100 in real systems. The diffraction factor is small

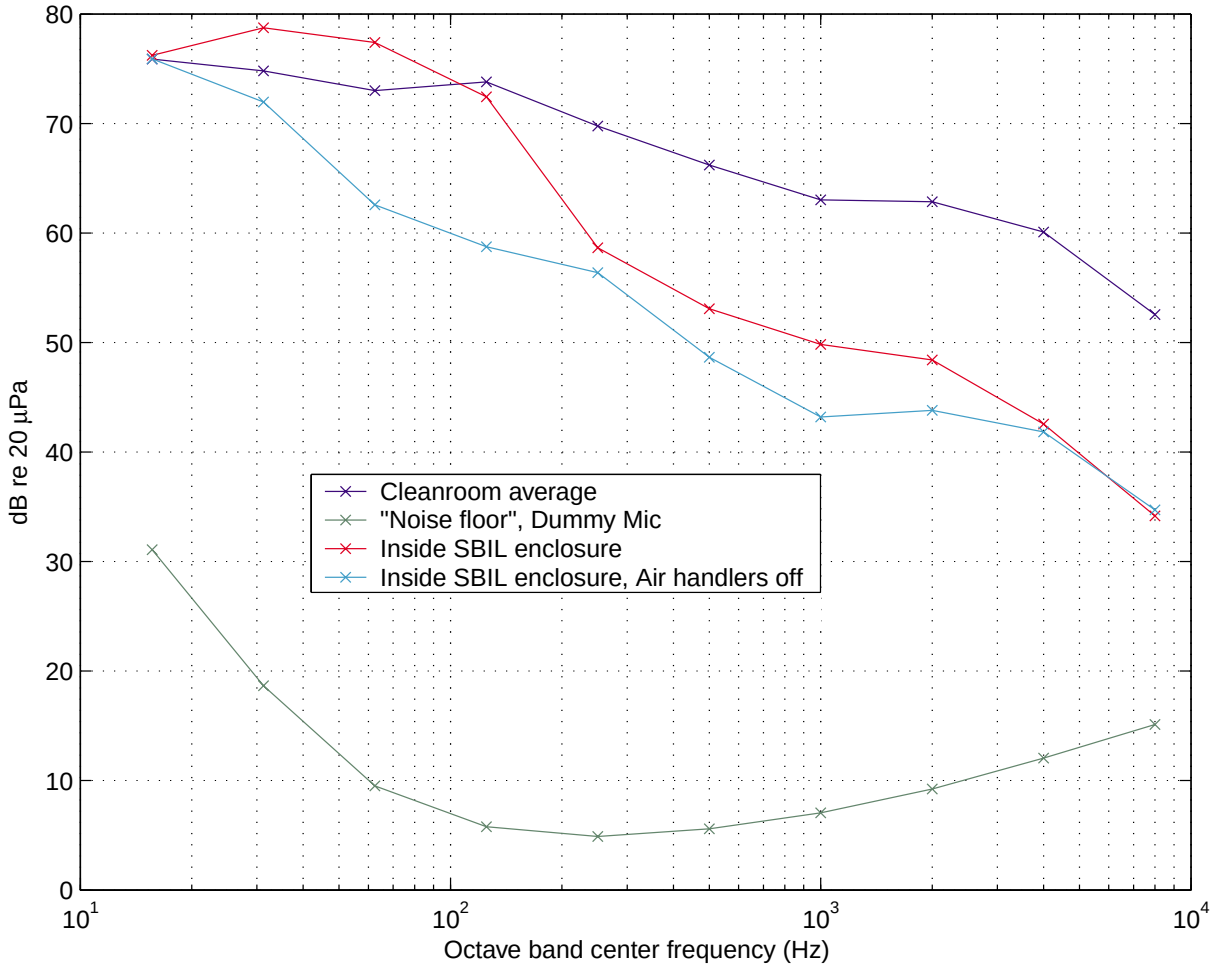

Figure 8-35: Sound pressure level measurements for the cleanroom, inside the SBIL enclosure, and inside the SBIL enclosure with the air handlers off. The noise floor of the acoustic measurement is also shown.

when the wavelength of sound is much longer than the dimensions of the base. For a plane wave crossing a rectangular geometry and the assumption that the base does not distort the sound field, the diffraction factor is

$$D(j\omega) = \exp\left(\frac{j\omega h}{v2}\right) - \exp\left(-\frac{j\omega h}{v2}\right) = 2\sin\frac{\pi h f}{c_s}. \tag{8.40}$$

Here c_s is the speed of sound (340 m/s for air). At frequencies where $f = c_s/(2h)$ the diffraction factor is the maximum of two. Since the granite base is 0.30 m thick, the diffraction factor is expected to be a maximum at about 560 Hz. In practice, uncertainties in D, Q, and transparency of materials make it difficult to predict the

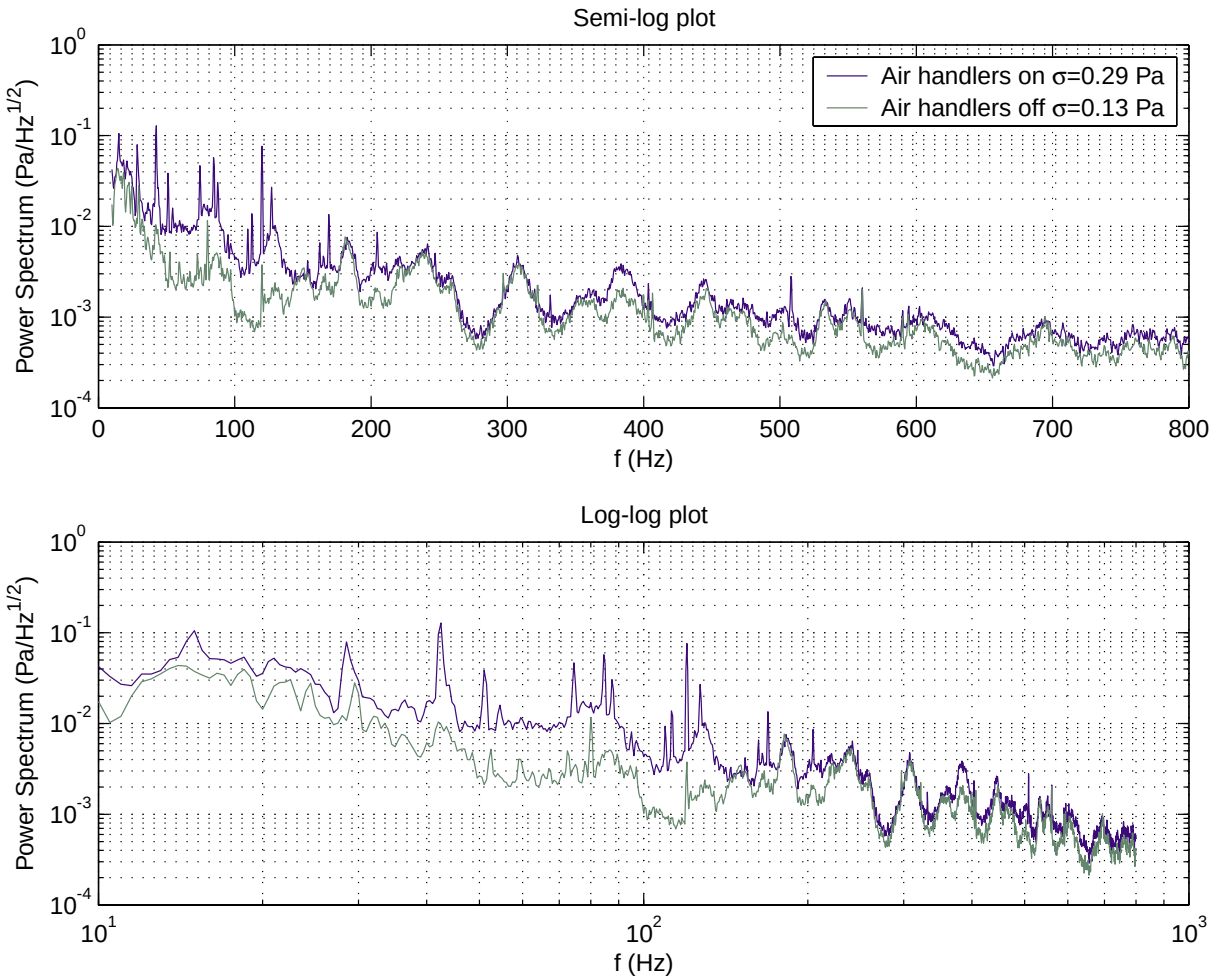

Figure 8-36: High resolution power spectral density of sound pressure inside the SBIL enclosure with and without the air handlers running. The same data is shown on semi-log and log-log plots.

acoustically induced accelerations in advance. However, Equation 8.39 provides some insight into the problem.

Figure 8-37 shows the power spectrum of x_{ue} with the air handlers on and off in the top plot. The bottom plot shows the ratio of the pressures from Figure 8-36 and the ratio of x_{ue}. Since the change in acoustic pressure is small and vibration errors do not dominate over the whole spectrum, the data must be evaluated carefully. Vibrational errors occur at the obvious resonances in the x_{ue} data. However, in between the resonances there is a noise floor not due to vibrations. The data confirms the resonances around 145 Hz and 185 Hz have magnitude linearly proportional to

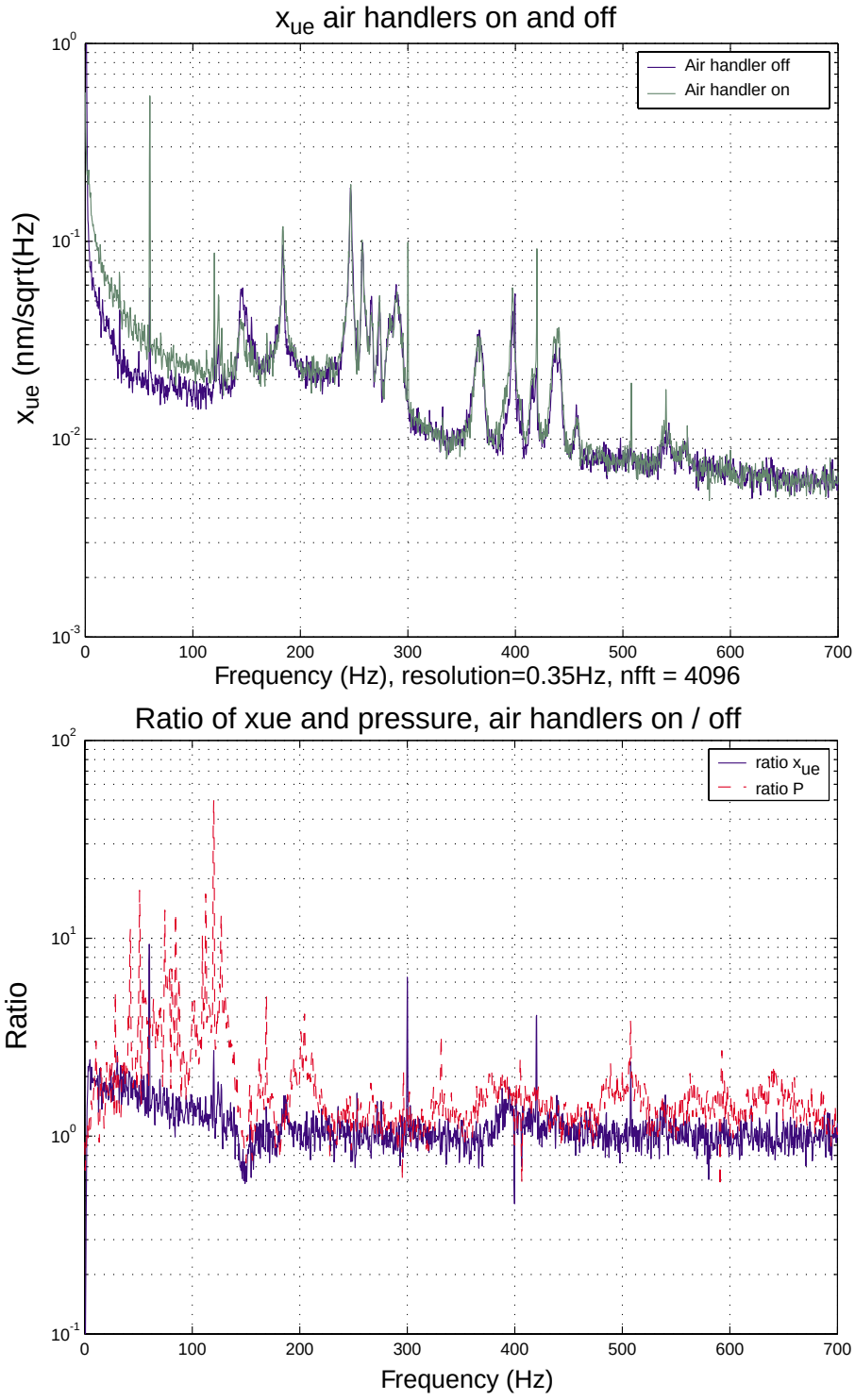

Figure 8-37: The top plot contains the power spectrum of the unobservable error with the air handlers on and off. The bottom plot compares the ratio of the unobservable error and pressure with air handlers on and off.

pressure. The acoustic pressure change in the range of 240 Hz to 300 Hz is too small to evaluate any changes. In the range of 380 to 450 Hz, the resonances are confirmed to be proportional to acoustic pressure. The x_{ue} noise between 100 and 700 Hz with the air handler on and off is 0.59 and 0.57 respectively, thus the air handler acoustics has a small effect.

The data in Figure 8-37 shows an increase in x_{ue} between 2 and 100 Hz with the air handler on. Except for the 60 Hz noise, the additional errors between 2 and 100 Hz with the air handlers on are attributed to index variations caused by parcels of moving air that have varying temperature. The noise between 10 and 59.5 Hz is 0.38 nm 1σ with the air handlers on versus 0.21 nm 1σ with the air handlers off. For this data, the total noise between 0 and 100 Hz is 0.84 nm 1σ with the air handler on. Removing the 60 Hz noise will bring the 1σ down to 0.75 nm for this range. The spikes at 60 Hz, 300 Hz, and 420 Hz for x_{ue} are all larger than the increase in sound pressure. These spikes are likely due to electrical ground loop issues in the SBIL electronics. The noise between 59.5 Hz and 60.5 Hz with the air handlers on is 0.38 nm 1σ compared to 0.04 nm 1σ with the air handlers off.

When the enclosure was first installed, the stage error was dominated by 60 Hz noise and its harmonics. The large contamination was traced to the SCR's[2] in the air handlers, which cause huge surges in currents through electrical heater coils. The 60 Hz stage errors were greatly reduced when only the SCR's were shut down. The air handler is on a totally different breaker than the SBIL electronics, therefore the interference must be radiated. The problem for the stage was resolved after making a direct connection with several 12 gauge wire leads between the stage amplifier and the VME rack ground. Some of the 60 Hz noise in x_{ue} may in fact be vibration but since x_{ue} increases much more at 60 Hz than the acoustic pressure, most of this noise is electrical and can probably be corrected by more direct leads between the VME rack and the remaining electronics. In Section 8.5, I verify the stage amplifier is not the source of the 60 Hz noise by observing no decrease in x_{ue} at this frequency when the amplifier is shut off.

[2]Silicon Controlled Rectifier model Robicon SSRP Series 1-15-P

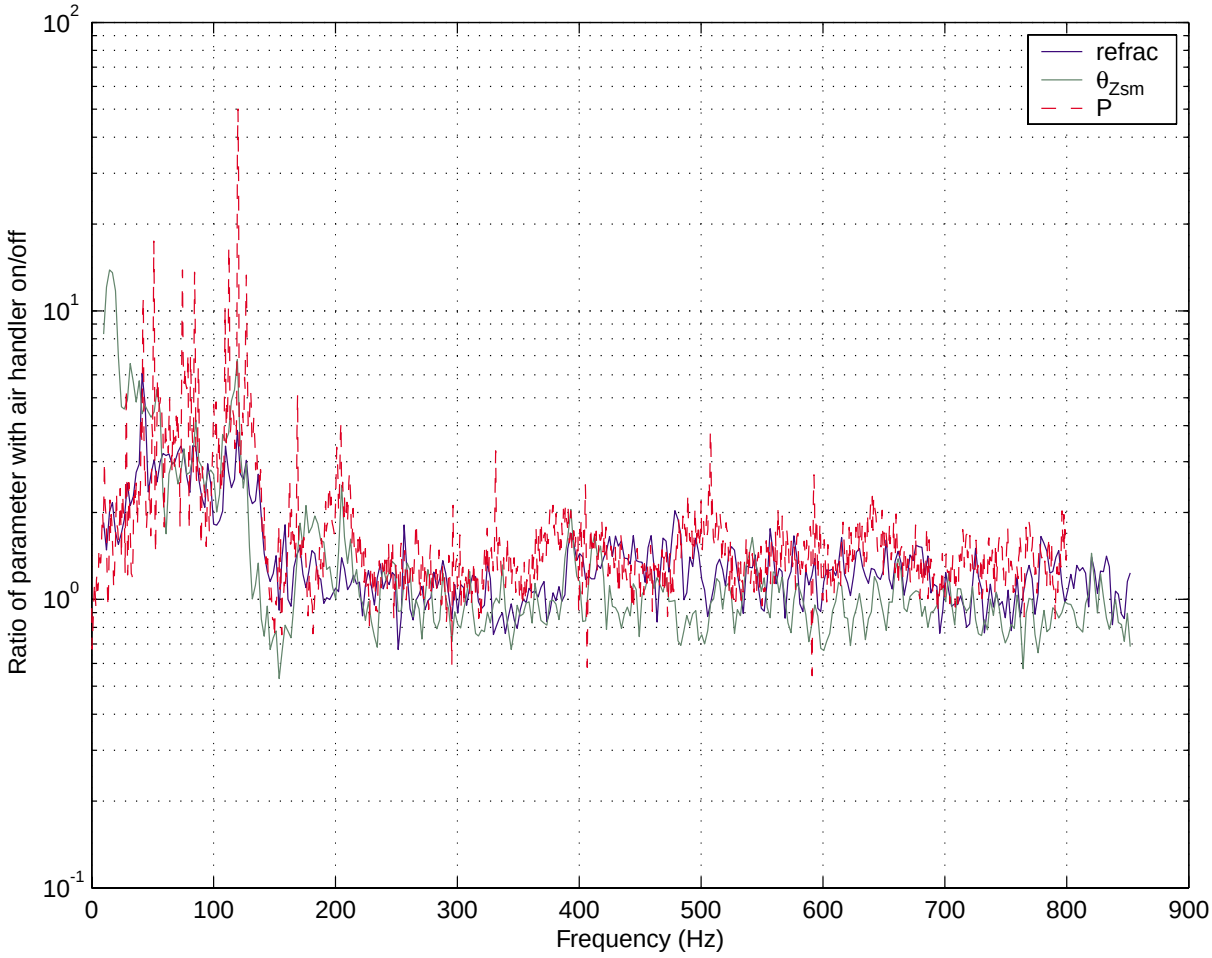

Figure 8-38: Ratio of refractometer, θ_{Zsm}, and pressure with air handlers on and off.

Figure 8-38 shows the ratio of the power spectral densities for the refractometer, θ_{Zsm}, and pressure with the air handler on and off. The measurement θ_{Zsm} is the differential yaw motion between the stage and the metrology block measured by the angle axis of the stage x axis interferometer. Between 10 and 140 Hz there is very good correspondence between acoustic pressure and the refractometer. With the air handler on the 1σ for this frequency range is 0.85 ppb for the refractometer and 0.27 Pa for the pressure. This measured sensitivity of 3.1 ppb/Pa is not far from the expected sensitivity to adiabatic pressure changes of 1.9 ppb/Pa. It is not clear why the measured sensitivity is higher than the theoretical sensitivity, however. The measured sensitivity is closer to the constant temperature pressure sensitivity of 27 ppb/Pa. The larger sensitivity than measured could be attributed to reflection of

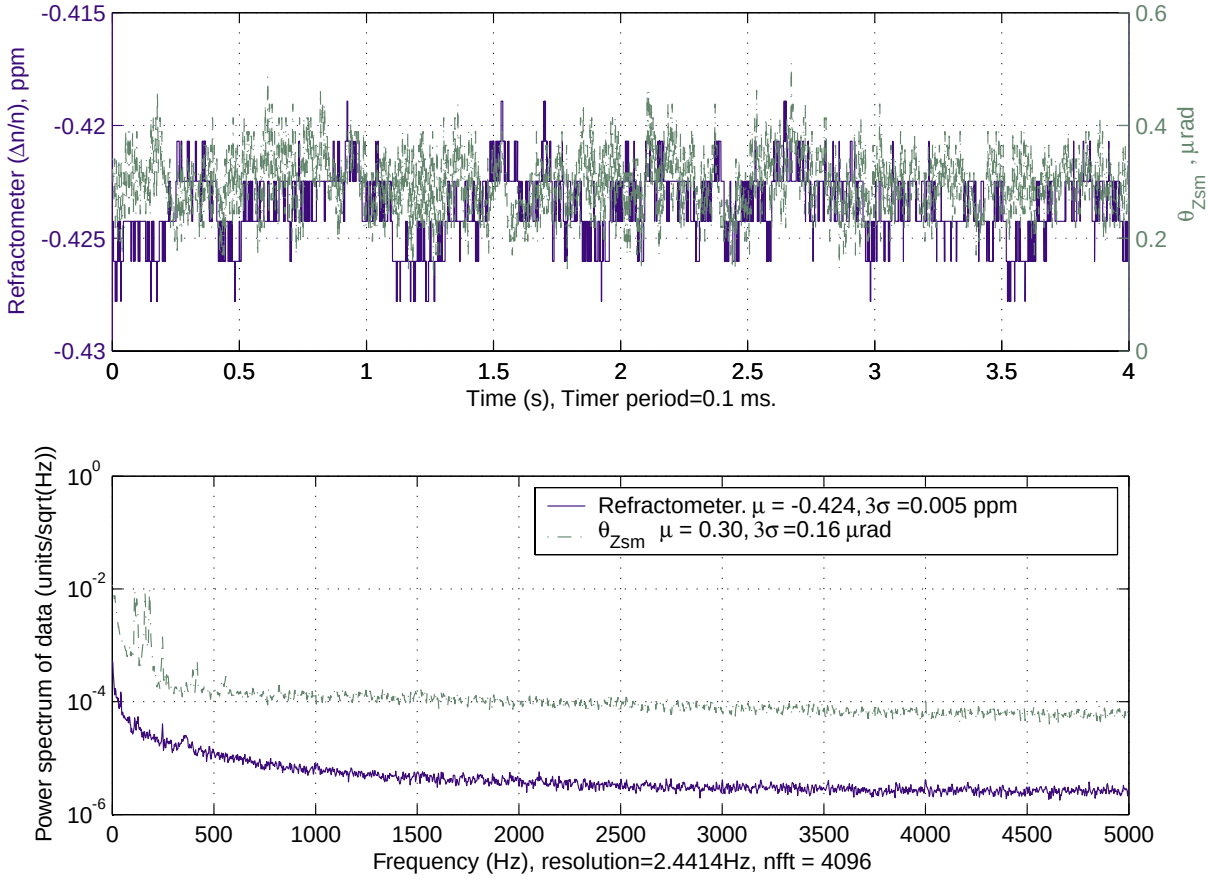

Figure 8-39: Refractometer and θ_{Zsm} data when the air handlers are on.

the sound waves from the face of the metrology block. However, I did not measure significant increases in pressure when the microphone was moved very close to the refractometer beam paths. The figure also shows that θ_{Zsm} has a large increase at low frequency ranges. I suspect this is turbulence related and not real angle variations. The refractometer and angle data used is shown in Figure 8-39 for the air handlers on and in Figure 8-40 for the air handler off. When the air handler is off, the large θ_{Zsm} variation is evident at low frequency. In general, I have observed large sensitivity to air index nonuniformity on the θ_{Zsm} axis. Nonuniformity with spatial period components on the order of 5 centimeters or twice the maximum separation of the beams produces the largest errors for the angle axis interferometer.

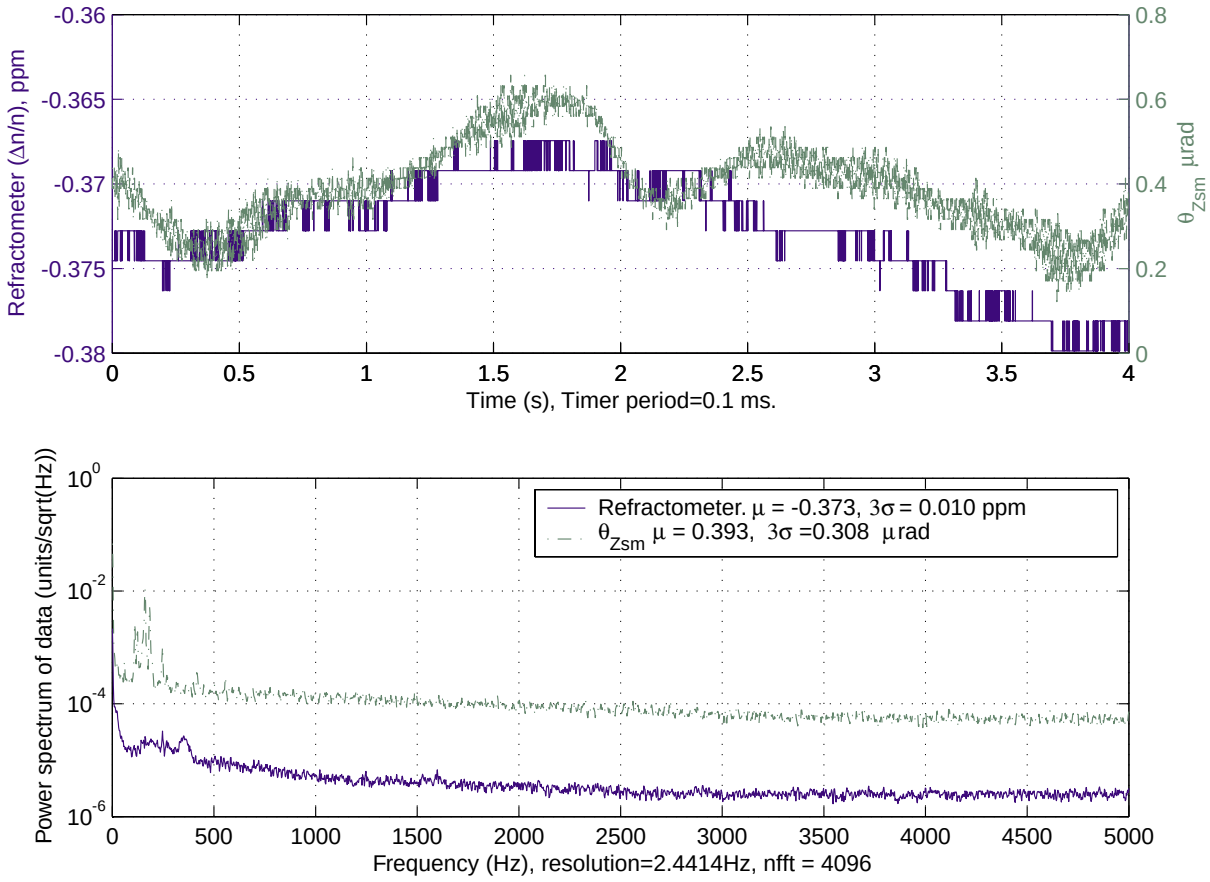

Figure 8-40: Refractometer and θ_{Zsm} data when the air handler is off.

8.4 Stage control

The stage control is based on classical frequency response techniques. The form of the controller is similar to that discussed in my masters thesis [60]. In Chapter 6 of that thesis, I developed the controls for a single degree of freedom scanning stage. The control form is a lead-double lag compensator. The double lag produces a controller with zero steady state error for a ramp input while the lead is necessary for stability. Since the residual stage error can be locked out by the high speed fringe locking control, the stage error is not critical for SBIL. However, poor stage control would be an indication of high disturbances. Furthermore, it is desirable for the control and profiling to not introduce disturbances during constant velocity scanning. Extra disturbance can also lead to unobservable errors due to vibration of the components and the metrology frame. The stage control does differ from my previous efforts in that it also includes feedforward of the stage acceleration. The stage more closely follows the position profile with this addition. The control system also feedforwards an analog signal proportional to the stage acceleration and position to the isolation system. The isolation system is configured with motors to cancel reaction forces caused by accelerations and changes in the position of center of gravity of the stage.

Figure 8-41 shows the frequency responses for the stage x axis. The first data plotted is the experimental frequency response obtained by injecting a white noise disturbance into the system and outputting the loop input and loop outputs to the DAC's. The signals were analyzed by the digital signal analyzer. The experimental plant is used to design the control system. However, the simplest model of the plant is

$$G(s) = \frac{K_G}{s^2 + \frac{b}{m}s}. \tag{8.41}$$

The ratio $\frac{b}{m}$ is the ratio of the dashpot constant to the stage mass, which was determined to be 7.9 rad/s from a force step. The gain K_G is an experimentally determined constant. The plotted second order plant uses this model. The second order plant is pretty good in the range of a few Hz to about 100 Hz. At high frequency, the column dynamics and the compliance of the stage cause deviations from the model. At low

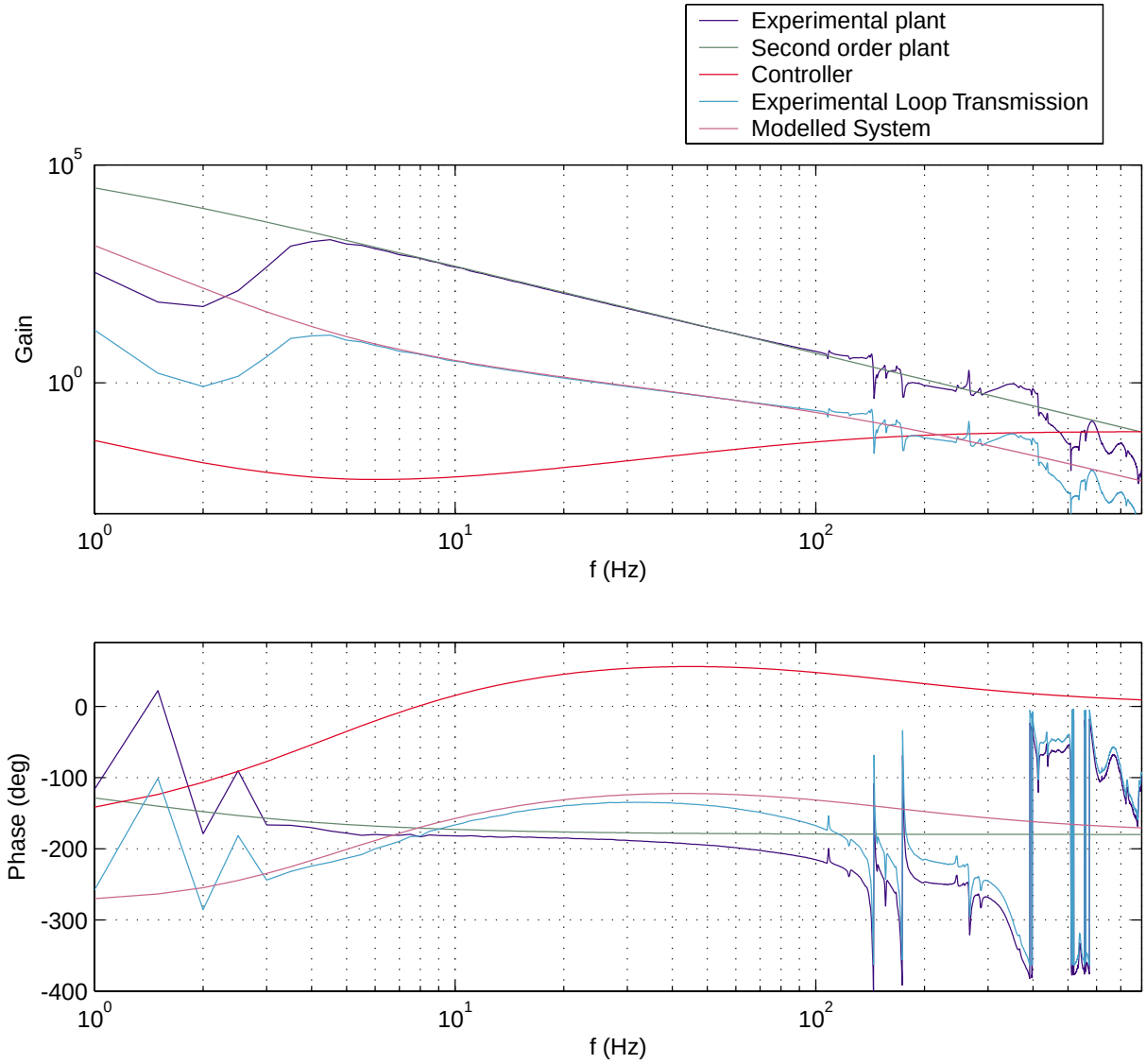

Figure 8-41: Experimental and modeled frequency responses for the stage x axis.

frequency, the disturbance injection was not sufficient to provide clean data. There is also an effect to be discussed further that I believe is due to the magnetic preloading.

The double lag, lead controller has the form

$$H(s) = \frac{K_H(s+z)^3}{s^2(s+p)} \tag{8.42}$$

The locations of the pole and zeros are determined from the design equations

$$w_c = \sqrt{p\,z} \tag{8.43}$$

and

$$p = \gamma z. \tag{8.44}$$

The nominal cross over frequency is w_c and γ is a design parameter chosen to provide sufficient phase margin. The x axis uses $\gamma = 33$ and $w_c = 2\pi \times 25$ rad/s. The system gain was adjusted for cross over at 25 Hz where the loop transmission achieved a phase margin of 45°. The pole is located at 144 Hz and the zeroes are located at 4.4 Hz. The continuous time controller was converted to its discrete time form using Matlab's "c2d" function, zero-order-hold, and a sampling rate of 10 KHz. For bandwidths about 25% faster, the column resonance at around 168 Hz had significant amplification. The bandwidth was conservatively chosen to prevent amplification of disturbances by no more than 6 dB.

On this stage, there is an interesting effect at low frequencies. Figure 8-42 shows the experimental frequency response of the plant at low frequency. The stage actually appears connected to the payload by a spring. The effect has nothing to do with the vibration isolation system, since the response is similar for the case when the granite is down on its hard stops as shown. For small differences in the stage position, the spring constant varies. The magnetic preloading is believed to produce forces on the stage that are dependent on the stage position. The force is also felt when moving the stage around by hand. The spring constant and hence the natural frequency of the system is shown to be dependent and repeatable with the stage position. The effect on the control system design is minimal since these dynamics don't affect the stability of the system. However, the reduced gain at low frequency will decrease the disturbance rejection. Also, this data shows the gain at 10 Hz is fairly independent of position while the force gradient is not. The varying forces on the stage with position disturb the stage during scans.

The frequency responses for the y axis are plotted in Figure 8-43. The ratio $\frac{b}{m}$ was determined to be 3.1 rad/s from a force step. The y axis uses $\gamma = 40$ and $w_c = 2\pi \times 40$ rad/s. The system gain was adjusted for cross over at 40 Hz where the loop transmission achieved a phase margin of 45°. The pole is located at 250 Hz

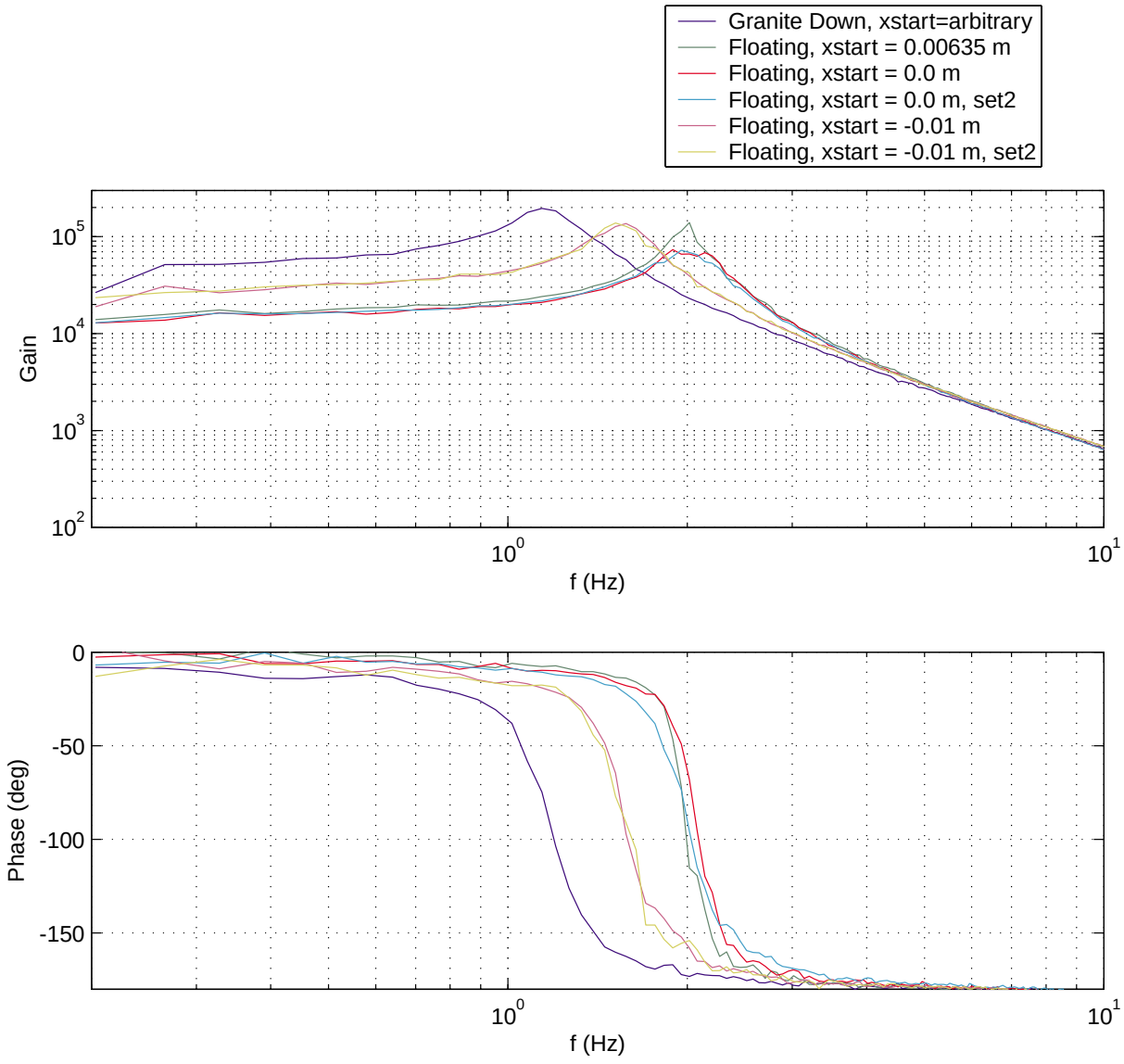

Figure 8-42: Experimental frequency responses of the x axis plant at low frequency.

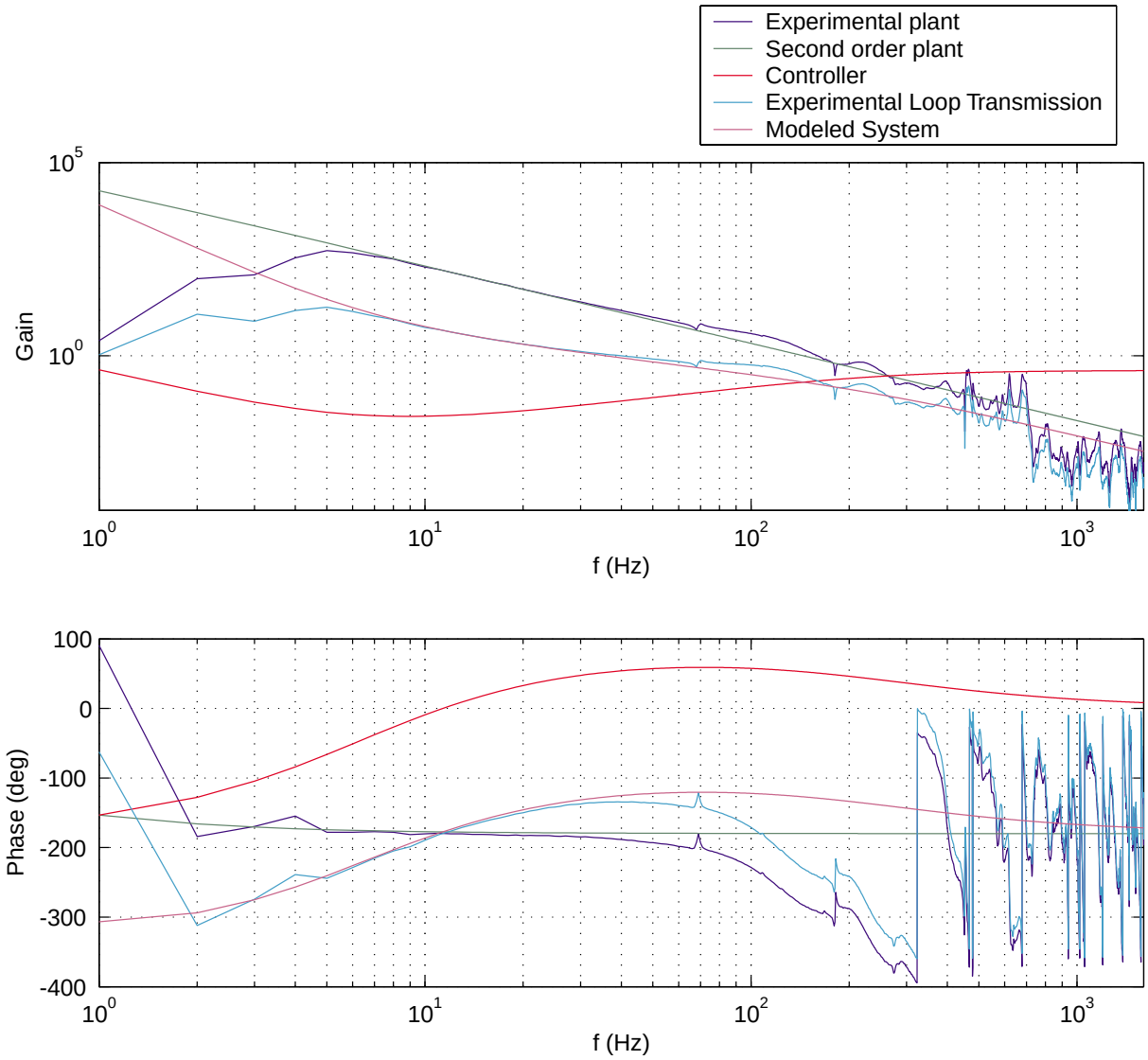

Figure 8-43: Experimental and modeled frequency responses for the stage y axis.

and the zeroes are located at 2.5 Hz. For bandwidths of 50 Hz on the y axis, the x axis would start resonating at 168 Hz. Thus, the coupling between the x and y axis control limits the control performance. In particular, the resonance at 168 Hz, limits both axes.

A plot of the x and y axis stage error when the stage is stationary is in Figure 8-44. The x axis 3σ error is 28 nm while the y axis 3σ error is 11 nm. The power spectrum of the error is plotted in Figure 8-45. The x axis error is worse than the y axis for at least two reasons. Since the x axis has a lower bandwidth controller,

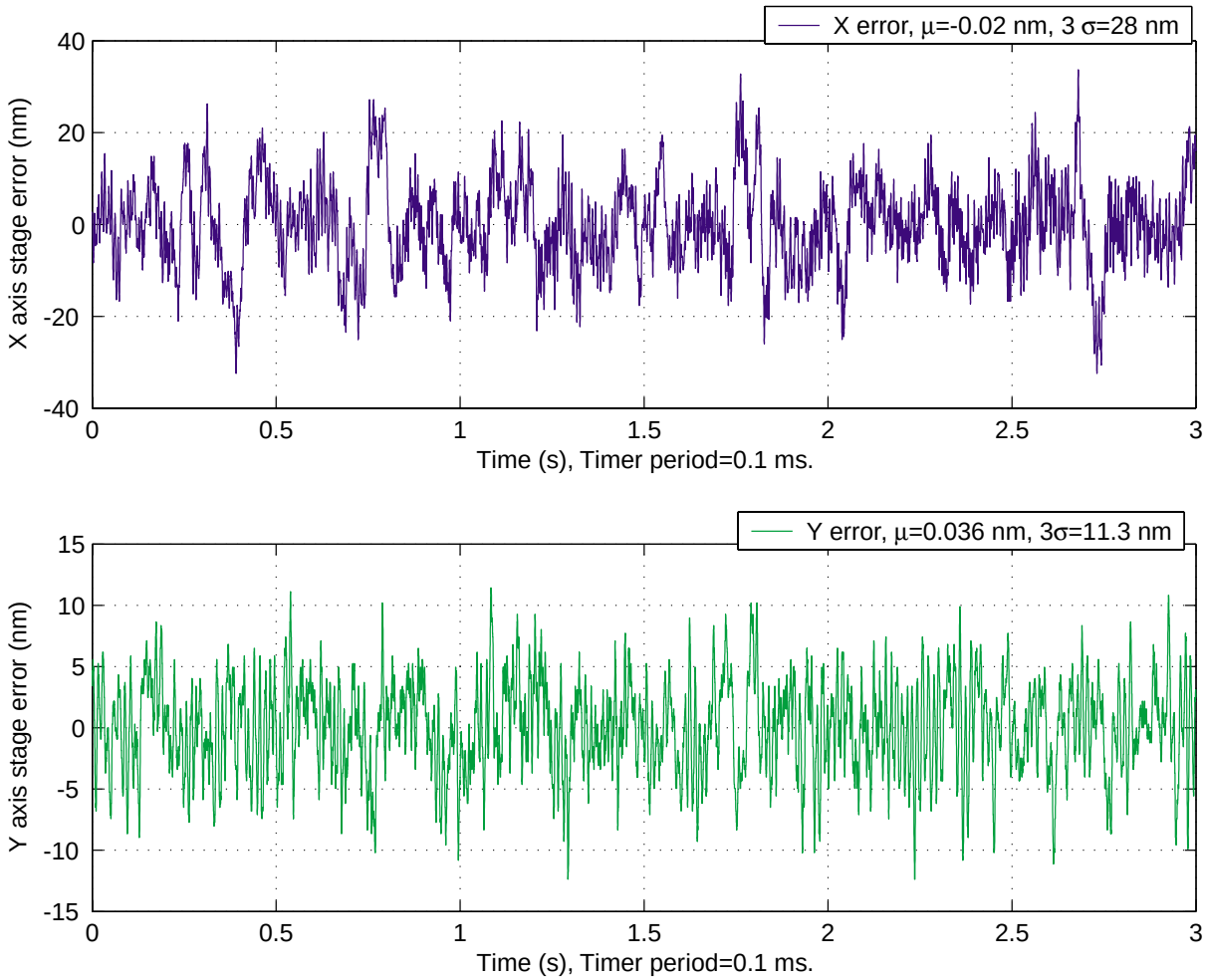

Figure 8-44: Position error plots for the stage when it is nominally stationary.

the disturbance rejection at low frequencies is worse as seen in the power spectrum. Secondly, the x axis interferometer is column referenced while the y axis is not. The relatively large optical bench structure has more vibration than the relatively rigid tower supporting the y axis interferometer head. The high frequency x axis error is largely the column mirror vibrating and not the stage moving.

Although the stage uses air bearings, which are very smooth, the stage does experience forces that depend on the stage position. Motor ripple force, amplifier commutation issues, and external forces associated with the magnetic preload and perhaps the cabling cause stage errors during scanning. The stage system can scan at speeds of 300 mm/s and accelerate at 0.3 g's. Typical velocities and accelerations for writing were 50 mm/s and 0.05 g however. In this thesis, the scanning performance

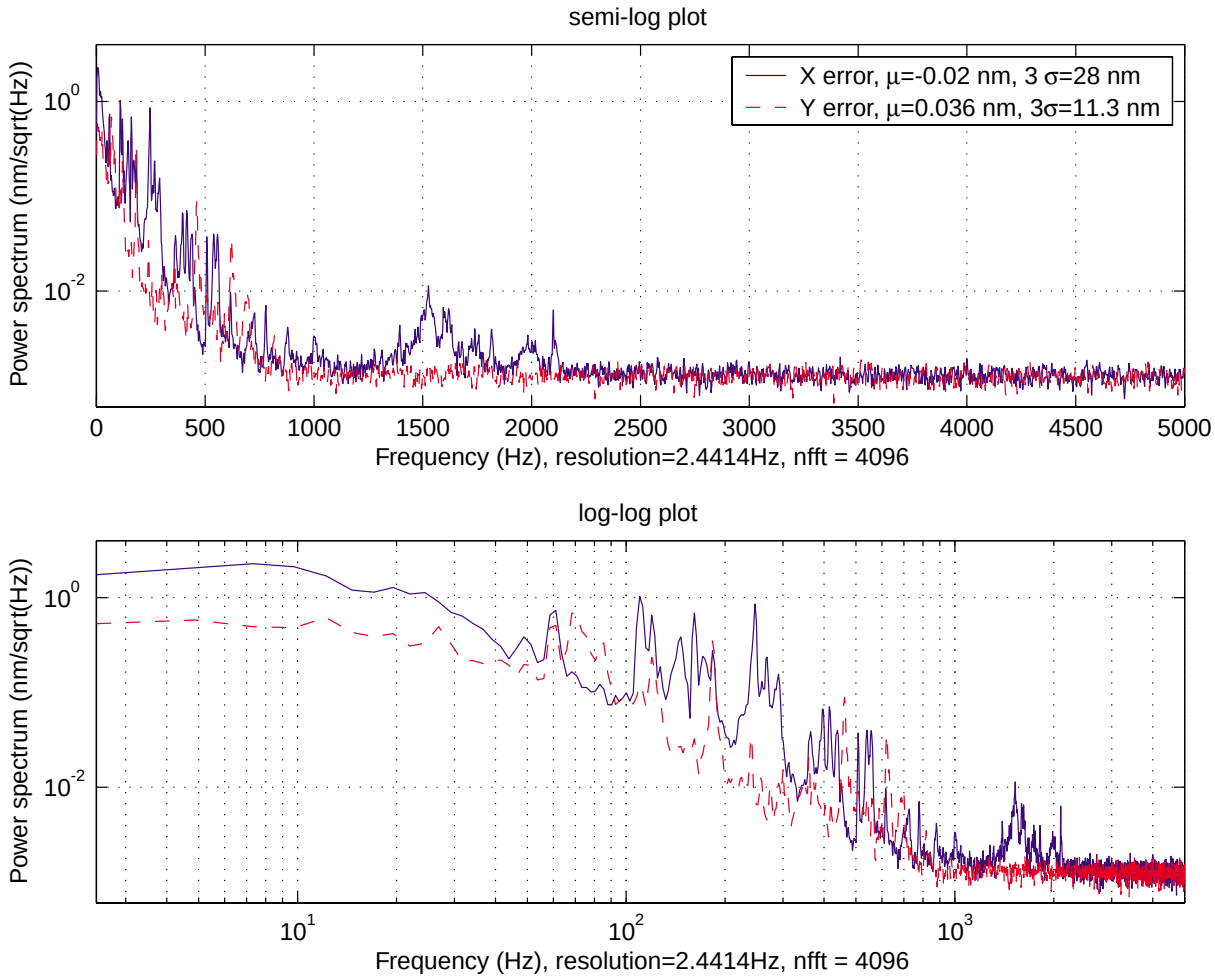

Figure 8-45: Power spectrum of the stage errors on semi-log and log-log plots. The data to calculate the power spectrums is from Figure 8-44.

is mainly evaluated at 100 mm/s, a speed even faster than that used to write.

Figure 8-46 shows the y axis error during the constant velocity portion of a 0.1 m/s scan. There is clearly a periodic error consisting of three strong frequency components indicated in the FFT in the lower plot. The harmonic at the 3.3 Hz corresponds to the first harmonic of the motor spatial period of 3 cm. The second and fourth harmonics at 6.6 Hz and 13 Hz contribute significant errors too. The y axis scanning, though seemingly bad, is still sufficiently smooth. The x axis scanning is much worse than the y axis as seen in the x axis error data during a constant velocity 0.1 m/s scan in Figure 8-47. The disturbance at the first harmonic is at least partly due to a bad commutation. Offset currents in the phases would produce the first harmonic

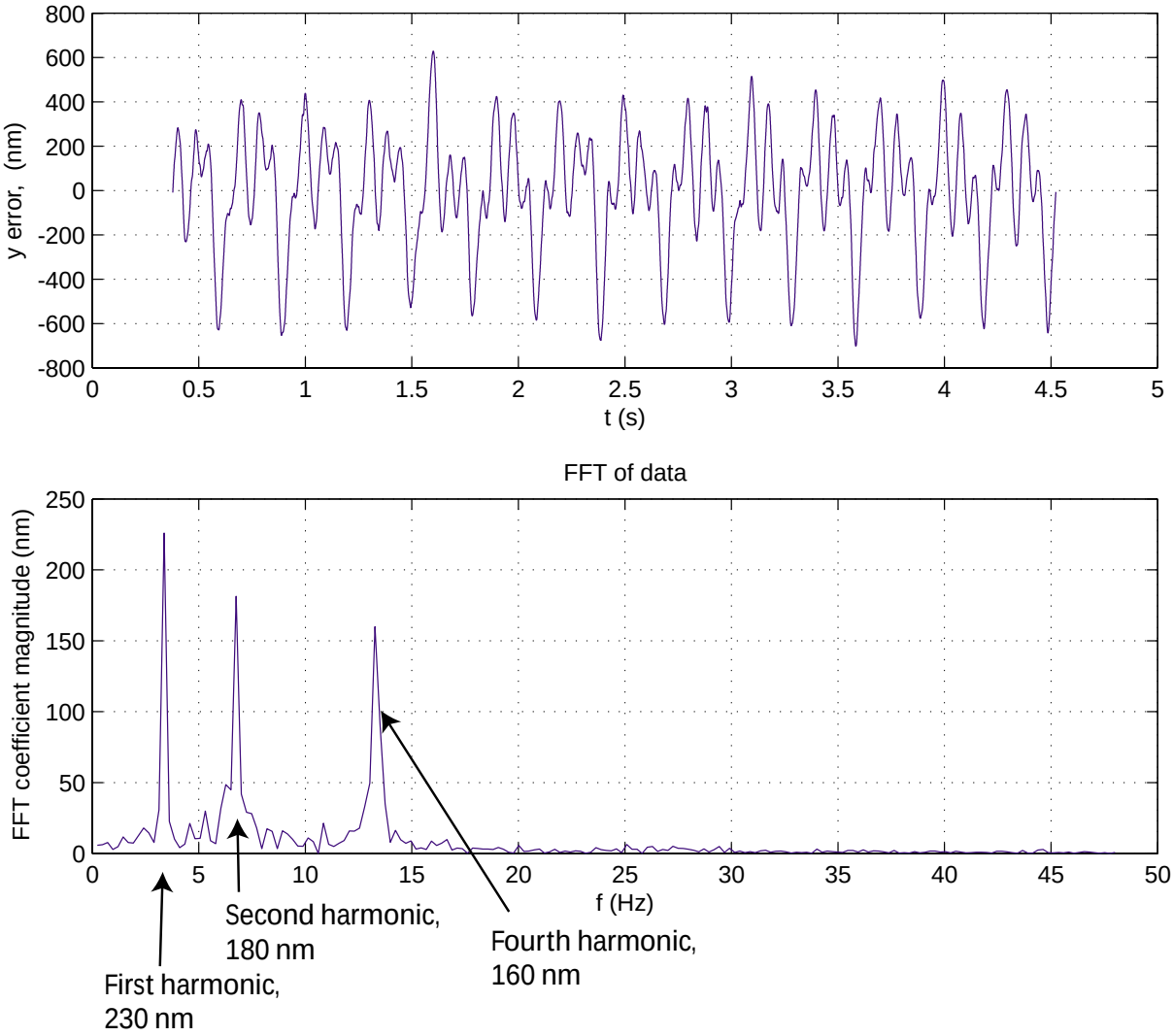

Figure 8-46: The top plot is the y axis error during constant velocity portion of a 0.1 m/s scan. The bottom plot is the FFT of the data. The harmonics correspond to the motor spatial period.

error. Since fast scanning is not performed in the x axis, the poor high speed x axis error is inconsequential. Any variation in the motor force constant as a function of position is an issue for the x axis acceleration estimation, however. The feedforward performance is affected by the acceleration estimation but the short steps of the x axis do not demand the best rejection of reaction forces either.

The stage scan shows periodic ripple due to the motor design and nonideal commutation. Some of the ripple is inherent in a motor built from block magnets and discrete coil arrays [56, 55]. A Halbach magnet array design and additional coils per period would reduce this contribution to the force ripple. However, some of the forces during scanning are due to the tolerances of the magnets and coils, offset currents in the stage amplifier, and nonideal magnetic preloading among other possible causes. A repetitive control strategy [73] may provide the best solution for smoother scanning. Or simply force mapping and linearizing the motor output may significantly enhance the scanning performance. Adaptive control schemes have also been applied to ripple force problems [105]. Although better scanning performance could certainly be attained, the performance demonstrated is sufficient for an angstrom level error budget for vibration.

Figure 8-48 shows the x and y axis accelerations during a 0.1 m/s scan along the y axis and the associated Gaussian filtered data where $d/v = 20$ ms. The accelerations were computed by filtering the position error data in Figure 8-46 with a double differentiator and a four pole Butterworth filter. The poles were place at 800 Hz. The transfer function of the filter is plotted in Figure 8-49. The filtering was implemented using Matlab's "lsim" function.

During scanning the stage accelerations increase as a result of disturbances. For the data in Figure 8-48, the Gaussian filtered accelerations are 99 μg, 3σ and $\pm$ 130 μg peak-to-valley for the x axis. This is much larger than the ± 25 μg peak-to-valley accelerations for the x axis when the stage is still. The y axis accelerations are 310 μg, 3σ and $\pm$ 260 μg peak-to-valley. Again, these accelerations are much larger than the still condition where the stage y acceleration is ± 15 μg. The payload will accelerate roughly 20 times less than these stage induced accelerations since the payload is 20

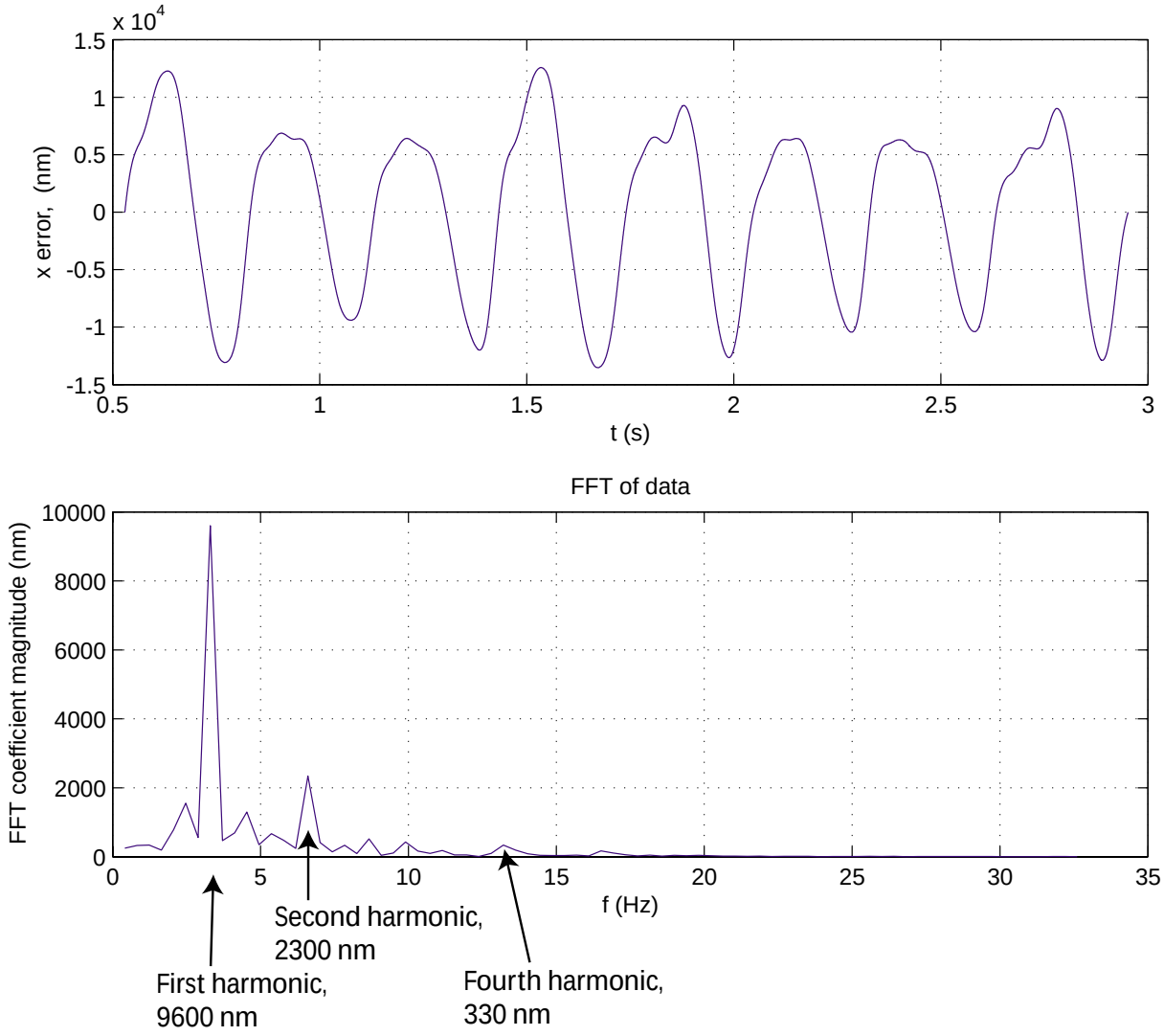

Figure 8-47: The top plot is the x axis error during constant velocity portion of a 0.1 m/s scan. The bottom plot is the FFT of the data. The harmonics correspond to the motor spatial period.

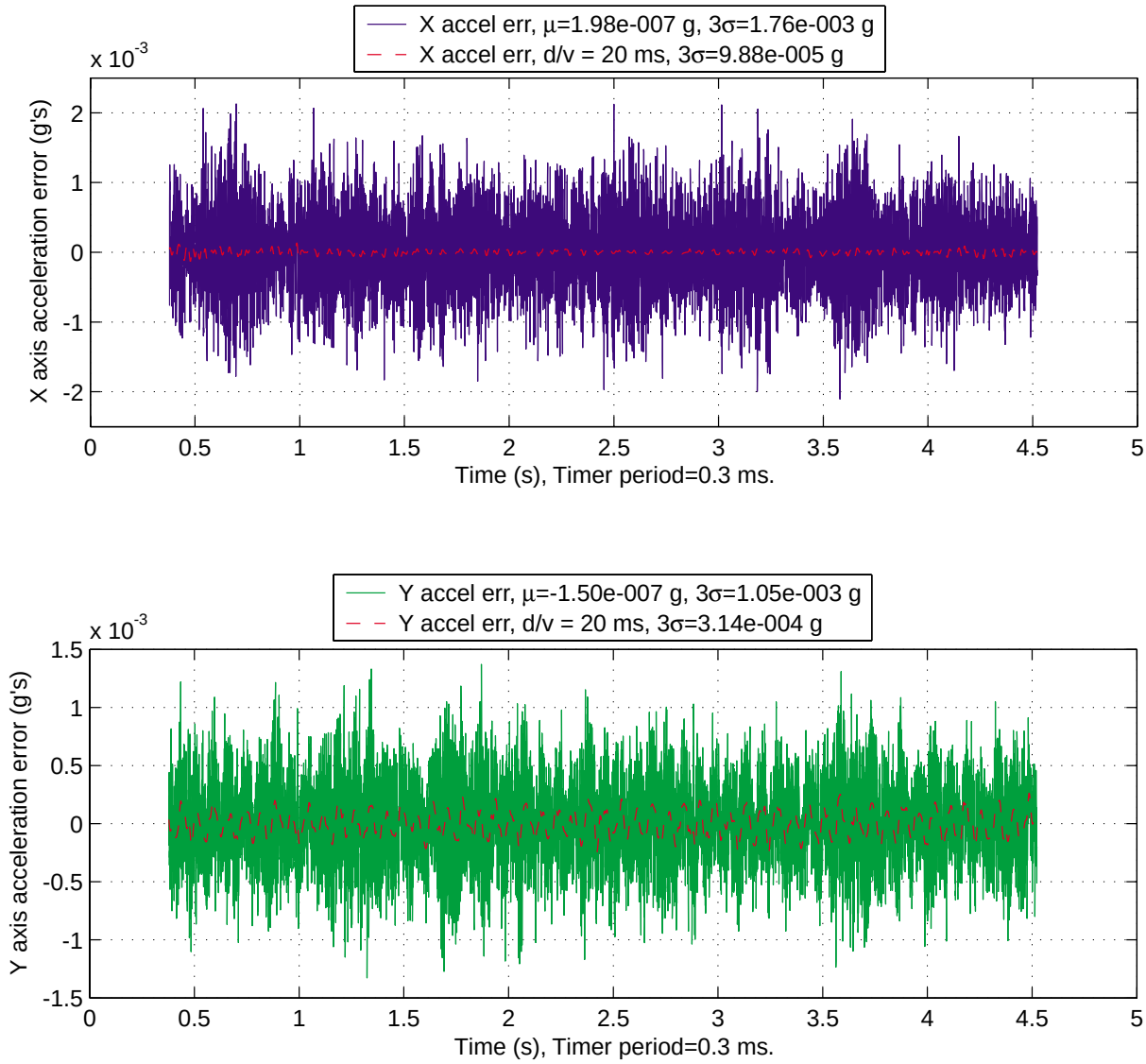

Figure 8-48: The x and y axis accelerations during a 0.1 m/s scan velocity in the y axis.

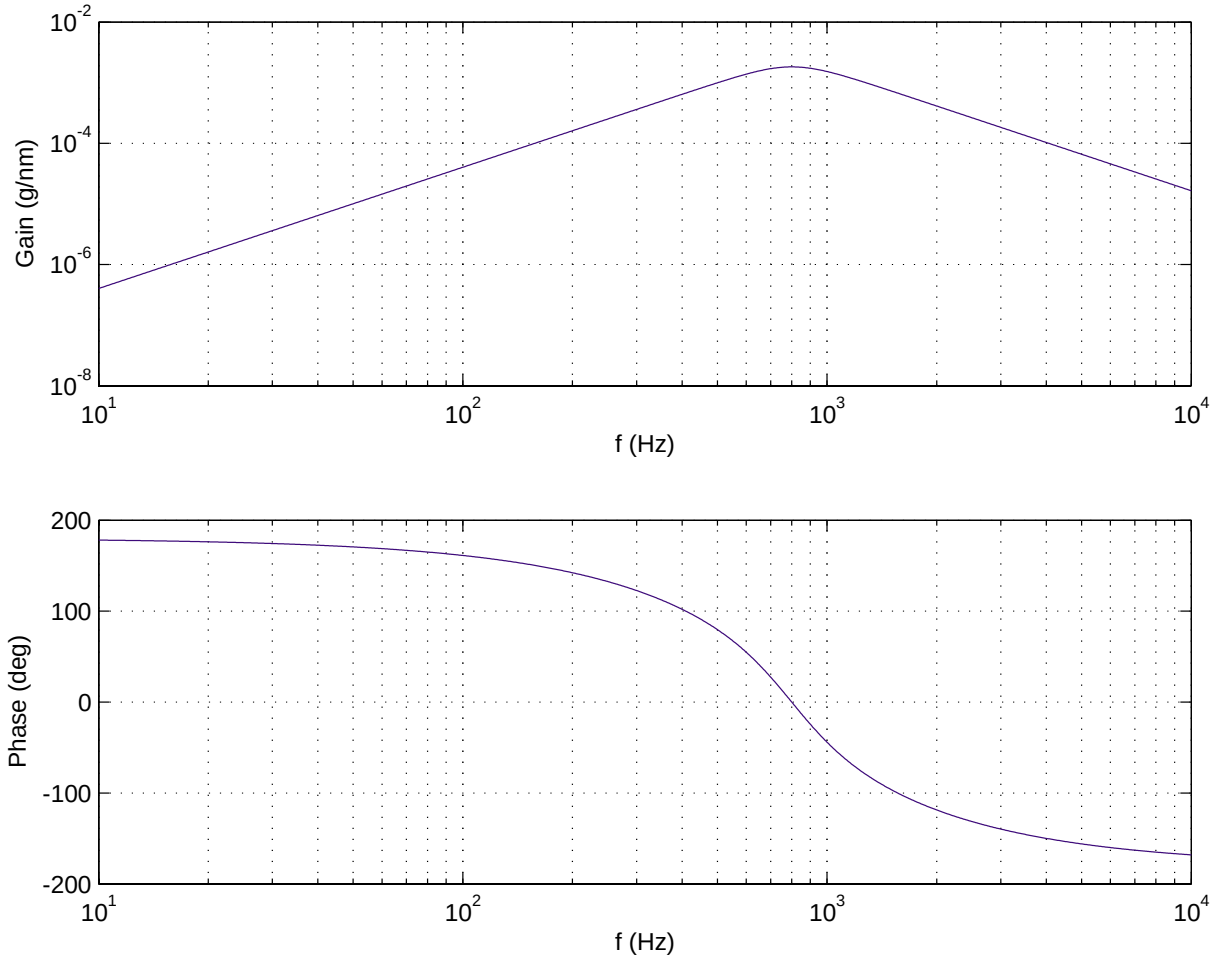

Figure 8-49: Transfer function of position to acceleration filter.

times more massive than the stage mass. Since the chuck has a vibration sensitivity of 0.050 nm/mg, these accelerations are expected to be acceptable for sub-angstrom error budgets for the chuck.

The stage does not perform fast scanning in the x axis, thus the dynamic performance at high speed are inconsequential for this axis. However, for the sake of completeness, the stage was calculated to have x axis accelerations of ± 1.5 mg peak-to-valley for x and ± 95 μg peak-to-valley for y during the 0.1 m/s x axis scan in Figure 8-47. These values are the Gaussian filtered accelerations with $d/v = 20$ ms.

8.5 The unobservable error with the stage amplifier off and with the stage air bearings down.

To test whether the stage electronics are contributing any significant electrical noise such as the 60 Hz noise noted in Section 8.3, I measured x_{ue} when the stage amplifier was off. This experiment, where the stage is freely floating on its air bearings, also determines the significance of the stage control's disturbance rejection on the unobservable errors. It was also of interest to measure x_{ue} while air to the bearings was shut off since the stage is more stable resting on its pads than any control could probably attain (except at very low frequencies where thermal expansion dominates). Figure 8-50 shows the power spectral density of x_{ue} when the stage amplifier is off, when the stage air is off and when the stage was controlled. To show the difference more clearly, Figure 8-51 shows the ratio of the power spectrums. When the amplifier is off, the SBIL error is within a factor of two for most of the data. Over the range of frequency shown, from 0 to 715 Hz, the 1σ is 1.05 nm when the stage is controlled. The case when the amplifier was off and the stage was floating had a 1σ is 1.11 nm and the case when the stage air was off had a 1σ of 1.08 nm. The difference is not statistically significant. Since the 60 Hz noise and 120 Hz noise is present when the stage amplifier is off, this noise is not associated with the amplifier – or at least some other source dominates. There is a difference at 300 Hz and 420 Hz but this noise is small to begin with and it is really to fast to be a concern.

When the stage was freely floating the fringe locking correction was large because the 3σ stage x error was 1.7 μm. Also, the 3σ stage x velocity was computed to be 1.7 μm/s when the stage is floating compared to 0.029 μm/s when controlled. The nonlinearity (discussed in Section 9.4) of the interferometers spreads to higher frequencies in the x_{ue} data when the stage has larger amplitude of error and higher velocities. I attribute the small increase in x_{ue} up to about 100 Hz when the stage is freely floating to the transfer of the nonlinearity to higher frequency.

From the results of this experiment, it can be concluded that the additional stage error has little effect on the SBIL error. The stage control does reject disturbances at

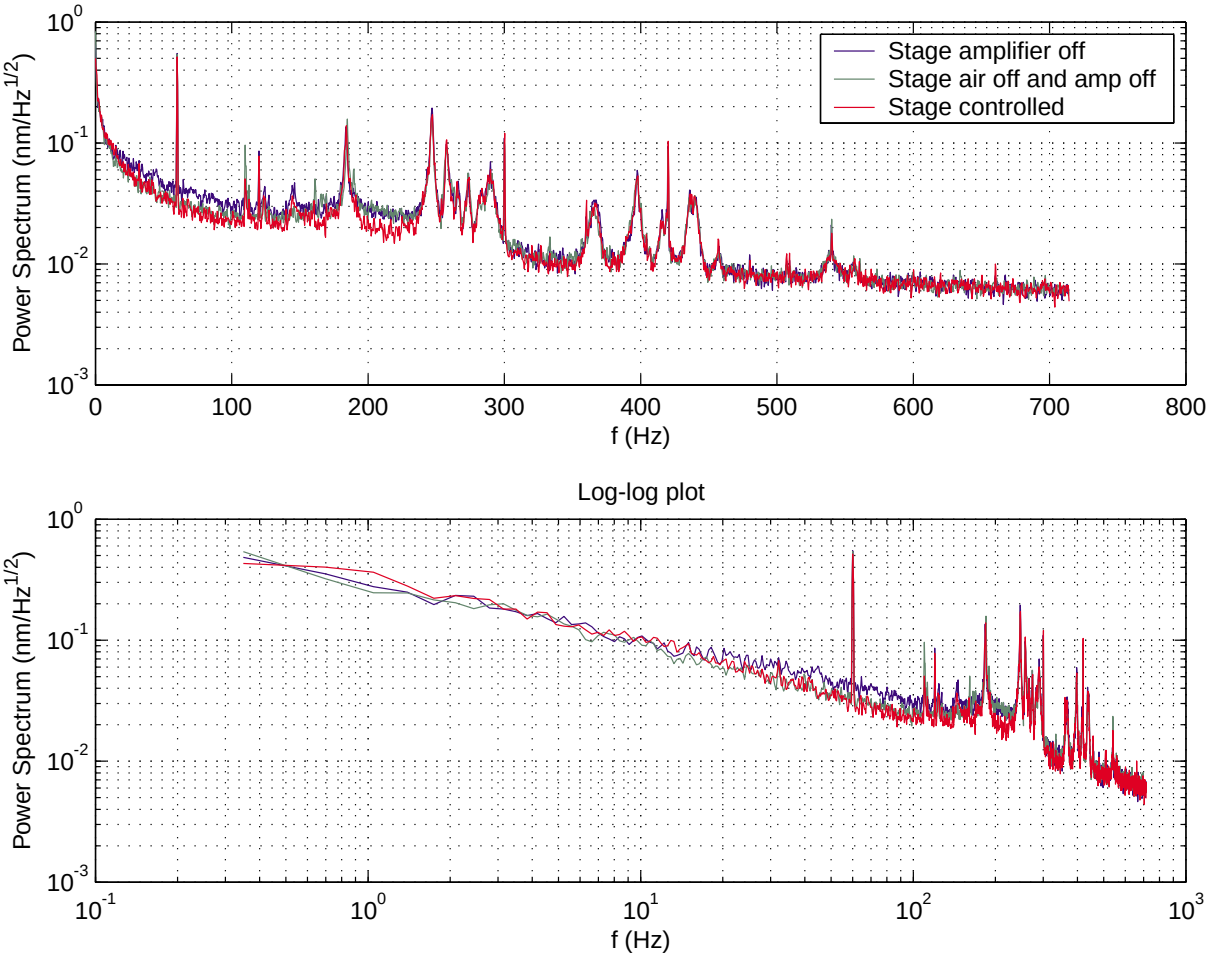

Figure 8-50: Power spectral density of x_{ue} when the stage amplifier is off, when the stage air is off, and when the stage is controlled.

low frequency, however, these disturbances are low enough that they don't introduce significant errors when the stage control is off. Thus, for this system, the error is insensitive to the stage performance for the ambient disturbances.

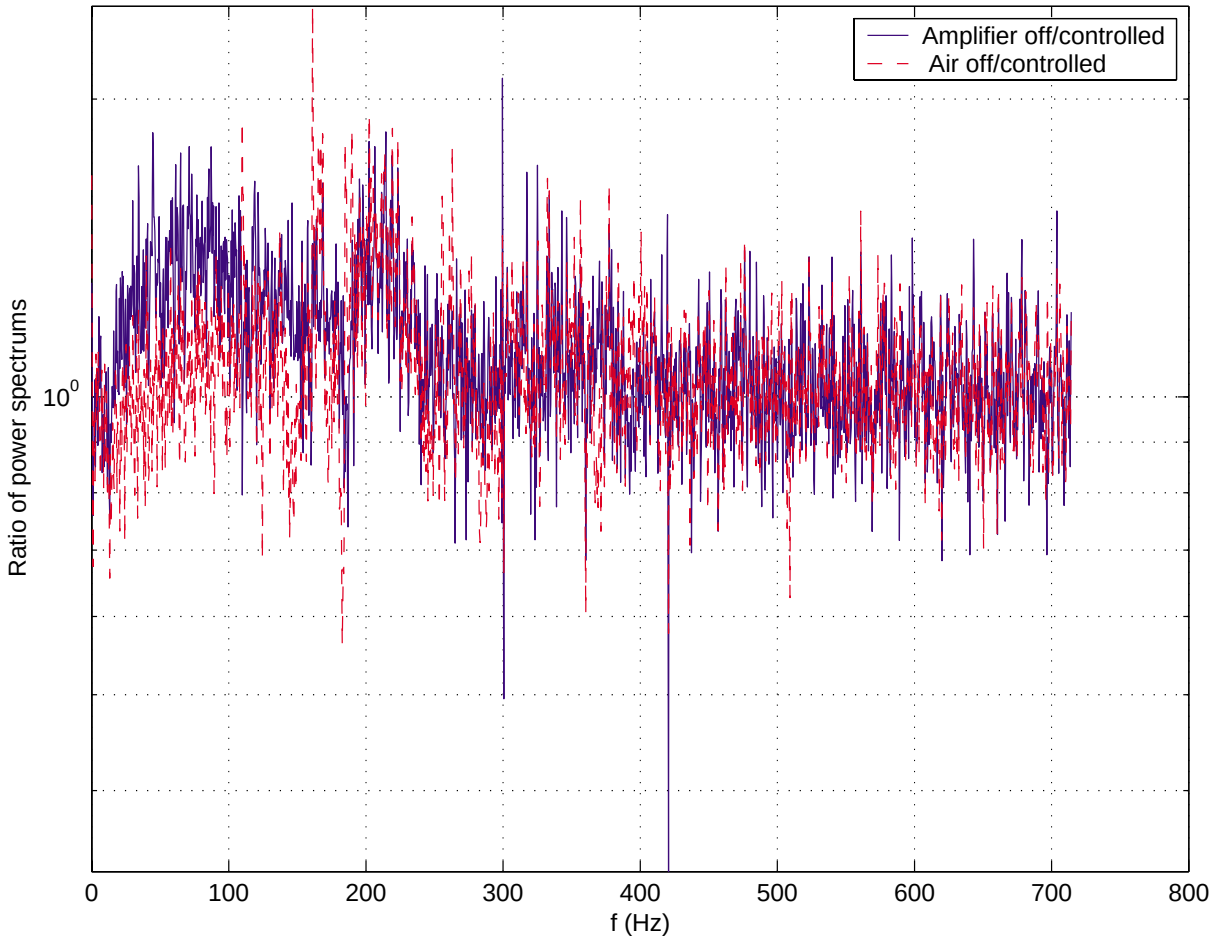

Figure 8-51: Ratio of power spectral densities of x_{ue}. The plot shows ratio x_{ue} when the stage amplifier is off over when the stage is controlled. Also, the ratio when the stage air is off over when the stage is controlled is shown.

Chapter 9

System Performance

This chapter discusses the system writing and reading performance. Static stability and the dynamic errors associated with scanning are demonstrated. Writing and reading performance is evaluated from phase maps of SBIL written gratings.

9.1 Short term stability

The grating-to-fringe placement is the fundamental performance metric for SBIL. Figure 9-1 shows x_4 over four seconds sampled at the 10 KHz. The raw data is taken directly from the Zygo phase meters that have an internal filter with a -3 dB bandwidth of 15 KHz. The raw 3σ error in x_4 is 3.89 nm. The Gaussian data uses the d/v parameter of 20 ms, which corresponds to a stage velocity of 100 mm/s and a 2 mm diameter beam. The 3σ error for the Gaussian filtered data is 1.94 nm. The x_4 data includes the unobservable error and the residual fringe locking error. Based on x_4, the normalized dose amplitude error is better than -0.03%. Thus, the fringe jitter is small enough to provide excellent contrast.

In the x_4 data, most of the residual fringe locking error is averaged by the Gaussian filter; the unobservable error at the same time in Figure 9-2 is very nearly the same as x_4 for the Gaussian filtered data. The Gaussian filtered x_{ue} is 1.95 nm 3σ versus 1.94 nm for x_4. The slightly worse x_{ue} is attributed to rounding associated with the data acquisition. The unfiltered x_{ue} is notably better than x_4 with a 3σ of 3.34 nm.

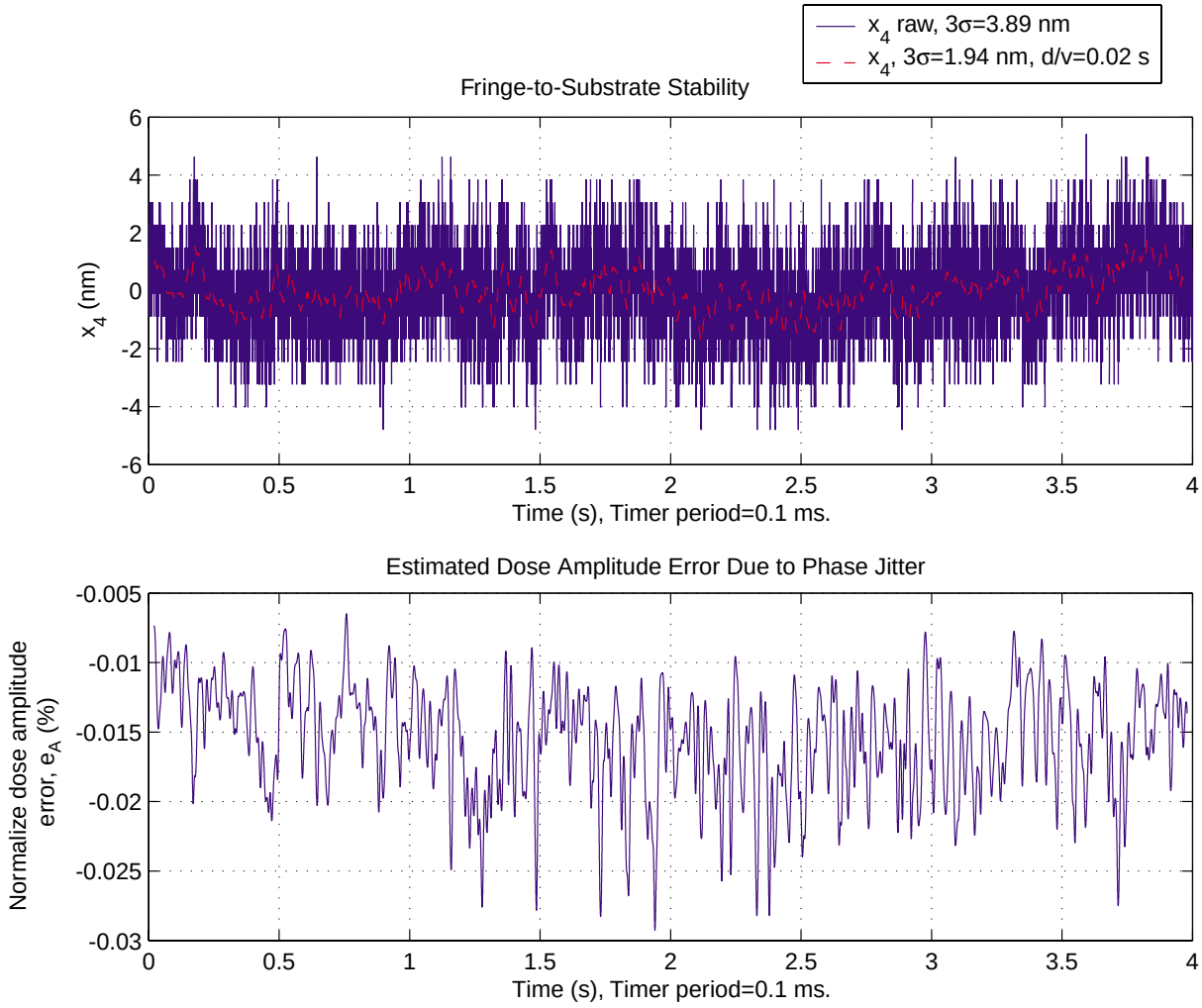

Figure 9-1: The upper plot is the grating-to-fringe stability, x_4, sampled at 10 KHz. The lower figure plots the calculated normalized dose amplitude error due to the x_4 assuming d/v=.02 s.

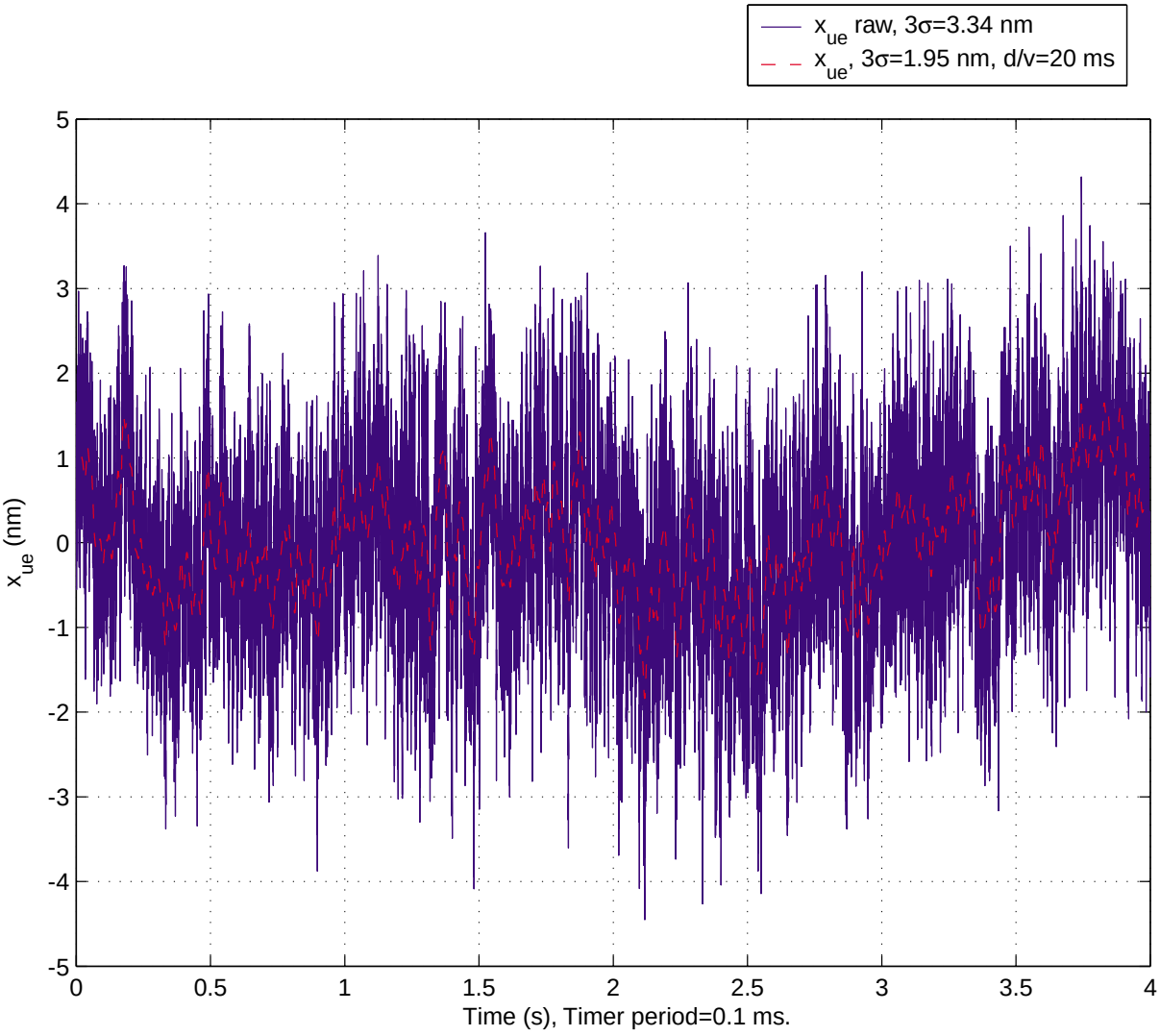

Figure 9-2: The unobservable error, x_{ue}, sampled at the same time as the data shown in Figure 9-1.

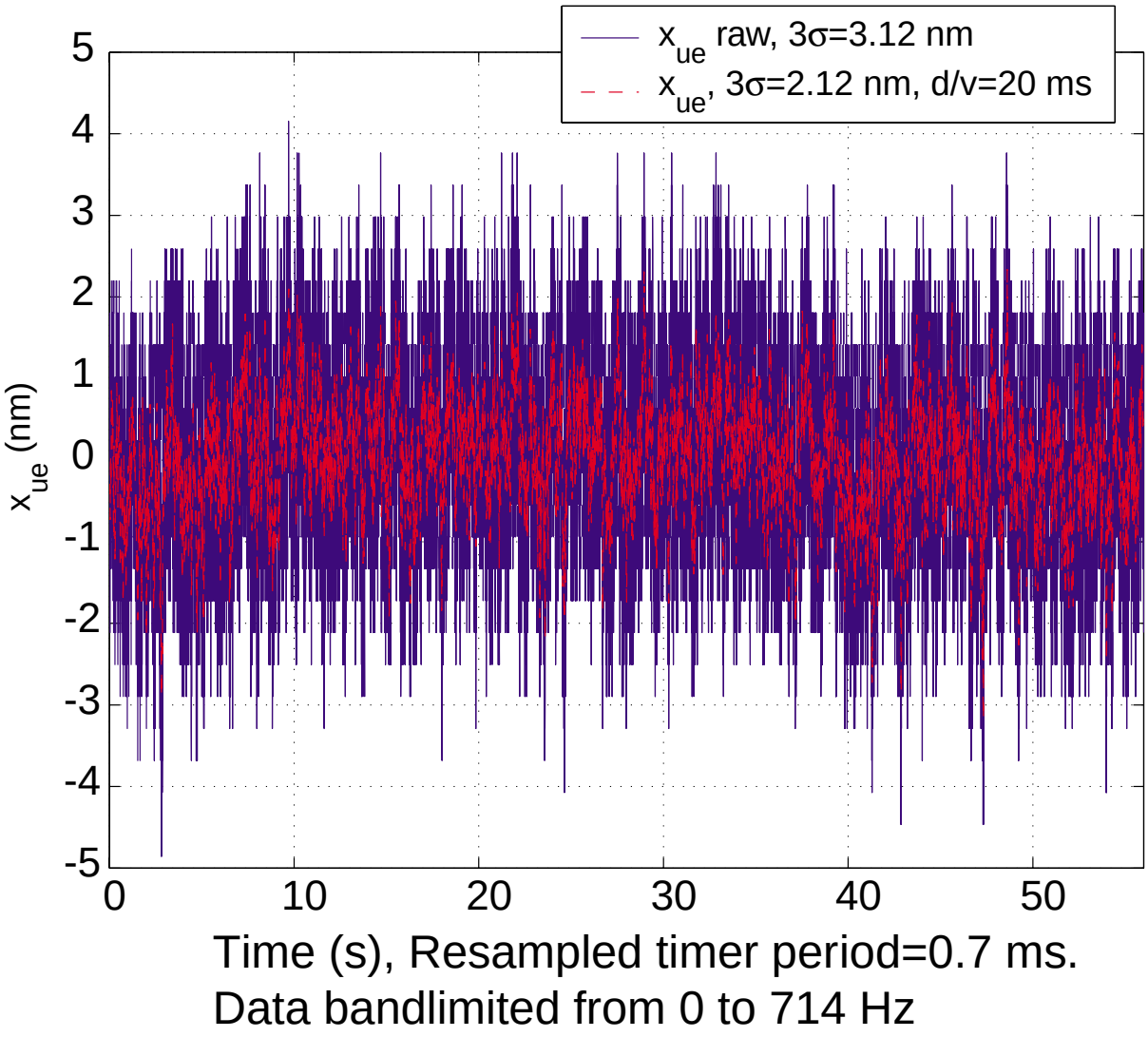

Figure 9-3: Unobservable error over 56 seconds while the stage is static. Raw data and Gaussian filtered data are shown.

Figure 9-3 shows x_{ue} over 56 seconds. The data was downsampled seven times from 10 KHz sampled data and it was filtered with a 714 Hz cut off frequency for band limited data. The raw x_{ue} data has a 3σ variation of about 3 nm and about 2 nm, 3σ for the Gaussian filtered data. To give another idea of what the static x_{ue} data looks like on shorter time scales, Figure 9-4 contains just the first 7 seconds of the data of Figure 9-4.

The (square root) power spectrum of the x_{ue} data from Figure 9-3 is shown in Figure 9-5. I have noted distinctive error regions in the Figure. Note the fast cut off

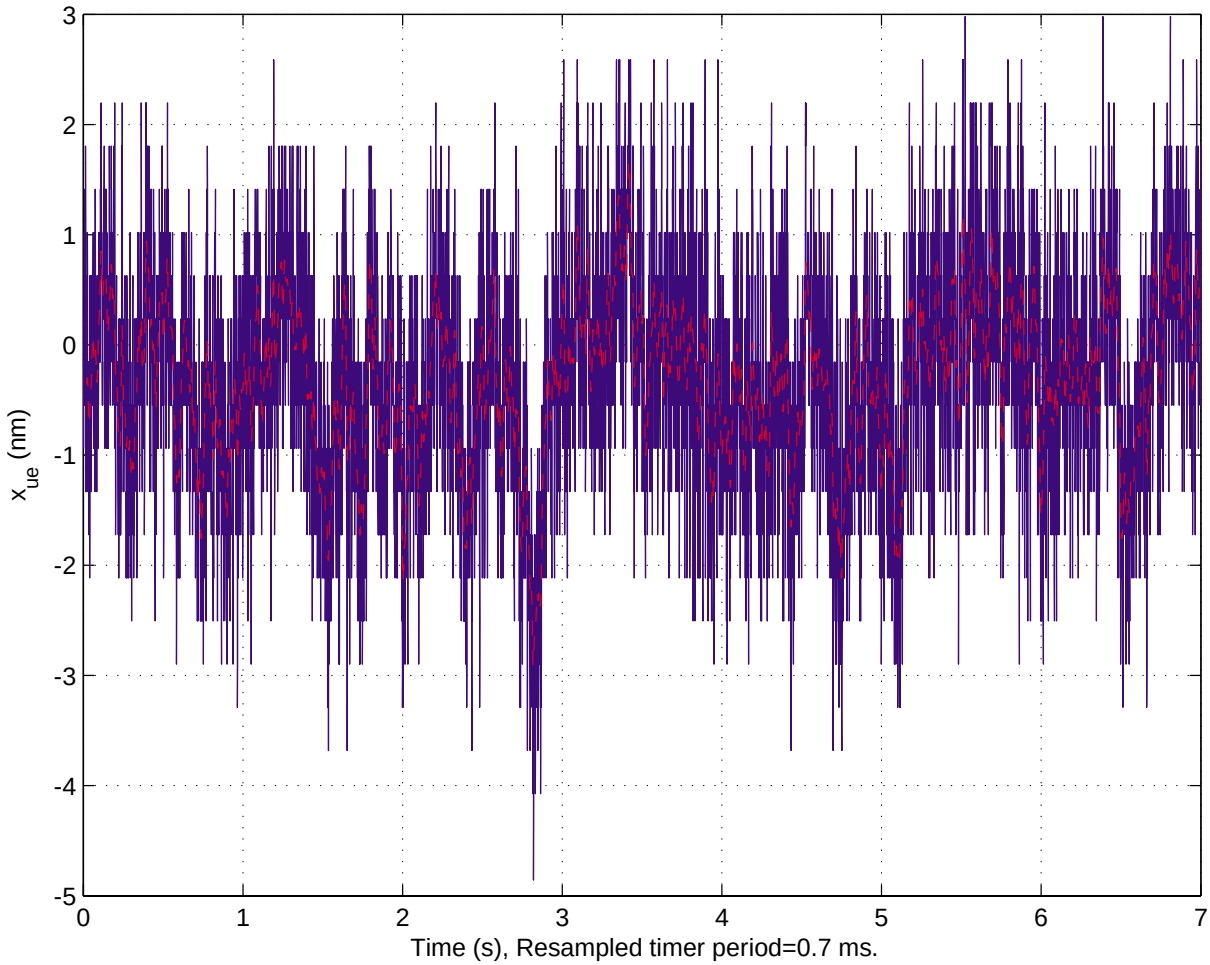

Figure 9-4: Unobservable error over seven seconds while the stage is static. Raw data and Gaussian filtered data are shown.

for the Gaussian filtered data. The errors at high frequency that are filtered include those due to vibrations and most of the electrical noise. Even the 60 Hz electrical noise is filtered by a factor of 6× when $d/v = 20$ ms. The 3σ values shown in the figure were computed by integrating the power spectrum of the raw data. The air index nonuniformity and the part expansion errors, which occur at low frequencies, limit the performance of the system. Between 0 and 59.5 Hz the unobservable error is 2.3 nm, 3σ. The nonlinearity of the interferometers is also included in the low frequency errors. In section 9.4, I determine that the nonlinearity errors are much smaller compared to the remaining errors at low frequency.

Scanning slow is beneficial. The standard deviation versus v/d can be computed

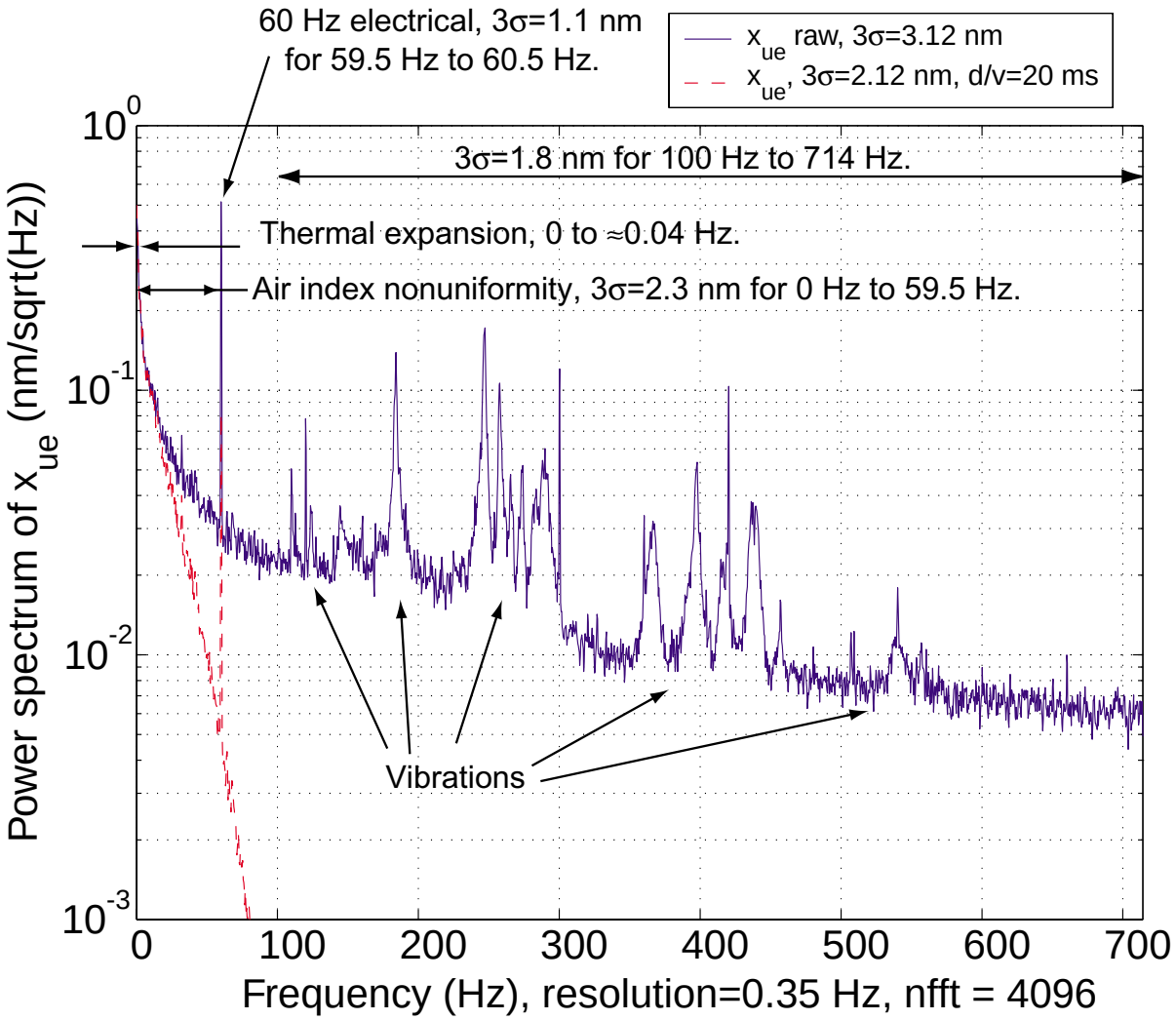

Figure 9-5: Power spectrum of x_{ue} computed from the data in Figure 9-3. The Gaussian filtered data shows the very fast cutoff. Dominant error sources in different frequency bands are indicated.

from

$$\sigma_{ue}^2(v/d) = \int_{-\infty}^{\infty} S_{ue}(f) \left[\exp\left(-\frac{1}{8} \left(\frac{\pi f d}{v} \right)^2 \right) \right]^2 \mathrm{d}f. \tag{9.1}$$

This relation follows from Equation 8.16 and the definition for M_G given in Equation 3.51. In practice the integration limits range from 0 Hz to the Nyquist frequency. The three sigma x_{ue} versus v/d is shown in Figure 9-6. This data indicates the placement repeatability versus scan speed assuming the dynamic errors are negligible. In Section

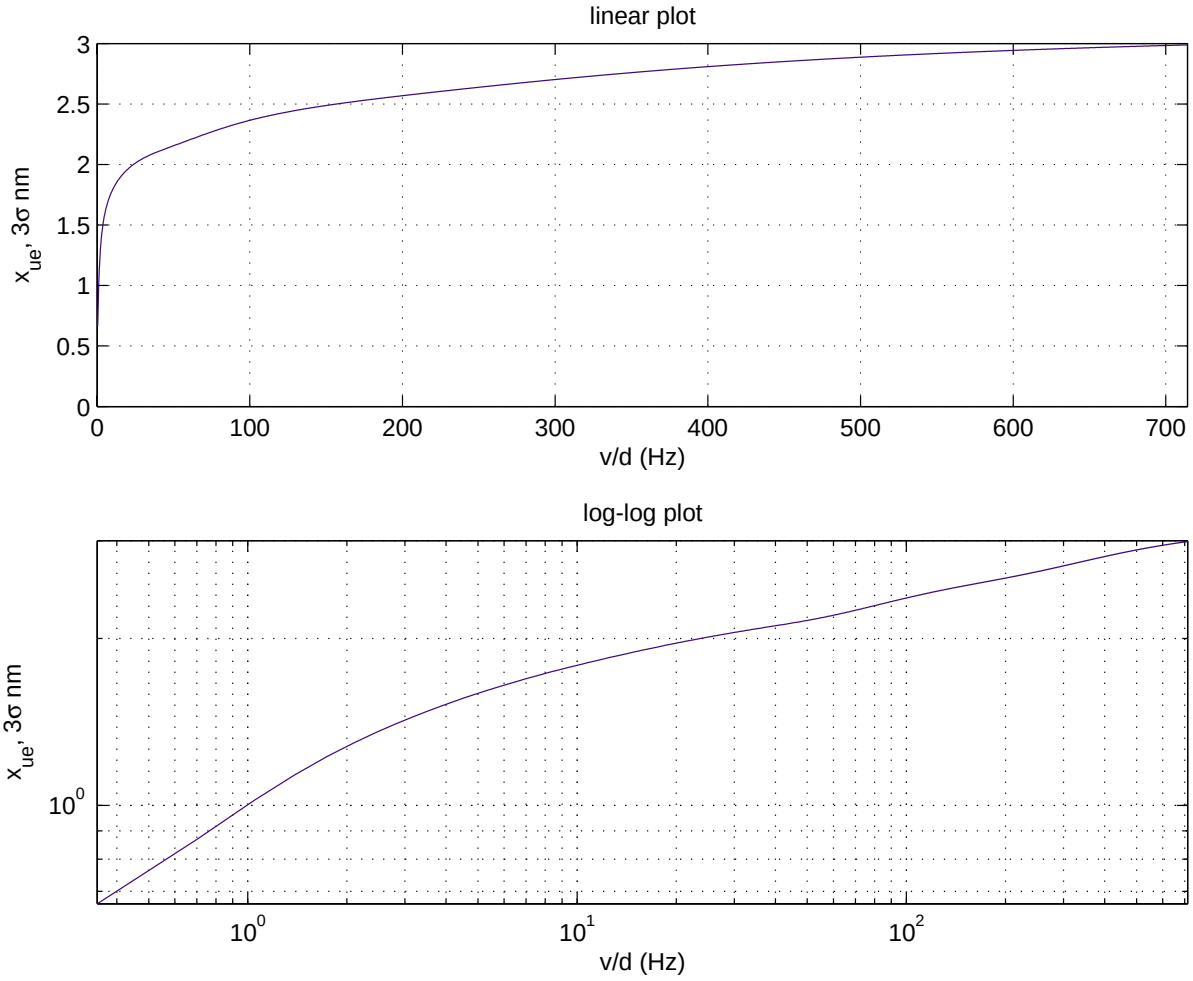

Figure 9-6: The $x_{ue}, 3\sigma$ computed by integrating the power spectrum versus v/d. The same data is shown on linear and log-log plots.

9.3, I experimentally confirm the dynamic errors, which essentially superpose with the static errors, are indeed negligible. When $v/d = 1$ Hz, $x_{ue} = 1.0$ nm, 3σ compared with $x_{ue} = 1.8$ nm, 3σ at $v/d = 10$ Hz and $x_{ue} = 2.1$ nm, 3σ at $v/d = 50$ Hz. Increasing the performance with reduced speed is expensive – a $50\times$ drop in throughput improves the performance by only $2.1\times$. The filtering behavior of overlapping multiple scans might be considered in future work.

Since the data set used to compute the power spectrum in Figure 9-5 was only 56 seconds long, there is some additional error at very low frequencies not included. However, the integral of the power spectrum from 0 to 1.4 Hz equals the 1.4 nm 3σ for data that was bandlimited from 0 to 1.4 Hz taken over an hour. That longer data is

discussed in the next section. Thus, very little additional noise power is contributed over longer time scales. Moving the stage through air with temperature gradients will in practice lead to additional low frequency errors however.

9.2 Long term stability and refractometer calibration

Interferometer systems with deadpath in air, such as the stage DMI, must be corrected [102] to achieve long term stability better than about 10 ppm. The SBIL system uses an interferometer-based refractometer to correct for instability in the vacuum wavelength and air index. Accurate refractometer calibration coefficients compensate not only for the deadpath in the DMI but also for any deadpath in the metrology block interferometer. The deadpath in the metrology block interferometer although nominally zero was expected to be less than a centimeter based on assembly tolerances of the optics on the block. Since an uncompensated 1 cm deadpath would contribute a nanometer of error for 0.1 ppm index change, empirically based refractometer coefficients that capture all deadpath terms significantly enhances the accuracy of the system. In this section I discuss the refractometer calibration procedure that also indicates the effectiveness of the correction.

The refractometer correction is applied to the stage x axis whose phase is given by

$$\phi_x = \frac{2\pi(L_s - L_m)n}{\lambda_{DMI,air}} + \phi_{x,o} \tag{9.2}$$

where the distance $L_s - L_m$ is the deadpath or the difference between the stage beam path and the column beam path. The arbitrary start phase $\phi_{x,o}$ depends on where the axis was zeroed. The interference scale factor n is 4 for a double pass interferometer. The stage position relative to the metrology block reference is calculated as

$$L_s - L_m = \frac{(\phi_x - \phi_{x,o})\,\lambda_{DMI,air}}{n2\pi} \tag{9.3}$$

To accurately measure the stage position to a nanometer, the wavelength of the DMI must be known to 1 nm over 0.15 m or to 7 ppb. For this SBIL project, it was decided to forego absolute accuracy that may be traceable to some national standard, at least for the foreseeable future. Instead, a repeatable length scale would suffice for the applications of interest. This repeatable length scale would be a grating written by SBIL that would then serve as a length scale calibration artifact. Before writing or reading a grating, the SBIL system would calibrate its scale to the length of a fixed number of periods of the artifact grating. Then the refractometer would compensate for any air index or laser vacuum wavelength changes that occur after the calibration. For my work, I did not end up implementing the artifact grating because time ran out. Furthermore, the length scale does not affect the linearity of the gratings but only the period. At this phase in the research, demonstrating linear gratings was considered the necessary first step. Low CTE substrates will be another important consideration for maintaining the scale accuracy of the written gratings. The chuck is already designed to accommodate a grating length scale.

The grating length scale can be extremely stable if it and the chuck is fabricated from a low CTE material. For instance, when using Zerodur Expansion Class 0, which has a CTE of 20 ppb/C, in an environment controlled to 5 mK the length scale can be stable to 0.1 ppb. This is much better than the uncertainty of laser wavelength calculated from temperature, pressure, humidity, and CO_2 concentrations, which can be $\pm$30 ppb [8, 9]. Furthermore, the Zygo laser has a lifetime wavelength accuracy of $\pm$ 100 ppb and a stability of $\pm$ 10 ppb over 24 hours.

The refractometer correction is extremely important to the stability of the system during the time of writing, which may be from 10 minutes to perhaps several hours. However, for most writing scenarios the time should be under an hour with typical refractivity changes of 0.1 ppm. Therefore, the refractometer typically corrects for 15 nm of error if 150 mm deadpath is assumed.

The refractometer interferometer phase is given by

$$\phi_R = 2\pi Rn\left(\frac{1}{\lambda_{DMI,air}} - \frac{1}{\lambda_{DMI,air,o}}\right) = 2\pi Rn\frac{\Delta\lambda}{\lambda_{DMI,air}\lambda_{DMI,air,o}}. \qquad (9.4)$$

The distance R is the deadpath of the refractometer. The wavelength of the DMI at the time the refractometer axis was zeroed is $\lambda_{DMI,air,o}$. The change in wavelength $\Delta\lambda$ is defined as

$$\Delta\lambda = \lambda_{DMI,air} - \lambda_{DMI,air,o}. \tag{9.5}$$

Solving Equation 9.4 for $\lambda_{DMI,air}$ one obtains

$$\lambda_{DMI,air} = \frac{\lambda_{DMI,air,o}}{\frac{\phi_R \lambda_{DMI,air,o}}{2\pi R n} + 1} = \frac{\lambda_{DMI,air,o}}{\frac{\Delta\lambda}{\lambda_{DMI,air}} + 1} \tag{9.6}$$

For $\Delta\lambda/\lambda_{DMI,air} << 1$, this simplifies to

$$\lambda_{DMI,air} \approx \lambda_{DMI,air,o} - \frac{\Delta\lambda}{\lambda_{DMI,air}} = \lambda_{DMI,air,o}\left(1 - \frac{\phi_R \lambda_{DMI,air,o}}{2\pi R n}\right). \tag{9.7}$$

Substituting this relation into Equation 9.3, the stage position relative to the column reference is calculated as

$$L_s - L_m = \frac{(\phi_x - \phi_{x,o})\,\lambda_{DMI,air,o}}{2\pi n}\left(1 - \frac{\phi_R \lambda_{DMI,air,o}}{2\pi R n}\right). \tag{9.8}$$

The length scale obtained from measuring the grating would be used to repeatably establish $\lambda_{DMI,air,o}$.

Without refractometer compensation, there will be unobservable error that is linearly related to the refractometer measurement. By least squares fitting data, the refractometer coefficients that indicate the location of zero deadpath and the refractometer cavity length are calculated. The part of the refractometer cavity length built into the metrology block could be measured directly to high certainty using the SBIL system's own stage and a federal gauge. However, the built in deadpath of the DPMI is only specified to about ± 2 mm. Also, the zero deadpath location has uncertainty; the UV interferometer may have a deadpath and the dead path of the x axis interferometer head is not specified to any certainty. Because of the uncertainties, it is desirable to measure the refractometer coefficients directly. Also, the effectiveness

of the correction is evaluated from the experimentally verified performance.

Figure 9-7 shows the unobservable error with and without refractometer compensation along with the refractometer data taken at the same time. The data is bandlimited to 1.4 Hz and is an hour long. Over the course of an hour the refractivity varied by 0.15 ppm, which leads to about 10 nm of error in the data shown. For deadpaths of 0.15 meters, the drift would be 23 nm. Since the environment has very stable temperature and humidity, most of the variation is due to pressure changes. Over many hours, the refractivity can vary by 10 ppm in extreme cases because of weather related pressure. Non weather related pressure changes such as the clean room doors opening also produces sudden pressure changes that are effectively compensated.

The refractometer is not effective for index variations faster than about 0.04 Hz as indicated in Figure 9-8. The plot shows the (square root) power spectrum for the hour long data. PSD's for the compensated and uncompensated unobservable error as well as the refractometer correction are plotted. After 0.04 Hz the refractometer signal drops off much faster than the x_{ue} signals and the compensated data is no longer better than the uncompensated data. The larger x_{ue} at high frequency is expected since the velocity of the air in the refractometer beam path is believed to be much slower than the air velocity in the stage beam paths. Most of the error in the compensated data, which is about $\pm$ 2 nm peak to valley and 1.44 nm 3σ is attributed to the air index nonuniformity since much of the noise occurs over tens of seconds long time scales or faster. Between 0.04 and 1.4 Hz, the 3σ square root power is 1.26 nm.

Also, seen in the power spectrum is the spike in the refractometer correction data at 0.06 Hz that is not seen in the uncompensated data. This time scale suggests the thermal control as the source of this non uniformity. The residual error at frequencies below 0.04 Hz is probably largely associated with the expansion of the thermally sensitive assemblies. The 3σ square root power between 0 and 0.04 Hz is 0.7 nm. This data was taken with the system very well thermally equilibrated. Poor equilibration or motion of the stage through a temperature gradient, leads to additional errors.

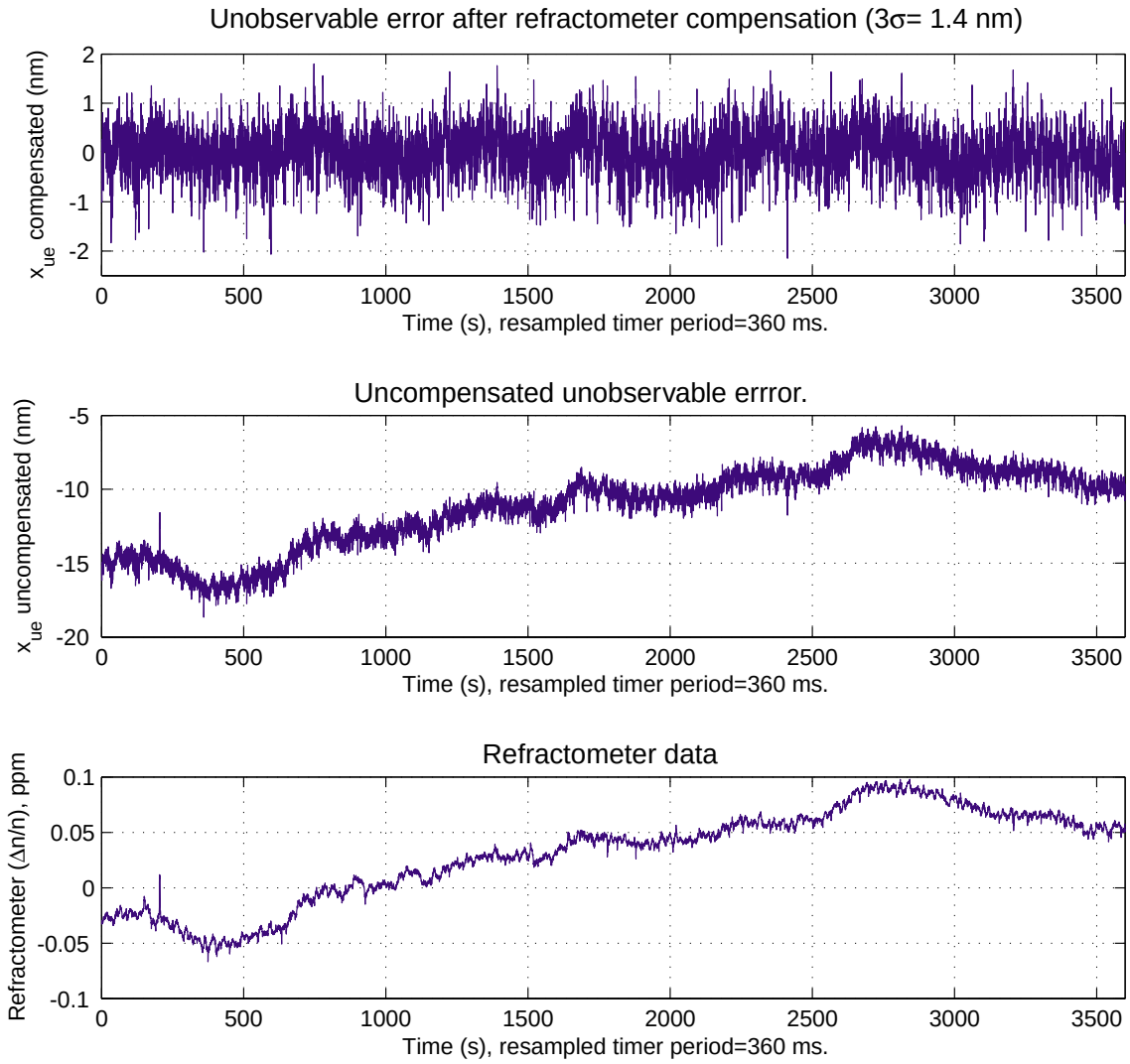

Figure 9-7: The top plot is the long term unobservable error with refractometer compensation. The middle plot is the unobservable error without refractometer compensation. The bottom plot is the refractometer data taken at the same time. The data is the bandlimited to 1.4 Hz.

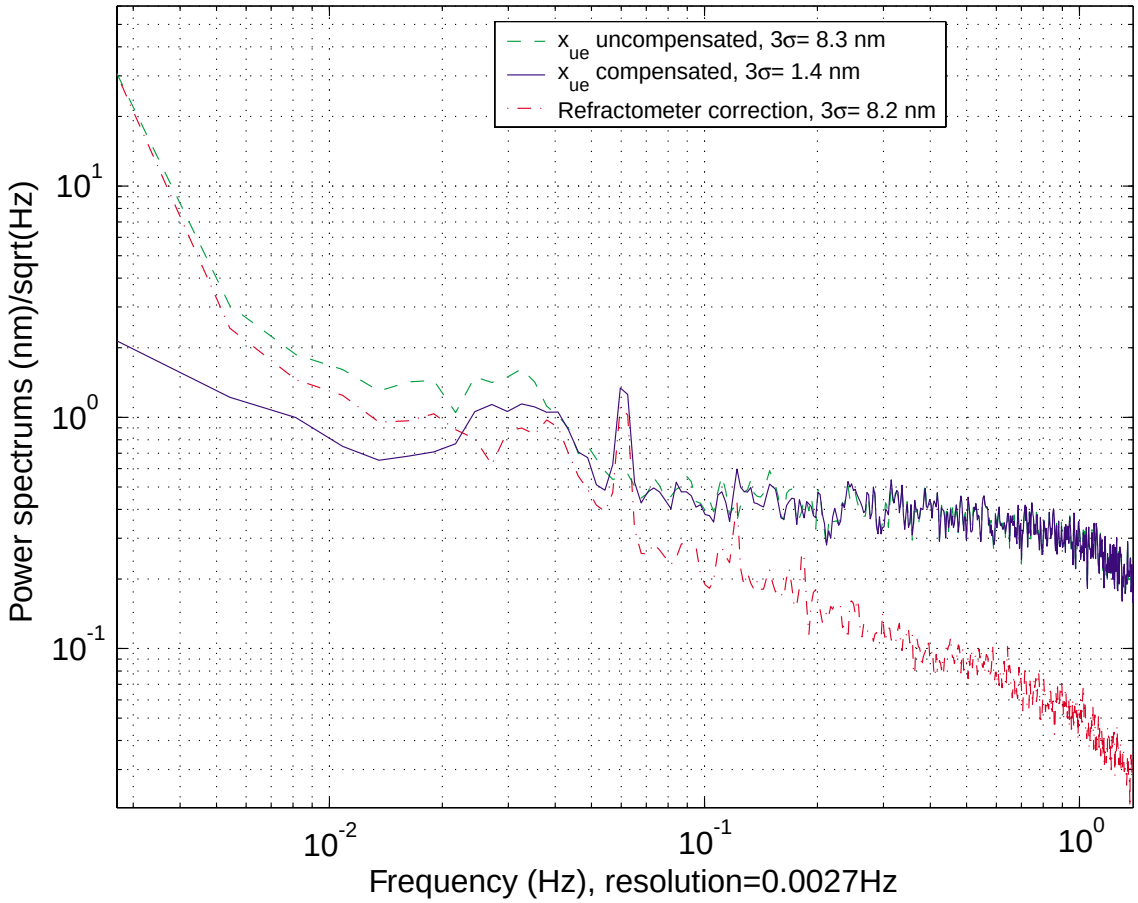

Figure 9-8: The power spectrums of the compensated and uncompensated x_{ue} data from Figure 9-7. The power spectrum of the refractometer correction signal is also shown. The refractometer compensation is effective up to about 0.04 Hz.

Since the uncompensated data is linearly proportional to the refractometer data, the refractometer signal is used as a correction. The refractometer calibration coefficients are obtained by least square fitting the refractometer measurements to the x_{ue} measurements. The doors of the clean room are opened and closed during the measurements to artificially cause a pressure and hence index changes. The positive pressure in the clean room falls when the doors are opened. Opening two sets of doors produces an index change of about 0.1 ppm. Figure 9-9 shows sample data from this procedure. The x_{ue} that is uncompensated in the top plot correlates well with the refractometer data in the bottom plot. The x_{ue} that is compensated using the experimentally derived refractometer coefficients shows much improved stability.

The top plot of Figure 9-10 shows the experimentally derived refractometer coef-

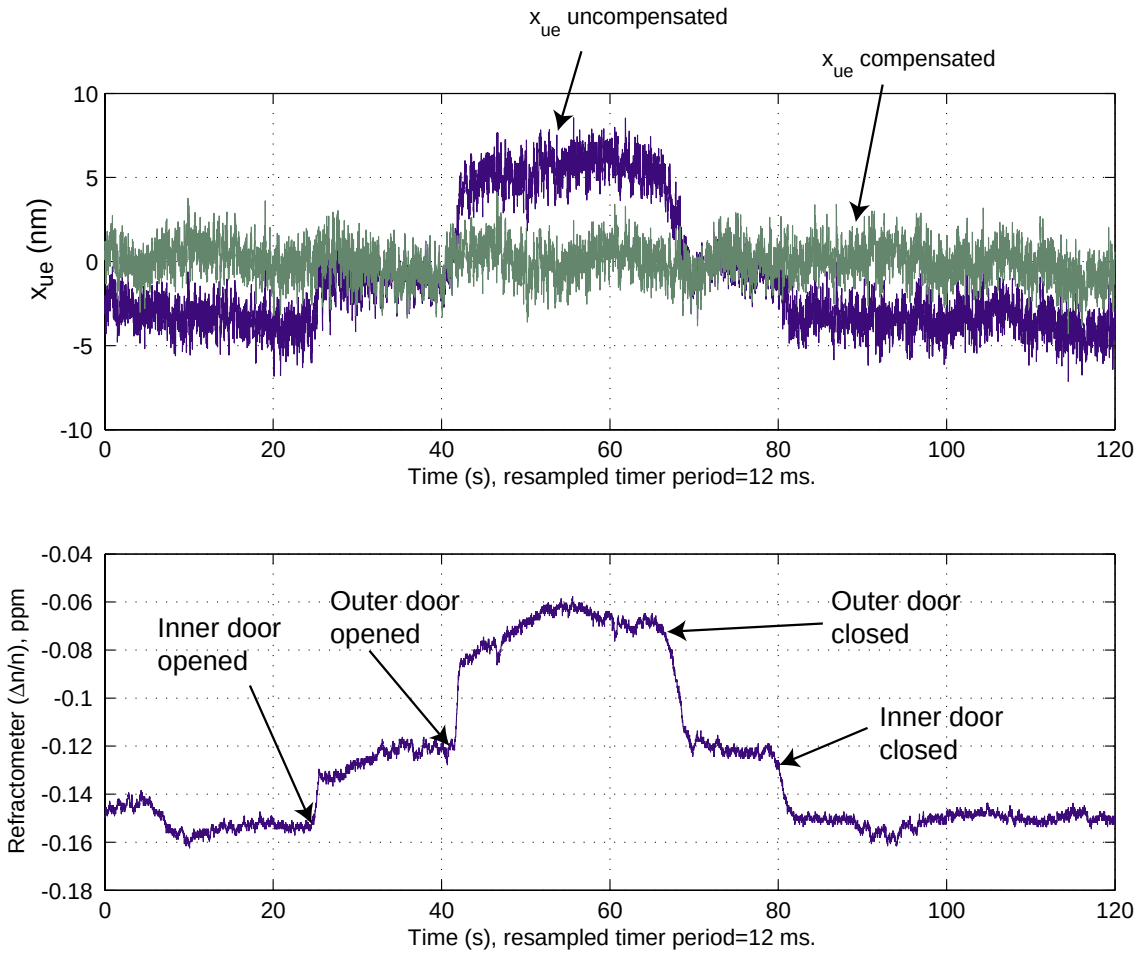

Figure 9-9: The top plot shows x_{ue} that is uncompensated by the refractometer and x_{ue} that is compensated. The bottom plot contains the refractometer measurement taken at the same time. The doors of the clean room were opened and closed to artificially produce a pressure change. The data is bandlimited to 42 Hz.

ficients versus the stage x position and the linear fit. The linear parameters obtained from the fit are used to correct the stage x axis position. The difference between the fit and the experimental data shown plotted against the left ordinate in the bottom plot is within $\pm$ 5nm/ppm. Thus, if the refractivity changes by 0.1 ppm, the error due to the refractometer is expected to be 0.5 nm. The deviation from the data from a straight line might be largely from periodic error of the refractometer. Since the change of 0.1 ppm produces a change of 0.11 periods on the refractometer phase meter, the nonlinearity is expected to be significant. Plotted against the right ordinate of the bottom plot is the unobservable error after removing the error proportional to

the refractometer measurement using the least squares fit. The residual errors at zero deadpath are much larger than any errors due to refractometer calibration. Close to the zero deadpath location, the error is not sensitive to the stage position. However, if the stage is moved far enough away, let's say to less than 0.16 m, the residual error increases with deadpath as expected for a system with nonuniform air index. When the deadpath is close to zero, the remaining component of the air index error is due to nonuniformity of the air index on spatial scales close to the separation of the measurement and reference beams of the interferometers. The residual error at x = 0.119 m where the deadpath is 0.11 m is about 3.48 nm, 3σ or about 1.1 times the 3.13 nm, 3σ at $x = 0.14$ where the deadpath is 0.09 m. Although more data points need to be taken to make a more reliable conclusion, the error appears to increase by about the ratio of the square root deadpath length. This type of increase is expected for random air index nonuniformity.

The zero deadpath position of the stage calculated from the fit to the refractometer coefficients is $x = 0.229$ meters, which is within the tolerances for the calculated location from the engineering drawings of $x = 0.231$ meters. Ideally, the zero deadpath location should be in the center of the stage travel, which would be $x = 0.158$. In an optimized system, the column reference mirror on the metrology block would be about 7 cm longer for the chuck used on the stage; the chuck mirror location was not known at the time of the metrology block design. The maximum deadpath on the system is about 22 cm versus 15 cm for an optimized design, assuming 300 mm diameter substrates. Thus, assuming the square root length relation, optimizing the maximum deadpath would improve the maximum errors by about 20%. This is a small improvement compared to what could be obtained by improving the index uniformity.

If the temperature gradient problem was improved, the refractometer calibration, correction accuracy, and residual errors should improve. Performing the calibration with larger gratings and larger deadpaths also should improve the calibration accuracy. The issue of the refractometer interferometer nonlinearity and nonlinearity in general is dealt with in Section 9.4.1.

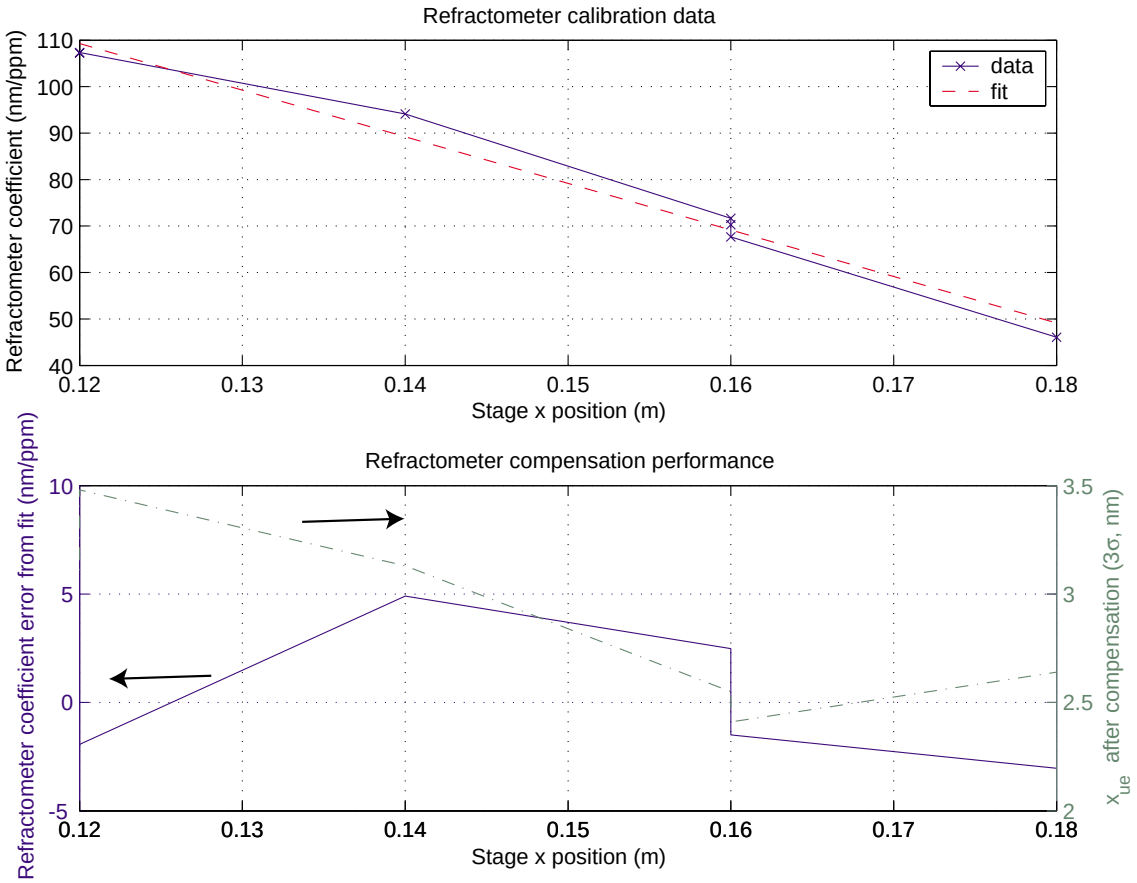

Figure 9-10: The top plot shows the experimentally derived refractometer coefficients versus the stage x position and the linear fit. The bottom plot shows the difference of the refractometer coefficients and the fit against the left ordinate. Additionally, the unobservable error with the error proportional to the refractometer measurement removed is plotted against the right ordinate.

9.3 Scanning performance

When the stage is scanning, disturbances in addition to the static ones are present – the static and dynamic disturbances linearly superpose. Dynamic errors occur because of stage accelerations. The stage must accelerate to reach a constant velocity and the stage accelerates in response to disturbance forces, which increase during scanning. Additional stage errors occur in both the scan direction and in the perpendicular scan direction. Errors result because the chuck distorts under its own inertial forces and the metrology block optics displace during payload accelerations. Although most of the reaction forces that disturb the payload are compensated by

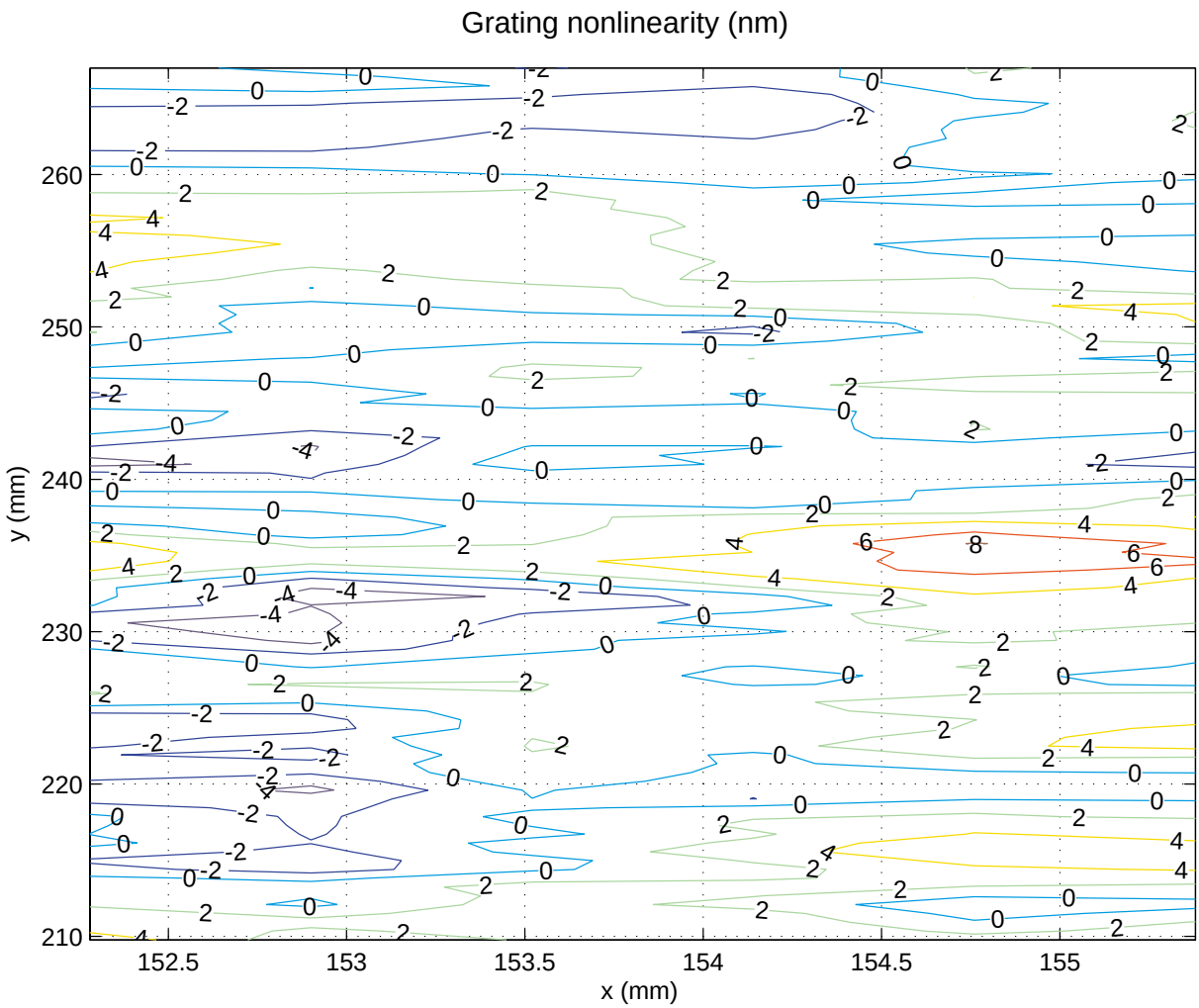

Figure 9-11: Nonlinear phase map of a strip of grating used in the experiments to assess the dynamic performance of the system. The nonlinearity is shown in nanometers versus the stage x and y positions. Note that the x and y scales are very different.

feedforward to the isolation system motors, they are never completely canceled. The unobservable errors due to vibration and deflections will be direct errors. The observable errors can be corrected by the fringe locking controller. At some point, the finite disturbance rejection of the controller is also an issue.

To assess the dynamic performance of the system, a grating was read while scanning the stage. Figure 9-11 shows the nonlinear phase map of a 7 cm $\times$ 0.3 cm portion of the grating used in this experiment. The grating lines are nominally aligned with the y axis. The nonlinearity is shown in nanometers versus the stage x and y posi-

tions. This data was obtained by serpentine scannning the stage. The data shown occured while the stage reference profile was at the constant velocity of 1 cm/s. The spatial resolution of the plot is 0.62 mm in x and 0.58 mm in y. The stage was stepped over by 0.62 mm in x. The data was downsampled 578 times from 10 KHz sampled data. The low pass filter used in the downsampling had a cutoff frequency of 8.7 Hz to provide bandlimited data. The shortest spatial period within the band corresponds to 1.2 mm. This filtering applies to data along the scan direction – the y axis. The data along the x axis is not spatially bandlimited but some filtering is provided by the laser beam, which is bigger than the x step size. This grating was written by the SBIL system. Since the grating has some repeatable nonlinearity, the measured nonlinearity was used to correct the data taken while the stage was scanning. Higher resolution data taken while scanning the stage along $x = 154$ mm, where the grating nonlinearity appeared lowest, was used for correction in the scanning experiments. Figure 9-12 shows the average x_{nl} of two scans along $x = 154$ mm. The stage traveled at a velocity of 1 cm/s during these 8 cm long scans except for the outer 400 μm on each side where the stage was accelerating. The data was filtered with a 50 Hz cutoff frequency, which would also filter spatial period information smaller than 0.2 mm. Since the beam is about 10 times bigger than this spatial frequency, this resolution should be sufficient. The difference between the two scans is shown in Figure 9-13. This data gives an indication of how much error there is in the measurement. The total range is less than ± 4 nm. The average data should be repeatable to less than ± 4 nm.

To assess the dynamic effects in the scanning data, the static stability of the system must be known. I refer the reader to the previously discussed Figure 9-4 and Figure 9-3 for comparison data.

For the gratings that I wrote, I typically used stage speeds of about 50 mm/s and maximum accelerations of 0.05 g. These scanning parameters provide reasonable throughput where a 100 mm wafer can be written in less than 10 minutes. Considering that the system should be allowed to equilibrate for longer than 10 minutes after loading the wafer, the actual writing time was never the limiting throughput

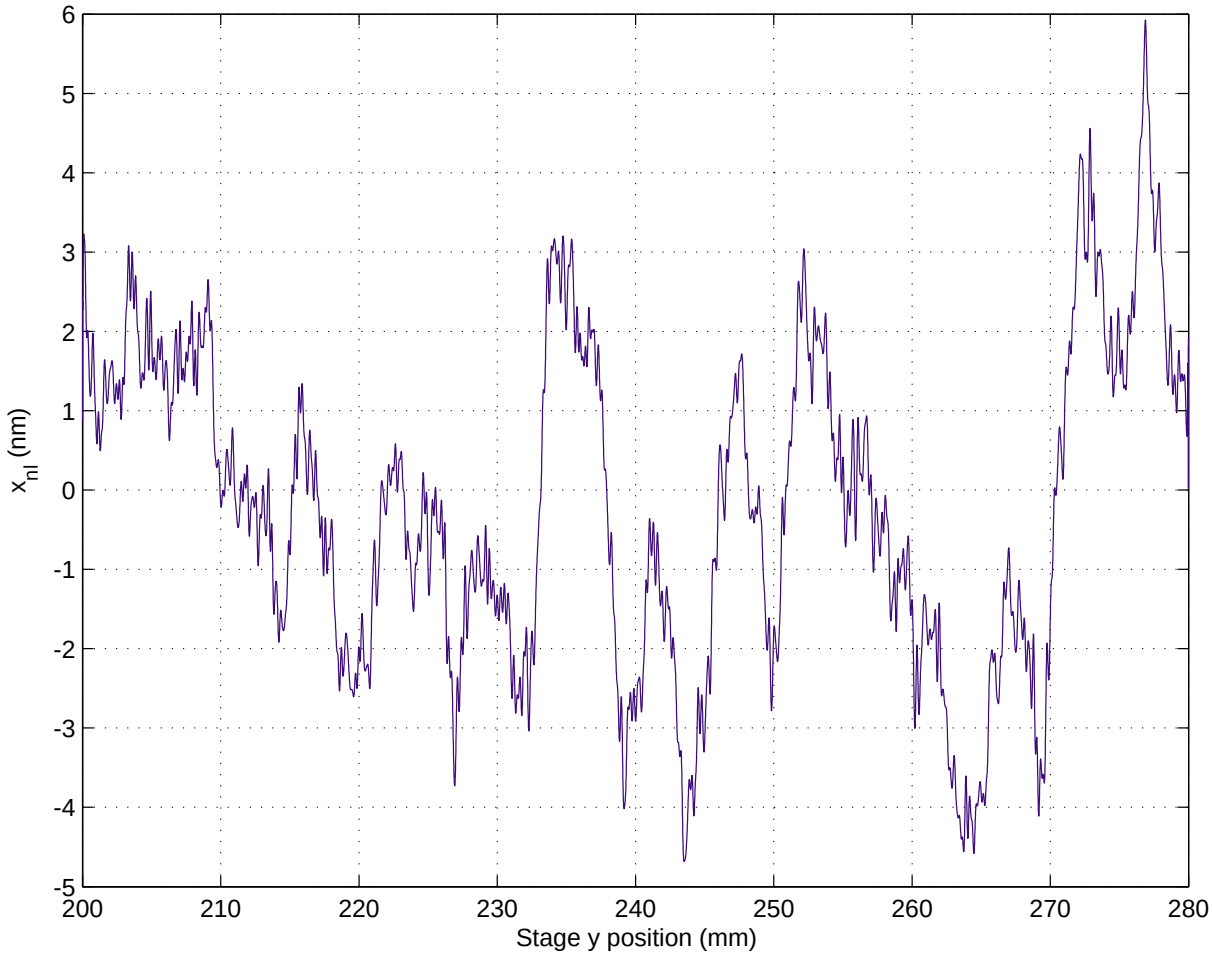

Figure 9-12: Average x_{nl} of two scans measured along $x = 154$ mm.

consideration. Furthermore, if only a few wafers are written, the setup time and substrate preparation is much more time consuming than the writing. Faster profiles are an issue only for large lots of large wafers. Robotic substrate loading would also be necessary to turn the throughput limitation into a stage speed problem.

It is of interest to demonstrate the dynamic performance and reasonable throughput capability however. Furthermore, I will demonstrate negligible dynamic errors at even higher speeds than the ones I used for writing. Figure 9-14 shows x_{ue} during a stage scan with 100 mm/s peak velocity and 0.1 g peak acceleration. The vertical lines denote the start and stop of the stage profile motion. The stage profile for the moving portion is shown in Figure 9-15. The unobservable error shows noticeable response during the stage accelerations but no obviously worse performance during

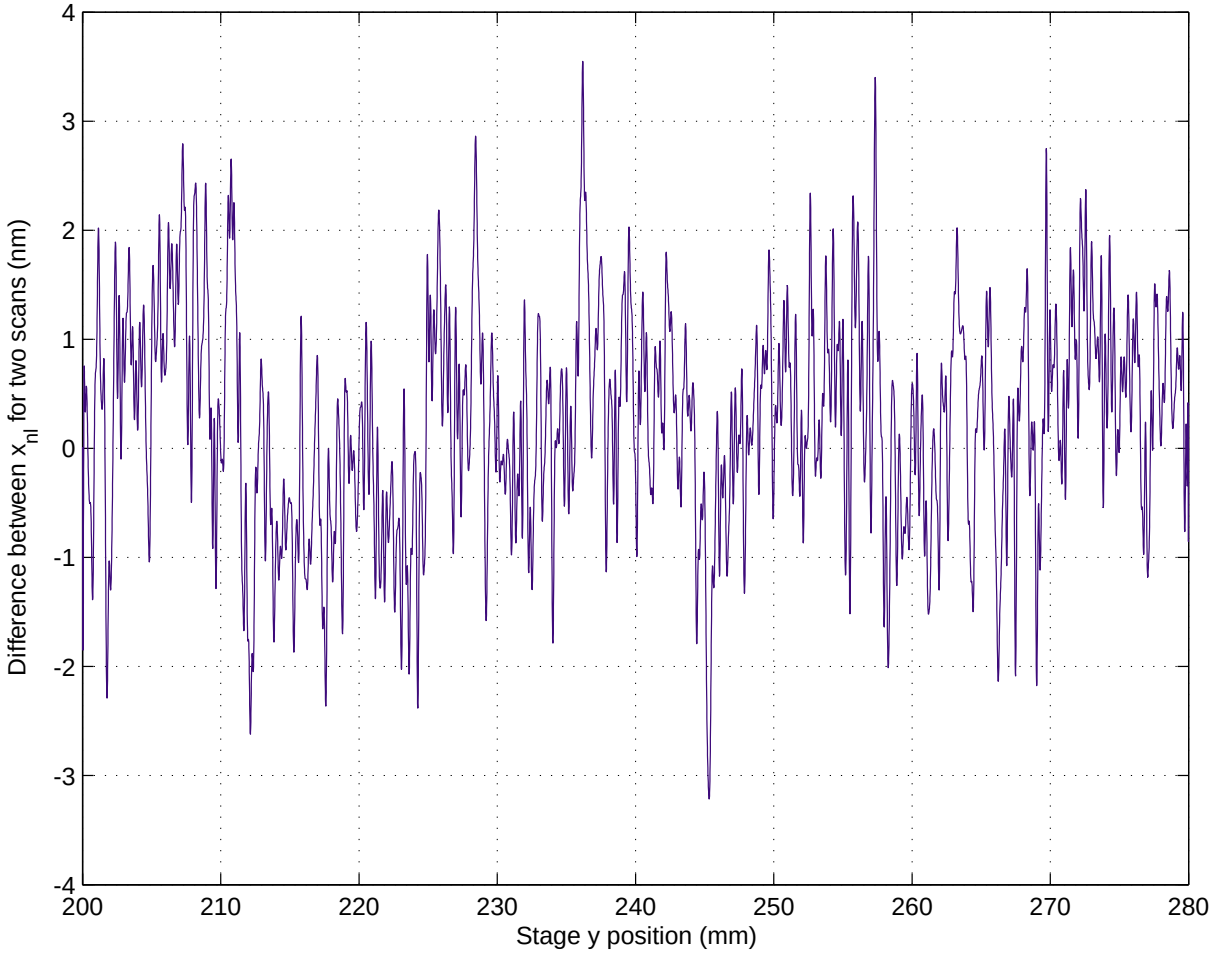

Figure 9-13: Difference between x_{nl} for two scans at 1 cm/s. The data was filtered with a 50 Hz cutoff frequency.

the constant velocity portion of the scan or after the stage stops. The data while the stage is moving is corrected using the x_{nl} of Figure 9-12 and is expected to have additional noise due to the correction having noise. Because the SBIL system exposes the substrate during the constant velocity portion of the scan, the additional x_{ue} during acceleration is not a concern. This additional error during the acceleration is mainly due to deflections of the chuck and possibly abbe offset error. The stage is shown later in this section to yaw during acceleration; any abbe offset will contribute to the error during acceleration. Figure 9-16 shows data from the repeated experiment. Again there is no obviously worse error during the constant velocity portion of the scan or after the stage stops.

During the scan, the stage has significant additional error in the scan axis and

the perpendicular scan axis. The stage error during the experiment of Figure 9-14 is plotted in Figure 9-17. The error in the y axis during the constant velocity is largely associated with motor ripple force as discussed in 8.4. The x axis motion is coupled with the y axis motion as indicated by the 300 nm x axis error. The additional x axis error is correlated with the stage y axis control effort. The stage yaw during acceleration may explain this coupling. The additional x axis error is an extra disturbance for the fringe locking. The fringe locking error during the same time is plotted in Figure 9-18. Within 0.1 sec of the beginning of constant velocity portion of the scan the fringe locking error is ± 0.4 nm peak to valley until the stage decelerates for the Gaussian filtered data. Once the stage has stopped and settled the fringe locking error is $\pm$ 0.2 nm peak to valley. The additional error is still small compared to the unobservable error during the constant velocity portion of the scan. However, the additional error can easily be wiped out by adding an integral-lag term to the controller. Moreover, the power spectrum shows that noise power exists at the low frequency range where the gain can easily be increased. Reducing the x axis error would also reduce the fringe locking error. At this point, since the unobservable error is so much larger than the x_{fle}, the better controller performance would not significantly improve the writing performance.

The feedforward of the stage accelerations and positions to the vibration isolation motors is critical to the system working at all. For long scans, even at the very slow stage velocity of 1 cm/s, the beam steering system fails due to lost dynamic range. For short and long scans, the system can also bang into the isolation hard stops. This causes ringing as can be seen in Figure 9-19. If the system bangs into the hard stops prior to entering the constant velocity portion of the scan, the vibrations will unacceptably diminish the contrast of the exposure. The stage for this data was scanned with the 100 mm/s, 0.1 g profile in Figure 9-15.

To prevent the stage from crashing into the hardtops for the 8 cm scan length, the peak velocity was slowed to 0.05 m/s and the peak acceleration was slowed to 0.05 g according the profile of Figure 9-21. The plot of the unobservable error for this profile with the isolation feedforward off is in Figure 9-20. There is no significant

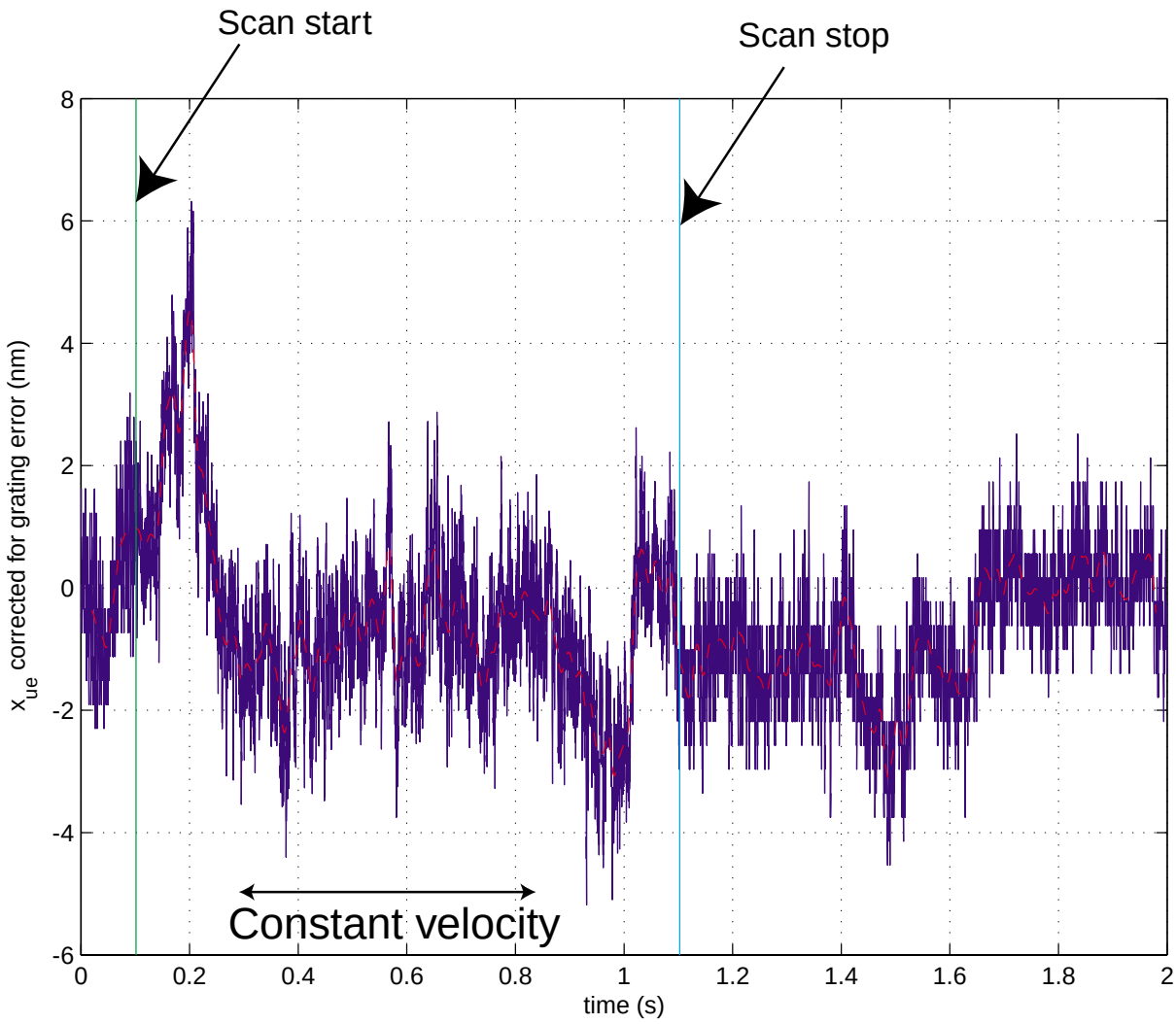

Figure 9-14: Unobservable error while the stage is scanning with 100 mm/s peak velocity and 0.1 g peak acceleration. Raw data and Gaussian filtered data are shown. The vertical lines denote the scan start and stop.

increase in x_{ue} despite the feedforward being off. The payload does acquire significant extra vibrations but they are still too small to show a significant effect. The payload vibrations do worsen the stage control. The stage error during the 50 mm/s scan profile with the feedforward on is shown in Figure 9-22. The comparison plot when the isolation feedforward is off is shown in Figure 9-23. Both the x and y axes have significant extra error with the isolation feedforward off. The stage control has bandwidths of 25 Hz and 40 Hz for the x and y axes respectively; the disturbance rejection is not sufficient to reject the 2 Hz rocking of the granite entirely.

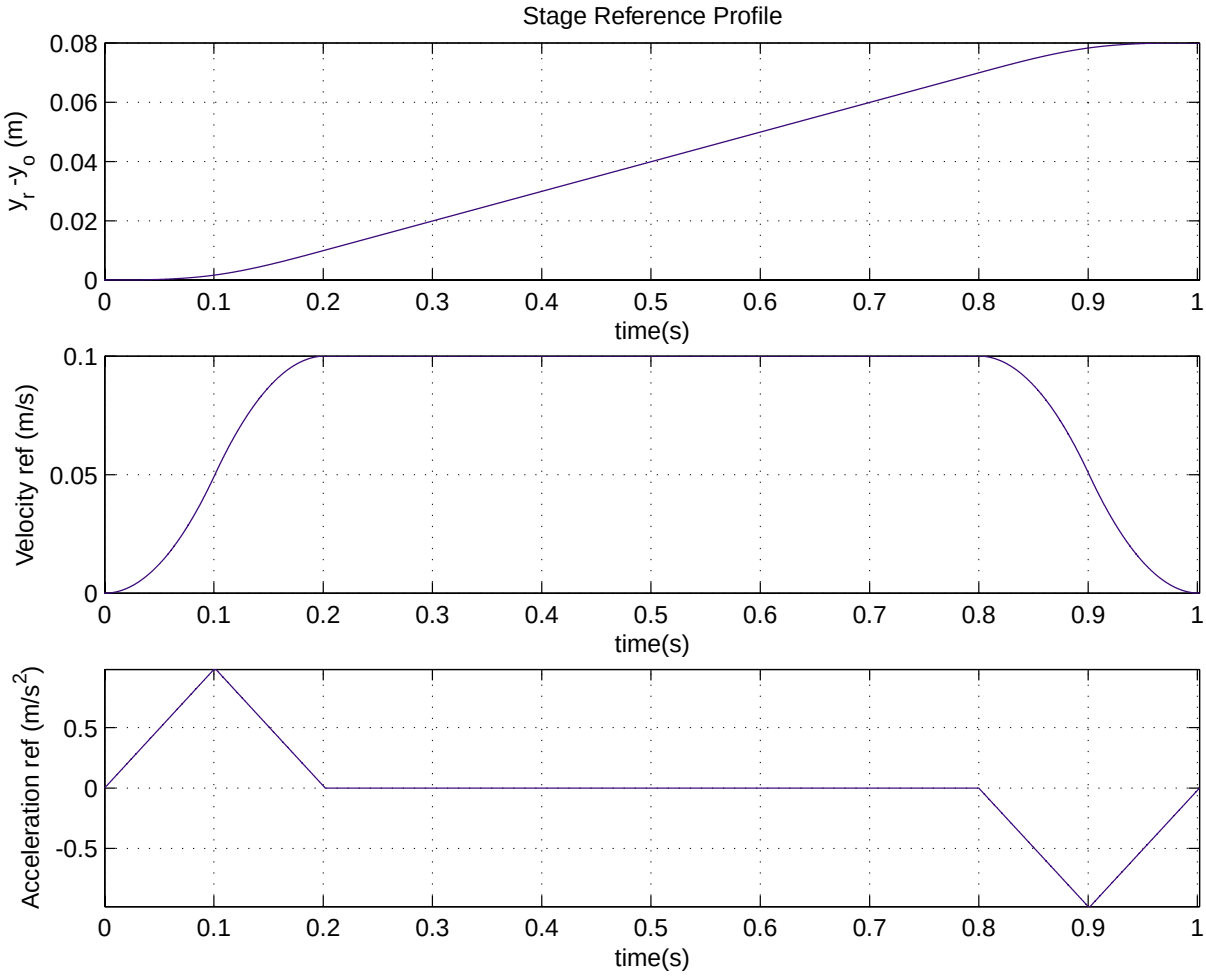

Figure 9-15: Stage reference profile for an 8 cm scan length (top plot). The middle plot shows the velocity reference with the maximum scan velocity of 0.1 m/s. The bottom plot is the acceleration reference with maximum acceleration of 0.1 g.

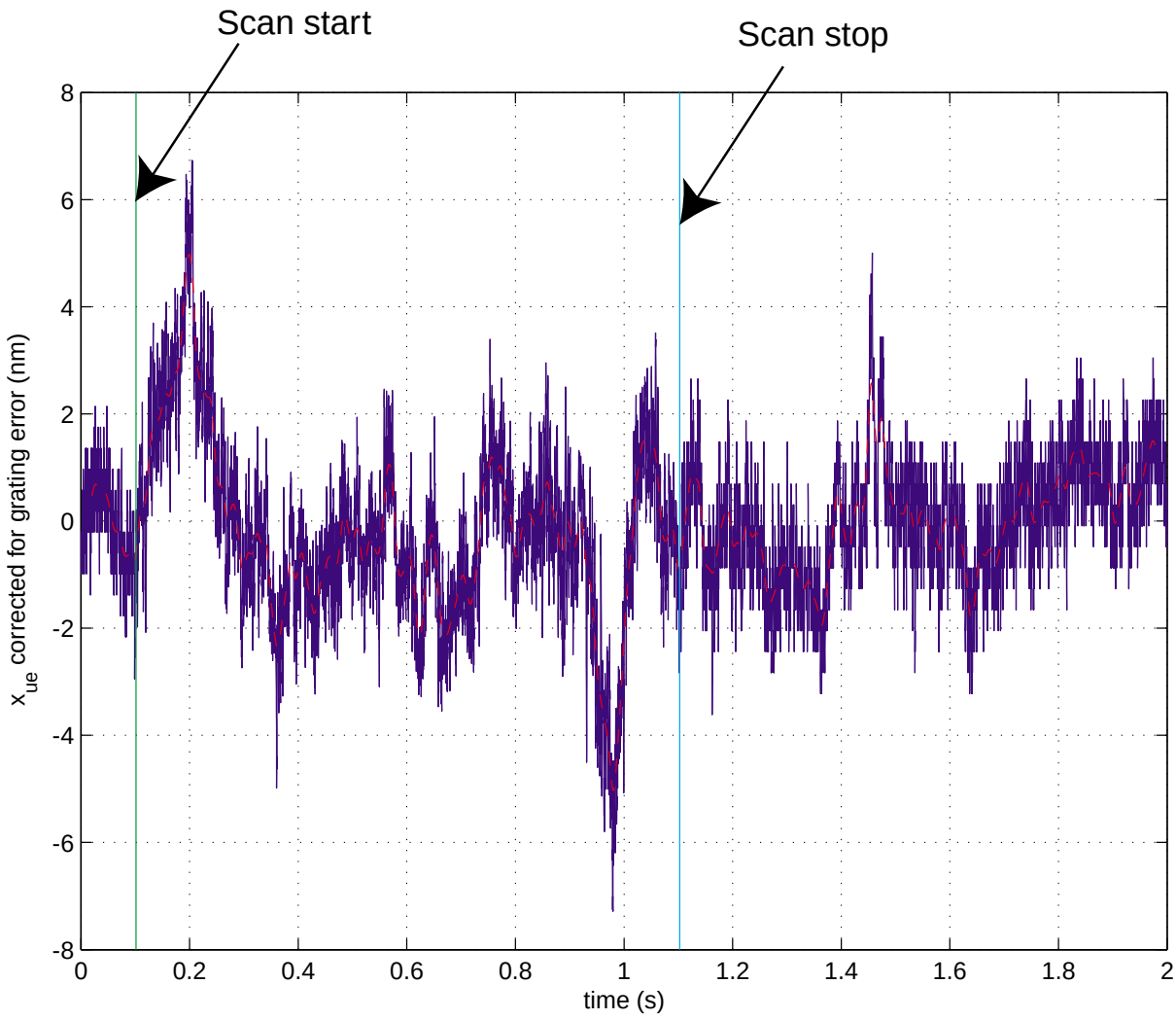

Figure 9-16: Unobservable error, x_{ue} while the stage is scanning. The same scan parameters as those for Figure 9-14 were used.

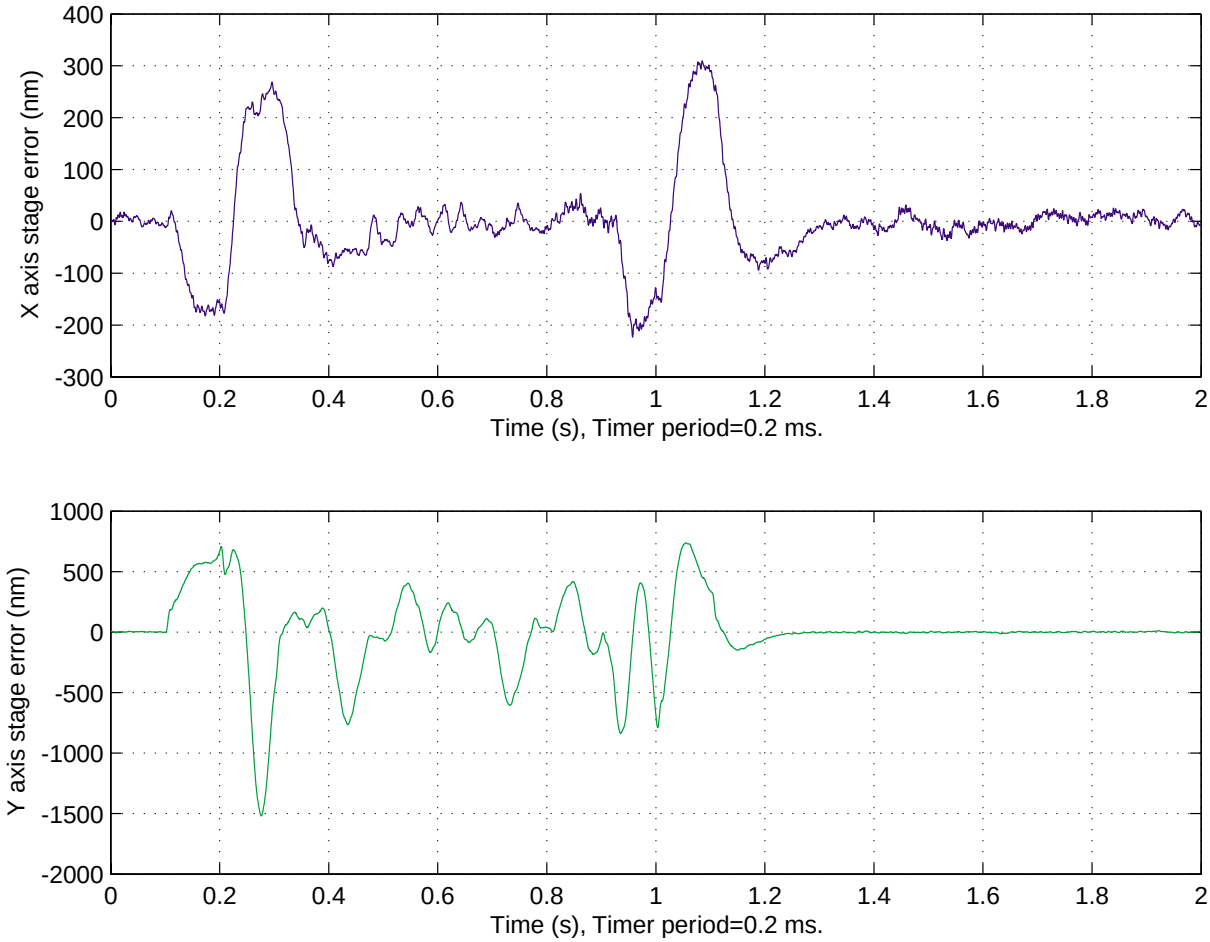

Figure 9-17: Stage error during the same time as data of Figure 9-14. The stage reference profile was 100 mm/s scan velocity, 0.1 g peak acceleration. The stage errors for both the x and y axis increases when the stage accelerates in the y axis.

With the feedforward off, the payload will accelerate approximately by the stage acceleration times the ratio of stage moving mass to the granite moving mass. Since the stage y moving mass is about 1/20 the payload mass, the granite accelerates approximately 1/20 the stage acceleration. When the stage nominally stops accelerating the granite motion slowly damps out. Because of the accelerations, parts will deflect. Payload components of most interest include the metrology block and its optics and the x axis interferometer head.

The payload rocking can be simulated given the stage accelerations assuming one dimensional motions. The transfer functions of payload acceleration to stage

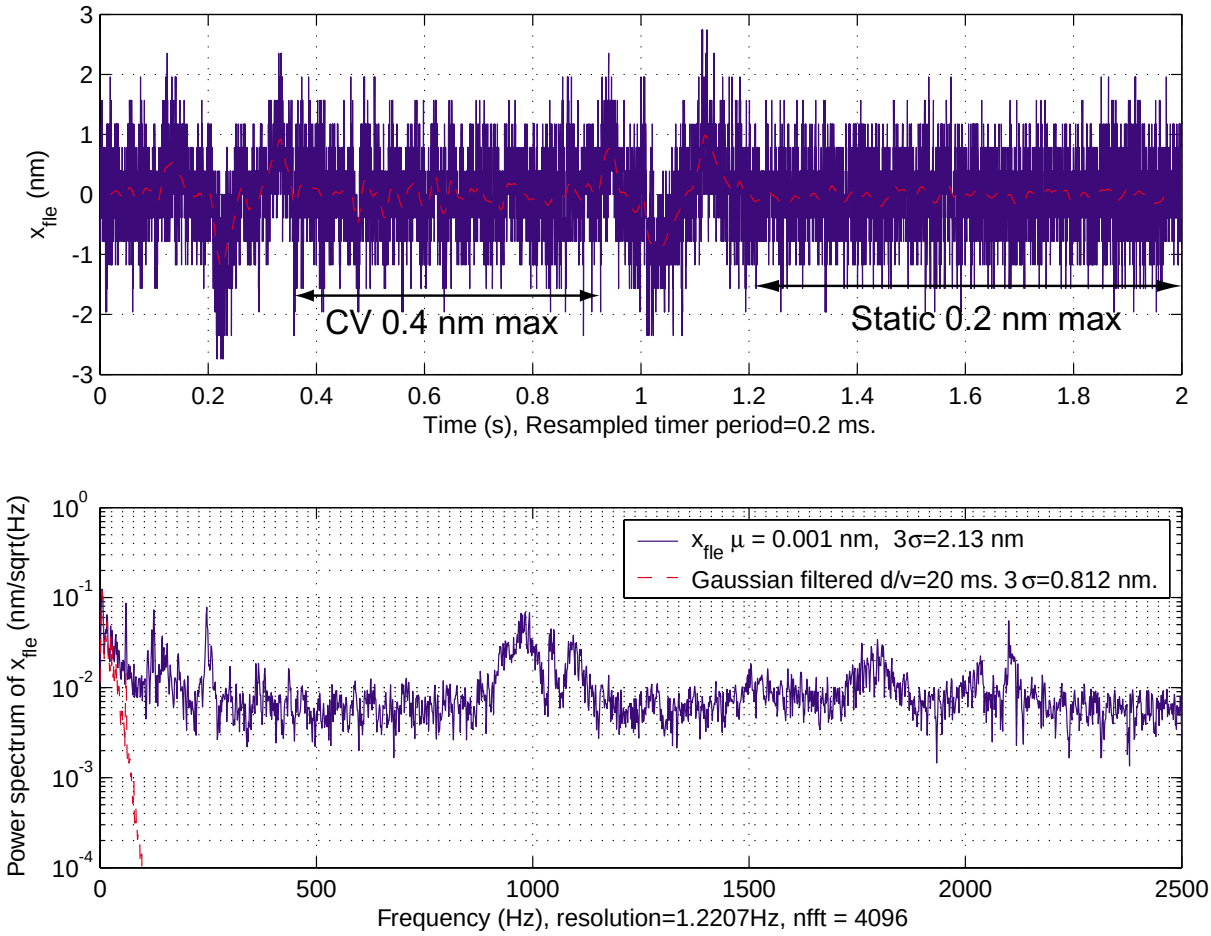

Figure 9-18: Fringe locking error during the same time as the data of Figure 9-14. Additional fringe locking error occurs because of additional stage x error.

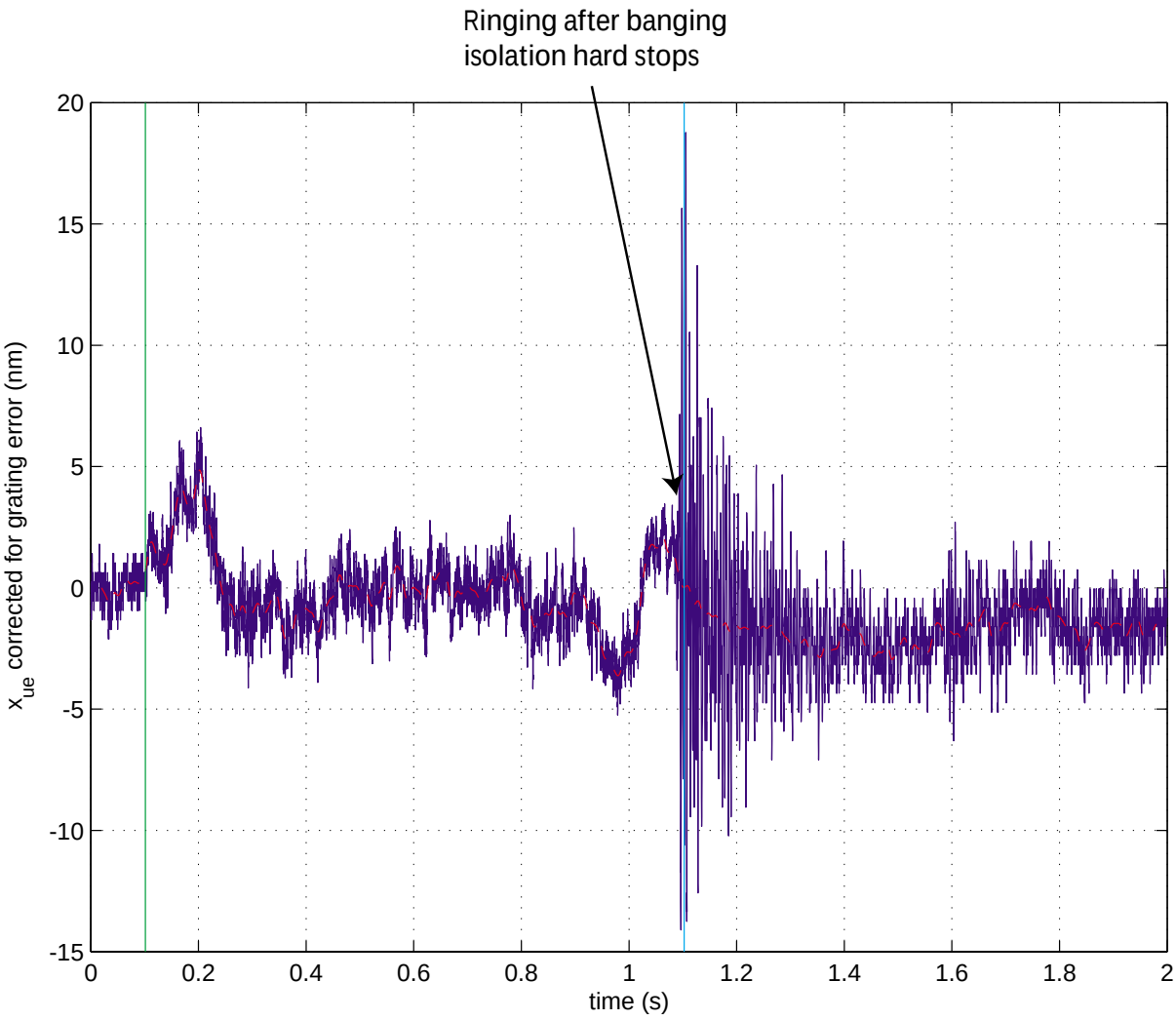

Figure 9-19: The unobservable error during a 100 mm/s, 0.1 g peak acceleration scan when the feedforward is off.

acceleration is given by

$$\frac{A_1(s)}{A_s(s)} = \frac{s^2 m_s/m_1}{s^2 + 2\zeta_1\omega_{n,1}s + \omega_{n,1}^2}. \tag{9.9}$$

Here, $A_1(s)$ is the Laplace transform of the payload accelerations, ζ_1 is the damping factor of the isolation system, $\omega_{n,1}$ is the natural frequency of the isolation system, and the ratio m_s/m_1 is the ratio of stage to payload mass.

Figure 9-24 simulates the payload accelerations using Equation 9.9 and assuming the stage acceleration profile of Figure 9-21 without isolation feedforward. The parameters are $\omega_{n,1} = 2\pi \times 2$ rad/s, $\zeta_1 = 0.05$, and $m_s/m_1 = 1/20$. The simulated payload

acceleration is a maximum of 2.8 mg. Although the payload accelerations remaining after the stage completes accelerating depends on the duration and magnitude of the stage accelerations, for many profiles the maximum payload accelerations can be approximated by the maximum stage acceleration times the ratio of m_s/m_1. Using this estimation, the predicted payload acceleration was 2.5 mg.

If the payload is accelerating at 2.8 mg as expected for the experiment in Figure 9-20 and the coupling between a metrology block optic and the metrology frame is described by a resonant frequency of 500 Hz as found in Section 8.2, the expected amplitude of the vibration is 2.8 nm. However, the vibration is not visible at this level in Figure 9-20. It is hard to say what additional vibration is there because the static errors are too large. However, any dynamic errors are safely under a nanometer. Thus, the metrology block sensitivity to the y axis accelerations is better than for the x axis accelerations. This was expected because the optics on the metrology block are mirror symmetric about the y axis. Any deflections due to y axis acceleration will be balanced on both sides of the interferometer and not appear as an error. Since the accelerations of the payload with the feed forward off is much greater than the system would experience with the feedforward on, the stage induced payload acceleration error is negligible for the operating condition.

The accelerations of the stage during writing is also a concern because the chuck will distort. The acceleration error from the 0.1 m/s, 0.1 g scan computed from the x and y axis error in Figure 9-17 is shown in Figure 9-25. The acceleration error was computed using the filter discussed in Section 8.4 with the transfer function shown in Figure 8-49. Both the x and the y axis have acceptable extra acceleration during the constant velocity portion of the scan. During the acceleration portion, the y axis has a maximum acceleration error of 3 mg but the spike in acceleration occurs in push pull pairs over about 10 ms. The force impulses integrate to impart very little momentum to the payload. It is important for the stage acceleration to closely follow the acceleration reference since the feedforward acceleration signal to the isolation system is the acceleration reference. The acceleration error shown is very much acceptable for the reference to be used as the feedforward signal. It was important to also feedforward

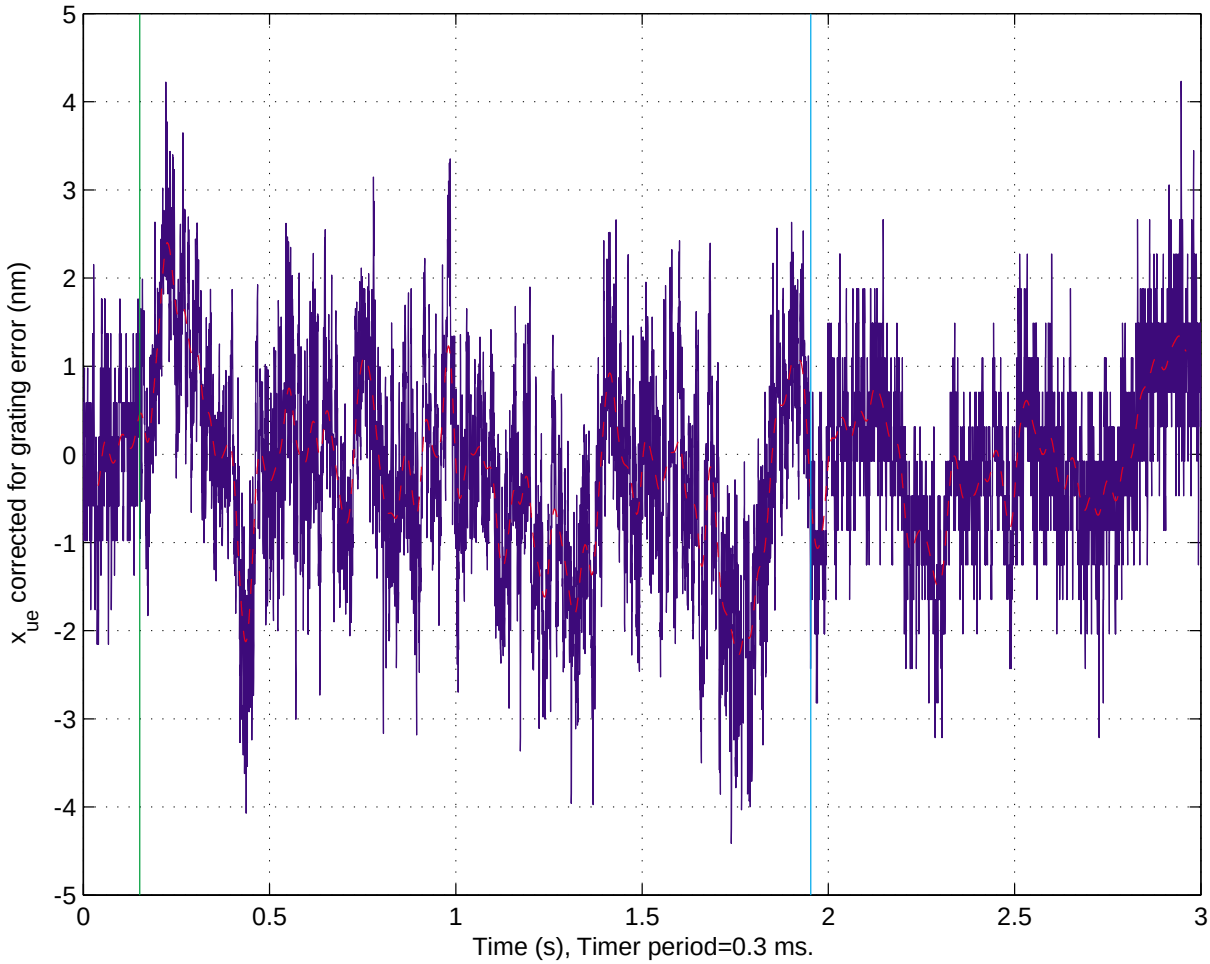

Figure 9-20: The unobservable error during a 50 mm/s, 0.05 g peak acceleration scan when the feedforward is off.

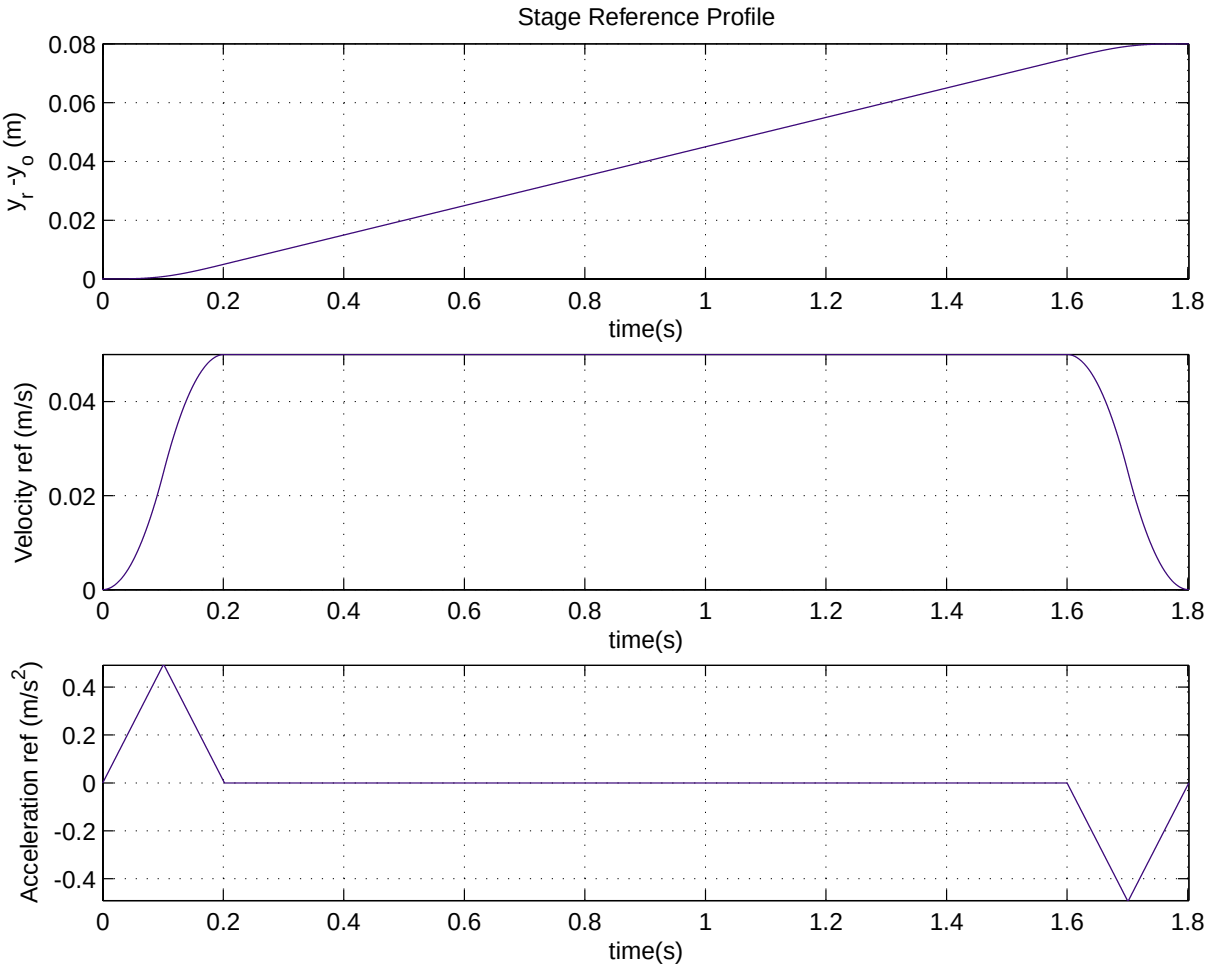

Figure 9-21: Stage reference profile for an 8 cm scan length, maximum acceleration of 0.05 g, and scan velocity of 0.05 m/s.

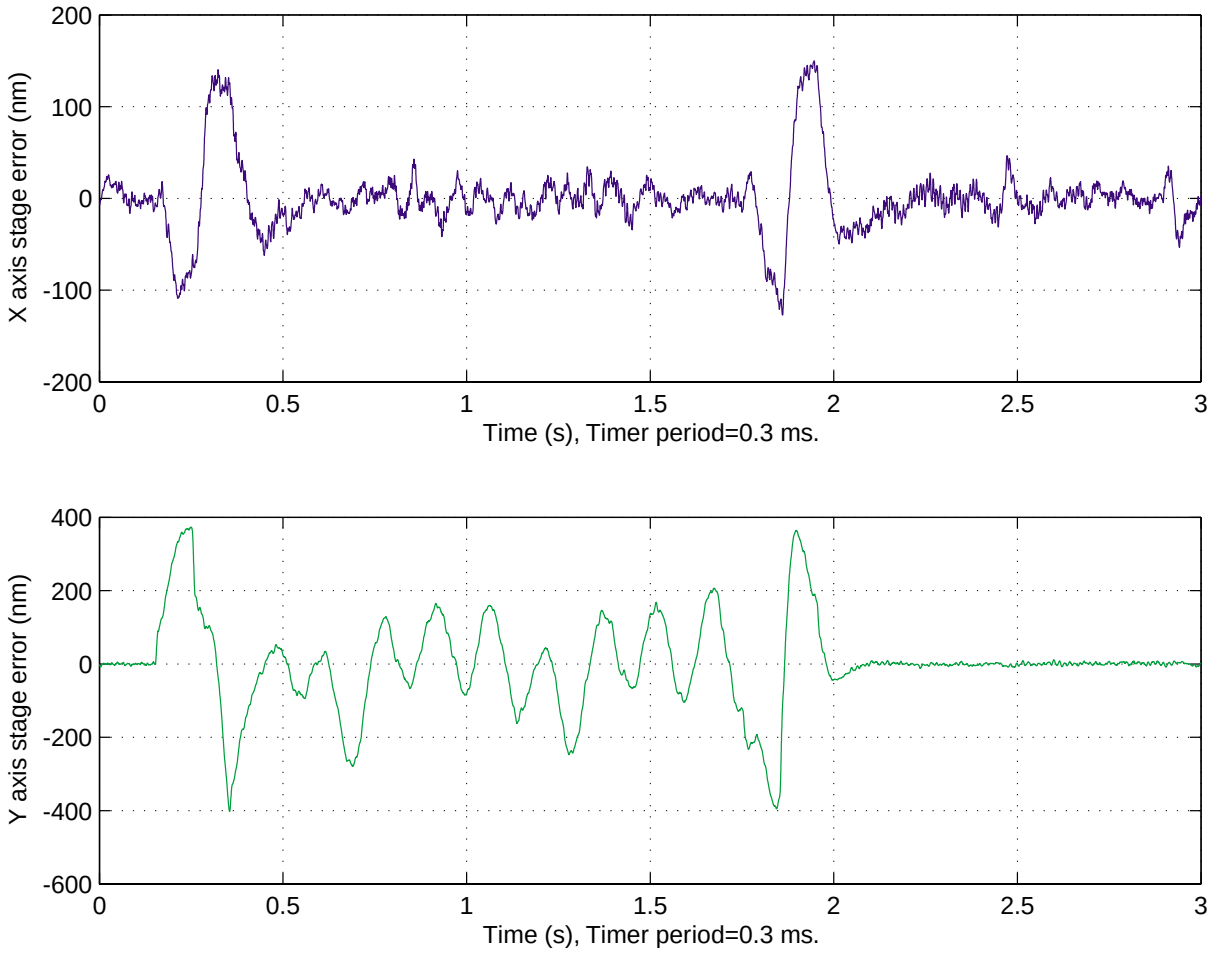

Figure 9-22: The stage error during the 50 mm/s scan profile when the isolation feedforward is on.

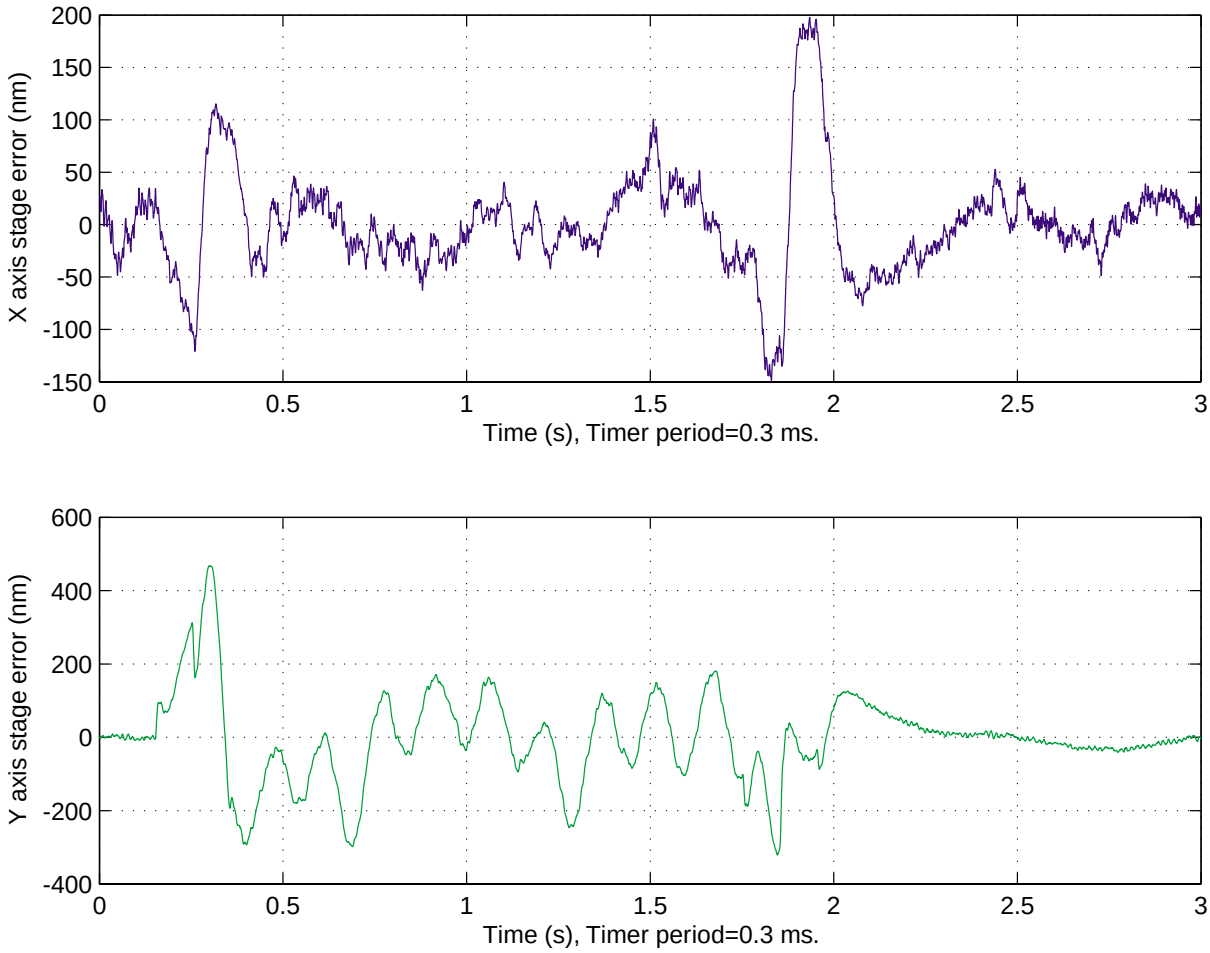

Figure 9-23: The stage error during the 50 mm/s scan profile when the isolation feedforward is off.

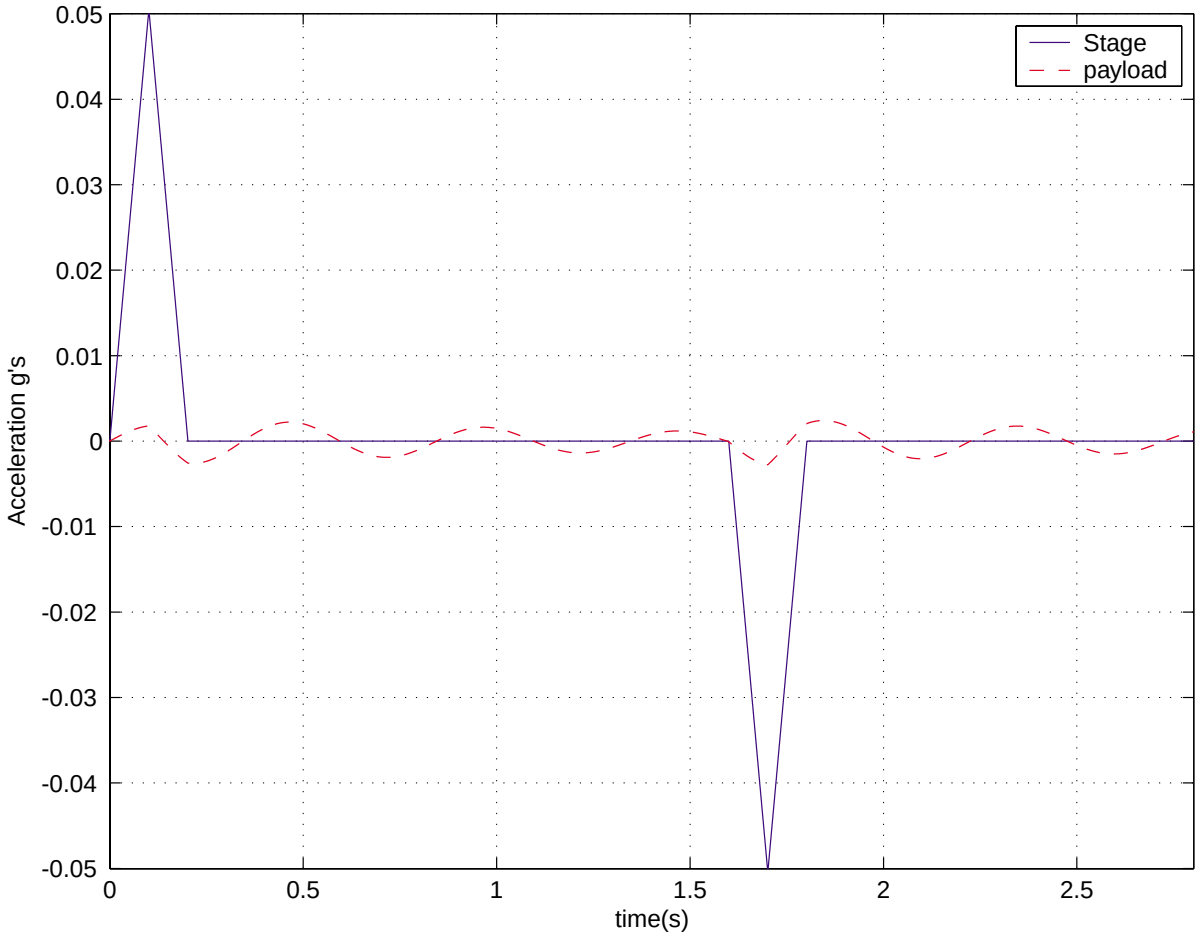

Figure 9-24: Simulated payload accelerations from the stage accelerations with the feedforward off.

the acceleration reference to the stage controller to achieve this performance. The ability for the stage to track the acceleration reference is limited largely by the ripple force discussed in Section 8.4. Most of the raw acceleration error is at high frequency as evidenced by the much lower accelerations for the Gaussian filtered data. During the constant velocity portion of the profile, the Gaussian filtered data has maximum magnitudes of 85 μg for the x axis and 240 μg for the y axis. Once the stage has stopped and settled, the maximum magnitude of the Gaussian filtered data is 25 μg for the x axis and 15 μg for the y axis. Although the accelerations do get much worse during the constant velocity profile, the system is rigid enough that the accelerations are still too small to be a concern for even 0.1 nm errors.

The stage and isolation system have been verified to have the capability to generate

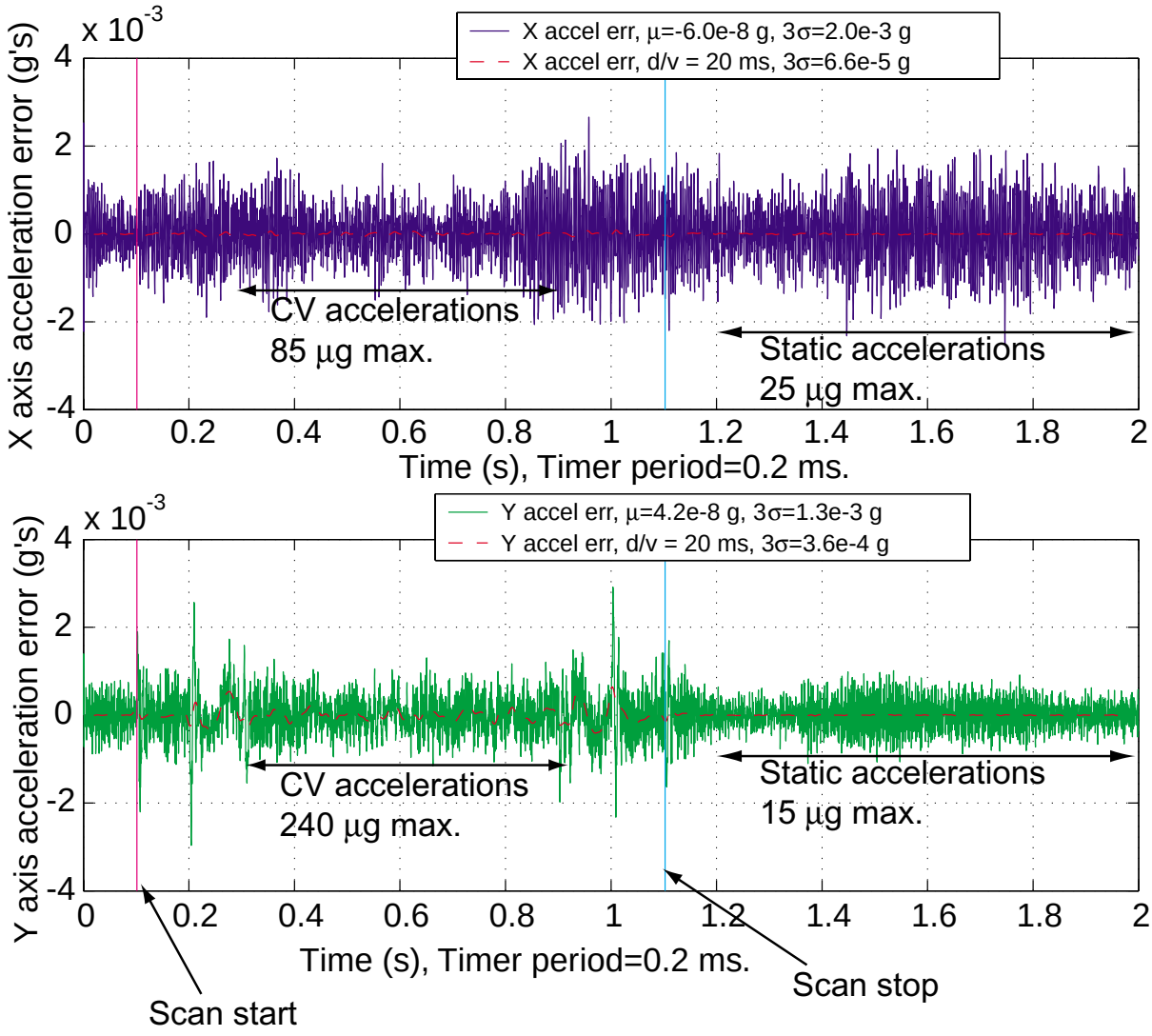

Figure 9-25: Stage acceleration error computed from the position error data of Figure 9-17. The stage reference profile was 100 mm/s scan velocity, 0.1 g peak acceleration. The vertical lines denote the start and stop times for the scan. The maximum accelerations during the constant velocity (CV) and static portions of the scans are noted.

the forces necessary to scan the stage at 0.3 g and 300 mm/s. It would be ideal to use a 300 mm grating substrate to evaluate the performance for the faster profiles. However, the processing capability for larger than 100 mm wafers was not available. A scan at 0.25 g and 300 mm/s does not leave much length to evaluate the constant velocity portion of the scan on the 100 mm substrates. Nevertheless, the unobservable error from this scan is shown in Figure 9-26. The Gaussian filtered data uses the d/v parameter of 6.7 ms, which is consistent with a 300 mm/s scan with 2 mm beam diameter. During acceleration there is an increase in the unobservable error but during the small constant velocity section and after the stage stops, there is no obvious increase in the error. The asymmetry of the unobservable error when the stage is accelerating versus when it is decelerating is probably associated with the strain distribution of the chuck. The approximately 50 nm/g of error is partly due to the abbe offset errors and partly due to the strain of the chuck.

Figure 9-28 shows the stage yaw interferometer measurement, θ_{Zsm} when the stage was scanned in the y axis. The peak velocities and accelerations are shown in the legend. The 1 mm/s scan is slow enough that there are negligible dynamic effects except in the very tiny region where the stage accelerates. The repeatable yaw over the plotted range is about 2 μrad peak to valley. Some of this measurement may be due to the stage mirror flatness. When the stage is accelerating, the stage has additional yaw proportional to the stage acceleration. For the higher velocity and higher acceleration scans the deviations at the end of the scan from the slow scan corresponds to when the stage was accelerating. When the stage motor forces are not centroided about the stage center of mass, the stage frame is torqued when the stage accelerates. Since both y axis motors are wired in parallel the stage is not configured to balance the reaction yaw forces. The stage yaw due to the motor forces will be dependent on the x axis position since the x axis position changes the center of mass. The stage yaw for the 50 mm/s scan is essentially the same as the slow scan except when the stage is accelerating. During acceleration, the stage yaws by about 23 μrad per g of acceleration. The 100mm/s scan shows a small and tolerable decrease in stage yaw stability during the constant velocity portion of the scan. This scan profile

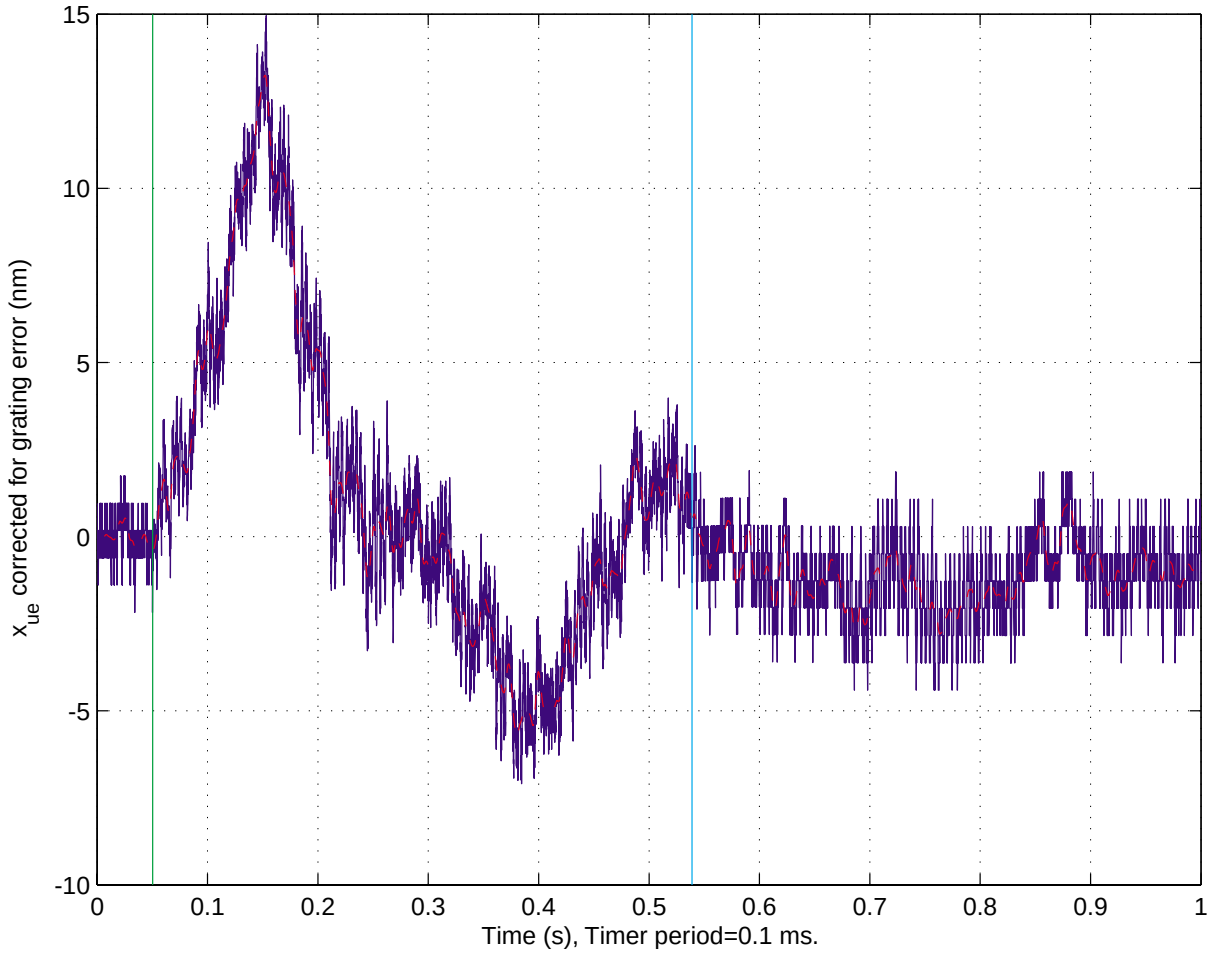

Figure 9-26: The unobservable error during a fast scan. The stage reference profile was 300 mm/s scan velocity, 0.25 g peak acceleration. The vertical lines denote the start and stop times for the scan.

is shown in Figure 9-15. The additional yaw instability is likely due to additional y axis control effort. The 300 mm/s scan is shown in Figure 9-27. During most of this 300mm/s scan the stage is accelerating except for the middle 14 mm. Irregularities in θ_{Zsm} of about 0.5 μrad are evident. The scan speed of 300 mm/s is much faster than required. Most importantly, the yaw stability appears very good under more usual operating profiles such as the 50 mm/s profile. Modifying the system to control each of the y motors independently might be important to achieve very high throughput. The independent y motor control would also allow correction of the repeatable stage yaw at the several μrad level. The abbe yaw offset could also be determined very accurately by slowly yawing the stage and observing the errors. The effect of the yaw

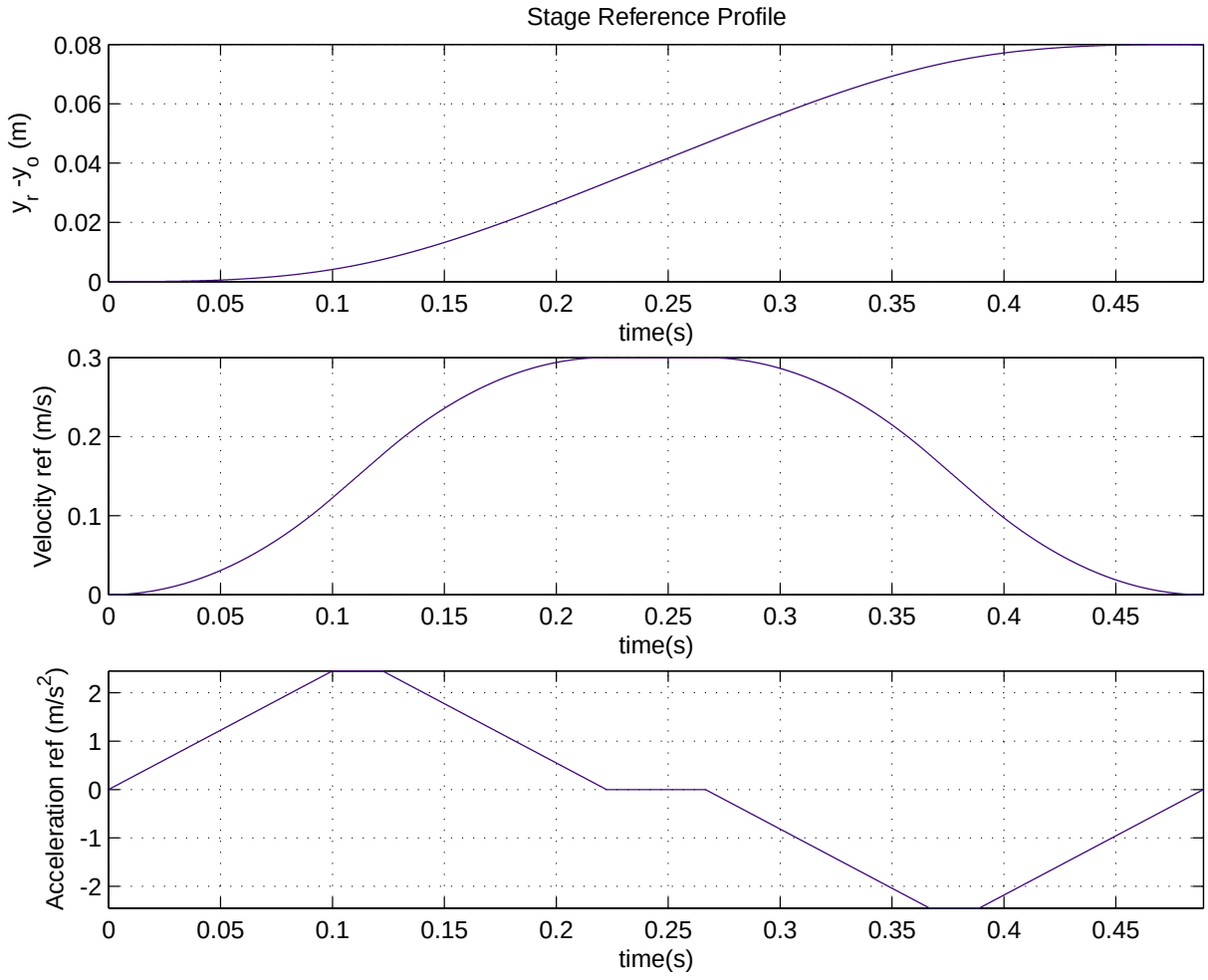

Figure 9-27: Stage reference profile for an 8 cm scan length, maximum acceleration of 0.25 g, and scan velocity of 0.3 m/s.

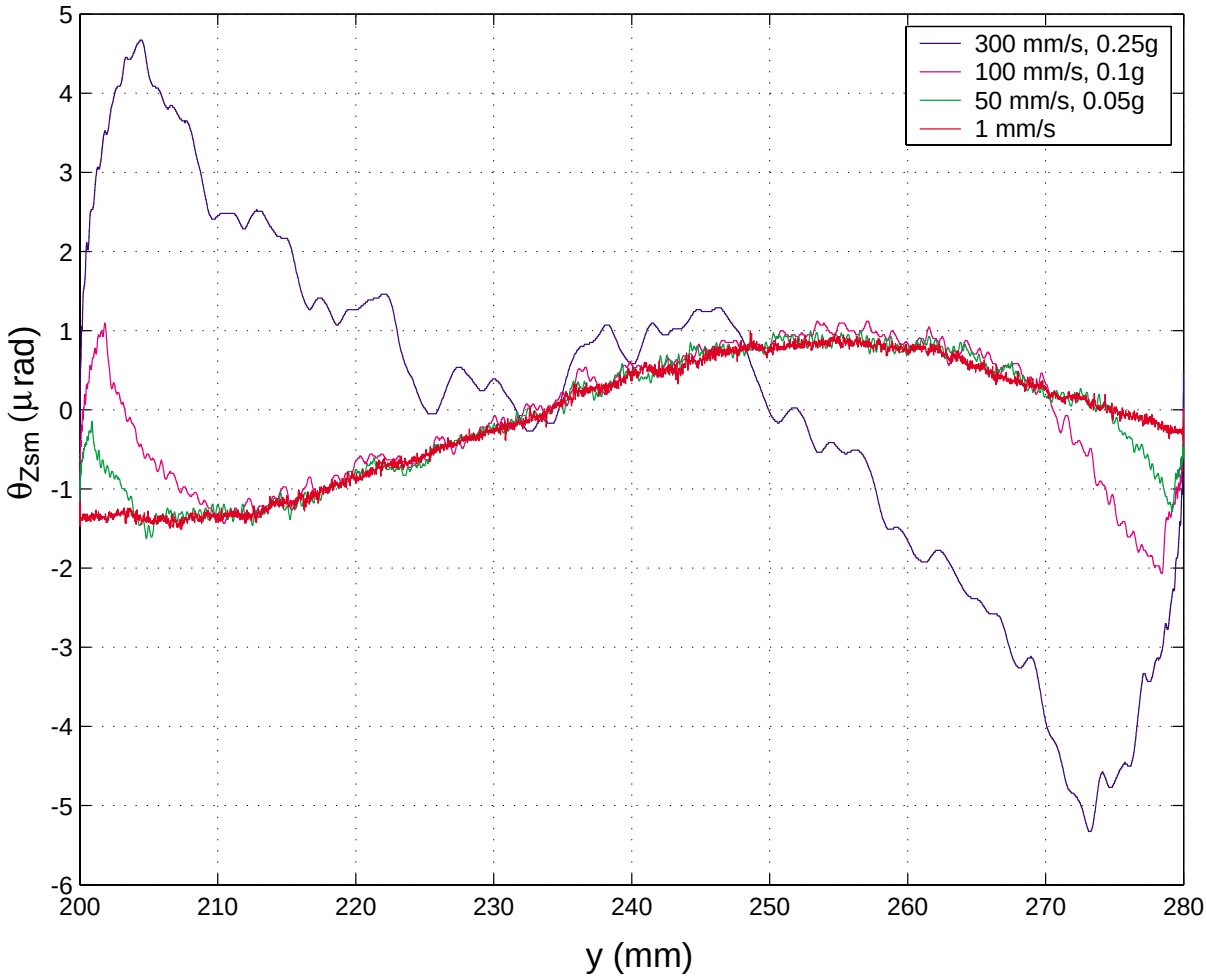

Figure 9-28: Stage yaw interferometer measurement for different scan profiles.

right now is largely a small contrast loss. The repeatable errors will show up in the error map produced from the future calibration and will be readily corrected.

Some of the error during acceleration is due to the stage Abbe yaw error. Since the Abbe yaw offset was determined to be ±1 mm, the Abbe yaw error would account for at most 23 nm/g. The stage is expected to have Abbe pitch errors less than the Abbe yaw since the y motor forces nominally don't pitch the stage and the stage pitch offset, Δ_z, (per Figure 4-9) is estimated to be smaller – about ± 400 μm.

The approximately 50nm/g of error, which corresponds to an effective resonant frequency of 2300 Hz, is really remarkable. To help put this in perspective, before installing my chuck design, the system had an unobservable error of 2600 nm/g for the y axis acceleration! The relatively poor performance of the old chuck is largely

attributed to the significant compliance in its interferometer mirror mounts.

The fact that the acceleration is perpendicular to the grating helps somewhat. However, there is always strain perpendicular to the stretching direction too. The ratio of the strain in the perpendicular direction to the strain in the pulled direction is the Poisson's ratio (0.23 for super Invar) at best. Because of the flexure mounting of the chuck, the strain distribution in the chuck is not expected to be very one dimensional for stage accelerations. Future work might characterize the strain due to x and y axis accelerations over 300 mm wafers. However, I expect the chuck will be more than adequate for better than Angstrom level vibrational errors with the level of disturbances present. Wafer loading and equilibration time aside, the motor heating is expected to limit the maximum throughput rather than vibration.

9.4 Periodic errors

The periodic error in interferometry has been a topic of extensive research interest. The periodic error arises due to polarization and frequency mixing [10, 84]. The polarization mixing error results when the interferometer allows light of the wrong polarization to leak into the wrong path of the interferometer. For instance, if the beam splitter in the interferometer has some finite extinction ratio there will be polarization mixing. The frequency mixing arises because the two frequencies are not perfectly orthogonally polarized. The modeling of the periodic error based on the mixing and the nonideal properties of optics in the interferometer has been studied [30, 112, 17]. The modeling has shown errors periodic in the first and second harmonic. Various researchers have measured and investigated compensating periodic errors [47, 48, 114, 6]. Novel interferometer designs with inherently low nonlinearity have also been demonstrated [113, 62, 117]. These interferometer designs appear to have inherently worse thermal stability and alignment difficulty however.

In the original error budget, the stage interferometer was budgeted to have ± 2 nm of error due to polarization mixing per the Zygo specification. This was the single largest error term. Therefore, it was of interest to explore the magnitude of the

nonlinearity of the phase measurement. Fortunately, the measured nonlinearity in the SBIL system's x axis interferometer was measured to be ± 0.6 nm peak-to-valley making this error much less of an immediate concern. After some advances in other areas, it will be important to achieve nonlinearities of 0.1 nm for SBIL. In this section, I discuss the measurement of the periodic errors. Then in section 9.4.1, I develop a writing and reading strategy for SBIL that is immune to periodic errors.

To measure the periodic errors, I first scanned the stage perpendicular to the grating and removed the linear grating phase to get x_{nl}. The data is plotted in Figure 9-29. I chose the scan velocity of 127 μm/s such that the first harmonic of the stage interferometer nonlinearity would show up at 800 Hz. The nonlinearity is more clearly revealed by comparing the power spectrums when the stage is scanning to when the stage is stationary. Figure 9-30 compares the power spectrums when the stage is stationary and when the stage is moving at 127 μm/s. The top plot shows the power spectrums of x_{nl} and the bottom plot shows the ratio of the moving/stationary power spectrums. The clear peaks at 800 Hz and 1600 Hz were expected and correspond to the first and second harmonics of the stage interferometer. These harmonics are not sharp because the velocity is not perfectly constant – there was stage error of 29 nm 3σ. The peaks at 630 and 1260 Hz were not expected. These frequencies correspond to the second and fourth harmonics of the $PM4$ interferometer. Additional higher harmonics are also visible in the data. The $PM4$ peaks are very sharp because x_4 has a relatively constant velocity – the x_4 error is less than 4 nm 3σ. Also, from the bottom plot of Figure 9-30 it is seen that scanning the stage pulled noise power out of the lower frequency band where the stage error has the most power.

I obtained a map of the nonlinearity of the stage interferometer and the PM_4 interferometer to quantify the magnitude of these errors. Figure 9-31 shows the first step of this process. In this figure, I have plotted the x_{nl} as a function of the modulus of PM_x after division by $p = 512$. Since the stage was scanning at a constant velocity, many data points in each phase bin were obtained. Figure 9-32 shows the number of points obtained versus phase bin. More than 60 points in each bin are used to calculate the average. The Fourier transform of the average x_{nl} produces coefficients

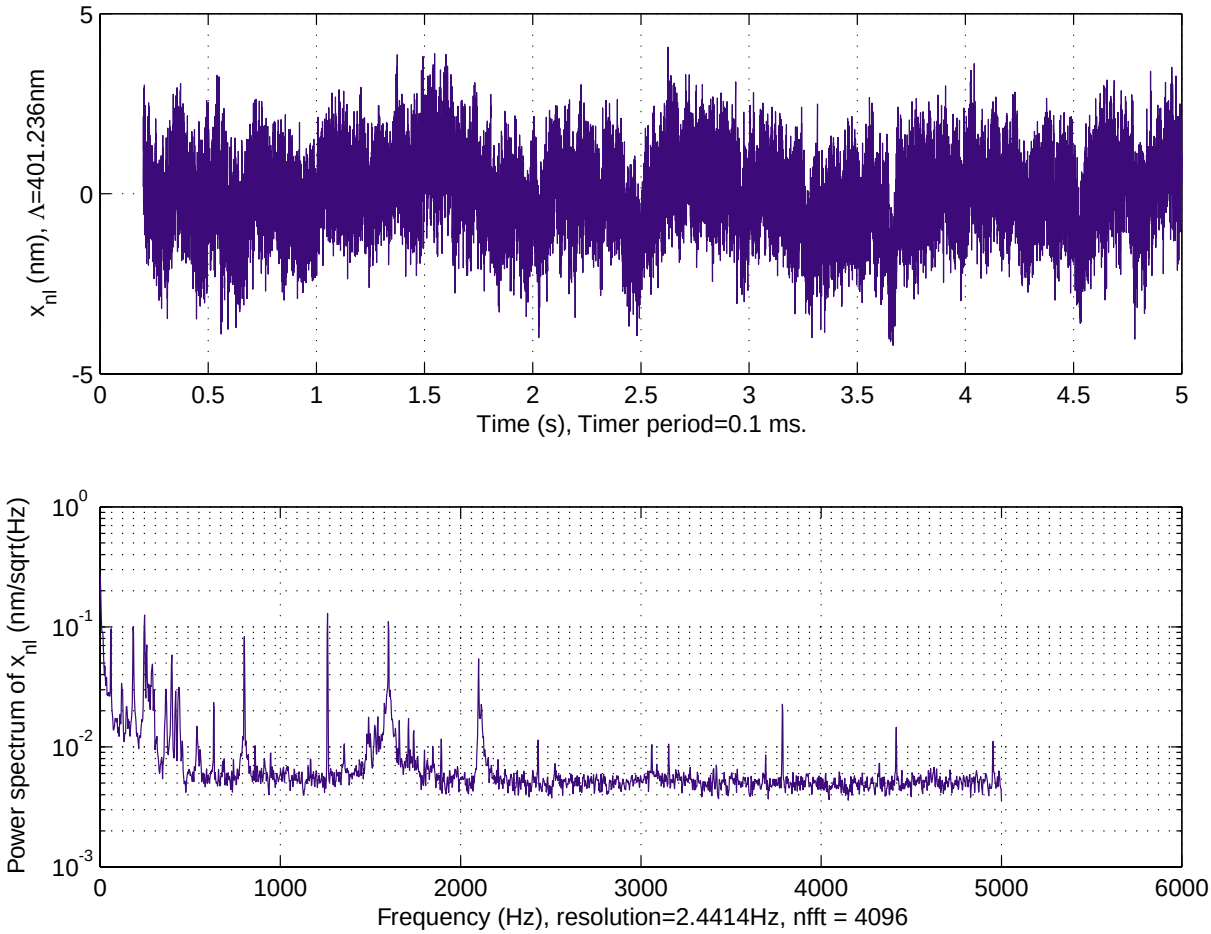

Figure 9-29: Plot of x_{nl} when the stage is scanning perpendicular to a grating at 127 μm/s. The top plot is x_{nl} versus time and the bottom plot shows the power spectral density of this data.

with the magnitudes plotted in Figure 9-33. The first and second harmonics have strong contributions as expected. Figure 9-34 shows the data used in the FFT and the reconstruction by the inverse FFT using the DC component and the first two harmonics. The reconstruction clearly shows that the DC and the first two harmonics capture most of the error. The nonlinearity of the stage interferometer is thus shown to be $\pm$ 0.6 nm. Its standard deviation is calculated to be 0.35 nm. To confirm that the algorithm used to obtain the FFT coefficients effectively removes the nonlinearity. I corrected the x_{nl} data using the map obtained from the FFT coefficients. The data and the corrected data is shown in 9-35. The power spectrum of the corrected data shows that 800 Hz and 1600 Hz peaks are now gone. Thus the correction produces the

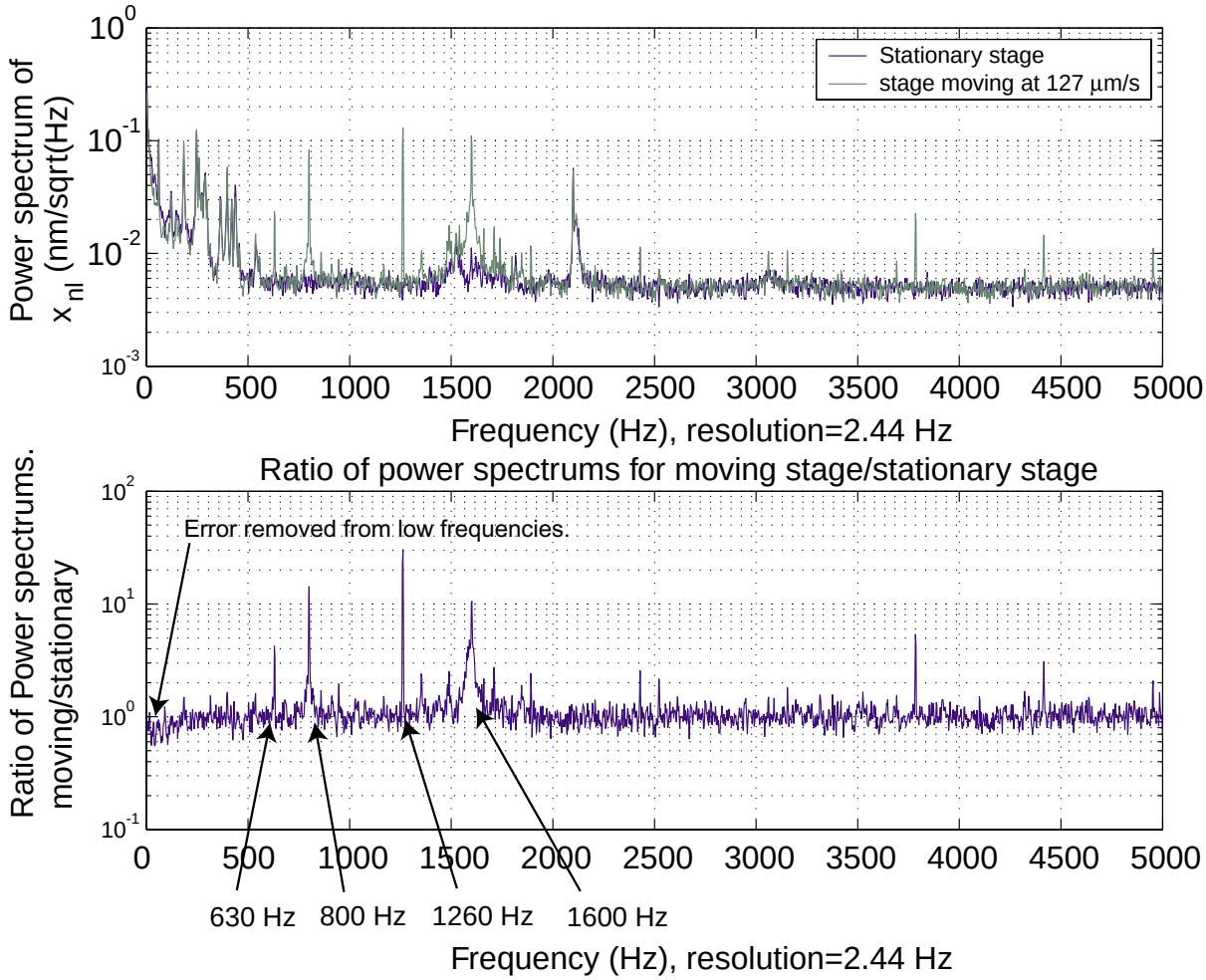

Figure 9-30: The top plot shows the power spectrums of x_{nl} for the moving stage and the stationary stage. The bottom plot shows the ratio of power spectrums of the moving stage to the stationary stage. The peaks due the interferometer nonlinearity are evident.

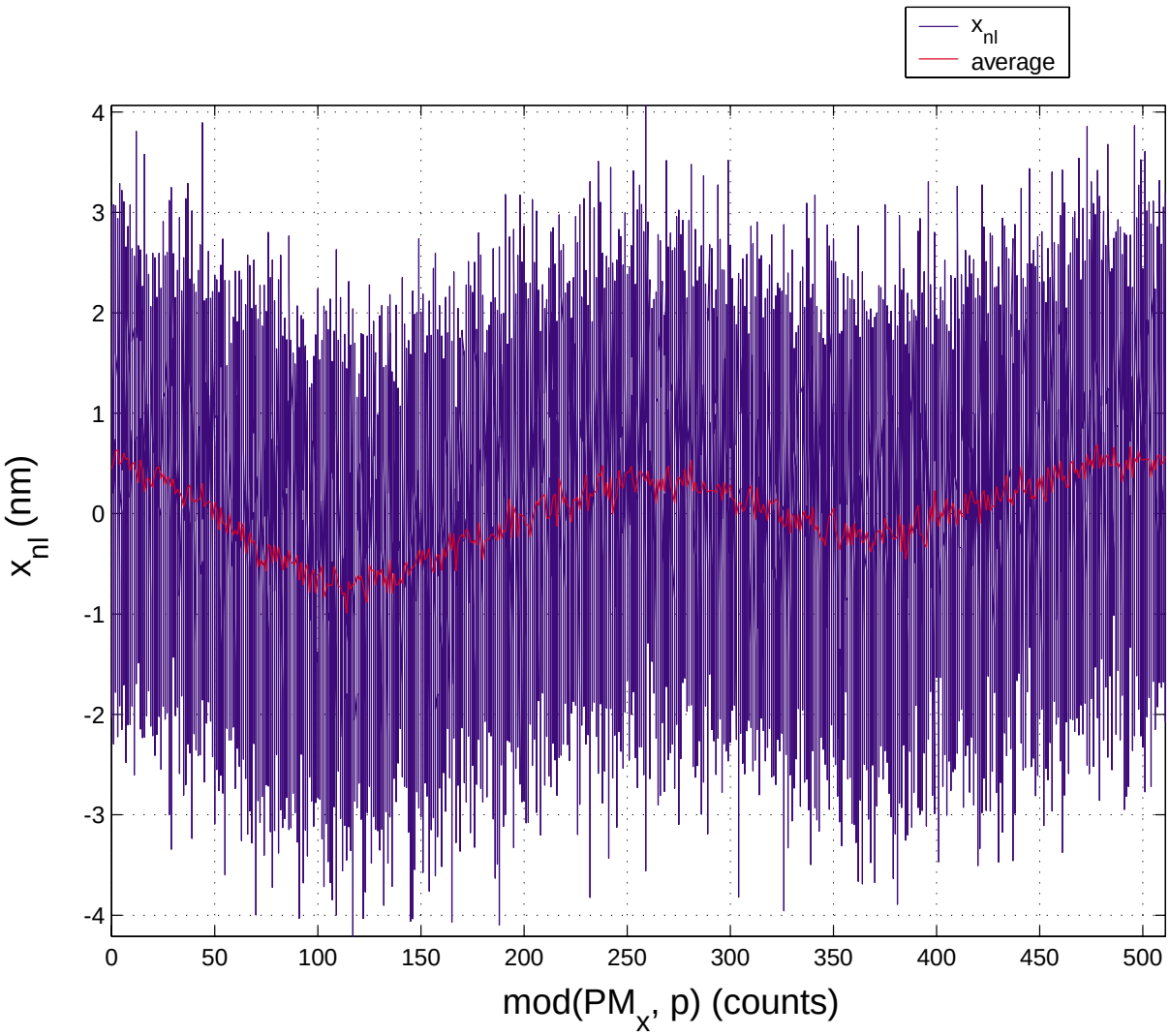

Figure 9-31: Plot of x_{nl} versus the modulus of PM_x. The average of the data points in each phase bin shows the linearity.

expected result. The rms error goes from 1.05 nm to 0.99 nm due with the correction. This is the same improvement estimated by the assuming root sum square addition of the nonlinearity rms error.

The nonlinearity associated with PM_4 was not expected because it is unlikely that the reflected beam can leak into the diffracted beam path and vice versa. However, if the optics can reflect a beam(s) back to the substrate after it had already reflected or diffracted from the substrate then mixing would occur. Nevertheless, the magnitude of this nonlinearity can be quantified using a procedure similar to that applied to PM_x. The nature of the calculated harmonics also provides insight into the source

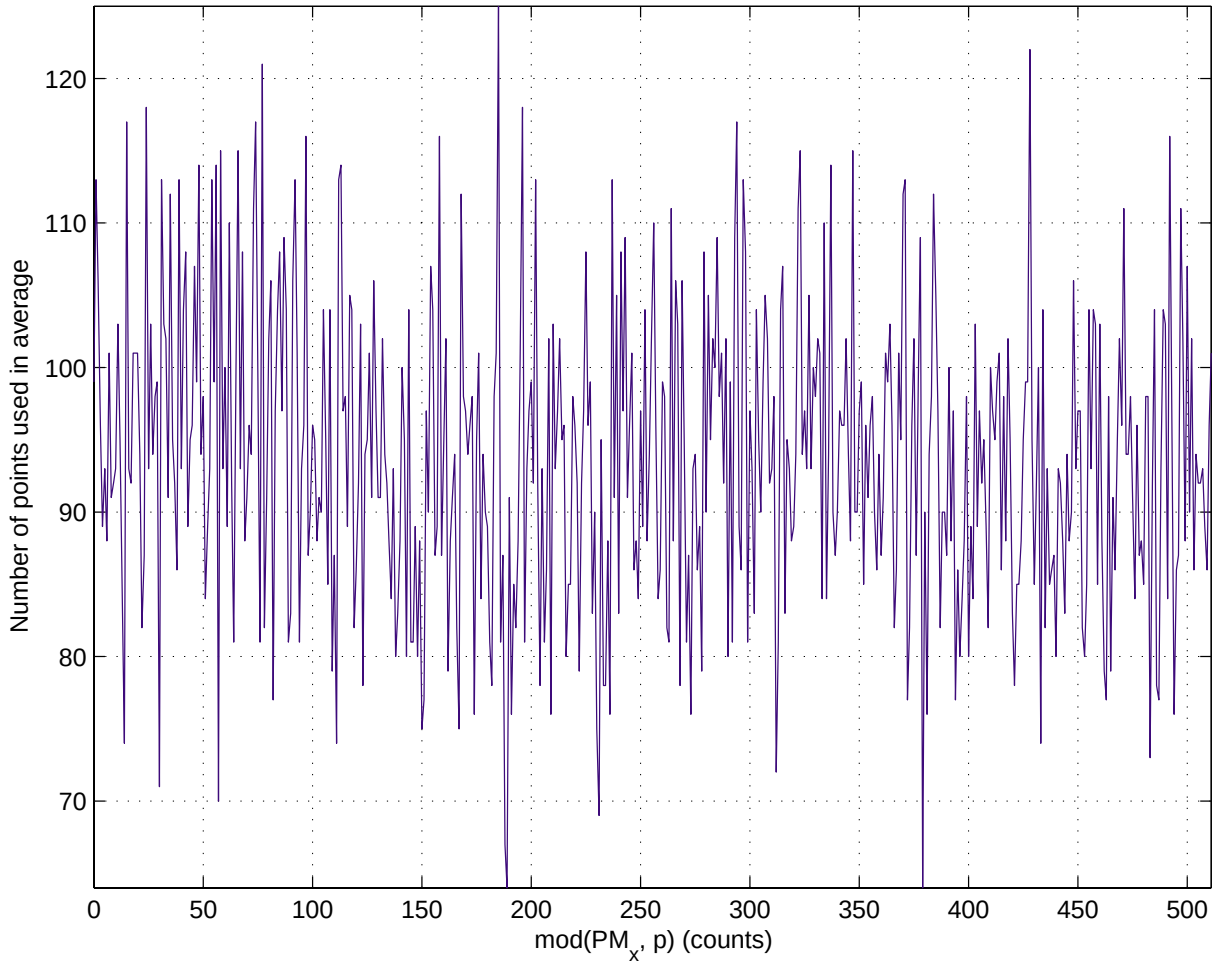

Figure 9-32: Plot of the number of points in each phase bin.

of the nonlinearity. The corrected data from Figure 9-35 is plotted as a function of the modulus of PM_4 after division by $p = 512$ in Figure 9-36. The FFT coefficient magnitude is plotted in Figure 9-37. Although the harmonics are not as clean as for PM_x, the second and fourth harmonics capture most of the nonlinearity. The reconstruction obtained from the inverse FFT using just the DC, the second harmonic coefficient, and the fourth harmonic coefficient is shown in Figure 9-38. The reconstructed data has a peak-to-valley magnitude of ± 0.4 nm and an rms value of 0.26nm. The peak to valley corresponds closely to $\pm 1/2$ LSB of $PM4$. The nonlinearity data including high order harmonics appear to be repeatable. Figure 9-39 shows the result of subtracting one data set like that shown in 9-38 data from a second data set. The "data" is repeatable to about twice the noise level of a single data set or ± 0.4 nm.

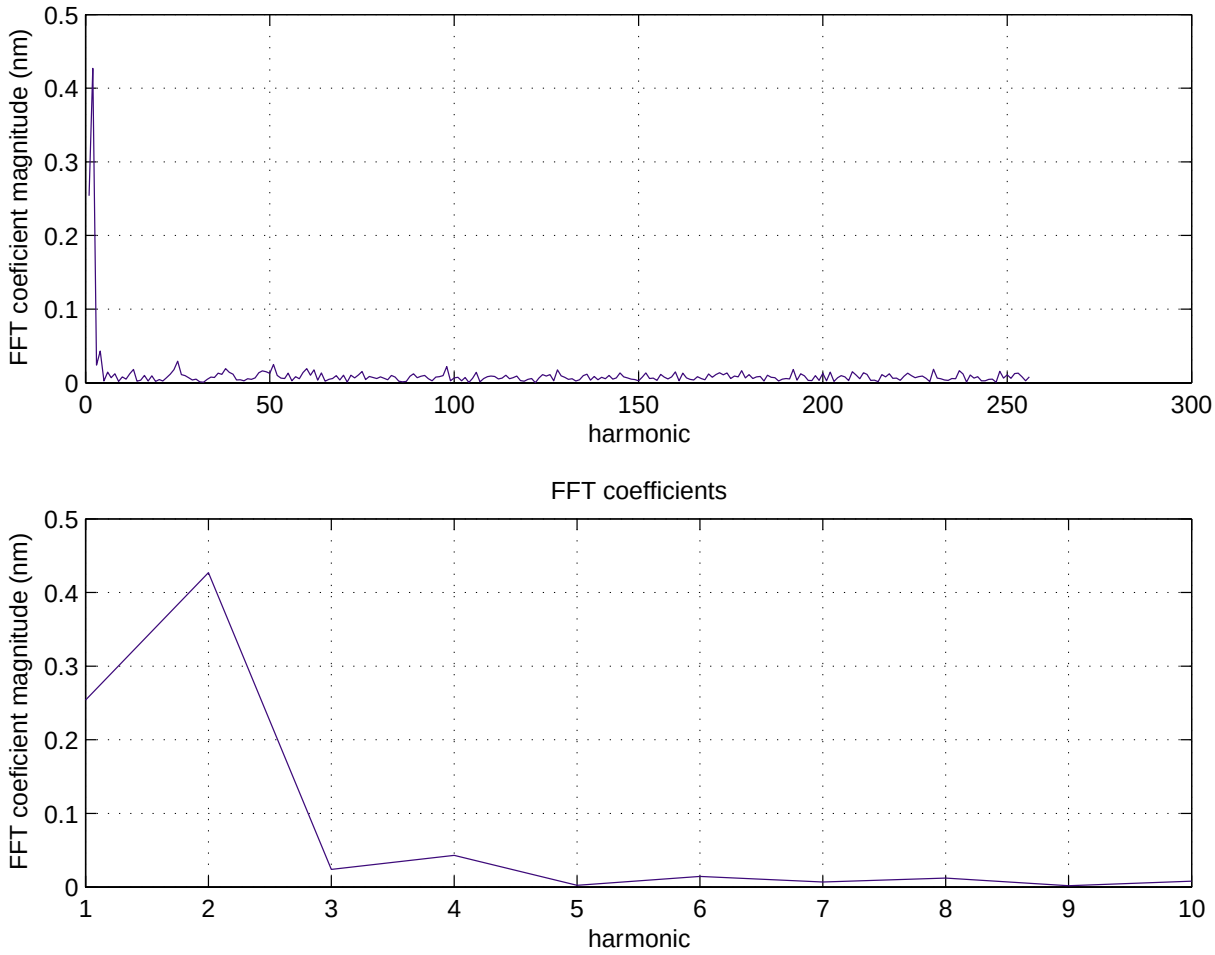

Figure 9-33: Plot of the magnitude of the FFT coefficients for PM_x periodic error obtained from the average x_{nl} data. The top plot shows the magnitude of all 256 harmonics. The bottom figure shows a magnified plot containing just the coefficient magnitudes for the first 10 harmonics.

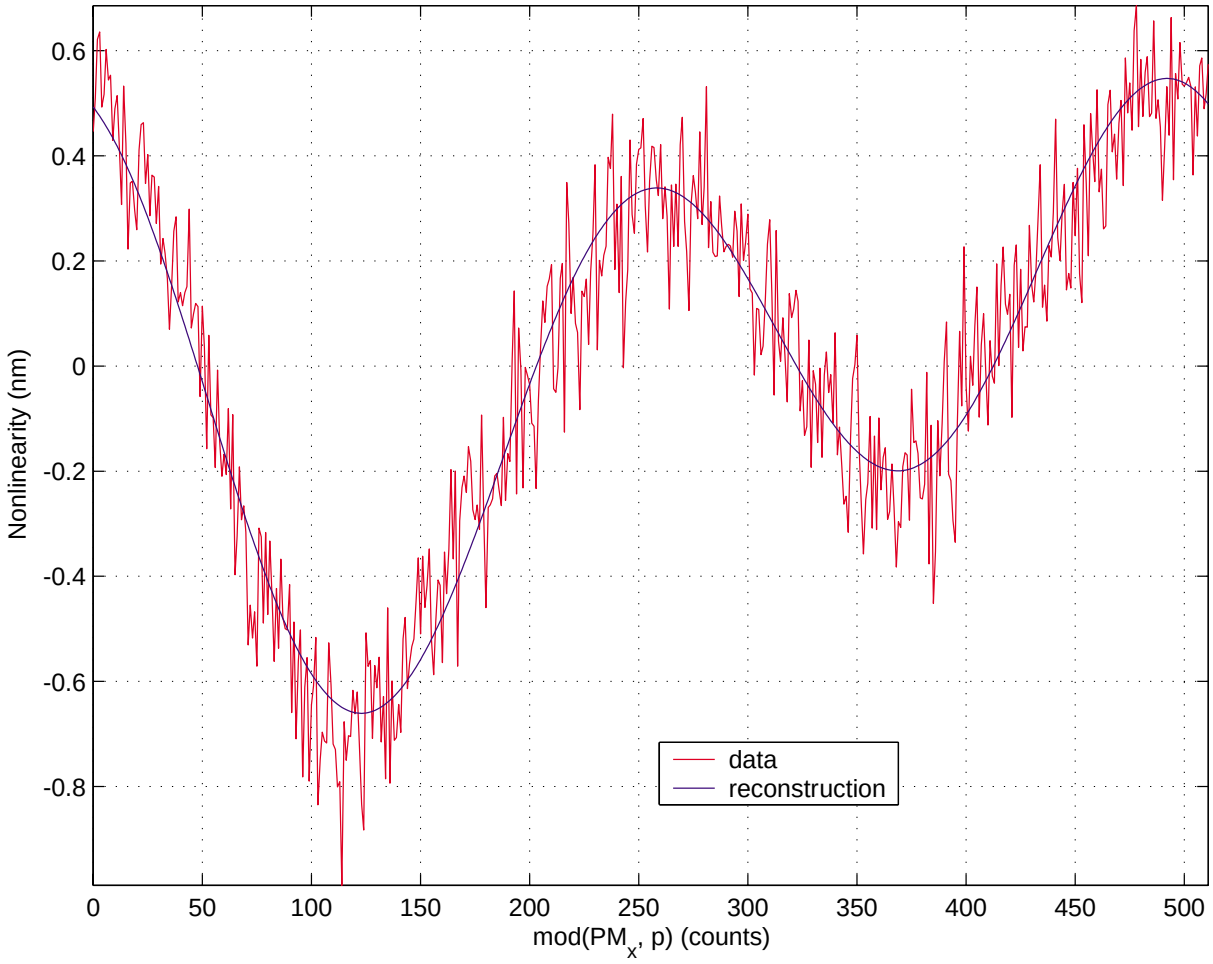

Figure 9-34: Plot of data used in the FFT and the reconstruction by the inverse FFT using the DC component and the first two harmonics

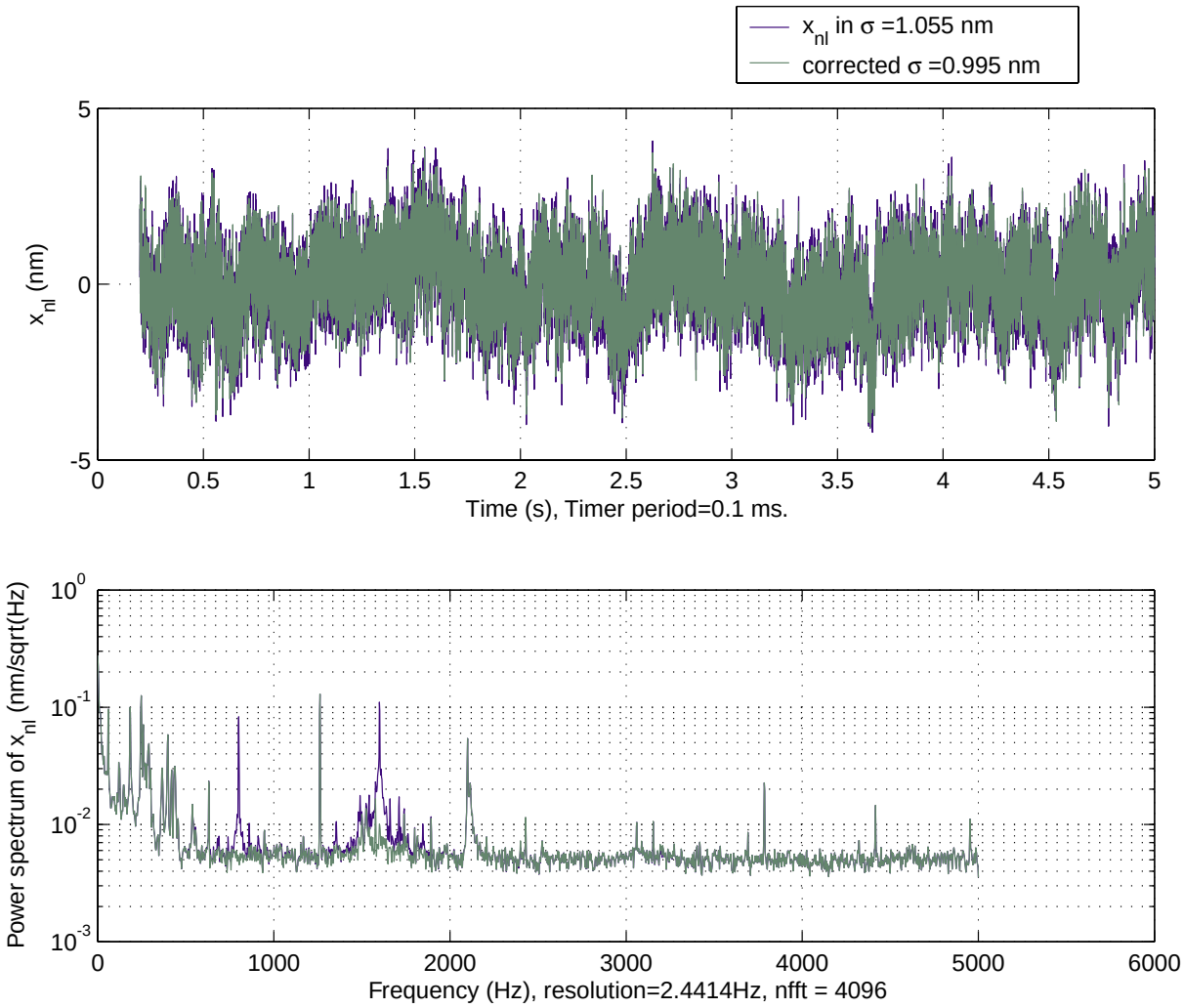

Figure 9-35: Plot of x_{nl} data and this data corrected for the x-axis nonlinearity. The power spectrum for the corrected data shows the 800 and 1600 Hz peaks are gone in the corrected data.

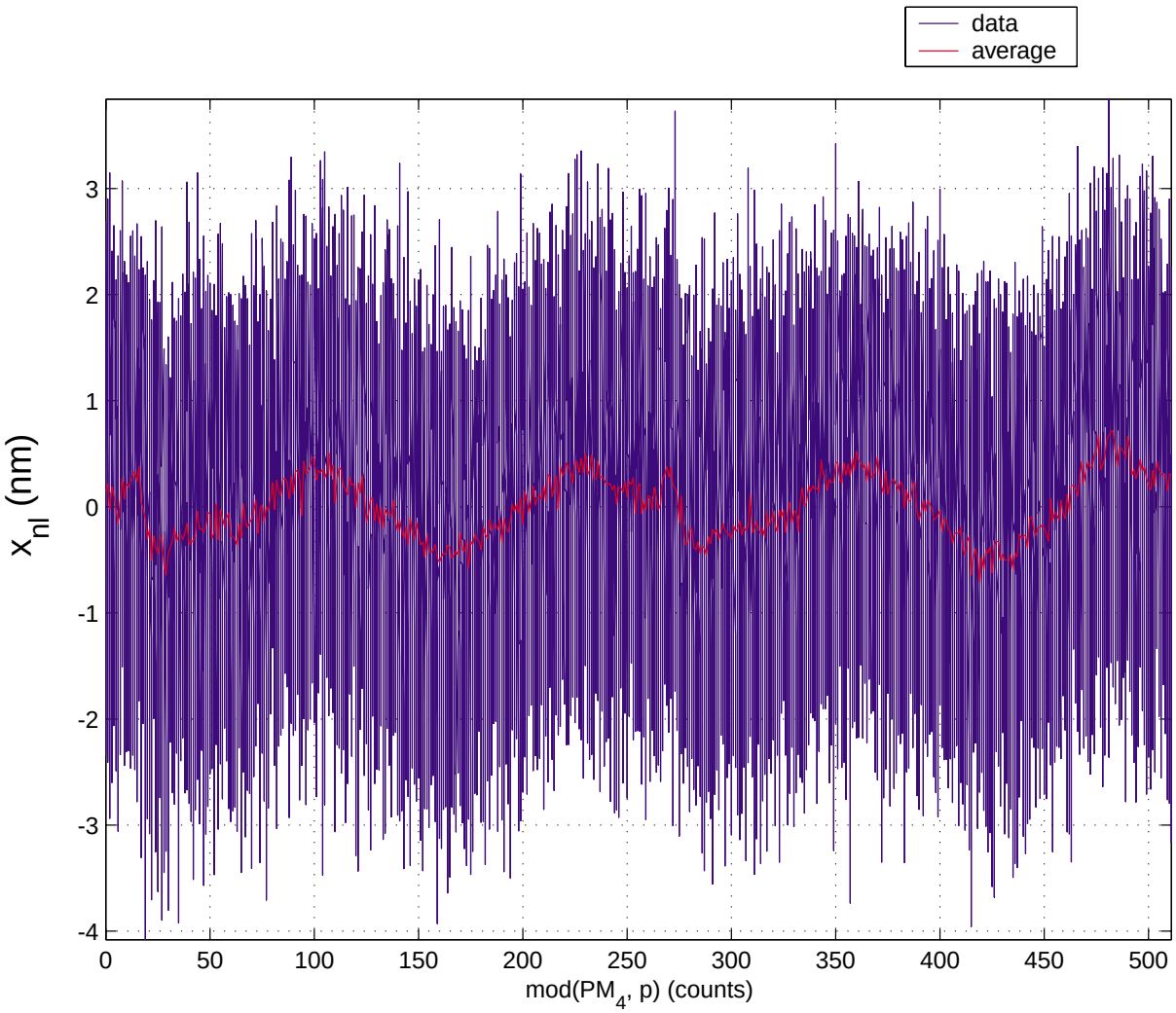

Figure 9-36: Plot of x_{nl} versus the modulus of PM_4. The average of the data points in each phase bin shows the linearity.

The reconstruction using the FFT coefficients is repeatable to about ± 0.01 nm. This data serves to show that the anomalous looking higher order harmonic nonlinearity is not anomalous noise. Six minutes elapsed between the data sets. The verification that the second and fourth harmonics of PM_4 are removed by the calculated coefficients is shown in Figure 9-40. The corrected data shows an improved rms of 0.96 nm. This is the same improvement predicted by assuming the root sum square of the rms errors.

The fact that the nonlinearity shows up in the second and fourth harmonics is strange since all analysis that I've seen of nonlinearity show error components only in

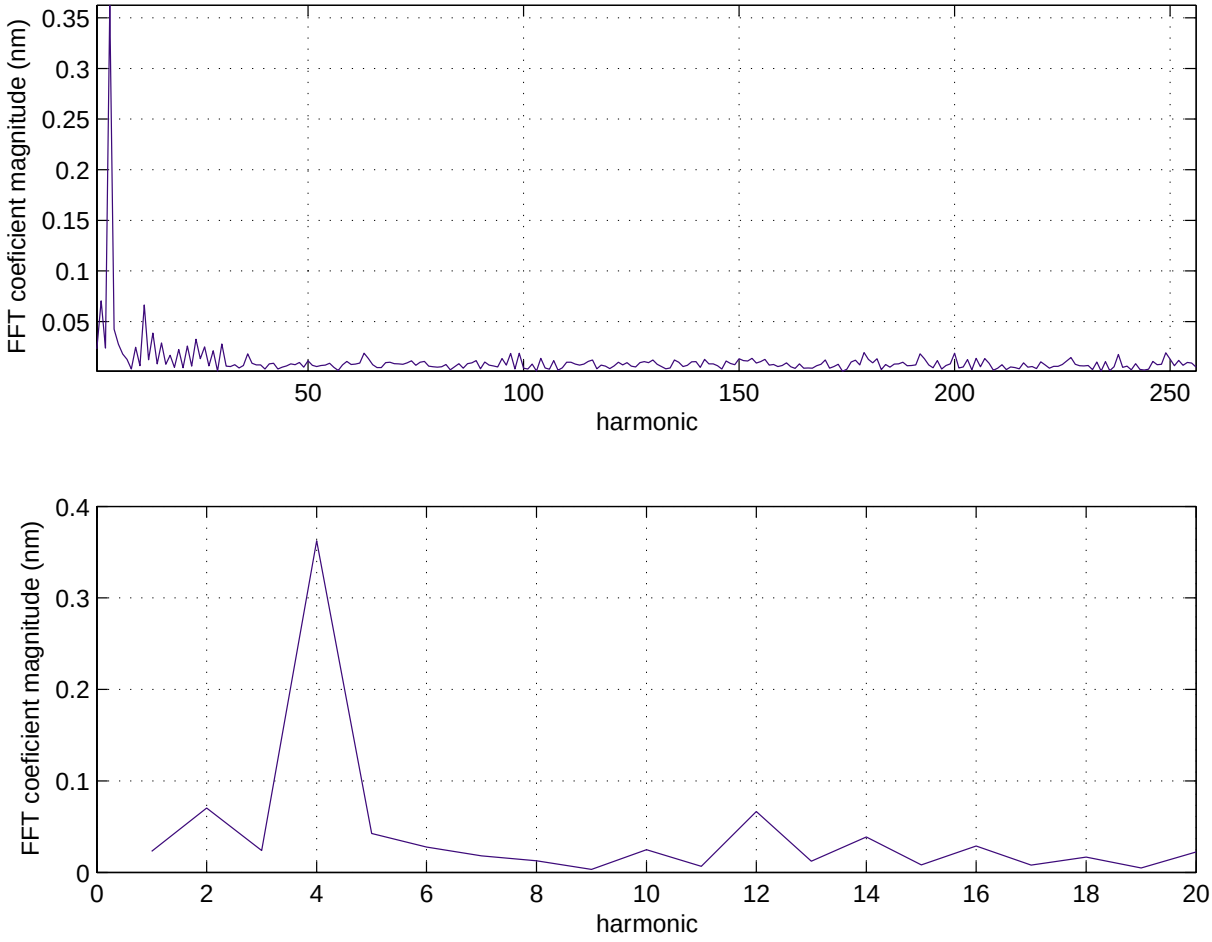

Figure 9-37: The magnitude of the FFT coefficients for PM_4 periodic error obtained from the average x_{nl} data. The top plot shows the magnitude of all 256 harmonics. The bottom figure shows a magnified plot containing just the coefficient magnitudes for the first 20 harmonics.

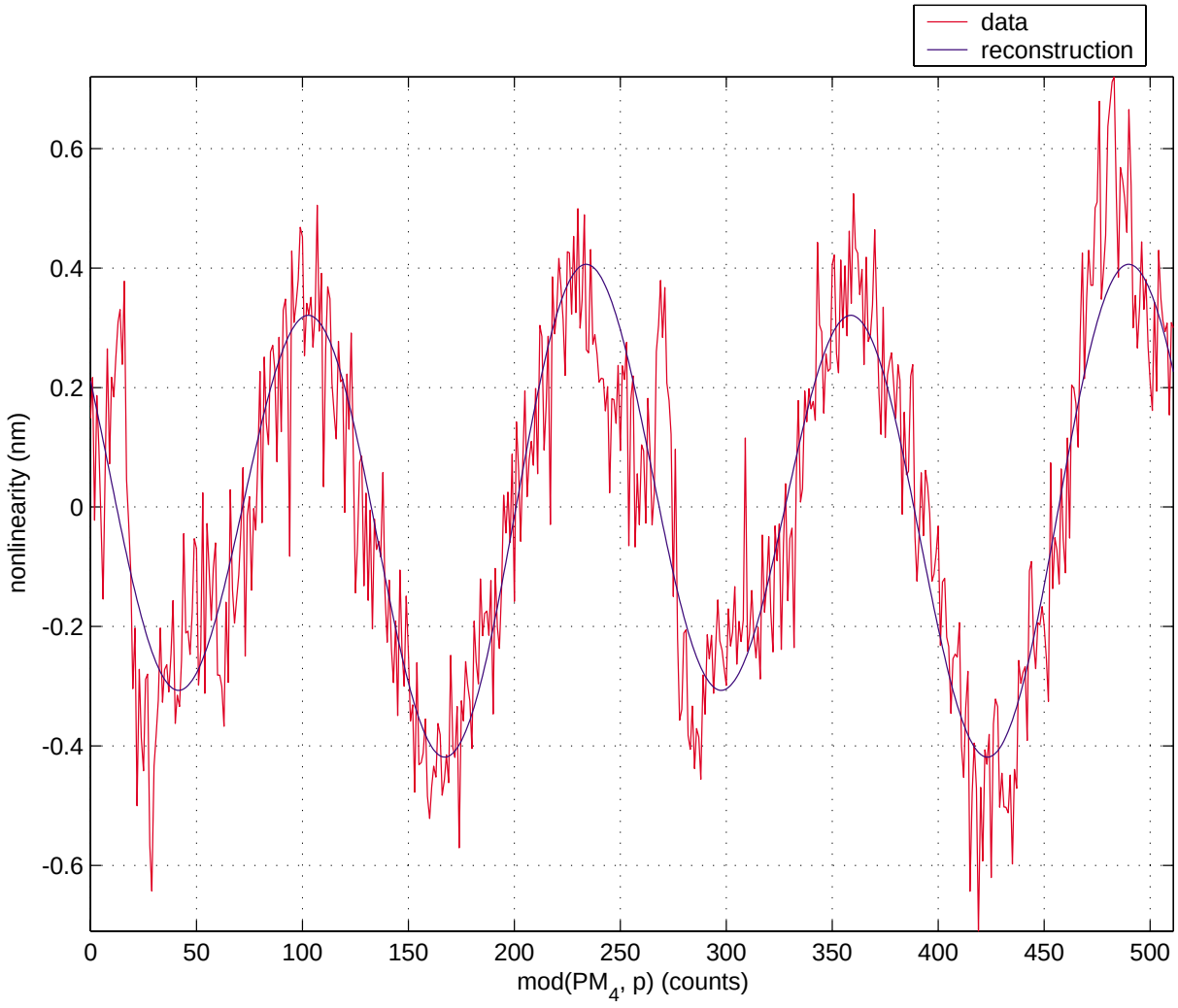

Figure 9-38: Plot of data used in the FFT and the reconstruction by the inverse FFT using the DC component and the second and fourth harmonics.

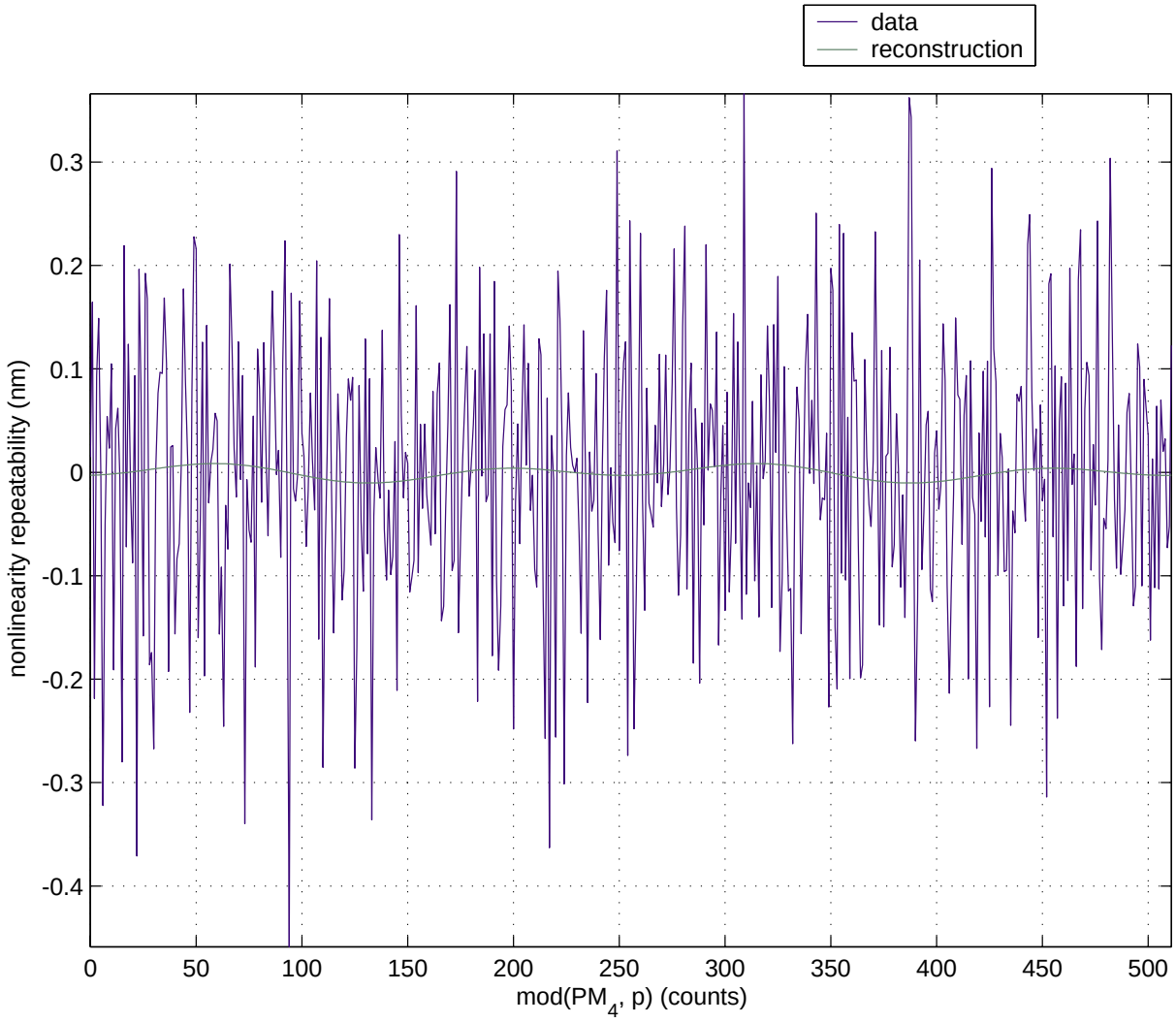

Figure 9-39: Repeatability of PM_4 nonlinearity. This data is difference between the average x_{nl} periodic error from two experiments.

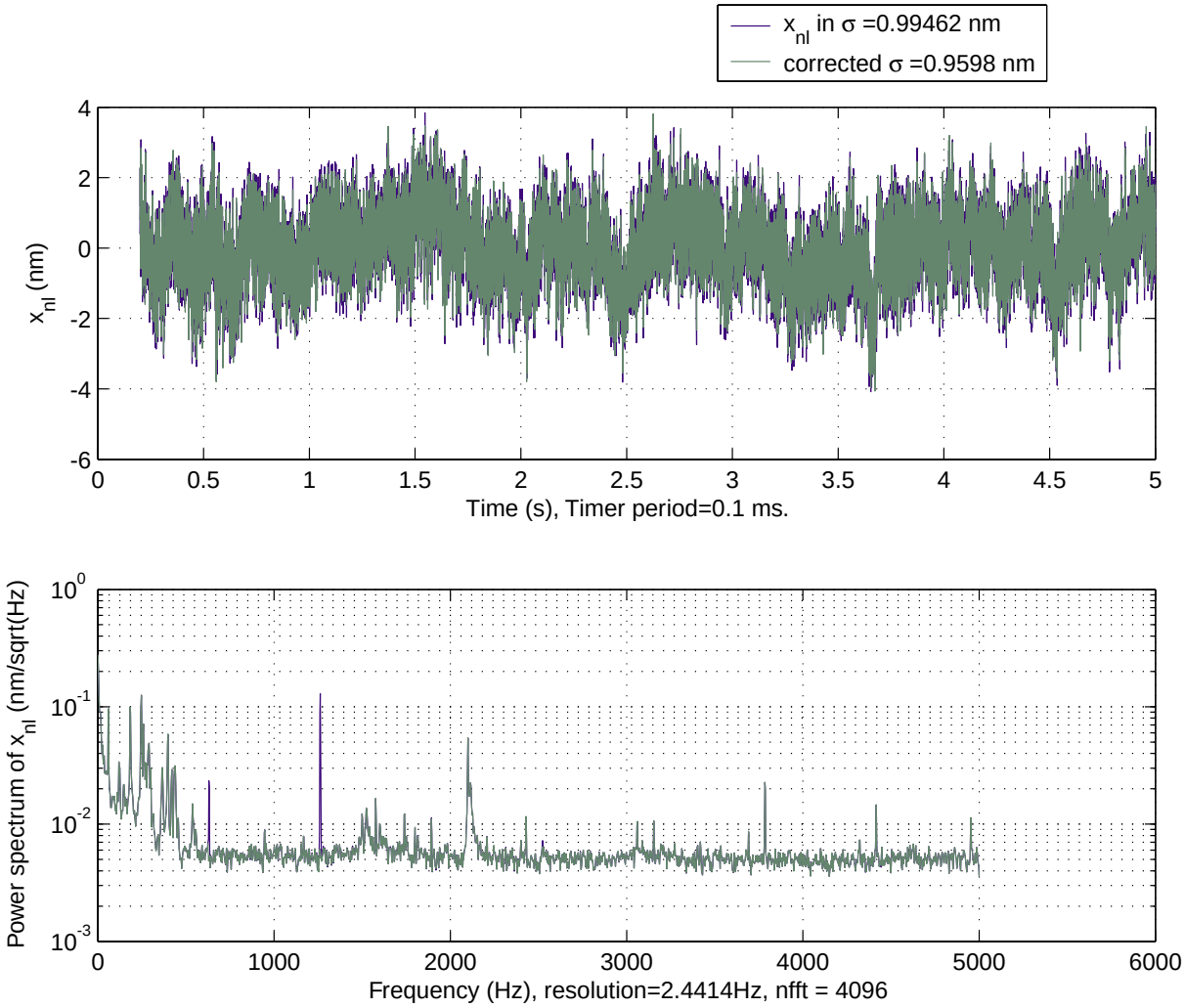

Figure 9-40: Plot of x_{nl} data that was already corrected for the PM_x nonlinearity and the same data corrected for the PM_4 axis nonlinearity. The power spectrums show the 630 and 1260 Hz peaks are gone in the corrected data.

the first and second harmonics. To verify that the nonlinearity is not somehow actually written into the SBIL grating, I analyzed x_{nl} taken when reading a holographic grating. This grating was produced by staff in the Space Nanotechnology Laboratory on the setup described in [27]. The holographic grating is expected to have a smooth phase. Figure 9-41 shows the power spectrum of x_{nl} with a stage velocity of 316 μm/s perpendicular to the holographic grating. The power spectrum clearly shows the first and second harmonic of the stage interferometer at 2 and 4 KHz respectively. The peaks at 1577 Hz and 3154 Hz correspond to the second and fourth harmonics of PM_4. All the nonlinearity component frequencies scale with the velocity as expected. Thus, the nonlinearity observed is not a phase nonlinearity somehow written into the grating. Since the nonlinearity occurs at very unusual harmonics, I tend to think the error is electronic related. Reference [18] includes data on the phase meters showing electronic error ranging from about ± 1 LSB with some periodicity in the data obvious in the second harmonic. If the problem is in fact electronic, it is strange that the same harmonics don't occur in the PM_x data though. Further testing by swapping phase meter boards may shed some further light on the electronic related issue.

The PM_4 nonlinearity contributes to inaccuracy in the grating phase mapping and corrupts the assumption of the x_{ue} measurement. For now, the error is still small compared to the other errors so the definition of x_{ue} is valid. The assumption was never intended to be better than the electronic inaccuracy of the phase meter any way.

The evidence of this nonlinearity raises the question whether there is periodic error in PM_3. Furthermore, PM_1 and PM_2 may have the periodic error too. If the PM_1, PM_2, and PM_3 nonlinearities are at the level of PM_4, then the nonlinearity errors are not the dominant errors. However, to achieve subnanometer level placement repeatability will require that all these nonlinearities and the refractometer nonlinearity be addressed. In the next subsection, I propose a relatively easy solution to the nonlinearity.

Finally, I will show a non obvious effect seen on the θ_{Zsm}-axis interferometer caused by scanning the stage. The data shown in 9-42 is from the angle axis of the x

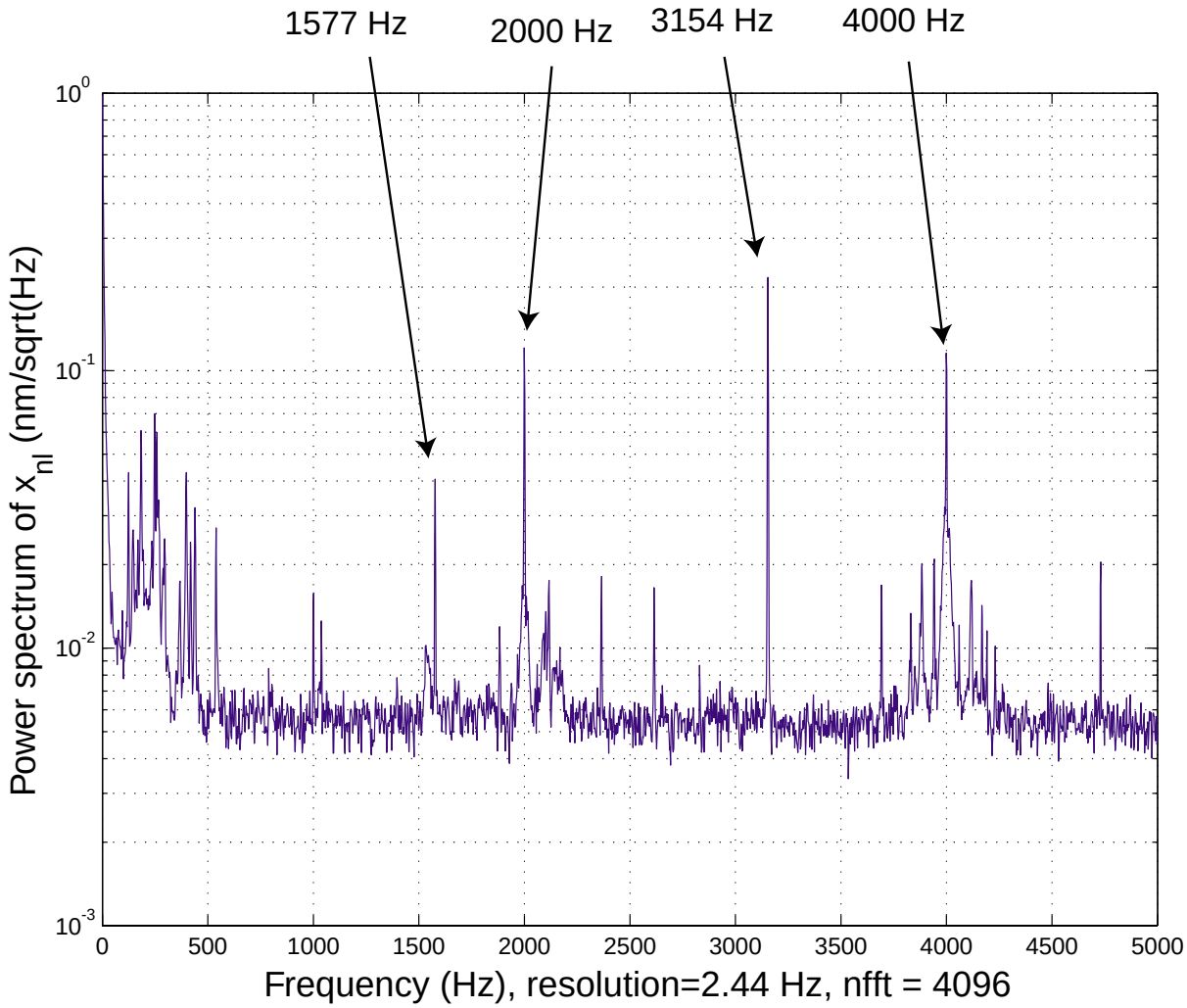

Figure 9-41: Plot of the power spectrum of x_{nl} with a stage velocity of 316 μm/s perpendicular to holographic grating.

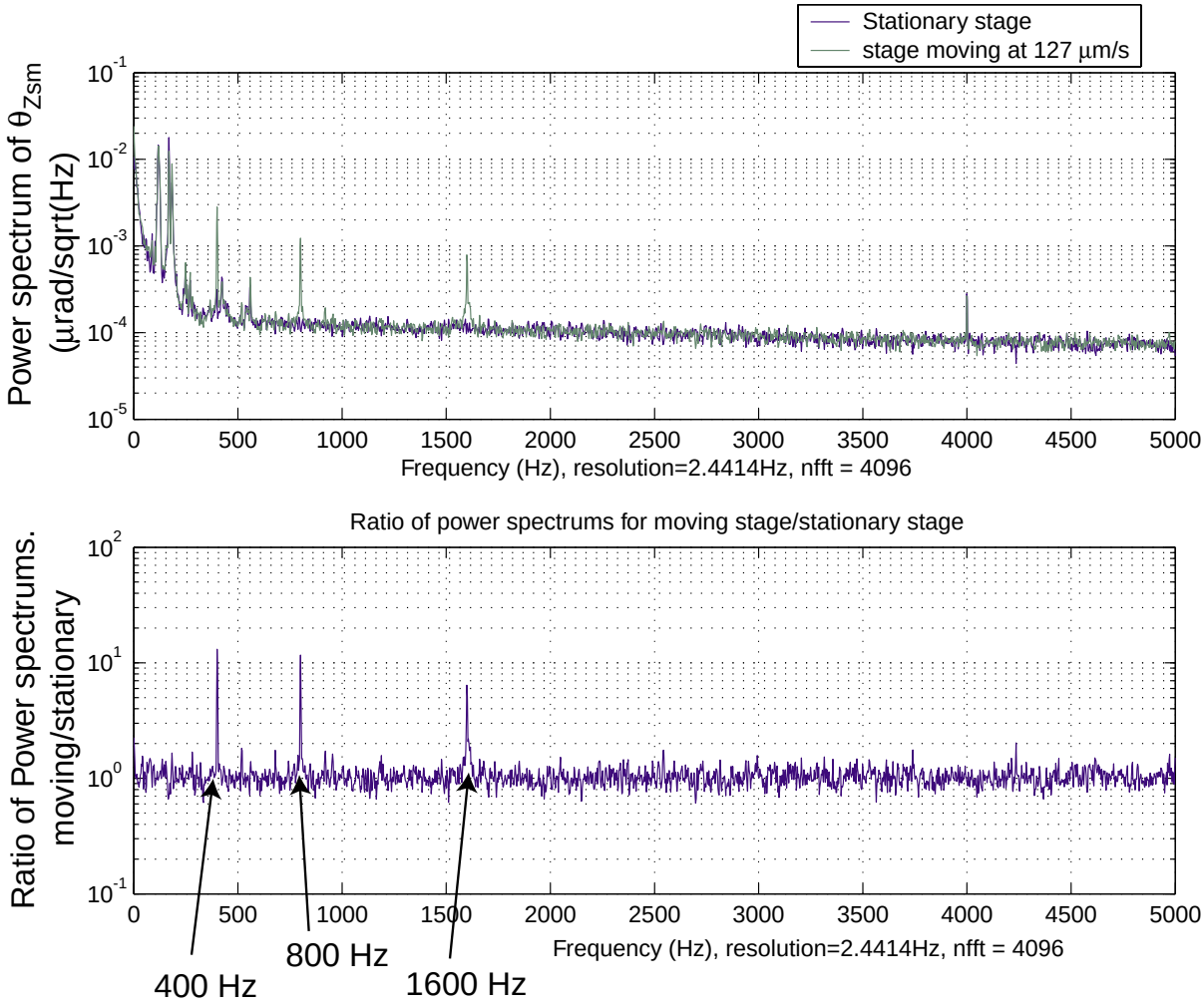

Figure 9-42: Comparison of the θ_{Zsm} axis power spectrums for a stationary and moving stage. The bottom plot shows the ratio of the power spectrums shown in the top plot.

interferometer head while the stage was scanning in the x axis at 127 μm/s. This scan speed produces the first harmonic on the translation axis at 800 Hz. It is surprising to see any effect at all on the θ_{Zsm} axis because scanning the stage nominally does not cause any optical path difference on the angle axis. However, there is obviously some leakage causing the peaks at 400 Hz, 800 Hz, and 1600 Hz. The linear-angle axis interferometer topology has never been analyzed for nonlinearity to my knowledge. The noise power in counts for the frequency ranges where the harmonics occur is shown in Table 9.1. This effect raises a profound question about whether it would even be possible to use mapping to compensate nonlinearity. If the phase measurement

changes when there is no optical path difference such as when both the measurement and reference beams are scanned equally, the nonlinearity mapping won't be stable if the reference beam path length changes. In systems where the reference beam is very stable, this won't be an issue. However, in our system, the column path does have significant displacement. Reference [48] observes and analyzes drift of nonlinearity for different interferometer topologies. While it would be possible to investigate this effect further on the SBIL system, I suggest a preferred method for reducing periodic errors in the next section.

Stage condition	395 to 405 Hz	795 to 805 Hz	1595 to 1605 Hz	root sum square
Stationary σ	0.0306	0.0153	0.0149	0.0373
Moving σ	0.2252	0.1042	0.0703	0.2579

Table 9.1: Integrated noise power in frequency ranges for the theta axis. Units are counts.

9.4.1 Reading and writing strategy for reduced periodic errors

One potential way to reduce the periodic errors is to map them and then correct for them. This may work for some interferometer topologies if the optical leakage parameters don't change [48]. Mapping is not a desirable proposition, however, because periodic electronic errors may necessitate the complication of mapping every interferometric axis. Furthermore, the periodic errors seen on the θ_{Zsm} axis when there was no change in optical path difference raises the question of whether mapping will be stable for systems where both the reference and measurement arms change optical path length. An easier and more reliable way to negate the periodic errors is to scan all the axes such that the periodic errors bump up to a fast enough frequency that they are averaged out. In writing, the averaging occurs because of the exposure integration time. The amplitude of the periodic errors fortunately is small enough that the fringe jitter of about a nanometer will have very little effect on the image contrast. In reading, the minimum scan frequency would need to be fast enough that the periodic errors are filtered out. From Equation 3.51, if $f_G = 2$, the error will

be attenuated to 0.7%. This is more than sufficient attenuation of the small non-linear errors. For v/d equal to 100 Hz, the scan frequency of the heterodyne signal fundamental would need to be at 200 Hz.

In writing, the UV axes are easy to scan. By simply adjusting the reference frequency f_3 to produce a nominal measurement frequency different from the phase meter reference frequency, PM_1 and PM_2 will scan. There is plenty of room in the 36 bit position word on the Zygo phase meters since they would take days to fill up at 200 Hz. Actually, even just using the lower 32 bits would be sufficient for more than 11 hours – much longer than any necessary write time. At this low frequency, data age is not significant problem either. The stage would also need to be scanned in the x axis at a small velocity. The scan angle between the x and y axis is calculated by setting

$$f = \frac{v f_G}{d} = \frac{v_x nm}{\lambda} \tag{9.10}$$

and solving

$$\frac{v_x}{v} = \frac{f_G \lambda}{dnm}. \tag{9.11}$$

Using $f_G = 2$, $n = 4$, m =1 for the first harmonic, $d = 2$ mm, and $\lambda = 633$ nm, the ratio of velocities is 1.6×10^{-4}. The stage would thus need to scanned from the y axis by only 160μrad. It is desirable for the velocity of the stage perpendicular to the grating to be low because disturbances are highest in the scan direction. Also, motor heating on the x axis could be problematic. The fringes could purposely be aligned to α equal or greater than 160μrad. However, it really should make no difference for the accuracy if $\alpha = 0$ μrad since the x axis velocities are too small to introduce significant additional disturbance or control effort. The important consideration is that the shifting of the UV fringes necessary to keep up with the stage ensures that $f_G = 2$ or more for the lowest harmonic of interest.

In reading mode, the UV axes are similarly easy to scan by setting a small offset between $f_1 - f_2$ and the heterodyne frequency. Phase meter signals PM_3 and PM_4 would then have a nominal scan frequency. The setting of the reference frequency on the UV axes obviously should account for the stage velocity perpendicular to grating

since this will affect the frequency seen at PM_4, which needs to scan at some minimum f_G.

In an alternative writing scheme, the stage might be scanned nominally perpendicular to the fringes while the fringes are shifted at relatively high frequency to be stationary on the substrate. In this approach there is a limit to the maximum frequency shift and hence the maximum scan speed because the angle change caused by the AOM frequency shift will result in clipping in the spatial filters (assuming writing in both scan directions). Assuming clipping was not a problem, the perpendicular scan scheme would provide a large x axis velocity and certainly would eliminate the periodic error for the x axis. It is of interest to understand the dependence of the image and reference periods on the printed period. The image period is set to ≈ 1 ppm whereas we desire a printed period repeatable to a few ppb. To determine the printed period, the intensity during the exposure with x axis velocity is written as

$$I(x,t) = \exp\left(-2\frac{(x+vt)^2}{w^2}\right)\left(B + A\cos\left(2\pi\left(\frac{x+vt}{\Lambda_0}\right) + \phi_r\right)\right). \tag{9.12}$$

Here x is the position on the substrate and v is the velocity of the image relative to the substrate. I am assuming a Gaussian intensity envelope. The fringes cannot be allowed to smear during writing so the reference phase needs to be set to

$$\phi_r(t) = \left(-\frac{2\pi vt}{\Lambda_r} + \phi_o\right) \tag{9.13}$$

The desired reference period Λ_r may be off from the actual image period Λ_0 by some small amount, limited by the period stability, the period setting tolerance, and period measurement accuracy.

The exposure dose is obtained by integrating over time as

$$D_{scan}(x) = \int_{-\infty}^{\infty} \exp\left(-2\frac{(x+vt)^2}{w^2}\right)\left(B + A\cos\left(2\pi\left(\frac{x}{\Lambda_0} + \left(\frac{1}{\Lambda_0} - \frac{1}{\Lambda_r}\right)vt\right) + \phi_o\right)\right)dt. \tag{9.14}$$

After substituting

$$h = x + vt, \tag{9.15}$$

$$dt = dh/v, \tag{9.16}$$

and assuming that $v > 0$, the dose becomes

$$D_{scan}(x) = \frac{1}{v}\int_{-\infty}^{\infty} \exp\left(-2\frac{h^2}{w^2}\right)\left(B + A\cos\left(2\pi\left(\frac{x}{\Lambda_0} + \left(\frac{1}{\Lambda_0} - \frac{1}{\Lambda_r}\right)(h-x)\right) + \phi_o\right)\right) dh. \tag{9.17}$$

This equation is simplified as

$$D_{scan}(x) = \frac{1}{v}\int_{-\infty}^{\infty} \exp\left(-2\frac{h^2}{w^2}\right)\left(B + A\cos\left(2\pi\left(\frac{x}{\Lambda_r} + \left(\frac{1}{\Lambda_0} - \frac{1}{\Lambda_r}\right)h\right) + \phi_o\right)\right) dh \tag{9.18}$$

and can be evaluated using the identities of Equations 1.15 and 3.44 to obtain

$$D_{scan}(x) = \sqrt{\frac{\pi}{2}}\frac{w}{v}\left(B + A\exp\left(-\frac{\pi^2 w^2}{2}\left(\frac{1}{\Lambda_0} - \frac{1}{\Lambda_r}\right)^2\right)\cos\left(\frac{2\pi x}{\Lambda_r} + \phi_o\right)\right). \tag{9.19}$$

For the case when $v < 0$, the integration limits need to range from negative infinity to positive infinity and the scanned dose will have a negative sign. However, the dose is the same since the negative velocity term will cancel the negative sign.

The result of Equation 9.19 shows that the printed pattern will be the desired reference period and not the image period. In fact, the printed pattern is the reference period no matter how far off Λ_o may be. If the image period is too far from the reference period, the contrast will be unacceptable however. In the parallel scan and step strategy, the error in the image results in a periodic error that does not accumulate. Reference [15] indicates that with several parts per million of image period inaccuracy, the periodic error is easily sub angstrom for a step over distance of 0.9 the Gaussian beam radius.

Scanning perpendicular to the fringes at high speed does have problems in addition to the clipping at the spatial filters. The disturbances on the stage and payload in the critical direction – perpendicular to the fringes will be greater. Also, the data age compensation becomes important at very fast velocities. The uncompensated data

age uncertainty on the ZMI-2000 cards is about 10 ns. Thus, velocities greater than 1 cm/s justify data age compensation for this error budget term to be less than 0.1 nm. With data age compensation, the uncertainty can be about 1 ns, which would limit velocities to 0.1 m/s.

Scanning perpendicular to the grating at some small velocity solves the nonlinearity problem for the stage and UV interferometers while preserving most of the benefits of scanning parallel to the grating. However, the refractometer linearity is still an issue. The refractometer nonlinearity might be mapped from the refractometer and pressure measurements, if the temperature and humidity are stable enough to have negligible influence. If necessary, temperature and humidity measurements could be incorporated into the refractivity calculation. The effect seen with the θ_{Zsm} axis interferometer still raises the question about whether the nonlinearity will be stable. Therefore, abandoning the interferometer based refractometer for weather-based calculations [20] is perhaps the better alternative. Under stable room conditions (no doors opening and closing), the relatively slow weather instruments [99] should be fine. Enclosing the stage beams in vacuum evacuated bellows and using a monolithic optic for the metrology block optics, which is the even better alternative, will eliminate the need for the refractometer altogether. The vacuum wavelength stability of the Zygo ZMI 2000 laser, which is specified to be stable to ± 10 ppb over 24 hours is still likely to be a problem. Other lasers are available with better stability, including the directly compatible 7712 Laser Head from Zygo with the specified one hour stability of 0.5 ppb.

9.5 Interference image distortion

Ideally, the interference image would be a perfect linear grating of the desired period. In actuality, the image distortion was measured to be $\pm\Lambda/15$ for the experimental results that I discuss.

A phase shifting interferometry (PSI) system was developed by another student to measure the wavefront distortion of the image grating [13, 15]. Figure 9-43 shows the

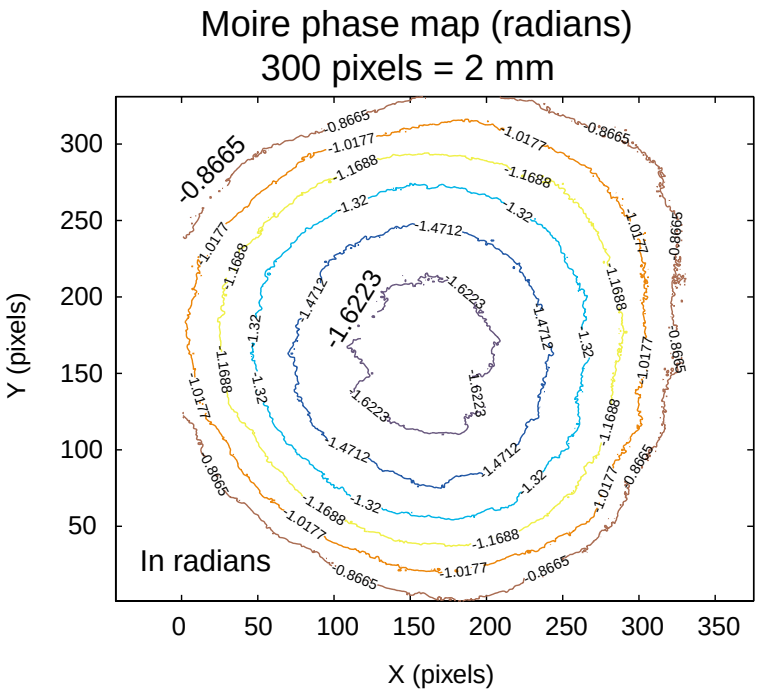

Figure 9-43: A phase map of the interference image. This is the Moire image between the image grating and a holographically produced grating.

phase map produced from the moire image between the grating image and a substrate grating [13]. The substrate was a holographically produce grating. The phase map shows the distortion in radians versus the pixel spacing of 6.7 μm. The peak-to-valley phase distortion is 53 nm. The repeatability of the PSI was assessed to be 3.3 nm 3σ from 24 data sets that were taken before several major improvements such as the environmental enclosure and the latest chuck were installed. The repeatability of the phase map would probably be significantly better after these improvements. The phase measurement shown is the average of the 24 sets.

The $\pm\Lambda/15$ level of distortion in the image was present during my experimental work. The spherical distortion contains a component of "chirp" that leads to printed errors. The image and written errors will convolve to diminish the repeatability. This error contributes to some of the nonlinear phase measurement seen when the written grating is read. Also, if the image grating is nonlinear another significant error during reading results if the substrate has non uniform diffraction efficiency.

The substrates that I used contain defects in the spin coatings. Some of these defects are visible as "comets" produced when either the ARC or resist is spun on the substrate containing particles. Varying grating height also changes the diffraction efficiency. If the image is distorted and the diffraction efficiency changes within the spot, the measured phase will show an error. These errors will occur even if the grating was perfect and the system was totally stable. Thus, the measured repeatability of the system contains more sources of error than the phase placement repeatability, which was my primary effort. While process improvements would reduce the diffraction non uniformity problem, the image grating can also be improved. Nevertheless, even with large image distortions and defective substrates, the written phase distortions (discussed in Section 9.8) are better than the moire distortions, except in the area of obvious defects, which indicates that a lot of the image distortion did not print. The scanning the grating image, is thus demonstrated to be advantageous over static exposure strategies.

9.6 Dose stability

Most of the dose fluctuation in our system is actually due to change of power of the laser beams as a result of spatial filtering. Whereas the measured power stability before the spatial filter's pinhole was ± 1%, after the beam pickoff it was measured to be about ± 3%. To fairly assess the dose, the beam power measurement really should be Gaussian filtered. The ± 3% beam power fluctuation is a worst case estimate. A 3% variation in dose is expected to produce 2% CD control for high contrast fringes per Equation 1.21.

9.7 Processing

A scanning electron micrograph of a SBIL written grating after exposure and development is shown in Figure 9-44. The silicon substrate has anti-reflection coating (ARC) with thickness designed for the 400 nm period grating exposure. The 200 nm

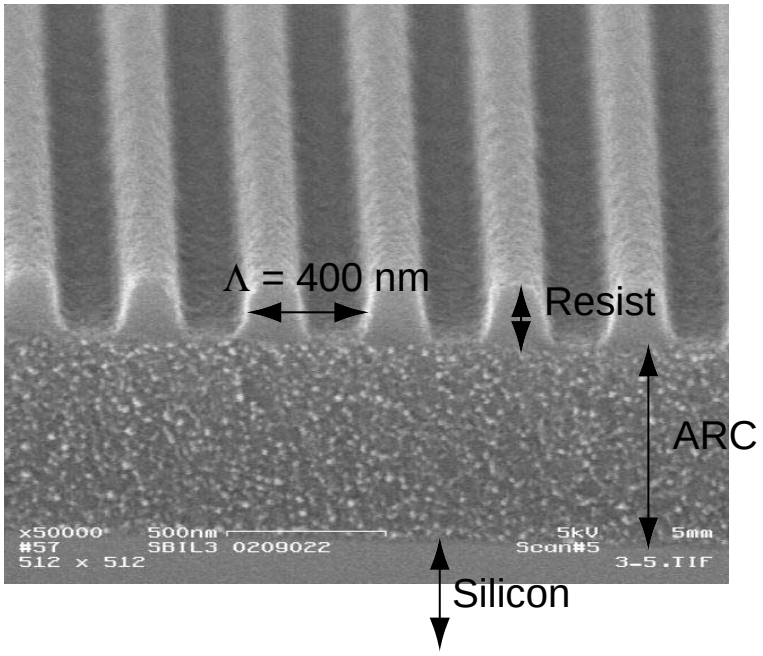

Figure 9-44: Scanning electron micrograph of SBIL written grating after exposure and development.

thick resist is Sumitomo PFI-34 and the 600 nm thick ARC is Brewer ARC-XL. The developer is Arch Chemical OPD 262, which is a solution of tetramethyl ammonium hydroxide. The side walls of the grating are not exceptionally vertical, indicating contrast improvements can be made. The image distortion is probably largely responsible for the reduced contrast. Posts and grids can also be fabricated by SBIL by using two crossed exposures. Figure 9-45 is the scanning electron micrograph of SBIL written posts after two crossed exposures and development.

Most grating applications would require further processing to achieve high diffraction efficiency and good durability. Figure 9-46 shows the scanning electron micrograph of SBIL written grating part way through the processing of a metal grating. The grating is shown after exposure, development, reactive ion etch of the interlayer, reactive ion etch of the ARC, and nickel plating. In the next step of the process, RCA cleaning removes the ARC to leave the metal grating. The tri-level resist process used to make this grating is discussed in Reference [85]. This process can be used to create very vertical grating lines even if the resist lines are not very vertical. The very

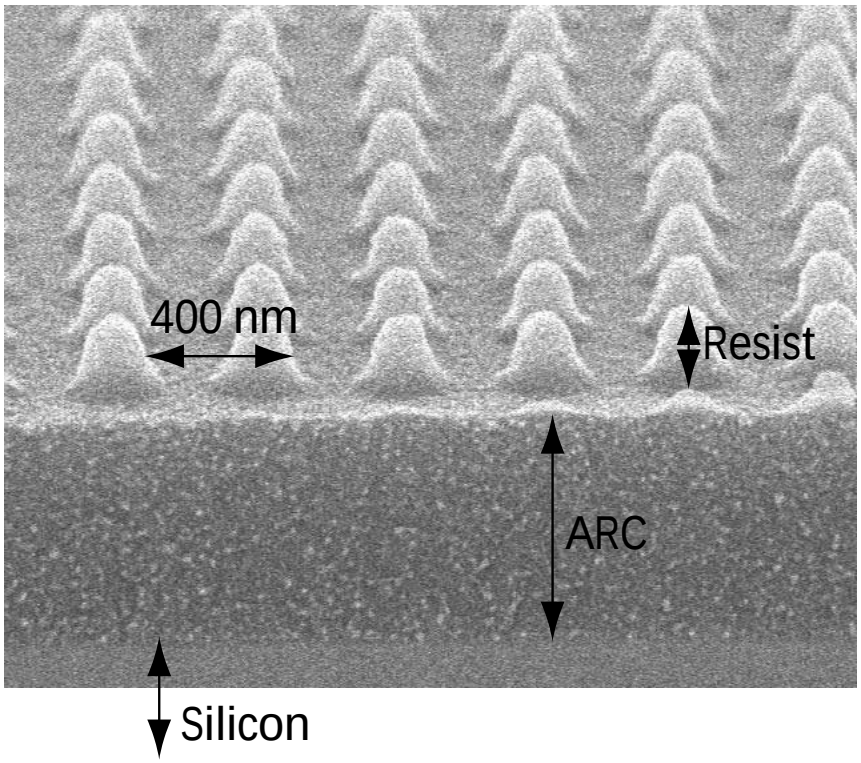

Figure 9-45: Scanning electron micrograph of SBIL written posts after two crossed exposures and development.

vertical ARC sidewalls are shown in the figure.

For SBIL self evaluation, minimal processing is required since developed resist gratings can be read. However, evaporation of gold or another metal over the resist requires relatively little extra effort while greatly enhancing the diffraction efficiency.

9.8 Reading maps

The grating phase across the entire wafer can by mapped via SBIL. The repeatability of the wafer mapping is plotted in Figure 9-47. This data is the difference between two wafer maps taken with a stage scan speed of 1 cm/s, while low pass filtering with a cut off frequency of 8.7 Hz. The wafers take about 10 minutes to map at this speed. The repeatability is ±4.0 nm peak-to-valley and 2.9 nm, 3σ. Since integrating the power spectrum for x_{ue} in Figure 9-5 from 0 to 8.7 Hz produces a 3σ of 1.9 nm and subtracting two data sets should account for a $\sqrt{2}$ greater error, the 3σ of 2.7 nm

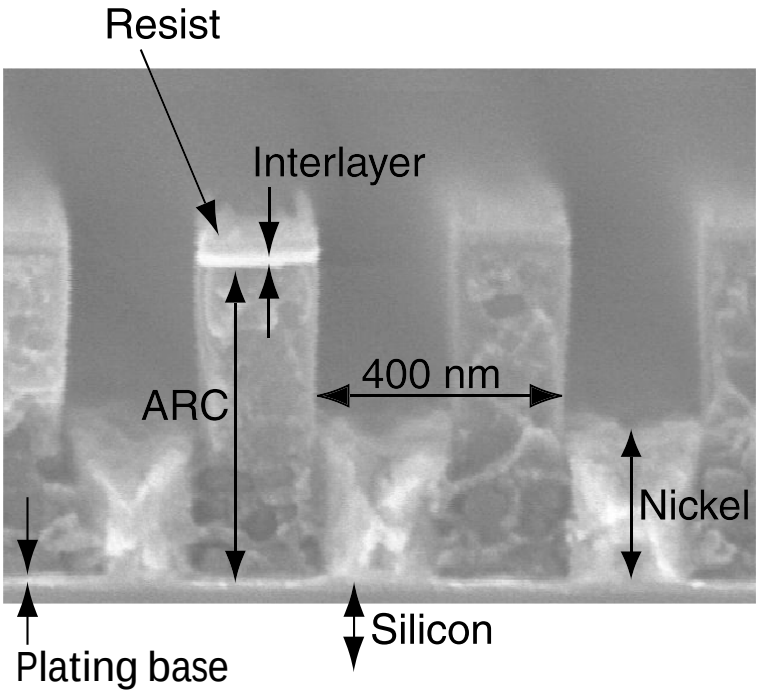

Figure 9-46: Scanning electron micrograph of SBIL written grating after exposure, development, RIE of interlayer, RIE of ARC, and nickel plating.

was expected by just considering the static data. Because the mapping requires stage motion, the associated thermal gradients and larger deadpath is expected to cause the slightly larger mapping error. The period was measured to be consistent to 6 ppb and the rotation angle of the wafer was consistent to 1 nrad between the two data sets. The grating period measurement may be the most repeatable ever performed.

A surface plot of the nonlinearity of a grating written by SBIL is in Figure 9-48. This grating was written at a scan speed of 55 mm/s with a step between scans of 857 μm. The wafer was written in about 10 minutes. The only processing performed on this substrate after exposure was development. The grating was returned to the same location on the chuck as when it was written to about ± 2 mm. The contour plot of the same data is in Figure 9-49. Figure 9-50 shows the same data but with the tighter contour spacing of 2.5 nm ranging from ± 10 nm. The largest source of grating nonlinearity is associated with particle defects. Also, the edges of the map show larger errors. Since the spin coatings and the diffraction efficiency are known

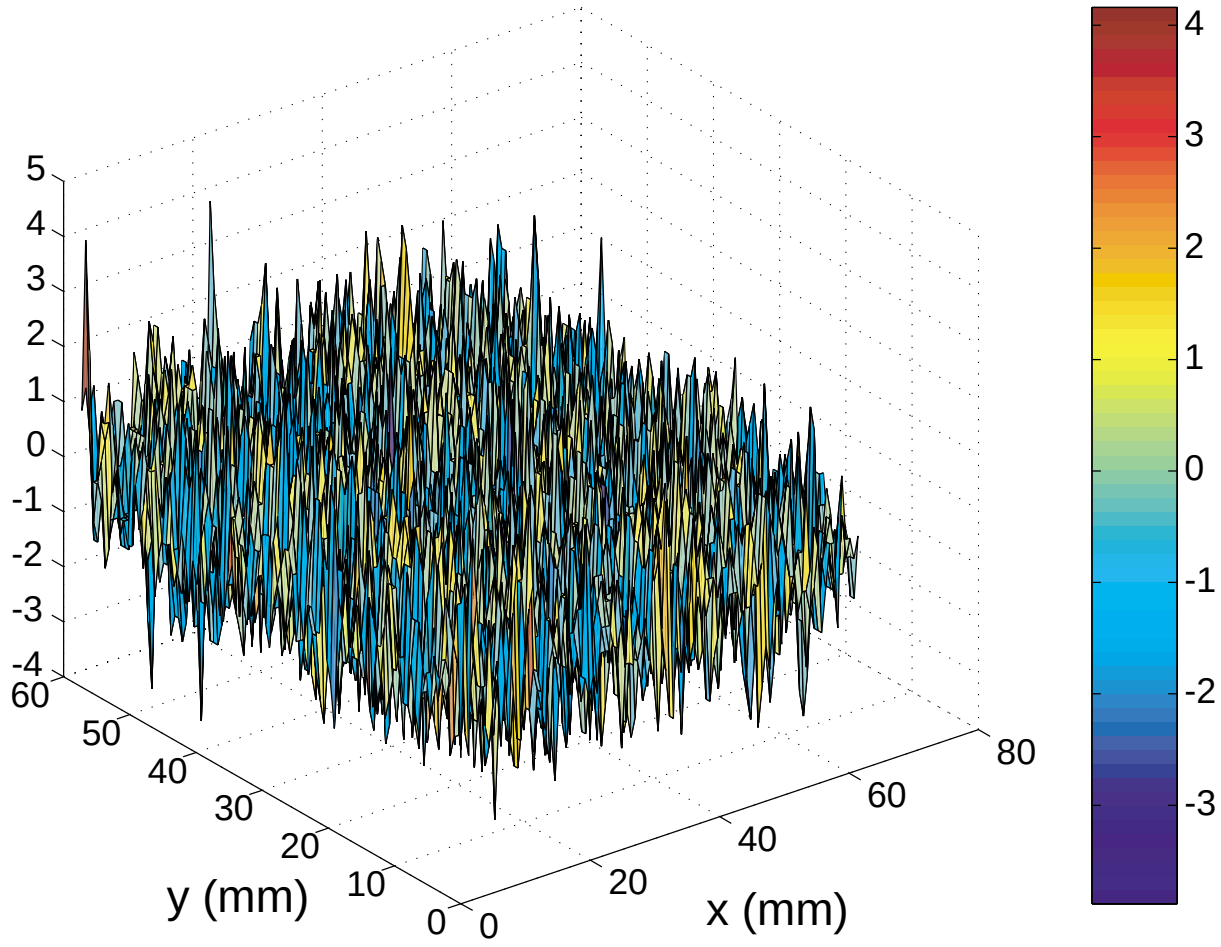

Figure 9-47: The difference between two wafer maps of the same un-rechucked wafer. The origin on this figure corresponds to the stage x position of 0.125 m and the stage y position of 0.207 m.

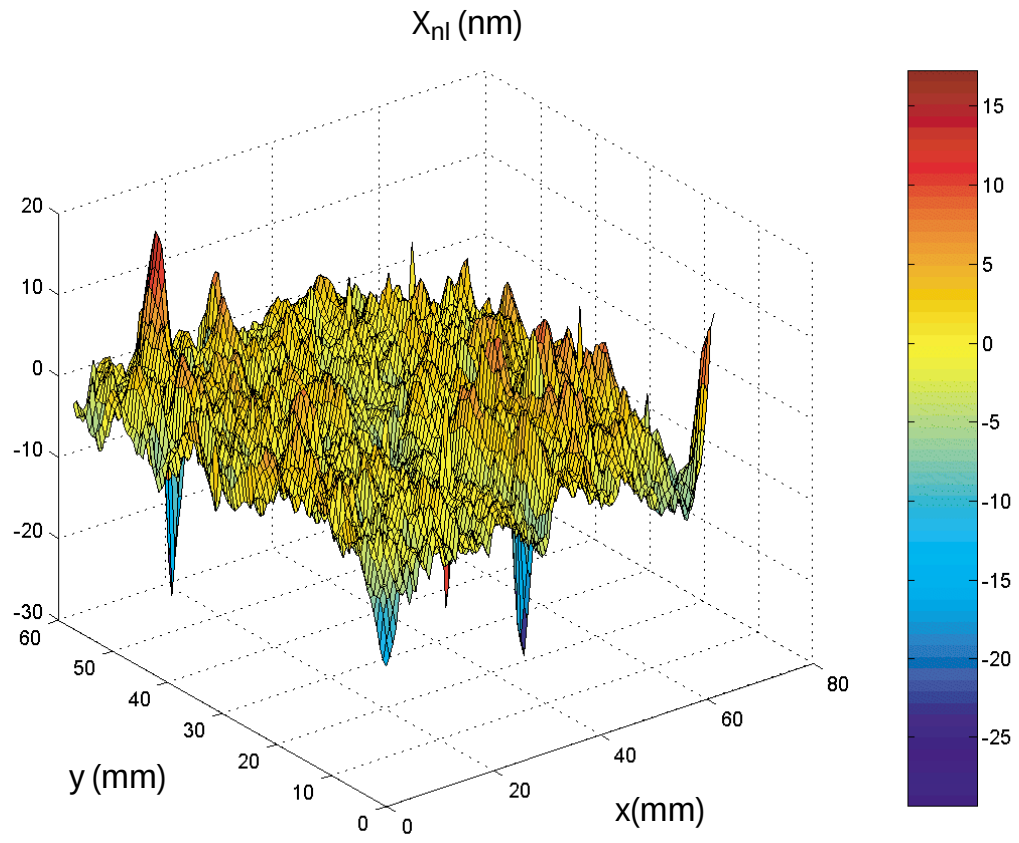

Figure 9-48: Nonlinearity of a grating written by SBIL.

to be inconsistent at the edges of the wafers, the observed larger errors there may validate the claim that the wavefront distortion of the image in the presence of varying diffraction efficiency causes significant inaccuracy. The repeatability of mapping for this wafer was ±6 nm. The worse repeatability here than that shown in Figure 9-47 was due to an alignment problem that was later resolved. During the mapping of this data, the beams were slightly clipped and were slightly misaligned. Both factors contributed to unobservable errors that had a power spectrum similar to the beam steering system stability. But with the larger error the repeatability is still better than the errors observed due to the defects. Except for the obvious particle defects and parts of the edges where the diffraction efficiency was low, the grating is measured to be linear to better than ±10 nm. Included in this error is the repeatability of the mapping.

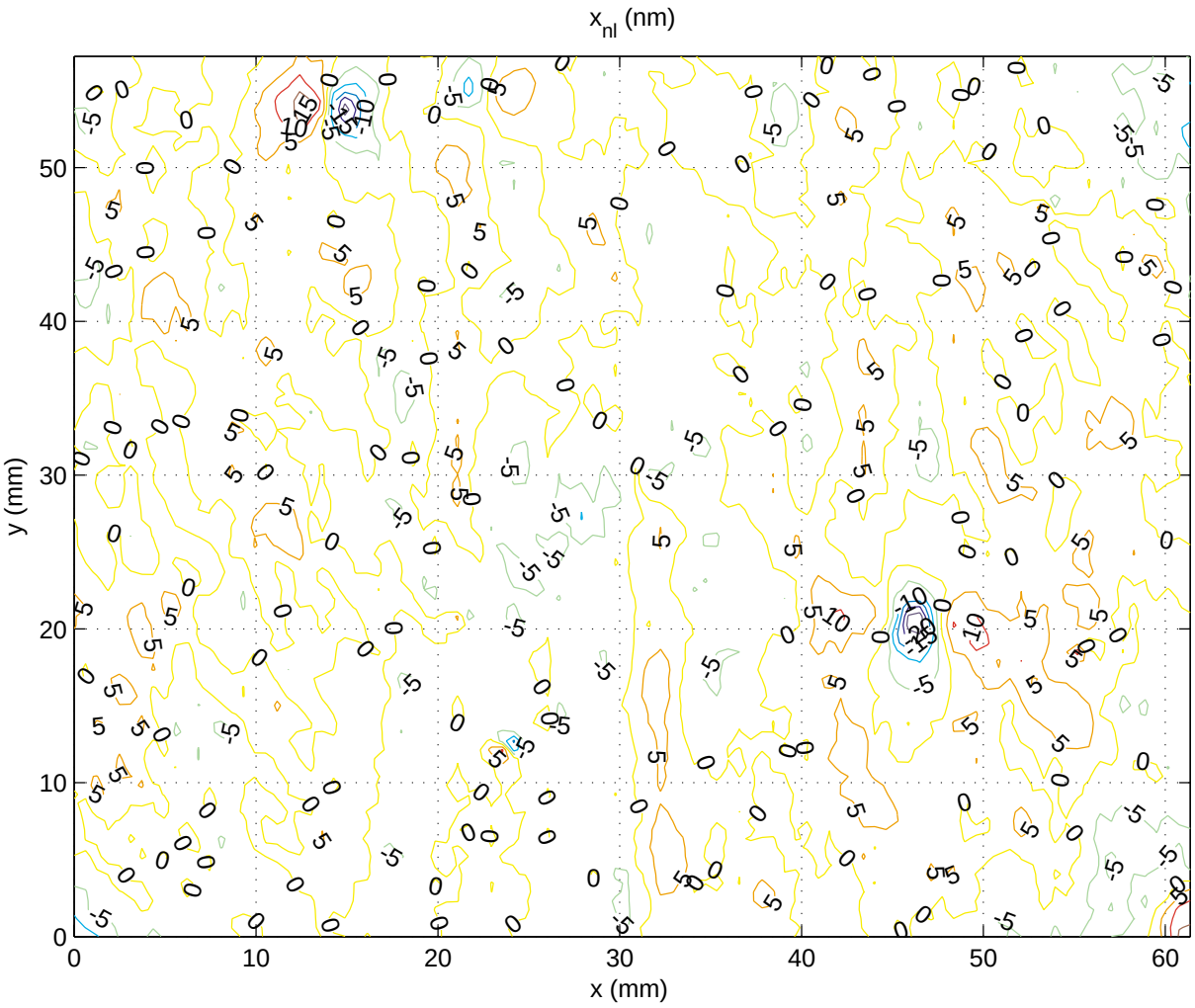

Figure 9-49: Contour plot of the nonlinearity of a grating written by SBIL.

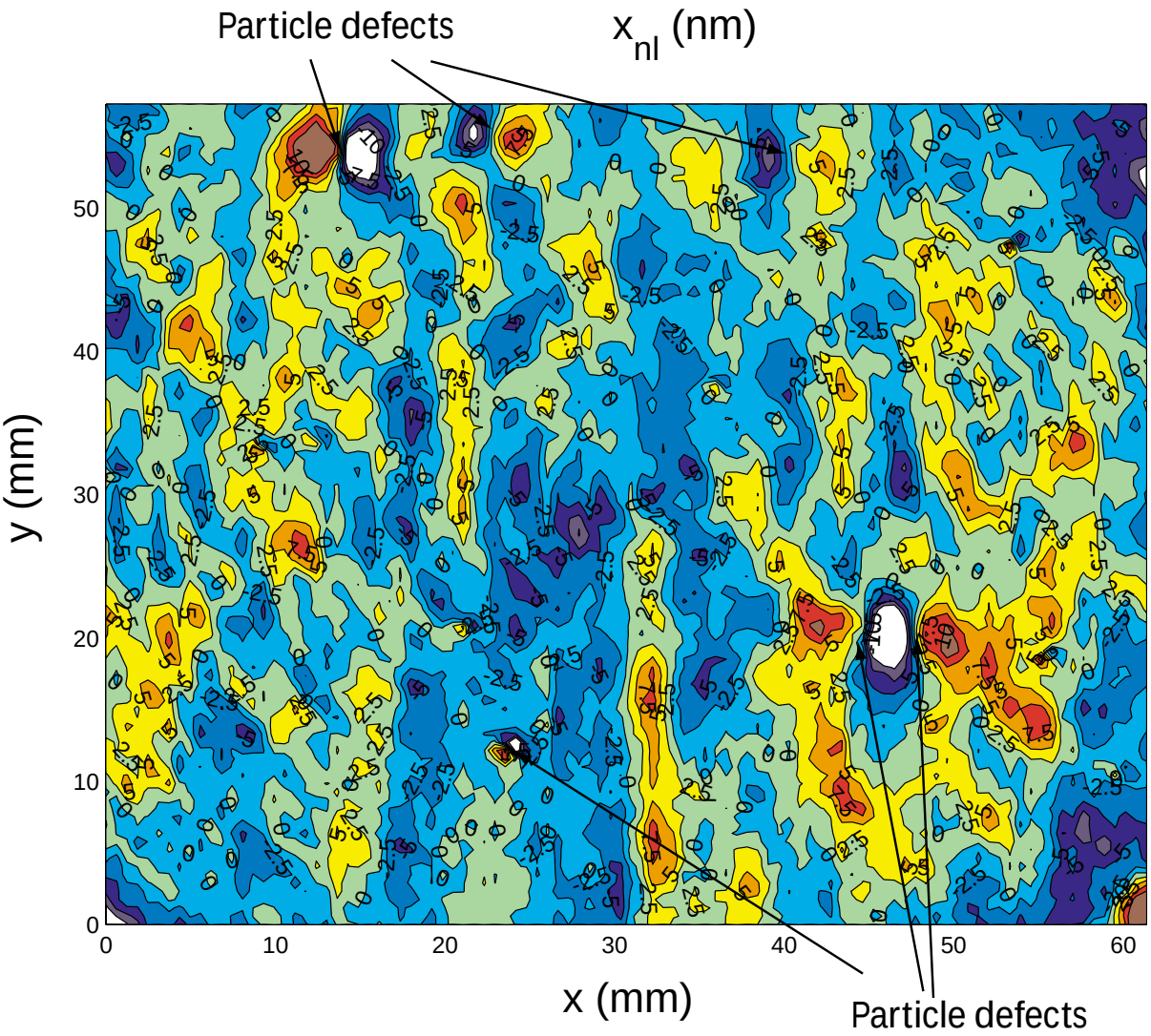

Figure 9-50: Contour plot of the nonlinearity of a grating written by SBIL with tighter contour spacing. Locations of obvious particle defects are indictated.

Aside from the defects, the larger measured nonlinearity for the written wafers compared to the reading repeatability is largely attributed to the nonuniform diffraction efficiency and the wavefront distortion of the image. That is, the written wafers may actually be more linear than measured, at least over the long spatial periods. The image distortion probably contributed a periodic written error too. But these errors should be constant along the scan direction. Another factor explaining the larger errors is that the system may not have been as well thermally equilibrated for the written gratings. The stage was positioned in a corner in between loading and writ-

ing. The temperature gradients in the system would lead to thermal expansion errors of the chuck and possibly more air index nonuniformity. The longer scan lengths of 25 cm used during writing may have also increased the index nonuniformity related errors. Both the temperature gradient problem and the wavefront distortion are areas for future work. Also, the stage during writing was scanned at 5.5 cm/s but based on the scanning performance, this faster writing speed than the reading speed does not fully explain the additional errors in the written wafer. Another issue affecting the repeatability is whether the wafer was returned to exactly the same place on the chuck when it was written. The ±2 mm return position error may have been a factor in the errors observed. If time had allowed, the wafer could have been located against pins during reading and writing to improve the wafer location repeatability to perhaps a few microns. Nevertheless, despite all these problems that have room for dramatic improvement, the ± 10 nm linearity over 6 cm × 6 cm exceeds the repeatability of any patterning that I have found in literature.

After the desired repeatability has been demonstrated by returning the wafer to the same place when written, absolute testing should be applied to achieve absolute accuracy (not including the length scale). Moreover, there is nonlinearity that cannot be measured by the system by returning the grating to its original location on the chuck. By rotating the grating 180° the mirror symmetric errors are observed. Figure 9-51 depicts mirror symmetric and rotationally symmetric errors. Mirror symmetric errors are symmetric about the plane parallel to the grating lines that passes through the rotation point. Figure 9-51 a) shows a mirror symmetric error that when rotated by 180° as in b) will produce a measurable nonlinearity that is twice the actual nonlinearity. Rotationally symmetric errors are depicted in c) and won't be observable when the substrate is rotated by 180° as in Figure d). The substrate needs at least three measurements to fully characterize the repeatable errors. The 0° measurement, 180° measurement, and a translation in either orientation needs to be performed to measure the absolute nonlinearity. Furthermore, the substrate cannot be distorted when its position is changed. Distortions due to wafer chuck flatness [98] and sagging in the vacuum grooves will lead to errors. The chuck was specified to be flat to 1

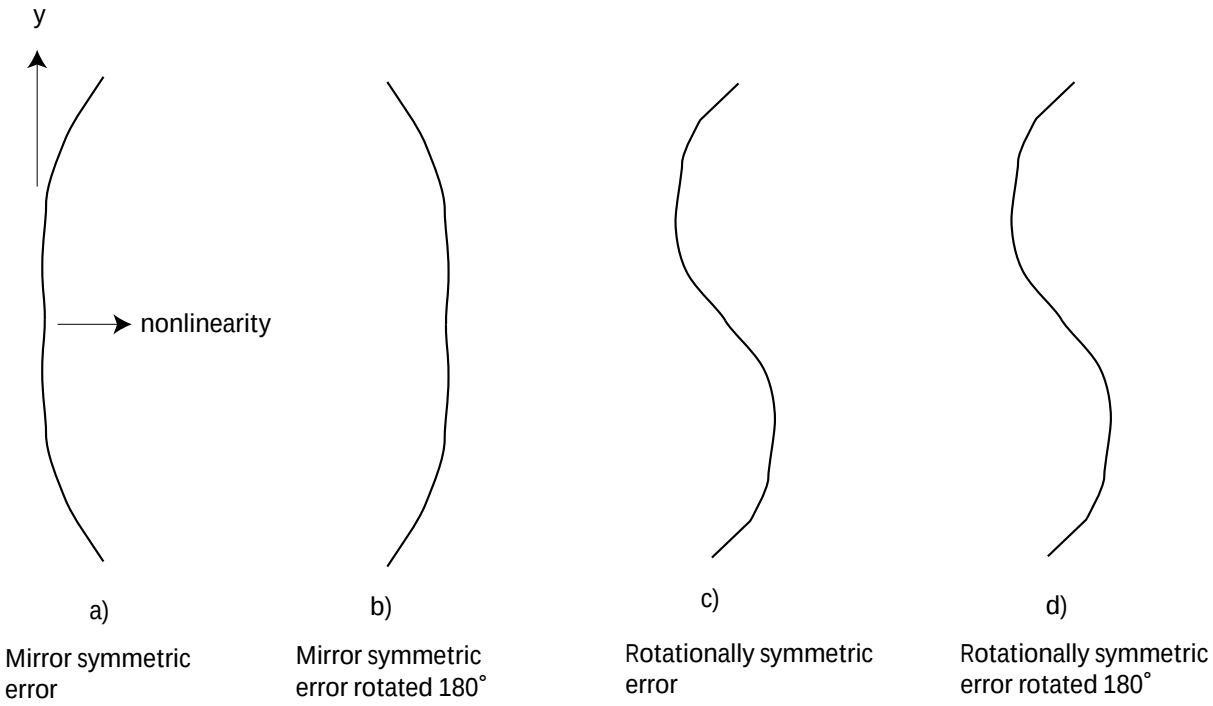

Figure 9-51: Figure a) depicts a mirror symmetric error. When the substrate with the nonlinearity of a) is rotated 180° the nonlinearity appears as shown Figure b). The metrology tool will measure twice the mirror symmetric error. Figure c) depicts a rotationally symmetric error. Rotationally symmetric errors are not observable when the substrate is rotated 180° as in Figure d).

μm over most of its area. Depending on the spatial period of the flatness, several nanometers of distortion are expected from the chuck. Also, in-plane distortion due to vacuum sag is expected to be about a nanometer. These errors are repeatable if the wafer is located to the same place that it was written in – the chuck was designed to meet only repeatability requirements.

The contour plot of the same grating in Figure 9-49 when it is rotated by 180° is shown in Figure 9-52. The purpose of this measurement is mainly to characterize the particle defects. Obvious nonlinearity caused by particle defects that were written into the substrate are labeled as an "anti-particle". The anti-particle is a defect produced when writing a wafer that is strained by vacuuming a wafer onto a chuck that has a particle on it. In the rotated state when the grating is pulled against the vacuum chuck to a flat state, which it was not in during writing, the characteristic anti-particle nonlinearity is evident. The anti-particle nonlinearity has opposite sign

as the particle nonlinearity. The particles in the labeled locations are embedded into the chuck. A contour plot with tighter contour spacing ranging from -10 nm to 10 nm is in Figure 9-53.

The in-plane-distortion due to a particle measured perpendicular to the grating is shown in Figure 9-54 (a). This data from Figure 9-52, where the x and y values correspond, is an enlarged plot of an area around a particle defect. The out-of-plane distortion, w, can be calculated from the in-plane distortion by the well known [110] relationship

$$w(x_2) - w(x_1) = -\frac{2}{h}\int_{x_1}^{x_2} u(x)\,dx. \tag{9.20}$$

Here u is the in-plane distortion, which is measured as x_{nl}. The total thickness of the substrate h was 500 μm. The calculated out-of-plane distortion shown in Figure 9-54 (b) unmistakably looks like that caused by a particle. The calculated maximum height is 300 nm. Here is a good place to consider the effect of the chuck nonflatness. From Equation 9.20, the in-plane distortion as a function of the chuck slope is

$$u = -\frac{h}{2}\frac{\mathrm{d}w}{\mathrm{d}x}. \tag{9.21}$$

If the chuck has 1 μm / 0.2 m of slope, then the chuck will induce an in-plane distortion of 1.3 nm of in-plane distortion for a 500 μm thick wafer. The chuck slope and the in-plane distortion is probably much worse since only the overall flatness of 1 μm was specified.

The finite-size of the Gaussian beam tends to underestimate the in-plane distortion on small spatial scales because the measured error is really the convolution of the Gaussian beam with the grating. For small spatial scales the averaging effect is significant. The out-of-plane particle distortion can be visualized directly as seen in the photograph in Figure 9-54 (c). The photograph is the white light interferogram formed between a vacuumed quartz wafer and the chuck. The radial period of the vacuum grooves is 2.4 mm. The location of rings due to a particle defect preventing contact of the wafer with the chuck is indicated with the arrow. Assuming that the effective wavelength of visible light is 500 nm and three fringes, the maximum out-

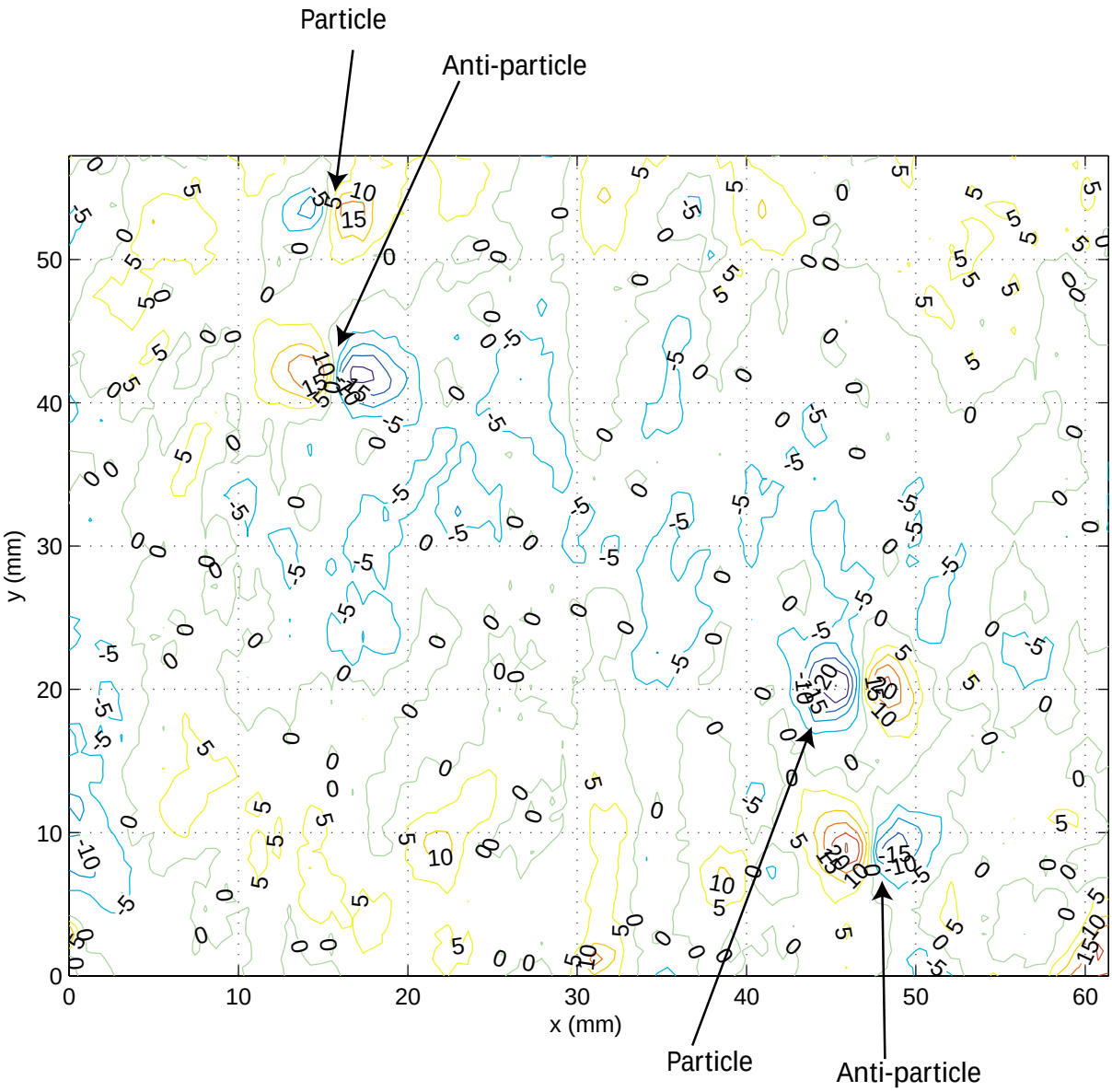

Figure 9-52: Contour plot of the same grating in Figure 9-49 when it is rotated by 180°.

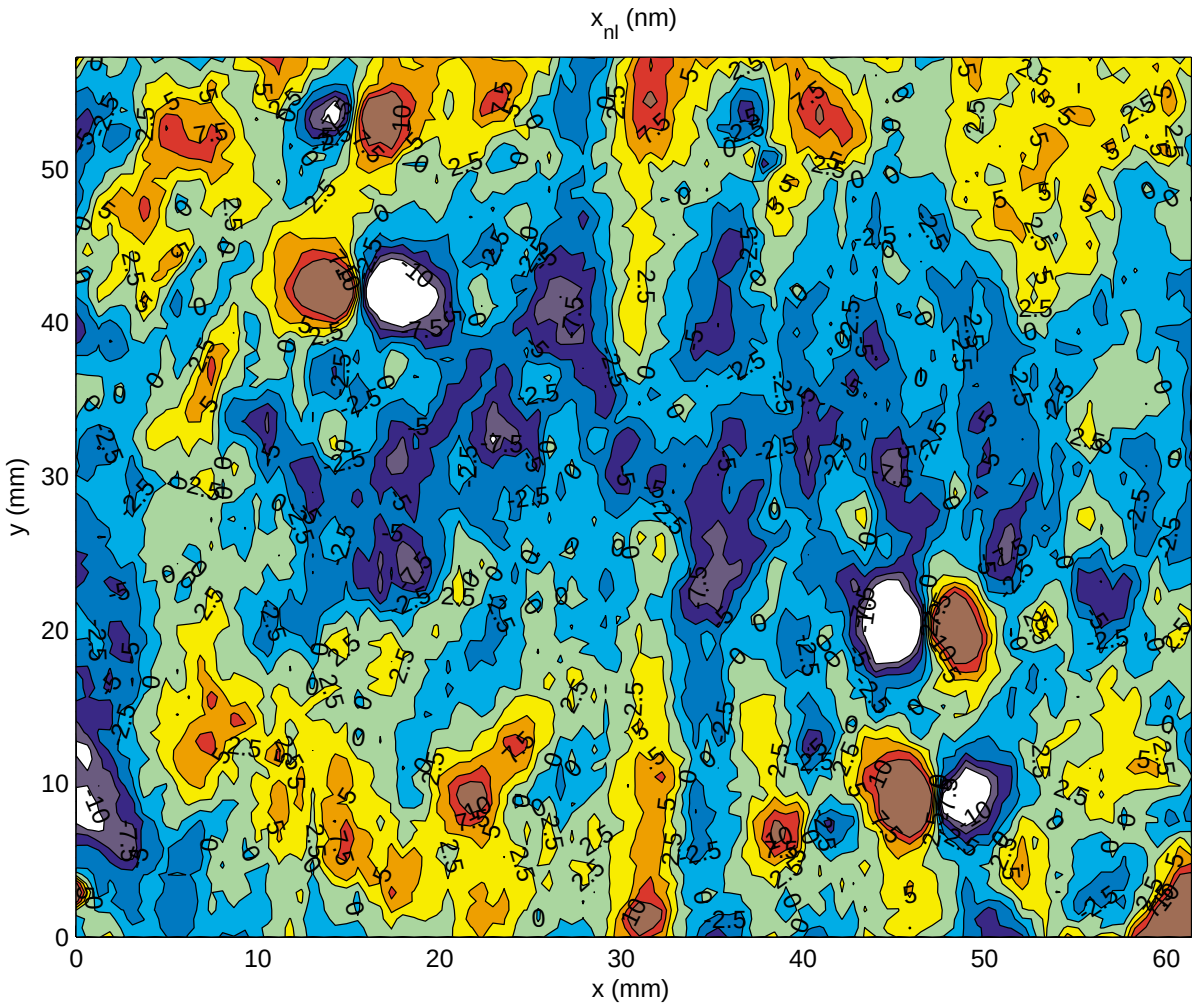

Figure 9-53: Contour plot of the same grating in Figure 9-49 when it is rotated by 180°. The contours range between -10 and 10 nanometers.

of-plane distortion is 750 nm or more than twice that calculated from the in-plane distortion. Issues such as the contact mechanics with the silicon versus quartz (i.e. different Young's modulus and yield strength), local roughness on the substrates (the back side of the silicon wafer was not polished), and particle deformation may have contributed to the discrepancy. However, the averaging provided by the finite sized beam may explain most of the difference.

Most importantly, the quartz wafer can be used to identify particle defects buried in the chuck without the relatively time consuming process of writing and reading a wafer. Unfortunately, some particles such as those in the nonlinearity maps were not

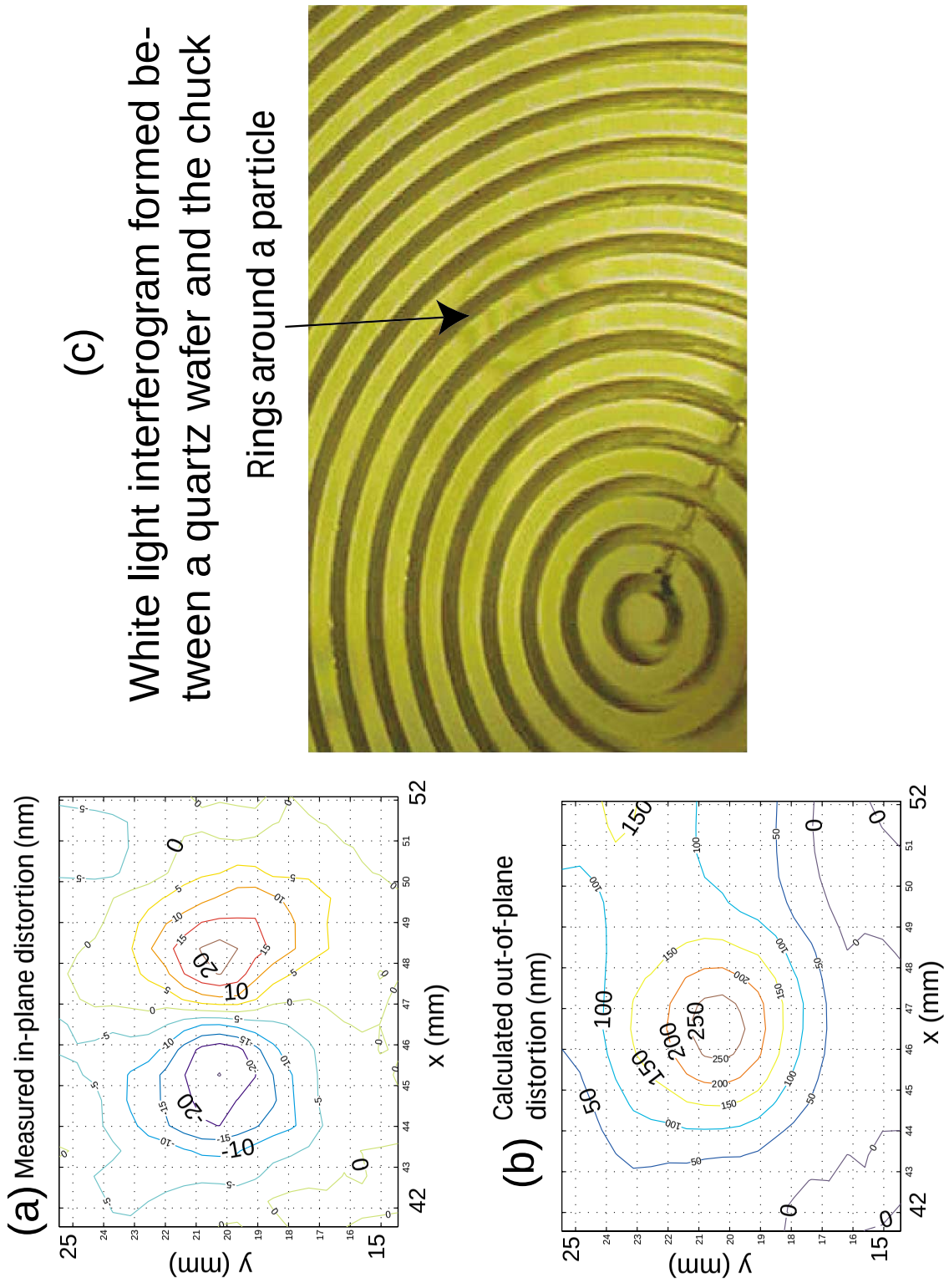

Figure 9-54: The measured in-plane distortion in the region of a particle defect (a) and the calculated out-of-plane distortion (b). The photograph (c) is the white light interferogram formed between a vacuumed quartz wafer and the chuck.

cleanable with acetone.

The particles are by far the largest source of error in the system. However, there are many potential solutions to this problem that I never pursued. Stoning the identified areas or otherwise refurbishing the surface of the chuck needs to be performed. After that, experiments should demonstrate whether it would even be possible for a human operator to reliably load a substrate without introducing particles. These experiments would be performed with quartz wafers. Very special attention to clean room attire will be essential considering that humans emit 10^5 particles per minute [92]. Furthermore, inspection of the backside of the substrates before writing needs to be performed – the substrates themselves can have debris on them, at least in my experience. The inspection could be performed with a quartz chuck.

I supect that robotic loading of the substrates is probably necessary for reliably loading wafers. At least some lithographic scanners are connected to track systems with all robotic material transport. In these systems, the wafers may never see environments worse than Class 0.1. This type of system would be ideal.

Also, a pin chuck with denser pin spacing and smaller contact area will reduce the chance of particle contamination. The pin spacing would need to be denser because the wafer sags more for the boundary condition where the wafer doesn't contact the chuck surface between grooves. The small pins will require special tooling for inspection. Some applications favor thick substrates. The thick substrates that are kinematically mounted will be immune to particles. Thick substrates will also be less sensitive to process induced distortions.

After future improvements in chuck refurbishment, contamination, wavefront quality, wafer placement, and process defects, the writing repeatability is expected to approach the repeatability of reading an un-rechucked wafer.

Chapter 10

Conclusions

The metrology system built into SBIL is ideal for assessing errors. For the first time, the unobservable errors of a patterning tool were measured in real time, on the fly, and at arbitrary locations across the substrate. This metrology capability was used to study the major sources of errors including: thermal expansion, air index, periodic errors, electronic noise, vibration, substrate clamping, and control. Many of these error terms also exist in other lithography and metrology paradigms. The experimental results and models enhance the understanding of ultra-precision patterning.

Based on my results and modeling, I conclude that SBIL is capable of satisfying sub nanometer placement requirements. In my work I have demonstrated long term (1 hour) fringe placement stability of 1.4 nm, 3σ (0 to 1.4 Hz). Also, the short term placement stability is less than 4 nm, 3σ (0 to 5 kHz). When considering the integrated intensity of the scanned image traveling at 100 mm/s, the dose placement stability is 2.1 nm, 3σ. The wafer mapping repeatability was shown to be 2.9 nm, 3σ while measuring a 100 mm substrate. The repeatability is consistent with error models.

Analysis of the error budget summary in Figure 3-1 indicates the suggested improvements. The errors by physics provides the most insight into the limitations of the system. All errors larger than a nanometer need to be improved to achieve sub nanometer repeatability. The air index uniformity is the largest source of error. I

expect that large improvements are possible on the air index uniformity. Specifically, the large temperature gradient across the x axis beam path should be diagnosed and corrected. Also, better temperature control is possible. In lieu of these improvements, the air paths of the x axis interferometer can be enclosed in vacuum. Some type of sliding vacuum containment or bellows would be required. The phase sensing optics will also require a more compact design and possibly containment in vacuum. Implementing a more stable laser and eliminating the refractometer will also be necessary. The next largest source of error is the thermal expansion error. Most of this error is associated with moving the Super Invar chuck through the large temperature gradient. A straight forward solution here is to use a lower coefficient of thermal expansion material. However, improvements in the temperature gradient might lead to more immediate improvements. Additionally, it may be possible to measure the temperature of the chuck and somewhat correct for its expansion. The next largest error term is the substrate clamping distortion. The budgeted error does not include particle induced distortions. For near term repeatability demonstrations, locating the substrate against pins will remove the non repeatable substrate clamping errors. In the far term, a system for performing absolute calibration techniques needs to be designed and implemented. The substrates will require rotation and translation without distortion. Since applications for grating-based metrology exist for both thick and thin substrates, the substrate clamping issue must be addressed for both types of substrates in the far term. Furthermore, solutions for the particle problem, as discussed in Section 9.8, need to be pursued. Finally, the periodic error will need to be addressed. Implementation of the writing and metrology strategy discussed in Section 9.4.1, will essentially eliminate these errors.

The index of air uniformity and the thermal stability of assemblies currently limit the repeatability. Meanwhile, the improvement of the periodic error and substrate clamping repeatability is expected to be straightforward and can be accomplished relatively quickly. Therefore, the improved system of thermal control, enclosed beam paths, and lower coefficient of thermal expansion components is critical for demonstrating sub nanometer placement repeatability. For the case of demonstrating defect

Improvements	Error budget, static [±nm]	Error budget, worst case [±nm]
Error without improvements	2.39	5.88
Error without thermal expansion and index terms	1.12	1.87
Error without periodic term	2.16	5.79
Error without thermal expansion, index, and periodic terms	0.46	1.57
Error without thermal expansion, index, periodic, and substrate clamping terms	0.46	0.68

Figure 10-1: Error budget considering potential improvements

free gratings, considerable investment into the particle problem may be required.

The repeatability of mapping an un-rechucked wafer is expected to be better than the phase maps of a written wafer. After future improvements in chuck refurbishment, particle contamination, wavefront quality, wafer placement, and process defects, the writing repeatability is expected to approach the repeatability of reading an un-rechucked wafer. My results on mapping rechucked wafers should be considered only preliminary considering that there are so many areas for improvement.

Demonstrating a repeatable length scale is another area for future work. The pressure compression error (see Section 5.1) and substrate thermal expansion need to be addressed. A pressure correction and low CTE substrate will be required for sub nanometer length scale repeatability.

This thesis is a major step toward nanometer accurate gratings. The application of the nanometer accurate gratings to mastering, replication and process induced distortions can solve the placement metrology requirements of the semiconductor industry.

Appendix A

Error Budget

The error budget by subsystem is contained within Figure A-1 and Figure A-2. Each error category is further broken down into sub-categories. I assume the exposure integration is described by the d/v parameter of 20 ms. The error budget columns contain errors associated with the design parameters described to their right. All errors are three sigma. The errors for some rows are blank or are designated OP (operating parameters). In these cases, the error depends on more than one design parameter and the error is included only in the row with the last associated design parameter. For rows where the error is blank, the requirement/specification is calculated from the operating parameters above. There are two columns for the errors. The first one will predict the fringe stability for a small deadpath ($<$ 7 cm) and a well thermally equilibrated system. Also, it does not include errors associated with clamping the substrate. The second error budget column is the worst case scenario accounting for errors when patterning a 300 mm wafer. The worst case scenario includes extra thermal expansion errors associated with moving the chuck through a temperature gradient and extra index errors due to the longer dead path and stage movement. The worst case errors also include terms associated with clamping the wafer. But I do not include particle induced distortions. Errors that are smaller than an angstrom may have been dropped from the error budget. The error budget summary by subsystem and by physics is shown in Figure 3-1.

The error budget does not include two errors that would mainly affect the repeata-

Table A

Error Category	Sub-Category	Error budget [±m]	Error budget, worst case [±m]	Design parameters	Units	Requirement/ specification
Displacement interferometer	Thermal expansion	OP		Interferometer thermal drift coefficient	nm/C	30
		1.50E-10	1.50E-10	Interferometer thermal stability	C	5.00E-03
	Electronics error	OP		Nominal electronics resolution, phase meter	m	3.09E-10
		OP		Electronics accuracy, phase meter	counts	1.2
				Maximum electronics error, phase meter	m	3.71E-10
		3.211E-11	3.21E-11	Printed electronics error, phase meter	m	3.21E-11
		1.27E-10	1.27E-10	60 Hz noise error	m	1.27E-10
	Periodic error	6.00E-10	6.00E-10	Periodic error	m	6.00E-10
	Air index	1.41E-09		Air index nonuniformity error, small travel	m	1.41E-09
			4.80E-09	Air index nonuniformity error, large travel	m	4.80E-09
	Refractometer	OP		DPMI therrmal coefficient	nm/C	10
		5.00E-11	5.00E-11	DPMI thermal stability	C	5.00E-03
		OP		Refractometer cavity therrmal coefficient	nm/C	40
		8.00E-11	8.00E-11	Refractometer cavity thermal stability	C	2.00E-03
		6.00E-10	6.00E-10	Periodic error	m	6.00E-10
		3.21E-11	3.21E-11	Printed electronics error, phase meter	m	3.21E-11
	rss displacement interferometer error [m]	1.66E-09	4.88E-09			

Table B

Error Category	Sub-Category	Error budget [±m]	Error budget, worst case [±m]	Design parameters	Units	Requirement/ specification
Fringe locking interferometer	Control	4.00E-10	4.00E-10	Control residual error	m	4.00E-10
	Electronics error	OP		Nominal electronics resolution, phase meter	m	7.81E-10
		OP		Electronics accuracy, differential fringe locking measurement, phase meter	counts	1.70
				Maximum electronics error, phase meter	m	1.33E-09
		1.148E-10	1.15E-10	Printed electronics error, phase meter	m	1.15E-10
		1.27E-10	1.27E-10	60 Hz noise error	m	1.27E-10
	Periodic error	5.66E-10	5.66E-10	Periodic error, two axes	m	5.66E-10
	Air index	1.41E-09	1.41E-09	Air index nonuniformity error	m	1.41E-09
	rss fringe locking interferometer error [m]	1.58E-09	1.58E-09			

Table C

Error Category	Sub-Category	Error budget [±m]	Error budget, worst case [±m]	Design parameters	Units	Requirement/ specification
Metrology block frame	Thermal expansion	OP		Metrology block therrmal coefficient	nm/C	40
		8.00E-11	8.00E-11	Metrology block thermal stability	C	2.00E-03
		OP		Beam splitter mount therrmal coefficient	nm/C	100
		5.00E-10	5.00E-10	Beam splitter mount thermal stability	C	5.00E-03
	Column reference mirror-to-fringe vibration	OP		Assembly vibration sensitivity	nm/g	1000
		6.00E-11	6.00E-11	Metrology block acceleration	g	6.00E-05
	rss metrology block frame error [m]	5.10E-10	5.10E-10			

Figure A-1: Error budgets for the displacement interferometer (Table A), fringe locking interferometer (Table B), and the metrology block frame (Table C)

Table D

Error Category	Sub-Category	Error budget [±m]	Error budget, worst case [±m]	Design parameters	Units	Requirement/ specification
Substrate frame	Vacuum clamping distortion		1.00E-09	Chuck flatness distortion	m	1.00E-09
			1.00E-09	Vacuum sag in groove distortion	m	1.00E-09
	Substrate thickness variation / fringe tilt	OP		Fringe tilt	µrad	50
			5.00E-10	Substrate thickness variation	µm	10
	Thermal expansion	OP		Therrmal coefficient chuck	nm/C	200
		4.00E-10		Chuc thermal stability, static	C	2.00E-03
			2.40E-09	Chuck, thermal stability, moving	C	1.20E-02
	Substrate-to- interferometer mirror vibration	OP		Chuck vibration sensitivity	nm/g	50
		1.50E-11	1.50E-11	Chuck acceleration	g	3.00E-04
	rss substrate frame error	4.00E-10	2.83E-09			

Table E

Error Category	Sub-Category	Error budget [±m]	Error budget, worst case [±m]	Design parameters	Units	Requirement/ specification
Rigid body error motions	Metrology bock-to-interferometer head pitch	OP		Abbe pitch offset, hi	m	1.91E-02
		OP		Pitch thermal coeficient	rad/C	1.05E-06
		1.00E-10	1.00E-10	Pitch thermal stability	C	5.00E-03
		5.00E-11	5.00E-11	Pitch stability, vibration (guess)	rad	2.62E-09
	Stage-to-interferometer head pitch	OP		Abbe pitch offset, z	m	4.00E-04
		2.00E-11	2.00E-11	Pitch stability, thermal (guess)	rad	5.00E-08
	Metrology block-to-stage yaw	OP		Abbe pitch offset, y	m	1.00E-03
		5.00E-11	5.00E-11	Yaw stability, thermal (guess)	rad	5.00E-08
	rss rigid body error motions [m]	1.24E-10	1.24E-10			

Figure A-2: Error budgets for the substrate frame (Table D) and rigid body error motions (Table E)

bility of length scale. For future work that aims to demonstrate the length scale, the pressure compression error (see Section 5.1) and substrate thermal expansion need to be addressed. Moreover, a pressure correction and low CTE substrate will be required for sub nanometer length scale repeatability. Additionally, errors associated with the period control and image distortion are not included in this error budget.

Bibliography

[1] Analog Devices Inc., Norwood, MA http://www.analog.com. *AD 9852, CMOS 300 Mhz Complete-DDS*.

[2] Analog Devices Inc., Norwood, MA http://www.analog.com. *A Technical Tutorial on Digital Signal Synthesis*.

[3] E. K. Anderson, V. Boegli, M.L. Schattenburg, D. Kern, and H.I. Smith. Metrology of electron-beam lithography systems using holographically produced reference samples. *J. Vac. Sci. Technol. B*, 9(6):3606–3611, November-December 1991.

[4] Howard Anton. *Elementary Linear Algebra*. John Wiley and Sons, 1991.

[5] ASTM, West Conshohocken, PA. *ASTM F 1684-99 Standard specification for iron-nickel and iron-nickel-cobalt alloys for low thermal expansion applications*, 1999.

[6] V. G. Badami and S. R. Patterson. A frequency domain method for the measurement of nonlinearity in heterodyne interferometry. *Precision Engineering*, 24:41–49, January 2000.

[7] L. Berger. Grating interferometry for positioning the x-y stages of a wafer stepper. *SPIE Application, Theory, and Fabrication of Periodic Structures*, 503:130–134, 1984.

[8] K. P. Birch and M. J. Downs. An updated edlen equation for the refractive index of air. *Metrologia*, 30:155–162, 1993.

[9] K. P. Birch and M. J. Downs. Correction to the updated edlen equation for the refractive index of air. *Metrologia*, 31:315–316, 1994.

[10] Norman Bobroff. Residual errors in laser interferometry from air turbulence and nonlinearity. *Applied Optics*, 26(13):2676–2682, July 1987.

[11] Norman Bobroff. Recent advances in displacement measuring interferometry. *Meas. Sci. Technol*, 4:907–926, 1993.

[12] R.D. Boyd, J. A. Britten, B. W. Shore, and et al. High-efficiency metallic diffraction gratings for laser applications. *Applied Optics*, 34(10):1697–1706, April 1995.

[13] C. G. Chen, P. T. Konkola, R. K. Heilmann, C. Joo, and M.L. Schattenburg. Nanometer-accurate grating fabrication with scanning beam interference lithography. *Proceedings of SPIE*, 4936(126), November 2002.

[14] C. G. Chen, P. T. Konkola, R. K. Heilmann, G.S. Pati, and M.L. Schattenburg. Image metrology and systems controls for scanning beam interference lithography. *J. Vac. Sci. Technol. B*, 19(6):2335–2341, November-December 2001.

[15] Carl G. Chen. *Beam Alignment and Image Metrology for Scanning Beam Interference Lithography – Fabricating Gratings with Nanometer Phase Accuracy.* PhD dissertation, Massachusetts Institute of Technology, Department of Electrical Engineering and Computer Science, 2003.

[16] Carl Gang Chen. Microcomb fabrication for high accuracy foil x-ray telescope and vector gaussian beam modeling. Master's thesis, Massachusetts Institute of Technology, 2000.

[17] S. Cosijns, H. Haitjema, and P. Schellekens. Modeling and verifying nonlinearities in heterodyne displacement interferometry. *Precision Engineering*, 26:448–455, 2002.

[18] Frank C. Demarest. High-resolution, high-speed, low data age uncertainty, heterodyne displacement measuring electronics. *Meas. Sci. Technol.*, 9:1024–1030, 1998.

[19] T.J. Edwards. Observations on the stability of thermistors. *Rev. Sci. Instum.*, 54(5):613–617, May 1983.

[20] W. Tyler Estler. High-accuracy displacement interferometry in air. *Applied Optics*, 24(6):808–815, March 1985.

[21] Etec Systems Inc., Hayward, CA. *MEBES 5500 Doc. 0999-0313A*.

[22] Chris Evans. *Precision Engineering an Evolutionary View*. Cranfield Press, 1989.

[23] Chris J. Evans, Robert J. Hocken, and W. Tyler Estler. Self-calibration: reversal, redundancy, error separation, and "absolute testing". *CIRP Annals*, 45(2):617–634, 1996.

[24] Jennifer Eyre. The digital signal processor derby. *IEEE Spectrum*, pages 62–68, 2001.

[25] J. Ferrera, M.L. Schattenburg, and H.I. Smith. Analysis of distortion in interferometric lithography. *J. Vac. Sci. Technol. B*, 14(6):4009–4013, November-December 1996.

[26] J. Ferrera, V. Wong, S. Rishton, V. Boegli, E. Anderson, D. Kern, and H.I. Smith. Spatial-phase-locked electron-beam lithography: Intial test results. *J. Vac. Sci. Technol. B*, 11(6):2342–2345, November-December 1993.

[27] Juan Ferrera. *Nano-meter scale placement in Electron-Beam Lithography*. PhD dissertation, Massachusetts Institute of Technology, Department of Electrical Engineering and Computer Science, June 2000.

[28] Gene F. Franklin, J. David Powell, and Abbas Emani-Naeini. *Feedback Control of Dynamic Systems*. Addison-Wesley, 1991.

[29] Gene F. Franklin, J. David Powell, and Michael L. Workman. *Digital Control of Dynamic Systems*. Addison-Wesley, 1994.

[30] J. M. Freitas and M. A. Player. Polarization effects in heterodyne interferometry. *Journal of Modern Optics*, 42(9):1875–1899, 1995.

[31] H. Fujimoto, M. Tanaka, and K. Nakayama. Noise reduction in an optical interferometer for picometer measurements. *IEEE Transactions on Instrumentation and Measurement*, 44(2):471–474, April 1995.

[32] R. G. Gibson. *Principles of composite material mechanics*. McGraw Hill Company, 1994.

[33] Joseph W. Goodman. *Introduction to Fourier Optics*. McGraw-Hill, 1996.

[34] S. Grafström, U. Harbath, J. Kowalski, R. Neumann, and S. Noehte. Fast laser beam position control with submicroradian precision. *Optics Communications*, 65(2):121–126, January 1988.

[35] George R. Harrison. The production of diffraction gratings i. development of the ruling art. *Journal of the Optical Society of America*, 39(6):413–426, June 1949.

[36] George R. Harrison. The diffraction grating – an opinionated appraisal. *Applied Optics*, 12(9):2039–2049, September 1973.

[37] M. E. Harvey. Precision temperature-controlled water bath. *The Review of Scientific Instruments*, 39(1):13–18, January 1968.

[38] H A Haus. *Waves and Fields in Optical Electronics*. Prentice-Hall, 1984.

[39] Eugene Hecht. *Optics*. Addison Wesley Longman, 1998.

[40] Heidenhain, http://www.heidenhain.com. *Digital Linear and Angular Metrology*.

[41] Heidenhain, http://www.heidenhain.de, D-83301 Traunreut, Deutschland. *General Catalog*, 1999.

[42] Ralf K. Heilmann, Paul T.Konkola, Carl G. Chen, G. S. Pati, and Mark L. Schattenburg. Digital heterodyne interference fringe control system. *J. Vac. Sci. Technol. B*, 19(6):2342–2346, November-December 2001.

[43] P. D. Henshaw and D. P. DeGloria. Atmospheric metrology using the air turbulence compensated interferometer. *J. Vac. Sci. Technol. B*, 14(6):3955–3959, November-December 1996.

[44] R.R. Hershey and E.N. Leith. Grating interferometers for producing large holographic gratings. *Applied Optics*, 29(7):937–943, March 1990.

[45] K. Hibinio and Z.S. Hegedus. Aberration compensation in a grating interferometer. *Applied Optics*, 33(19):4156–4163, July 1994.

[46] K. Hibinio and Z.S. Hegedus. Hyperbolic holographic gratings: analysis and interferometric tests. *Applied Optics*, 33(13):2553–2559, May 1994.

[47] W. Hou and G. Wilkening. Investigation and compensation of the nonlinearity of heterodyne interferometers. *Precision Engineering*, 14(2):91–98, April 1992.

[48] W. Hou and X. Zhao. Drift of nonlinearity in the heterodyne interferometer. *Precision Engineering*, 16(1):25–35, January 1994.

[49] John T. Houghton. *The Physics of Atmospheres*. Cambridge University Press, 1989.

[50] R. S. Huang, C. Tarn, P.P. Banerjee, and D. Cao. Laser beam profile deformation effect during bragg acousto-optic interaction: a non-paraxial approximation. *Opt. Eng.*, 38(7):1122–1126, July 1999.

[51] M. C. Hutley. *Diffraction gratings*. Academic Press, 1982.

[52] International Technology Roadmap for Semiconductors, http://public.itrs.net. *International Technology Roadmap for Semiconductors*, 2001.

[53] International Technology Roadmap for Semiconductors, http://public.itrs.net. *International Technology Roadmap for Semiconductors Update*, 2002.

[54] Akira Ishida. Two-wavelength displacement-measuring interferometer using second-harmonic light to eliminate air-turbulence-induced errors. *Japanese Journal of Applied Physics Part 2*, 28(3), March 1989.

[55] Won jong Kim. *Planar Magnetic Levitation*. PhD dissertation, Massachusetts Institute of Technology, Department of Electrical Engineering and Computer Science, June 1997.

[56] W. J. Kim and D. L. Trumper. Force ripple in surface-wound permanent-magnet linear motors. *IEEE Intermag*, April 1996.

[57] L. E. Kinsler, A. R. Frey, A. B. Coppens, and J. V. Sanders. *Fundamentals of Acoustics*. John Wiley and Sons, 2000.

[58] P. Konkola, C. G. Chen, R. Heilmann, G.S. Pati, and M. L. Schattenburg. Scanning beam interference lithography. *Proceedings of the 16th Annual Meeting of the American Society of Precision Engineering, Crystal City, Virginia*, November 2001.

[59] P. Konkola, C. G. Chen, R. Heilmann, and M. L. Schattenburg. Beam steering system and spatial filtering applied to interference lithography. *J. Vac. Sci. Technol. B*, 18(6):3282–3286, November-December 2000.

[60] Paul Thomas Konkola. Magnetic bearing stages for electron beam lithography. Master's thesis, Massachusetts Institute of Technology, February 1998.

[61] J. P. Laude, J. Flammand, A. Thevenon, and D. Lepere. Classical and holographic gratings design and manufacture. *ESO Conference on Very Large Telescopes and Their Instrumentation*, 2:967–989, 1988.

[62] John Lawall and Ernest Kessler. Michelson interferometry with 10 pm accuracy. *Review of Scientific Instruments*, 71(7):2669–2676, November-December 2000.

[63] K.M. Lawton and S.R. Patterson. A high-stability air temperature control system. *Precision Engineering*, 24:174–182, 2000.

[64] K.M. Lawton and S.R. Patterson. Long-term relative stability of thermistors. *Precision Engineering*, 25:24–28, 2001.

[65] K.M. Lawton and S.R. Patterson. Long-term relative stability of thermistors: Part 2. *Precision Engineering*, 26:340–345, 2002.

[66] Leica Microsystems Wetzlar GmbH, 35578 Wetzlar, Germany. *Leica LMS IPRO fully automated mask and wafer metrology system*, 1999.

[67] John Lekavich. Basics of acousto-optic devices. *Lasers and Applications*, 31:59–64, April 1986.

[68] J. M. Lerner, J. Flamand, J. P. Laude, G. Passereau, and A. Thevenon. Diffraction gratings ruled and holographic – a review. *SPIE Periodic Structures, Gratings, Moire Patterns and Diffraction Phenomena*, 240:82–88, 1980.

[69] M.H. Lim, T.E. Murphy, J. Ferrera, J.N. Damask, and Henry I. Smith. Fabrication techniques for grating-based optical devices. *J. Vac. Sci. Technol. B*, 17(6):3208–3211, November-December 1999.

[70] E. G. Loewen, R. S. Wiley, and G. Portas. Large diffraction grating ruling engine with nanometer digital control system. *SPIE Application and theory of periodic structures, diffraction gratings and moire phenomena III*, 815:88–95, 1987.

[71] Jennifer E. Logan, Peter G. Halverson, Martin W. Regehr, and Robert E. Spero. Automatic alignment of a displacement-measuring heterodyne interferometer. *Applied Optics*, July 2002.

[72] Stephen Joseph Ludwick. Control of a six degree of freedom magnetic/fluidic motion control stage. Master's thesis, Massachusetts Institute of Technology, 1996.

[73] Stephen Joseph Ludwick. *A rotary fast tool servo for diamond Turning of Asymmetric Optics*. PhD dissertation, Massachusetts Institute of Technology, Department of Mechanical Engineering, June 1999.

[74] Wayne R. Moore. *Foundations of Mechanical Accuracy*. Moore Tool Company, 1970.

[75] B. Munson, D. Young, and T. Okiishi. *Fundamentals of Fluid Mechanics*. John Wiley and Sons, 1994.

[76] Nikon Precision Inc, 1399 Shoreway Road, Belmont, CA. *Nikon Model XY-6i Laser Interferometric Measuring System, Code No. 4CE-SWSH-2 (9703-02) K*, 1997.

[77] S. Ohki, T. Watanabe, Y. Takeda, T. Morosawa, K. Saito, T. Kunioka, J. Kato, A. Shimizu, and T. Matsuda. Patterning performance of eb-x3 x-ray mask writer. *J. Vac. Sci. Technol. B*, 18(6):3084–3088, November-December 2000.

[78] Alan V. Oppenheim, Ronald W. Schafer, and John R. Buck. *Discrete-Time Signal Processing*. Prentice Hall, 1999.

[79] David Oxtoby and Norman Nachtrieb. *Modern Chemistry*. Saunders College Publishing, 1990.

[80] C. Palmer. *Diffraction grating handbook, fourth edition*. Richardson Grating Laboratory, 2000.

[81] E. K. Popov, L. V. Tsonev, and M. L. Sabeva. Technological problems in holographic recording of plane gratings. *Optical Engineering*, 31(10):2168–2173, October 1992.

[82] L. R. Rabiner, C. A. McGonegal, and D. Paul. *Programs for Digital Signal Processing, Chapter 5.2: FIR Windowed Filter Design Program-WINDOW*. IEEE Press, 1979.

[83] M. R. Raugh. Two-dimensional stage self-calibration: Role of symetry and invariant sets of points. *J. Vac. Sci. Technol. B*, 15(6):2139–2145, November-December 1997.

[84] A. E. Rosenbluth and N. Bobroff. Optical sources of nonlinearity in heterodyne interferometers. *Precision Engineering*, 12:7–11, 1990.

[85] M.L. Schattenburg, R.J. Aucoin, and R.C. Fleming. Optically matched trilevel resist process for nanostructure fabrication. *J. Vac. Sci. Technol. B*, 13(6):3007–3011, November-December 1995.

[86] M.L. Schattenburg, C. Chen, P.N. Everett, J. Ferrera, P. Konkola, and H.I. Smith. Sub-100 nm metrology using interferometrically produced fiducials. *J. Vac. Sci. Technol. B*, 17(6):2638–2642, November-December 1999.

[87] Gunter Schmahl. Holographically made diffraction gratings for the visible, uv, and soft x-ray region. *Journal of the Spectroscopical Society of Japan*, 23(1):3–11, 1974.

[88] R. Schodel and B. Bonsch. Interferometric measurements of thermal expansion, length stability and compressibility of glass ceramics. *Proceedings Third Euspen International Conference*, pages 691–694, May 2002.

[89] V.A. Skormin, T.E. Busch, and M.A. Givens. Model reference control of a fast steering mirror of a pointing, acquisition and tracking system for laser communications. *Proceedings of the IEEE 1995 National Aerospace and Electronics Conference*, 2:907–913, 1995.

[90] Alexander H. Slocum. *Precision Engineering*. Society of Manufacturing Engineers, 1992.

[91] B. Sluijk and et al. Performance results of a new generation of 300 mm lithography systems. *Proceedings of SPIE, The 26th Annual Symposium on Microlithography, Feb 25-Mar 2*, 2001.

[92] H. I. Smith. *Submicron- and nanometer-structures technology*. NanoStructures Press, Sudbury, MA, 1996.

[93] H.I. Smith. Japan could dominate industry with x-ray lithography. *Semiconductor International*, February 2001.

[94] H.I. Smith, S. D. Hector, M.L. Schattenburg, and E.H. Anderson. A new approach to high fidelity e-beam and ion-beam lithography based on an in situ global-fiducial grid. *J. Vac. Sci. Technol. B*, 9(6):2992–2995, November-December 1991.

[95] S. Sohail, H. Naqvi, H. Zaidi, S.R. J. Brueck, and J. R. McNeil. Diffractive techniques for lithographic process monitoring and control. *J. Vac. Sci. Technol. B*, 12(6):3600–3606, November-December 1994.

[96] G. E. Sommargren. A new laser measurement system for precision metrology. *Precision Engineering*, 9:179–184, 1987.

[97] J.P. Spallas, A. M. Hawryluk, and D. R. Kania. Field emitter array mask patterning using laser interference lithography. *J. Vac. Sci. Technol. B*, 13(5):1973–1995, September-October 1995.

[98] H. Stauch, K. Simon, H. U. Scheunemann, and H. L. Huber. Impact of chuck flatness on wafer distortion and stepper overlay – comparison of experimental and fem results. *Microelectronic engineering*, 23:197–201, 1994.

[99] C. R. Steinmetz. Sub-micron position measurement and control on precision machine tools with laser interferometry. *Precision Engineering*, 12(1):12–24, January 1990.

[100] J. T. M. Stevenson and J. R. Jordan. Use of gratings and periodic structures as alignment targets on wafer steppers. *Precision Engineering*, 11(2):64–70, April 1989.

[101] StockerYale, http://www.lasiris.com, 3549 Ashby Street, St-Laurent, Quebec Canada. *Lasiris purelight phase mask*, 2001.

[102] J. Stone and S. D. Phillips. Corrections for wavelength variations in precision interferometeric displacement measurements. *Journal of Research of the National Institute of Standards and Technology*, 101(5):671–674, September-October 1996.

[103] M. Suzuki and A. Une. An optical-heterodyne alignment technique for quarter-micron x-ray lithography. *J. Vac. Sci. Technol. B*, 7(6):1971–1976, November-December 1989.

[104] M. T. Takac, M. R. Raugh, J. Ye, and et al. Obtaining a physical two-dimensional cartesian reference. *J. Vac. Sci. Technol. B*, 15(6):2173–2176, November-December 1997.

[105] K. K. Tan, S. N. Huang, and T. H. Lee. Robust adaptive numerical compensation for friction and force ripple in permanent-magnet linear motors. *IEEE Transactions on Magnetics*, 38(1):221–228, January 2002.

[106] Arnold Teimel. Technology and applications of grating interferometers in high-precision measurement. *Precision Engineering*, 14(3):147–154, July 1992.

[107] Brian J. Thompson. *Selected Papers on Diffraction Gratings, SPIE Milestone Series Volume MS 83*. SPIE Optical Engineering Press, 1970.

[108] I. D. Torbin and A. M. Nizhin. The use of polymerizing cements for making replicas of optical surfaces. *Soviet Journal of Optical Technology*, 40(3):192–196, March 1973.

[109] David Trost. Using air bearings in vacuum to control stage vibration. *Semiconductor International*, July 2002.

[110] Chi-Teh Wang. *Applied Elasticity*. McGraw Hill Book Company, 1953.

[111] William L. Wolfe and George J. Zissis. *The Infrared Handbook, revised edition.* The Infrared Information Analysis Center, 1989.

[112] C. Wu and R. Deslattes. Analytical modeling of the periodic nonlinearity in heterodyne interferometry. *Applied Optics*, 37(28):6696–6700, October 1998.

[113] C. Wu, J. Lawall, and R. Deslattes. Heterodyne interferometer with subatomic periodic nonlinearity. *Applied Optics*, 38(19):4089– 4094, July 1999.

[114] C. Wu, C. Su, and G. Peng. Correction of nonlinearity in one-frequency optical interferometry. *Meas. Sci. Technol.*, 7:520–524, 1996.

[115] Amnon Yariv. *Optical Electronics.* Saunders College Publishing, 1991.

[116] Jun Ye, C. N. Berglund, and R. F. W. Pease. Spatial frequency filtering using multiple-pass printing. *J. Vac. Sci. Technol. B*, 12(6):3455 – 3459, November-December 1994.

[117] F. Zhao, R. Diaz, P. Dumont, and et al. Development of sub-nanometer race-track laser for external triangulation measurement for the space interferometry mission. *Proceedings ASPE annual meeting, Arlington Virginia*, pages 349–352, November 2001.

[118] Zygo Corporation, PO Box 448, Laurel Brook Road, Middlefied, CT. *Zygo 2/20 Integrated Interferometer System Reference Manual OMP-0229B*, 1993.

[119] Zygo Corporation, PO Box 448, Laurel Brook Road, Middlefied, CT. *ZMI 2002 Measurement Board P/N 8020-0211-01 Operation Manual OMP-0413F*, 1999.